

Integrated analysis of hydrochemical, geophysical, hydraulic and structural geology data to improve characterisation and conceptualisation of faults for use in regional groundwater flow models

Editors: Mallants D, Underschultz J, Simmons C

This report was commissioned by the Department of the Environment and Energy and was prepared by CSIRO.

2018

© Commonwealth Scientific and Industrial Research Organisation 2018. To the extent permitted by law, all rights are reserved and no part of this publication covered by copyright may be reproduced or copied in any form or by any means except with the written permission of CSIRO.

Citation

Mallants D, Underschultz J, Simmons C (eds) (2018). Integrated analysis of hydrochemical, geophysical, hydraulic and structural geology data to improve characterisation and conceptualisation of faults for use in regional groundwater flow models, prepared by the Commonwealth Scientific and Industrial Research Organisation (CSIRO) in collaboration with University of Queensland (UQ) and Flinders University of South Australia (FUSA).

Important disclaimer

CSIRO advises that the information contained in this publication comprises general statements based on scientific research. The reader is advised and needs to be aware that such information may be incomplete or unable to be used in any specific situation. No reliance or actions must therefore be made on that information without seeking prior expert professional, scientific and technical advice. To the extent permitted by law, CSIRO (including its employees and consultants) excludes all liability to any person for any consequences, including but not limited to all losses, damages, costs, expenses and any other compensation, arising directly or indirectly from using this publication (in part or in whole) and any information or material contained in it.

CSIRO is committed to providing web accessible content wherever possible. If you are having difficulties with accessing this document please contact csiroenquiries@csiro.au.

Contents

Contents	iii
Figures ix	
Tables xxiii	
Acknowledgements	xxv
Abbreviations	xxvi
Glossary	xxvii
Symbols	xxxii
Executive summary	xxxiv
Background	xxxiv
Key Results	xxxv
Conclusions and Recommendations.....	xxxviii
1 Introduction	1
1.1 Faults, aquitards and modelling project: overall goals	1
1.2 Fault component of the project	2
1.3 Project study area: Gloucester Basin.....	3
1.4 References	4
2 Gloucester basin case study description	6
2.1 Introduction	6
2.1 Resource exploration history.....	7
2.2 Pre-existing hydrogeological conceptualisation.....	10
2.3 Fieldwork schedule	17
2.4 References	20
3 Shallow electromagnetic (EM) analysis	22
3.1 Introduction	22
3.2 Methods.....	22

3.3	TEM data quality analysis	24
3.4	Results from TEM data analysis.....	24
3.4.1	North line NanoTEM.....	26
3.4.2	South line NanoTEM.....	26
3.4.3	Alpha line TEM.....	27
3.5	Frequency-dependent response in the TEM data.....	33
3.6	Comparison of TEM results with existing seismic data	36
3.7	Integrated analysis of geophysical results supporting hydrogeological characterisation	38
3.8	References	39

4 Hydraulic analysis of pre-existing subsurface data 40

4.1	Introduction.....	40
4.2	Methods.....	42
4.2.1	Formation pressure analysis	42
4.2.1.1	Hydraulic head.....	42
4.2.1.2	Data processing	43
4.2.1.3	Well test data detection.....	43
4.2.1.4	Monitoring bore data	43
4.2.2	Hydrochemistry of deep boreholes.....	46
4.2.2.1	Introduction.....	46
4.2.2.2	Groundwater chemistry data collection and processing	48
4.2.2.3	Multivariate statistical analysis of hydrochemical data.....	48
4.3	Results 49	
4.3.1	Initial hydraulic head analysis	49
4.3.2	Hierarchical cluster analysis and principal component analysis.....	56
4.3.2.1	Layers 1-12 all bores/wells	56
4.3.2.2	Other grouping of data.....	64
4.3.2.3	Total Dissolved Solids	65
4.4	References	67

5 Hydrogeochemical and environmental tracer analysis 70

5.1	Introduction.....	70
-----	-------------------	----

5.2	Methods.....	72
5.2.1	Surface water and groundwater sampling.....	72
5.2.2	Major element, methane, isotope and noble gas analyses	74
5.3	Results	76
5.3.1	Synoptic river survey	85
5.3.1.1	Chloride, $\delta^{18}\text{O}$ and $\delta^2\text{H}$	85
5.3.1.2	Radon and helium-4	86
5.3.1.3	Surface water methane	87
5.3.2	Major ions in groundwater.....	88
5.3.3	Methane in groundwater	90
5.3.4	Stable isotopes of water.....	93
5.3.5	^{222}Rn and dissolved non-radioactive noble gases in groundwater	94
5.3.6	Tritium and carbon-14.....	95
5.4	Discussion	97
5.4.1	Groundwater – surface water mixing processes.....	99
5.4.2	Inferring the groundwater flux from surface water radon, methane and helium trends.....	101
5.4.3	Methane	102
5.4.4	Estimating the vertical groundwater flux based on helium and methane profiles	104
5.5	Integrated analysis supporting hydrogeological conceptualisation.....	109
5.6	References	110

6	Structural geology analysis	117
----------	------------------------------------	------------

6.1	Introduction.....	117
6.2	Methods.....	119
6.2.1	Borehole image log analysis	119
6.2.1.1	Methodology and Classification	120
6.2.1.2	In-situ stress analysis.....	123
6.2.1.3	Borehole fracture characterisation	124
6.2.1.4	In-situ stress and fracture relationship with permeability.....	130
6.2.2	Three-dimensional deep seismic analysis	132

6.3	References	137
-----	------------------	-----

7	Data integration, fault seal analysis and hydrogeological conceptualisation	139
----------	--	------------

7.1	Introduction	139
7.2	Methods for integration	140
7.3	Integrated analysis supporting a hydrogeologic conceptualisation.....	140
7.3.1	Seismic Interpretation with NanoTEM.....	142
7.3.2	Revised hydraulic Head Maps and Cross Sections	144
7.3.2.1	Hydraulic Head Distribution for Layers 11-14.....	145
7.3.2.2	Hydraulic Head Distribution for Layer 10.....	149
7.3.2.3	Hydraulic Head Distribution for Layer 8.....	149
7.3.2.4	Hydraulic Head Distribution for Layer 1-6.....	149
7.3.2.5	Vertical flow analysis (cross sections)	153
7.3.3	Salinity distribution in shallow aquifers	156
7.4	References	158

8	Regional scale groundwater flow modelling of fault conceptualisations	159
----------	--	------------

8.1	Introduction	159
8.2	Approach to incorporate geological information in regional-scale groundwater modelling	160
8.2.1	Model design	161
8.2.1.1	Model Conceptualisation	161
8.2.1.2	Model Design.....	161
8.2.1.3	Model Boundary Conditions.....	166
8.2.2	Fault Implementation.....	166
8.2.3	CSG water production curves.....	168
8.2.4	Model Parameterisation	169
8.2.4.1	Workflow	169
8.2.4.2	Permeability Estimation	171
8.2.4.3	Coal seam connectivity.....	175
8.2.4.4	Bulk Permeability Estimation	178
8.2.5	Additional fault features: Chimneys.....	182
8.2.6	Implementing chimneys in MODFLOW	183

8.2.7	Modelling scenarios	187
8.3	Simulated groundwater response	189
8.3.1	Groundwater flow for a natural system.....	190
8.3.1.1	Connected model simulations.....	190
8.3.1.2	Disconnected model simulations	193
8.3.2	Groundwater flow for a stressed system.....	195
8.3.2.1	Connected model simulations.....	195
8.3.2.2	Disconnected model simulations	201
8.3.3	Impact of chimney flow on groundwater heads	208
8.3.3.1	Single chimney simulations	208
8.3.3.2	Cluster of chimneys	211
8.4	Key findings of groundwater flow modelling	213
8.5	References	216

9	3D geomechanical deformation modelling	218
----------	---	------------

9.1	Introduction.....	218
9.2	Geo-model setup	218
9.2.1	Geomechanical simulator FLAC3D	218
9.2.2	Model stratigraphy and structure	220
9.2.3	Mechanical and hydraulic properties.....	222
9.2.4	Initial model conditions.....	222
9.2.5	Scenarios for modelling.....	224
9.3	Simulation results	226
9.3.1	Results of the models with a reverse faulting stress regime	226
9.3.2	Model results for normal faulting stress regime.....	234
9.3.3	Model results for strike-slip faulting stress regime	239
9.4	Conclusions.....	240
9.5	References	241

10	Summary and conclusions	243
-----------	--------------------------------	------------

10.1	Fault investigations: a multiple lines of evidence approach	243
10.2	Shallow geophysical survey	244

10.3	Hydrochemistry and environmental tracer data.....	244
10.4	Hydraulic analysis	246
10.5	Structural geology analysis	246
10.6	Data integration and proposed regional scale conceptual model	247
10.7	Regional scale groundwater flow modelling	248
10.8	Geomechanical deformation modelling.....	250

11	Benefits of research findings	252
-----------	--------------------------------------	------------

11.1	Benefits to the coal seam gas industry.....	253
11.2	Remaining knowledge gaps and recommendations	254
11.3	Outcomes and impacts	255
11.4	References	256

APPENDIX A	Sampling of dissolved gases in groundwater at in-situ pressure: a new methodology	257
APPENDIX B	Continuous air sampling: CO₂, methane and its stable isotopes	272
APPENDIX C	Sampling locations for surface water	275
APPENDIX D	Additional Fault Features: Chimneys	279

Figures

Figure 2-1 Locations of open-cut mining (identified by owner), Petroleum Exploration Licence 285 (PEL 285), and field sampling area “Waukivory” in the Gloucester subregion (Modified from: Hodgkinson et al., 2014).	8
Figure 2-2 Base map of the Gloucester Basin (left) with the region of CSG appraisal indicated in red. Right: the stratigraphic nomenclature for the Gloucester Basin (Modified from: Ward et al. [2001] and Weber and Smith [2000]).	9
Figure 2-3 Schematic west-east cross section of the Gloucester Basin. Note the small area covered by the Quaternary alluvial aquifer (Source: Parsons Brinckerhoff [2013]).	12
Figure 2-4 Conceptual hydrodynamic cross-section of the Gloucester Basin indicating the gravity driven flow systems and resident time for formation water on various flow paths (Source: Colin et al. [2013], modified from Winter et al. [1998] and Waller [2013]).	12
Figure 2-5 Interpreted regional groundwater contours for the shallow most aquifer in the Gloucester Basin. Yellow arrows indicate the groundwater migration direction (Source: Parsons Brinckerhoff [2013]).	13
Figure 2-6 Hydraulic conductivity of coal seams and interburden with depth for the Gloucester Basin strata (Source: Parsons Brinckerhoff [2015]).	14
Figure 2-7 A schematic diagram demonstrating the fault zone architecture common for strike slip systems (Source: Parsons Brinckerhoff [2013]).	15
Figure 2-8 Seismic cross section near the Stratford 4 gas well with the interpreted strike slip fault and location of monitoring bores. Drawdown at each of the bores is shown after 72 hrs of pumping at the TTPB well (Source: Parsons Brinckerhoff [2013]).	17
Figure 2-9 Location map of the Gloucester region, NSW Australia and the field study site. The location of the shallow TEM lines are also shown.....	19
Figure 3-1 Primary and secondary electromagnetic fields generated in the subsurface and voltage (V) decay during a TEM survey.....	23
Figure 3-2 Idealised resistivity-depth section showing conceptual model for identification of faults in the TEM data sets shown in this section. The colours used in this section are similar to those used in the actual data sections, with redder colours indicating relatively electrically conductive zones and bluer colours indicating relatively resistive zones. Many of the faults interpreted in these sections appear as conductors; this is consistent with the observations in Figure 6-11 and Figure 6-12 that the shallow fracturing observed in bores Waukivory 11 and 12 were characterised as either “conductive fractures” (Waukivory 12) or “mixed fractures” (Waukivory 11), i.e. are not “resistive fractures” ...	25
Figure 3-3 North line resistivity depth section from the NanoTEM near surface geophysical survey. With (top) and without (bottom) vertical height exaggeration.....	28

Figure 3-4 South line resistivity depth section from the NanoTEM near surface geophysical survey. With (top) and without (bottom) vertical height exaggeration.....	28
Figure 3-5 Alpha line Tiedmans property TEM near surface geophysical survey from Alpha GeoScience (Parsons Brinckerhoff 2013).....	29
Figure 3-6 (top) Near surface geophysical NanoTEM (North line and South line) and TEM (Alpha line) 2D transects overlain on Google Earth including the inferred structural lineaments at ground surface; (middle) zoomed in detail of North line transect; (bottom) zoomed in detail of South line transect.....	32
Figure 3-7 Borehole resistivity logs for a) bore GW080841-2 and b) bore Waukivory 14. In (a) note that there is no consistent change in resistivity that matches the change seen in the NanoTEM section. In (b) tuffs are logged to occur from 172 to 180 m depth; there is only a small change in resistivity at that depth. The resistivity scales in a) and b) are different.	34
Figure 3-8 Comparison of (a) modelled decay data with (b) field decay data. The field data are from South Line, station 3240.	35
Figure 3-9 Comparison of North Line NanoTEM with seismic section cut from 3D cube on the same traverse. Red, ochre and purple lines show deeper fault locations determined from seismic data. Blue circles indicate zones in shallower seismic section that are heavily faulted. Both red faults may extend to surface. Ochre and purple faults appear to be cut off below bottom of Cloverdale.....	37
Figure 3-10 Comparison of South Line NanoTEM with seismic section cut from 3D cube on the same traverse. Blue lines indicate faults interpreted from seismics. Blue circle shows zone of concentrated faulting in near-surface.	38
Figure 4-1 A detailed stratigraphic nomenclature for the northern Gloucester Basin with equivalent layer numbers of the AGL Petrel model (after Brown et al. (1996), AECOM (2009) SRK (2010), Pacific consulting (2012) and the Australian Stratigraphic Names Database).	41
Figure 4-2 South to north cross-section of the AGL surfaces within the Petrel static model of the Gloucester Basin.....	42
Figure 4-3 Geothermal gradient for the entire study area (blue line).	44
Figure 4-4 Geothermal gradient for Waukivory sub-area (red line).....	45
Figure 4-5 Geothermal gradient for Stratford sub-area (green line).	45
Figure 4-6 Generic representation of aquifer interactions along the recharge flow path and methane generation. Note: These processes are shown along the flow path, but they do not necessarily occur sequentially (Dahm et al., 2014).....	48
Figure 4-7 Hydraulic head values of study area. Well locations with multiple hydraulic head values along the vertical showing a consistent gradient are indicated by red arrows. The red circles show regions of significant hydraulic head differences across a fault. The	

fault traces highlighted in red have been selected as likely being significant to fluid flow.	51
Figure 4-8 Fresh water hydraulic head isolines (bold black contours) for L11-14. Inferred flow arrows are in blue. Fault traces likely significant to fluid flow are shown in red.....	52
Figure 4-9 Fresh water hydraulic head isolines (bold black contours) for L10. Some well data are posted with hydraulic head-elevation plots and well test data tables to show the data QC process. Inferred flow arrows are in blue. Fault traces likely significant to fluid flow are shown in red.	53
Figure 4-10 Fresh water hydraulic head isolines (bold black contours) for L8. Some well data are posted with hydraulic head-elevation plots and well test data tables to show the data QC process. Inferred flow arrows are in blue. Fault traces likely significant to fluid flow are shown in red.	54
Figure 4-11 Fresh water hydraulic head isolines (bold black contours) for L1-L6 with the hydraulic head value posted next to each well/bore. Data from the alluvium is in khaki green and data from the shallow fractured bedrock is in bright green. Inferred flow arrows are in blue. Fault traces likely significant to fluid flow are shown in red.....	55
Figure 4-12 HCA result for layers 1-12 labelled by bore ID. Black horizontal lines represent where the dendrogram would be cut at a height of 15 creating; group 1 circled in light blue and group 2 circled in red, and at a height of 10 creating; group 1 circled in dark blue, group 2 circled in dark red and group 3 circled in pink.	57
Figure 4-13 HCA result for layers 1-12 labelled by the geological model layer that was sampled.....	57
Figure 4-14 PCA result for layers 1-12.	59
Figure 4-15 HCA results plotted spatially with bores assigned to one of two groups by cutting the dendrogram at a height of 15 (see Figure 4-12).	61
Figure 4-16 HCA results plotted spatially with bores assigned to one of three groups at a height of 10 (see Figure 4-12).....	62
Figure 4-17 HCA results Piper diagram of average proportion of major anions and cations for each bore. Colours represent the HCA group with the dendrogram cut at 15; red = group 1, blue = group 2.....	63
Figure 4-18 Piper diagram of average proportion of major anions and cations for each bore. Colours represent the HCA group with the dendrogram cut at 10; red = group 1, blue = group 2, pink = group 3.	64
Figure 4-19 Salinity (total dissolved solids) distribution for layers 1-6.	66
Figure 5-1 Typical compositional ranges of methane from different sources (Coleman, 1995).	71

Figure 5-2 Surface water sampling locations along the Waukivory River and Avon River, Gloucester, NSW. Sampled groundwater wells completed in the alluvial, interburden aquifers and coal seams are also shown.	73
Figure 5-3 Run of river showing streamflow and chloride concentration versus distance upstream of Jacks Rd river crossing (observation point A0 on the Avon River).....	86
Figure 5-4 Run of river showing the stable isotope of water, $\delta^{18}\text{O}$, versus distance. The distance of 0 meters upstream of Jacks river crossing corresponds to observation point A0 on the Avon River.	86
Figure 5-5 Run of river showing ^{222}Rn and ^4He (right axis) concentration versus distance. The distance of 0 meters upstream of Jacks river crossing corresponds to observation point A0 on the Avon River. Solubility equilibrium with the atmosphere for helium is $4.1 - 4.5 \times 10^{-8} \text{ cm}^3 \text{ STP g}^{-1}$ between 10 and 30°C	87
Figure 5-6 Run of river showing methane (μgL^{-1}) and $\delta^{13}\text{C-CH}_4$ (right axis) versus distance. Data labels show the $\delta^2\text{H-CH}_4$ values for a subset of samples measured.	88
Figure 5-7 Piper diagram of 22 surface water and 26 groundwater samples collected 22 nd February to 2 nd March 2016 from the Gloucester study area.....	89
Figure 5-8 Measured surface water and groundwater dissolved methane concentrations and $\delta^{13}\text{C-CH}_4$ values in the study area.	91
Figure 5-9 CH_4 versus $\delta^{13}\text{C-CH}_4$ of surface water and groundwater samples. Diamond symbols represent samples collected in this study. Circular symbols represent samples collected by AGL throughout 2011-2015.....	92
Figure 5-10 Methane concentration of surface water and groundwater samples versus depth. Methane solubility curves (at 10 and 20 degrees C) are also shown. Samples to the right of the blue curves will tend to degas if in situ pressures are not maintained during sampling.....	92
Figure 5-11 Stable isotopes of water of surface water and groundwater samples from the Gloucester study site. LMWL for Brisbane $\delta^2\text{H} = 7.6\delta^{18}\text{O} + 12.8$. Diamond symbols represent samples collected in this study. Circular symbols represent samples collected by AGL throughout 2011-2015.	93
Figure 5-12 Stable isotopes of water of surface water and groundwater samples from the Gloucester Basin. Diamond symbols represent samples collected in this study. Circular symbols represent samples collected by AGL throughout 2011-2015.....	94
Figure 5-13 Comparison of measured concentrations of nitrogen, argon, helium and neon in groundwater with expected concentrations based on equilibrium solubility of atmospheric gases in water at temperatures between 5 and 30°C and excess air volumes up to $10 \text{ cm}^3 \text{ kg}^{-1}$. Note that helium is plotted on a logarithmic scale, whereas the scale for the other gases is linear.	95

Figure 5-14 (a) ^3H , (b) ^{14}C and (c) ^4He concentrations versus depth in groundwater samples. Diamonds represent samples collected in this study; circles represent samples collected by AGL throughout 2011-2015. Error bars represent well screen lengths..... 96

Figure 5-15 Measured surface water and groundwater ^4He concentrations and ^{222}Rn in the study area. The size of the circles represent ^{222}Rn concentration and the numbers next to them are the ^4He concentrations..... 98

Figure 5-16 Conceptual representation of a solute mixing profile below a gaining river generated by a combination of flood pulses and hyporheic exchange..... 100

Figure 5-17 Summary diagram for the different components of the radon mass-balance along a river reach. F_{in} is the surface water radon flux to the reach, F_{out} is the surface water radon flux out of the reach, F_{a} is the flux to the atmosphere by gas evasion (degassing), F_{p} the radon loss by pumping, $F_{\text{gw_in}}$ is the groundwater discharge of radon, $F_{\text{gw_out}}$ is the loss of radon by groundwater recharge, F_{hyp} is the flux from hyporheic exchange, and L_{decay} is the loss during transit from radioactive decay. 102

Figure 5-18 $\delta^{13}\text{C}\text{-CH}_4$ versus $\delta^2\text{H}\text{-CH}_4$ of surface water and groundwater samples compared to other coal basins. Diamond symbols represent samples collected in this study. Circular symbols represent samples collected by AGL throughout 2011-2015. Classification system from Whiticar et al. ((1986)) with other Australian coal bed methane reservoir data taken from Faiz and Hendry ((2009)). 104

Figure 5-19 Examples of tracer distribution in an aquitard under low and high, and upward and downward groundwater velocity (from Smith et al., 2018), assuming no internal production..... 105

Figure 5-20 Modelled helium concentrations using three models (model 1, S5MB, S4MB)..... 107

Figure 5-21 Modelled methane concentrations using two pore-water velocities (8×10^{-5} and 4×10^{-5} m year $^{-1}$). When concentrations exceed solubility, bubble formation may occur..... 108

Figure 5-22 Conceptual model of a dual permeability porous medium. The matrix continuum represents the interburden rock mass while the fracture continuum represents the fault zone damage zone. Flow direction can be upwards or downwards (Source: Altman et al., 1996). 109

Figure 6-1 (A) Location map of Gloucester Basin (Source: McVicar et al., 2014) (B) Regional geological map of the Gloucester Basin (Source: Parsons Brinckerhoff, 2013). 118

Figure 6-2 Simplified regional cross-section for the Gloucester Basin (Source: Roberts et al., 1991). This figure is not covered by a Creative Commons Attribution licence. It has been reproduced with the permission of NSW Trade & Investment..... 119

Figure 6-3 Map showing location of wells with image log data. 121

Figure 6-4 Image log analysis methodology flow chart adopted in this study..... 122

Figure 6-5 Image log interpretation classification scheme.....	122
Figure 6-6 Example of structural features observed in borehole image and how they were used in the interpretation.....	123
Figure 6-7 Fracture abundance measures (source: Dershowitz and Herda, 1992; Mauldon and Dershowitz, 2000).....	124
Figure 6-8 Map showing in-situ horizontal stress (S_{Hmax}) distribution within the Gloucester Basin.....	125
Figure 6-9 Summary map showing faults and fracture distribution within Gloucester Basin.....	126
Figure 6-10 Individual well details on in-situ stress, faults and fracture distribution along B – B' cross section.....	127
Figure 6-11 (A) Waukivory 11 S_{Hmax} and fracture distribution along depth; (B) Waukivory 11 fracture dip azimuth distribution along depth; (C) Stereonet contour of faults and fractures dip azimuth in Waukivory 11 well; (D) Waukivory 11 fracture dip range histogram.	128
Figure 6-12 (A) Waukivory 12 S_{Hmax} and fracture distribution along depth; (B) Waukivory 12 fracture dip azimuth distribution along depth; (C) Stereonet contour of faults and fractures dip azimuth in Waukivory 12 well; (D) Waukivory 12 fracture dip range histogram.	129
Figure 6-13 Seismic and well section showing structural complexity, in-situ stress and fracture character variation along depth within Waukivory 12.....	130
Figure 6-14 Cross-section along Waukivory pilot area and further south showing in-situ stress and fracture character variation spatially and along depth with the measured permeability data using well tests.....	131
Figure 6-15 Interpreted permeability relationship with angle between S_{Hmax} and fracture orientation.	132
Figure 6-16 Gloucester Basin – Morgani 3D location and basin outline.	134
Figure 6-17 Morgani 3D Coherency Attribute volume, example time slice (left) and profile (right). The magenta lines represent the bounds of the shear zone with right lateral displacement (magenta arrows). Yellow lines represent interpreted fault segments. Red polygon is an interpreted fault plane. The orange transects mark the NanoTEM lines. .	135
Figure 6-18 Fault pattern change from Stratford to Waukivory. Left panel: Magenta lines are previous AGL fault interpretations and orange transects mark the NanoTEM lines. Right Panel: Top red box highlights the area of Figure 6-17 and the bottom red box highlights the area of Figure 6-19. The orange transects mark the NanoTEM lines and the yellow lines represent interpreted fault zones.	136

Figure 6-19 Detailed coherency slice from Stratford area. Key features are ~W-E faulting which occur at “bend” in structural trend. This deformation may form flow boundary to compartmentalize the observed salinity anomaly. 137

Figure 7-1 Conceptual model of the hydrodynamic system of the Gloucester Basin. Dimensions are not to scale. Circles with plus signs indicate flow into the page; circles with dots indicate flow out of the page..... 142

Figure 7-2 Coherency example from Waukivory area integrated with NanoTEM Profile 3 (orange). Profile shows the shallow extent of discontinuous, en-echelon faulting, also shown in Figure 6-17). 143

Figure 7-3 Profile along NanoTEM3 (orange in previous figure), shallow resistivity anomalies are observed to coincide with seismic faulting..... 143

Figure 7-4 Updated faults (black lines) for the Gloucester Basin from AGL with different fault trace locations per stratigraphic interval. Stratigraphic levels are as follows: L1-L6 (Bindaboo), L8 (Fairbairns),L10 (Bowens), and L11-L14 (Avon). 146

Figure 7-5 The Digital Elevation Model (masl) for the study area with key wells/bores marked. The surface drainage is posted in blue..... 147

Figure 7-6 Fresh water hydraulic head distribution (bold black contours) for L11-L14 (Avon)..... 148

Figure 7-7 Fresh water hydraulic head distribution (bold black contours) for L10 (Bowens Road). 150

Figure 7-8 Fresh water hydraulic head distribution (bold black contours) for L8 (Fairbairns). 151

Figure 7-9 Fresh water hydraulic head distribution (bold black contours) for L1-L6 (Bindaboo) with well/bore data control (hydraulic head value posted next to each well/bore with data from the alluvium flagged khaki green and shallow fractured bedrock flagged bright green..... 152

Figure 7-10 Fresh water hydraulic head distribution (black contours) along a W-E cross-section through the Waukivory area with well/bore data control (yellow stars are test data/monitoring bore data and green stars are controls from previously described hydraulic head maps). The location of cross-section is the black line shown in base map on the bottom right of the diagram. Black arrows show the interpreted flow direction, upward in the red squares and downward in the blue square. Interpreted faults are shown by red lines. 154

Figure 7-11 Fresh water hydraulic head distribution (black contours) along a S-N cross-section through the Waukivory area with well/bore data control (yellow stars are test data/monitoring bore data and green stars are controls from previously described hydraulic head maps). The location of cross-section is the black line shown in base map on the bottom right of the diagram. Black arrows show the interpreted flow direction, upward in the red square. Interpreted faults are shown by red lines. 155

Figure 7-12 fresh water hydraulic head distribution (black contours) along a W-E cross-section through the Stratford area with well/bore data control (yellow stars are test data/monitoring bore data and green stars are controls from previously described hydraulic head maps). The location of cross-section is the black line shown in base map on the bottom right of the diagram. Black arrows show the interpreted flow direction, upward in the red squares. Interpreted faults are shown by red lines..... 155

Figure 7-13 3D seismic cube with a horizontal map of coherency that indicates small fault segments in the Stratford area. Map on the left is a regional view while the red square is highlighted in more detail on the right..... 156

Figure 7-14 Salinity map (mg/L) for L1-L6 with added control of the hydraulic head cross-sections and detailed coherency map interpretation to help constrain the TDS plume geometry..... 157

Figure 8-1 Gloucester Basin major fault traces (grey lines) and depth structure maps extracted from the eroded and faulted geological model for the coal-bearing geological Gloucester Basin area modelled in three dimensions. (a) Alum Mountain Volcanics, (b) Durallie Road Formation, (c) Mammy Johnsons Formation, (d) Waukivory River Formation, (e) Dog Trap Creek Formation, (f) Speldon Formation, (g) Wenham Formation Wards River Conglomerate and (h) Jilleon Formation TVDss = total vertical depth subsea reported to the Australian Height Datum; negative values represent elevation above sea level – grey lines represent the main fault trends (Source: Frery et al., In Prep). 163

Figure 8-2 Alluvial model of the Gloucester Basin. Extent of the Gloucester basin model is indicated by the red box. 164

Figure 8-3 (a) Extent of the Gloucester numerical model showing the major faults (red lines), well field location (hashed box), and chimney location (green star). The alluvial aquifer (beige) and drains (blue lines) are also indicated. (b) Plan view with numerical layer numbers (variability in layer numbers at the surface is due to fault juxtaposition), with model boundary conditions also indicates (NFB: no flow boundary, and CHB: constant head boundary). (c) Cross-sectional view of the model (cross-section identified in (b)). Figure based on Fig 17 from McCallum et al. (2018). 165

Figure 8-4 Implementation of the modified continuum method in MODFLOW-Unstructured Grid, based on McCallum et al. (2018)..... 167

Figure 8-5 Conceptual model of fault relative permeability (Rel Perm) for different fault types. Based on Figure 4 McCallum et al. (2018). 167

Figure 8-6 Relationship between the fault permeability multiplier and (a) fault throw (m) and (b) the throw ratio (throw/maximum throw)..... 168

Figure 8-7 Total water production rate used for the P50 scenario (blue; Peeters et al. (In Prep)) and the MODFLOW-simulated water production rates (red)..... 169

Figure 8-8 Workflow to generate a 3D bulk permeability field to inform model parameterisation. The data block shows the available drill stem test (DST) data used to

determine the depth-permeability relationship for coal k_c and interburden k_i , and the cumulative distribution function (CDF) of the coal fraction data. The simulations block includes Gaussian simulations to generate variability in the coal seam permeability (Permeability Estimation) and spatial connectivity of the coal seams (Coal Seam Connectivity). The DST CDF and coal seam connectivity and fraction were used to estimate the bulk permeability (Bulk Permeability Estimation)..... 170

Figure 8-9 Schematic diagram showing a layered model structure (a) pre deformation and the faulted model structure post deformation (b). Figure based on Figure 13(b) in McCallum et al. (2018). 171

Figure 8-10 (a) Bulk permeability (k) data from Drill Stem Tests in the Waukivory area in the Gloucester Basin at various depths (black dots) and corrected coal seam DST permeability estimates (corr. k_c) based on the DST data for bulk permeability and coal seam fraction present for each data point. Blue line represents a log-linear regression of the corrected coal seam permeability estimates (equation and r^2 stated in the figure). (b) Simple model of permeability for the coal fraction (k_c : blue) and assumed interburden model (k_i : black). The dotted line indicates the base of the weathered zone. 172

Figure 8-11 Images of the 3D Gaussian domain of spatially correlated values with a mean of zero and a variance of $\ln(\text{permeability})$ of 2.85 ($\sigma^2 \epsilon$ in Equation 8-3) determined from the Drill Stem data (where permeability is depth-detrended). Subplots (a) – (c) show vertical slices through the 3D domain at different locations (labelled on (d)). (d) shows a plan view of the 21st layer in the field. 174

Figure 8-12 Image of the 3D natural log of the coal permeability ($\ln(k_c)$) based on the depth relationship (Equation 8-3) and the spatial variability depicted in Figure 8-11. Subplots (a) – (c) show vertical slices through the 3D domain at different locations (labelled on (d)). (d) shows a plan view of the 21st layer in the domain. 175

Figure 8-13 Location of coal seams in four CSG wells in the Waukivory (WAUK) area, Gloucester Basin. Black lines represent the location and depth of the coal seam. 176

Figure 8-14 Images of the disconnected multi-Gaussian domain of spatially correlated random values with a mean of zero and a unit variance. Subplots (a) – (c) show vertical slices through the 3D domain at different locations (labelled on (d)). (d) shows a plan view of the 21st layer in the domain. 177

Figure 8-15 Images of the connected multi-Gaussian domain of spatially correlated random values with a mean of zero and a unit variance. Subplots (a) – (c) show vertical slices through the 3D domain at different locations (labelled on (d)). (d) Plan view of the 21st layer in the domain. 177

Figure 8-16 Cumulative Distribution function (CDF) of the (a) connected (Con) and disconnected (Discon) domain ($H(\epsilon)$) and (b) the coal fraction in the each of the Drill Stem Test data ($F(cf)$)(black line). The arrows indicate how a value of ϵ is mapped to a coal fraction..... 178

Figure 8-17 Images of the 3D coal fraction field, obtained by a normal-score transform of the potential coal connectivity (disconnected: Figure 8-14) and the likely coal fraction present (Figure 8-16). Subplots (a) – (c) show vertical slices through the 3D field at different locations (labelled on (d)). (d) shows a plan view of the 21st layer in the field.. 180

Figure 8-18 Images of the 3D coal fraction field, obtained by a normal-score transform of the potential coal connectivity (connected: Figure 8-15) and the likely coal fraction present (Figure 8-16). Subplots (a) – (c) show vertical slices through the 3D field at different locations (labelled on (d)). (d) shows a plan view of the 21st layer in the field.. 181

Figure 8-19 Comparison of the bulk hydraulic conductivity domains in the north of the Gloucester model for the (a) facies model, (b) connected *K* domain, and (c) disconnected *K* (m/day) domain. The red area (high *K* zone) is associated with the alluvial aquifer. ... 182

Figure 8-20 (A) TDS anomaly and the head boundaries used for the plume analysis, chimney location indicated by the red circle (based on Figure 7-14). Solid yellow lines represent the no-flow boundaries, and the dashed lines represent the constant head boundaries, and open black circles represent well locations. (B) Schematic diagram of the aquifer area used in the mass balance analysis showing the boundary conditions (NFB: no flow boundary and CHB: constant head boundary) and chimney location (red circle). (C) Schematic cross-section through (B) showing the chimney connectivity between high hydraulic conductivity layers at depth and the overlying alluvial aquifer/weathered zone..... 183

Figure 8-21 (a) Schematic geological cross-section through a chimney conduit showing the faults (red dashed line) and layer deformation and offset. The grey lines indicate areas of enhanced flow due to brecciation process during faulting. The grey area represents the alluvial aquifer and weathered zone, the groundwater table is shown (thin blue line and triangle). The approximate location of the chimney is indicated. (b) Conceptual representation of the chimney as implemented in the numerical model. The blue cylinder represents the chimney conduit, which receives groundwater from the high hydraulic conductivity aquifers (labelled). The radius of the conduit and its hydraulic conductivity are required as inputs. 185

Figure 8-22 Connected Linear Network configuration for the single CLN chimney simulation showing the CLN nodes (green) and the connection between layers, (b) plan view of the CLN for a single chimney (CLN # 1: red square) and the cluster of five chimneys (5 CLN: red and black squares) simulations. 186

Figure 8-23 Hydraulic conductivity of the groundwater nodes connected to the CLN chimney (single CLN) for the connected (black) and disconnected (red) simulations. 187

Figure 8-24 Cross-sections for the connected (a) and disconnected (b) models, and the location of the chimney (white line). 189

Figure 8-25 Cross-sectional view of steady-state head distribution for a connected model for (a) high permeability fault, (b) medium permeability fault, and (c) low permeability

fault. Dotted line indicates the main fault location. See Figure 8-3 for cross-section location.	191
Figure 8-26 Plan view of the surficial hydraulic head contours in the north of the Gloucester model for the connected model and (a) high permeability fault, (b) medium permeability fault, and (c) low permeability fault. The alluvial aquifer is identified by the transparent white area. Grey areas within the model area indicate model cells whose hydraulic head are outside of the range depicted here.	192
Figure 8-27 Cross-sectional view of steady-state head distribution for a disconnected model across the well field for (a) high permeability fault, (b) medium permeability fault, and (c) low permeability fault. Dotted line indicates the main fault location. See Figure 8-3 for cross-section location.	193
Figure 8-28 Plan view of the surficial hydraulic head distribution in the north of the Gloucester model for the disconnected model for (a) high permeability fault, (b) medium permeability fault, and (c) low permeability fault. The alluvial aquifer is identified by the transparent white area. Grey areas within the model area indicate model cells whose hydraulic head are outside of the range depicted here.	194
Figure 8-29 Cross-section through the well field of the hydraulic heads (a,b, and d) and drawdown (c and e) for the connected simulation using a high flow across fault conceptualisation at different time (steady state, 1 year of pumping, and 10 years of pumping). The location of the fault is indicated in (a), (b) and (d) (dashed line) and the location of the stream is identified. See Figure 8-3 for cross-section location.	195
Figure 8-30 Cross-section through the well field of the hydraulic heads (a,b, and d) and drawdown (c and e) for the connected simulation using a medium flow across fault conceptualisation for different times (steady state, 1 year of pumping, 10 years of pumping). See Figure 8-3 for cross-section location.	196
Figure 8-31 Cross-section through the well field of the hydraulic heads (a, b, and d) and drawdown (c and e) for the connected simulation using a low flow across fault conceptualisation for different time (steady state, 1 year of pumping, 10 years of pumping). See Figure 8-3 for cross-section location.	197
Figure 8-32 Comparison of the cross-section through the well field of the hydraulic heads for the connected simulation using a high (a, b, and c), medium (d, e, and f) and low (g, h, and i) flow across fault conceptualisation at different times. Steady-state heads are shown in (a), (b), and (c); heads after 1 year of pumping are shown in (d), (e), and (f); and heads 10 years into the production period (pumping has almost ceased at this point) (g), (h), and (i). See Figure 8-3 for cross-section location.	199
Figure 8-33 Plan view of the surficial drawdown in the north of the Gloucester model for the connected model after 1 year of pumping. The alluvial aquifer is identified by the transparent white area. Grey areas within the model area indicate model cells whose hydraulic head are outside of the range depicted here.	200

Figure 8-34 Cross-section of hydraulic conductivity through the well field for the disconnected <i>K</i> model. Location of the fault indicated by a white rectangle, white box identifies the well locations.	201
Figure 8-35 Cross-section through the well field of the hydraulic heads (a, b, and d) and drawdown (c and e) for the disconnected simulation using a high flow across fault conceptualisation for different times (steady-state, 1 year of pumping, and 10 years of pumping). See Figure 8-3 for cross section location.	203
Figure 8-36 Cross-section through the well field of the hydraulic heads (a, b, and d) and drawdown (c and e) for the disconnected simulation using a medium flow across fault conceptualisation for different times (steady-state, 1 year of pumping, and 10 years of pumping). See Figure 8-3 for cross-section location.	204
Figure 8-37 Cross-section through the well field of the hydraulic heads (a, b, and d) and drawdown (c and e) for the disconnected simulation using a low flow across fault conceptualisation for different times (steady- state, 1 year of pumping, and 10 years of pumping). See Figure 8-3 for cross-section location.	205
Figure 8-38 Comparison of the cross-section through the well field of the hydraulic heads for the disconnected simulation using a high (a, b, and c), medium (d, e, and f) and low (g, h, and i) flow across fault conceptualisation at different times. Steady-state heads are shown in (a), (b), and (c); heads after 1 year of pumping are shown in (d), (e), and (f); and heads 10 years into the production period (pumping has almost ceased at this point) (g), (h), and (i). See Figure 8-3 for cross-section location.	206
Figure 8-39 Plan view of the surficial drawdown in the north of the Gloucester model for the disconnected model after 1 year of pumping. Well field location indicated by white box. The alluvial aquifer is identified by the transparent white area. Grey areas within the model area indicate model cells whose hydraulic head are outside of the range depicted here. Dashed white line is a fault.	207
Figure 8-40 Cross-sectional views of the hydraulic heads for the connected simulation using a high (a, b, and c), medium (d, e, and f) and low (g, h, and i) flow across-fault conceptualisation at different times. Steady-state heads are shown in (a), (b), and (c); heads after 1 year of pumping are shown in (d), (e), and (f); and heads 10 years into the production period (pumping has almost ceased at this point) (g), (h), and (i). See Figure 8-3 for cross-section location. The chimney (CLN) location is marked with a white dashed line).	209
Figure 8-41 Cross-sectional view of the hydraulic heads for the disconnected simulation using a high (a, b, and c), medium (d, e, and f) and low (g, h, and i) flow across fault conceptualisation at different times. Steady-state heads are shown in (a), (b), and (c); heads after 1 year of pumping are shown in (d), (e), and (f); and heads 10 years into the production period (pumping has almost ceased at this point) (g), (h), and (i). See Figure 8-3 for cross-section location. The chimney (CLN) location marked with a white dashed line.....	210

Figure 8-42 Single chimney (CLN) hydraulic head (a) and groundwater flux (b) a for the different K fields (connected: con, and disconnected: discon) and fault scenarios (low, medium, and high flow across the fault) for a period of 20 years (pre-pumping (0 years) to post pumping (> 10 years)). The head values are taken from the top CLN node. 211

Figure 8-43 Cross-sectional view of the hydraulic heads (a, b, and d) and drawdown (c and e) for the connected simulation using a medium across-fault flow conceptualisation for different times (steady-state, 1 year of pumping, 10 years of pumping). See Figure 8-3 for cross-section location. The centre of the chimney cluster is indicated by the dashed white line. 212

Figure 8-44 Hydraulic head (a) and groundwater flux (b) through each chimney (CLN) for the clustered simulations (5 CLNs numbered 1-5; see Figure 8-22), for the different K fields (connected: con, and disconnected: discon) and fault scenarios for a period of 20 years (pre-pumping to post pumping)..... 213

Figure 9-1 (A) Schematic illustration of stress-strain relationship for the Mohr-Coulomb elastic-plastic material. (B) Mohr's circle diagrams for point-1 (pre-yield) and point-2 (yield) in A. Mohr's circle is a two-dimensional graphical presentation of principal stresses (σ_1 and σ_3 are the maximum and minimum principal stresses). Mohr's circle will touch the failure envelope (straight line) when mechanical yield or failure occurs. The vertical dash line and T define the tension cut off (tensile failure) point, where the effective minimum principal stress is tensile and equal to tensile strength..... 219

Figure 9-2 Model geometry. (A) Full model. (B) Model internal structure with 11 coal layers and a single generic fault. 221

Figure 9-3 Schematic illustration of stress gradients and fault movement for (A) reverse-faulting stress, (B) normal-faulting stress, and (C) strike slip-faulting stress cases. σ_v is the vertical stress, σ_{Hmax} is the maximum horizontal stress and σ_{Hmin} is the minimum horizontal stress..... 223

Figure 9-4 Initial pore pressure of the model..... 224

Figure 9-5 Illustration of four well locations for depressurisation simulations (A) and depressurisation locations on coal seam units (B). Numbered open circles in (A) show approximate depth levels of pore pressure and shear stress tracking locations in the model. Also note that interburden units are not plotted in (B) and red triangles are fault segments exposed between coal units..... 225

Figure 9-6 Pore pressure variations with depressurisation at locations for the four-well scenario in the model (reverse faulting stress regime). Note that all pore pressure curves start from hydrostatic conditions. See Figure 9-5 for the locations and depth levels of datum-tracking points in the model. 227

Figure 9-7 Pore pressure variations with fast depressurisation at a number of locations in the model (reverse faulting stress regime). See Figure 9-5 for the locations and depth levels of datum-tracking points in the model..... 228

Figure 9-8 Final pore pressure distribution on an E-W vertical cross section truncating depressurisation locations through the model (reverse faulting stress regime). Three images are for the models with fault permeability of 10 mD (top), 0.1 mD (middle) and 50 mD (bottom). Coal permeability is 20 mD in all models. Circles on top image show approximate depressurisation locations (i.e. CSG wells intersection coal layers). 229

Figure 9-9 Final pore pressure patterns on an E-W vertical cross section for the models with coal permeability = 1.0 and 50 mD, respectively. Fault permeability is kept at 10 mD in both models. Circles on top image show approximate depressurisation locations..... 230

Figure 9-10 Plots of shear stresses in the fault and coal beds in the model with a reverse faulting stress regime. See Figure 9-5 for the locations and depth levels of datum-tracking points in the model. 231

Figure 9-11 Mohr’s circle diagrams showing stress variation with respect to failure envelopes under a reverse faulting stress regime. σ_1 , σ_2 and σ_3 are the maximum, intermedium and minimum principal stresses, respectively. σ_v is the vertical stress, and σ_{Hmax} and σ_{Hmin} are the maximum and minimum horizontal stress, respectively. 232

Figure 9-12 Plots of fluid flow velocity vectors on a vertical cross section for models with fault permeability of (A) 10 mD (the base model) and (B) 0.1 mD. Maximum flow velocity is $\sim 7.9 \times 10^{-7}$ m/s in both models. Circles on (A) show approximate depressurisation locations. 233

Figure 9-13 Fluid flow velocity contours and vectors on a vertical cross section. (A) Model with coal permeability = 1 mD. (B) Model with coal permeability = 50 mD. Fault permeability is kept at 10 mD in both models. Note different flow velocity scales in the images for best visualization of fluid flow velocity contours and vectors. High flow velocity locations on coal beds are depressurisation locations (also see Figure 9-12A for these locations). 234

Figure 9-14 Plots of shear stresses in fault and coal in the model with a normal faulting stress regime. See Figure 12-5 for the locations and depth levels of datum-tracking points in the model. 235

Figure 9-15 Mohr’s circle diagrams showing stress variation with respect to failure envelopes under a normal faulting stress regime. 236

Figure 9-16 Mohr’s circle diagrams showing initial stresses in a fault in a model with low fault cohesion of 2 MPa and a variable stress ratio from 0.5 to 0.65 from shallow depth (500 m) to greater depth (1000 m). Note that the fault is critically-stressed from shallow to greater depth. 237

Figure 9-17 Illustration of failure status in fault and Mohr-circle stress plot for a fault experiencing failure in one or several locations. 238

Figure 9-18 Mohr-circle stress plot for a location in coal beds in a model with a very low coal cohesion of 1 MPa. 238

Figure 9-19 Plots of shear stresses in the fault and coal in the model with a strike-slip faulting stress regime. See Figure 9-5 for the locations and depth levels of datum-tracking points in the model. 239

Figure 9-20 Mohr’s circle diagrams showing stress variation with respect to the failure envelope for the fault under a strike-slip faulting stress regime. 240

Figure 10-1 Conceptual model of the hydrodynamic system of the Gloucester Basin. Dimensions are not to scale. Circles with plus signs indicate flow into the page; circles with dots indicate flow out of the page..... 248

Tables

Table 2-1 Hydrostratigraphic nomenclature for the Gloucester Basin (Source: Parsons Brinckerhoff, 2013). 11

Table 4-1 Estimated geothermal gradients (from Figure 4-3, Figure 4-4, and Figure 4-5) of the Gloucester Basin study area (combined data) and sub-regions. 46

Table 4-2 HCA Bore IDs, model layer assignment and HCA group assignments. 58

Table 4-3 Component weightings and proportion of explained variance from the Principal Components Analysis. Highlighted values show the largest positive and negative weighting for the first two components..... 60

Table 5-1 Construction details of the groundwater wells sampled as part of this study. TOC = top of casing; C-DEPTH = completion depth; SWL = standing water level; RSWL = relative standing water level. 74

Table 5-2 Measured field parameters and major ion analyses of the collected 22 surface water samples, 22nd February to 2nd March 2016. TDPG = total dissolved gas pressure... 77

Table 5-3 Measured field parameters and major ion analyses of the collected 26 groundwater samples, 22nd February to 2nd March 2016. TDPG = total dissolved gas pressure. 79

Table 5-4 Stable isotopes of water ($\delta^{18}\text{O}$ and $\delta^2\text{H}$), methane concentrations, $\delta^{13}\text{C}\text{-CH}_4$, $\delta^2\text{H}\text{-CH}_4$, dissolved gases (^4He , ^{20}Ne , ^{22}Ne , N_2 , O_2 , ^{40}Ar), ^{14}C , $\delta^{13}\text{C}$, ^{222}Rn , and ^3H analyses of the collected 22 surface water samples, 22nd February to 2nd March 2016. Note that not all tracers were measured on every sample..... 81

Table 5-5 Stable isotopes of water ($\delta^{18}\text{O}$ and $\delta^2\text{H}$), methane concentrations, $\delta^{13}\text{C}\text{-CH}_4$, $\delta^2\text{H}\text{-CH}_4$, dissolved gases (^4He , ^{20}Ne , ^{22}Ne , N_2 , O_2 , ^{40}Ar), ^{14}C , $\delta^{13}\text{C}$, ^{222}Rn , and ^3H analyses of the collected 26 groundwater samples, 22nd February to 2nd March 2016. Samples from coal monitoring wells have their Well ID underlined. Note that not all tracers were measured on every sample..... 83

Table 8-1 Chimney CLN parameters. 184

Table 8-2 Outline of the simulations using the different fault configurations, geostatistical permeability fields and the number of Connected Linear Networks (chimneys) in the model. 188

Table 8-3 Simulated steady-state flux (m³/day) through the single chimney for the different scenarios. (positive fluxes are upward). 209

Table 9-1 Summary of model properties. (1 mD corresponds to 7.5×10⁻⁴ m/d or 8.62×10⁻⁹ m/sec). IB = interburden; BU = Basal “basement unit. 222

Acknowledgements

The authors would like to acknowledge the Commonwealth Department of the Environment and Energy for funding the project “Research to improve treatment of faults and aquitards in Australian regional groundwater models to improve assessment of impacts of CSG extraction”. The report was subject to internal peer review processes during its development and benefitted from reviews undertaken by Dr. Rod Dann (Department of Environment and Energy), Dr. Emanuelle Frery (CSIRO Energy), Dr. Laurent Langhi (CSIRO Energy), Dr. Ludovic Ricard (CSIRO Energy), Dr. Praveen Kumar Rachakonda (CSIRO Energy), Mr. Paul Wilkes (CSIRO Energy), Dr. Heather Sheldon (CSIRO Mineral Resources), Dr. Aaron Davis (CSIRO Mineral Resources), Dr. Matthias Raiber (CSIRO Land and Water), and Dr. Luk Peeters (CSIRO Land and Water). We gratefully acknowledge the Flinders University staff Lawrence Burk, Angela London, and David Poulsen for their participation in the field investigations. Many thanks to AGL staff John Ross, Douglas Ferry, James Duggleby, Andrew Adorini, and Ben Eastwood for their help during the field investigations at Gloucester. Special thanks to John Williams, Chris Rumpf, and Ross Beasley (NSW Department of Primary Industry), Timothy Pippett (Alpha Geoscience), Duncan Massie (TerraTEM), Carolina Sardella (Parsons Brinkerhoff), and Bob Corbett (Gloucester Resources Limited) for providing support with the field investigations at Gloucester. UQ acknowledges Schlumberger for use of their Petrel software.

Abbreviations

Abbreviation	Description
CSG	Coal Seam Gas
CSIRO	Commonwealth Scientific and Industrial Research Organisation (Australia)
HSU	HydroStratigraphic Unit
masl	Metres above sea level
MC	Monte Carlo (sampling methodology)
mD	milliDarcy
MPa	MegaPascals
μD	microDarcy
NSW	New South Wales
OGIA	Office of Groundwater Impact Assessment (Queensland)
CDF	Cumulative Density Function
PDF	Probability Density Function
Psi	Pound per square inch
Qld	Queensland
TDS	Total Dissolved Solids
TEM	Time Domain Electromagnetic
TTPB	Tiedman Property Parsons Brinckerhoff

Glossary

Term	Description
Anastomosing Shear Splays	A strike slip fault with related splay faults in a branching structure
Aquifer	Rock or sediment in a formation, group of formations or part of a formation, which is saturated and sufficiently permeable to transmit quantities of water to wells and springs
Aquitard	A saturated geological unit that is less permeable than an aquifer and incapable of transmitting useful quantities of water. Aquitards often form a confining layer over aquifers
Coal seam	Individual layers containing mostly coal. Coal seams store both water and gas. Coal seams generally contain more salty groundwater than aquifers that are used for drinking water or agriculture
Coal seam gas	A form of natural gas (generally 95 to 97% pure methane, CH ₄) typically extracted from permeable coal seams at depths of 300 to 1000 m. Also called coal seam methane (CSM) or coalbed methane (CBM)
Confined aquifer	An aquifer that is isolated from the atmosphere by an impermeable layer. Pressure in confined aquifers is generally greater than atmospheric pressure
Confining pressure	The combined hydrostatic stress and lithostatic stress; i.e. the total weight of the interstitial pore water and rock above a specified depth
Darcy flow	Liquid flow that conforms to Darcy's law
Darcy's law	A constitutive equation that describes the flow of a fluid through a porous medium such as rock or soil
Depressurisation	The lowering of static groundwater levels through the partial extraction of available groundwater, usually by means of pumping from one or several groundwater bores or gas wells
Dewatering	The lowering of static groundwater levels through complete extraction of all readily available groundwater, usually by means of pumping from one or several groundwater bores or gas wells
Drawdown	A lowering of the water table of an unconfined aquifer or of the potentiometric surface of a confined aquifer, typically caused by groundwater extraction
Drill stem test	A procedure to determine the productive capacity, pressure, permeability or extent (or a combination of these) of a hydrocarbon reservoir, involving the circulation of drilling fluids and the use of inflatable bladders ('packers') to isolate the vertical extent of the test
Dual permeability	In a dual-permeability porous medium (reservoir, aquifer, aquitard), fluid flow occurs in both primary and secondary porosity systems
Effective porosity	The fraction of pores that are connected to each other and contribute to flow. Materials with low or no primary porosity can become very permeable if a small number of highly connected fractures are present
Facies	All lithological and sedimentological features of a particular sedimentary rock, from which the depositional environment may be inferred

Term	Description
Fault core	The fault core is composed of structural elements that accommodate the majority of fault displacement. The fault core is often represented by a low permeability, continuous clay smear or a deformation band shear
Fault damage zone	<p>Damage Zones are a result of brittle deformation along a fault zone where rocks are ground and crack in various orientations in response to stress. Some structures in damage zones are:</p> <ul style="list-style-type: none"> • Wing Cracks—Extension fractures associated with small amounts of displacement; • Horsetail Splay—Occur along larger faults and create a series of secondary pinnate shear fractures; • Synthetic Branch faults—When deformation at a fault tip causes shear of the same sense of the motion of the fault; and • Antithetic faults—when deformation at a fault tip causes shear of the opposite sense as the main fault. This creates rotation of the block in the damage zone.
Fault displacement	The offset between two sections of the same geological formation caused by uplift during or following fault activation
Fault throw	The vertical displacement caused by fault activation
Fault zone	The complete volume of rock deformed when lithospheric stresses cause two tectonic blocks to move in relation to one another; commonly comprised of two architectural elements - a fault core and damage zone
Geomechanical	Relating to the movement/expansion/contraction of soil and rock
Groundwater	Water occurring naturally below ground level (whether in an aquifer or other low-permeability material), or water occurring at a place below ground that has been pumped, diverted or released to that place for storage. This does not include water held in underground tanks, pipes or other works
Groundwater (single phase) flow model	A numerical solution to a partial differential equation used to describe the flow of water in the subsurface. Groundwater flow models involve the flow simulation of a single fluid phase (i.e. water). Common parameters used in groundwater flow models are hydraulic conductivity, specific yield and specific storage
Hydraulic conductivity	A coefficient of proportionality describing the rate at which a fluid can move through a permeable medium
Hydraulic gradient	The difference in hydraulic head between different locations within or between hydrostratigraphic units, as indicated by water levels observed in wells constructed in those units
Hydraulic head	The potential energy contained within groundwater as a result of elevation and pressure. It is indicated by the level to which water will rise within a bore constructed at a particular location and depth. For an unconfined aquifer, it will be largely subject to the elevation of the water table at that location. For a confined aquifer, it is a reflection of the pressure that the groundwater is subject to and will typically manifest in a bore as a water level above the top of the confined aquifer, and in some cases above ground level

Term	Description
Hydraulic pressure	The total pressure that water exerts on the materials comprising the aquifer. Also known as pore pressure
Hydrostratigraphic unit	A formation, part of a formation, or group of formations of significant lateral extent that compose a unit of reasonably distinct (similar) hydrogeologic parameters and responses
Interburden	Material of any nature that lies between two or more bedded ore zones or coal seams
Intrinsic permeability	The permeability of a given medium independent of the type of fluid present
Juxtaposition analysis	An assessment of the strata located directly across a fault plane from one another.
Lithospheric stress	Stress in the outer solid part of the Earth (lithosphere)
Lithological facies	A mappable subdivision of a stratigraphic unit that can be distinguished by its facies or lithology-the texture, mineralogy, grain size, and the depositional environment that produced it
Matrix (rock matrix)	The finer grained mass of rock material in which larger grains/crystals are embedded
Mohr - Coulomb failure envelope	The linear envelope that is obtained from a plot of the shear strength of a material versus the applied normal stress
Multi-rate well test (MRT)	Multi-rate well test is used to estimate the flow efficiency or skin factor to quantify formation damage and understand its impact on hydrocarbon production. Several stabilized flow rates and corresponding stabilized flowing bottomhole pressures can be obtain in this test.
Normal stress	The stress which acts perpendicularly to the plane to which a force has been applied
Permeability	The measure of the ability of a rock, soil or sediment to yield or transmit a fluid. The magnitude of permeability depends largely on the porosity and the interconnectivity of pores and spaces in the ground
Porosity	The proportion of the volume of rock consisting of pores, usually expressed as a percentage of the total rock or soil volume
Preferential flow	Preferential flow refers to the uneven and often rapid and short-circuiting movement of water and solutes through porous media characterised by small regions of enhanced flux (such as faults, fractures or other high permeability pathways), which contributes most of the flow, allowing much faster propagation of pressure differences and transport of solutes through that pathway
Radioactive isotope	Natural or artificially created isotope of a chemical element having an unstable nucleus that decays, emitting alpha, beta, or gamma rays until stability is reached
Recharge	The process whereby water (such as from rainfall runoff or irrigation) after percolating through the ground replenishes to the water table
Regional-scale groundwater flow models	Models that encompass an entire groundwater system, geological basin or other significant area of interest that extends well beyond the measurable influence of individual bores or borefields
Relative permeability	The permeability of a medium for a specific fluid relative to the intrinsic permeability for a porous medium containing more than a single fluid phase (e.g., air and water or oil, gas, and water)

Term	Description
Reservoir (hydrocarbon)	Porous or fractured rock formations that contain significant reserves of hydrocarbons. Naturally-occurring hydrocarbons such as crude oil or natural gas are typically trapped in source or host rocks by overlying low permeability formations
Robustness (of model predictions)	Insensitivity of model predictions to data outliers or other small departures from assumptions required by a predictive model, including the types of parametric distributions assumed
Saturated flow	Flow through a porous medium (such as soil or rock) in which the void space within the porous medium is entirely occupied by water (as opposed to water and gas)
Seismic	Relating to earthquakes or other vibrations of the earth and its crust.
Seismic lines/data and interpretation	Seismic Interpretation is the extraction of subsurface geologic information from seismic data. The seismic wavelet starts as the pulse of seismic energy generated by an energy source, it travels down through the earth, is reflected and travels back up to the surface receivers carrying the geological information with it. Seismic data is recorded into what is termed the time-domain. Several common processing routines transform the data into a new domain (such as depth), perform various operation and then the inverse routine is used to reverse the transform
Solute	The substance present in a solution. However, for convenience, water is generally considered the solvent (not the solute) even in concentrated solutions with water molecules in the minority
Stratigraphy	An arrangement of sedimentary, metamorphic and/or igneous rocks
Strike-slip	A fault in which rock strata are displaced mainly in a horizontal direction, parallel to the line of the fault
Tensile stress	A normal stress (negative compressive stress) which pulls apart the material on either side of a plane. Tensile stress greatly weakens rocks, reducing the amount of shear stress that is needed to produce failure in them
Transmissibility	Synonym for transmissivity. The hydraulic conductivity of an aquifer multiplied by the thickness of that unit
Transmissibility multiplier	Transmissibility multipliers account for the reduced or increased permeability for each cross-fault connection
Transmissivity	The rate at which a fluid is transmitted through a unit width of a hydrostratigraphic unit under a hydraulic gradient
Transtensional Regime	A tectonic regime where both extensional (normal faulting) and shear (strike slip faulting) forces affect the strain
Unconfined aquifer	An aquifer in which there are no confining beds between the zone of saturation and land surface
Unconventional gas	Natural gas found in a very low permeability rock, such as coal seam gas, shale gas, and tight gas. Unconventional gas such as coal seam gas is trapped in coal beds by adsorption of the gas molecules to the internal surfaces of coal. It cannot migrate to a trap and form a conventional gas deposit. This distinguishes it from conventional gas resources, which occur as discrete accumulations in traps formed by folds and other structures in sedimentary layers

Term	Description
Unlithified rock	Soft sediments that have little strength and are readily deformed under pressure
Upscaling	Upscaling is the process of transforming the detailed description of hydraulic parameters in a grid constructed at measurement scale to a coarser grid with less detailed description. It replaces a heterogeneous domain with a homogeneous one in such a way that both domains produce the same response under some upscaled boundary conditions
Well	Borehole in which a casing (e.g. steel piping) has been placed to restrict connection to specific ground horizons/depths

Symbols

Symbol	Brief description and unit of measurement
C	Cohesion [Pa]
c	Concentration [mgL^{-1} or BqL^{-1}]
c_i	Concentration in groundwater inflow [Bq L^{-1}]
d	Mean stream depth [m]
D_e	Effective diffusion coefficient [m^2/sec]
$D_{0,w}$	Free-water diffusion coefficient = 7.22×10^{-9} [m^2/s]
f	Factor chosen to represent a fault in dilation ($f = 1.0$) or compression ($f = 10^{-5}$).
F	Flux from the hyporheic zone [$\text{Bq m}^{-1} \text{s}^{-1}$]
F_m	Fault permeability multiplier [-]
g	Internal production rate of the tracer [$\text{cc STPg}^{-1}\text{year}^{-1}$]
g	Gravitational constant [$9.81 \text{ m}\cdot\text{sec}^{-2}$]
G	Geothermal gradient [$^{\circ}\text{C m}^{-1}$]
h	Hydraulic head [m]
H	Depth to calculating point for t [m]
k	Bulk permeability [mD or m^2]
k_c and k_f	Coal and interburden permeability [mD or m^2]
k_h	Horizontal permeability [mD or m^2]
k_v	Vertical permeability [mD or m^2]
K	Hydraulic conductivity [m day^{-1}]
k_g	Gas transfer velocity across the water surface [m day^{-1}]
K_h	Horizontal hydraulic conductivity [m day^{-1}]
K_v	Vertical hydraulic conductivity [m day^{-1}]
l	Groundwater flow rate per unit stream length [$\text{m}^3 \text{m}^{-1} \text{day}^{-1}$]
L	Rate of surface water loss by pumping or to groundwater [$\text{m}^3 \text{m}^{-1} \text{day}^{-1}$]
λ	Radioactive decay constant [day^{-1}]
n_e	Effective porosity [-]
φ	Friction angle [degree]
Φ	Porosity [%]
q	Darcy flux [m day^{-1}]
Q	Stream discharge [$\text{m}^3 \text{day}^{-1}$]

Symbol	Brief description and unit of measurement
ρ_b	Saturated rock bulk density [kg m^{-3}]
ρ_f	Fluid density [998.23 kg.m^{-3} at 20°C and 0.1 MPa for water]
ρ_g	Grain or rock density [kg m^{-3}]
(S_{Hmax})	<i>In-situ</i> horizontal stress [MPa]
τ_m	Maximum shear stress [MPa]
σ_n	Normal stress [MPa]
t	Temperature at the midpoint of the perforated interval [$^\circ\text{C}$]
t_f	Throw of a fault [m]
t_0	Mean annual surface temperature [$^\circ\text{C}$]
V	Linear fluid flux [m day^{-1}]
V_z	Vertical groundwater velocity [m year^{-1}]
w	Width of the river [m]
x	Distance in the direction of flow [m]
z	Elevation of the pressure gauge [m]
Z	Sample depth [m]

Executive summary

Background

The project “Research to improve treatment of faults and aquitards in Australian regional groundwater flow models to improve assessment of impacts of coal seam gas (CSG) extraction” focuses on method development to underpin the risk assessments associated with deep groundwater extraction and depressurisation from energy resource development. The project aims to develop methods and techniques that will improve the predictive capability of regional groundwater flow models used in this context, specifically with respect to the representation of faults and aquitards. The project has three components:

1. an examination of aquitards;
2. an examination of faults; and
3. an examination of the upscaling of aquitard and fault properties such that they can be adequately represented in regional groundwater flow models.

The objective of this research is to contribute to an improved conceptualisation, representation and parameterisation of aquitards and faults in groundwater flow models to reduce uncertainty in regional and local groundwater flow and pressure simulation.

Specifically, this report provides an overview of:

1. complementary methodologies for assessing fault properties in coal seam gas reservoirs and their impact on local and regional groundwater flow; and
2. numerical modelling based investigations of faults at regional scale and their influence on groundwater flow and solute migration from deep systems to shallow aquifers and surface water.

This report documents the methods and workflows that have been developed to improve the characterisation of subsurface rock properties, in particular faults, and how this informs developing regional scale groundwater flow models. The Gloucester Basin, NSW, was selected as case study area for investigating faults from local to regional scale, involving both field work and desktop subsurface studies. The field sampling was designed to both take advantage of existing bores and water courses, and focus on geophysical transects running perpendicular to the main north-south structural geological features such that there was an increased chance of identifying hydrodynamic signatures of upwards fluid migration along these structures. The field campaign included sampling well bores for water chemistry and dissolved gases, collection of atmospheric samples for methane, acquisition of shallow geophysics along certain transects, and a run of river surface water sampling campaign of Waukivory River and the Avon River for water chemistry and dissolved gases. The desktop

subsurface study used coal seam gas exploration well data and water bore records to constrain a conceptual model of the formation water hydrochemistry and hydrogeology. Well bore image logs were examined to determine *in situ* stress and small scale strain; seismic data was examined to interpret the fault zone architecture. From those investigations multiple lines of evidence were derived that formed the basis of a conceptual hydrogeological model that included fault zone architecture and its hydrodynamic properties.

Key Results

Evidence for near-surface expressions of geological faults (i.e. in the top 50 to 100 m) was derived from a shallow Time domain Electromagnetic (TEM) survey. Near-surface expressions of faults were identified in high resolution TEM data, with corresponding deeper fault traces being evident from analysis of seismic data. Analysis of environmental tracers (e.g. helium - ^4He) in the Avon and Waukivory Rivers and groundwater near inferred fault traces were indicative of a source of groundwater with a much longer residence time coming from greater depth and mixing with the shallow groundwater. This suggests that some of the helium is more concentrated in groundwater in the close vicinity of lineament features as a result of a higher fracture density and an existing inter-connection with flow pathways of increased residence time.

Inference of fault traces from the combination of near-surface geophysics and deeper seismic analysis, together with evidence from tracer analysis indicated the presence of both slow moving groundwater (i.e. diffusion-driven mass transport) and faster moving groundwater (i.e. advection-driven mass transport). The former was inferred from one-dimensional modelling of methane and helium profiles, while evidence of the latter was found in tracer hotspots along the Avon and Waukivory Rivers. Such a combined low and high velocity flow system was conceptualised at the local scale as a dual-permeability type rock. The majority of the interburden acts as a relatively low permeability rock (between 0.01 mD at depths of about 800 m and 100 mD at depths of about 200 m) where mass transport is governed by molecular diffusion. The fault zone with its damage zone acts as the more permeable rock (with permeabilities at least one to two order of magnitude higher than the unperturbed rock) with mass transport likely governed by advection (i.e. flowing water). The conceptual model of a dual permeability rock represents the fracture and matrix domain as separate continua. This conceptual model was confirmed at the regional scale based on analysis of hydraulic, salinity and structural geology data.

While the dual permeability conceptual model provides a simple yet plausible working hypothesis, several additional mixing processes have been identified. For instance, stable isotopes of water ($\delta^{18}\text{O}$ and $\delta^2\text{H}$) provided further insights into the various mixing processes between deeper and shallow groundwater and surface water. The groundwater samples from the major aquifer units showed some overlap and are isotopically lighter than the surface water samples and less enriched than the average weighted rainfall. The coal seam samples are far more depleted in stable isotopes than the alluvial samples indicating

groundwater recharge under different climatic conditions to present day. Overall, the patterns in stable isotopes of water are consistent with a binary mixing system between a surface water end-member and a groundwater end-member at the scale of the alluvial aquifer and adjoining interburden. Two hypotheses are put forward that could explain the observed isotope line. The first hypothesis assumes a process with overall low vertical groundwater advection velocity or spatially constrained flows, possibly linked to permeable fault zones. The second hypothesis, however, considers a dynamic alluvial aquifer setting, where solutes such as stable isotopes are continuously exchanged between surface water and groundwater by flood cycles and hyporheic processes. While each of these hypotheses separately could explain the observed features, a more likely explanation would involve a combination of the two hypotheses.

The presence of zones characterised by upward water movement nearby fault traces was further confirmed at the regional scale using well head and salinity data. At several locations in the Stratford area, fault traces existed where there appeared to be a closed hydraulic head high against the fault line at a certain stratigraphic interval indicating a source of formation water emanating from the fault. On the other (i.e. east) side of the same fault, downward groundwater flow was apparent due to a sink with a closed low head against the eastern side of the selected fault. At least two high total dissolved solids (TDS) areas separated by faults were identified. The fault separating the two high TDS zones may play a significant role in providing for groundwater discontinuity laterally but may also be a source of upwelling higher salinity formation water.

Further evidence of enhanced vertical hydraulic connection between the coal seam gas reservoirs and adjacent aquifers due to faults was obtained from an evaluation of resistivity and acoustic borehole image logs. In doing so the contribution of faults, fractures and present-day maximum horizontal principal stress orientations S_{Hmax} was assessed. By cross-plotting the *in-situ* horizontal stress S_{Hmax} and fracture orientations with measured permeability data, a causal relationship was found that may assist in predicting potential permeability pathways for fluid movement. Large variations in *in-situ* stress orientation, spatially as well as vertically within individual wells, further indicated a strong influence of local structures, i.e. fractures or faults.

Analysis of 3D seismic volumes showed a dominant north-south structural fabric with a local bend in the Stratford area. The Stratford and Waukivory areas are distinguished from one another by the difference in spatial fault morphology. In the Stratford area, faulting within the shallower section is characterized by a series of en-echelon displacements. These had been mapped previously as continuous faults. However upon closer examination many of these faults are seen to be discontinuous along strike with “en echelon” patterns consistent with shear deformation.

Fault damage zones, relay structures and fractures that enhance permeability are likely to have an observable influence on fluid flow. Therefore, characterising *in-situ* stress along with small scale fractures associated with seismically observable faults or areas of distributed strain in relays was shown to be a powerful method to demonstrate that the

Waukivory area displayed slightly increased permeability when fracture orientations are sub-parallel to the S_{Hmax} stress orientations. At a similar depth, interpreted permeability was an order of magnitude greater when fracture orientation is parallel or sub-parallel to S_{Hmax} orientation.

The combined desktop investigations and analysis of field data resulted in multiple lines of evidence regarding expressions of the impacts of fault hydraulic properties on local and regional groundwater flow. Based on this combined evidence, a regional scale conceptual model of the Gloucester Basin subsurface was developed, consistent with the local-scale dual-permeability conceptual model. Combinations of data suggestive of preferential upwards vertical fluid migration include:

1. the Stratford area with at least two wells indicating an upward hydraulic gradient and the TDS map for the shallow aquifer indicating two salinity plumes;
2. the Waukivory River with measured surface water methane and helium concentration anomalies that coincided with resistivity change in the TEM data that could be related to a fault; and
3. the Waukivory area where at least two wells indicated an upward hydraulic gradient and the TDS map for the shallow aquifer indicates an above background salinity plume.

The proposed conceptual model for the Gloucester Basin includes a series of bedrock coal zones and interburden with a bulk permeability of 1 mD or less. The upper part of the bedrock immediately beneath the alluvium is weathered and has an enhanced permeability in the 10s of mD. The alluvium has a permeability in the 100s of mD. The overall flow system is controlled by recharge at the high topographic eastern and western edges of the basin with discharge generally into the basin's central drainage. Given the overall permeability distribution, the bulk of the flux is within the alluvium and shallow weathered bed rock. The flux through the deeper part of the basin is focused in a few locations where the fault zone architecture provides slightly enhanced permeability (e.g., from 0.1 mD matrix permeability to 1 mD enhanced permeability). At some locations the fault segments form barriers to flow with hydraulic head discontinuities across them. At other locations certain fault segments and their associated damage zones provide slightly enhanced permeability relative to the host rock and thus focus flux upwards to shallower aquifers. At these locations upwelling groundwater may explain high salinity plumes from water emanating from a fault into a fresher water shallow aquifer. These same migration pathways may be locations of methane and helium migration that can be detected in the shallow aquifer or surface water.

Numerical groundwater flow simulations were undertaken for the Gloucester Basin to demonstrate the relationship between different fault properties and aquifer responses. Impacts of faults on groundwater flow were tested by modifying fault properties to represent high, medium, and low across-fault flow. Results showed that as the fault permeability decreased, the effect on heads became more evident with a sharp head contrast developing across the fault. Under the conditions of well-connected hydraulic conductivity (K) fields for the coal seam layers, this head build-up quickly dissipated in the

directions along the fault. Simulated anomalous head distributions were similar in nature to those measured in the field.

Field observations of salinity anomalies across the basin had been interpreted as “chimney-like” structures, i.e. highly localised preferential flow features associated with fault damage zones enhancing connectivity between deeper and shallower groundwater. By implementing such chimney features in the groundwater model, the magnitude of the flow through the chimney for the connected K field was shown to be similar in magnitude to independent mass balance estimates.

A final set of simulations involved three-dimensional (3D) numerical geomechanical deformation modelling to investigate the geomechanical effects of depressurisation in coal seams on the stability of a pre-existing fault (referred-to as fault reactivation potential). The sedimentary coal layers of the Gloucester Basin were subjected to simulated depressurisation from coal seam gas extraction to model the 3D distribution and partitioning of strains and stresses. By coupling geomechanical processes to flow modelling, the geomechanical deformation simulations were used to assess the dynamic behaviour of faults and the impact of pressure variation on flow pathways.

It should be noted that the findings from the case study analysis are specific to the Gloucester Basin geology; they may not be typical of coal basins more generally. In particular the bulk permeability of strata below the shallow weathered bedrock is very low (generally less than 1 mD). This means that the impact of fault sealing (i.e., permeability reducing mechanisms in faults) is less important since the bulk permeability of the matrix is so low already. In the case of the Gloucester Basin, it is the locations of fault processes that locally enhance permeability that become important for regional groundwater flow. In other basins the reverse may be true. It is therefore important to look at this report (and its support reports) as identifying a wide range of possible fault influences on permeability and a wide range of methodologies to characterize faults and estimate their rock properties that are transferable to many basins. The Gloucester case study represents an example of how the workflows can be applied; however a meaningful application of workflows needs to be tailored to the particular characteristics of the rocks in each case. This includes determining which aspects of the generic workflows are most important in a particular geological setting, the availability of data and the maturity of the Coal Seam Gas development

Conclusions and Recommendations

Main conclusions from the near-surface geophysical investigations and deep seismic analysis are:

1. Conjunctive analysis of high-resolution Time domain Electromagnetic data and deep seismic survey data provided evidence for respectively near-surface expressions of faults and deeper fault traces that are likely connected;

2. At locations where inferred fault traces intersected with the Avon and Waukivory Rivers, groundwater appeared to be originating from greater depths with a much longer residence time and some mixing with the shallow groundwater; and
3. The spatial coverage of near-surface geophysical investigations could be improved by using specialised airborne electromagnetic systems that collect high-resolution data over large areas economically,

Conclusions regarding the hydrochemical investigations in surface waters, shallow and deep groundwater are summarised as follows:

1. a similar chemical composition (Na-HCO₃-Cl or Na-Cl water type) for surface water and shallow alluvial aquifer samples indicated a highly connected surface water-groundwater system with considerable mixing; the only distinctive difference between groundwater samples from the interburden and coal seams (Na-HCO₃, Na-HCO₃-Cl and Na-Cl water types) and the alluvial aquifers is the higher concentration of Ca and Mg for the latter;
2. the coal seam samples are far more depleted in stable isotopes than the alluvial samples indicating groundwater recharge under different climatic conditions to present day;
3. tritium results show that most of the groundwater samples within the study area are more than 50 years old, while analysis of ¹⁴C and ⁴He suggests that the deeper groundwater (interburden and coal seams) has an apparent groundwater age that is greater than approximately 30,000 years;
4. based on a one-dimensional advection-dispersion transport model interpretation of helium and methane depth profiles, an upward vertical advective or diffusive flux for methane and helium could occur through the interburden. Even in the absence of preferential flowpaths via faults and fractures, a small methane and helium flux through the interburden matrix is plausible; and
5. the methane concentration, stable isotopes of methane, hydrochemistry, stable isotopes of water, noble gases and apparent age tracer data identified locations of the surface water and the shallow alluvial aquifer system within the study area that are likely to be influenced by structural geological features, in particular preferential flow paths along faults between the deeper coal seams.

Conclusions from an analysis of hydraulic and structural geology data are summarised as follows:

1. on the basis of regional scale well head and salinity data, fault zones were shown to produce locally upward water movement in some areas whereas at other locations fault traces are coincident with locally downward groundwater flow. Also, based on the head observations certain fault locations seemed to behave hydraulically as a barrier to east-west flow across the fault;

2. the influence of local structures such as faults or fault zones is expressed by large variations in in-situ stress orientation observable on image logs;
3. the dominant fracture orientations in most of the wells within the Waukivory area are parallel or sub-parallel to the maximum horizontal principal stress orientation SHmax. The higher fracture density and multiple fracture orientations within some of the Waukivory wells develops the conditions conducive to creating pathways for fluid movement in the shallower aquifers;
4. plumes of high salinity water observed in an area with fault traces are indicative of locations with upwelling groundwater. A possible conclusion is that certain fault segments and their associated damage zones provide a slightly enhanced permeability relative to the host rock and focus fluxes upwards to shallower aquifers;
5. from a methodological point of view, the integrated analysis of hydraulic, chemical, and structural geology data has proven valuable in developing a data-driven conceptualisation that can be implemented in a groundwater flow model for hypothesis testing.

The regional-scale groundwater flow simulations provided the following conclusions:

1. the degree to which coal seam layers are connected in space has a direct and profound impact on the head build-up across faults and on the distance over which this head build-up dissipates in the directions along the fault;
2. wherever high permeability zones form connected pathways, drawdown was focussed and extended laterally within the connected pathways. For the less connected fields, the drawdown is more diffuse. This underscores the need that the characterisation of the hydraulic conductivity of hydrogeological formations should include establishment of the degree of lateral connectivity as a basis for realistic groundwater flow simulations in which such spatial correlations are implemented;
3. the faults included in the groundwater flow simulations had no material impact on the maximum drawdown in the fractured rock or alluvial aquifer, in part because they were sufficiently far from the depressurisation zone (about 1 km), and in part because only the few large faults were included (all at a considerable distance from the well field). Several smaller faults and disturbed zones were shown to be present in the area, however, they were not included in the model; and
4. the transferability of the current methods to other faulted areas has not been explicitly tested, although the novel numerical modelling tool for incorporation of fault conceptualisations in groundwater flow models is expected to be applicable to many other basins. The method provides a sound basis for predicting hydraulic and/or chemical expressions of faults and their subsequent verification using the previously discussed suite of hydraulic, chemical, and structural geology data. However, further testing is required to get better understanding of the computational limits of such models for large-scale applications, and under which

circumstances it is equally appropriate to simulate faults by the much more cost-effective equivalent porous media approach.

Key conclusions from the present geomechanical modelling are:

1. Under static tectonic conditions, depressurisation in coal seams leads to important stress alterations. In models with reverse-faulting (i.e. the dominant stress regime in eastern Australia) or strike-slip faulting stress regimes, shear stresses decrease as the result of depressurisation;
2. Based on the conventional Mohr-Coulomb elastic-plastic theory, failure in the coal and fault is unlikely under reverse-faulting or strike-slip faulting stresses due to the combined effects of shear stress decrease and effective stress increase; and
3. In the present geomechanical models with reverse-faulting, normal-faulting or strike-slip stress conditions, no geomechanical failure in coal strata or fault reactivation was observed.

Conclusions regarding methodological developments:

1. Through the case study a new methodology of integrating different existing techniques was developed (i) that was successful in deriving multiple lines of evidence about hydraulic-chemical expressions of faults, (ii) which was used for fault conceptualisation, and (iii) that is verifiable through numerical groundwater flow modelling; and
2. To successfully apply these workflows to any particular case study one needs to consider the geology and available data and the problem trying to be addressed and then select the most fit for purpose combination of tools and methods that has the best chance of success.

1 Introduction¹

1.1 Faults, aquitards and modelling project: overall goals

Coal seam gas production and coal mining have the potential to affect both surface water and groundwater resources and their associated ecosystems (Barrett et al., 2013). Groundwater extraction is typically required for coal mining (dewatering) and coal seam gas production (depressurisation) (Moore, 2012). Almost all coal seam gas production, and a large proportion of coal mining, occurs at depths from which the water resource impacts are within groundwater systems. The rate and extent of pressure decline and propagation is strongly linked to the continuity and distribution of low permeability geobodies and structural features such as aquitards (Turnadge et al., 2018a, b) and faults (Underschultz et al., 2018). Forecasting impacts puts a high level of reliance upon accurate characterisation, simulation, and forecast of groundwater flow and pressure change to inform planning and approval decisions (Turnadge et al., 2018c).

This project focuses on developing methods and workflows that improve the characterisation of subsurface rock properties, in particular faults and aquitards, and then meaningfully incorporate them into regional groundwater flow models. Recent research, discussion with the Independent Expert Scientific Committee on Coal Seam Gas and Large Coal Mining Development (IESC) and consultation with industry stakeholders identified the need for a project to specifically address the following three issues. Each issue forms a component of this research project.

1. **Aquitards**

Improve characterisation and representation of aquitards in regional-scale groundwater flow model, by improved characterisation of vertical hydraulic conductivity and its spatial heterogeneity at a spatial scale commensurate with the scale of cellular flow models. This work has been discussed in Smith et al. (2018) and Turnadge et al. (2018a).

2. **Faults**

Review of conceptual representations of different groundwater flow conditions associated with faults in sedimentary basins. This review is available from Underschultz et al. (2018).

¹ Contribution authors: D Mallants

Improve methods for determining geological fault properties and their representation in regional groundwater flow models (this report).

Improve conceptualisation, representation and parameterisation of faults in regional groundwater flow models to reduce uncertainty in regional and local groundwater flow and pressure simulation (this report).

Investigate faults at various spatial scales and their influence on potential for propagation of depressurisation to adjacent aquifers and surface water systems (this report).

3. **Modelling**

Provide a comprehensive overview of aquitard and geological fault simulation approaches in regional scale assessments of coal seam gas extraction impacts. This review is available from Turnadge et al. (2018a).

Improve techniques to represent faults in numerical models for regional groundwater application. This work has been discussed in McCallum et al. (2018).

Improve conceptualisation, representation and parameterisation of aquitards in groundwater flow models to reduce uncertainty in regional and local groundwater flow and pressure simulation (Turnadge et al. 2018b).

Based on improved understanding of the most appropriate approach to include aquitards and faults in groundwater modelling for predicting impacts of CSG extraction, guidance will be provided on:

- various methods, their strengths and limitations, including improved characterisation, conceptualisation, and representations of aquitards and faults in regional groundwater flow models for predicting potential impacts of CSG; and
- how different data types and their spatio-temporal distribution contribute to constraining models of groundwater flow. Guidance on usefulness of upscaling techniques, depending on questions being asked and specifics of the local hydrogeology.

1.2 Fault component of the project

The purpose of the fault component of this project is to demonstrate complementary methods for the characterisation of faults and the way they are included in regional groundwater flow models with a particular interest in the assessment of impacts from CSG extraction on groundwater and surface water. The detailed characterisation of fault zones requires:

- the development of a methodology and workflow for estimating fault zone architecture and hydraulic properties;

- a case study application as an example that includes an integrated analysis of field data (Sections 3 to 7 of this report); and
- a numerical modelling component (Section 8 of this report).

A broad range of these are largely described by Underschultz et al. (2018). It should be noted that the most appropriate methodologies and workflows from this broad range, for application to a particular geological scenario may be quite different.

The Gloucester Basin, NSW, was selected as an example case study area for the fault investigations. Data was compiled from industry reports and from a dedicated field investigation designed, planned and executed as part of this project. As part of the fieldwork component, the following items have been undertaken:

1. Analysis of hydrogeology/hydrochemistry, hydraulic and groundwater age data for exploring evidence, or potential evidence (where available), of the influence of geological structure features on baseline groundwater flow processes (pre-resource development); and
2. Analysis of image logs and seismic data to infer the presence of fault zones and their most likely hydraulic function (barrier, conduit, or a combination).

As part of the numerical modelling component, the analyses focuses on testing the significance of faults and their parameterisation on the predictions of regional groundwater flow models (e.g., under what circumstances do faults significantly control local-scale and regional-scale groundwater flow?).

1.3 Project study area: Gloucester Basin

The Gloucester Basin was chosen as a case study example area for this investigation as CSIRO had already developed a hydrogeological understanding of the Gloucester subregion (for their Bioregional Assessment Programme, see Hodgkinson et al. [2014], McVicar et al. [2014], Peeters et al. [In Prep]) and hence it was an opportunity to:

- 1) build upon existing information; and
- 2) develop and test methods for determining impacts of faults zones on local and regional groundwater flow using a combination of pre-existing and new field data.

The availability of high quality data at sites investigated by AGL (the Tiedman Property and the Waukivory River study site) were also an important selection criteria. The data used in this project has two main sources:

- Pre-existing data on the Gloucester subregion collated from the DIGS database and data provided by AGL; and
- New data collected from field investigations by the project team.

1.4 References

- Barrett DJ, Couch CA, Metcalfe DJ, Lytton L, Adhikary DP and Schmidt RK (2013). Methodology for bioregional assessments of the impacts of coal seam gas and coal mining development on water resources. A report prepared for the Independent Expert Scientific Committee on Coal Seam Gas and Large Coal Mining Development through the Department of the Environment. Department of the Environment, Australia.
- Hodgkinson JH, Pinetown KL, Wilkes PG, McVicar TR and Marvanek SP (2014) Coal and coal seam gas resource assessment for the Gloucester subregion. Product 1.2 for the Gloucester subregion from the Northern Sydney Basin Bioregional Assessment. Department of the Environment, Bureau of Meteorology, CSIRO and Geoscience Australia, Australia.
- McCallum J, Simmons C, Mallants D and Batelaan O (2018). Simulating the groundwater flow dynamics of fault zones. MODFLOW Un-Structured Grid: A comparison of methods for representing fault properties and a regional implementation. School of the Environment, Flinders University, South Australia.
- McVicar TR, Langhi L, Barron OV, Rachakonda PK, Zhang YQ, Dawes WR, Macfarlane C, Holland KL, Wilkes PG, Raisbeck-Brown N, Marvanek SP, Li LT and Van Niel TG (2014). Context statement for the Gloucester subregion. Product 1.1 from the Northern Sydney Basin Bioregional Assessment. Department of the Environment, Bureau of Meteorology, CSIRO and Geoscience Australia, Australia.
- Moore T (2012). Coalbed methane: A review. *International Journal of Coal Geology* 101: 36-81.
- Peeters LJM, Dawes WR, Rachakonda PR, Pagendam DE, Singh RM, Pickett TW, Frery E, Marvanek SP and McVicar TR (In Prep) Groundwater numerical modelling for the Gloucester subregion. Product 2.6.2 for the Gloucester subregion from the Northern Sydney Basin Bioregional Assessment. Department of the Environment and Energy, Bureau of Meteorology, CSIRO and Geoscience Australia, Australia.
- Smith S, Mathouchanh E and Mallants D (2018). Characterisation of fluid flow in aquitards using helium concentrations in quartz, Gunnedah Basin, NSW, prepared by the Commonwealth Scientific and Industrial Research Organisation (CSIRO), Canberra.
- Turnadge C, Mallants D and Peeters L (2018a). Overview of aquitard and geological fault simulation approaches in regional scale assessments of coal seam gas extraction impacts, prepared by the Commonwealth Scientific and Industrial Research Organisation (CSIRO). Canberra.
- Turnadge, C, Esteban, L, Emelyanova, I, Nguyen, D, Pervukhina, M, Han, T, Mallants, D (2018b). Multiscale aquitard hydraulic conductivity characterisation and inclusion in groundwater flow models: Application to the Gunnedah Basin, New South Wales,

prepared by the Commonwealth Scientific and Industrial Research Organisation (CSIRO). Canberra.

Turnadge C, Mallants D and Peeters L (2018c). Sensitivity and uncertainty analysis of a regional-scale groundwater flow system stressed by coal seam gas extraction, prepared by the Commonwealth Scientific and Industrial Research Organisation (CSIRO), Canberra.

Underschultz J, Esterle J, Strand J and Hayes S (2018). Conceptual representation of fluid flow conditions associated with faults in sedimentary basins. Prepared for the Department of the Environment by The University of Queensland Centre for Coal Seam Gas, Queensland.

2 Gloucester basin case study description²

2.1 Introduction

The investigations aimed at improving characterisation and conceptualisation of faults for use in regional groundwater flow models are firstly grounded in a report on the “Conceptual representation of fluid flow conditions associated with faults in sedimentary basins” (Underschultz et al., 2018). This report provided a literature review on particular groundwater flow features caused by geological faults and an overview of current fault analysis techniques that can be applied to estimate the hydraulic properties of faults in various geological scenarios. The learnings summarised by Underschultz et al. (2018) were subsequently incorporated into the groundwater modelling flow study “Simulating the groundwater flow dynamics of fault zones” (McCallum et al., 2018). These authors explored and implemented novel methodologies for incorporating current fault characterisation of both fault zone architecture and associated hydraulic properties into functional regional groundwater flow models. Such models can then be used as integrators of various data types to test, in a first instance, plausible conceptual models by comparing model predictions with field observations. The aim of such comparison is primarily to constrain the conceptual model, and possibly to constrain a plausible range of hydrogeological system parameters.

The main objective of this study is to identify, for a case study example, those lines of field-based evidence that would i) capture any effects of geological faults on groundwater heads, chemistry, and temperature, ii) allow developing conceptual models of a groundwater system with presence of faults, and iii) serve as “ground truthing” of numerical modelling methodologies describing flow behaviour within fault zones in a regional groundwater flow model. To this end a case study area was sought where sufficient data was available to test the fault related groundwater flow concepts. The Gloucester Basin of New South Wales was selected as a preferred case study for the following reasons:

- Previous work on the structural geology and hydrogeology had been undertaken by the CSIRO as part of the Bioregional Assessments Programme (McVicar et al., 2014). As a result a considerable database previously compiled was accessible to serve as a starting point from which to develop a dedicated and targeted field investigation;
- The Gloucester Basin contains a reasonable quantity of data, including coal exploration holes, groundwater monitoring bores, historical oil and gas and modern CSG exploration wells, a number of consultant reports on the geology, hydrogeology, surface water hydrology, and seismic data including a modern 3D seismic volume

² Contributing authors: J Underschultz

collected by AGL. Additional public domain geological data and reports are available from the NSW Department of Industry Resources and Energy DiGS database;

- Whilst there have been open pit coal mine developments, and coal seam gas exploration and pilot testing (Hodgkinson et al., 2014), there has been no significant oil and gas development activity so far³ meaning that the basin is amenable to understanding near baseline conditions (i.e. unaffected by depressurisation of the coal seam target formations);
- The geography provided reasonable access for field work involving collecting surface-based geophysical data and water bore, surface water and atmospheric sampling; and
- The Gloucester Basin is intensely faulted making it a test case area with a high likelihood to detect the effects of faults on groundwater heads and chemistry.

2.1 Resource exploration history

The Gloucester Basin is a relatively small (approximately 10 km × 40 km) Permian basin (Figure 2-1) within the broader Southern New England Fold Belt (Figure 2-2), which probably opened in response to the transtensional regime that also caused extension in the Sydney-Gunnedah-Bowen basin systems. It represents a broadly synclinal structure and contains both coal and hydrocarbon resources (Figure 2-1 and Hodgkinson et al., 2014), but is highly deformed with significant E-W shortening and intense faulting recording multiple deformation episodes (Ward et al., 2001).

Although the Gloucester Basin has been known for its coal resources since the late 1800's, a stratigraphic definition was only first proposed by Loughnan (1954). During the 1970's and early 1980's there was an active coal exploration and appraisal program of mapping, and drilling bores, with Noranda Australia drilling in excess of 300 shallow holes and BMI Mining Pty Ltd with Esso Resources drilling some 990 open cut holes (Lucas Energy, 2007) resulting in BMI Mining Pty. Ltd. defining some 20 million tonnes of saleable coal. In 1982, liquid hydrocarbons from both coal and interburden zones were found in a well intersecting the Durallie Rd, Speldon and Buckets Way formations. Esso Australia investigated the nature of the oil (Thornton, 1982; Burns, 1982) and discovered the oil to be C9-30, of terrestrial source, biodegraded and occurring between approximately 50 and 300 m depth. This spurred a new exploration phase in the 1980's that included a seismic acquisition program and the drilling of 93 wells, some which obtained core (Hughes et al., 1984).

³ In February 2016, AGL announced it would not proceed with the Gloucester Gas Project.

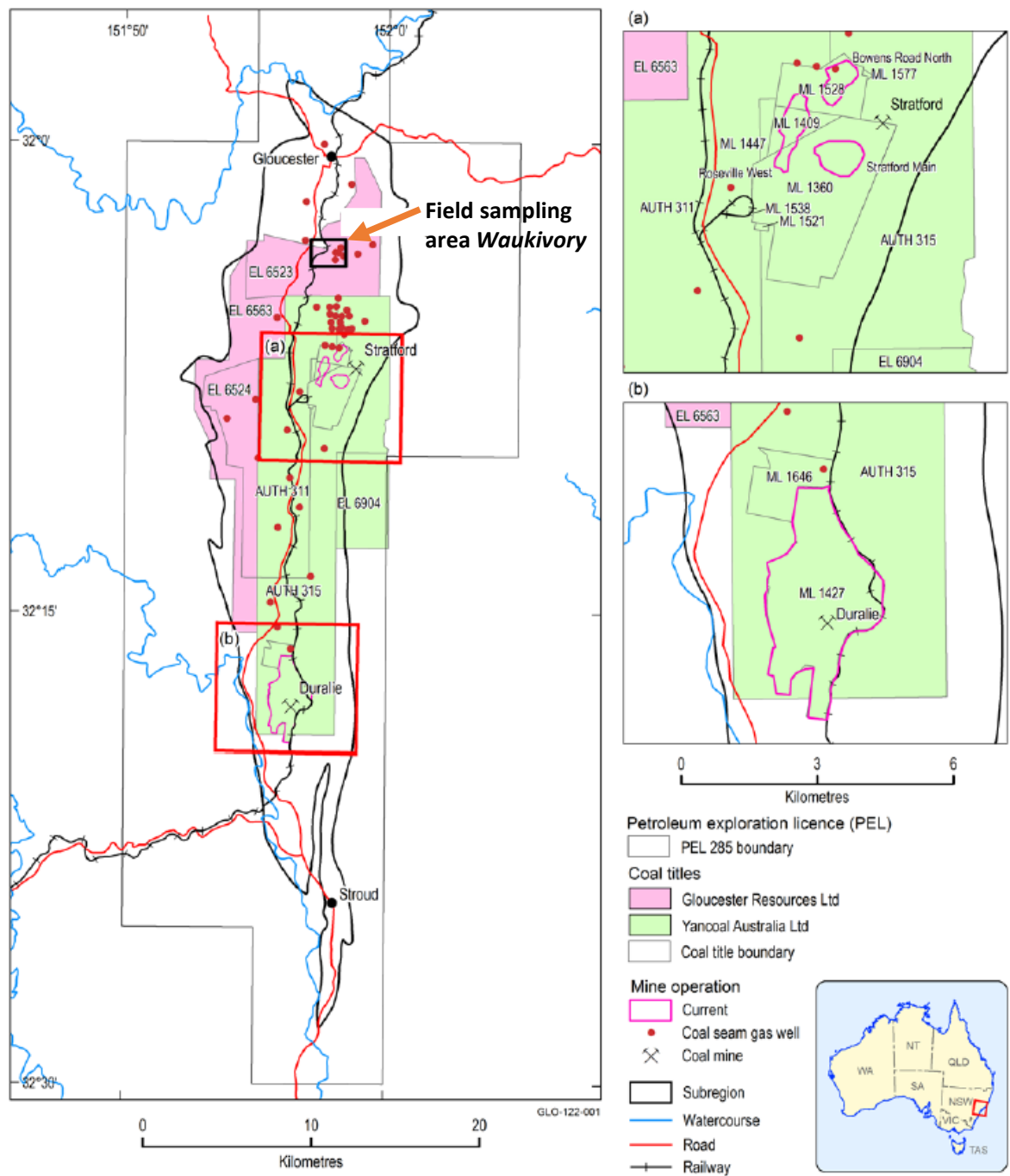


Figure 2-1 Locations of open-cut mining (identified by owner), Petroleum Exploration Licence 285 (PEL 285), and field sampling area “Waukivory” in the Gloucester subregion (Modified from: Hodgkinson et al., 2014).

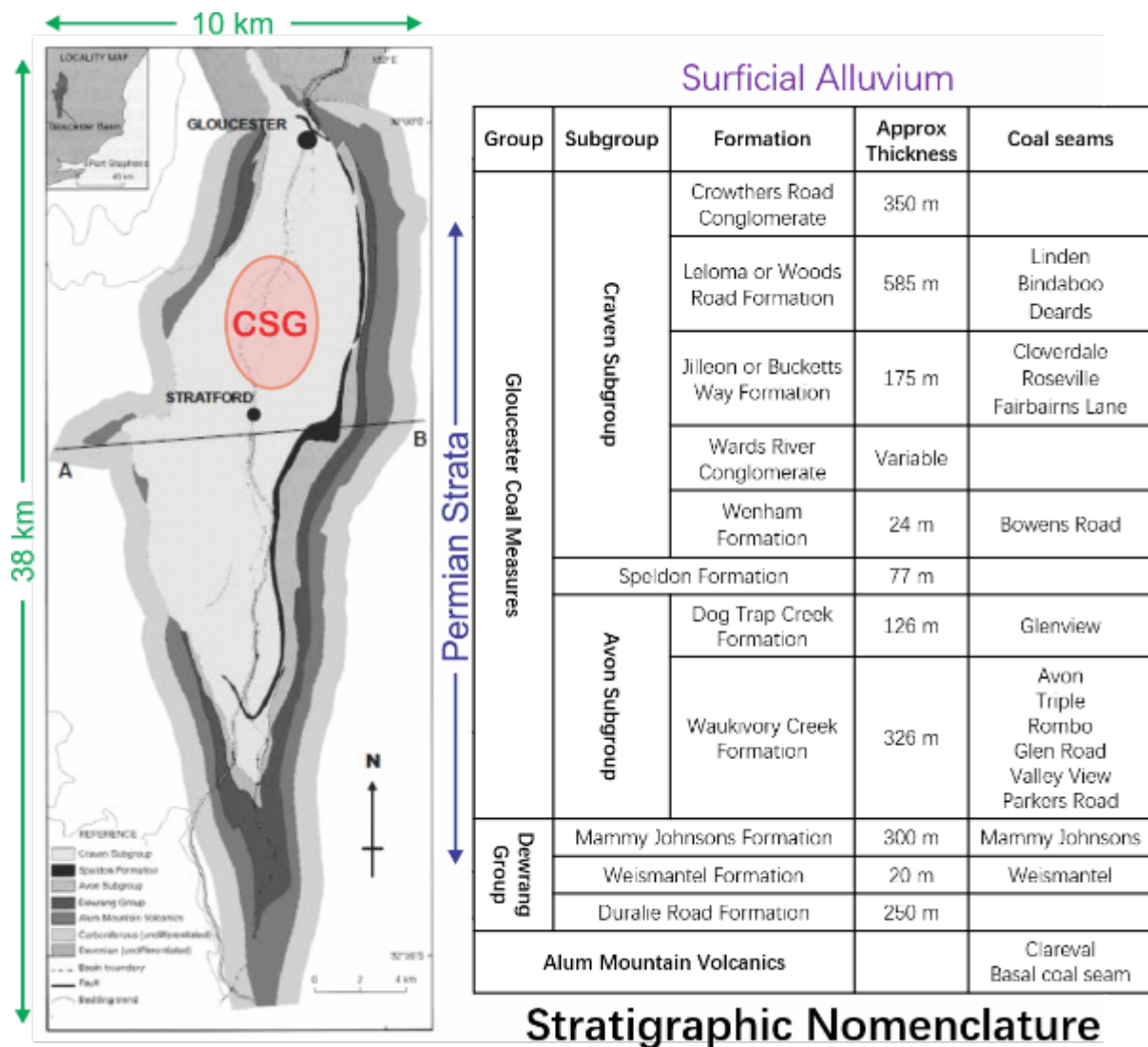


Figure 2-2 Base map of the Gloucester Basin (left) with the region of CSG appraisal indicated in red. Right: the stratigraphic nomenclature for the Gloucester Basin (Modified from: Ward et al. [2001] and Weber and Smith [2000]).

Analysis of the new data (Hughes et al., 1984) suggested that the Gloucester Basin was characterised by:

- A complexly faulted steeply dipping eastern margin;
- A less complexly faulted but steeply dipping western margin;
- A relatively flat lying central portion;
- Containing source rocks that have generated hydrocarbons widespread across the basin and these hydrocarbons were mobile; and
- Little well preserved porosity and permeability other than that associated with faults and fractures.

The next economic exploration activity in the Gloucester Basin was a geothermal energy investigation in the late 2000's that included the evaluation of existing wells and the drilling of some new exploration bores. Finally, since 1993 a phase of CSG exploration saw Pacific Power and the Gloucester joint venture (Lucas Energy Pty Ltd (Lucas) and Molopo Australia Limited (Molopo)) drill 22 wells (Lucas Energy, 2007) followed by AGL who drilled and tested 15 wells by 2014 designed to characterise the coal seam gas potential (Hodgkinson et al., 2014). This investigation involved 200 km² of coal-bearing strata, targeting 11 major coal seams of greater than 2.5 m thickness and an average total thickness of 30 to 60 m (Hodgkinson et al., 2014).

The Gloucester Basin stratigraphy (Figure 2-2) is floored by Devonian and Carboniferous volcanics. The Permian section begins with the Alum Mountain Volcanics that also include clastic sediments and coal zones. Overlying is a series of Early Permian coal members with variable interburden of mudstone, siltstone and sandstone that together make up the Dewrang Group. The Late Permian Avon Subgroup coal measures overly the Dewrang Group. The Avon Subgroup consists of nine coal members with variable interburden of mudstone, siltstone and sandstone. The overlying Speldon Formation is a sandstone with marine influences. The overlying Craven Subgroup contains eight coal measures with sandstone and siltstone interburden topped by the Crowthers Road Conglomerate. The Avon and Craven Subgroups contain the economically interesting CSG resources that have been tested by AGL (see Figure 2-2). A Quaternary alluvium associated with the current surface drainage covers much of the region.

2.2 Pre-existing hydrogeological conceptualisation

As part of the due diligence work of AGL in the evaluation of the coal seam gas potential, a number of hydrogeological evaluations were commissioned to establish the baseline conditions of the region. Two reports "Gloucester Basin stage 1 gas field development project: Preliminary assessment and initial conceptual hydrogeological model" by SRK (2010) and "Phase 2 groundwater investigations" by Parsons Brinckerhoff (2012) form the key data and analysis of the Gloucester Basin hydrogeological conceptualisation. From this work there was recognition that faults may play an important role in hydraulic communication (or lack thereof). Thus a study was commissioned by AGL on "Hydrogeological Investigation of a strike slip fault in the northern Gloucester Basin" by Parsons Brinckerhoff (2013).

The generalized hydrostratigraphy as defined by Parsons Brinckerhoff (2013) is shown in Table 2-1. Note that the alluvium and a layer of fractured bedrock form the upper two aquifers. Below that, the coal measures are treated separately from the interburden.

Table 2-1 Hydrostratigraphic nomenclature for the Gloucester Basin (Source: Parsons Brinckerhoff, 2013).

Unit	Aquifer Type	Formation name	General lithology	Hydraulic characteristics
Alluvium	Semi-confined, clay capped, porous, granular	Quaternary alluvium	Clay/mixed gravels	Heterogeneous, highly variable permeability associated with varying lithology
Shallow Rock (<150m)	Semi-confined, fractured rock	Upper Permian Coal Measures, Alum Mountain Volcanics	Interbedded sandstone/siltstone with bedding plane fractures	Heterogeneous, high and low permeability domains associated with fault zones and fracturing
Interburden	Confined, fractured rock	Upper Permian Coal Measures	Interbedded indurated sandstone/siltstone and claystone	Low permeability associated with sparse fractures, permeability decreases with depth
Coal Seams	Confined, fractured rock	Upper Permian Coal Measures	Coal/shale	Low permeability associated with cleating and fractures in coal seams, permeability decreases with depth

The Parsons Brinckerhoff conceptual model (2013) shows a schematic cross section of the Gloucester Basin that indicates faulted bedrock consisting of Permian coal measures and interburden with an upper weathered “Shallow Rock” aquifer and an alluvial aquifer as part of a closed hydrogeological system (Figure 2-3). The alluvial aquifer has a limited lateral and vertical extent (15 m thick or less) as it has developed in close proximity to the Gloucester and Avon Rivers in the north and the Karuah River in the south but is connected to a geographically widespread fractured bedrock aquifer that together form the upper unconfined aquifer system for the basin. High topography on the eastern and western edges of the basin impose a gravity driven flow system with discharge into the alluvium and surface drainage system (Avon River) that trends north-south (perpendicular to the line of section) in the middle axis of the basin (Figure 2-3). The water table is marked by the light blue dashed line near the land surface and the forecast piezometric surface for the “post production” coal zones is shown by the dark blue dashed line. Ward and Kelly (2013) presented a conceptual hydrodynamic cross section that described the gravity driven flow system with indicative formation water residency times for the various flow paths (Figure 2-4). While this presents a useful overall conceptual model as a starting point of further investigations, it obviously lacks detail of the geological influences that define fluid migration pathways in the basin.

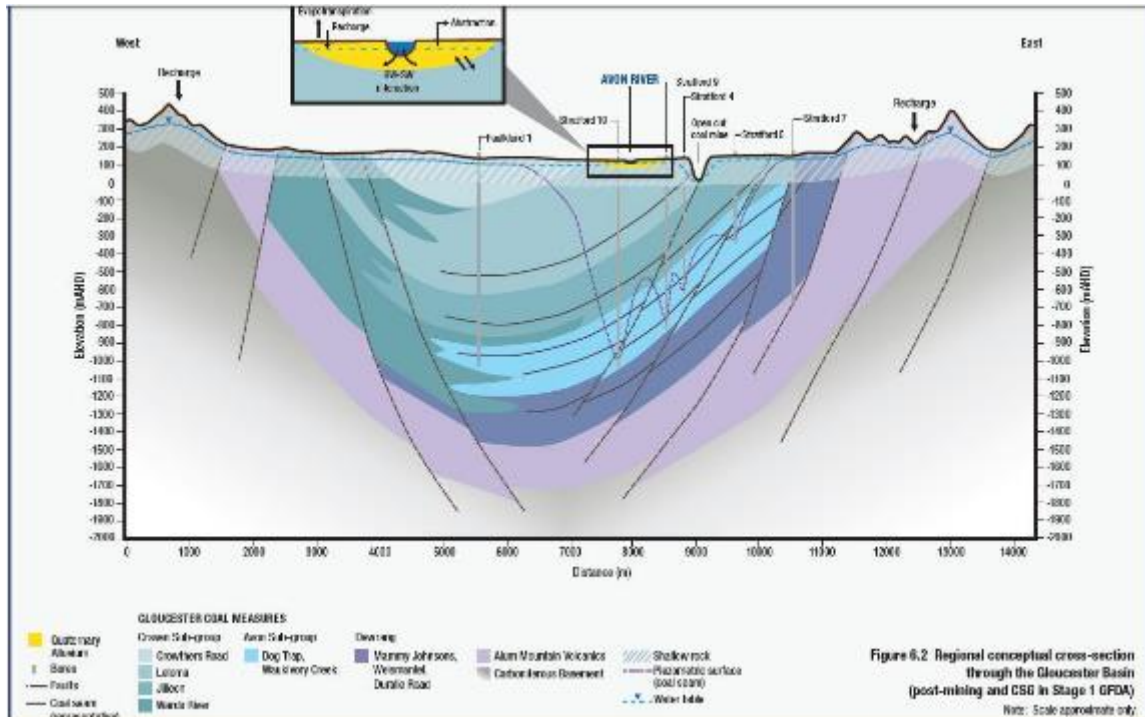


Figure 2-3 Schematic west-east cross section of the Gloucester Basin. Note the small area covered by the Quaternary alluvial aquifer (Source: Parsons Brinckerhoff [2013]).

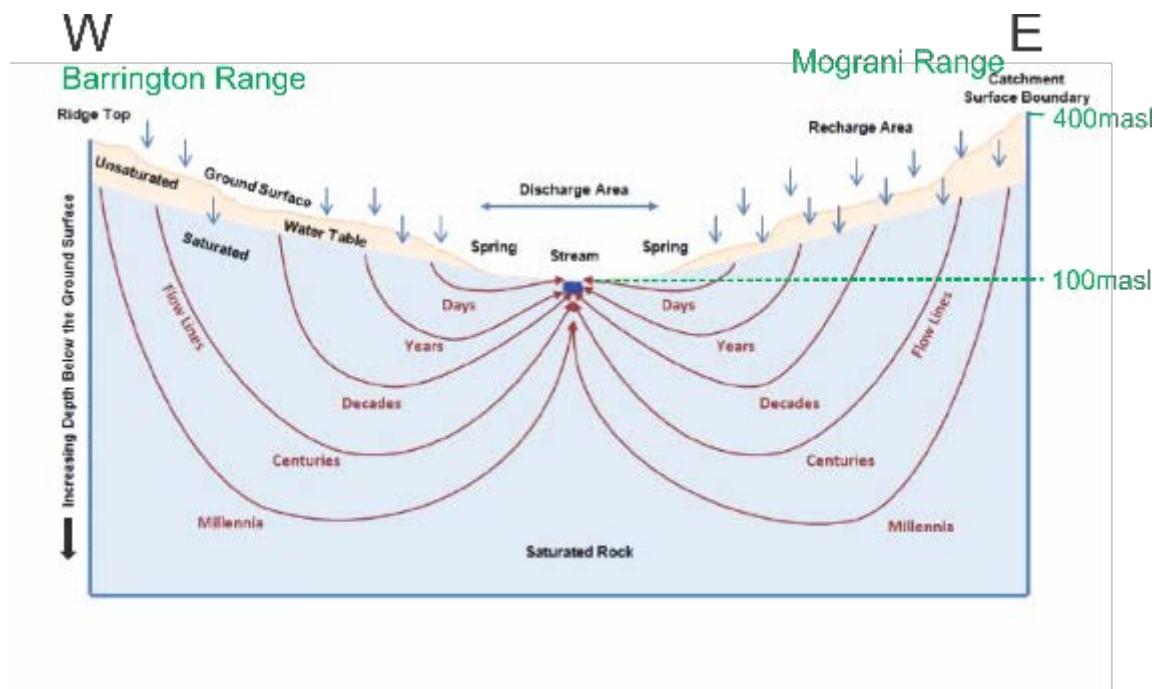


Figure 2-4 Conceptual hydrodynamic cross-section of the Gloucester Basin indicating the gravity driven flow systems and resident time for formation water on various flow paths (Source: Colin et al. [2013], modified from Winter et al. [1998] and Waller [2013]).

In plan view, Parsons Brinckerhoff (2013) present a hydraulic head distribution for the shallow most (i.e. alluvial plus fractured bedrock) aquifer (Figure 2-5). This supports the

notion of recharge from the high topography regions on the western and eastern edges of the basin discharging to the central surface drainage. From the central area groundwater flows north in the upper Gloucester Basin and south in the lower Karuah River Basin as a result of the groundwater divide in the central latitudes of the basin (Figure 2-5).

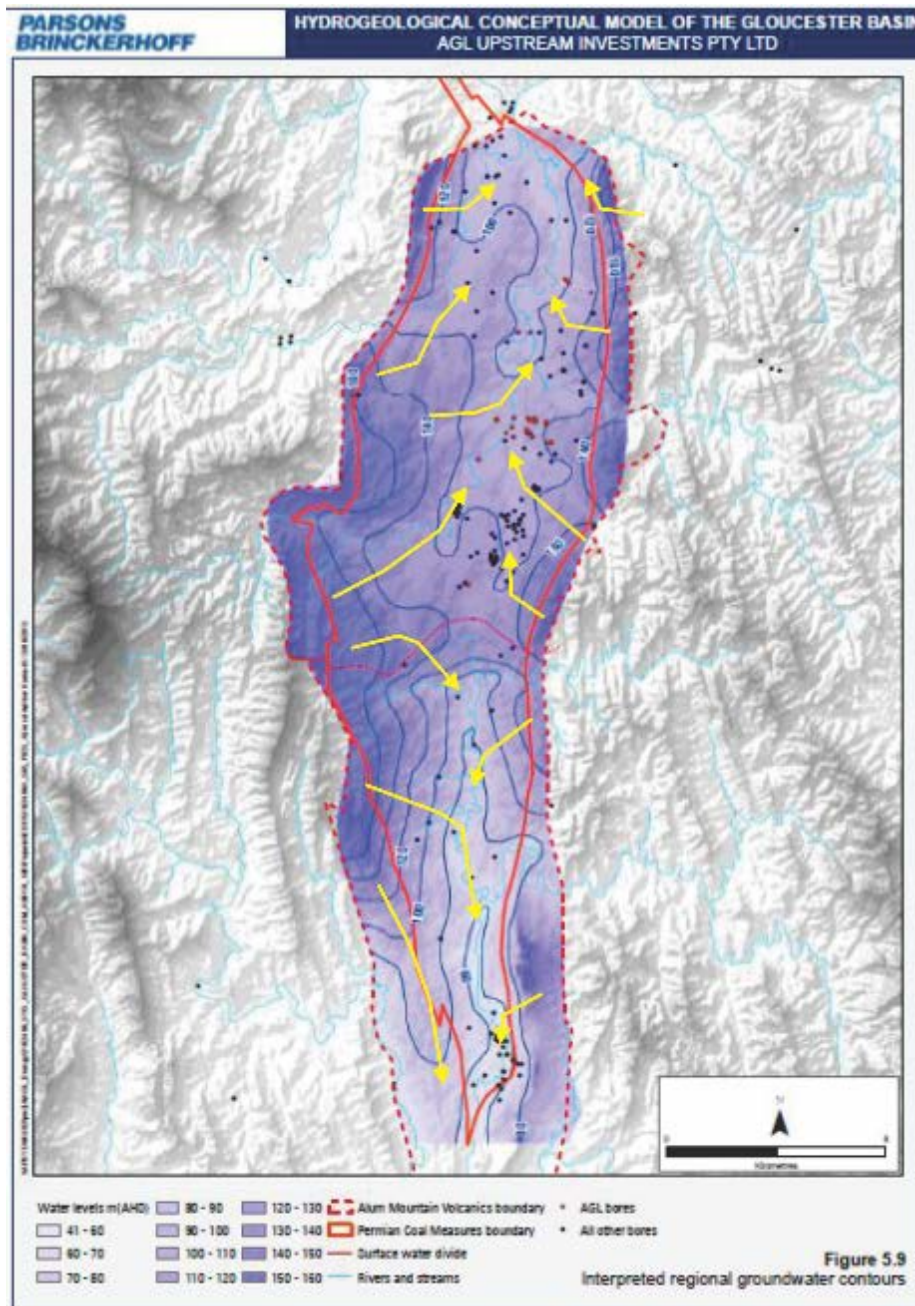


Figure 2-5 Interpreted regional groundwater contours for the shallow most aquifer in the Gloucester Basin. Yellow arrows indicate the groundwater migration direction (Source: Parsons Brinckerhoff [2013]).

Permeability data obtained from drill stem tests and core analysis for various strata in the basin have been reported by a number of different public domain studies. SRK (2010)

presented an initial overview of permeability data of coal seams plotted by depth; a more recent overview of hydraulic conductivity (related to permeability through fluid viscosity) data of coal seams and interburden is provided by Parsons Brinckerhoff (Figure 2-6). Here it can be seen that hydraulic conductivity K in the m/day occur in the shallow strata but these values rapidly drop to 10^{-3} m/day or less by approximately 300-400 m depth. This roughly corresponds to the alluvium being in the m/day, the weathered bedrock layer being in the 10^{-3} m/day and the deeper Permian coal measures and interburden being about 10^{-4} m/day (permeability k of ~ 1 mD) or less.

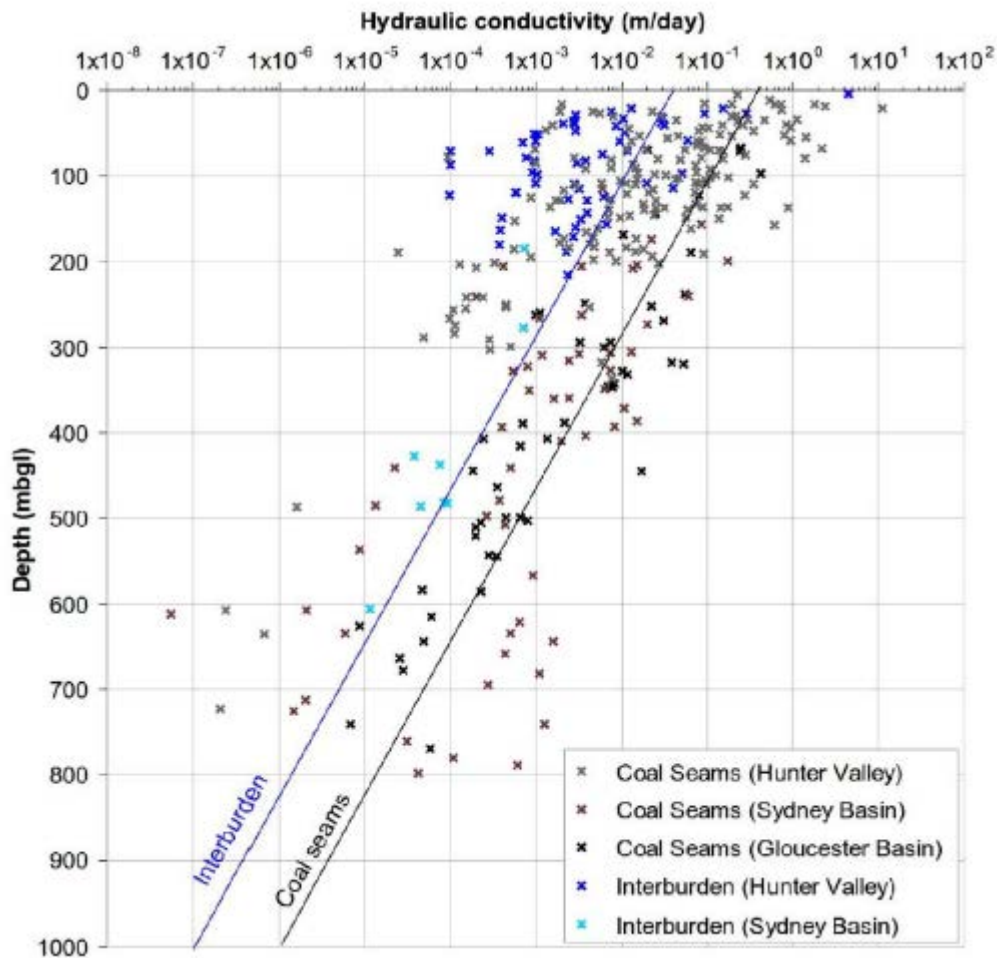


Figure 2-6 Hydraulic conductivity of coal seams and interburden with depth for the Gloucester Basin strata (Source: Parsons Brinckerhoff [2015]).

The “Hydrogeological Investigation of a strike slip fault in the northern Gloucester Basin” by Parsons Brinckerhoff (2013) took a more detailed look at the implications of faulting for hydraulic communication between coal zones and shallow aquifers. They presented a conceptual model of a fault zone architecture in scenarios of strike-slip faulting (see Figure 9-3 for a schematic illustration of fault types) with either a compressional or tensional component that produce either flower or horse tail type structures (Figure 2-7).

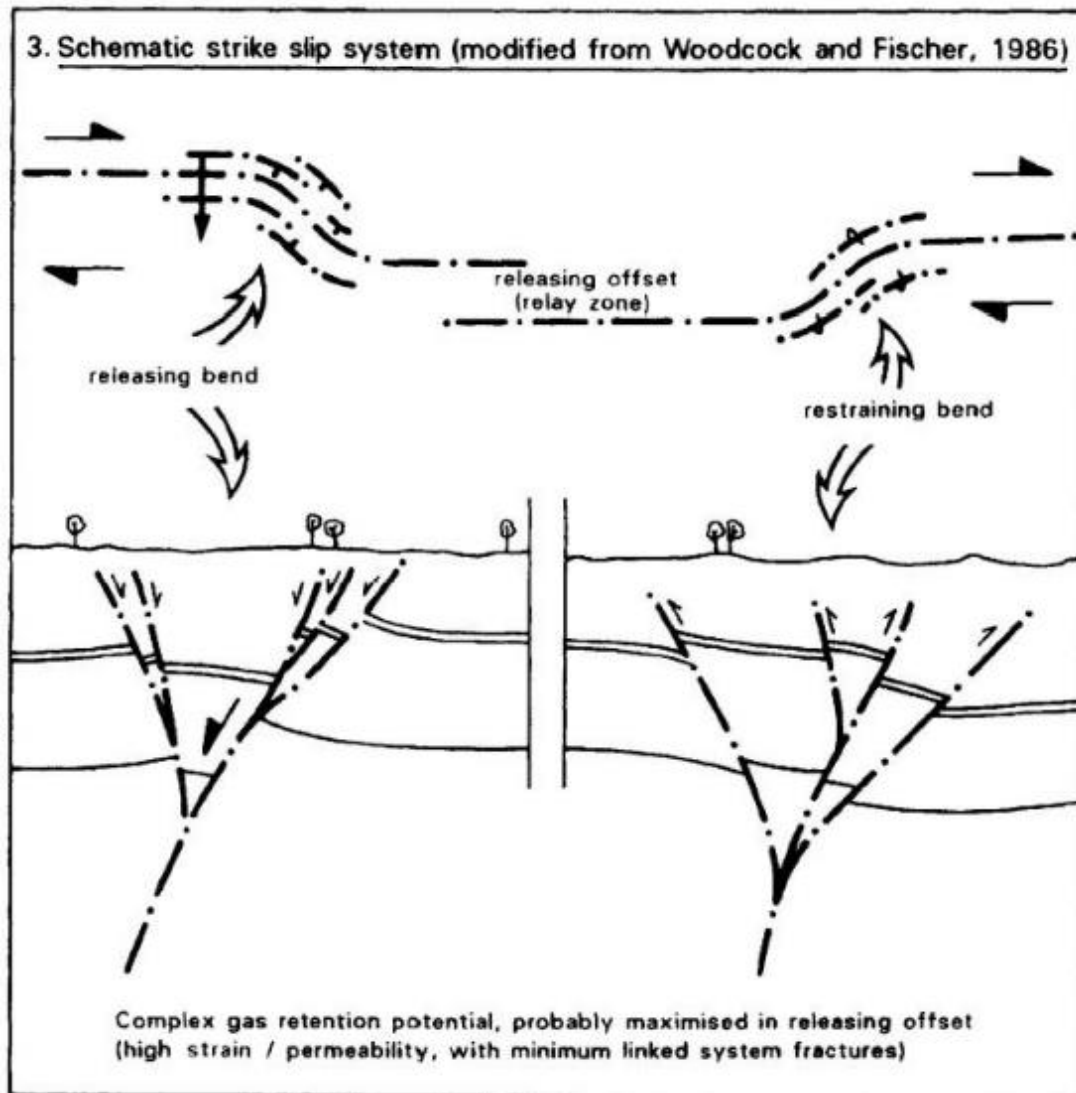


Figure 2-7 A schematic diagram demonstrating the fault zone architecture common for strike slip systems (Source: Parsons Brinckerhoff [2013]).

Parsons Brinckerhoff also examined the seismic data in the area of the Tiedman Property near the Stratford 4 well and interpreted a series of westerly dipping thrust faults and high angle easterly dipping oblique faults that they interpreted to be strike slip (Figure 2-8). One of these easterly dipping strike slip faults was interpreted to come to surface some 300 m east of the Stratford 4 gas well. A number of relatively shallow groundwater monitoring wells were installed in this area (Figure 2-8) and a pumping test at the TTPB (Tiedman Property Parsons Brinckerhoff) well was designed to observe the aquifer response in the area of the interpreted strike slip fault.

The TTPB well was pumped for 72 hours and water levels were monitored in the other wells nearby. The pressure time series for the TTPB well demonstrated generally radial flow with no obvious transmissivity barriers within the radius of investigation. The monitoring bores showed water level decline in response to pumping at TTPB. They interpret an area in the

shallow subsurface of enhanced hydraulic conductivity (orange polygon on Figure 2-8) and an area of “surface splinter zone” due to the strike slip fault (blue polygon on Figure 2-8). The Parsons Brinckerhoff (2013) report concludes the following:

- “Compared with other bores, anomalously high drawdown is seen in TTMB02 (7.4 m drawdown at 43 m from TTPB) and in TCMB01 (0.32 m drawdown at ~540 m from TTPB). This implies that there is enhanced hydraulic connection (higher permeability) towards the SSW of the pumping bore and fault surface trace;
- In contrast, other monitoring bores, S4MB02, S4MB03, TTMB01 and the Farley bore all show drawdown due to pumping, but less than would be expected in an isotropic aquifer (assuming that TTMB02 and TCMB01 define a valid straight line). These responses imply a poorer hydraulic connection (lower permeability) between the pumping bore and the screened intervals of these monitoring bores;
- There may be a weak relationship between drawdown and the stratigraphic interval screened by the bores. Monitoring bores that register no drawdown (S4MB01 and the S5-series) have screened intervals that are stratigraphically higher and lower (respectively) than the pumping bore suggesting that the poor connection with these bores is partly due to low vertical permeability in the stratigraphic sense;
- However it is noted also that the S5-series bores are located well outside of the inferred fault zone in an area shown by slug testing to have generally lower permeability (by about an order of magnitude);
- Although the fault zone appears to be slightly more permeable than other (non-fractured) parts of the shallow rock aquifer, there is no evidence for preferred groundwater flow (i.e. anisotropy in hydraulic conductivity) in the direction of the fault trace. Rather, the drawdown data are consistent with preferred flow in multiple anastomosing shear splays within a broad zone of faulting; and
- It is noted that many of the monitoring bores did not fully recover to pre-test groundwater levels by 72 hours after the test finished. This implies that parts of the fracture network are of limited extent and/or have limited storage capacity, taking longer to recharge than an ideal porous aquifer.”

The overall conclusion of the test pumping is that in the natural system, the faults do not form barriers to flow in the near surface, nor cause strong preferred longitudinal flow, but may form weakly transmissive zones, relative to unfractured shallow-rock domains (Parsons Brinckerhoff [2013] page 42).

Subsequent to the TTPB pumping test the Stratford 4 well was flowed for 29 days at a variable rate of between 15-40 m³/day. Some of the monitoring bore showed only a slight decline but the results were indeterminate if this was due to the Stratford 4 production or due to dry climatic conditions. The final conclusion of the Parsons Brinckerhoff (2013) report was that the strike slip fault zone is likely providing a slightly enhanced hydraulic conductivity in the near surface but do not indicate being across fault barriers. It should be

noted that the pumping test was conducted in the shallow subsurface associated with the shallow fractured bedrock.

The previously described hydrogeological characterisation described here from the amalgamation of a number of reports and publications that can be found in the public domain form the basis on which the current examination of faults and their influence on hydrodynamic systems in the Gloucester Basin is now conducted. From this point forwards we focus our investigation on the northern part of the Gloucester Basin (north of the surface water and groundwater divide (Figure 2-5)).

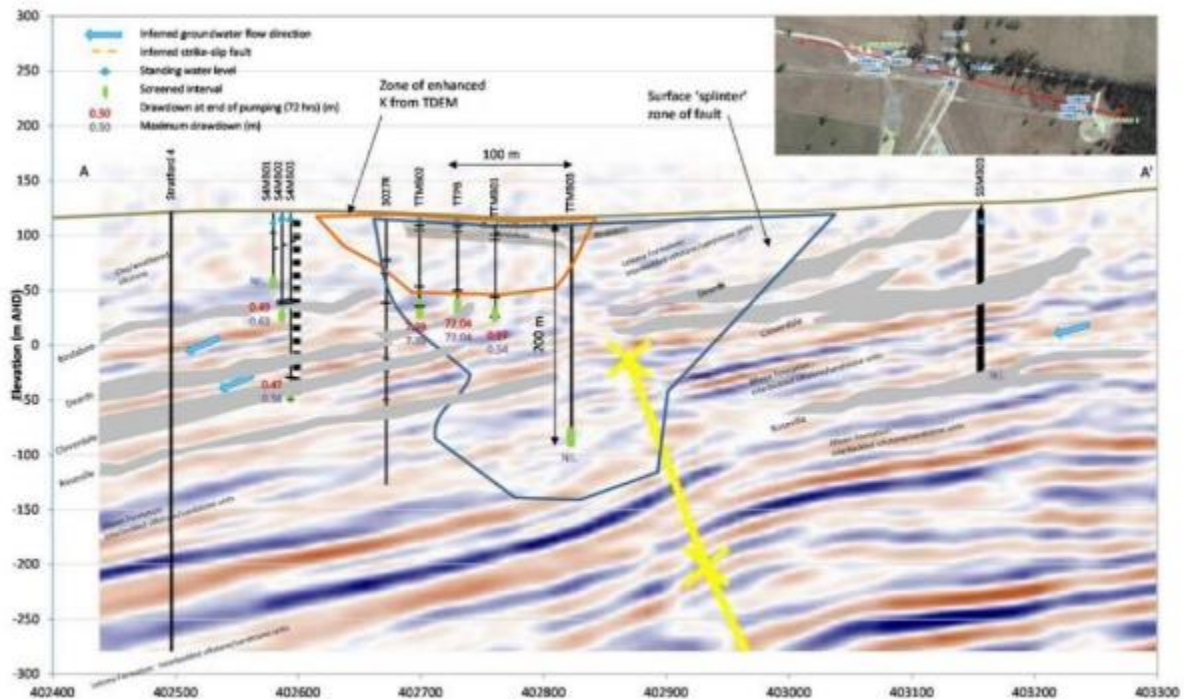


Figure 2-8 Seismic cross section near the Stratford 4 gas well with the interpreted strike slip fault and location of monitoring bores. Drawdown at each of the bores is shown after 72 hrs of pumping at the TTPB well (Source: Parsons Brinckerhoff [2013]).

2.3 Fieldwork schedule

Based on the current conceptualisation developed within the Bioregional Assessments Programme (Peeters et al., In Prep), the surface water features provide some opportunity for groundwater discharge, particularly from the alluvial groundwater system. The proportion of deep versus shallow groundwater discharge, however, is unknown. Thus, there is particular interest in focusing some of the fieldwork on the Waukivory River and Avon River and applying a number of different approaches to investigate surface water-groundwater exchanges and the influence of faults, whether as barriers or conduits, to groundwater flow and possibly surface water flow. The local and regional maps showing the structural lineaments indicate that there are a number of locations where there is a high density of faults running perpendicular to the surface water features. These features provide the best opportunity for undertaking chemical and tracer analysis on surface water

samples. The study area for the fieldwork was located within a large mining lease (PEL285) held by AGL and Gloucester Resources Limited (Figure 2-9). The study area was selected because of the high density of available drill holes that had been constructed as part of stage 1 exploration and testing phase of a major coal seam gas project (AGL Gloucester Gas Project; www.agl.com.au), as well as other groundwater monitoring bores that had been installed by Gloucester Resources Limited and the New South Wales Department of Primary Industries. In February 2017 AGL announced it would not proceed with the Gloucester Gas Project, however, access was still made available for the fieldwork program to be undertaken as part of this investigation

A combined multi-tracer, hydrochemistry and surface-based geophysical approach was used in this field study, combining both spatial measurements of deep and shallow groundwater hydrochemistry (including environmental tracers), surface water hydrochemistry (including environmental tracers) and shallow subsurface geophysics. The study also included a re-analysis of data that had been collected and published in earlier reports for AGL Upstream Investments Pty Ltd (Parsons Brinckerhoff 2012) of the same area for greater sample density (for further details see Section 4.2.2).

The subsequent Sections provide a detailed discussion and analysis of the near surface geophysics fieldwork (Section 3) and the hydrogeochemical and environmental tracer sampling campaign of surface water and groundwater within the study area (Section 5). Specific details on the sampling techniques used for sampling surface water and groundwater and the laboratory analytical methods are described in Appendix A.

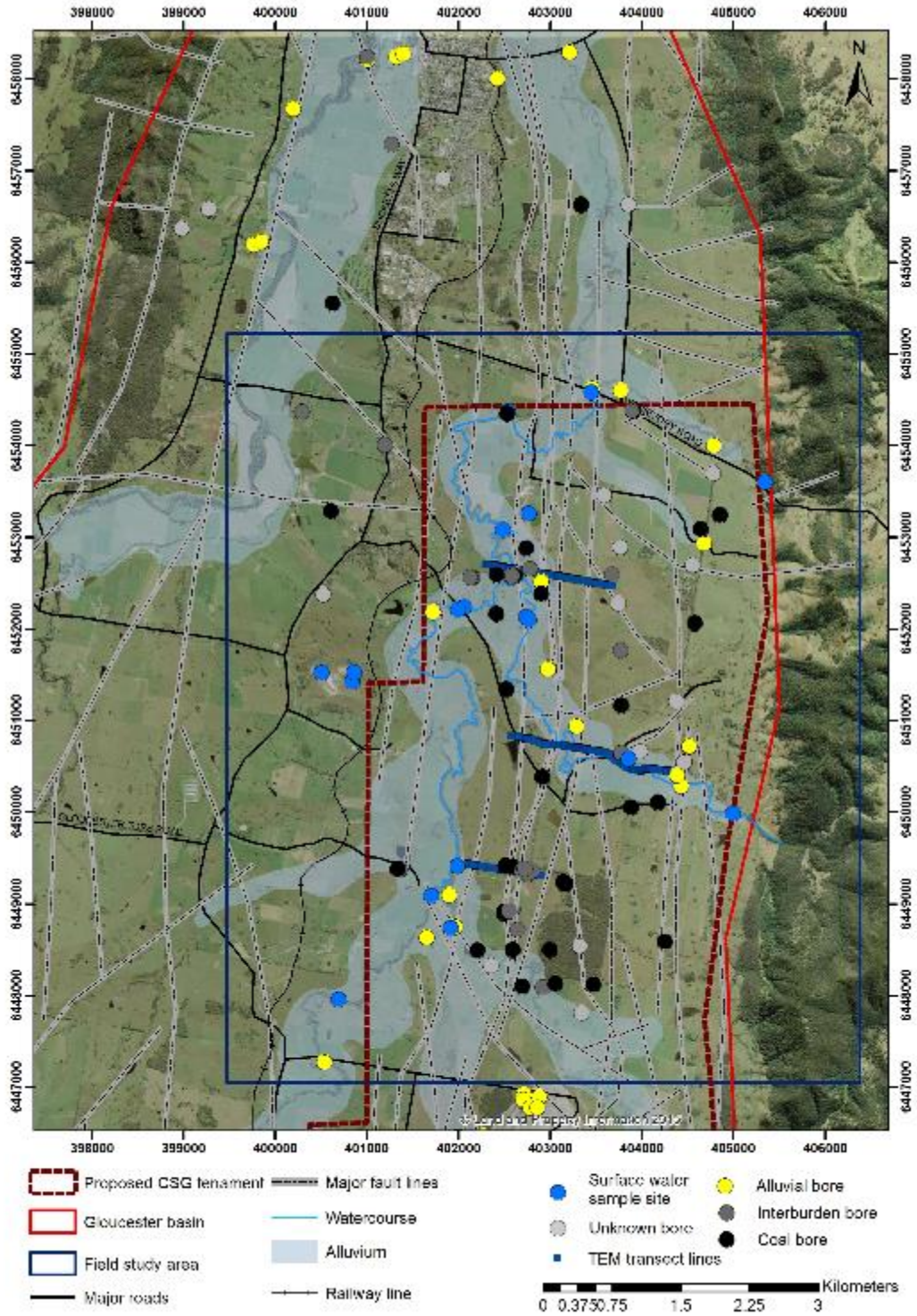


Figure 2-9 Location map of the Gloucester region, NSW Australia and the field study site. The location of the shallow TEM lines are also shown.

2.4 References

- Burns BJ (1982). Geochemistry report, Esso Australia Ltd.
- Hodgkinson JH, Pinetown KL, Wilkes PG, McVicar TR and Marvanek SP (2014). Coal and coal seam gas resource assessment for the Gloucester subregion. Product 1.2 for the Gloucester subregion from the Northern Sydney Basin Bioregional Assessment. Department of the Environment, Bureau of Meteorology, CSIRO and Geoscience Australia, Australia.
- Hughes WW, Wilcox RD and Wilcock SW (1984). Regional Exploration of the Gloucester Basin. Esso Australia Ltd.
- Loughnan FC (1954). The Permian coal measures of the Stroud-Gloucester Trough. J Roy Society NSW. 88.
- McCallum J, Simmons C, Mallants D and Batelaan O (2018). Simulating the groundwater flow dynamics of fault zones. MODFLOW Un-Structured Grid: A comparison of methods for representing fault properties and a regional implementation. School of the Environment, Flinders University, South Australia.
- McVicar TR, Langhi L, Barron OV, Rachakonda PK, Zhang YQ, Dawes WR, Macfarlane C, Holland KL, Wilkes PG, Raisbeck-Brown N, Marvanek SP, Li LT and Van Niel TG (2014). Context statement for the Gloucester subregion. Product 1.1 from the Northern Sydney Basin Bioregional Assessment. Department of the Environment, Bureau of Meteorology, CSIRO and Geoscience Australia, Australia.
- Parsons Brinckerhoff (2012). Phase 2 groundwater investigations. Report to AGL. 199. Parsons Brinckerhoff Australia Pty Limited, Sydney.
- Parsons Brinckerhoff (2013). Hydrogeological Investigation of a strike slip fault in the northern Gloucester Basin. Report to AGL. 90. Parsons Brinckerhoff Australia Pty Limited, Sydney.
- Parsons Brinckerhoff (2015). Updated conceptual hydrogeological model of the Gloucester Basin 1699 Technical report by Parsons Brinckerhoff Australia Pty Limited for AGL Upstream 1700 Investments Pty Ltd. Parsons Brinckerhoff Australia Pty Limited, Sydney.
- Peeters LJM, Dawes WR, Rachakonda PR, Pagendam DE, Singh RM, Pickett TW, Frery E, Marvanek SP and McVicar TR (In Prep). Groundwater numerical modelling for the Gloucester subregion. Product 2.6.2 for the Gloucester subregion from the Northern Sydney Basin Bioregional Assessment. Department of the Environment and Energy, Bureau of Meteorology, CSIRO and Geoscience Australia, Australia.
- SRK (2010). Gloucester Basin stage 1 gas field development project: Preliminary groundwater assessment and initial conceptual hydrogeological model. Report to AGL. 78.

- Smith S, Mathouchanh E and Mallants D (2018). Characterisation of fluid flow in aquitards using helium concentrations in quartz, Gunnedah Basin, NSW, prepared by the Commonwealth Scientific and Industrial Research Organisation (CSIRO), Canberra.
- Thornton RCN (1982). Oil occurrence in Esso stratigraphic corehole C7029 Gloucester Basin. Coal and Synthetic Fuels Department Esso Australia Ltd.
- Underschultz J, Esterle J, Strand J and Hayes S (2018). Conceptual representation of fluid flow conditions associated with faults in sedimentary basins. Prepared for the Department of the Environment by The University of Queensland Centre for Coal Seam Gas, Queensland.
- Waller RM (2013). Groundwater and the Rural Homeowner. US Department of Interior, US Geological Survey.
- Ward CR, Bocking M and Ruan CD (2001). Mineralogical analysis of coals as an aid to seam correlation in the Gloucester Basin, New South Wales, Australia. *International Journal of Coal Geology* 47: 31–49.
- Ward CR and Kelly BFJ (2013). Background paper on NSW Geology with a focus on basins containing coal seam gas resources. Office of NSW Chief Scientist and Engineer. J083550. 91.
- Weber CR and Smith BC (2000). Stratford Coal Bed Methane Prospect, PEL 285, Gloucester Basin, New South Wales: Coal Bed Methane Resource Estimate. Unpublished Report, Pacific Power, Sydney.
- Winter TC, Harvey JW, Franke OL and Alley WM (1998). Ground Water and Surface Water: A Single Resource. US Geological Survey Circular 1139.

3 Shallow electromagnetic (EM) analysis⁴

3.1 Introduction

Time Domain electromagnetic (TEM) surveys were interpreted to locate structural geological features within approximately 100 m depth of the surface in the study area. Electromagnetic surveying methods make use of the response of the subsurface to the propagation of an electromagnetic field. This response will vary depending on the electrical conductivity of the subsurface sediments and rocks.

TEM data shown in this report were collected using either a Zonge Engineering NanoTEM system or a Monex GeoScope TerraTEM system. The NanoTEM data were collected in February 2016 as part of the field investigations of this project; the TerraTEM data were previously collected for AGL/Parsons Brinckerhoff by Alpha Geoscience (Parsons Brinckerhoff, 2013). The transect lines were selected in a way that they crossed the major inferred structural lineaments in an east-west direction (Figure 2-9).

3.2 Methods

TEM is an inductive time domain geophysical technique frequently used in the mining industry most often targeting conductive ore bodies. Zonge Engineering's NanoTEM technique⁵ was developed in the early 1990s as a low-powered, fast-sampling modification of the mining exploration systems, designed specifically to provide high resolution images of the top 50 to 80 m. The TerraTEM system was developed in the early 2000s by Monex GeoScope⁶, as an offshoot of research performed at Monash University. The system used in this survey is also designed to image the near surface. Information about both systems is given below.

For the NanoTEM data shown in this report, the transmitting system output was set to 2 amps through each single-turn, 20 m x 20 m square transmitter loop. The 5 m x 5 m receiving antenna is located in the centre of the transmitter loop and is also made of a single turn of wire. Data are collected at a sampling rate of approximately 625,000 samples per second, stacking 256 cycles at a repetition rate of 32 hertz. The transmitter turnoff is about 2 microseconds; the combination of the fast transmitter turn off and high sampling rate allow data to be collected quite close to the surface, with good resolution.

⁴ Contributing authors: M Hatch, E Banks

⁵ <http://zonge.com/geophysical-methods/electrical-em/nanotem/>

⁶ <http://www.monexgeoscope.com.au/index.php/terratem/terratem-specifications/>

For the TerraTEM data shown in this report, the transmitting system output is about 9 amps through each single-turn 50 m x 50 m square transmitter loop. The receiving antenna, set up in the centre of the loop, is reported to be a compact, multi-turn antenna, with an effective area of 105 m² (the manufacturer is not specified). Data are collected at a sampling rate of 500,000 samples per second, stacking about 256 cycles at a repetition rate of 25 hertz. The transmitter turn off is recorded by the system for every data set and is approximately 40 microseconds. This system is designed with a more powerful transmitter than the Zonge system and a slightly slower sampling rate and slower transmitter turnoff; the focus of the system is to get good shallow resolution, as well as to collect data to greater depths than the Zonge system.

The “raw” data that are recorded in a TEM survey are decays of the vertical magnetic field induced by the horizontal transmitter loop into the earth (Figure 3-1). These decays are recorded as voltages from the central receiving antenna that become weaker with time (i.e. the receiver is measuring a decaying field). Readings are made after the turnoff of the transmitted signal to at least 2 milliseconds after turnoff.

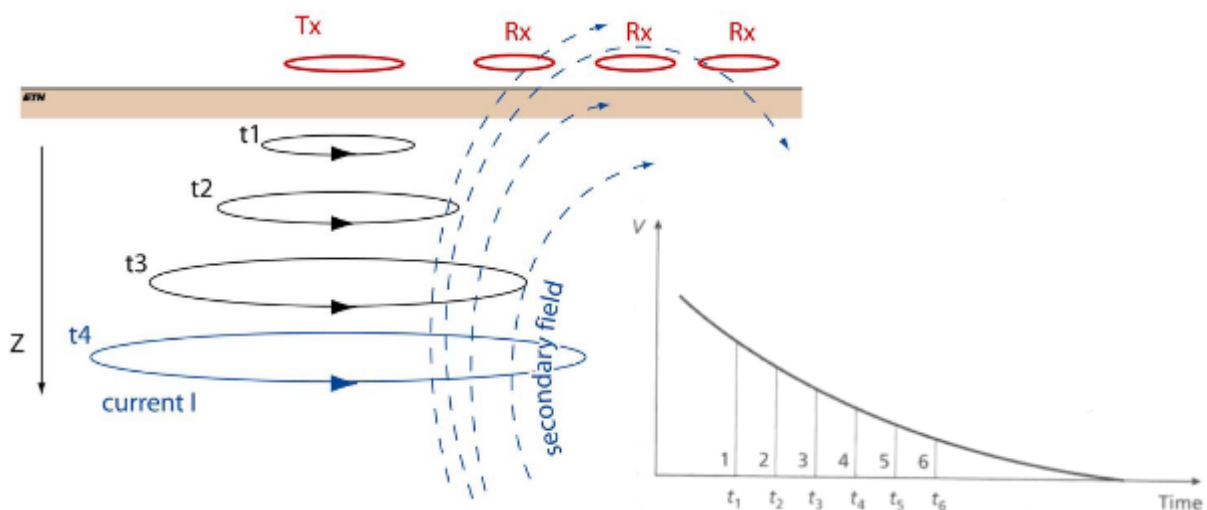


Figure 3-1 Primary and secondary electromagnetic fields generated in the subsurface and voltage (V) decay during a TEM survey.

The TEM data were processed by averaging each of the data stacks collected; any of the late time data that are no longer true decay were discarded. The averaged data were run through an inversion routine that converts observed magnetic field decay data (i.e. measured voltages and times) at each location to depths and electrical resistivities. All of the TEM data shown in this report have been processed using Zonge Engineering’s STEMINV routine ((MacInnes 2005)). This is a smooth-model, minimum-structure 1D inversion for which no model parameters are set a priori (other than smoothness and fit to starting model parameters). Each sounding is inverted individually; the result is a vertical “sounding” made up of many layers, each assigned an estimated resistivity, which varies smoothly with depth. Results for a complete line are then presented as a depth section by combining individual inversion results for each station and then contouring inverted resistivities against depth (i.e. to make resistivity-depth sections).

The 1D inversion program assumes a fairly simple model of the earth, that greatly simplifies the mathematics and therefore the time required for the inversion routine to run. The program assumes that the entire earth is a laterally non-varying “layer cake” of resistivities, which only vary vertically. The program looks at each sounding individually, processing each using the 1D assumption. This assumption, while not always valid, appears to be mostly valid in many shallow environments, where predominantly sedimentary processes have created fairly flat lying, smoothly varying layering that extend for large distances laterally (Hatch et al., 2010). Furthermore, to the authors’ knowledge there is no 2D program available to invert TEM data. The “smooth model”, “minimum structure”, “Occams” inversion model selection assumes that the 1D layer cake is made up of a large number of thin layers, with fixed thickness where only the resistivity assigned to each layer is allowed to vary. This means that where there are sharp boundaries between layers they may be poorly defined. Again, in this environment, it is probably not unreasonable to assume that contacts are mostly smooth.

3.3 TEM data quality analysis

The data from the NanoTEM surveys were determined to be of high quality. There was one zone where the data appeared to be affected by local noise sources. This was located on the North Line between stations 1000 and 1120. There were no obvious noise sources noted in the area (i.e. power lines or other aboveground features), however there was evidence of shallow subsurface horizontal drilling activity for underground pipelines as part of the CSG wells which may have been the source of noise interference. Reported data for the Alpha line were also stated to be of high quality, with no issues with the data.

3.4 Results from TEM data analysis

It was intended that the TEM lines would provide information about the local hydrogeology to help with the interpretation of the hydrogeochemical data, particularly to assist in locating faults that terminated at or near the ground surface (within 100 metres depth). Two transect lines of NanoTEM data were collected during the survey in February 2016 (see Figure 2-9 for line locations) – these will be referred to as the North Line and the South Line. Results are also shown for a transect line of TerraTEM data collected in September 2011 – called the Alpha Line. Specifically, the TEM survey results were used to: (1) identify major hydrogeological zones along each line, (2) examine each section in conjunction with geological and geophysical bore logs to correlate known features in the geology logs with the geophysics, and (3) identify the location of faults along each line and attempt to interpret whether they intersect the surface or are terminated at some depth below the surface. The TEM results were correlated with the topography, surrounding land usage and geomorphology of the surface water system using Google Earth images and other spatial GIS datasets. A limited number of nearby monitoring wells with available geological and geophysical logs were also used for comparison and interpretation of the data.

The conceptual model that was adopted in the interpretation process for identifying faults or fault damage zones was to identify narrow vertical to dipping electrical conductors that extend to depth in each section, that were associated with apparent shifts in the stratigraphy to either side of the interpreted fault location (Figure 3-2). Identifying the faults as conductors is based on the assumption that the surrounding rock would be relatively undeformed (and therefore relatively electrical resistive) and that the faults would be filled with re-worked bedrock material and clays, and would therefore be more conductive than the surrounding rock (see, for example, inverted airborne EM results, Figure 22 in Fitzpatrick et al., 2011). Also, as the groundwater in this area has been classified as being brackish to moderately saline, i.e. with water resistivity that ranges from 0.5 ohm-m to 6.25 ohm-m (Parsons Brinckerhoff 2015), fluids filling the fault zone would add to the conductive response of the fault in the TEM results. Termination depth of each fault was estimated by examining the section and then to determine the apparent depth that each interpreted fault terminated within the section. It is worth noting that the TEM sections presented here are probably only providing resistivity information to depths within 70 to 80 m of the surface and the inferred structural lineaments in the study have been based on seismic data interpretation which generally has low resolution at 0 to 200 m depth. As these intervals coincide with the weathered interburden, it may be difficult in some circumstances to infer where faults would end near the surface. It is likely that even if a fault is interpreted to terminate before it reaches the surface, the top of the fault may not be sealed and therefore gases, using the fault as a conduit, may diffuse to the surface from the top of the fault.

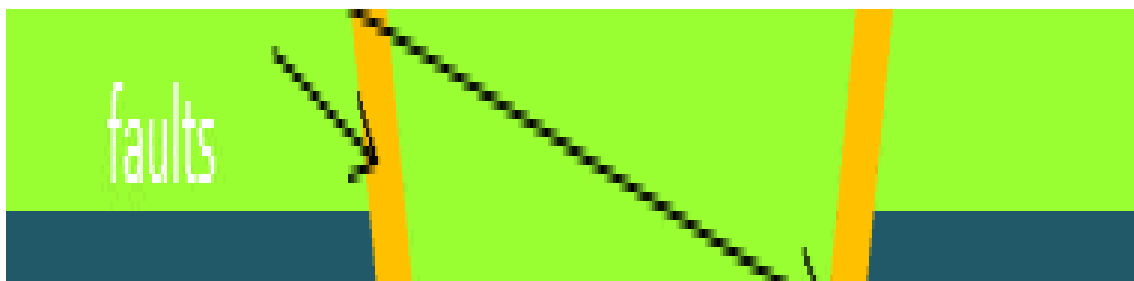


Figure 3-2 Idealised resistivity-depth section showing conceptual model for identification of faults in the TEM data sets shown in this section. The colours used in this section are similar to those used in the actual data sections, with redder colours indicating relatively electrically conductive zones and bluer colours indicating relatively resistive zones. Many of the faults interpreted in these sections appear as conductors; this is consistent with the observations in Figure 6-11 and Figure 6-12 that the shallow fracturing observed in bores Waukivory 11 and 12 were characterised as either “conductive fractures” (Waukivory 12) or “mixed fractures” (Waukivory 11), i.e. are not “resistive fractures”.

The field setting for all three of the transect lines discussed here are similar. The lines ran across mixed-use farmland, dominated by grasslands, used primarily for cattle and sheep grazing. The transect lines were positioned in an east-west direction that ran across or are near to the Waukivory/Avon River system. The North Line crosses the Avon River, just north of the confluence between the Waukivory and the Avon River systems, at approximately

station⁷ 900 (see Figure 2-9 for the location of this line). The South Line runs subparallel to Waukivory River for much of its length, and crosses the river at approximately stations 3680, 4150 and 4600. The Alpha TEM Line ends about 50 m east of the Avon River. As such, much of the shallow hydrogeology is dominated by reworking of near-surface sediments as the river system has meandered over time.

Based on the examination of the geological borelogs on the North Line, the location of the watertable and the top of the alluvial gravel layer generally coincide. At depths below the alluvial material, much of the variation in the resistivity profiles would be consistent with vertical faults, also observed in the seismic data. The direction and orientation of the river course looks to be largely determined by the location of the faults or fault zones, as there is evidence of faulting in or near each intersection with the river system.

The following Sections 3.4.1 to 3.4.3 describe the interpretation of each line. Note that for the two NanoTEM lines the top depth section in each figure is presented with a 5:1 vertical to horizontal exaggeration, while the bottom section is presented without exaggeration (Figure 3-3 and Figure 3-4). For the Alpha TEM section both sections are presented without vertical exaggeration (Figure 3-5).

3.4.1 North line NanoTEM

Much of the near-surface (to a depth of approximately 40 m), from station 900 towards the east, appears to be dominated by a sedimentary sequence that starts at the surface with a layer of conductive soils and clays; this is followed by a more resistive gravel layer and the bottom layer is made up of mixed siltstones and sandstones, and intermixed tuffaceous layers, extending to depth (Figure 3-3). To the west of station 900, the sequence appears similar, mostly without the gravel layer.

Only two of the faults observed on this line appear to extend to the surface (others may, as indicated below). If the faults are terminated by the reworking of the near surface by the river system in that area, this would indicate that faulting has not been reactivated since the river has moved from one of its original positions. Major faulting, possibly associated with the river, is interpreted to occur at stations 950 and 1040 and appear to extend to the surface. Faults are also interpreted at stations 600, 800, 1370 1430, 1700 and 1860. The faults at stations 1370 and 1430 may extend to the surface. However, the other inferred faults appear not to extend to the surface.

3.4.2 South line NanoTEM

This line runs sub-parallel with Waukivory River. Thus much of the near surface resistivity changes could be associated with the meandering of the creek that occurred since neo-tectonic fault activity ended in this area (Figure 3-4). The effects of river meandering are

⁷ Stations represent horizontal distance (m) on a local coordinate system

apparent from station 3650 to the east, as evidenced by variable depths to conductive layers (clays) and less resistive layers (gravels). From station 3650 to the west, the line climbs out of the river valley, and the section is similar to the west end of the North Line. The resistivity log shown for bore GW080841-2 at station 3460 shows increasing resistivities from where logging started at 8.5 m below the ground surface to approximately 20 m depth; coincident with the change in resistivity shown in the TEM data (interpreted to be shallow clays and soils, overlying mixed siltstone, sandstone and tuffs – similar to the west end of the North Line). Interestingly, most of the faults in this area appear to extend to the surface, suggesting that they postdate the meandering of the river. Major faults are interpreted to occur at stations 3100, 3680, 4050, 4250 and 4470.

3.4.3 Alpha line TEM

The TerraTEM system used along the Alpha line provides information to approximately 120 m below the surface but comprises the level of detail at the near surface which is picked up with the NanoTEM system (Figure 3-5). The surface clays and soils that are resolved as the surface conductive layer in the NanoTEM are not resolved using the TerraTEM system in this area. It is likely that the relatively resistive layer at approximately 30 m depth is related to gravel layers (although they are not noted in the log for bore S4MB03). Faults are interpreted to occur at stations 460, 550 and 770, with the faults at 460 and 770 interpreted to extend to the surface.

The overall findings of the near surface geophysical surveys using TEM techniques showed that the creek geometry and the shallow alluvial system is likely to be shaped by the high density of vertical faults in the area. The locations of the inferred faults based on the TEM data tended to match up with the existing inferred structural lineaments as identified with the previous seismic surveys (Parsons Brinckerhoff, 2013) and the combination of both datasets improves the confidence that these faults and fault zones extend towards the ground surface at a number locations in the study area.

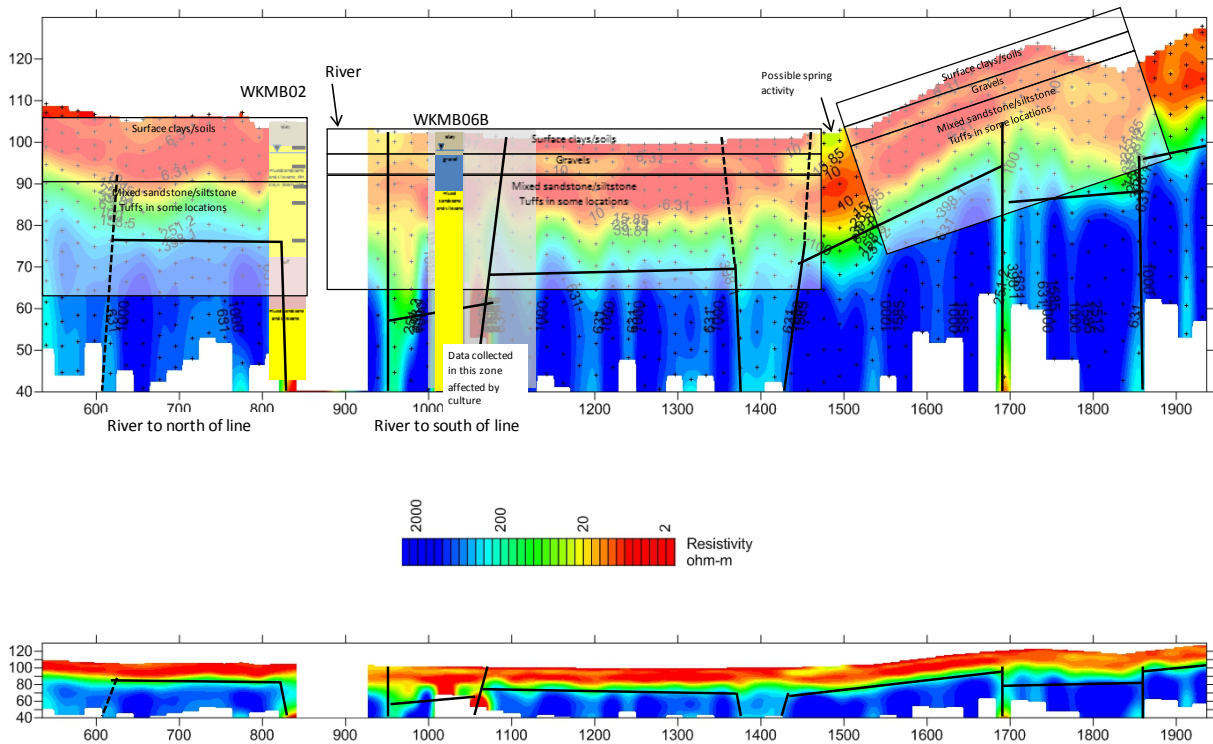


Figure 3-3 North line resistivity depth section from the NanoTEM near surface geophysical survey. With (top) and without (bottom) vertical height exaggeration.

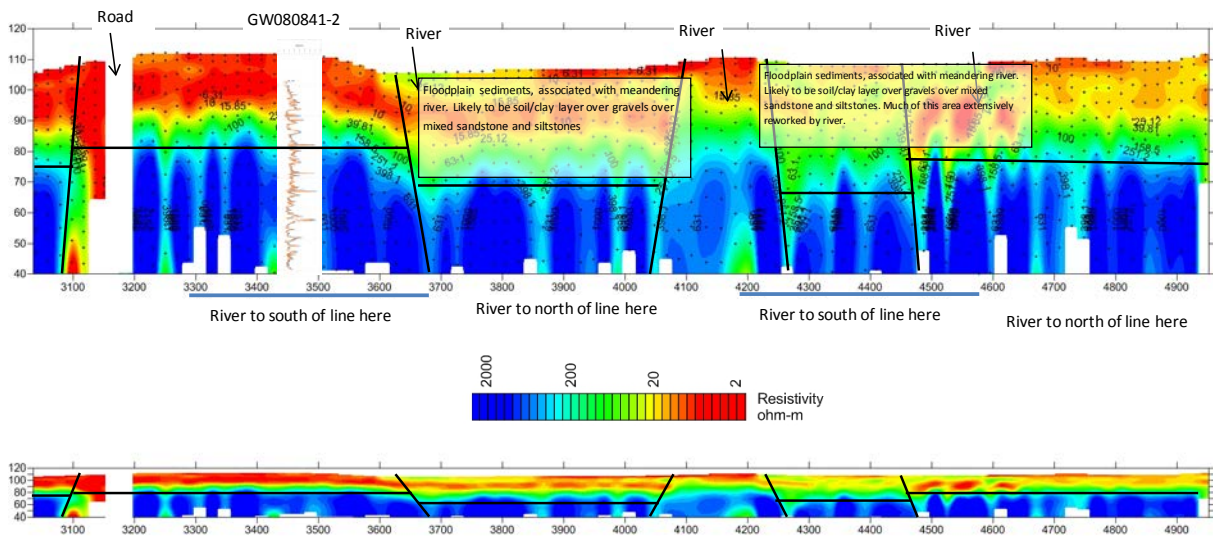


Figure 3-4 South line resistivity depth section from the NanoTEM near surface geophysical survey. With (top) and without (bottom) vertical height exaggeration.

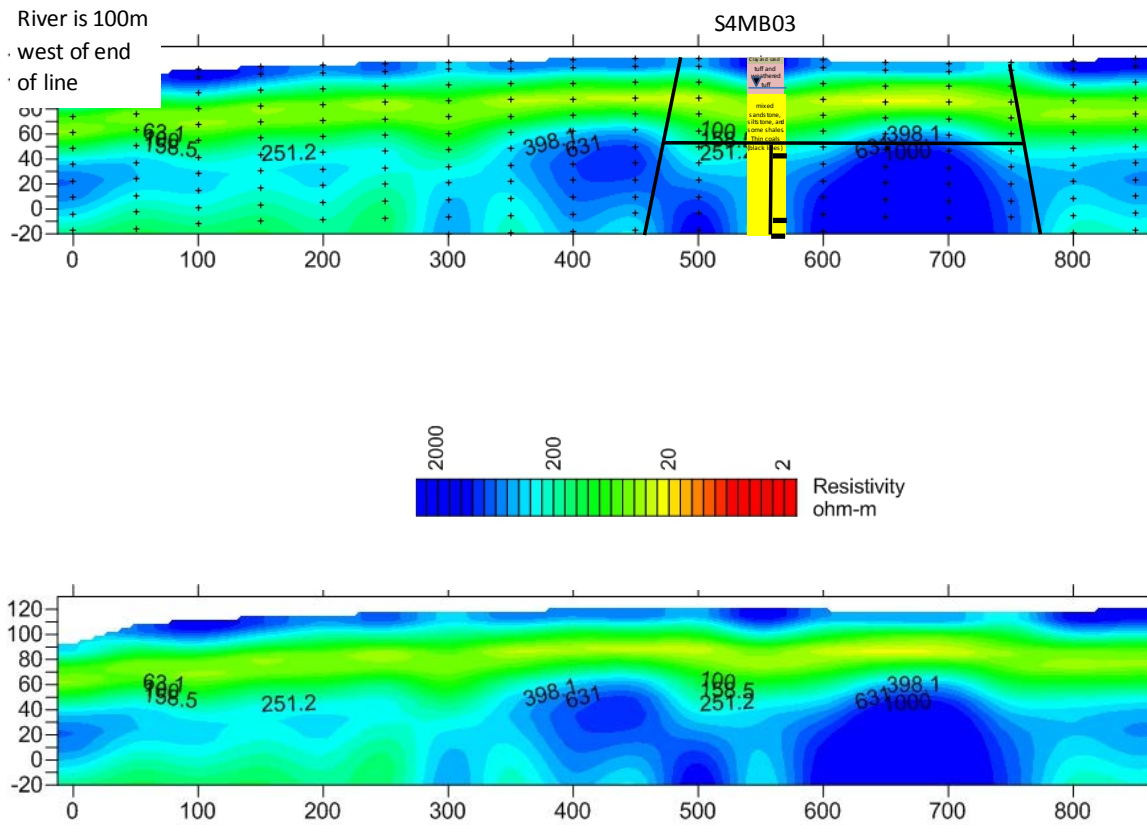
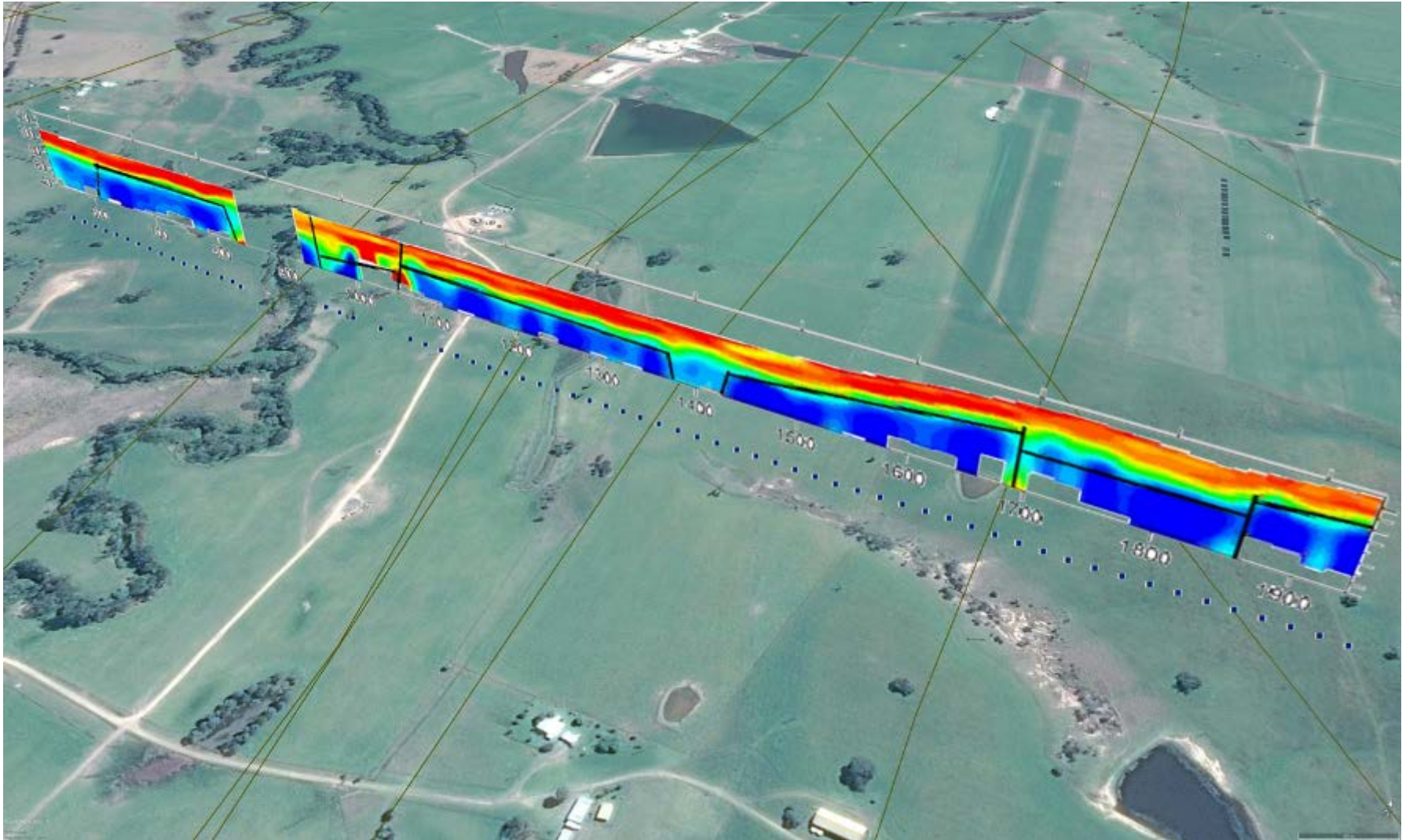


Figure 3-5 Alpha line Tiedmans property TEM near surface geophysical survey from Alpha GeoScience (Parsons Brinckerhoff 2013).



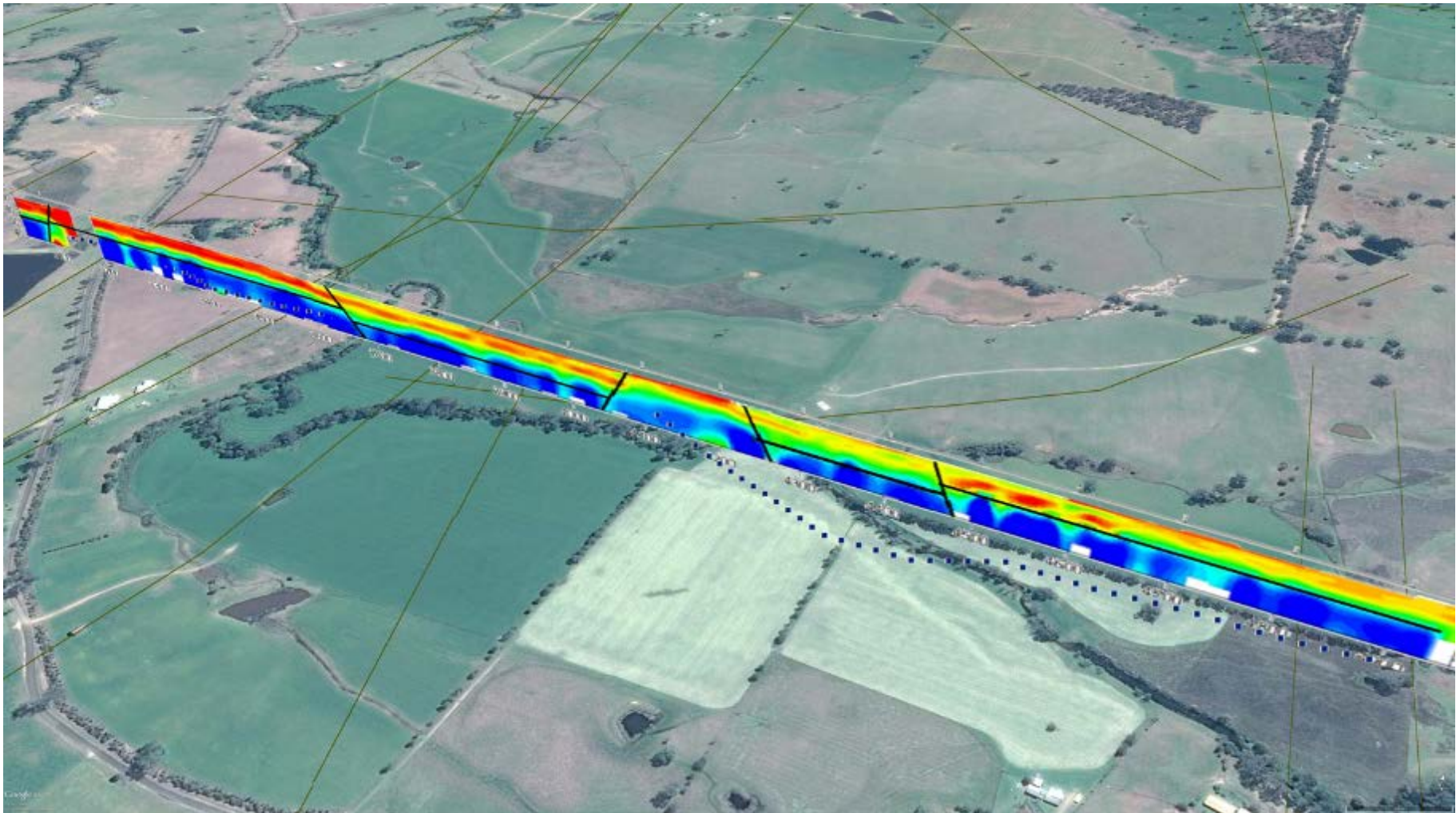


Figure 3-6 (top) Near surface geophysical NanoTEM (North line and South line) and TEM (Alpha line) 2D transects overlain on Google Earth including the inferred structural lineaments at ground surface; (middle) zoomed in detail of North line transect; (bottom) zoomed in detail of South line transect.

3.5 Frequency-dependent response in the TEM data

Nearly all of the TEM data collected for this work (including the older Alpha data set) showed an apparent increase in the resistivity data at approximately 30 to 40 m depth below ground. In each of the TEM sections it appears that the resistivity increases abruptly from 10s of ohm-meters to values >100 ohm-m to >1000 ohm-m. Examination of the available borelog-derived geological information (see borelog insets at stations 840 and 1020 on the North Line, and station 550 on the Alpha Line [(Parsons Brinckerhoff 2013) show no correlation with a change in geology at or near these depths. Additionally, examination of available downhole, induction-based resistivity logs (see Figure 3-6 which shows downhole resistivity log for bore WKMB04, located about 225 m south-west of the western end of the North Line and bore GW080841-2, located south of the South Line transect western end), do not show an overall increase in magnitude of the resistivity that correlates with the measured resistivity change of the TEM data. A large resistivity change might be related to the occurrence of tuffs, however, this relationship was not consistent based on the observed depth locations of the tuffs according to the geological logs and measured downhole resistivity logs to explain the sharp increase in resistivity. For example, the S4MB03 borelog on the Alpha Line at station 560 shows a tuffaceous layer from 19 to 24 m depth; this layer is at a much shallower depth than where the resistivity increases on that line. Additionally, there is no increase in resistivity in other geophysical logs that intersect tuffs. The borelog for bore Waukivory 14, that is known to intersect tuffs, shows only a small increase in resistivity at the approximate location of the tuffs (approximately 172 to 180 m depth), and the change in the resistivity log is much smaller than the response noted in the TEM data.

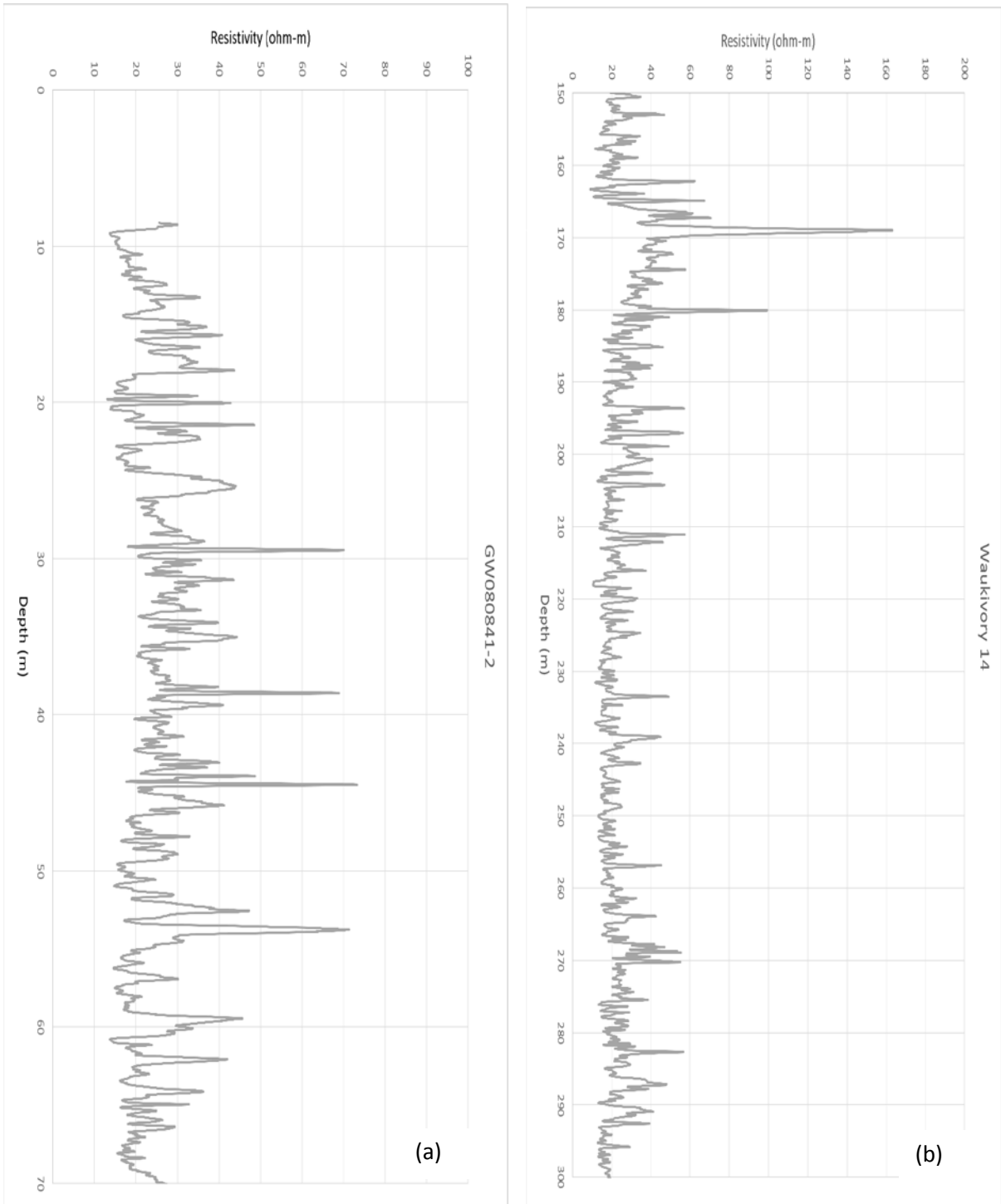


Figure 3-7 Borehole resistivity logs for a) bore GW080841-2 and b) bore Waukivory 14. In (a) note that there is no consistent change in resistivity that matches the change seen in the NanoTEM section. In (b) tuffs are logged to occur from 172 to 180 m depth; there is only a small change in resistivity at that depth. The resistivity scales in a) and b) are different.

Further examination of the TEM data suggests that the sudden increase in resistivity in the TEM sections around 30 to 40 m depth may be a frequency-dependent response, related to a non-resistive change in mineralogy in the ground that increases the rate of decay, making the response appear more resistive than it actually is. An example of this, that is occasionally seen in the literature, is accelerated decay due to the IP (induced polarisation) effect; see for example Flis et al. (1989). It is unknown what mineral combination is affecting the data in this way in this survey as there is nothing out of the ordinary noted in the geological bore logs. However, some clays are known to produce IP effects ((Telford *et al.* 1976) and it is possible a particular clay-rich layer common to the local stratigraphy is causing this response.

In order to examine the possibility that ground conditions not related to resistivity variation (i.e. an IP effect) has influenced the data, an attempt was made to forward model this response to match the character of the responses seen in the shallow TEM data. Previous work by CSIRO Mineral Resources Group have used the Leroi program (<http://p223suite.sourceforge.net/descriptions.html>) to forward model a simple ground response similar to what was observed in this project. The model consisted of a 5 m thick, 20 ohm-m layer at the surface, overlying an infinitely thick second layer that was 100 ohm-m. The top layer has enhanced IP response and the Cole-Cole parameters are set such that chargeability (m) = 0.8, time constant (tau) = 0.1 and frequency dependence (c) = 0.5) (Pelton et al. 1978). Figure 3-8a shows the results of this model, with the response decaying rapidly to negative values at $\sim 10^{-4}$ seconds. This response is similar to the field example shown in Figure 3-8b. Obviously this model only confirms the possibility that a conductive surface layer (possibly a clay) with some IP response could affect the data as seen here. Further modelling is necessary to better focus the response and it should be noted that the fact that the responses look similar does not necessarily mean that IP effect explains the strong decay and late-time negative data; this should be confirmed with other data.

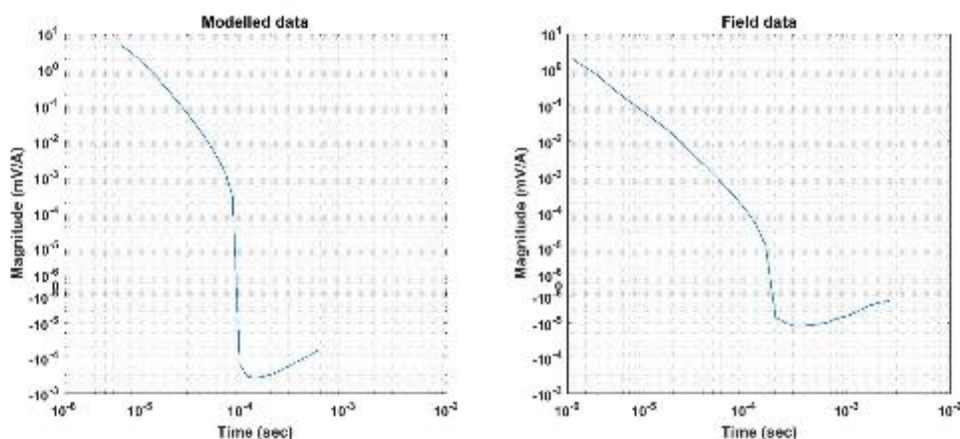


Figure 3-8 Comparison of (a) modelled decay data with (b) field decay data. The field data are from South Line, station 3240.

3.6 Comparison of TEM results with existing seismic data

In this section we compare the NanoTEM results with existing 3D seismic data collected by AGL (Parsons Brinckerhoff, 2013), and described in Section 6. These data have been combined into a 3D cube of the survey area; this type of data cube makes further analysis of this large data set possible, but also allows the data to be sliced and sections made of traverses where the data were not directly collected. These slice sections are shown in Figure 3-9 and Figure 3-10.

Most seismic reflection data does not provide good resolution of the “near-surface”; this can be seen in the seismic data shown in Figure 3-9, which shows poor resolution of the top 100 to 200 m over the survey area. If information is needed in this zone, shallow EM techniques, like the NanoTEM system used here (and airborne EM), have the potential ability to fill in information on this zone. While we do not expect all faults identified in the NanoTEM to show up in the seismic sections and vice versa, it is encouraging when the two are at least similar and identify similar features.

In Figure 3-9 the North NanoTEM line is aligned with the appropriate section slice through the seismic cube of data for this area. There is generally good alignment of faulting in the TEM data with what is interpreted in the seismic data, with some faulting seen in the NanoTEM appearing to extend to depth in the seismic data (e.g. the two faults highlighted in red in Figure 3-9).

Similarly, in Figure 3-10, there is generally good correlation between the locations of shallow faulting interpreted from the seismic data when compared with the NanoTEM data collected in the same area.

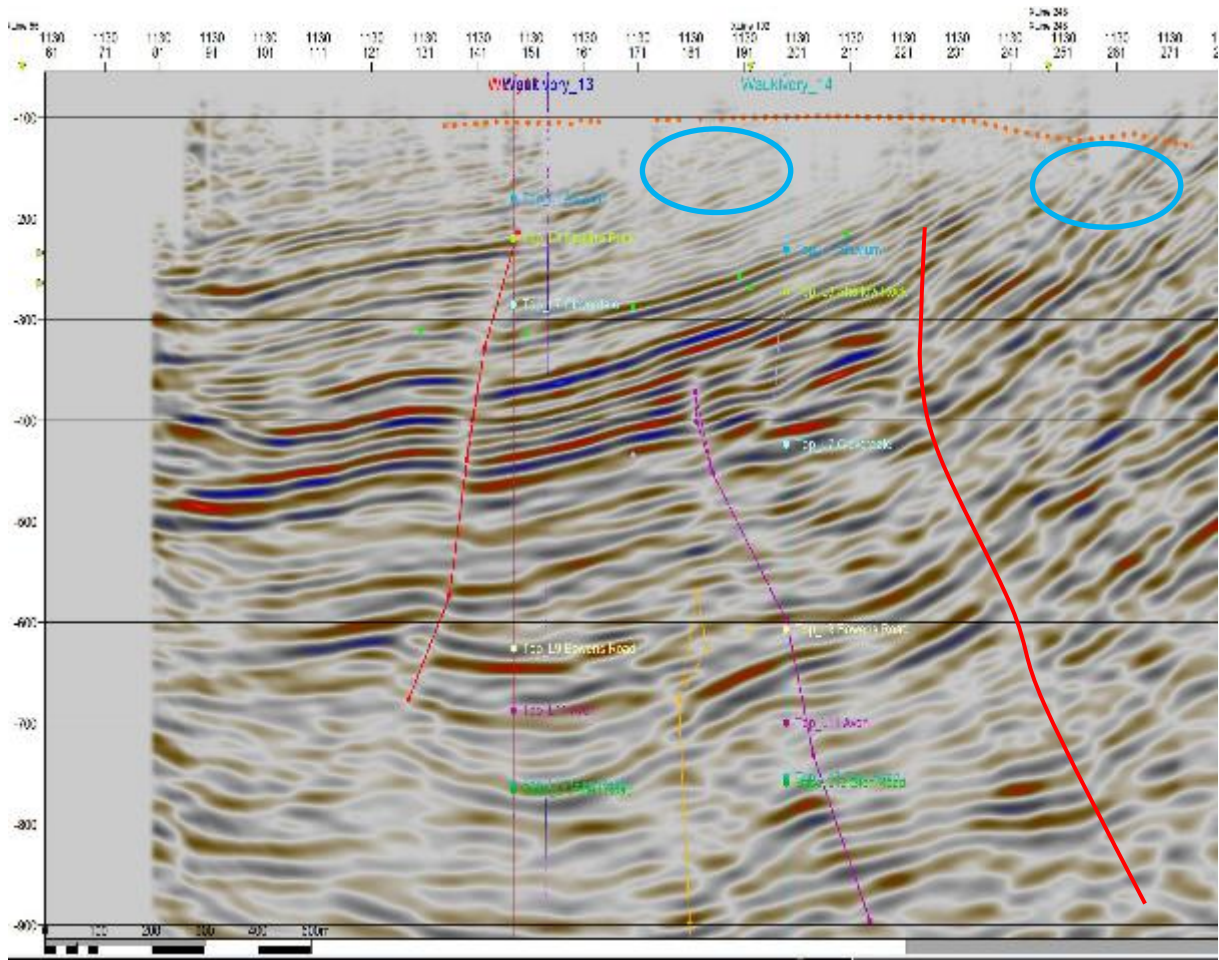


Figure 3-9 Comparison of North Line NanoTEM with seismic section cut from 3D cube on the same traverse. Red, ochre and purple lines show deeper fault locations determined from seismic data. Blue circles indicate zones in shallower seismic section that are heavily faulted. Both red faults may extend to surface. Ochre and purple faults appear to be cut off below bottom of Cloverdale.

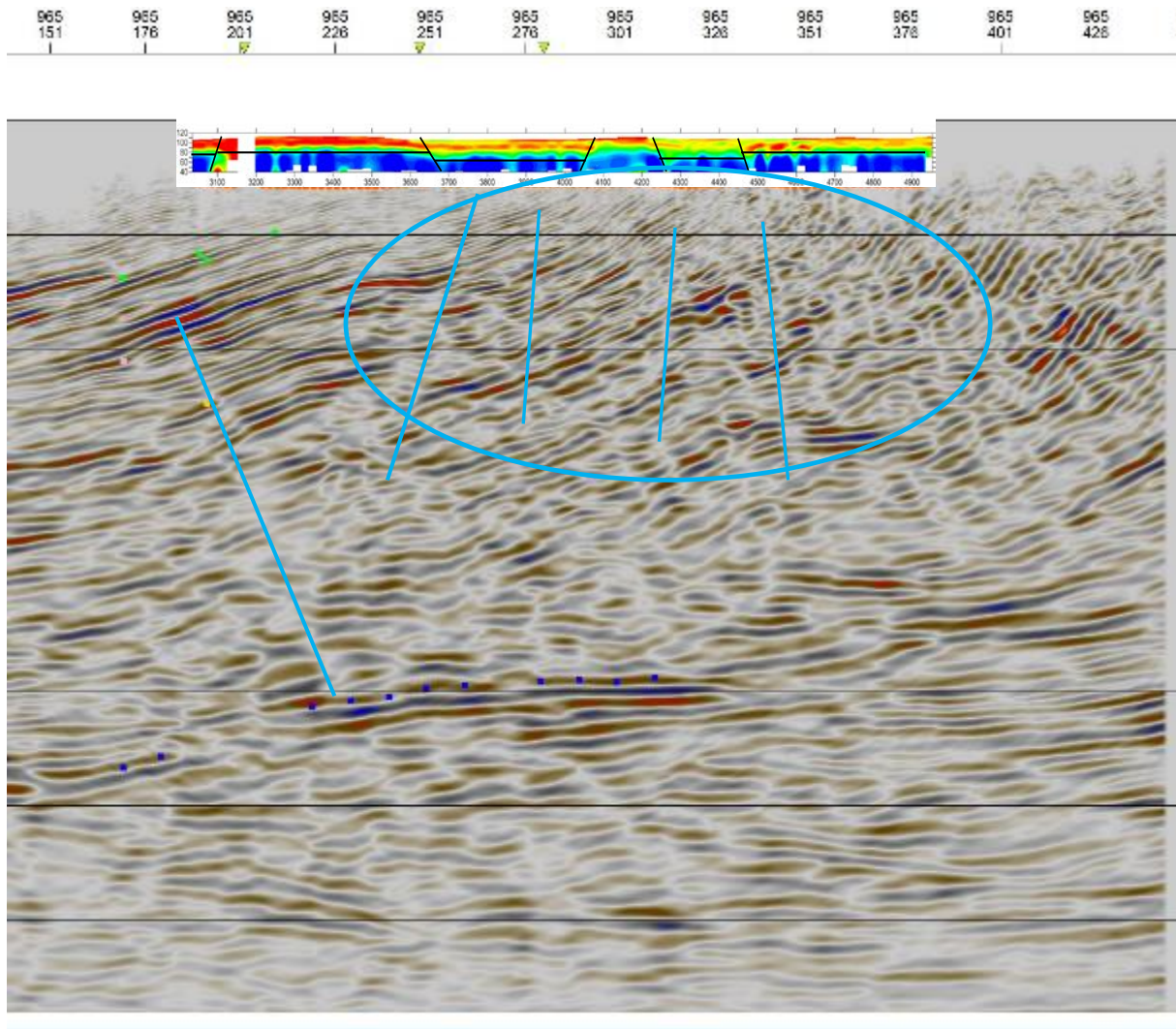


Figure 3-10 Comparison of South Line NanoTEM with seismic section cut from 3D cube on the same traverse. Blue lines indicate faults interpreted from seismics. Blue circle shows zone of concentrated faulting in near-surface.

3.7 Integrated analysis of geophysical results supporting hydrogeological characterisation

The shallow geophysical surveys based on electromagnetic induction techniques have been successful in identifying the geological structure in the near surface and provide additional information to the hydrogeological characterisation of the aquifer in the near stream environment. The large resistivity/conductivity changes in the near-surface along the transect lines can be attributed to faulting in the top 80 to 100 m of sediments. A number of sub-vertical faults were identified, that appeared to extend to below the depth of investigation of the shallow TEM techniques used here. While the shallow seismic survey data sets (interpreted in Section 6 of this report) are not able to accurately inform us about faulting in the near surface, examination of the shallow parts of the relevant seismic sections confirm that zones associated with shallow faulting in the seismic data also coincide with faults identified in the shallow TEM data sets.

3.8 References

- Fitzpatrick A, Munday TM, Cahill K, and Stelfox, L (2011). A regional, reconnaissance scale AEM survey to aid the definition of surface water - groundwater processes beneath a large unregulated river system: Fitzroy River, Western Australia. CSIRO Technical Report No: CESRE P2010/1235 pp. 106.
- Flis MF, Newman GA, and Hohmann GW (1989). Induced-polarization effects in time-domain electromagnetic measurements. *Geophysics* 54(4): 514-523.
- Hatch MA, Munday TJ and Heinson G (2010). A comparative study of in-river geophysical techniques for defining variations in riverbed salt load as an aid to managing river salinization. *Geophysics* 75(4): WA135-147.
- MacInnes S (2005). STEMINV: Smooth model TEM Inversion, edited, Zonge Engineering, Tucson, AZ.
- Parsons and Brinckerhoff (2013). Hydrogeological Investigation of a strike slip fault in the northern Gloucester Basin. Report to AGL. 90. Parsons Brinckerhoff Australia Pty Limited, Sydney.
- Pelton WH, Ward SH, Hallof PG, Sill WR and Nelso PH (1978). Mineral discrimination and removal of inductive coupling with multi-frequency IP. *Geophysics* 43(3): 588-609.
- Telford WM, Geldart LP, Sheriff RE, and Keys DA (1976). *Applied Geophysics*, Cambridge, England, Cambridge University Press.

4 Hydraulic analysis of pre-existing subsurface data⁸

4.1 Introduction

Section 2 presented a summary of the previous work on characterizing the hydrogeology of the Gloucester Basin including hydraulic head, hydrochemistry and some work on the possible impacts of faults. This initial characterisation provides a starting point for the current investigation. A key aspect to framing the current evaluation is the most recent available geological description of the northern part of the basin that has been developed by AGL through its evaluation of CSG resource potential, particularly at the Waukivory and Stratford areas (the AGL Petrel static geological model and the complimentary 3D seismic volume (Morgani 3D) were made available to the research project). This includes new wells and seismic data used to define a static geological model. The AGL static geological model was provided to the project and imported into the Schlumberger Petrel software. Figure 4-1 shows the detailed stratigraphic nomenclature for the northern part of the Gloucester Basin including a definition of individual coal and interburden members of each formation. To the right of this stratigraphic chart is indicated the AGL layer number that has been interpreted within the Petrel Static model. The identified odd numbered layers match the economically interesting coal sections of the geology. Between these (unlabelled in Figure 4-1) are the even numbered layers mainly representing interburden. The AGL interpreted layers are displayed as a cross section of the Petrel block model in Figure 4-2. We use these layers to allocate each data point derived from wells, to a geological layer within the AGL Petrel static model. This includes hydrochemistry data, formation pressure data, drill stem test (DST) permeability data, petrophysical well log and image log data, and core data. For data derived from a "completed interval" such as a DST, the mid-point of the interval was used to allocate the data to one of the layers within the 16-layer AGL Petrel static geological model. It is on the basis of this allocation that maps such as hydraulic head of formation water salinity can be constructed for individual layers. The AGL Petrel layer number are referred to throughout the remainder of this report.

⁸ Contributing authors: J Underschultz, H Xu, A Wolhuter

AGE	FORMATION	LITHOLOGY	HYDROSTRATIGRAPHY	
Quaternary	Alluvium	sand, gravel	aquifer	L1 Alluvium
Late Permian Clouanater Coal measures	Crowthers Road Conglomerate	conglomerate, minor sandstone	interburden or aquifer if fractured	100 to 90 masl
	Leloma Formation	sandstone, minor siltstone and coal	interburden or aquifer if fractured	L3 Shallow Rock 40 to -50 masl
		Linden Coal Member	water bearing zone	
		marker/ID Coals Member	water bearing zone	
		Jo Both Tuff	interburden (as aquitard)	
		Bindaboo Coal Member	water bearing zone	
	Lilleon Formation	Deards Coal Member	water bearing zone	L5 Bindaboo -115 to -117 masl
		sandstone, minor siltstone and coal	interburden (as aquitard)	
		Cloverdale Coal Member	water bearing zone	
		conglomerate, sandstone, siltstone	interburden (as aquitard)	
	Wards River Conglomerate	Roseville Coal Member	water bearing zone	L7 Cloverdale -204 to -216 masl
		Fairbairns Lane - Terree Coal Member	water bearing zone	
		Wards River Conglomerate	conglomerate, sandstone	
	Late Permian Dewarung Group	Bowen Road Coal Member	water bearing zone	L9 Bowens Road
		Wenham Formation	siltstone	
Speldon Formation		marine influenced sandstone	interburden (as aquitard)	
Glenview Coal Member		water bearing zone		
Avon Subgroup	Dog Trap Creek Formation	Bucketts Way Coal Member		-499 to -513 masl
		Marker Two Coal Member		
		sandstone, siltstone	interburden (as aquitard)	
	Waukivory Creek Formation	Avon Coal Member	water bearing zone	L11 Avon -670 to -682 masl
		Triple Coal Member	water bearing zone	
		Rombo Coal Member	water bearing zone	
		Glen Road Coal Member	water bearing zone	
		sandstone, siltstone	interburden (as aquitard)	
		Valley View Coal Member	water bearing zone	
		Parkers Road Coal Member	water bearing zone	
siltstone, mudstone	interburden (as aquitard)			
Mammy Johnsons Formation	sandstone, siltstone, mudstone	interburden (as aquitard)	L13 Glen Road -778 to -788 masl	
	Intra-Mammy Johnsons Member	water bearing zone		
	bioturbated sandstone	interburden (as aquitard)		
Weismantels Formation	siltstone, mudstone	interburden (as aquitard)	L15 Clareval -914 masl to deeper	
	Weismantels Coal Member	water bearing zone		
Early Permian	Duralie Road Formation	marine sandstone, conglomerate	interburden (as aquitard)	
		Clareval Coal Member	water bearing zone	
	Alum Mountain Volcanics	conglomerate, coal	interburden (as aquitard)	
Carboniferous	Sequences	ryholite, basalt, welded tuff	interburden (as aquitard)	
		basal Coal Member	water bearing zone	

Figure 4-1 A detailed stratigraphic nomenclature for the northern Gloucester Basin with equivalent layer numbers of the AGL Petrel model (after Brown et al. (1996), AECOM (2009) SRK (2010), Pacific consulting (2012) and the Australian Stratigraphic Names Database).

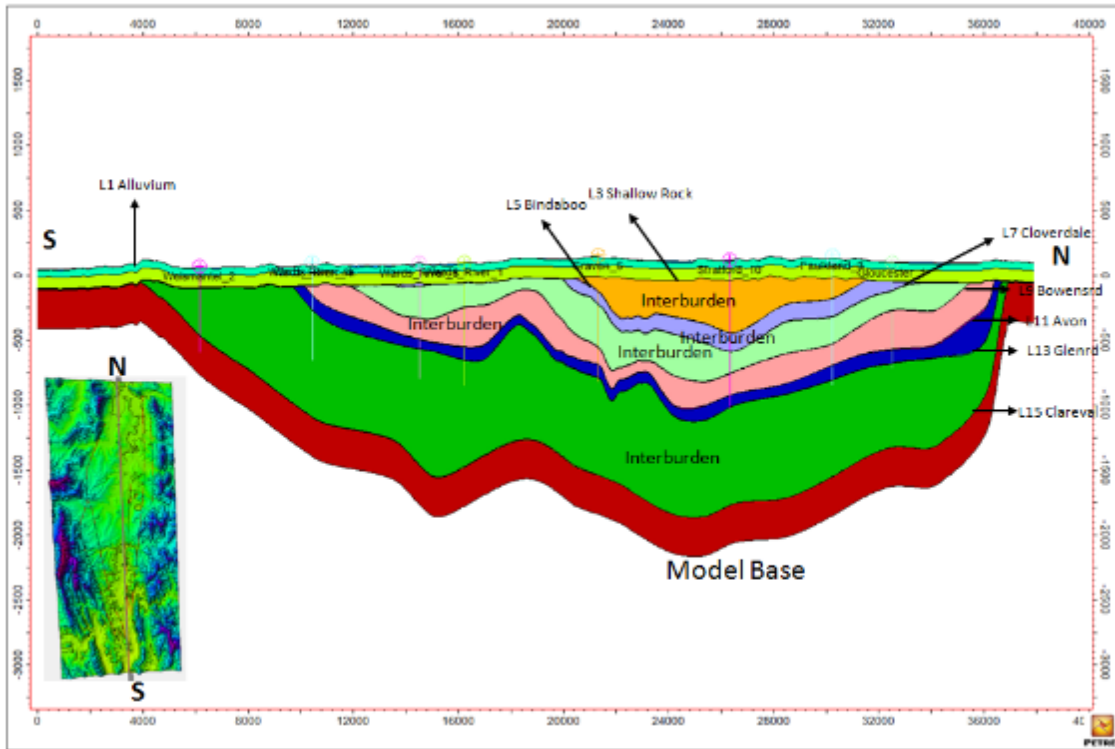


Figure 4-2 South to north cross-section of the AGL surfaces within the Petrel static model of the Gloucester Basin.

4.2 Methods

4.2.1 Formation pressure analysis

The formation pressure analysis conducted in this study mainly involves the conversion of formation pressure values to hydraulic head and then interpreting the potential for flow.

4.2.1.1 Hydraulic head

Hydraulic head h is a specific measurement of liquid potential energy relative to a geodetic datum (Raymond, 2004). We use hydraulic head converted from formation water pressure P to measure the energy of the fluid and the potential for it to flow. The details of calculating hydraulic head (h) can be found in various publications including Fetter (1994) and Lusczynski (1961) such that:

$$h = z + \frac{P}{\rho_f G} \quad (4-1)$$

where z is the elevation of the pressure gauge, ρ_f is the fluid density and G is the gravitational constant. With Equation (4-1), one can calculate fresh water head assuming a fluid density of 1.

4.2.1.2 Data processing

We used data from both petroleum wells and groundwater monitoring bores for calculating hydraulic head. Pressure data is obtained for petroleum wells from well completion reports or pressure test reports (DST, MDT, FRT and etc.) available through the New South Wales Department of Industry Resources and Energy which hosts the DiGS database. But for groundwater monitoring bores, we need to first use raw data including water level, temperature, salinity and perforation depth to calculate the pressure in aquifer at the elevation of the bore completion interval. This pressure can then be converted to a hydraulic head value.

4.2.1.3 Well test data detection

In this study, DST and wireline tests (FDT, FRT) provided formation pressure data in wells from AGL that can be used to calculate hydraulic head directly. After we collected test data, it was passed through a Quality Control (QC) system that evaluates the reliability (Otto et al, 2001). The quality of the test determines the confidence level of calculated hydraulic head. Some pressure data recorded in DST test reports as part of well completion report may not provide the pressure-time increments required to conduct a Horner extrapolation (Hortle et al., 2013). These data, listed only as a final shut-in pressure, are considered to be of low confidence particularly as the general permeability of the strata being tested is low (in the 1mD range).

For wells containing multiple formation pressure measurements we used pressure-elevation plot analysis to identify spurious data and assess the vertical hydraulic continuity and the strength of seals.

4.2.1.4 Monitoring bore data

Obtaining hydraulic head values from groundwater bore observations requires some corrections. The formation water pressure at the midpoint of the completed interval is required before this value can be converted to a hydraulic head. This can be obtained from knowledge of the groundwater density and column height within the observation bore. The density of the groundwater can be calculated from the temperature and salinity. The column height of groundwater within a bore is associated with the measured water level relative to the completed interval. Each bore was subjected to basic QA/QC for confidence testing in water level which can be affected by seasonal, atmospheric, and human activities. Since this study is interested in the natural baseline conditions, bore data was screened to select data that suits this need. To obtain the formation water density a calculator tool was used (Wadhams, 2000 and Rowe and Chou, 1970) that required salinity and temperature. The formation water salinity is obtained from the water analysis collected on the bore water samples.

Temperature (t) of the bore water is calculated using the geothermal gradient according to:

$$t = t_0 + GH \quad (4-2)$$

where t is temperature at the midpoint of the perforated interval, t_0 is mean annual surface temperature, G is geothermal gradient in the study area and H is depth to calculating point for t . The mean annual surface temperature in study area, t_0 , is 18.78 °C obtained from Bureau of Meteorology, Commonwealth of Australia.

The geothermal gradient for the study area is estimated by collecting all bottom hole temperature data measured for petrophysical logging runs and reported in well completion reports for O&G wells (combined data). All the data for the region was plotted on a single temperature depth plot (Figure 4-3). Since there are a number of reasons why a measured temperature may yet have had time to equilibrate but there are few explanations of why a temperature measurement may be recorded higher than the actual in situ temperature, the entire data set is used to define a best estimate of the in-situ temperature gradient by the high temperature edge of the cloud of data (Figure 5-3). We also constructed a separate temperature-depth plot for the Waukivory and Stratford areas (Figure 4-5 and Figure 4-4 respectively) to test if there were any differences.

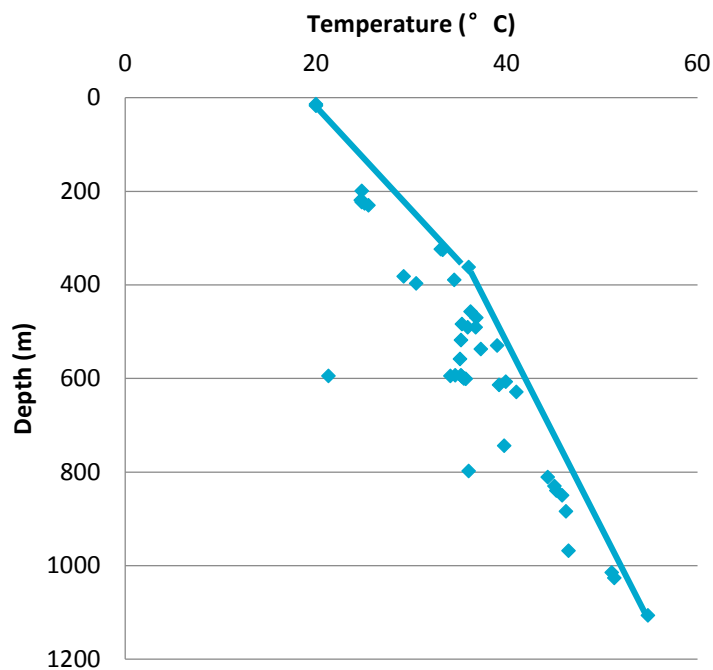


Figure 4-3 Geothermal gradient for the entire study area (blue line).

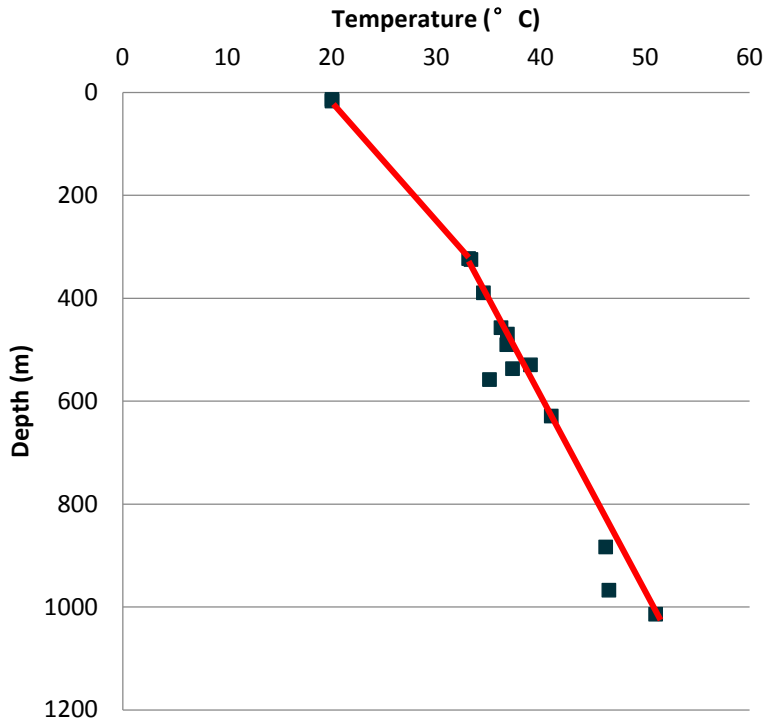


Figure 4-4 Geothermal gradient for Waukivory sub-area (red line).

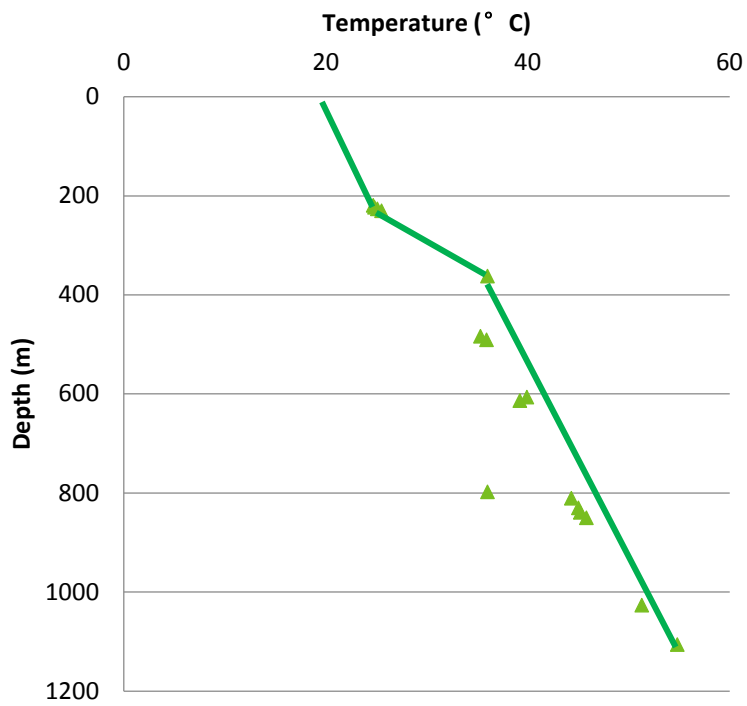


Figure 4-5 Geothermal gradient for Stratford sub-area (green line).

The geothermal gradient shows two distinctive values for the shallow and deep sections. This could be related to the relatively low thermal conductivity of coal that provide an insulating effect. Table 4-1 shows the calculated geothermal gradient for Gloucester Basin based on the data in the whole study area and for each sub-region.

Table 4-1 Estimated geothermal gradients (from Figure 4-3, Figure 4-4, and Figure 4-5) of the Gloucester Basin study area (combined data) and sub-regions.

GRADIENT(°C/KM)	SHALLOW PART	DEEP PART
All data	46.4	25.3
Waukivory area data	39	26.4
Stratford area data	23.3	80.6
		25.3

4.2.2 Hydrochemistry of deep boreholes

4.2.2.1 Introduction

Many of the biogeochemical processes that are known to control groundwater chemistry (such as mineral dissolution and precipitation, oxidation/reduction processes and mixing of different quality waters) are also important within coal seams and coal bearing strata. In general, groundwater chemistry is influenced by rainfall composition, interactions with soils during recharge, interactions with rock strata during through-flow and biological processes (Gibbs 1970; Drever 1988; Stumm and Morgan 1996; Appelo and Postma 2007).

Investigation of groundwater chemistry where coal seams are present requires an understanding of the dominant biogeochemical processes that can occur within coal seams and how these interact with the regional groundwater flow system (see section 4.3.3). There is an abundance of literature on the influence of various geological factors on groundwater chemistry and the general trends in groundwater chemistry that might be expected to occur as a result of sequences of hydrogeochemical evolution along groundwater flow paths (Güler and Thyne, 2004; Skrzypek et al., 2013; Somaratne and Frizenschaf, 2013). The literature surrounding groundwater chemistry within coal seams is more limited but there have been a sufficient number of investigations worldwide to enable us to summarise the general hydrochemical character of such waters and the key processes expected to control coal seam water chemistry. Some of the important features of coals that are expected to influence groundwater geochemistry include (Duvert et al., 2015; Owen et al., 2015; Papendick et al., 2011):

- the co-existence of water and gas;
- gas composition (methane plus higher hydrocarbons and other non-hydrocarbon gases such as CO₂);
- the stage of coal maturity;

- coal seam inter-burden mineralogy; and
- local geological and hydrogeological features.

Interactions between the groundwater and gas within coal bearing strata are expected to have an influence on groundwater composition. Any transfer of gas or water between the coal matrix and the coal fractures may further influence groundwater composition. Coal seam production waters associated with high gas production tend to be characterised by low concentrations of Ca and Mg and high concentrations of Na with high alkalinity and dissolved inorganic carbon values where the gases are interpreted to be of microbial or mixed origin on the basis of methane and water stable isotope compositions (Golding *et al.* 2013). In contrast, waters from areas of thermogenic gas production have lower alkalinity values and dissolved inorganic carbon concentrations (Golding *et al.* 2013). The Ca/Mg ratio and alkalinity of subsurface waters including coal seam production waters largely reflect reactions involving carbonate dissolution and precipitation and the extent of methanogenesis (Golding *et al.* 2013).

Despite these variations in major ion concentrations, there are some generalisations that can be made about the hydrochemical character of coal seam water. Coal seam water often predominantly consists of sodium and bicarbonate (and, where influenced by connate water of marine association, also chloride) and is essentially devoid of sulphate, calcium and magnesium (Van Voast 2003b; Cheung *et al.* 2010). Low sulphate concentrations are the result of the biochemical sulphate reduction reactions that commonly precede methanogenesis (Van Voast 2003b; Rice *et al.* 2008). The predominant process for calcium and magnesium depletion is likely to be the inorganic precipitation of calcite and dolomite cement due to reduced solubility in the presence of the elevated bicarbonate concentrations (Van Voast 2003b).

The degree of interactions between neighbouring formations via groundwater leakage and mixing along migration pathways influences the final hydrogeochemical character. Higher chloride concentrations within certain sections of a series of coal measures (generically) can indicate interactions with saline waters such as trapped (or sluggish) brines in marine sedimentary strata (Cheung *et al.* 2010) or longer residency times in the subsurface. As is depicted in Figure 4-6, recharge areas are characterised by weathering of pyrite (FeS_2) and marcasite (polymorphs of FeS_2) present in the coal and weathering of gypsum (CaSO_4); both processes produce high-sulfate (SO_4^{2-}) coal seam waters. Ion exchange with clays may also result in increasing sodium (Na^+) concentrations and decreasing calcium (Ca^{2+}) and magnesium (Mg^{2+}) concentrations (uptake from groundwater) and Na^+ (release into groundwater) (Lee, 1981). Further along the flow path with increasing residency time in the subsurface coal seam waters evolve as a result of anaerobic microbial sulfate reduction, bicarbonate (HCO_3^-) enrichment and calcium and magnesium depletion (Van Voast, 2003). As oxygen (O_2) concentration decreases with depth, sulfate-reducing bacteria convert dissolved sulfate and organics to sulfide (S^{2-}) (which is re-precipitated) and bicarbonate, respectively. The increase in bicarbonate concentration may lead to the precipitation of

calcite (CaCO_3) and dolomite ($\text{CaMg}(\text{CO}_3)_2$) that will reduce the concentration of calcium and magnesium in the coal seam waters (Van Voast, 2003).

4.2.2.2 Groundwater chemistry data collection and processing

Groundwater data was obtained from AGL surface and groundwater monitoring reports. The data was then organised and passed through a quality control procedure. Groundwater chemistry samples were automatically excluded from analysis if the charge balance error was greater than 15%, if the pH was 12 or above, or if the reports had noted that there was an issue with the sample. Well or bore depth information was used to assign each well or bore to a layer of the geological model. The data measured in this project (discussed in Section 5) was not available at the time this statistical analysis was undertaken.

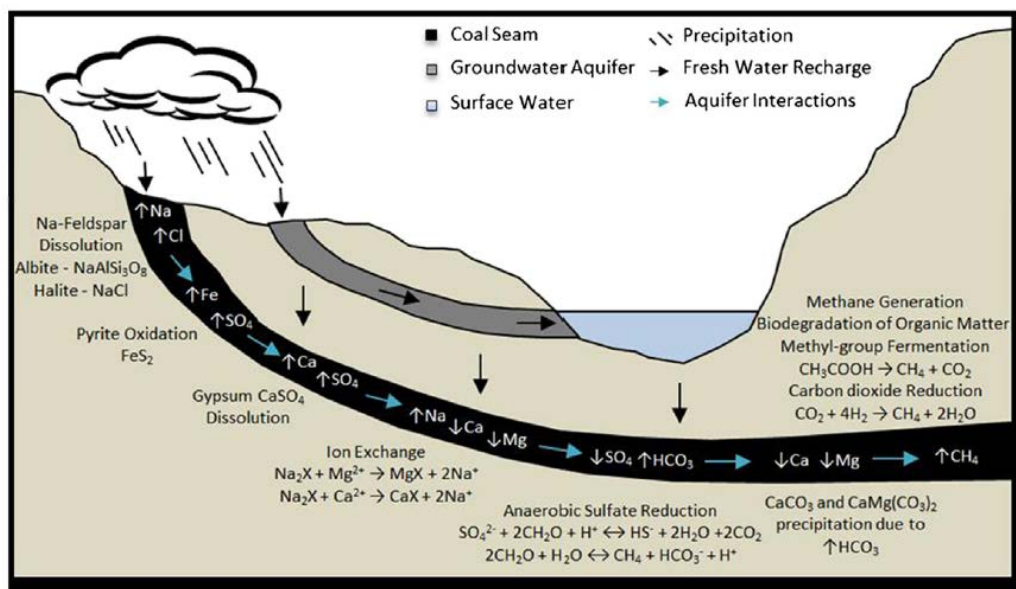


Figure 4-6 Generic representation of aquifer interactions along the recharge flow path and methane generation. Note: These processes are shown along the flow path, but they do not necessarily occur sequentially (Dahm et al., 2014).

4.2.2.3 Multivariate statistical analysis of hydrochemical data

Hierarchical cluster analysis (HCA) and Principal Component Analysis (PCA) were performed on all of the bore and well water quality data (combined data) as well as on different subsets of the data. The different analyses conducted include:

- Layers one to 12 of the geological model with all bores and well data in the Gloucester basin (combined data);
- Layers one to six of the geological model from wells across the Gloucester basin (subset 1);

- Layers one to six of the geological model from bores/wells in the area of interest around faults (subset 2);
- Layer eight of the geological model (subset 3); and
- Layer eight to 14 of the geological model (subset 4).

Not all parameters were included in the analysis. Parameters were excluded from the analysis if they were not measured in a significant number of the samples, or if more than approximately one third of the measurements were at the detection limit. Parameters that were highly correlated with other parameters (such as TDS with EC) were also not included. Remaining measurements at the detection limit were converted to half of the detection limit for analysis.

A hierarchical cluster analysis may be undertaken to identify any spatial patterns in hydrochemical parameters. All parameters, except pH, were logged, and all parameters were standardised by dividing by the standard deviation prior to HCA. All analysis was performed in R using Euclidean distances and Ward.D2 clustering for the HCA. Principal components analysis (PCA) is typically used to simplify the original data by representing the same observations in fewer than the original number of variables. It is also referred to as eigenvector analysis (Kutzbach, 1967; Gray, 1981), empirical orthogonal functions (Lorenz, 1956; Gilman, 1957), and singular decomposition (Rasmusson et al., 1981). These so-called reduced space techniques attempt to find a smaller number of dimensions (variables) that contain most of the information in the original space (Green and Carroll, 1978). Principal components try to find linear combinations of the original variables. The most important properties of these combinations are i) the factor scores have maximal variance, and ii) the combinations are uncorrelated with previously computed combinations. PCA was used here to synthesize the data set and find patterns (clustering of wells) that could be explained by the new variables (principal components).

4.3 Results

4.3.1 Initial hydraulic head analysis

With all available pressure data converted to fresh water hydraulic values, these were then allocated to the 16 horizons from the AGL static model. The alluvial aquifer, shallow weathered bedrock aquifer and Layer 8 contained the most data. An initial hydraulic head distribution was mapped for each of these. The patterns for the alluvial and weathered bedrock aquifers were similar so these two datasets were combined. A few data points were available from Layer 6 and these also matched the hydraulic head distribution of the alluvial-weathered bedrock combined map. The Layer 8 map exhibited sufficient differences to map it separately. A similar process was followed for other layers in an effort to group units showing similar trends. The first iteration of hydraulic head maps used faults from the

AGL static model, from CSIRO as part of the bioregional assessment work (McVicar et al., 2014) and from Parson and Brinckerhoff (2013) to help constrain the hydraulic head distributions following the general approach described by Underschultz et al. (2005). The 2D fault traces from these various sources were without other information such as dip, and the fault population was quite dense making it difficult to know a-priori which faults are important to flow. A first-pass approach was taken to plot hydraulic head data on the total fault population and to look for large variations in hydraulic head across a fault (Figure 4-7). Here, a series of lineations highlighted in red, were selected as marking significant breaks in hydraulic head. This set of lineations was used in constraining a first iteration of hydraulic head maps with the expectation that these maps would change as more information was brought to bear on constraining the flow systems as the project progressed.

The deepest hydraulic head map in the study area is for layers 11-14 (Figure 4-8). With data only available on the eastern part of the maps a head distribution is defined in that area with a general southwesterly gradient terminating against the red highlighted fault.

The layer 10 data set was restricted mainly to the west side of the red highlighted fault (Figure 4-9). It should be noted that there are often more than one DST or WLT in the same well for the same layer. As the bulk permeability is generally on the order of 1 mD there is a high incidence of miss runs or poor pressure build-up making an estimate of formation pressure uncertain. Figure 4-9 gives an example where insets are displayed of the data tables, i.e. hydraulic head depth plots that were used to assess the quality of the individual data points. The distribution of head for Layer 10 defines a generally northwards gradient on the west side of the selected red fault trace in contrast to the previous map for layer 11-14 (Figure 4-8).

The next shallower mappable unit is Layer 8 (Figure 4-10) where there is sufficient data to establish a distribution on either side of the selected red fault trace. The eastern side demonstrated a similar trend of decreasing head to the southwest as was previously observed in L11-14. On the west side of the selected red fault trace there appear to be two sources of fluid marked by closed hydraulic head highs with flow emanating from the fault. At the same time there remains a hydraulic head discontinuity across the red fault trace at several locations. Multiple test data at Waukivory 11 show a vertical profile of decreasing hydraulic head beginning with 118m decreasing to 89m by the Fairbairns Lane strata below. To the east of the selected red fault, hydraulic head in both Waukivory 12 and Waukivory 14 have multiple test data that define upward flow with decreasing head upwards with the lowest value at 89m comparable to the surface elevation in Waukivory River.

The shallowest unit with mapped hydraulic head is the combined Layers 1-6 (Figure 4-11) that includes both the alluvium and the shallow fractured bedrock.

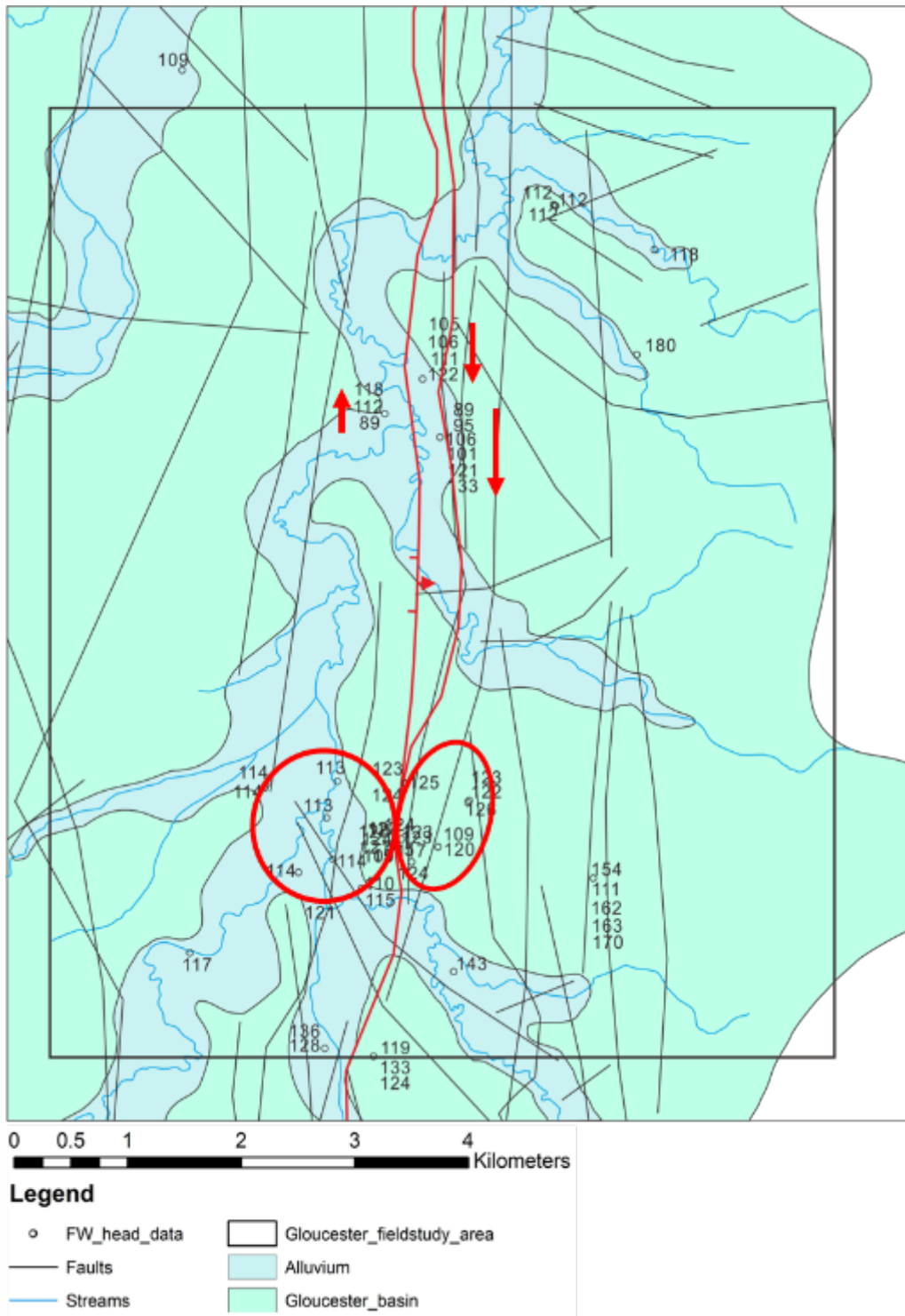


Figure 4-7 Hydraulic head values of study area. Well locations with multiple hydraulic head values along the vertical showing a consistent gradient are indicated by red arrows. The red circles show regions of significant hydraulic head differences across a fault. The fault traces highlighted in red have been selected as likely being significant to fluid flow.

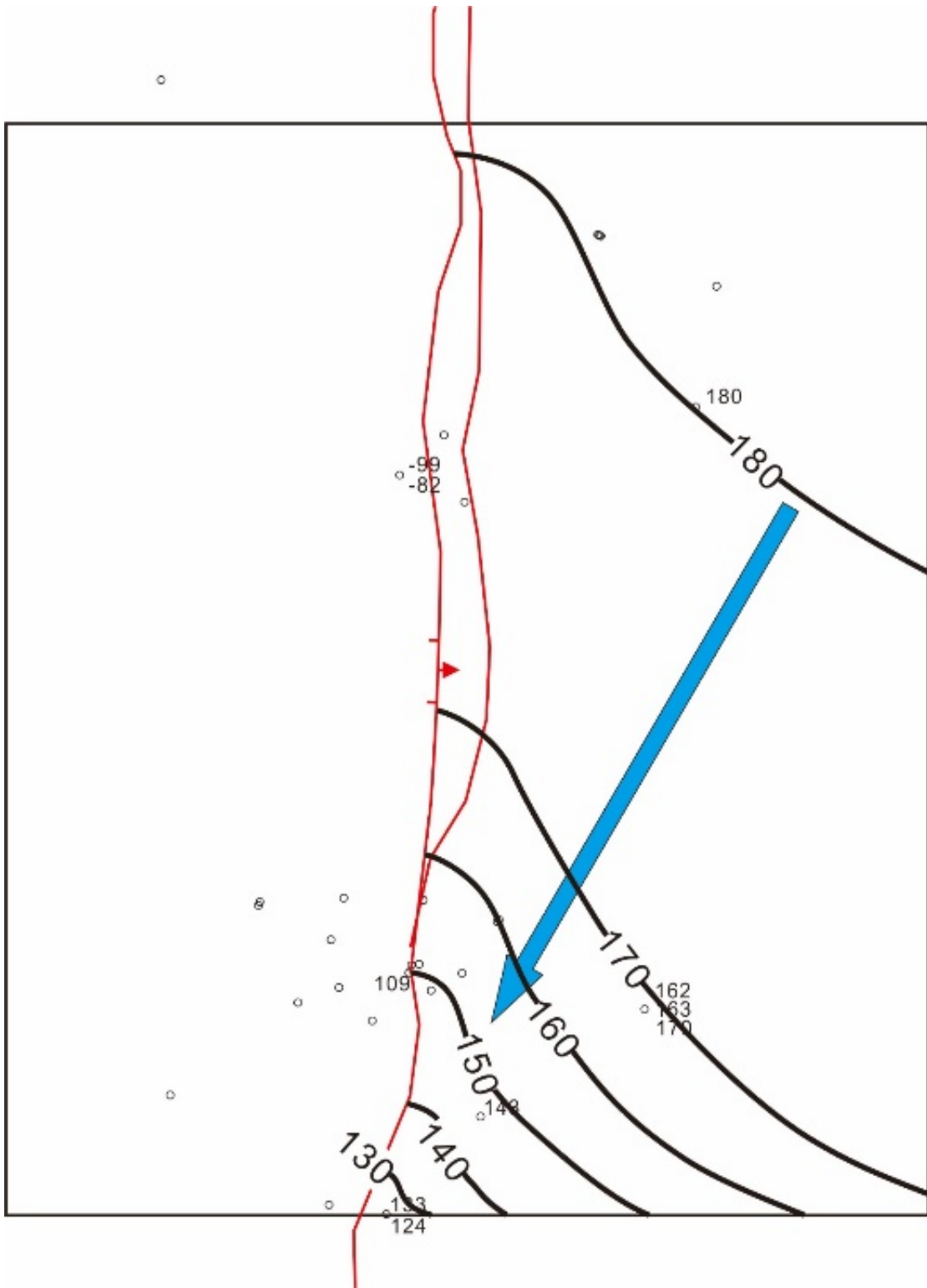


Figure 4-8 Fresh water hydraulic head isolines (bold black contours) for L11-14. Inferred flow arrows are in blue. Fault traces likely significant to fluid flow are shown in red.

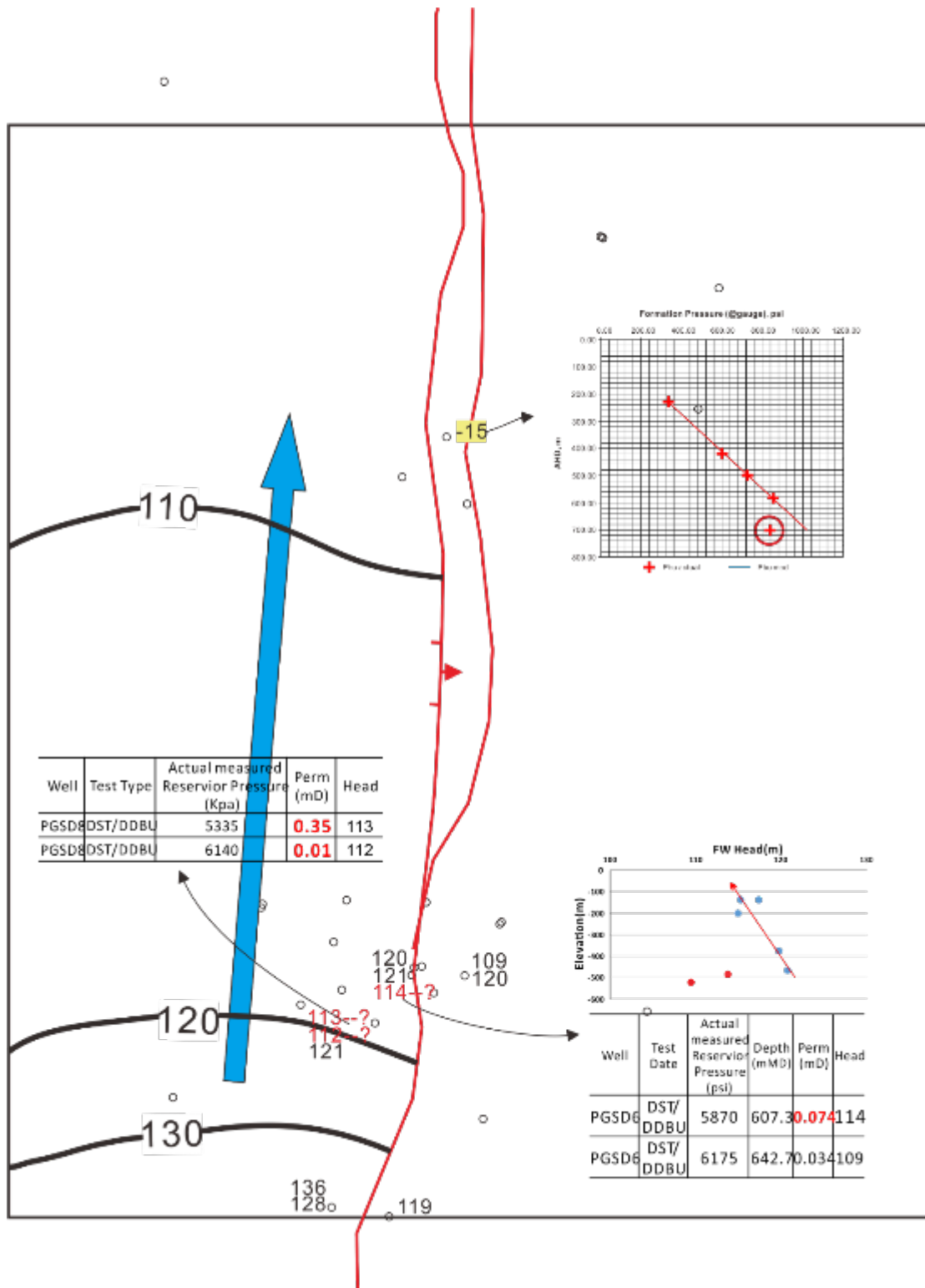


Figure 4-9 Fresh water hydraulic head isolines (bold black contours) for L10. Some well data are posted with hydraulic head-elevation plots and well test data tables to show the data QC process. Inferred flow arrows are in blue. Fault traces likely significant to fluid flow are shown in red.

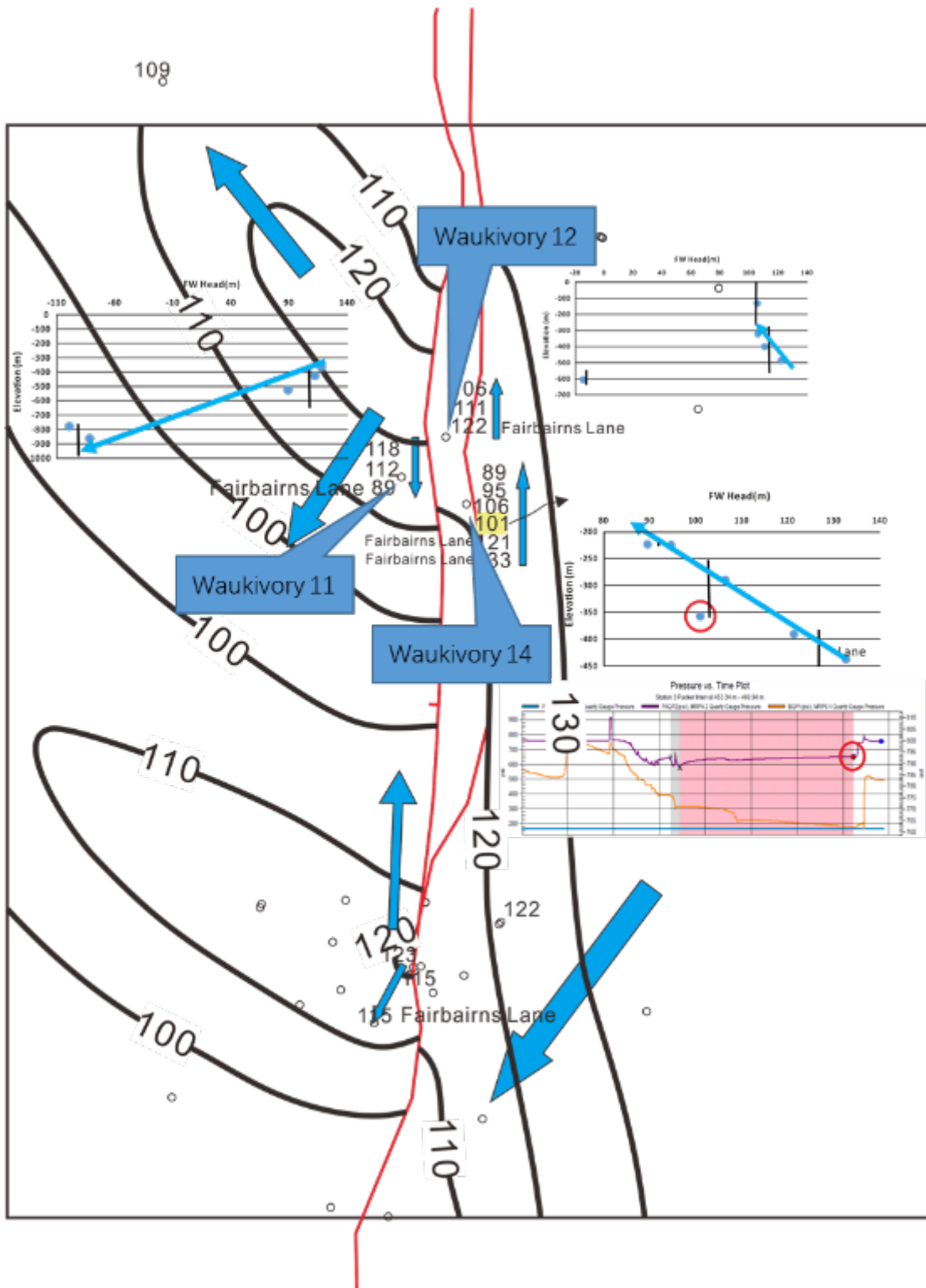


Figure 4-10 Fresh water hydraulic head isolines (bold black contours) for L8. Some well data are posted with hydraulic head-elevation plots and well test data tables to show the data QC process. Inferred flow arrows are in blue. Fault traces likely significant to fluid flow are shown in red.

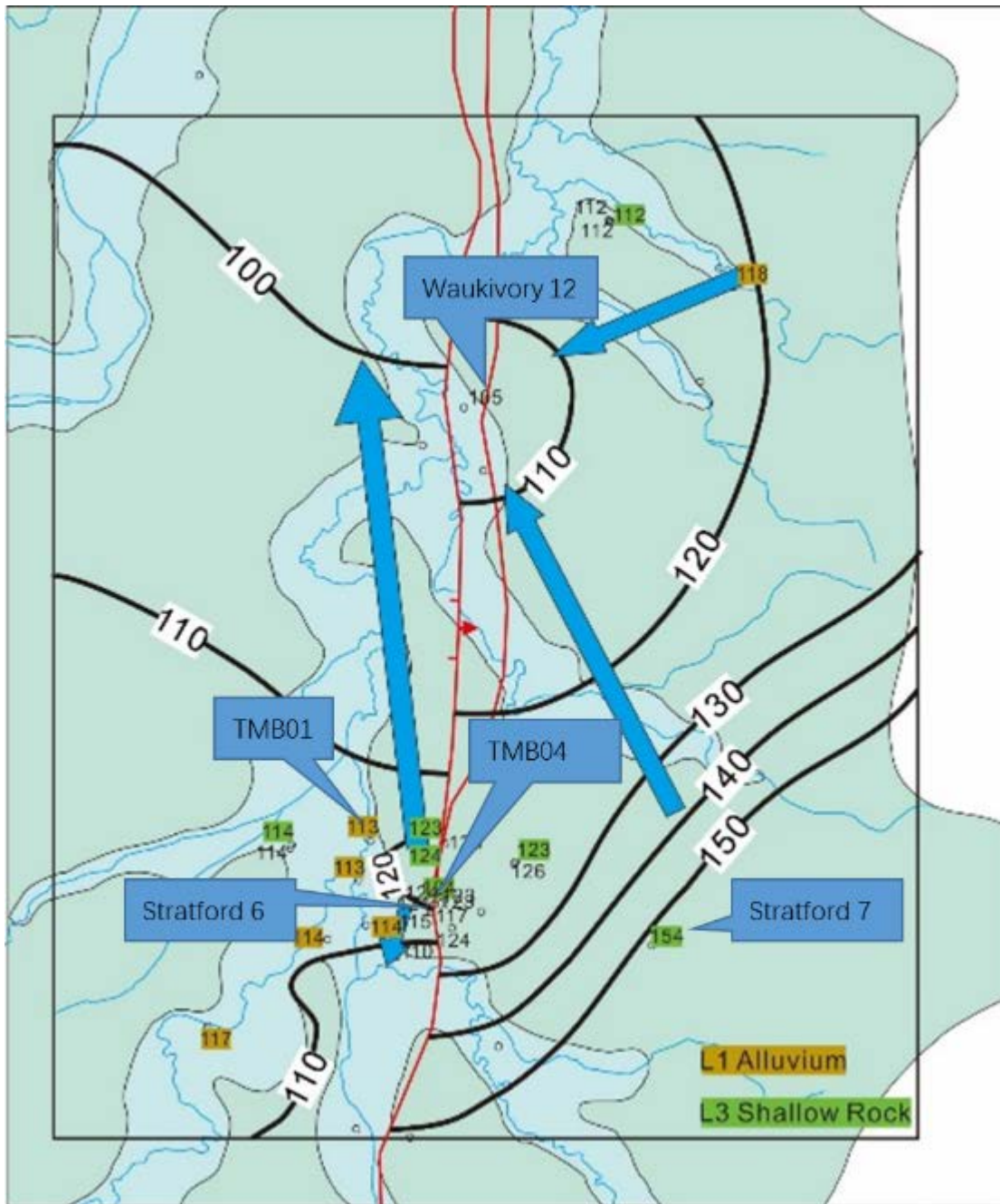


Figure 4-11 Fresh water hydraulic head isolines (bold black contours) for L1-L6 with the hydraulic head value posted next to each well/bore. Data from the alluvium is in khaki green and data from the shallow fractured bedrock is in bright green. Inferred flow arrows are in blue. Fault traces likely significant to fluid flow are shown in red.

The Stratford area has higher hydraulic head values than the Waukivory area (Figure 4-11). To the west of the selected red fault trace near TCMB 04 there appears to be a closed hydraulic head high against the fault indicating a source of formation water emanating from the fault. From here there is a general gradient to lower values in the north with flow roughly parallel to the red selected fault. On the east side of the selected red fault, Stratford 7 in the southeast shows the highest value of hydraulic head at 154m. This defined a

northwards gradient towards a low value at Waukivory 12 (105m) that appears to define a sink with a closed low against the eastern side of the selected red fault.

4.3.2 Hierarchical cluster analysis and principal component analysis

4.3.2.1 Layers 1-12 all bores/wells

Averages for each parameter at a sampling location (bore/well) were used in the analysis as there were enough sampling locations to conduct HCA and PCA with one measurement per location. Figure 4-12 shows the result of the HCA with each leaf in the dendrogram labelled by the bore ID. Figure 4-13 shows the same results, but with each leaf labelled by the geological model layer that from which the bore water sample was sourced. To analyse the results of the HCA, bores were assigned to two groups by cutting the dendrogram at a height of 15, and to three groups by cutting the dendrogram at height of 10 (Figure 4-12). Figure 4-12 sets out the bore identifications, which geological model layer each bore was assigned to and which group each bore would be assigned to, based on the results of the HCA. Figure 4-13 sets out which geological model layer each bore was assigned to. The PCA scores for components one and two are shown in Figure 4-14. Table 4-3 sets out the component weightings and proportion of explained variance across all components of the PCA. No distinct pattern could be detected in groundwater chemistry composition; either by geological layer (Figure 4-14), or geographically across the basin (Figure 4-15 and Figure 4-16) was evident when all bores were analysed together.

Figure 4-17 and Figure 4-18 show Piper diagrams of the average proportion of major anions and cations for each bore, with the symbol colours indicating which group the bore was assigned to in the HCA. No clear link between water type (as shown by the Piper diagram) and bore group assignment through HCA can be seen. This is not particularly surprising given that pH and methane (neither of which are displayed in the Piper diagram) were identified as the principle component differences between water samples.

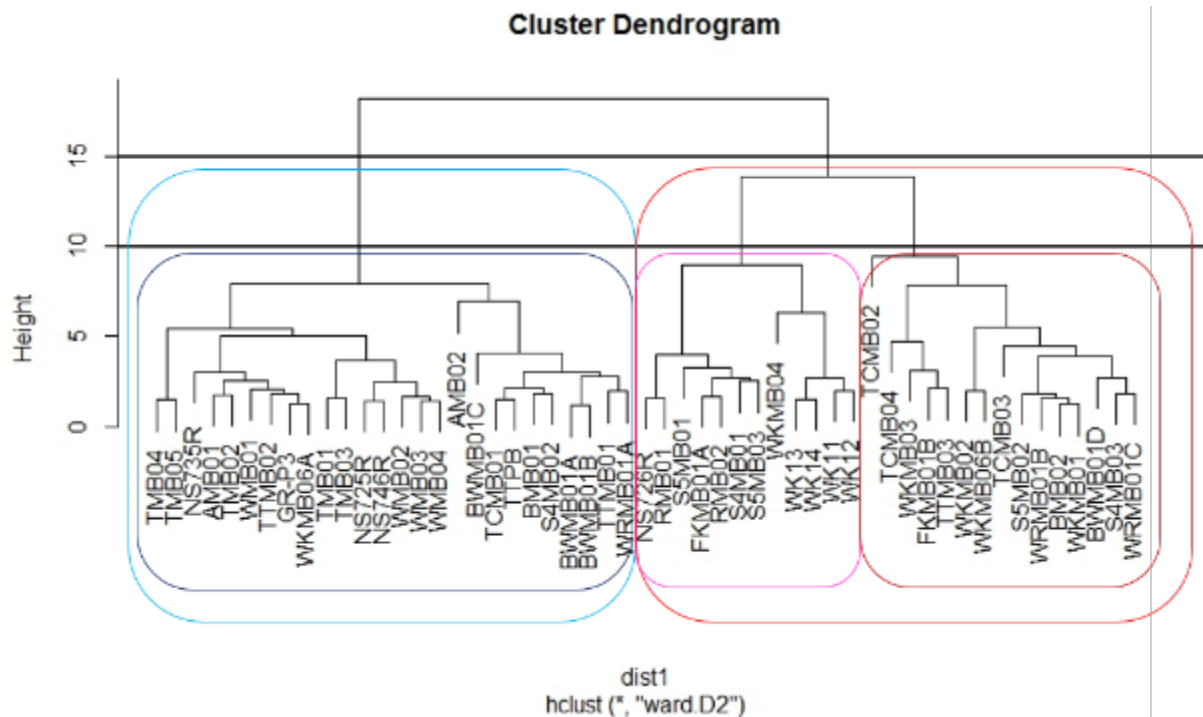


Figure 4-12 HCA result for layers 1-12 labelled by bore ID. Black horizontal lines represent where the dendrogram would be cut at a height of 15 creating; group 1 circled in light blue and group 2 circled in red, and at a height of 10 creating; group 1 circled in dark blue, group 2 circled in dark red and group 3 circled in pink.

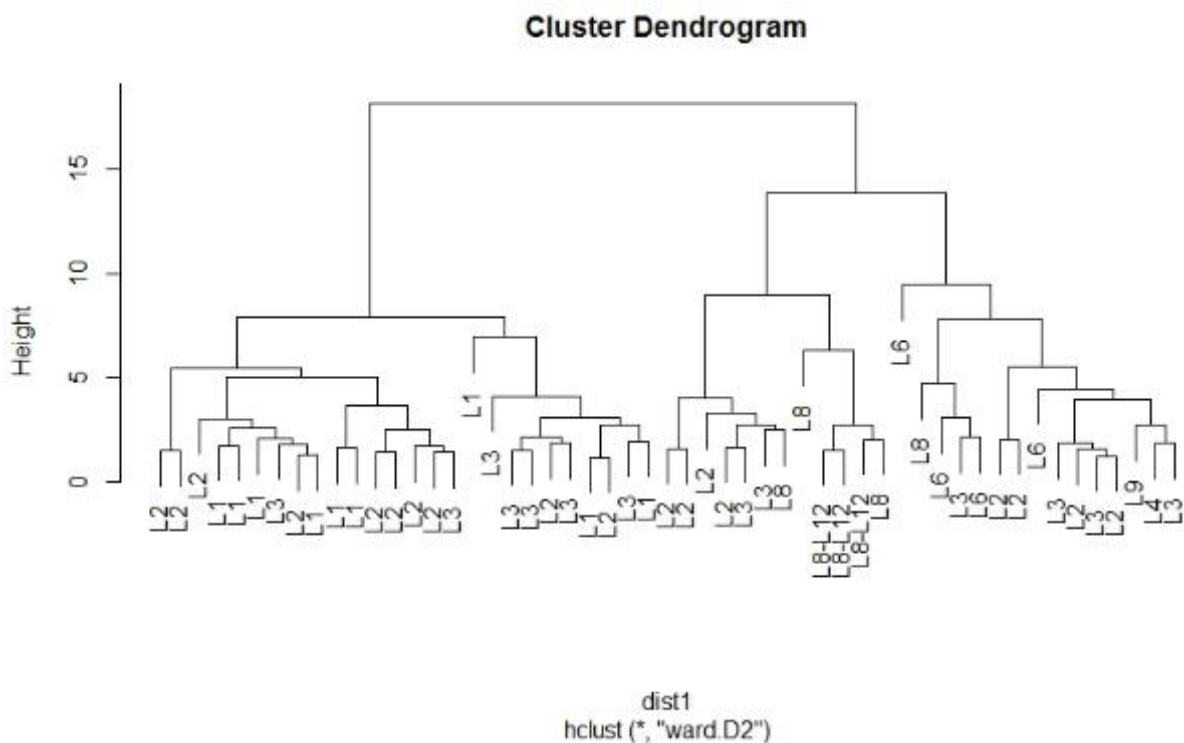


Figure 4-13 HCA result for layers 1-12 labelled by the geological model layer that was sampled.

Table 4-2 HCA Bore IDs, model layer assignment and HCA group assignments.

BORE/WELL	MODEL LAYER	CUT 15	CUT 10	BORE/WELL	MODEL LAYER	CUT 15	CUT 10
AMB01	L1	1	1	TTMB02	L3	1	1
AMB02	L1	1	1	TTMB03	L6	2	2
BMB01	L2	1	1	TTPB	L3	1	1
BMB02	L3	2	2	WK11	L8-L12	2	3
BWMB01A	L1	1	1	WK12	L8	2	3
BWMB01B	L2	1	1	WK13	L8-L12	2	3
BWMB01C	L3	1	1	WK14	L8-L12	2	3
BWMB01D	L9	2	2	WKMB01	L2	2	2
FKMB01A	L2	2	3	WKMB02	L2	2	2
FKMB01B	L3	2	2	WKMB03	L6	2	2
GR-P3	L2	1	1	WKMB04	L8	2	3
NS725R	L2	1	1	WKMB06A	L1	1	1
NS726R	L2	2	3	WKMB06B	L2	2	2
NS735R	L2	1	1	WMB01	L1	1	1
NS746R	L2	1	1	WMB02	L2	1	1
RMB01	L2	2	3	WMB03	L2	1	1
RMB02	L3	2	3	WMB04	L3	1	1
S4MB01	L3	2	3	WRMB01A	L1	1	1
S4MB02	L3	1	1	WRMB01B	L2	2	2
S4MB03	L4	2	2	WRMB01C	L3	2	2
S5MB01	L2	2	3				
S5MB02	L3	2	2				
S5MB03	L8	2	3				
TCMB01	L3	1	1				
TCMB02	L6	2	2				
TCMB03	L6	2	2				
TCMB04	L8	2	2				
TMB01	L1	1	1				
TMB02	L1	1	1				
TMB03	L1	1	1				
TMB04	L2	1	1				
TMB05	L2	1	1				
TTMB01	L3	1	1				

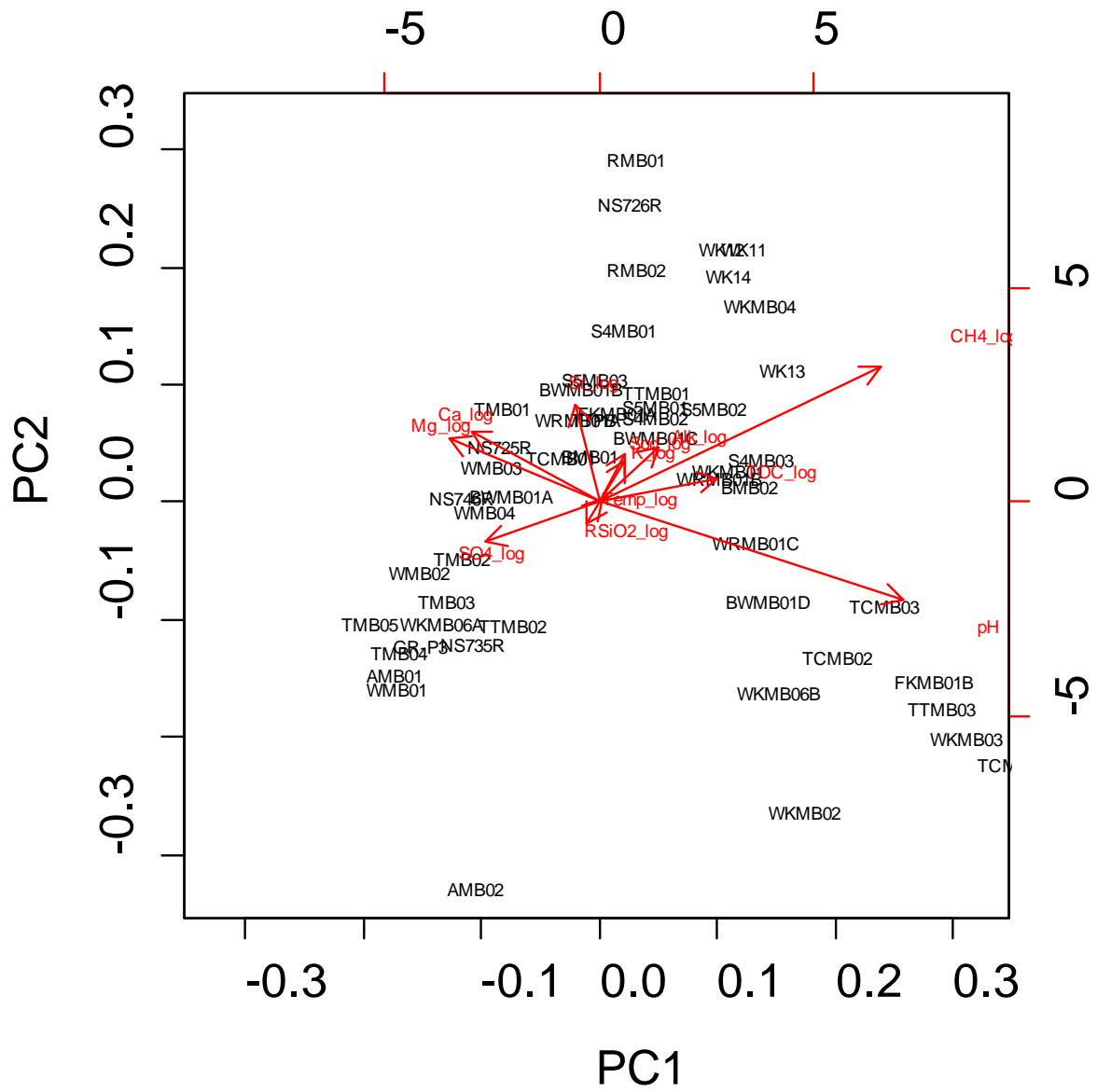


Figure 4-14 PCA result for layers 1-12.

Table 4-3 Component weightings and proportion of explained variance from the Principal Components Analysis. Highlighted values show the largest positive and negative weighting for the first two components.

	PC1	PC2	PC3	PC4	PC5	PC6	PC7	PC8	PC9	PC10	PC11	PC12
pH	0.617	-0.418	0.178	0.236	0.530	-0.183	0.027	0.155	0.063	0.106	0.057	0.001
Ca (log₁₀)	-0.261	0.300	0.078	0.124	0.201	0.140	0.076	0.515	-0.060	0.602	0.350	-0.039
Mg (log₁₀)	-0.305	0.269	0.129	0.095	0.608	0.058	0.114	-0.450	0.333	0.073	-0.324	-0.001
K (log₁₀)	0.053	0.174	0.365	-0.013	0.024	-0.087	0.647	-0.061	-0.613	-0.139	-0.082	0.006
Na (log₁₀)	0.050	0.206	0.200	-0.026	-0.004	-0.348	-0.151	-0.468	0.026	-0.030	0.741	-0.026
SO4 (log₁₀)	-0.230	-0.170	0.415	0.787	-0.320	0.025	-0.116	-0.044	0.045	-0.034	-0.066	0.003
Temperature (log₁₀)	0.006	0.011	0.002	0.001	-0.003	-0.045	-0.013	0.024	0.003	-0.047	-0.049	-0.996
Alkalinity as CaCO₃ (log₁₀)	0.120	0.229	0.170	-0.111	-0.140	-0.543	-0.390	-0.028	-0.195	0.428	-0.449	0.034
RSiO2 (log₁₀)	-0.024	-0.088	0.170	-0.085	0.260	0.508	-0.551	-0.156	-0.547	-0.042	0.0224	-0.022
Total organic carbon (log₁₀)	0.239	0.103	0.675	-0.381	-0.217	0.330	0.009	0.096	0.406	0.019	-0.038	-0.007
CH4 (log₁₀)	0.571	0.569	-0.273	0.359	-0.136	0.320	0.006	-0.144	0.005	0.047	-0.049	-0.009
Sr (log₁₀)	-0.049	0.409	0.109	0.075	0.232	-0.218	-0.262	0.478	0.039	-0.640	-0.015	0.060
Standard deviation	1.971	0.950	0.770	0.626	0.496	0.347	0.325	0.266	0.261	0.159	0.118	0.031
Cumulative proportion	0.605	0.745	0.838	0.899	0.937	0.956	0.972	0.983	0.994	0.998	0.999	1.000

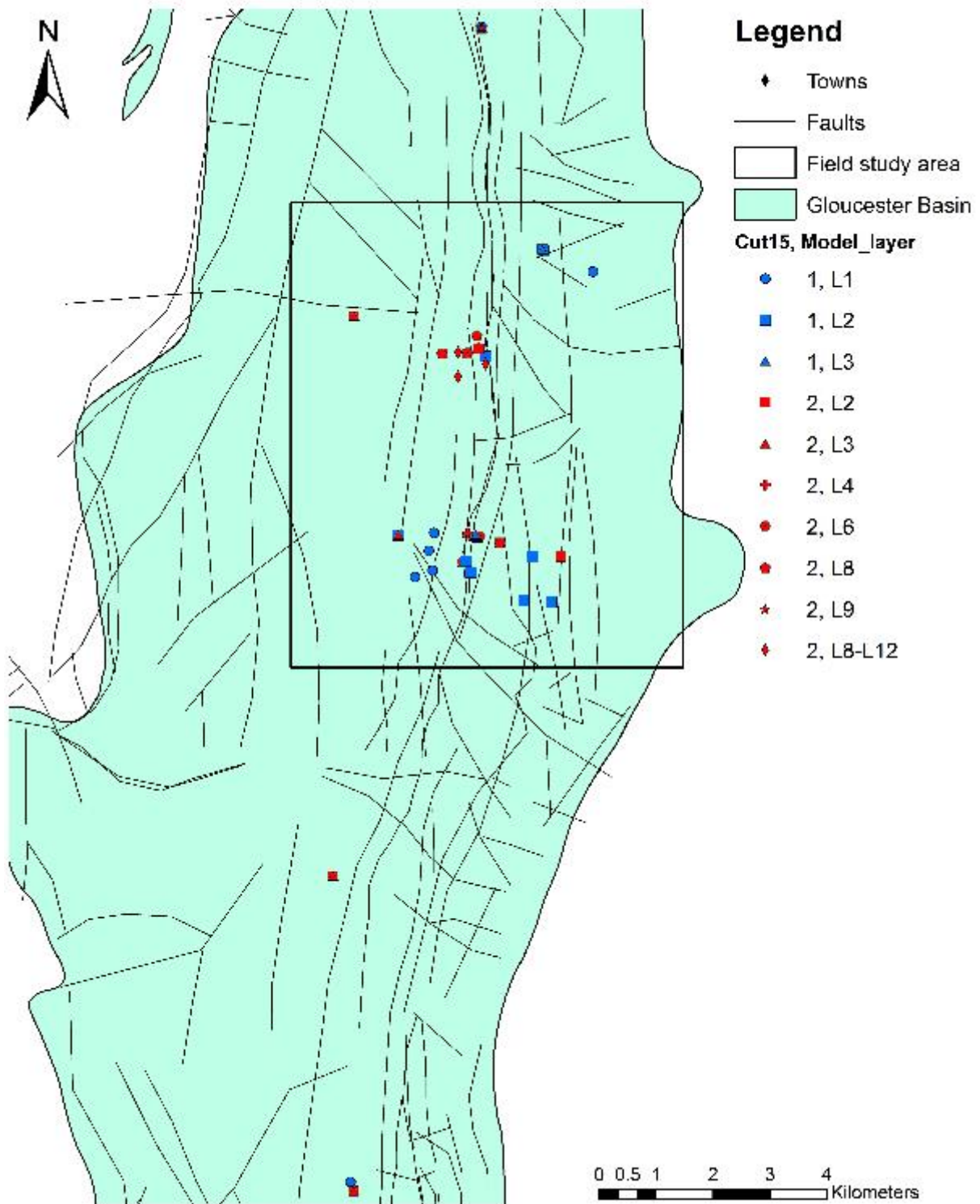


Figure 4-15 HCA results plotted spatially with bores assigned to one of two groups by cutting the dendrogram at a height of 15 (see Figure 4-12).

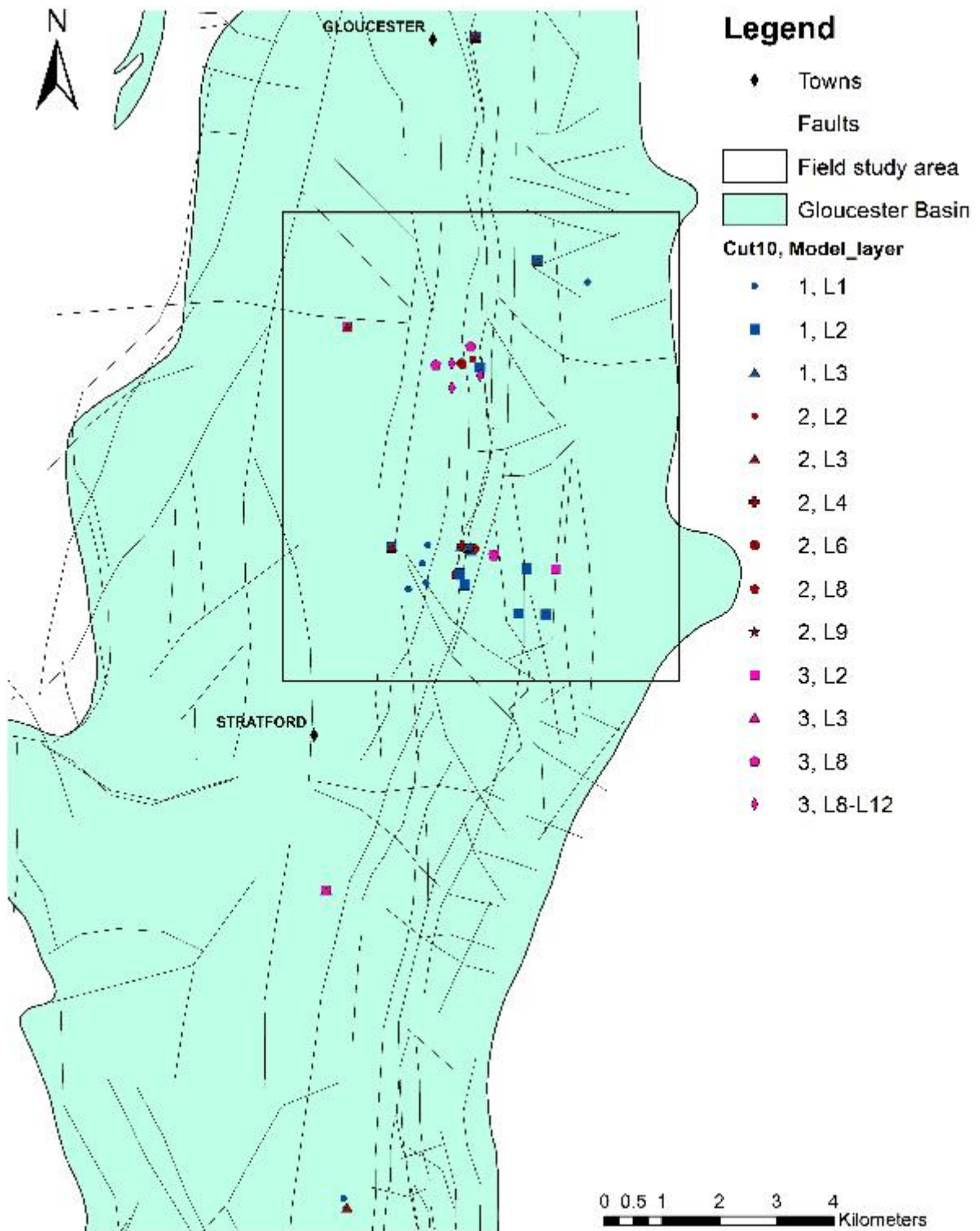


Figure 4-16 HCA results plotted spatially with bores assigned to one of three groups at a height of 10 (see Figure 4-12).

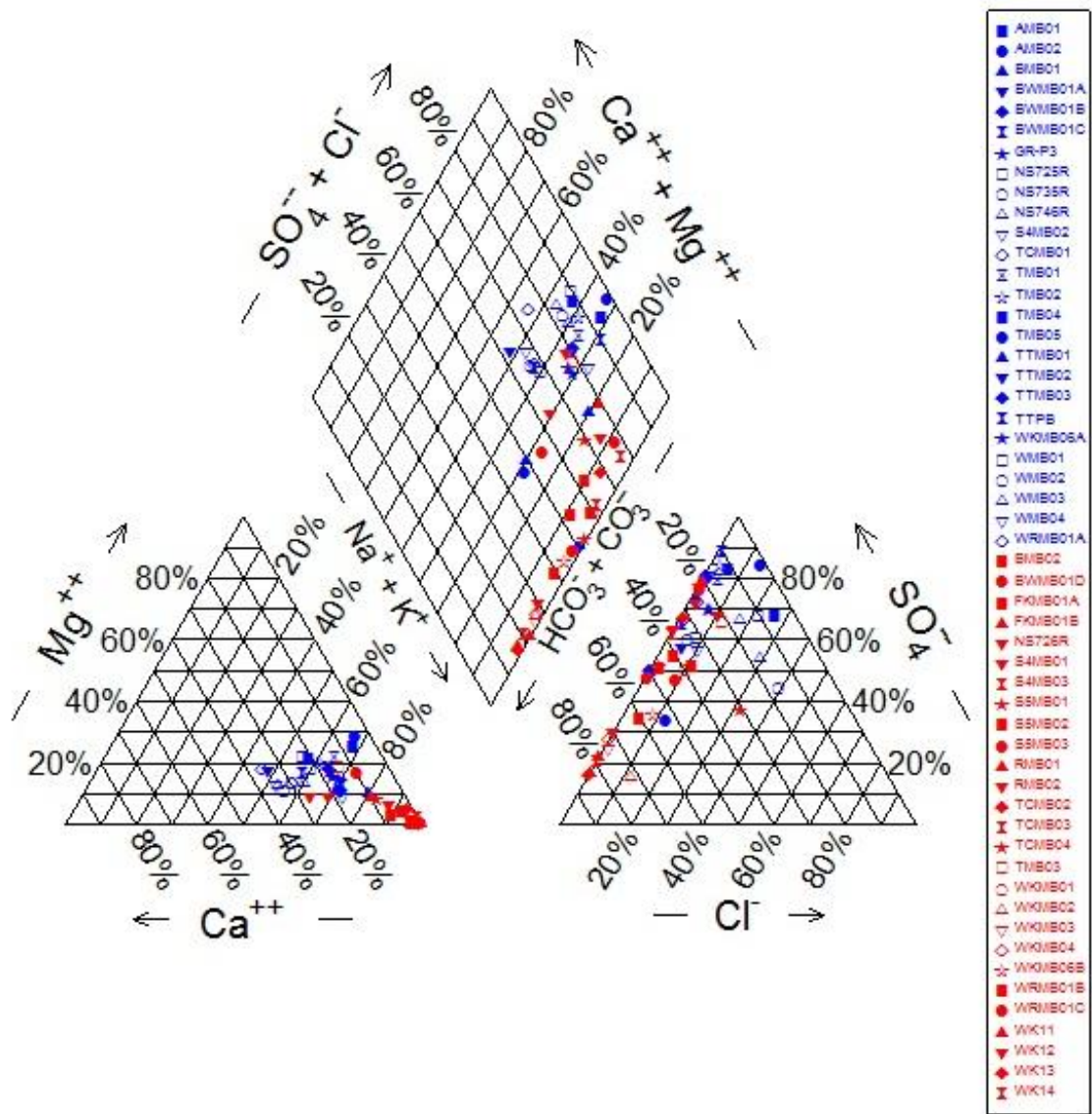


Figure 4-17 HCA results Piper diagram of average proportion of major anions and cations for each bore. Colours represent the HCA group with the dendrogram cut at 15; red = group 1, blue = group 2.

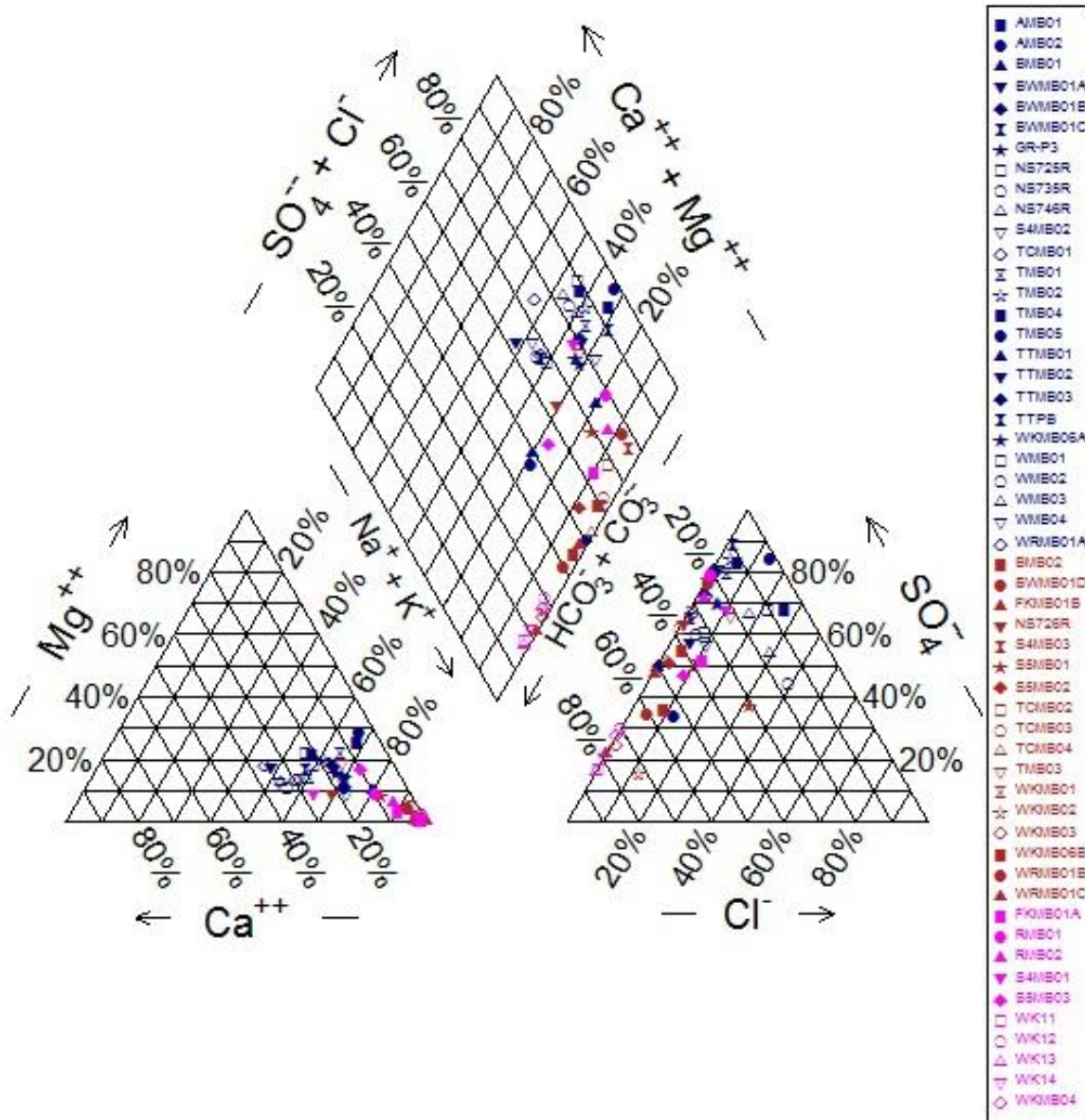


Figure 4-18 Piper diagram of average proportion of major anions and cations for each bore. Colours represent the HCA group with the dendrogram cut at 10; red = group 1, blue = group 2, pink = group 3.

4.3.2.2 Other grouping of data

The same procedure as described above was used to examine various possible groupings of data. For example data from layers 1-6, data from layer 8, data from layers 8-12, and bores located near to faults. Averages for each parameter at a sampling location (bore/well) were used in most of these analysis (except for layers 8-12) as there were enough sampling locations to conduct an HCA. To analyse the results of the HCA, bores were assigned to two groups by cutting the dendrogram at a height of 15, and to three groups by cutting the dendrogram at height of 10. Bore identifications and the geological model layer each bore was assigned to and which group each bore would be assigned to, based on the results of the HCA. The PCA scores for components one and two, sets out the component weightings

and proportion of explained variance across all components of the PCA. From all the variety of groupings that we examined, no distinct spatial pattern in groundwater chemistry composition was observed (resulting diagrams are not shown).

In the case of the Gloucester Basin, the HCA and PCA analysis did not reveal any striking and obvious trends in the hydrochemistry data. As a result we moved to simply mapping the salinity (TDS) distribution for each hydrostratigraphic layer.

4.3.2.3 Total Dissolved Solids

Within the study area, layers 1-6 contained the most water chemistry data and also showed the most variability in formation water salinity (TDS) as shown in Figure 4-19. In the Waukivory area the WKMB01 and WKMB03 wells have more than 2,000 mg/L salinity. In the Stratford area, there are also two high TDS areas separated by faults, TMB01 at 4,633 mg/L and TMB05 at 5,012 mg/L. The red marked fault between these 2 bores may play a significant role in groundwater discontinuity laterally but may also be a source of upwelling higher salinity formation water. Other than the high salinity anomaly the region is generally less than 2,000 mg/L. It is interesting that there is a sudden change in TDS between Stratford 6 and TMB04 but there are no identified faults in this area. Finally there is a region of more than 2,000 mg/l in the northeast part of the study area.

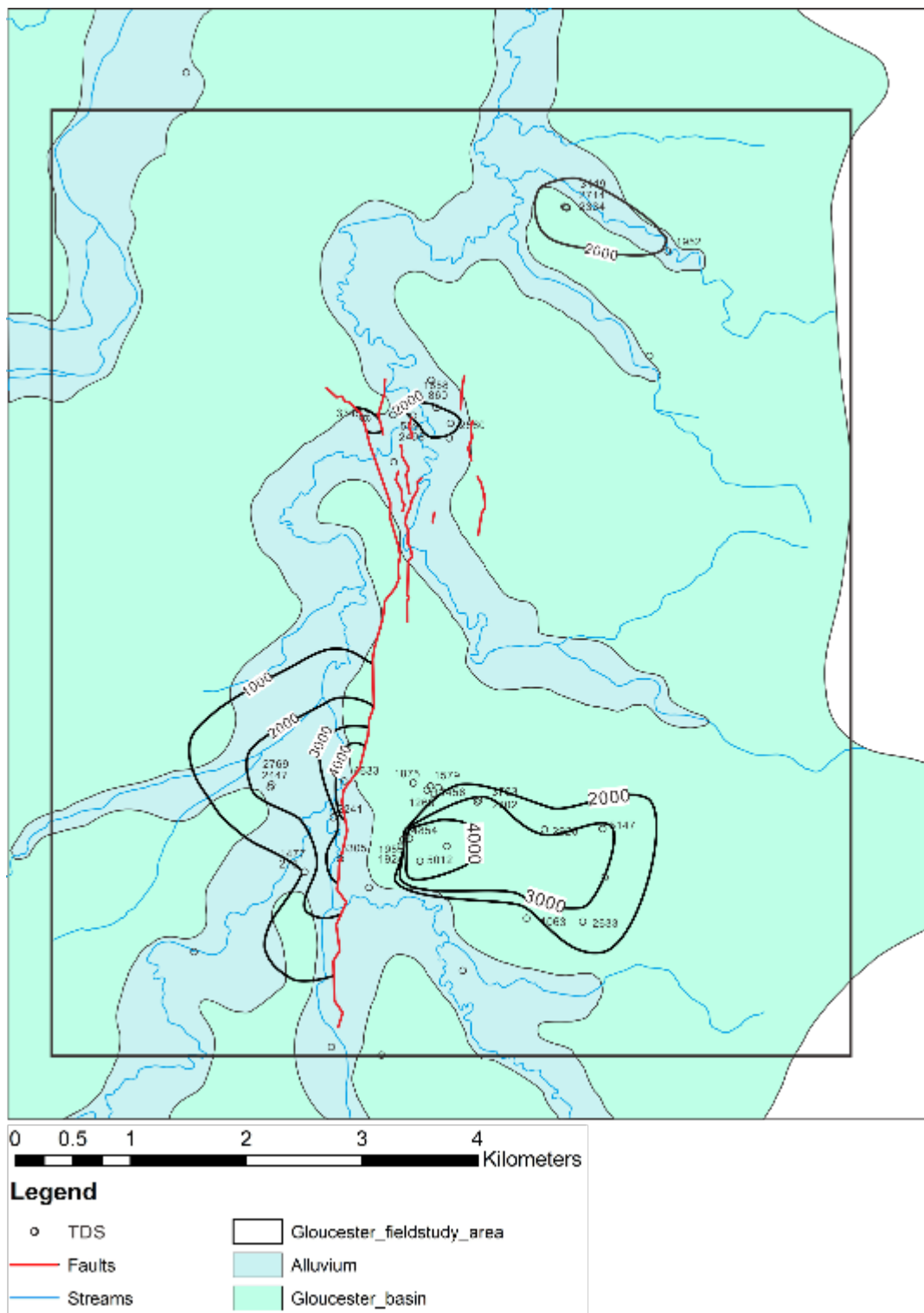


Figure 4-19 Salinity (total dissolved solids) distribution for layers 1-6.

4.4 References

- Appelo CA J and Postma D (2007). *Geochemistry, Groundwater and Pollution*. Amsterdam, The Netherlands, A.A.Balkema Publishers.
- Cheung K, Klassen P, Mayer B, Goodarzi F and Aravena R (2010). Major ion and isotope geochemistry of fluids and gases from coalbed methane and shallow groundwater wells in Alberta, Canada. *Applied Geochemistry* 25: 1307-1329.
- Dahm KG, Guerra KL, Munakata-Marr J and Drewes JE (2014). Trends in water quality variability for coalbed methane produced water. *Journal of Cleaner Production* 84: 840-848.
- Drever JI (1988). *The geochemistry of natural waters*. Englewood Cliffs, NJ, Prentice-Hal.
- Duvert CMR, Owen DDR, Cendón DI, Batiot-Guilhe C, and Cox ME (2015). Hydrochemical processes in a shallow coal seam gas aquifer and its overlying stream–alluvial system: implications for recharge and inter-aquifer connectivity. *Applied Geochemistry* 61: 146-159.
- Fetter CW (1994). *Applied Hydrogeology*, 4th ed. Macmillan College Publishing, Inc., New York, 113-119.
- Gibbs R (1970). Mechanisms controlling world water chemistry. *Science* 170: 1088-1090.
- Golding SD, Boreham CJ and Esterle JS (2013). Stable isotope geochemistry of coal bed and shale gas and related production waters: A review. *International Journal of Coal Geology* 120: 24-40.
- Gray BM (1981). On the stability of temperature eigenvector patterns. *Journal of Climatology* 1: 273-281.
- Green PE and Douglas Carroll J (1978). *Analyzing Multivariate Data*. John Wiley and Sons, 519 pp.
- Güler C and Thyne GC (2004). Hydrologic and geologic factors controlling surface and groundwater chemistry in Indian Wells-Owens Valley area, southeastern California, USA. *Journal of Hydrology* 285: 177-198.
- Hortle A, Otto C and Underschultz J (2013) A quality control system to reduce uncertainty in interpreting formation pressures for reservoir and basin pressure system analysis. *Journal of Petroleum Geology* 36 (2): 163-177.
- Kutzbach JE (1967). Empirical eigenvectors of sea-level pressure, surface temperature and precipitation complexes over North America. *Journal of Applied Meteorology* 6: 791-802.
- Lee RW (1981). *Geochemistry of water in the Fort Union Formation of the Powder River basin, Southeastern Montana*: U.S. Geological Survey Water-Supply Paper 2076, 17 pp.

- Lorenz E (1956). Empirical orthogonal functions and statistical weather prediction. Scientific Report No. 1, Contract AF19-(604) 1566, Dept. Meteor., MIT.
- Luszczynski NJ (1961). Head and Flow of Ground Water of Variable Density. *Journal of Geophysical Research*, Volume 66, No. 12.
- McVicar TR, Langhi L, Barron OV, Rachakonda PK, Zhang YQ, Dawes WR, Macfarlane C, Holland KL, Wilkes PG, Raisbeck-Brown N, Marvanek SP, Li LT and Van Niel TG (2014). Context statement for the Gloucester subregion. Product 1.1 from the Northern Sydney Basin Bioregional Assessment. Department of the Environment, Bureau of Meteorology, CSIRO and Geoscience Australia, Australia.
- Mulley R (2004). *Flow of Industrial Fluids: Theory and Equations*. CRC Press, 43–44.
- Otto CJ, Unterschultz JR, Hennig AL and Roy VJ (2001). Hydrodynamic analysis of flow systems and fault seal integrity in the North West Shelf of Australia. *APPEA Journal*, Volume 41: 347-365.
- Owen DR, Raiber M, and Cox ME (2015). Relationships between major ions in coal seam gas groundwaters and their application as indicators of hydrogeochemical processes: examples from the Surat and Clarence-Moreton basins, Queensland, Australia. *International Journal of Coal Geology* 137: 77-91.
- Papendick SL, Downs KR, Vo KD, Hamilton SK, Dawson GKW, Golding SD, and Gilcrease PC (2011). Biogenic methane potential for Surat Basin, Queensland coal seams. *International Journal of Coal Geology* 88: 123–134.
- Parsons Brinckerhoff (2013). Hydrogeological Investigation of a strike slip fault in the northern Gloucester Basin. Report to AGL. 90.
- Rasmusson EM, Arkin PA, Chen W-Y and Jalickee JB (1981). Biennial variations in surface temperature over the United States as revealed by singular decomposition. *Monthly Weather Review* 109: 587-598.
- Rowe AM and Chou JCS (1970). Pressure-Volume-Temperature-Concentration of aqueous NaCl solutions. *Journal of Chemical and Engineering Data* 15: 61-66.
- Skrzypek G, Dogramaci S, Grierson PF (2013). Geochemical and hydrological processes controlling groundwater salinity of a large inland wetland of northwest Australia. *Chemical Geology* 357: 164-177.
- Somaratne N and Frizenschaf J (2013). Geological Control upon Groundwater Flow and Major Ion Chemistry with Influence on Basin Management in a Coastal Aquifer, South Australia. *Journal of Water Resource and Protection* 5: 1170-1177.
- SRK (2010). Gloucester Basin stage 1 gas field development project: Preliminary assessment and initial conceptual hydrogeological model. Report to AGL. 78.
- Stumm W and Morgan JJ (1996). *Aquatic Chemistry: Chemical Equilibria and Rates in Natural Waters*. New York, John Wiley & Sons, Inc.

Van Voast WA (2003). Geochemical signature of formation waters associated with coalbed methane. AAPG Bulletin-American Association of Petroleum Geologists 87: 667-676.

Underschultz JR, Otto CJ and Bartlett R (2005). Formation fluids in faulted aquifers: examples from the foothills of Western Canada and the North West Shelf of Australia. *In*: P. Boulton and J. Kaldi (eds.), Evaluating fault and cap rock seals, American Association of Petroleum Geologists, Hedberg Series, 2, pp. 247-260.

Wadhams P (2000). Ice in the Ocean. Routledge Curzon, 364.

5 Hydrogeochemical and environmental tracer analysis⁹

5.1 Introduction

Recent development of coal resources in Australia, in particular coal seam gas (CSG), has raised a number of environmental concerns including the role of faults and fracture zones and their potential influence on flow pathways between deep hydrocarbon resources and shallow groundwater aquifers and their connected surface water systems ((Commonwealth of Australia 2014)). Surface water features such as streams, particularly gaining systems, may capture and integrate multiple groundwater flowpaths from shallow and deeper aquifer systems (Figure 2-4). Baseline environmental monitoring of both groundwater and surface water undertaken prior to, during and following such developments may give confidence that there are no detrimental impact to the adjacent water resources and communities ((Jackson *et al.* 2013; Vengosh *et al.* 2014). However, determining the location and source of groundwater contributing to river baseflow remains a challenge in most settings because several geological units can contribute groundwater to a stream and contribute to it by different mechanisms. Understanding solute discharge to streams and rivers from the subsurface adds another level of complexity because additional processes to groundwater discharge can be important. For example, even when no groundwater discharge occurs, a background diffusive flux for methane and other dissolved gases to the surface is still possible in environments containing hydrocarbon resources.

Environmental tracers are solutes or gases dissolved in water or properties of the water molecule itself that can be used to infer the source or the apparent age of water (or solutes). In groundwater – surface water interaction studies, common tracers include major ions (or salinity), the stable isotope ratios of the water molecule ($\delta^2\text{H}$ and $\delta^{18}\text{O}$), noble gases (including ^4He [helium-4]), the radioactive noble gas ^{222}Rn (radon-222), tritium (^3H), and ^{14}C (carbon-14) (Ellins *et al.*, 1990; Cook *et al.*, 2006; Lamontagne *et al.*, 2015). Radon-222 and helium-4 are often used in tandem to identify areas of groundwater discharge to surface water. Radon-222 is considered to represent total groundwater discharge (i.e., not to be source-specific) whereas helium-4 is more typically associated with regional (older) groundwater discharge (Ellins, 1990; Gardner *et al.*, 2011; Cartwright and Hoffman, 2016). This is because helium-4 gradually accumulates over time in groundwater whereas ^{222}Rn reaches equilibrium with aquifer material in less than a month owing to its short half-life (3.8 days) relative to that of its parent ^{226}Ra (1,600 years).

⁹ Contributing authors: E Banks, A Suckow, S Smith, S Lamontagne, D Mallants

Methane and its stable isotopes ($\delta^{13}\text{C-CH}_4$ and $\delta^2\text{H-CH}_4$) are often used as tracers of fugitive emissions at different phases of resource projects (Atkins *et al.* 2015; Eyer *et al.* 2015; Iverach *et al.* 2015). Other studies have also used stream-based methane concentrations to evaluate impacts of unconventional gas development ((Heilweil *et al.* 2013)) and the fate of methane in coastal stream environments ((Heilweil *et al.* 2016)). Methane is produced either by bacteria (biogenic methane) or by geologic processes involving heat and pressure (thermogenic methane). Biogenic methane is produced by the decomposition of organic matter through fermentation processes (e.g., in wetlands), or by the chemical reduction of carbon dioxide. Biogenic methane may also be found in shallow, organic rich water-bearing geologic formations, including coal seams. Thermogenic methane, on the other hand, is produced by the thermal decomposition of buried organic material. Thermogenic methane is found in rocks buried deeper within the earth than biogenic methane (typically greater than 600 m depth [Faiz and Hendry, 2006]).

Different types of analyses can be used in conjunction to help determine whether methane gas is of biogenic or thermogenic origin, or a mixture of the two (Coleman *et al.*, 1995; Kaplan *et al.*, 1997), including the stable isotopes of methane (Figure 5-1; Coleman, 1995). Some of the challenges with using methane as a tracer of impacts of CSG developments on adjacent water resources is that the concentration and isotopic composition can change due to the effects of microbial degradation and biogenic methane formation during transport in streams and aquifers ((Whiticar *et al.* 1986; Whiticar 1999; Chanton *et al.* 2005; Wang *et al.* 2015)).

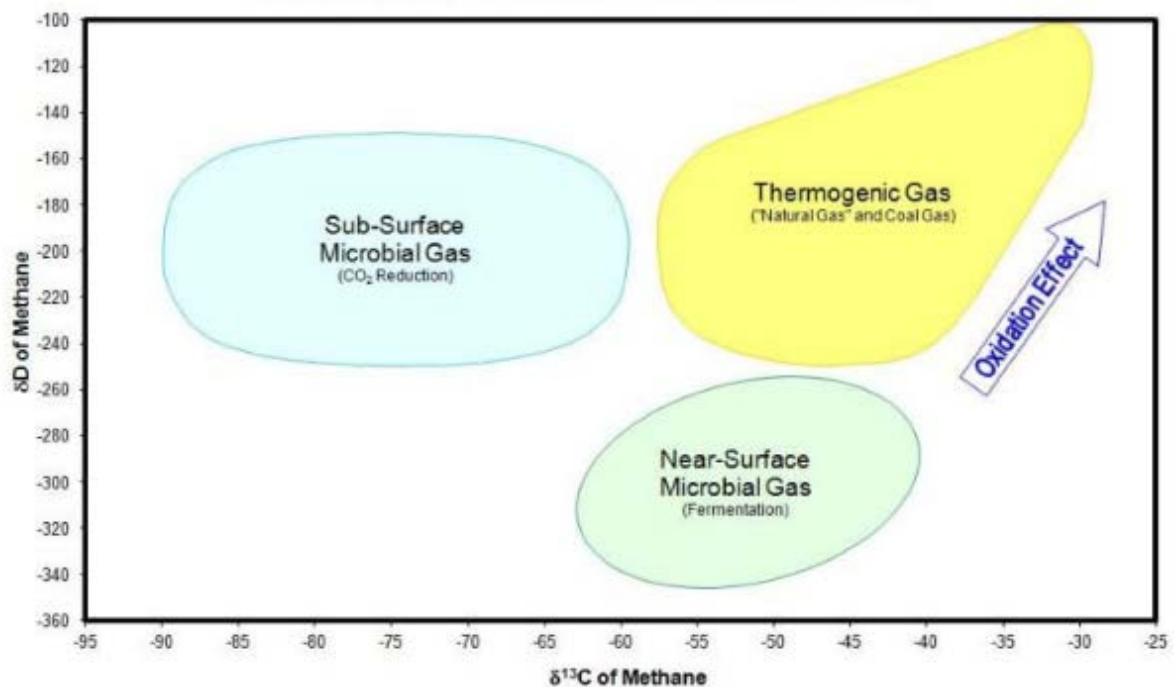


Figure 5-1 Typical compositional ranges of methane from different sources (Coleman, 1995).

In this component of the Gloucester Basin field study, a range of environmental tracers were sampled in surface water and in groundwater from the alluvium, interburden and coal seams formations. The objectives were to:

- Identify locations of preferential groundwater and methane discharge along Waukivory River and the Avon River using a synoptic (i.e. 'run-of-river') survey during a baseflow period;
- Evaluate the source of groundwater discharge and of methane to the rivers; and
- Using vertical concentration profiles across geological formations, evaluate the vertical advective and diffusive components of methane and helium transport at the scale of the river valley.

The results are used to formulate a conceptual model of groundwater – surface water interactions in the Gloucester Basin and to assess the potential role of faults as conduits for groundwater and solutes from deeper formations to the alluvium and river network.

5.2 Methods

5.2.1 Surface water and groundwater sampling

Surface water and groundwater from the Waukivory study site in the Gloucester Basin were sampled between the 22nd February and 2nd March 2016. Surface water sampling was conducted at 22 locations along the Avon and Waukivory Rivers (Figure 5-2).

Groundwater sampling was conducted on 26 monitoring wells completed in three major aquifer units (alluvial, interburden and coal seam) (for construction details about the wells sampled, see Table 5-1). In addition, previous sampling in surface water and the well network were used in the evaluation ((Parsons Brinckerhoff 2012)). The following parameters were analysed on the surface water and groundwater samples:

- alkalinity, pH, dissolved oxygen (DO), oxidation-reduction potential (ORP), specific electrical conductivity (SEC), and temperature;
- major ions, trace metals;
- environmental tracers (stable isotopes of water [¹⁸O, ²H], ²²²Rn, noble gases [He, Ar, Ne], ¹⁴C and tritium); and
- dissolved gases (CO₂, CH₄ and its isotopes $\delta^{13}\text{C-CH}_4$ and $\delta^2\text{H-CH}_4$).

In addition, air samples (mobile real-time survey) were collected for evaluating the spatial variations in atmospheric CH₄, CO₂, water vapour across the valley. A YSI™ multi-parameter meter (www.ysi.com) was used to measure pH, specific electrical conductance (SEC), dissolved oxygen (DO), oxidation-reduction potential (ORP) and temperature in the river and also during purging of the monitoring wells using a flow-through cell. The alkalinity (as CaCO₃) was measured in the field using a HACH™ titration kit (www.hach.com). Prior to sampling the monitoring wells, the static water level was measured from top of casing (TOC)

using an electric water level indicator. Purging of at least three volumes from the well screen was made prior to sampling whenever possible (but was occasionally less due to low yields in some wells). Groundwater sample collection was made by pumping to the surface, except for gas samples which were collected at in situ pressures by deploying a downhole sampler at the well screen (refer to Appendix A for details).

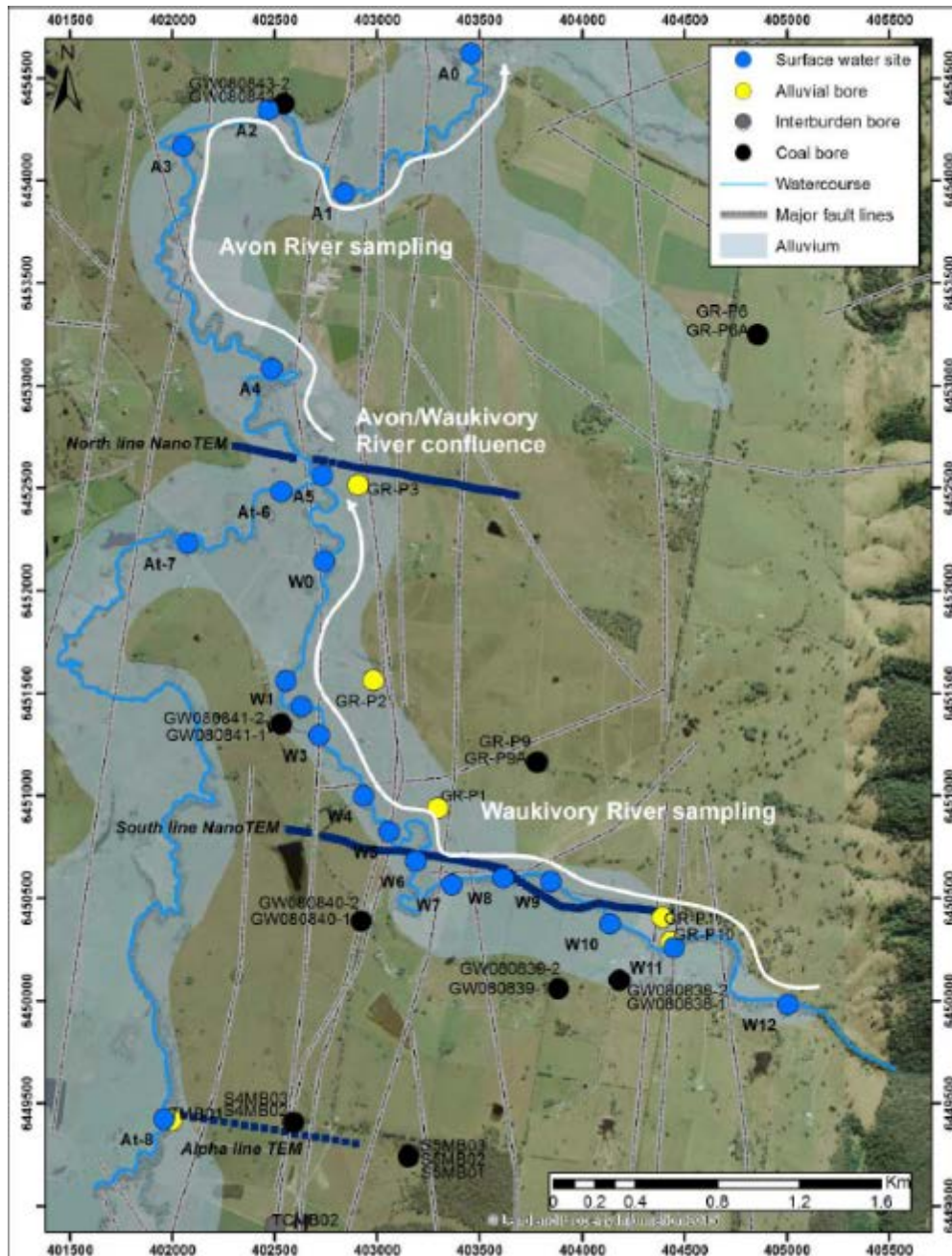


Figure 5-2 Surface water sampling locations along the Waukivory River and Avon River, Gloucester, NSW. Sampled groundwater wells completed in the alluvial, interburden aquifers and coal seams are also shown.

5.2.2 Major element, methane, isotope and noble gas analyses

Major element analyses were conducted on the surface water and groundwater samples, after filtration through a 0.45 µm membrane filter in the field. Samples for major cation and trace element analyses were acidified with nitric acid (1% v/v HNO₃) and analysed by a Spectro CIROS Radial Inductively Coupled Plasma Optical Emission Spectrometer at CSIRO Land and Water Analytical Services, Adelaide, South Australia. Major anions were analysed using a Dionex ICS-2500 Ion Chromatograph. All ion balances were typically better than ±5%.

All stable water isotope compositions were measured by a Picarro L2130-i Cavity Ring Down Laser Spectroscopy at Flinders University in Adelaide, South Australia. The results are reported as a deviation from Vienna Standard Mean Ocean Water (vs. VSMOW) in per mil (‰) difference using delta (δ) notation.

Table 5-1 Construction details of the groundwater wells sampled as part of this study. TOC = top of casing; C-DEPTH = completion depth; SWL = standing water level; RSWL = relative standing water level.

WELL_ID	LITHOLOGY	EASTINGS	NORTHINGS	TOC	C-DEPTH	MID SCREEN	SCREEN LENGTH	SWL	RSWL
				mAHD	mbg	mbg	m	mbTOC	mAHD
GW201186	Alluvial	403295	6450941	105.06	8.5	7.00	3	3.84	101.22
GR-P10	Alluvial	404434	6450290	110.43	8.5	7.00	3	4.81	105.62
GR-P11	Alluvial	404394	6450408	110.54	9.3	7.80	3	4.72	105.82
GW201185	Alluvial	402981	6451564	102.63	9	6.50	5	2.11	100.52
GW201184	Alluvial	402906	6452518	100.27	9	7.00	4	2.49	97.78
GR-P6	Interburden	404856	6453250	146.00	23	20.00	6	4.17	141.83
GR-P6A	Coal	404860	6453248	146.00	95	92.00	6	12.24	133.76
GR-P9	Interburden	403785	6451167	117.87	33	28.50	9	10.31	107.56
GR-P9A	Coal	403780	6451167	117.67	65	62.00	6	8.82	108.85
GW080838-1	Coal	404183	6450102	111.84	78	72.00	12	3.405	108.43
GW080838-2	Coal	404183	6450102	111.88	110	107.40	5	3.478	108.40
GW080839-1	Coal	403884	6450060	108.56	61	55.00	12	3.62	104.94
GW080839-2	Coal	403884	6450060	108.52	111	106.00	9	2.035	106.49
GW080840-1	Coal	402922	6450390	117.30	69	63.00	12	11.47	105.83
GW080840-2	Coal	402922	6450390	117.33	122	117.00	9	11.66	105.67
GW080841-1	Coal	402532	6451351	104.03	24	21.00	6	2.91	101.12
GW080841-2	Coal	402532	6451351	103.90	145	140.00	9	1.67	102.23
GW080843-1	Coal	402544	6454377	100.71	69	64.00	9	5.77	94.94
GW080843-2	Coal	402544	6454377	100.76	122	117.50	9	3.19	97.57
S4MB02	Interburden	402587	6449409	119.09	95	92.00	6	5.53	113.56
S4MB03	Coal	402592	6449408	119	168	165.00	6	4.66	114.34
S5MB01	Interburden	403156	6449250	130.5	58	55.00	6	14.14	116.36

WELL_ID	LITHOLOGY	EASTINGS	NORTHINGS	TOC	C-DEPTH	MID SCREEN	SCREEN LENGTH	SWL	RSWL
S5MB02	Interburden	403153	6449245	130.4	112	106.00	12	15.93	114.47
S5MB03	Coal	403151	6449240	130.32	164	161.00	6	17.41	112.91
TCMB02	Interburden	402502	6448904	123.85	181	178.00	6	10.1	113.75
TMB01	Alluvial	401997	6449420	107.6	10	8.50	3	4.63	102.97

A Picarro 2201-i cavity ring down spectrometer (CRDS) ((Crosson 2008)) was used to measure dissolved CH₄ concentrations, $\delta^{13}\text{C-CH}_4$ and CO₂ in water samples collected in the field using the surface water and groundwater sampling methodology as described in Appendix A. Continuous real-time CH₄, CO₂ and water vapour concentrations in air were also collected around the study area using the CRDS mounted as a mobile survey unit in a GPS and weather station-equipped vehicle (see Appendix B). Continuous sampling was maintained via a small pump and a short hose attached to the roof rack of the vehicle. There was a 40 s delay ($\pm 1\text{s}$) between a change in concentration being presented to the gas inlet, and that change being registered by the instrument. GPS location and time were recorded, so that the 40 s delay could be accounted for in the spatial analysis. CRDS data were recorded approximately every 3.7 seconds. Final results were calibrated¹⁰ both for concentration and isotopic ratios using a number of gases of known concentration and isotopic ratios.

Based on measurements from three tanks of “instrument grade” compressed air over the last three years, we have observed that the instrumental drift for CH₄ concentration has been <5 ppb (one standard deviation) since 2013. Additionally, the methane and CO₂ concentrations for all three of our tanks were measured by CSIRO, these measurements being referenced to a World Meteorological Organization standard (WMOX2004A). It was determined that our Picarro instrument measures approximately 30 to 40 ppb low (0.03 to 0.04 ppm) when measuring methane concentration (i.e. <2 % at background level). Because of the large variations observed between the field samples, no correction for instrument drift was required.

Headspace methane gas concentrations were converted to head gas concentrations in water using Henry’s Law. Additional samples for the analysis of the stable isotope ratios of carbon ($\delta^{13}\text{C}$) and hydrogen ($\delta^2\text{H}$) in methane were measured at the Stable Isotope facility at UC Davis Stable Isotope Laboratory at the University of California, using a ThermoScientific Precon concentration unit interfaced to a ThermoScientific Delta V Plus isotope ratio mass spectrometer (ThermoScientific, Bremen, Germany). Final results are expressed relative to the international standards V-PDB (Vienna PeeDee Belemnite) for

¹⁰ Performance specifications of the Picarro 2201-i for high precision and high dynamic range mode can be found at: http://www.picarro.com/products_solutions/isotope_analyzers/13c_for_ch4_co2.

carbon and V-SMOW (Vienna-Standard Mean Ocean Water) for hydrogen. Long-term standard deviation for $\delta^{13}\text{C-CH}_4$ and $\delta^2\text{H-CH}_4$ is 0.2‰ and 2‰, respectively.

Groundwater and surface water samples were also collected for analysis of ^{222}Rn activity. Groundwater samples were taken directly from the downhole sampler port using a syringe. A 14 mL sample was transferred to a pre-weighed 22 mL Teflon coated PTFE vial with 6 mL Packard NEN mineral oil scintillant, gently shaken for 30 s, sealed and the date and time recorded. The samples were submitted to the CSIRO Environmental Isotope Laboratory (Adelaide, South Australia) within 3 days of sample collection and counted by liquid scintillation on a LKB Wallac Quantulus counter ((Herczeg *et al.* 1994)). Surface water samples for ^{222}Rn activity were measured in the field using a portable radon-in-air monitor (RAD-7) combined with a Rad-Aqua (DurrIDGE Company Inc 2015)) using the methods described in Burnett *et al.* (2001).

Groundwater samples for measurement of dissolved noble gases (Ar, Ne, Xe, Kr and He) were collected in copper tubes ((Weiss 1970)) at in situ pressure using the downhole sampler. Samples were analyzed at the CSIRO Environmental Isotope Laboratory (Adelaide, South Australia) with a Stanford Research Systems RGA 220 quadrupole mass spectrometer with cryogenic separation ((Poole *et al.* 1997)). Samples for carbon isotope ratio ($^{13}\text{C}/^{12}\text{C}$), radiocarbon (^{14}C) and tritium (^3H) were collected in 1 L plastic bottles, unfiltered with zero head space and with no preservative, and analysed at GNS Laboratories, Lower Hutt, New Zealand. Stable carbon isotopes are reported using the delta notation ($\delta^{13}\text{C}$, ‰) relative to the Pee Dee Belemnite (PDB) standard, and radiocarbon activities are reported as percent modern carbon (pmC) according to Stuiver and Polach ((1977)).

5.3 Results

Hydrochemistry, isotopes, methane concentration, noble gases and apparent age tracer data were used to characterise the surface water and groundwater aquifer system and identify areas that may be influenced by structural geological features, in particular preferential flow paths along faults between the deeper coal seams and the overlying shallow aquifers and surface water system. Table 5-2 and Table 5-4 provide an overview of all parameters measured for the surface water; Table 5-3 and Table 5-5 list all parameters measured for the groundwater samples. Details about sampling location and sampling dates are provided in Appendix C. Results from this investigation and data collected in previous studies ((Parsons Brinckerhoff 2012)) in the study area have been combined in the spatial interpretation and analysis of the data for selected environmental tracers. In the following data is presented and preliminary inferences presented, with additional interpretation provided in the Discussion Section 5.4. For brevity, the mobile real-time atmospheric sampling is presented and discussed in Appendix B.

Table 5-2 Measured field parameters and major ion analyses of the collected 22 surface water samples, 22nd February to 2nd March 2016. TDPG = total dissolved gas pressure.

SITE ID	RIVER	TEMP	SEC	DO	FIELD PH	ORP	FIELD ALKALINITY AS HCO ₃	TDPG	FLOW	TOTAL ALKALINITY AS HCO ₃	Cl ⁻	Br ⁻	SO ₄ ⁻²	Ca ⁺²	K ⁺	Mg ⁺²	Na ⁺	TDS
		°C	µS cm ⁻¹	mg L ⁻¹		mV	mg L ⁻¹	mm Hg	m ³ s ⁻¹	mg L ⁻¹	mg L ⁻¹	mg L ⁻¹	mg L ⁻¹	mg L ⁻¹	mg L ⁻¹	mg L ⁻¹	mg L ⁻¹	mg L ⁻¹
A0	Avon	23.5	304	6.5	6.8	219.0	58.4	771	0.3455	84.7	58	0.62	3.7	13	2.6	8.3	31	202
A1	Avon	24.4	307	8.3	7.0	226.9	56.8	773	NA	78.8	58	0.08	4.1	13	3.8	8.5	30	196
A2	Avon	23.6	307	6.0	7.0	207.0	55.2	762	NA	72.6	59	0.09	5.3	12	3.7	8.8	31	192
A3	Avon	23.7	297	5.0	6.3	215.4	56.0	NA	NA	66.7	56	0.09	5.5	11	3.6	8.1	30	181
A4	Avon	24.6	319	3.8	6.3	178.4	71.1	742	0.162	60.6	73	0.11	10	10	3.2	8.2	35	201
A5	Avon	23.9	331	3.2	7.0	193.2	73.2	751	0.167	72.6	63	0.09	5.7	13	3.1	9.5	34	202
At-6	Avon	23.0	292	5.0	6.8	93.2	72.8	742	0.244	60.7	61	0.08	9.2	8.8	3.1	8.1	33	183
At-7	Avon	24.7	291	5.3	6.2	180.6	61.0	740	0.215	60.6	57	0.09	7.2	8.9	3.1	7.9	32	177
At-8	Avon	24.9	312	4.7	7.9	55.5	82.4	NA	NA	78.9	56	0.07	3.3	13	3.0	8.4	30	192
W0	Waukivory	23.6	440	1.3	7.0	117.5	95.3	750	0.045	114.5	81	0.11	2.6	24	3.4	12.4	40	278
W1	Waukivory	24.7	452	1.6	7.1	192.2	113.4	NA	0.041	114.5	89	0.10	3.1	25	3.3	12.6	42	289
W2	Waukivory	25.8	450	4.3	7.3	138.2	118.4	758	NA	114.8	85	0.11	3.7	24	3.3	12.4	42	285
W3	Waukivory	24.7	465	2.5	7.2	226.0	125.5	752	NA	113.7	94	0.09	3.4	25	3.3	13.3	44	297
W4	Waukivory	26.0	455	4.4	7.3	198.1	123.0	752	0.025	121.1	88	0.11	3.6	25	3.4	13.2	43	297
W5	Waukivory	23.2	472	2.3	7.1	99.7	114.6	758	0.043	121.1	98	0.13	3.7	26	3.5	13.3	45	311
W6	Waukivory	24.2	458	1.9	7.1	214.1	114.6	747	0.031	114.1	90	0.11	3.5	25	3.5	12.7	42	291
W7	Waukivory	23.6	427	2.4	7.0	199.4	114.6	NA	0.035	120.1	79	0.10	3.9	25	3.3	13.4	38	283

SITE ID	RIVER	TEMP	SEC	DO	FIELD PH	ORP	FIELD ALKALINITY AS HCO ₃	TDPG	FLOW	TOTAL ALKALINITY AS HCO ₃	Cl ⁻	Br ⁻	SO ₄ ⁻²	Ca ⁺²	K ⁺	Mg ⁺²	Na ⁺	TDS
W8	Waukivory	25.5	412	4.8	6.4	39.3	119.6	746	0.021	114.8	74	0.10	3.9	23	3.2	11.9	36	268
W9	Waukivory	25.8	411	4.1	7.0	208.6	123.3	742	0.015	114.5	76	0.10	3.7	24	3.3	12.6	37	271
W10	Waukivory	26.8	410	4.8	7.3	211.9	126.5	746	0.016	120.1	73	0.10	3.8	24	3.4	12.7	37	274
W11	Waukivory	22.7	395	3.7	6.4	265.0	150.4	741	0.025	114.8	68	0.09	3.8	23	3.3	11.7	35	260
W12	Waukivory	22.2	347	4.7	6.9	240.1	108.5	743	0.021	102.7	58	0.07	2.9	20	3.0	10.4	30	228

Table 5-3 Measured field parameters and major ion analyses of the collected 26 groundwater samples, 22nd February to 2nd March 2016. TDPG = total dissolved gas pressure.

WELL ID	LITHOLOGY	TEMP	SEC	DO	FIELD PH	ORP	FIELD ALKALINITY AS HCO3	TDPG	TOTAL ALKALINITY AS HCO3	Cl ⁻	Br ⁻	SO4 ⁻²	Ca ⁺²	K ⁺	Mg ⁺²	Na ⁺	TDS
		°C	µS cm ⁻¹	mg L ⁻¹		mV	mg L ⁻¹	mm Hg	mg L ⁻¹	mg L ⁻¹	mg L ⁻¹	mg L ⁻¹	mg L ⁻¹	mg L ⁻¹	mg L ⁻¹	mg L ⁻¹	mg L ⁻¹
GW201186	Alluvial		5711	2.02	6.63	82	441.6	NW	388	1840	1.68	77.5	182.0	3.5	118.0	886	3500
GR-P10	Alluvial	18.6	620.0	1.6	6.90	-14.7	144.1	NW	152	114	0.09	5.3	32.4	2.4	17.1	62	385
GR-P11	Alluvial	28.74	1215	2.04	6.62		349.4	NW	312	238	0.25	18.8	65.7	2.3	28.6	148	816
GW201185	Alluvial		2204	1.44	6.16	82	246.9	NW	173	661	0.60	17.5	90.8	2.2	50.4	255	1253
GW201184	Alluvial	20.7	4161	0.53	7.08	-29	596.8	NW	452	449	1.19	74.5	119.0	2.5	75.6	685	1860
GR-P6	Interburden	23.5	3034.0	?	7.16	-115	522.3	?	556	714	0.65	20.2	122.0	10.8	35.1	431	1891
GR-P6A	Coal	22.9	5525.0	?	6.89	-163.0	350.6	?	321	1531	1.62	411.9	404.0	18.9	112.0	638	3445
GR-P9	Interburden	20.4	7189	0.53	6.99	-123	748.5	NW	576	2340	1.64	413.4	300.0	10.1	249.0	1020	4915
GR-P9A	Coal	20.8	3940	0.6	6.78	-156	413.2	NW	304	1097	0.41	375.1	189.0	8.4	135.0	419	2530
GW080838-1	Coal	20.4	8152	0.51	7.41	-213	609.9	915	536	2647	2.66	0.05	251.0	9.0	59.9	1420	4945
GW080838-2	Coal	21.6	7798	0.35	11.80	-267	0.1	954	NA	2392	2.67	8.6	1.8	16.3	0.4	1630	4053
GW080839-1	Coal	21.9	3668	0.41	7.00	-180		851	269	960	0.78	394.1	166.0	7.3	69.6	560	2431
GW080839-2	Coal	21.45	3832	1.67	7.44	-227	1018.1	861	763	919	0.79	1.7	62.1	5.8	28.7	807	2591
GW080840-1	Coal	?	?	?	?	?		765.0	414	202	0.13	16.1	8.2	3.6	1.8	276	922
GW080840-2	Coal	?	?	?	?	?		960.0	1467	252	0.35	2.6	6.9	5.1	2.9	726	2464
GW080841-1	Coal	22.7	8718.0	0.4	7.55	-193.0	679.7	822.0	470	2809	3.62	2.1	201.0	7.7	136.0	1480	5120
GW080841-2	Coal	20.4	4169.0	0.9	8.97	-272.0	1976.0	1050.0	2034	436	0.33	48.8	7.1	10.3	2.3	1140	3679
GW080843-1	Coal	20.8	6689	0.43	8.15	-206	532.4	921	399	2325	2.40	6.2	56.4	7.4	24.6	1390	4221
GW080843-2	Coal	20.35	5187	0.71	9.03	-210	2579.7	NW	2410	565	0.55	0.05	5.9	13.8	3.1	1240	4239

WELL ID	LITHOLOGY	TEMP	SEC	DO	FIELD PH	ORP	FIELD ALKALINITY AS HCO3	TDPG	TOTAL ALKALINITY AS HCO3	Cl ⁻	Br ⁻	SO4 ²⁻	Ca ²⁺	K ⁺	Mg ²⁺	Na ⁺	TDS
S4MB02	Interburden	23.2	2280	0.4	8.12	-244	576.9	902	408	758	0.56	238.8	88.8	4.5	25.9	623	2156
S4MB03	Coal	21.02	3214	0.5	8.47	-260.7	308.8	867	331	950	0.74	0.1	16.0	3.6	4.5	720	2028
S5MB01	Interburden	NA	NA	NA	NA	NA	NA	968	NA	947	0.95	58.2	53.8	76.0	29.3	744	1915
S5MB02	Interburden	19.3	4386	0.6	7.01	-308	1306.8	NW	1201	1180	1.45	44.0	81.6	6.5	70.7	1050	3640
S5MB03	Coal	21.8	5143	0.8	7.15	-218	1317.6	NW	1017	1136	1.32	115.1	99.5	8.1	111.0	894	3387
TCMB02	Interburden	23.5	3578	0.29	11.76	-548	0.2	971	457	634	0.44	6.3	2.8	3.2	0.7	726	1832
TMB01	Alluvial	24.06	7333	4.71	7.03	-144.4	810.7		666	2406	1.82	74.7	199.0	3.6	211.0	1090	4657

Table 5-4 Stable isotopes of water ($\delta^{18}\text{O}$ and $\delta^2\text{H}$), methane concentrations, $\delta^{13}\text{C}\text{-CH}_4$, $\delta^2\text{H}\text{-CH}_4$, dissolved gases (^4He , ^{20}Ne , ^{22}Ne , N_2 , O_2 , ^{40}Ar), ^{14}C , $\delta^{13}\text{C}$, ^{222}Rn , and ^3H analyses of the collected 22 surface water samples, 22nd February to 2nd March 2016. Note that not all tracers were measured on every sample.

SITE ID	$\delta^2\text{H}$	$\delta^{18}\text{O}$	CH_4	$\delta^{13}\text{C}\text{-CH}_4$	$\delta\text{D}\text{-CH}_4$	^4He	^{20}Ne	^{22}Ne	N_2	O_2	^{40}Ar	^{14}C	^{14}C ERROR	$\delta^{13}\text{C}$	^{222}Rn	^3H	^3H ERROR
	‰ VSMOW	‰ VSMOW	$\mu\text{g L}^{-1}$	‰ V-PDB	‰ VSMOW	cm^3g^{-1}	cm^3g^{-1}	cm^3g^{-1}	cm^3g^{-1}	cm^3g^{-1}	cm^3g^{-1}	pmC		‰ PDB	Bq L^{-1}	TU	TU
A0	-17.89	-3.84	12.6	-35.2													
A1	-15.58	-3.45	19.5	-41.3											0.159		
A2	-13.31	-3.16	23.6	-46.1											0.124		
A3	-12.61	-3.08	18.5	-40.6											0.147		
A4	-10.89	-2.75	20.9	-39.4											0.247		
A5	-11.70	-2.88	46.7	-45.3											0.478		
At-6	-11.18	-2.82	18.4	-43.8		4.70E-08	1.84E-07	1.55E-08	1.15E-02	2.95E-04	9.61E-07				0.0912		
At-7	-11.06	-2.85	17.2	-42.7											0.129		
At-8	-15.16	-3.44	9.0	-33.6													
W0	-15.13	-3.14	444.2	-43.4	-216.8	4.41E-08	1.77E-07	1.53E-08	1.27E-02	3.16E-04	9.71E-07				0.399		
W1	-13.01	-2.72	166.8	-52.0	-231.5	4.81E-08	2.15E-07	1.16E-08	1.24E-02	3.29E-04	1.15E-06				0.622		
W2	-14.95	-3.11	23.7	-36.7	-127.1	4.33E-08	1.74E-07	1.55E-08	1.08E-02	3.30E-04	8.56E-07	93.9	0.29	-11.1	0.824	1.795	0.041
W3	-20.38	-3.98	62.0	-43.3											1.05		
W4	-14.68	-3.03	66.3	-49.4											1.34		
W5	-13.69	-2.88	33.1	-46.1											0.362		
W6	-20.47	-4.00	42.0	-35.7	-142.3	4.36E-08	1.67E-07	1.17E-08	1.16E-02	2.92E-04	1.05E-06				1.24		
W7	-11.39	-2.57	43.7	-19.9											0.372		
W8	-14.67	-3.07	85.1	-54.1	-260.8	4.39E-08	1.62E-07	1.38E-08	1.17E-02	2.87E-04	9.34E-07	92.86	0.29	-11.3	2.31	1.76	0.04

SITE ID	$\delta^2\text{H}$	$\delta^{18}\text{O}$	CH_4	$\delta^{13}\text{C-CH}_4$	$\delta\text{D-CH}_4$	^4He	^{20}Ne	^{22}Ne	N_2	O_2	^{40}Ar	^{14}C	^{14}C ERROR	$\delta^{13}\text{C}$	^{222}Rn	^3H	^3H ERROR
W9	-14.41	-3.02	18.4	-24.4	-88.3												1.51
W10	-20.71	-4.05	27.6	-26.6	-88.7												0.695
W11	-15.28	-3.23	207.7	-56.0		4.26E-08	1.79E-07	1.53E-08	1.10E-02	3.08E-04	8.65E-07						0.961
W12	-16.39	-3.39	30.5	-49.2													1.21

Table 5-5 Stable isotopes of water ($\delta^{18}\text{O}$ and $\delta^2\text{H}$), methane concentrations, $\delta^{13}\text{C}\text{-CH}_4$, $\delta^2\text{H}\text{-CH}_4$, dissolved gases (^4He , ^{20}Ne , ^{22}Ne , N_2 , O_2 , ^{40}Ar), ^{14}C , $\delta^{13}\text{C}$, ^{222}Rn , and ^3H analyses of the collected 26 groundwater samples, 22nd February to 2nd March 2016. Samples from coal monitoring wells have their Well ID underlined. Note that not all tracers were measured on every sample.

WELL ID	$\delta^2\text{H}$	$\delta^{18}\text{O}$	CH_4	$\delta^{13}\text{C}\text{-CH}_4$	$\delta\text{D}\text{-CH}_4$	^4He	^{20}Ne	^{22}Ne	N_2	O_2	^{40}Ar	^{14}C	^{14}C ERROR	$\delta^{13}\text{C}$	^{222}Rn	^{222}Rn ERROR	^3H	^3H ERROR
	‰VSMOW	‰VSMOW	$\mu\text{g L}^{-1}$	‰ V-PDB	‰ VSMOW	cm^3g^{-1}	cm^3g^{-1}	cm^3g^{-1}	cm^3g^{-1}	cm^3g^{-1}	cm^3g^{-1}	pmC		‰ PDB	Bq L ⁻¹	Bq L ⁻¹	TU	TU
GW201186	-22.05	-4.10	39.4	-44.1		2.84E-07	2.64E-07	2.49E-08	4.53E-02	4.82E-04	4.58E-04	79.38	0.27	-9	51.7	2.45	0.296	0.021
GR-P10	-14.58	-2.99	97.8	-39.0	-34.1	1.09E-07	2.48E-07	2.17E-08	2.42E-02	5.20E-05	3.86E-04	94.66	0.31	-12.2	65.4	1.31	1.573	0.038
GR-P11	-20.58	-4.17	463	-62.4	-174.7	1.67E-06	3.32E-07	3.05E-08	5.03E-02	2.44E-04	5.37E-04				59.1	2.81		
GW201185	-18.82	-3.37	3.7	-29.2	-53.7	6.40E-08	2.61E-07	1.59E-08	5.70E-02	1.37E-03	1.03E-03	96.13	0.3	-8.4	45.3	2.16	0.765	0.027
GW201184	-25.88	-4.54	8.1	-52.0	-200.4	1.20E-07	2.40E-07	2.13E-08	4.93E-02	1.37E-03	5.08E-04				43.3	0.91		
GR-P6	-34.19	-5.92	17.2	-66.4		8.00E-08	3.57E-07		5.58E-02		1.45E-03							
<u>GR-P6A</u>	-32.92	-5.83	13.3	-60.4		2.95E-07	3.10E-07	5.58E-08	4.44E-02	1.07E-03	8.41E-04	3.09	0.41	-11.2			-0.009	0.016
GR-P9	-30.98	-5.36	86.3	-58.6		4.20E-07	2.74E-07		5.28E-02		1.19E-03				2.2	0.15		
<u>GR-P9A</u>	-29.88	-5.15	83.9	-46.8		4.20E-07	3.19E-07	2.79E-08	4.78E-02	9.66E-04	5.57E-04	1.99	0.46	-12.1	0.2	0.07	-0.023	0.017
<u>GW080838-1</u>	-28.52	-5.04	56735	-55.9	-216.9	1.83E-05	2.00E-07	1.26E-08	5.41E-01	3.50E-04	2.30E-04	3.05	0.45	-15.1	13.0	0.44	-0.007	0.017
<u>GW080838-2</u>	-29.88	-5.35	146407	-50.5	-216.9	4.35E-06	1.27E-07	7.82E-09	1.33E+00	1.61E-04	7.00E-06				4.5	0.23		
<u>GW080839-1</u>	-28.53	-5.16	1571	-60.7								5.49	0.4	-13.5	0.7	0.12	0.009	0.017
<u>GW080839-2</u>	-31.76	-5.66	144481	-60.4	-201.3	2.03E-05	1.56E-07	1.48E-08	1.01E+00	5.57E-04	2.54E-05	0.67	0.46	2.6	5.9	0.29	-0.017	0.017
<u>GW080840-1</u>	-23.77	-4.40	47441	-54.9	-218.3	1.26E-06	2.28E-07	2.62E-08	2.74E-01	1.90E-04	1.98E-04	25.72	0.33	-11.1	0.5	0.11	1.241	0.029
<u>GW080840-2</u>	-31.21	-5.47	168135	-56.3	-222.3	8.37E-07	3.37E-08	-3.97E-08	1.06E+00	2.66E-03	4.59E-06	1.52	0.41	15.9	1.4	0.13	0.148	0.017
<u>GW080841-1</u>	-24.98	-4.49	5569	-55.8	-224.1	1.34E-06	2.25E-07	2.07E-08	5.18E-02	2.65E-04	3.95E-04	10.9	0.38	-15.7	2.1	0.18	-0.011	0.016
<u>GW080841-2</u>	-35.81	-6.08	153518	-47.1		4.00E-07	7.51E-08	-2.25E-08	9.60E-01	3.58E-03	1.71E-05	1.22	0.42	21.6	4.1	0.22	0.062	0.017

WELL ID	$\delta^2\text{H}$	$\delta^{18}\text{O}$	CH_4	$\delta^{13}\text{C-CH}_4$	$\delta\text{D-CH}_4$	^4He	^{20}Ne	^{22}Ne	N_2	O_2	^{40}Ar	^{14}C	^{14}C ERROR	$\delta^{13}\text{C}$	^{222}Rn	^{222}Rn ERROR	^3H	^3H ERROR
<u>GW080843-1</u>	-27.88	-4.85	35514	-76.9		9.28E-07	3.89E-07	4.29E-08	3.45E-01	1.74E-04	2.07E-04	4.81	0.44	-12.2	7.6	0.29	0.043	0.017
<u>GW080843-2</u>	-41.22	-6.29	88494	-54.5	-222.9	1.05E-06	4.00E-07	3.24E-08	1.00E+00	1.60E-04	1.27E-05				1.3	0.12		
S4MB02	-31.50	-5.54	14112	-81.9	-234.2	7.01E-07	3.47E-07	3.74E-08	8.75E-02	9.75E-05	7.88E-04				5.1	0.29		
<u>S4MB03</u>	-30.44	-5.47	218555	-59.8	-215.5	1.54E-05	1.91E-07	1.90E-08	1.53E+00	1.55E-04	2.11E-04				0.5	0.14		
S5MB01	-22.73	-4.18	11671	-69.4		8.00E-07	5.98E-07		7.48E-02		8.48E-04				1.0	0.20		
S5MB02	-26.18	-4.76	7486	-66.7	-194.5	7.24E-07	3.26E-07	3.34E-08	8.42E-02	1.27E-03	9.45E-04				0.6	0.09		
<u>S5MB03</u>	-25.01	-4.59	20327	-47.8	-232.3	2.18E-06	3.54E-07	3.39E-08	1.54E-01	9.51E-04	4.99E-04				0.3	0.08		
TCMB02	-27.26	-4.92	121132	-55.3	-235.2										0.6	0.10		
TMB01	-23.11	-4.22	61.4	-58.2		1.38E-07	3.97E-07	2.06E-08	5.00E-02	1.46E-03	5.68E-04				37.4	1.79		

5.3.1 Synoptic river survey

The synoptic survey covered part of the Avon River below its junction with Waukivory (starting at Jack's Road River crossing; Figure 5-3), the Waukivory River up to the transition between the valley and the Mograni Range, and two samples in the Avon River upstream the Waukivory junction. The rivers were gently flowing during the survey following recent rainfall, with the bulk of the flow carried in the Avon. Waukivory River had distinct pool – shallow riffles sequences, which were also present but less pronounced in the Avon.

Streamflow steadily increased in the downstream direction in both the Waukivory and Avon rivers (Figure 5-3). As there were no obvious surface water inputs along the study reach, this indicated the rivers were gaining throughout the valley. These observations are consistent with the findings in Parsons Brinckerhoff (2015), where the Avon and Karuah river systems are considered to be gaining even under low flow conditions.

5.3.1.1 Chloride, $\delta^{18}\text{O}$ and $\delta^2\text{H}$

Chloride concentrations were higher in Waukivory (58 –98 mg L⁻¹) than in the Avon upstream of its junction with Waukivory (56 – 61 mg L⁻¹; Figure 5-3). In Waukivory, chloride concentrations were lowest upstream, increased mid-reach, and decreased somewhat again before the confluence with the Avon (Figure 5-3). In the Avon, chloride concentrations peaked downstream of the confluence with Waukivory and declined thereafter. In general, the stable isotopes of water were more depleted (i.e. more negative) in the upstream reach of both rivers and furthest downstream in the Avon (Table 5-4 and Figure 5-4). For example, $\delta^{18}\text{O}$ was –3.44‰ upstream in the Avon, peaked –2.74‰ at station A4, and decreased to –3.84‰ at station A0. However, isotopic values were more variable in Waukivory than in the Avon, varying by 1.5‰ over less than 200 m. Overall, whilst the rivers may be gaining throughout the study reach, the variations in chloride and stable isotopes of water suggest the sources of groundwater may vary.

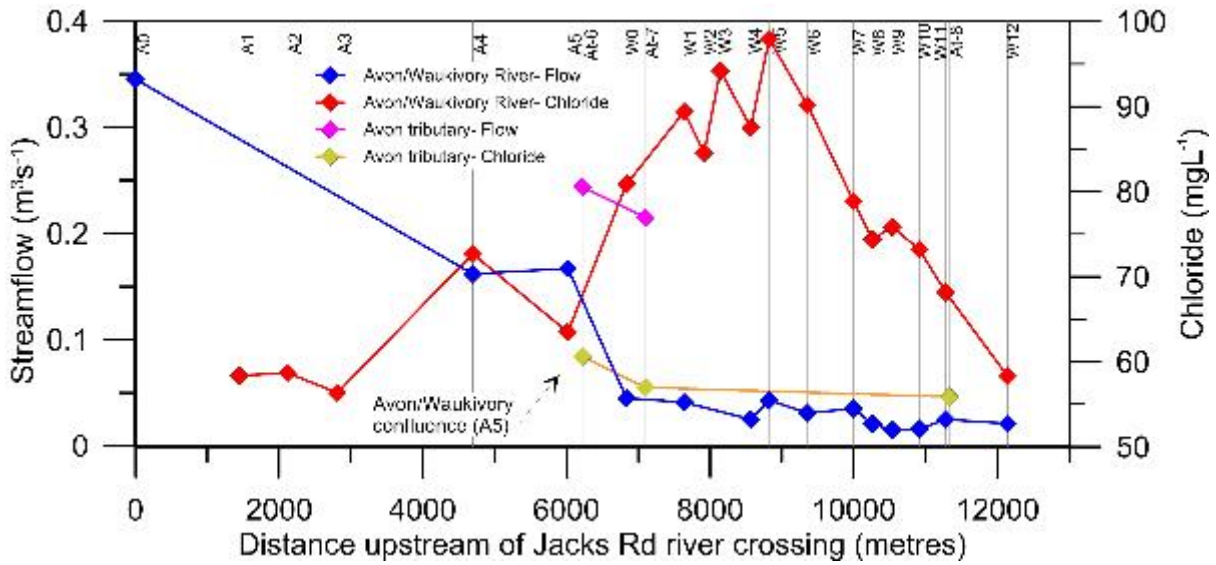


Figure 5-3 Run of river showing streamflow and chloride concentration versus distance upstream of Jacks Rd river crossing (observation point A0 on the Avon River).

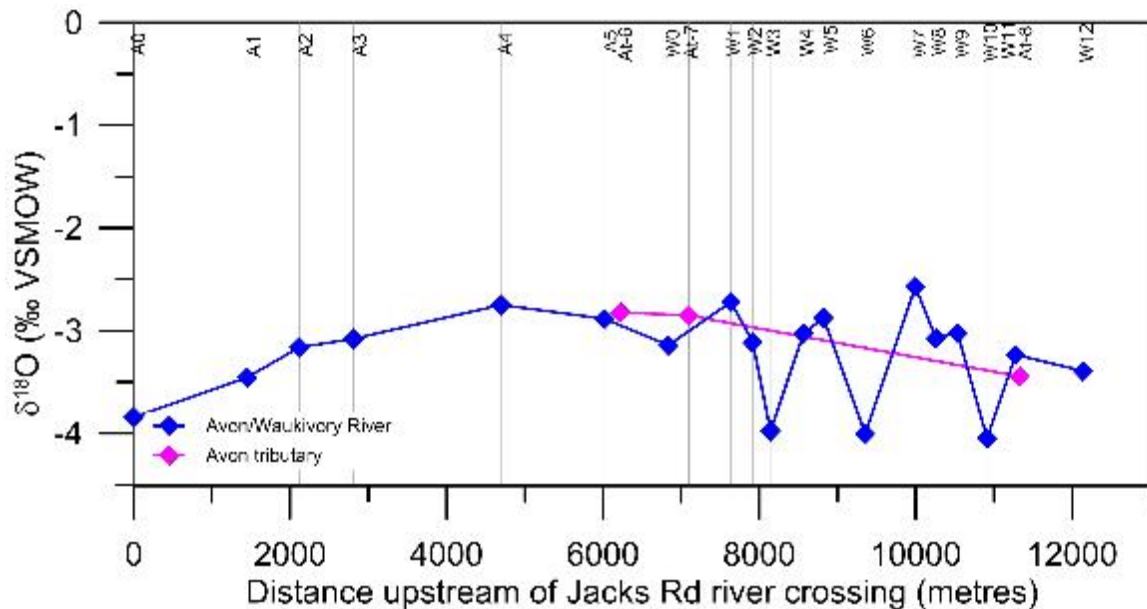


Figure 5-4 Run of river showing the stable isotope of water, $\delta^{18}\text{O}$, versus distance. The distance of 0 meters upstream of Jacks river crossing corresponds to observation point A0 on the Avon River.

5.3.1.2 Radon and helium-4

Radon activities were highest (and most variable) in the Waukivory River, with activities ranging between 0.3 and 2.1 Bq L⁻¹ (Figure 5-5). A number of radon concentration ‘hotspots’ were identified between sample sites W1 and W10, which may represent reaches with preferential groundwater discharge. Radon activity in the Avon River above its confluence was ~0.1 Bq L⁻¹ and <0.5 Bq L⁻¹ below. Most helium samples were near solubility equilibrium ($4.1 - 4.5 \times 10^{-8}$ cm³ STP g⁻¹, cubic centimetres of gas at standard temperature and pressure per gram of water, between 10 and 30°C), with the exception of one sample each in Waukivory and the Avon River just before their confluence (Figure 5-5). Relatively high ²²²Rn

across the synoptic survey is consistent with a generally gaining environment and the presence of helium above background at some sites suggests an older source of groundwater contributing there.

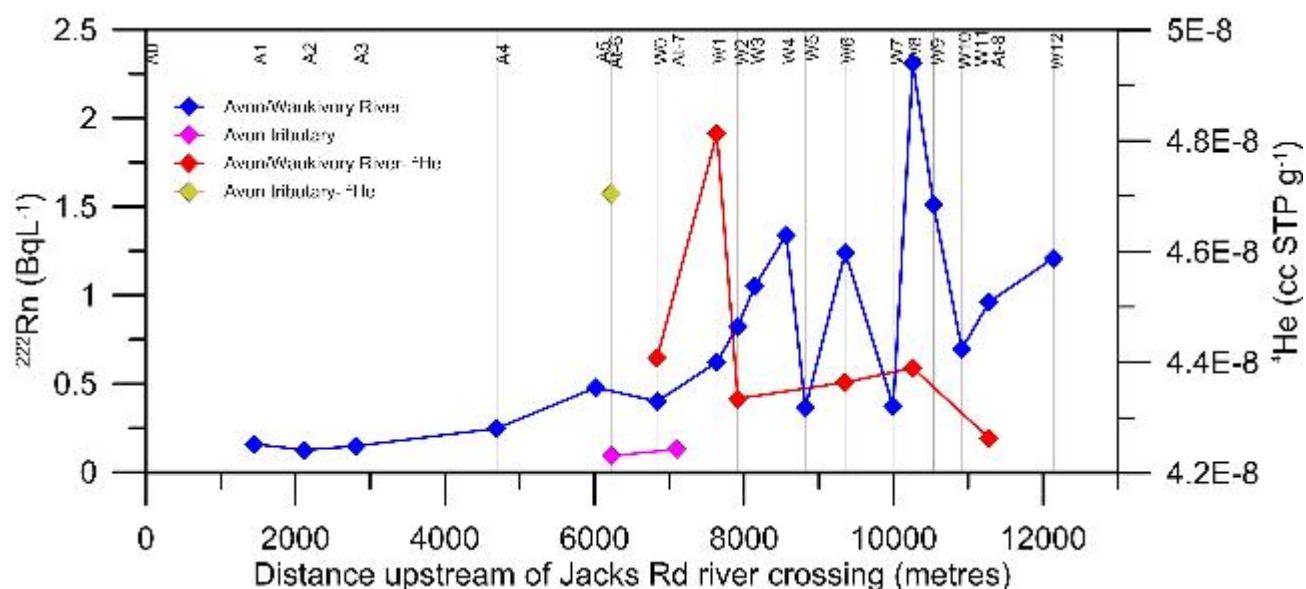


Figure 5-5 Run of river showing ²²²Rn and ⁴He (right axis) concentration versus distance. The distance of 0 meters upstream of Jacks river crossing corresponds to observation point A0 on the Avon River. Solubility equilibrium with the atmosphere for helium is 4.1 – 4.5 X 10⁻⁸ cm³ STP g⁻¹ between 10 and 30°C.

5.3.1.3 Surface water methane

Methane in surface water was >9 µg L⁻¹ throughout the synoptic survey (Figure 5-6). There were four notable methane concentration ‘hotspots’ (>60 µg L⁻¹) at the Waukivory River stations W1, W8 and W11 and especially at W0 (444 µg L⁻¹; Figure 5-6). The δ¹³C-CH₄ values at these sites ranged from -56 to -43.4‰ V-PDB, with values most variable at the upstream Waukivory stations. More limited sampling for δ²H-CH₄ also showed widely fluctuating values within the Waukivory reach (-231 to -88.3‰ VSMOW). Thus, the range in isotopic values suggest that both thermogenic and biogenic methane could be present.

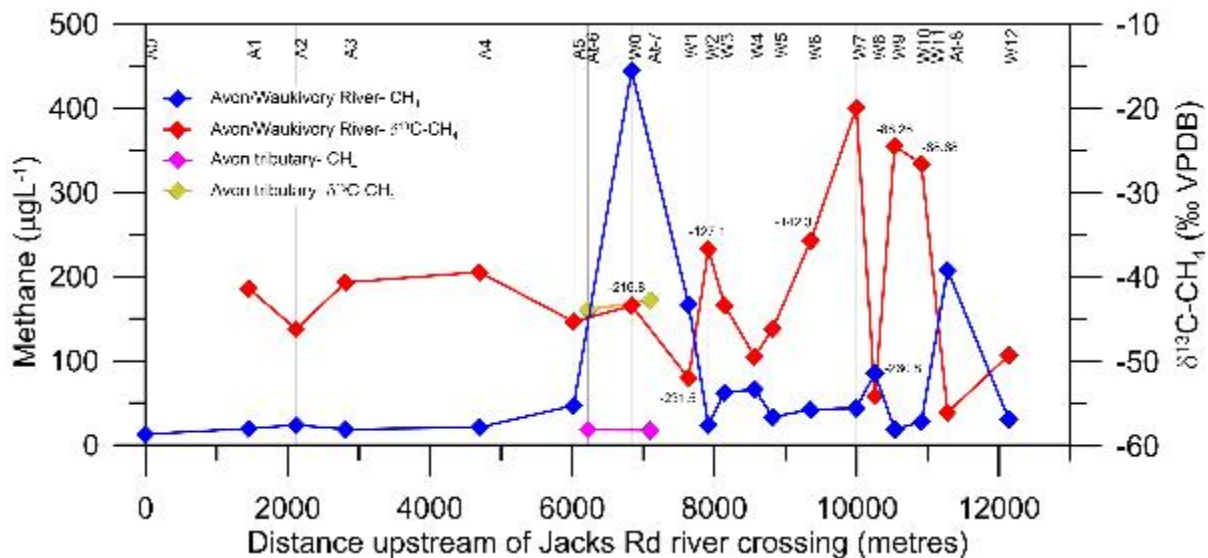


Figure 5-6 Run of river showing methane (μgL^{-1}) and $\delta^{13}\text{C-CH}_4$ (right axis) versus distance. Data labels show the $\delta^2\text{H-CH}_4$ values for a subset of samples measured.

5.3.2 Major ions in groundwater

In Section 4, major ions in groundwater were used to statistically identify distinct water types for different geological layers, with a focus on different coal seams. Here, a slightly different approach is used where water types were pooled a priori by broader geological units (that is, surface water, alluvium, interburden and coal seam). This approach will be used here for major ions and in subsequent subsections describing trends in methane and environmental tracers in groundwater. For major ions, the emphasis here was to evaluate a potential relationship with methane or methane isotopic composition and to evaluate potential sources of methane in the system and to help characterise groundwater – surface water interactions.

In the Piper diagram (Figure 5-7), surface water samples are relatively tightly clustered and characterised by a Na-HCO₃-Cl composition, with two of the shallow alluvial aquifer samples (GR-P10 and GR-P11) having a very similar composition to surface water. Other samples from the alluvial aquifer are of the Na-Cl type. Potential sources of, or mechanisms, explaining the high concentration Na-Cl type water in alluvial samples are evapoconcentration from transpiration by phreatophytes or mixing with more saline water from the underlying interburden.

The groundwater samples from the interburden and coal seams have water types ranging from Na-HCO₃, Na-HCO₃-Cl and Na-Cl, similar to other CSG studies globally ((Van Voast 2003a; Hamawand *et al.* 2013; Duvert *et al.* 2015)). High amounts of bicarbonate and low sulphate can also be used as indicators of high methane concentrations because bacterial sulphate reduction would precede methanogenesis (which consumes sulphate and produces alkalinity; see also Figure 4-6). This was consistent with anion ratios in monitoring wells completed within coals seams and with international studies (Van Voast 2003b; Cheung *et al.* 2010). Other hydrochemical investigations that have been reported on the

Hutton and Precipice sandstone in the Surat Basin, Queensland, have also found that coal seam water predominantly consists of sodium and bicarbonate and is essentially devoid of sulphate, calcium and magnesium (Ransley et al., 2015). Coal seam production waters associated with high gas production tend to be characterised by low concentrations of Ca and Mg and high concentrations of Na; the gases associated with such samples have been interpreted to be of microbial or mixed origin on the basis of methane and water stable isotope compositions (Golding *et al.* 2013). Further interpretation of the major ion data in the study area is provided in Section 4.3.2. Overall, there appears to be a gradual shift in major ion composition from surface water to deeper formations rather than a distinct grouping by broad geological units.

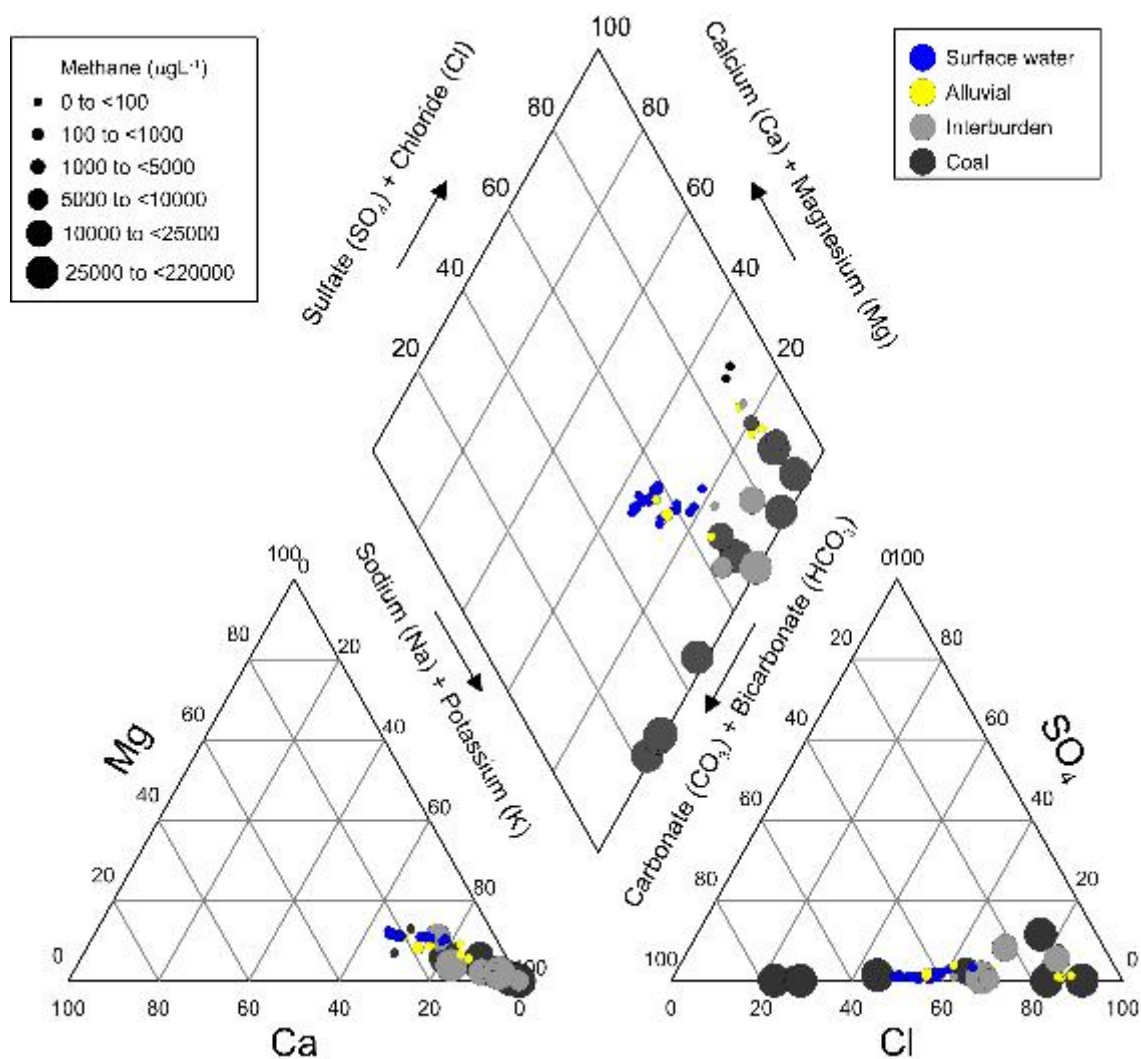


Figure 5-7 Piper diagram of 22 surface water and 26 groundwater samples collected 22nd February to 2nd March 2016 from the Gloucester study area.

5.3.3 Methane in groundwater

There was a very wide range in methane concentration and isotopic composition in groundwater (Figure 5-8 and Figure 5-9), with concentrations varying from 10 to >100,000 $\mu\text{g L}^{-1}$. In general, surface water and alluvial groundwater had the lowest concentrations (10 – 500 $\mu\text{g L}^{-1}$) and the interburden and coal seams had the highest concentrations (1,000 – >100,000 $\mu\text{g L}^{-1}$). However, there was an overlap in concentrations between geological units (Figure 5-9). Methane isotopic values also varied widely across all units ranging, for $\delta^{13}\text{C-CH}_4$, from -80 to -20‰ V-PDB . However, there was no surface water sample with $\delta^{13}\text{C-CH}_4$ more negative than -50‰ V-PDB . $\delta^2\text{H-CH}_4$ values were in the range -224 to -195 ‰VSMOW.

Because of the anticipated high methane concentrations, special care was taken in this study to sample groundwater at in situ pressures to prevent degassing during sampling. This appears warranted because many methane samples collected from all units were well above solubility equilibrium (Figure 5-10). Combining all methane values collected for the Gloucester Basin, the highest methane concentration (>100,000 $\mu\text{g L}^{-1}$) have been found in this study. However, as other factors varied as well between different studies (preservation and analytical techniques, etc.), it is not clear at present if groundwater methane concentrations have been underestimated in previous studies in the Gloucester Basin and whether this was due to a different sampling technique.

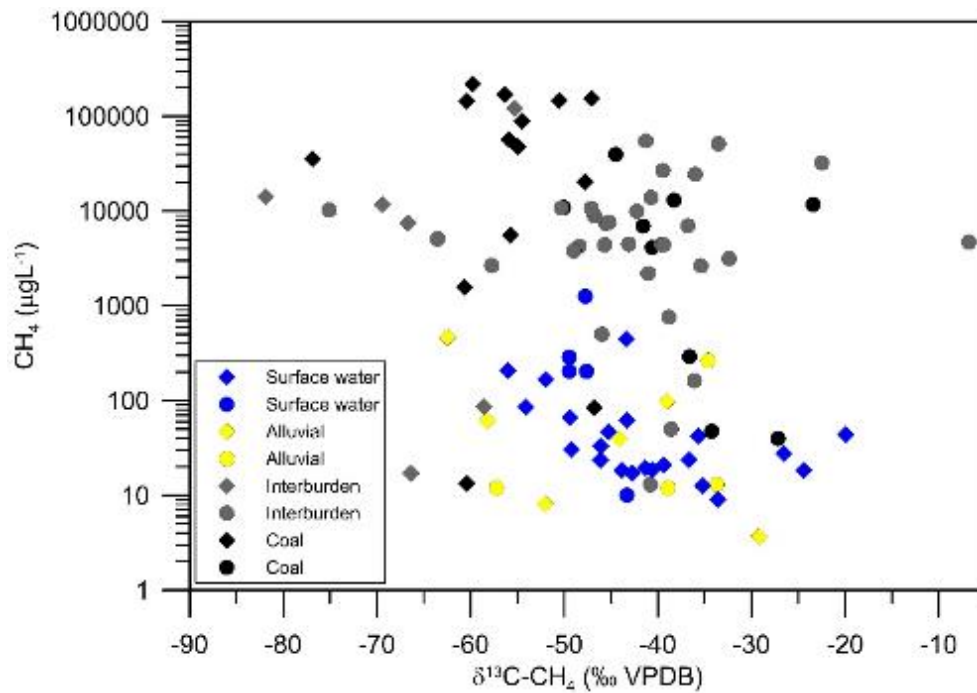


Figure 5-9 CH_4 versus $\delta^{13}\text{C}-\text{CH}_4$ of surface water and groundwater samples. Diamond symbols represent samples collected in this study. Circular symbols represent samples collected by AGL throughout 2011-2015.

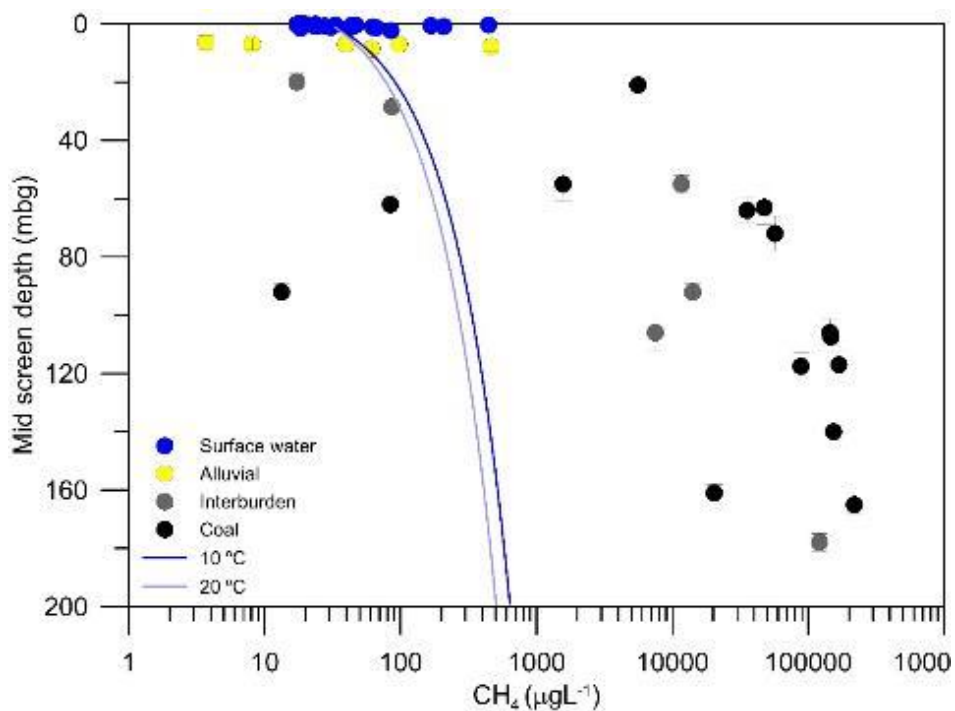


Figure 5-10 Methane concentration of surface water and groundwater samples versus depth. Methane solubility curves (at 10 and 20 degrees C) are also shown. Samples to the right of the blue curves will tend to degas if in situ pressures are not maintained during sampling.

5.3.4 Stable isotopes of water

The stable isotopes of water were used to identify the different water sources that may be contributing to the Avon and Waukivory Rivers (Table 5-4). The $\delta^{18}\text{O}$ and $\delta^2\text{H}$ values of the surface water and the groundwater samples from the alluvial, interburden and coal seams are plotted in Figure 5-11 relative to the meteoric water line (LMWL; $\delta^2\text{H} = 7.60 \delta^{18}\text{O} + 12.8$) for Brisbane. The surface water samples fall along an evaporation line (slope ~ 5.5) away from the LMWL and are more isotopically enriched than the Brisbane averaged weighted rainfall ($\delta^{18}\text{O} = -3.48$; $\delta^2\text{H} = -13.14$). Unevaporated surface water samples have a similar isotopic signature to alluvial groundwater. The groundwater samples from the major geological units show some overlap and are isotopically lighter than the surface water samples and less enriched than the average weighted rainfall. The coal seam samples are far more depleted than the alluvial samples indicating groundwater recharge under different climatic conditions to present day. Thus, a modern and older source of water are present.

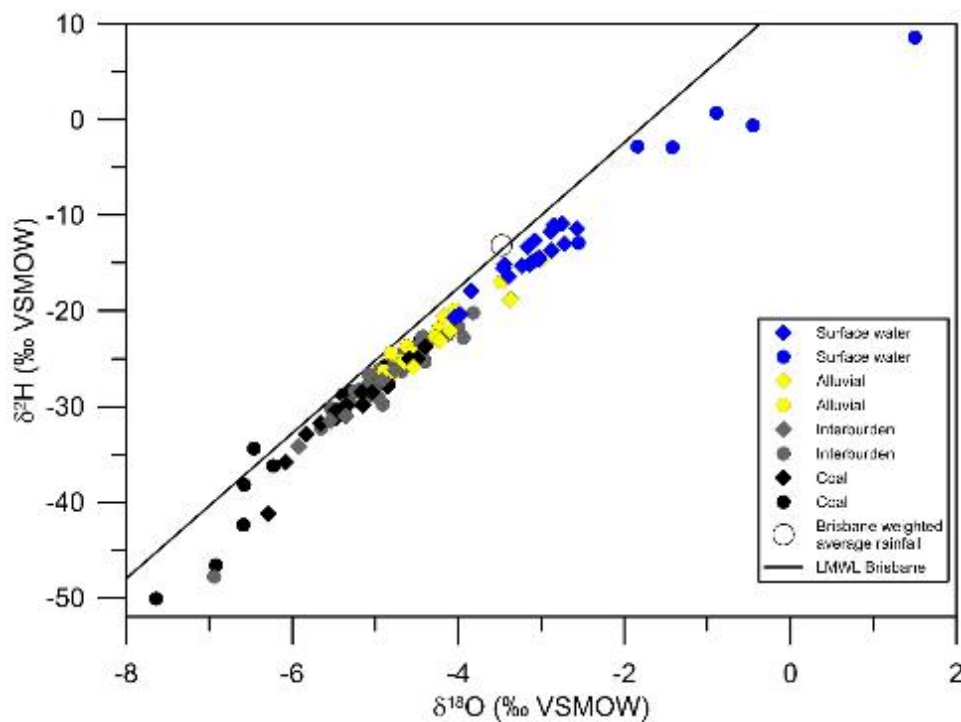


Figure 5-11 Stable isotopes of water of surface water and groundwater samples from the Gloucester study site. LMWL for Brisbane $\delta^2\text{H} = 7.6\delta^{18}\text{O} + 12.8$. Diamond symbols represent samples collected in this study. Circular symbols represent samples collected by AGL throughout 2011-2015.

Comparing $\delta^2\text{H}$ versus chloride shows that the bulk of the groundwater samples from the major aquifer units have higher chloride concentrations than the surface water and therefore can only provide a relatively small component of discharge to the surface water system (Figure 5-12). However, there are a few groundwater samples from the alluvium and interburden that have chloride concentrations similar to surface water and a similar isotopic compositions. As there is no evaporation signal in groundwater, the higher chloride

concentrations in the alluvium could be from a combination of transpiration by phreatophytes and saline groundwater discharge from deeper geological units.

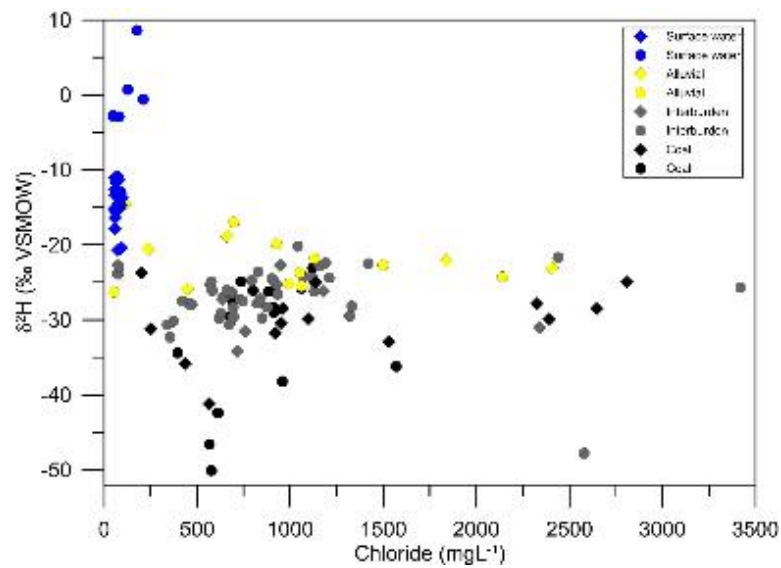


Figure 5-12 Stable isotopes of water of surface water and groundwater samples from the Gloucester Basin. Diamond symbols represent samples collected in this study. Circular symbols represent samples collected by AGL throughout 2011-2015.

5.3.5 ²²²Rn and dissolved non-radioactive noble gases in groundwater

The dissolved concentration of the atmospheric noble gases Ar, Ne, and He in water are determined by their solubility, which is a function of pressure, salinity and recharge temperature. In some cases, due to a process termed ‘excess air’, elevated concentrations of all gases can occur due to the entrapment and subsequent dissolution of air bubbles in recharging groundwater ((Heaton and Vogel 1981)). Other geochemical processes and subsurface production associated with radioactive decay (e.g., He by radioactive decay of thorium and uranium) can also affect dissolved gas concentrations. Measured noble gas concentrations were compared in groundwater with likely concentrations based on recharge temperatures between 5 and 30 °C and an excess air of less than 10 cm³ (Figure 5-13).

The dissolved helium concentrations in the surface water samples were close to atmospheric equilibrium (4.4×10^{-8} cm³ STP g⁻¹ at 20°C and 150 m elevation above sea level). Helium concentrations in the groundwater were typically much higher than what can be explained by equilibrium with atmospheric helium at the time of recharge and indicate subsurface production of helium within the aquifer and therefore evidence of an older groundwater end member (Table 5-5). Helium concentrations in the groundwater had a very large range in values from 6.4×10^{-8} to 2.0×10^{-5} cm³ STP g⁻¹) and were higher at depth than in the alluvium (Figure 5-14). One sample from the shallow alluvial aquifer (GR-P11) had a very high helium concentration (1.7×10^{-6} cm³ STP g⁻¹) indicating a source of groundwater coming from greater depth with a much longer residence time and mixing with the shallow groundwater (it also had a high methane concentration).

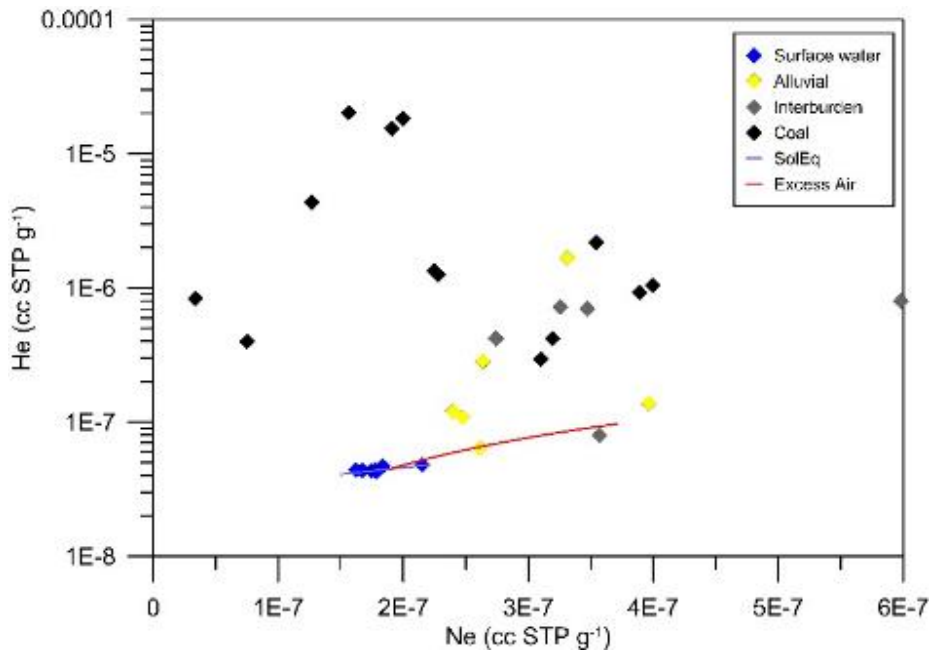


Figure 5-13 Comparison of measured concentrations of nitrogen, argon, helium and neon in groundwater with expected concentrations based on equilibrium solubility of atmospheric gases in water at temperatures between 5 and 30 °C and excess air volumes up to 10 cm³ kg⁻¹. Note that helium is plotted on a logarithmic scale, whereas the scale for the other gases is linear.

5.3.6 Tritium and carbon-14

Tritium results show that most of the groundwater samples within the study area are greater than 50 years old, with 8 out of 13 samples analysed from the February 2016 campaign less than background concentrations (less than 0.1 TU) (Table 5-5 and Figure 5-14). One sample from a well completed in the coal seam had tritium concentrations reflecting modern groundwater of 1.2 TU (GW080840-1), however, the other environmental tracers (¹⁴C and ⁴He) suggest that the water is much older, indicating that the sample may be contaminated by residual drilling fluid given that this was a newly constructed well only completed in late 2015. This would also mean that radiocarbon is too young.

The ¹⁴C activities in the groundwater samples analysed in February 2016 ranged from 0.7 to 96 pmC and the δ¹³C values ranged between -15.7 to 21.6 ‰ (Table 5-5). The alluvial samples were greater than 79 pmC, whilst the majority of the coal seam samples were less than 10 pmC. Changes to the total dissolved inorganic carbon (TDIC) or alkalinity via geochemical processes can potentially decrease the isotopic ratio of ¹⁴C/¹²C which can make the water sample appear 'older' than it actually is (Plummer and Glynn, 2013). Overall, the ¹⁴C data showed that groundwater apparent age increased within increasing depth and that some of the coal seam and interburden samples show signs of methanogenesis (Han et al., 2012).

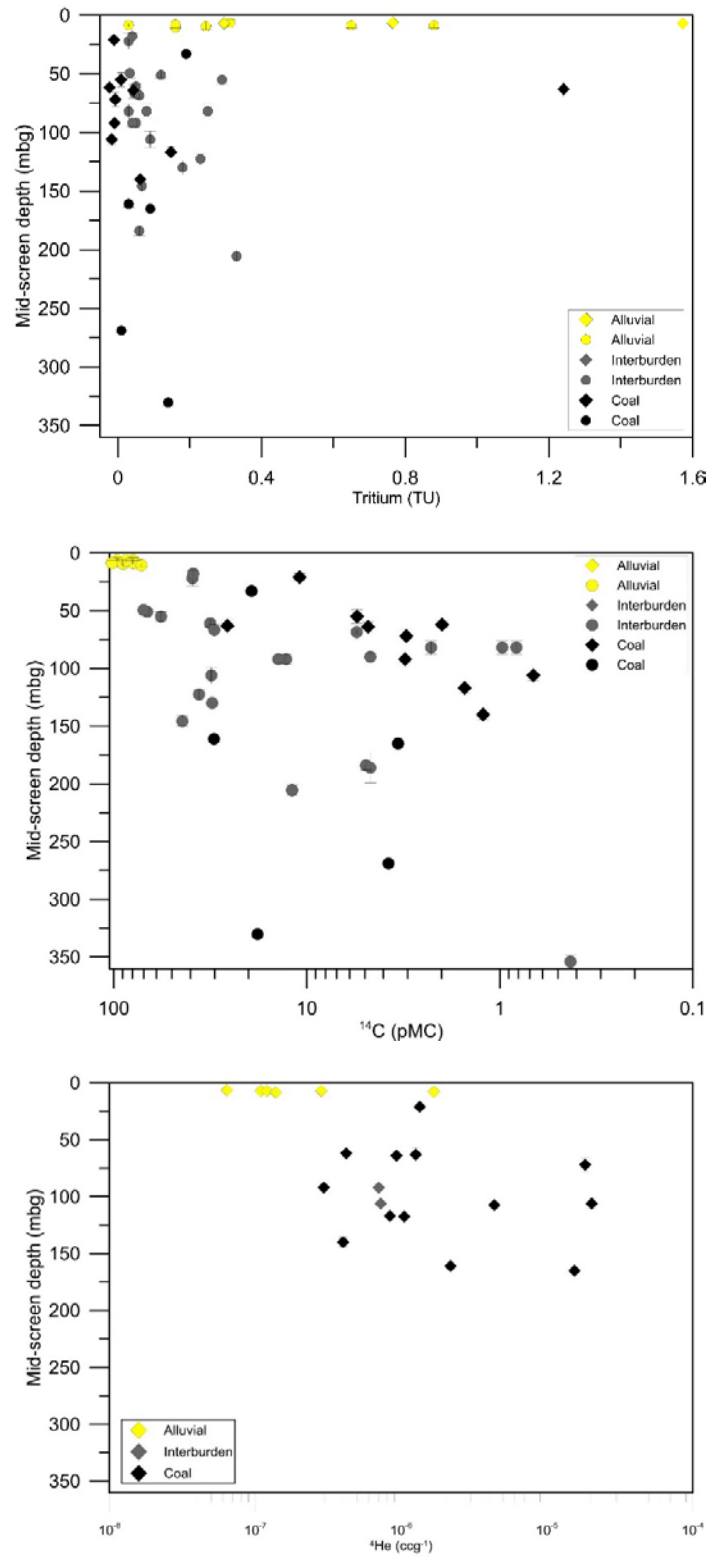


Figure 5-14 (a) ^3H , (b) ^{14}C and (c) ^4He concentrations versus depth in groundwater samples. Diamonds represent samples collected in this study; circles represent samples collected by AGL throughout 2011-2015. Error bars represent well screen lengths.

5.4 Discussion

Deeper groundwater in the Gloucester Basin is significantly enriched in potential environmental tracers of groundwater discharge to surface waters, including helium, methane and salinity. In general, the patterns in environmental tracers were consistent with the Waukivory and the Avon rivers being gaining environments and the main source of groundwater was the alluvium, owing to its lower salinity. However, helium, radon and methane trends in surface water all hinted at some preferential zones for groundwater discharge, including potentially from deeper sources. These tracer hotspots were associated with some of the fault zones identified with others techniques, including the fault zones at the junction of the Waukivory and Avon rivers (methane hotspot) and the one at the base of the Mograni Range on Waukivory River (helium hotspot; Figure 5-15). Other studies have found that helium is more concentrated in groundwater in the close vicinity of lineament features as a result of a higher fracture density and an existing inter-connection with flow pathways of increased residence time (Banwell and Parizek 1988). Thus, whilst the bulk of groundwater baseflow is via the alluvial aquifer, discharge from deeper sources is also likely.

In the following, the impact of groundwater – surface water mixing for the evaluation of deep groundwater discharge is discussed. The mass-balance for radon in rivers is reviewed to help with the interpretation of gas tracers in surface water in general. The potential causes for the broad range in methane isotope values in all geological units are reviewed. Finally, the potential for a background diffusive flux of methane and helium from deeper units to the alluvium is evaluated.

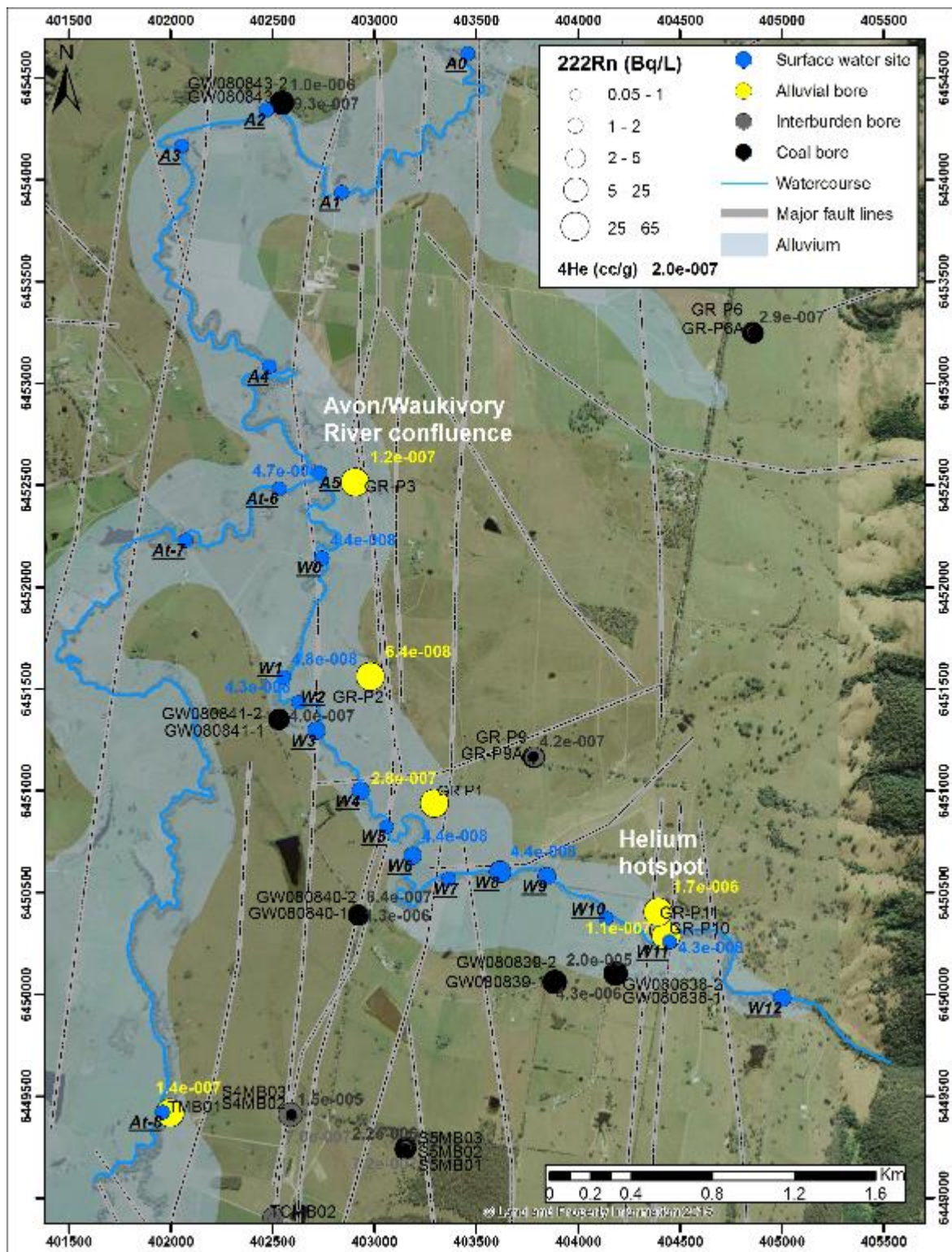


Figure 5-15 Measured surface water and groundwater ^4He concentrations and ^{222}Rn in the study area. The size of the circles represent ^{222}Rn concentration and the numbers next to them are the ^4He concentrations.

5.4.1 Groundwater – surface water mixing processes

Even in gaining environments, groundwater-surface water interaction is a two-way process with groundwater and surface water (and their solutes) continuously being exchanged at different spatial and temporal scales (Woessner, 2000). In an alluvial aquifer setting, flood cycles and hyporheic exchange will contribute to mixing between groundwater and surface water (Figure 5-16). Hyporheic processes occur at a range of scales, from the current-driven exchange due to flow over uneven streambeds to the larger exchanges promoted by head gradients between pools or across river meanders (Jones and Mullholland, 2000; Carthwright and Hofmann, 2016). Groundwater mixing during floods can occur as combination of floodplain inundation, rapidly rising and falling water tables, and bank recharge and discharge cycles (Lamontagne et al., 2005; Lamontagne et al., 2015b).

The implication for using tracers to evaluate groundwater discharge via faults from deeper geological formations is that the tracer signal will tend to be diluted by groundwater – surface water exchange within the alluvium. In other words, when an alluvium is present, the evidence for groundwater discharge from deeper geological units may be more obvious in the alluvium than in the rivers themselves. In addition, when discharge from deeper units is very saline, density stratification may develop in the alluvium (when a river-derived freshwater lens sits on top of the denser saline groundwater). These are common in many environments in Australia (Anderson and Morrison, 1989), including in catchments of the Hunter River region (Lamontagne et al., 2005a; Jasonsmith et al., 2017). Thus, when evaluating the potential for groundwater discharge from faults and fractures in CSG environments, both the surface water network and the alluvium need to be monitored.

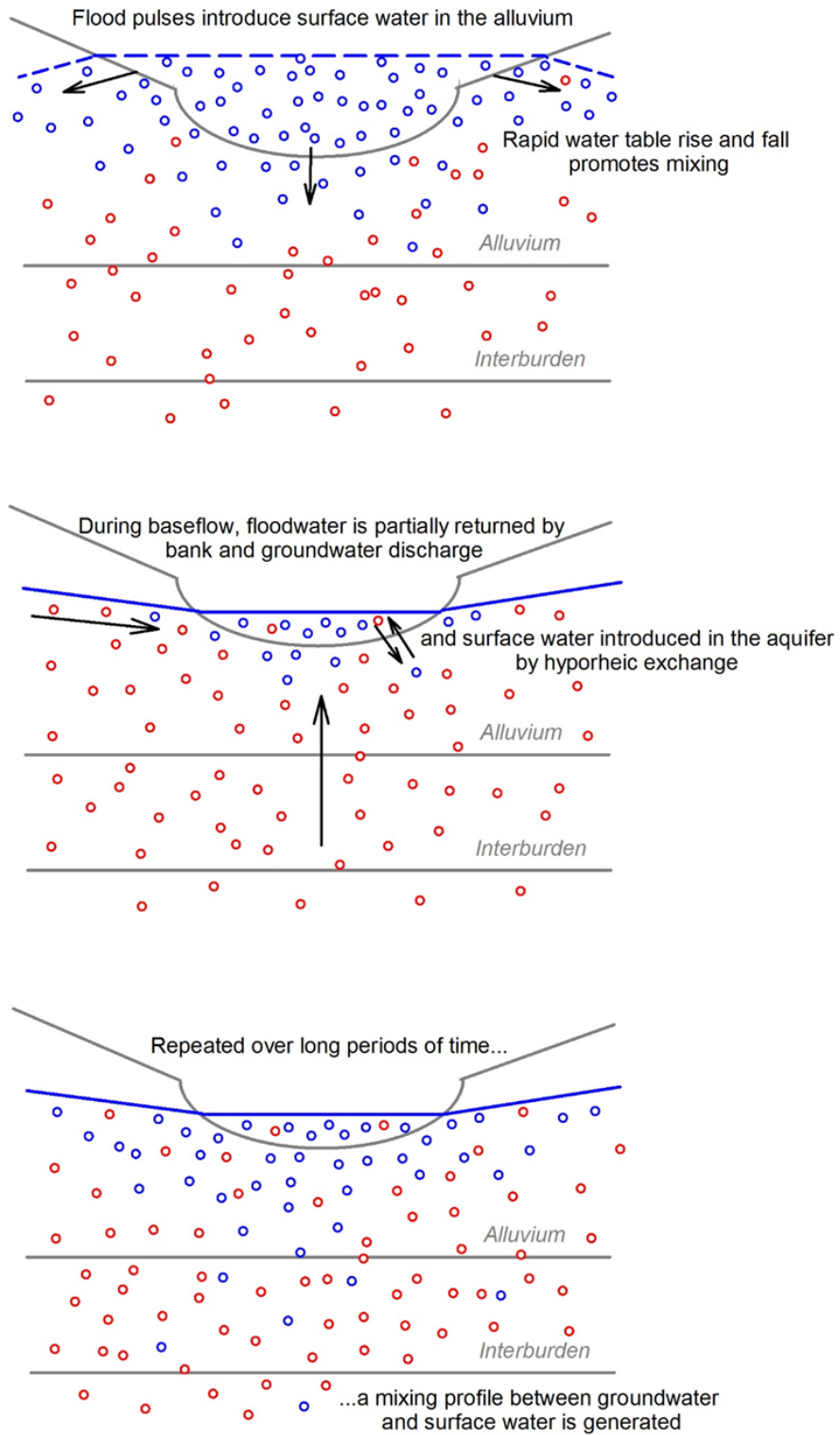


Figure 5-16 Conceptual representation of a solute mixing profile below a gaining river generated by a combination of flood pulses and hyporheic exchange.

5.4.2 Inferring the groundwater flux from surface water radon, methane and helium trends

Because they can be enriched in groundwater, dissolved gases like methane, helium and radon are useful tracers of groundwater discharge to surface waters. However, finding these gases in surface water does not necessarily 'prove' groundwater discharge takes place because they have several sources and sinks in surface water. These, including groundwater discharge, can be evaluated with a mass-balance for the tracers in the river (Figure 5-17). Using ^{222}Rn as an example, the variations in concentration along a groundwater-fed river follows (Cook et al., 2006):

$$\frac{\partial Qc}{\partial x} = Ic_i - k_gwc - \lambda dwc - cL + F \quad (5-1)$$

where Q is stream discharge ($\text{m}^3 \text{day}^{-1}$), c is the concentration (or activity) in the stream (Bq L^{-1}), c_i is the concentration in groundwater inflow (Bq L^{-1}), I is the groundwater flow rate per unit stream length ($\text{m}^3 \text{m}^{-1} \text{day}^{-1}$), L is the rate of surface water loss by pumping or to groundwater ($\text{m}^3 \text{m}^{-1} \text{day}^{-1}$), k_g is the gas transfer velocity across the water surface (m day^{-1}), λ is the radioactive decay constant (day^{-1}), d is the mean stream depth (m), w is the width of the river (m), x is distance in the direction of flow and F is the flux from the hyporheic zone ($\text{Bq m}^{-1} \text{s}^{-1}$).

Thus, an increase in ^{222}Rn at a given point along a river could be due to a combination of factors including: 1) an increase in groundwater discharge, 2) an increase in groundwater ^{222}Rn activity, 3) a lower degassing rate to the atmosphere, 4) the stream widening, and 5) an increase in hyporheic exchange. In general, ^{222}Rn activity in surface water is much lower than in groundwater because of the significance of degassing in the mass-balance. Thus, variations in radon activity in streams will tend to be larger when pronounced pool-riffle sequences are present because of the impact of turbulence on degassing rates. This is consistent with the large variations in ^{222}Rn observed in the Waukivory River relative to the Avon River downstream of Waukivory, as the former has well-defined pool-riffle sections along its course and the riffles are relatively wide (about 1–10 m) and shallow (about 5 – 20 cm). The mass-balance for helium is simpler than for radon because production by sediments is usually very small. However, it is more complex for methane because both production and consumption in sediment or the water column is possible. For all gas tracers, evaluating k is an important aspect of the mass-balance (see example in Cook et al., 2006).

Combining tracers together can also help constrain the sources of groundwater to a river (Gardner et al., 2011). Whilst ^{222}Rn is usually considered an indicator of total groundwater discharge, elevated ^4He is usually found in regional (older) groundwater sources. Helium-4 concentrations along the Waukivory River were all close to atmospheric values, suggesting groundwater originated from the alluvium rather than from deeper formations. On the other hand, because the k for helium is approximately 2.5 times larger than the one of radon (Gardner et al., 2011), the 'old' groundwater signature may have been lost at Waukivory due to more rapid ^4He degassing relative to radon.

Taken together, the evidence available from the synoptic river survey is consistent with a significant contribution of groundwater discharge to stream baseflow, principally from the alluvium. Whether groundwater discharge along the stream was continuous or via hotspots is less clear and would require additional field characterisation of processes such as degassing rates and hyporheic exchange.

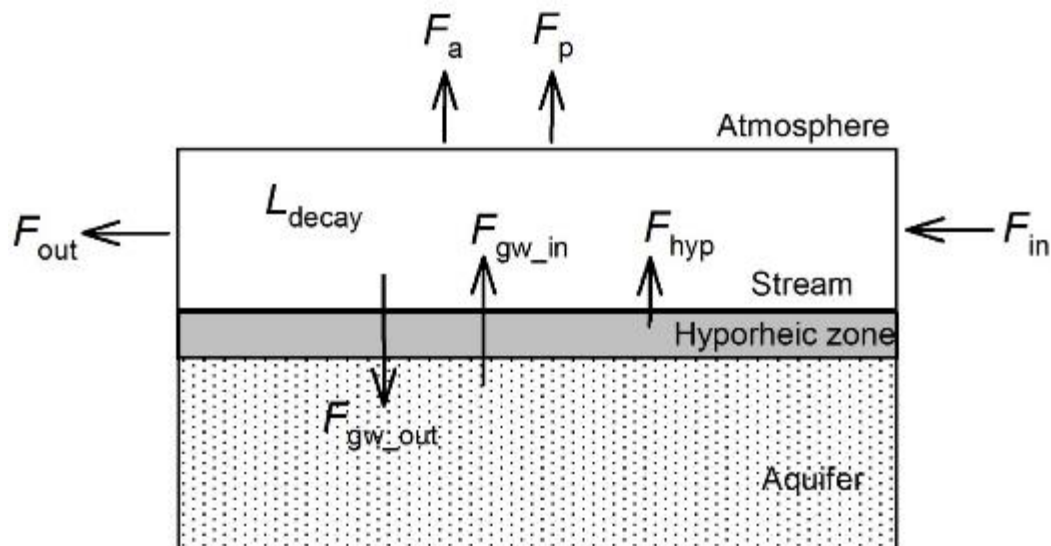


Figure 5-17 Summary diagram for the different components of the radon mass-balance along a river reach. F_{in} is the surface water radon flux to the reach, F_{out} is the surface water radon flux out of the reach, F_a is the flux to the atmosphere by gas evasion (degassing), F_p the radon loss by pumping, F_{gw_in} is the groundwater discharge of radon, F_{gw_out} is the loss of radon by groundwater recharge, F_{hyp} is the flux from hyporheic exchange, and L_{decay} is the loss during transit from radioactive decay.

5.4.3 Methane

A large range in methane isotopic composition was found in Gloucester Basin surface and groundwater, suggesting that more than one source for methane may be present (Figure 5-18). Numerous studies have investigated low-temperature thermal generation of hydrocarbon gases in sedimentary basins ((Rowe and Muehlenbachs 1999; Hamilton *et al.* 2014)) and used the stable isotopic compositions of methane, $\delta^{13}\text{C-CH}_4$ and $\delta^2\text{H-CH}_4$, to distinguish between the biogenic and thermogenic components of the methane source and depth of origin. For $\delta^{13}\text{C-CH}_4$, delta values between approximately -70 and -50‰ are interpreted as indicating a biogenic source. Similarly delta values between approximately -55 and -30‰ are interpreted to be from a thermogenic source ((Cicerone and Oremland 1988)). However, strict methane gas composition and classification as biogenic or thermogenic origin has been found to be problematic in systems which have mixtures of biogenic and thermogenic gases due to complex formation pathways and the hydro-biogeochemical reaction processes that take place in the subsurface ((Whiticar *et al.* 1986; Whiticar 1999; Kirk *et al.* 2015)). Additionally, some methane is created from the incomplete combustion of organic materials and the delta values for this methane are less negative than thermogenic methane ((Ferretti *et al.* 2005; Ferretti *et al.* 2007)). Data from Australian

coal basins show that there is extensive microbial activity, particularly in coal beds shallower than 600 m depth ((Faiz and Hendry 2006)). Microbial activity causes secondary biogenic gas generation, with CO₂ reduction being the main pathway of this secondary biogenic methane generation. Hence, CO₂ and biogenic methane are often the major constituents in Australian coal seam gas reservoirs (Kinnon et al., 2010). Stolper et al. ((2014a; 2014b; 2015)) have used a methane clumped isotope geothermometer approach to provide some additional constraints on the formation temperatures to determine the relative amounts of biogenic and thermogenic gases. However, in order to achieve this requires separating the individual isotopologues of methane during analysis of the sample.

The $\delta^{13}\text{C-CH}_4$ values in the Gloucester Basin fall into the range found during a baseline study of the Richmond River Catchment, NSW (−90.9 to −29.5‰ V-PDB), which concluded a bacterial methane source that had been subject to partial oxidation ((Atkins *et al.* 2015)). Additional biogeochemical effects may be anticipated in the vicinity of rivers, where both bacterial production and consumption may occur ((Bigeleisen and Wolfsberg 1958)). Partial methane oxidation in rivers would enrich the remaining methane pool and blur the distinction between thermogenic and biogenic methane ((Coleman *et al.* 1981)). Nevertheless, the combination of the $\delta^{13}\text{C-CH}_4$ and $\delta^2\text{H-CH}_4$ values provides some evidence for a thermogenic methane component in the Waukivory and Avon rivers (Figure 5-18). This would be consistent with either some deeper groundwater discharge, or some process favouring the migration of deeper methane to the surface. This latter process is evaluated next.

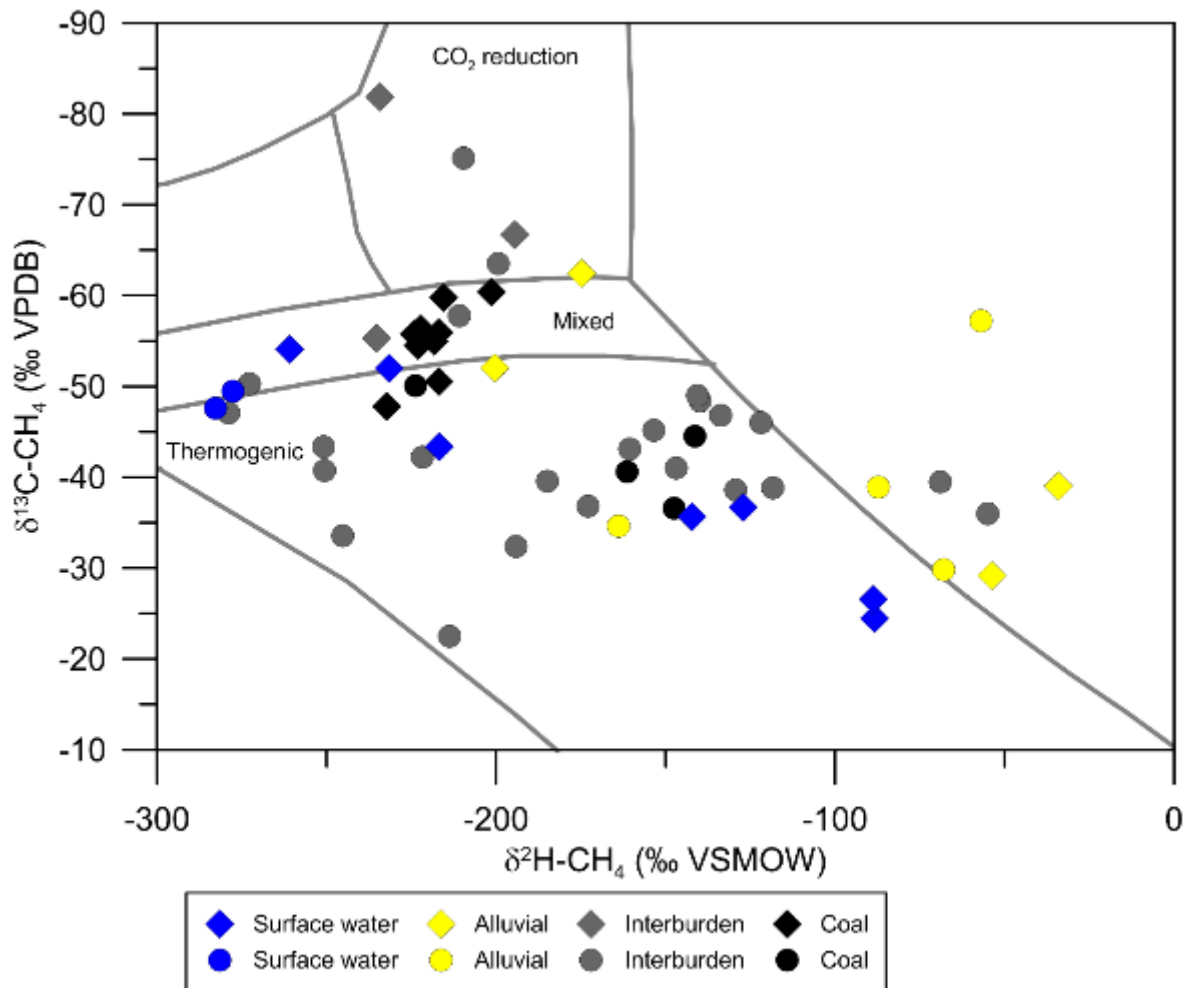


Figure 5-18 $\delta^{13}\text{C-CH}_4$ versus $\delta^2\text{H-CH}_4$ of surface water and groundwater samples compared to other coal basins. Diamond symbols represent samples collected in this study. Circular symbols represent samples collected by AGL throughout 2011-2015. Classification system from Whiticar et al. ((1986)) with other Australian coal bed methane reservoir data taken from Faiz and Hendry ((2009)).

5.4.4 Estimating the vertical groundwater flux based on helium and methane profiles

In low permeability environments, solutes can be transported by a combination of groundwater advection and diffusion through the geological matrix (Figure 5-19), with the latter process favoured when large concentration gradients are present. As methane and helium concentrations vary over several order of magnitudes between deeper geological units and the alluvium, an upward vertical diffusive flux for methane and helium is possible in the Gloucester Basin. To evaluate this, a simple one-dimensional (1D) transport model was set up in an attempt to describe the observed tracer profiles. The closer the model describes the observed data, the more likely it is that the hypothesized model is representative of real world processes.

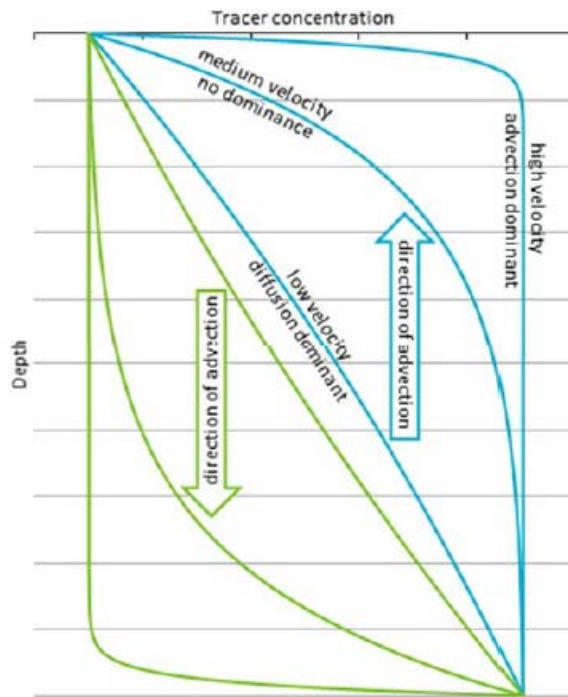


Figure 5-19 Examples of tracer distribution in an aquitard under low and high, and upward and downward groundwater velocity (from Smith et al., 2018), assuming no internal production.

1D-modelling of the helium and methane data was done using an analytical solution of the advection-dispersion-production equation (no production rate was considered for the methane case):

$$\frac{\partial C}{\partial t} + V_z \frac{\partial C}{\partial z} = D_e \frac{\partial^2 C}{\partial x^2} + \frac{g^*}{n_e} \quad (5-2)$$

where C is the concentration of the tracer ($\text{cm}^3 \text{ STP g}^{-1}$), V_z is the vertical groundwater velocity (m year^{-1}), D_e is the effective diffusion coefficient (as described below), g is the internal production rate of the tracer ($\text{cm}^3 \text{ STP g}^{-1}\text{year}^{-1}$), and n_e is the effective formation porosity. The porosity used was 0.3, which is suitable for the coal seams but may be an overestimation for the interburden material. For helium, the internal production rate is a function of the U and Th concentration within the aquifer. The production was estimated to be $1.2 \times 10^{-20} \text{ cm}^3 \text{ STP g}^{-1} \text{ s}^{-1}$ using average concentrations of U and Th of 1.9 ppm and 4.8 ppm, respectively. The U and Th concentrations are taken from Smith et al. (2018) and are representative of low-permeability formations in the Gunnedah Basin (Watermark [an upward coarsening sequence of silt grading to fine-grained sandstone] and Porcupine [an upward-fining conglomerate containing sandstones, siltstones and a few igneous intrusions] Formations).

The effective diffusion coefficient can be defined using the temperature-dependent free-water diffusion coefficient ($D_{0,w}$) (Jähne *et al.* 1987), which is multiplied by aquitard porosity (n_e) and flow path tortuosity (τ):

$$D_e = D_{0,w} n_e \tau \quad (5-3)$$

Because flow path tortuosity is typically not a well-constrained parameter, D_e is instead commonly approximated as:

$$D_e = D_{0,w} n_e^m \quad (5-4)$$

where $m = 2$ is the maximum expected porous media diffusion coefficient for helium (Mazurek *et al.* 2011). For deionised water at a temperature of 25 °C, the free-water diffusion coefficient $D_{0,w} = 7.22 \times 10^{-9} \text{ m}^2 \text{ s}^{-1}$ (Jähne *et al.* 1987).

The modelling of helium concentrations is constrained by the He concentrations used for the upper and lower boundary conditions (Figure 5-20). The upper boundary condition for the 1D model was taken as the measured helium concentrations in the shallow alluvial aquifer (GR-P2), whilst the geometric mean ($2.29 \times 10^{-6} \text{ cm}^3 \text{ STP g}^{-1}$) of the measured helium concentrations from the six sampled wells greater than 100 m depth was selected as the lower boundary. Taking the geometric mean of the helium concentration in the coal seams as the calibration target (Model 1), the 1D modelling resulted in a minimum upward velocity V_z of approximately 0.1 mm year^{-1} . This velocity represents a Darcy flux $q = V_z \times n_e = 3 \times 10^{-5} \text{ m year}^{-1}$ or $9.5 \times 10^{-13} \text{ m s}^{-1}$. Typically at such low velocities, helium transport is governed by molecular diffusion rather than by advection (Smith *et al.*, 2018). These results were obtained by fitting the model through approximately five data points which were either interburden (GR-P9 and S5MB01) or coal (GW080840-1, GW080843-1, GW080843-2, and S5MB03).

Two additional modelling scenarios were conducted for the two sets of nested wells, i.e. model S5MB (based on nested wells S5MB01 [interburden], S5MB02 [interburden], and S5MB03 [coal]) and model S4MB (based on nested wells S4MB02 [interburden] and S4MB03 [coal]). The upper boundary condition was the same as Model 1, however, $2.4 \times 10^{-6} \text{ cm}^3 \text{ STP g}^{-1}$ and $2.8 \times 10^{-6} \text{ cm}^3 \text{ STP g}^{-1}$ was used for the lower boundary for model scenarios S5MB and S4MB, respectively. Compared to the first model, the modelled vertical flux value for S5MB and S4MB was downward in order to closely match each of the measured He concentrations within the nested bores (S5MB01, S5MB02, and S5MB03 data were used to fit the S5MB model while the S4MB02 and S4MB03 data were used to fit the S4MB model). The downward flux for the S5MB and S4MB modelling scenarios was 0.2 and 0.9 mm year^{-1} , respectively and although, relatively low, this would be expected for the permeability of the interburden material.

Figure 5-21 shows measured methane concentrations versus depth and two fitted models that describe the data equally well, with upward pore-water velocities ranging from 4×10^{-5} to $8 \times 10^{-5} \text{ m year}^{-1}$, or from 10^{-7} to $2 \times 10^{-7} \text{ day}^{-1}$. These velocities are even lower (about one order of magnitude) than the ones based on the helium data.

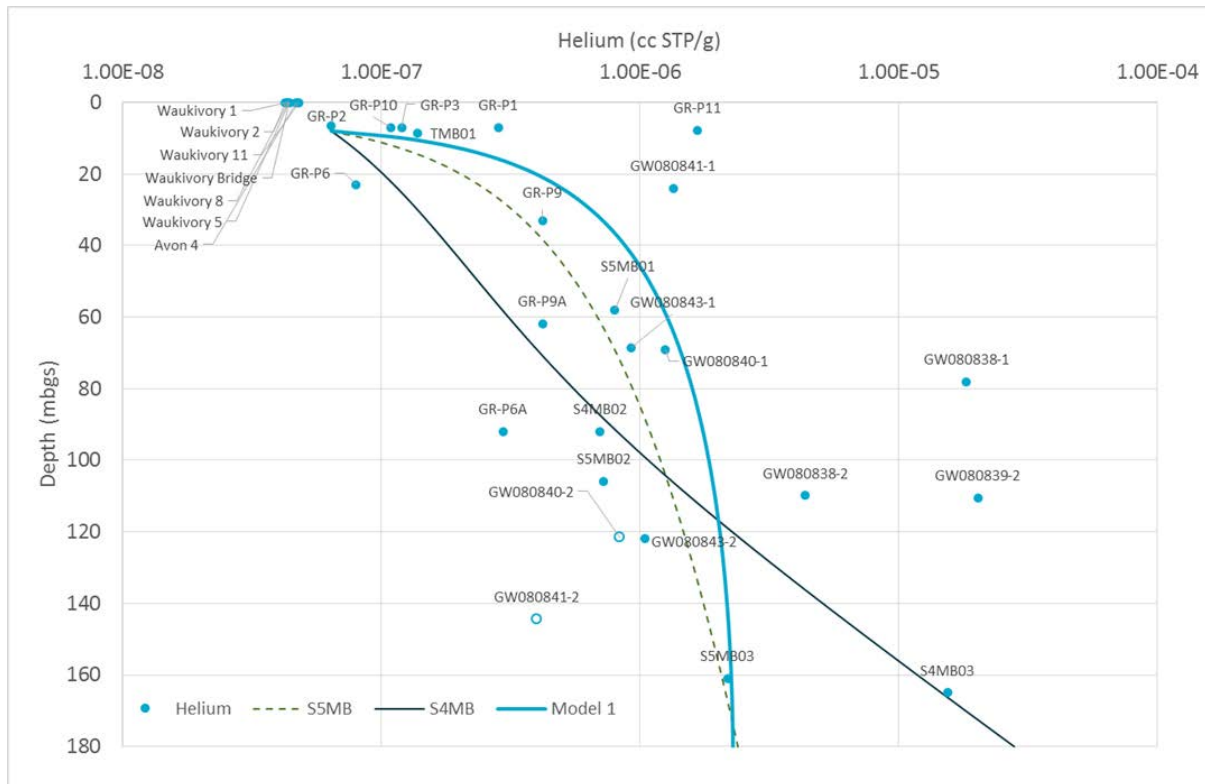


Figure 5-20 Modelled helium concentrations using three models (model 1, S5MB, S4MB)

The model was particularly sensitive to the values selected for vertical flux (V_z) and the effective porosity; similar models were obtained by modifying the direction from upwards to downwards flow and adjusting the porosity less than an order of magnitude. Also due to the geological complexity of the area with alternating bands of coal seam and interburden material, a dual porosity model would be more appropriate to try and reduce some of the model sensitivities. The presence of upward and downward flow in some areas is consistent with analysis of hydraulic head data (see Section 7.3.27.3.2; for example, Layer 1-6 in Figure 7-9) which shows a sink with a closed low head against the eastern side of the selected red fault. Taking in to consideration the observed hydraulic gradients in section 4 and the measured hydraulic conductivity data with depth in section 2.3 (see Figure 2-6) to obtain a Darcy flux of 10^{-5} m year⁻¹ (see model 1 above), the hydraulic gradient should not be larger than 10^{-2} m/m if $K_v = 10^{-3}$ m day⁻¹ and not larger than 10^{-3} m/m if $K_v = 10^{-2}$ m day⁻¹. A discussion on hydraulic gradients is provided in Section 7.3.2.

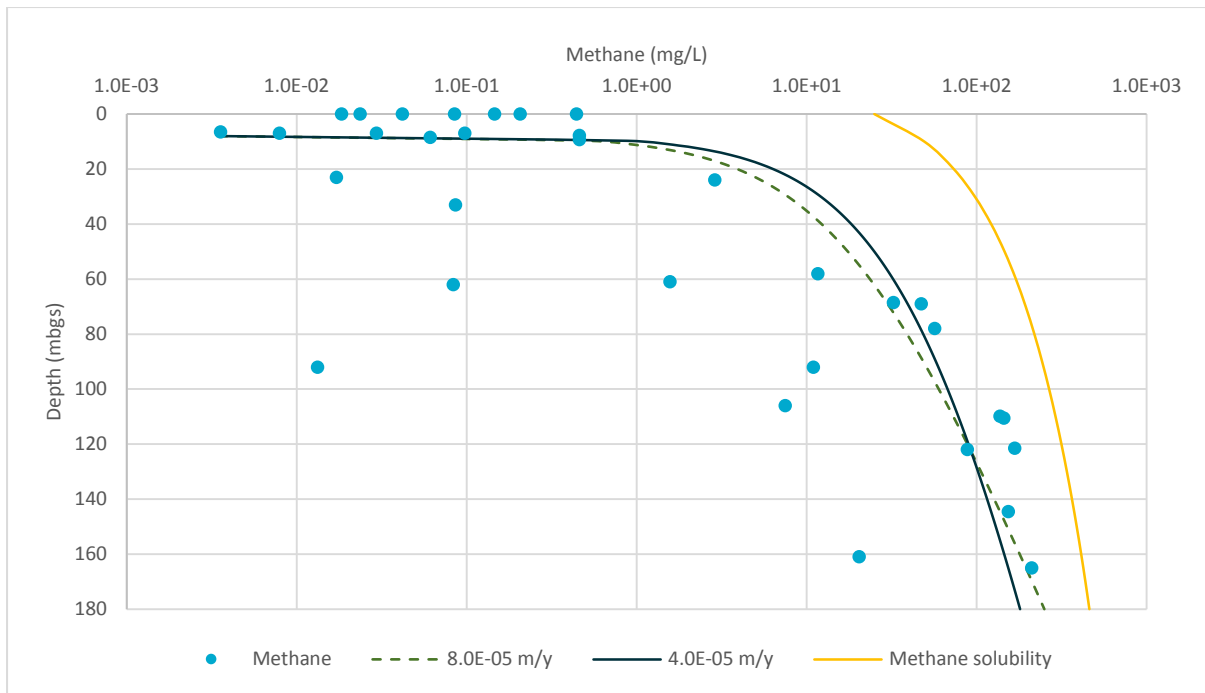


Figure 5-21 Modelled methane concentrations using two pore-water velocities (8×10^{-5} and 4×10^{-5} m year⁻¹). When concentrations exceed solubility, bubble formation may occur.

Overall, the inferences made from this simple modelling exercise should be used with caution considering the large range in concentration found in the subsurface and the simplified geological model used. In particular, upward advection could still be larger than what was estimated here and the velocity profile more complex, including areas of upward and downward flow. The key finding is that an upward vertical advective or diffusive flux for methane and helium could occur through the interburden. Thus, even in the absence of preferential flowpaths via faults and fractures, a small methane and helium flux through the interburden matrix could occur.

The above findings, together with evidence from subsequent Sections 7, indicate the presence of a dual-permeability type rock mass. The majority of the interburden acts as a relatively low permeability rock where mass transport is governed by molecular diffusion (see above). The fault zone with its disturbed zone acts as the more permeable rock with mass transport likely governed by advection (i.e. flowing water). The conceptual model of a dual permeability rock (Figure 5-22), represents the fractures and matrix domain as separate continua. Each continuum has its own permeability, i.e. flow exists in both continua. If a different pressure exists between fracture and matrix, flow occurs between the two continua.

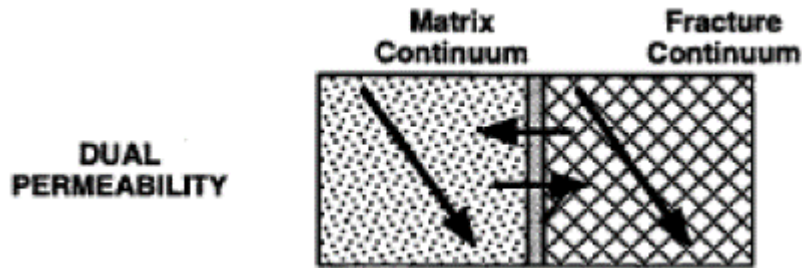


Figure 5-22 Conceptual model of a dual permeability porous medium. The matrix continuum represents the interburden rock mass while the fracture continuum represents the fault zone damage zone. Flow direction can be upwards or downwards (Source: Altman et al., 1996).

5.5 Integrated analysis supporting hydrogeological conceptualisation

The use of a multi-tracer approach helped identify some of the plausible factors that could be contributing to the surface water-groundwater exchange processes between the different water compartments in the Gloucester Basin and highlighted the complex nature of the heavily faulted hydrogeological system.

The synoptic river survey showed a gaining stream environment and an integration or capture zone of multiple flow pathways and groundwater sources. Radon and noble gas data identified that there is a significant contribution of groundwater discharge to stream baseflow, principally from the alluvium. The shallow alluvial aquifer acts a 'mixing bucket' for shallow and deeper groundwater from the interburden and coal seams prior to discharging into the river. Major ion chemistry and stable isotopes of water identified the key water types and provided some indication of cyclic mixing of young (<50 years) and old (>50 years) water in the near stream environment as a result of stream hydrological events and hyporheic exchange processes. The apparent age dating tracers (tritium, ^{14}C and ^4He) indicated that the surface water is relatively modern and that most of the groundwater are greater than 50 years with much older waters within the interburden and coal seams and a mix of young and old in the alluvial aquifer system.

Whether groundwater discharge along the stream was continuous or via localised discharge points related to the structural geological features of the basin is less clear. However, the surface water methane concentration 'hotspots' did tend to correlate to the location of the local and regional maps showing the structural lineaments (Hillis et al., 1999; Parsons Brinckerhoff, 2013) and major fault/damage zone features that were identified in this study (see Chapter 3 and Chapter 6). The stable isotopes of methane showed that there are both bacterial and thermogenic sources of methane which suggests that there may be some component of deeper groundwater migrating upwards to the alluvial and river system. The 1-D analytical modelling using the helium and methane data to estimate vertical

groundwater fluxes found that similarly good models were obtained by modifying the direction from upwards to downwards flow and adjusting the porosity less than an order of magnitude. Given the geological complexity of the area with alternating bands of coal seam and interburden material, a dual porosity model would be more appropriate to try and reduce some of the models' sensitivities.

Overall, the methane concentration, stable isotopes of methane, hydrochemistry, stable isotopes of water, noble gases and apparent age tracer data identified locations of the surface water and the shallow alluvial aquifer system within the study area that are likely to be influenced by structural geological features, in particular preferential flow paths along faults between the deeper coal seams.

5.6 References

- Altman SJ, Arnold B, Barnard R, Barr G, Ho C, McKenna S and Eaton R (1996). Flow calculations for Yucca Mountain groundwater travel time, report no. GWTT-95, Sandia National Labs, Albuquerque, NM, USA.
- Anderson JR and Morison AK (1989) Environmental consequences of saline groundwater intrusion into the Wimmera River, Victoria. *BMR Journal of Australian Geology and Geophysics* (11): 233-252.
- Atkins ML, Santos IR and Maher DT (2015). Groundwater methane in a potential coal seam gas extraction region. *Journal of Hydrology: Regional Studies* 4 Part B: 452-471, doi: <http://dx.doi.org/10.1016/j.ejrh.2015.06.022>.
- Banwell G and Parizek R (1988). Helium 4 and Radon 222 Concentrations in Groundwater and Soil Gas as Indicators of Zones of Fracture Concentration in Unexposed Rock. *Journal of Geophysical Research* 93(B1): 355-366.
- Bigeleisen J and Wolfsberg M (1958). Theoretical and experimental aspects of isotope effects in chemical kinetics. *Advances in Chemical Physics* 1: 15-76.
- Burnett WC, Kim G and Lane-Smith D (2001). A continuous monitor for assessment of ²²²Rn in the coastal ocean. *Journal of Radioanalytical and Nuclear Chemistry* 249(1): 167-172, doi: 10.1023/A:1013217821419.
- Cartwright I and Hofmann H (2016). Using radon to understand parafluvial flows and the changing locations of groundwater inflows in the Avon River, southeast Australia. *Hydrology and Earth System Sciences* 20(9): 3581-3600, doi: 10.5194/hess-20-3581-2016.
- Chanton J, Chaser L, Glasser P and Siegel D (2005). Carbon and Hydrogen Isotopic Effects in Microbial, Methane from Terrestrial Environments, in *Stable Isotopes and Biosphere Atmosphere Interactions*, edited, pp. 85-105.

- Cheung K, Klassen P, Mayer B, Goodarzi F and Aravena R (2010). Major ion and isotope geochemistry of fluids and gases from coalbed methane and shallow groundwater wells in Alberta, Canada. *Applied Geochemistry* 25: 1307-1329.
- Cicerone RJ and Oremland RS (1988). Biogeochemical aspects of atmospheric methane. *Global Biogeochemical Cycles* 2(4): 299-327.
- Coleman DD, Risatti JB and Schoell M (1981). Fractionation of carbon and hydrogen isotopes by methane-oxidizing bacteria. *Geochimica et Cosmochimica Acta* 45(7): 1033-1037, doi: [http://dx.doi.org/10.1016/0016-7037\(81\)90129-0](http://dx.doi.org/10.1016/0016-7037(81)90129-0).
- Coleman DC, Liu CH, Hackley KC, Pelphey SR (1995). Isotopic identification of landfill methane. *Environmental Geosciences* 2: 95-103.
- Coleman DC (1995). Advances in the use of Geochemical finger printing for gas identification. American Gas association operations Conference, San Francisco, CA, 1994 and Society of Petroleum Engineers Continuing Education Seminar "engineering applications for Michigan" mt Pleasant, MI, April 11-12 1995.
- Commonwealth of Australia (2014). Aquifer connectivity within the Great Artesian Basin, and the Surat, Bowen and Galilee Basins, Background review Rep., 209 pp, Department of the Environment, Canberra.
- Cook PG, Lamontagne S, Berhane D and Clark JF (2006). Quantifying groundwater discharge to Cockburn River, southeastern Australia, using dissolved gas tracers ^{222}Rn and SF_6 . *Water Resources Research* 42, W10411.
- Crosson ER (2008). A cavity ring-down analyzer for measuring atmospheric levels of methane, carbon dioxide and water vapor. *Applied Physics B: Lasers and Optics* 92: 403-408.
- Durrige Company Inc (2015). Rad7 Radon detector, (http://www.durrige.co.uk/products_rad7.shtml).
- Duvert C, Raiber M, Owen DDR, Cendón DI, Batiot-Guilhe C and Cox ME (2015). Hydrochemical processes in a shallow coal seam gas aquifer and its overlying stream-alluvial system: implications for recharge and inter-aquifer connectivity. *Applied Geochemistry* 61: 146-159, doi: <http://dx.doi.org/10.1016/j.apgeochem.2015.05.021>.
- Ellins KK, Roman-Mas A and Lee R (1990). Using ^{222}Rn to examine groundwater/surface discharge interaction in the Rio Grande De Manati, Puerto Rico. *Journal of Hydrology* 155: 319-341.
- Eyer S, Tuzson B, Popa ME, van der Veen C, Röckmann T, Rothe M, Brand WA, Fisher R, Lowry D, Nisbet EG, Brennwald MS, Harris E, Zellweger C, Emmenegger L, Fischer H, and Mohn J (2015). Real-time analysis of $\delta^{13}\text{C}$ - and δD - CH_4 in ambient air with laser spectroscopy: method development and first intercomparison results. *Atmospheric Measurement Techniques Discussion* 8(8): 8925-8970, doi: 10.5194/amtd-8-8925-2015.

- Faiz M and Hendry P (2006). Significance of microbial activity in Australian coal bed methane reservoirs — a review. *Bulletin of Canadian Petroleum Geology* 54(3): 261-272, doi: 10.2113/gscpgbull.54.3.261.
- Faiz M and Hendry P (2009). *Microbial Activity in Australian CBM Reservoirs Rep.*, CSIRO Petroleum, North Ryde, NSW, Australia.
- Ferretti DF, Miller JB, White JWC, Lassey KR, Lowe DC and Etheridge DM (2007). Stable isotopes provide revised global limits of aerobic methane emissions from plants. *Atmospheric Chemistry and Physics* 7: 237-241.
- Ferretti DF, Miller JB, White JWC, Etheridge DM, Lassey KR, Lowe DC, MacFarling Meure CM, Dreier MF, Trudinger CM, van Ommen TD, Langenfelds RL (2005). Unexpected changes to the global methane budget over the past 2000 years. *Science* 309: 1714-1717.
- Gardner WP, Harrington GA, Solomon DK and Cook PG (2011). Using terrigenic ^4He to identify and quantify regional groundwater discharge to streams. *Water Resources Research* 47, W06523.
- Golding SD, Boreham CJ and Esterle JS (2013). Stable isotope geochemistry of coal bed and shale gas and related production waters: A review. *International Journal of Coal Geology* 120: 24-40.
- Hamawand I, Yusaf T and Hamawand SG (2013). Coal seam gas and associated water: A review paper. *Renewable and Sustainable Energy Reviews* 22: 550-560, doi: <http://dx.doi.org/10.1016/j.rser.2013.02.030>.
- Hamilton SK, Golding SD, Baublys KA and Esterle JS (2014). Stable isotopic and molecular composition of desorbed coal seam gases from the Walloon Subgroup, eastern Surat Basin, Australia. *International Journal of Coal Geology* 122: 21-36, doi: <http://dx.doi.org/10.1016/j.coal.2013.12.003>.
- Han L-F, Plummer LN, Aggarwal P (2012). A graphic method to evaluate predominant geochemical processes occurring in groundwater systems for radiocarbon dating. *Chemical Geology* 318-19: 88-112.
- Heaton THE and Vogel JC (1981). "Excess air" in groundwater. *Journal of Hydrology* 50(0): 201-216, doi:10.1016/0022-1694(81)90070-6.
- Heilweil VM, Solomon DK, Darrah TH, Gilmore TE and Genereux DP (2016). Gas-Tracer Experiment for Evaluating the Fate of Methane in a Coastal Plain Stream: Degassing versus in-Stream Oxidation. *Environmental Science & Technology* 50(19): 10504-10511, doi: 10.1021/acs.est.6b02224.
- Heilweil VM, Stolp BJ, Kimball BA, Susong DD, Marston TM and Gardner PM (2013). A Stream-Based Methane Monitoring Approach for Evaluating Groundwater Impacts Associated with Unconventional Gas Development. *Groundwater* 51(4): 511-524, doi: 10.1111/gwat.12079.

- Herczeg AL, Dighton JC, Easterbrook ML and Salomons E (1994). Radon-222 and Ra-226 measurements in Australian groundwaters using liquid scintillation counting, paper presented at Proceeding of Workshop on Radon and Radon Progeny Measurements in Environmental Samples, Office of the Supervising Scientist, Canberra.
- Hillis RR, Enever JR & Reynolds SD (1999). In situ stress field of eastern Australia. *Australian Journal of Earth Sciences* 46: 813-825.
- Iverach CP, Cendón DI, Hankin SI, Lowry D, Fisher RE, France JL, Nisbet EG, Baker A and Kelly BFJ (2015). Assessing Connectivity Between an Overlying Aquifer and a Coal Seam Gas Resource Using Methane Isotopes, Dissolved Organic Carbon and Tritium. *Scientific Reports* 5: 15996, doi: 10.1038/srep15996
<http://www.nature.com/articles/srep15996#supplementary-information>.
- Jackson RE, Gorody AW, Mayer B, Roy JW, Ryan MC and Van Stempvoort DR (2013). Groundwater Protection and Unconventional Gas Extraction: The Critical Need for Field-Based Hydrogeological Research. *Groundwater* 51(4): 488-510, doi: 10.1111/gwat.12074.
- Jähne B, Heinz G, Dietrich W (1987). Measurement of the diffusion coefficients of sparingly soluble gases in water. *Journal of Geophysical Research* 92: 10767-10776.
- Jasonsmith JF, Macdonald BCT and White I (2017). Earth-tide-induced fluctuations in the salinity of an inland river, New South Wales, Australia: a short-term study. *Environmental Monitoring and Assessment* 189: 188, doi:1007/s10661-017-5880-z.
- Jones JB and Mullholland PJ (2000) *Streams and Ground Waters*, Academic Press, New York.
- Kaplan IR, Galperin Y, Lu S-T and Lee R-P (1997). Forensic Environmental Geochemistry: differentiation of fuel-types, their sources and release time. *Organic Geochemistry* 27(5/6): 289-317.
- Kinnon ECP, et al. (2010). Stable isotope and water quality analysis of coal bed methane production waters and gases from the Bowen Basin, Australia. *International Journal of Coal Geology* 82(3–4): 219-231.
- Kirk MF, Wilson BH, Marquart KA, Zeglin LH, Vinson DS and Flynn TM (2015). Solute Concentrations Influence Microbial Methanogenesis in Coal-bearing Strata of the Cherokee Basin, USA. *Frontiers in Microbiology* 6: 1287, doi: 10.3389/fmicb.2015.01287.
- Lamontagne S, Herczeg AL, Dighton JC, Jiwan JS and Pritchard JL (2005a) Patterns in groundwater nitrogen concentration in the floodplain of a subtropical stream (Wollombi Brook, New South Wales). *Biogeochemistry* (72): 169-190.
- Lamontagne S, Leaney FW and Herczeg AL (2005b) Groundwater – surface water interactions in a large semi-arid floodplain: implications for salinity management. *Hydrological processes* (19): 3063-3080.

- Lamontagne S, Taylor AR, Batlle-Aguilar J, Suckow A, Cook PG, Smith SD, Morgenstern U and Stewart MK (2015). River infiltration to a subtropical alluvial aquifer inferred using multiple environmental tracers. *Water Resources Research*, doi: 10.1002/2014WR015663.
- Maher D. T., Santos I. R. and Tait D. R. (2014). Mapping methane and carbon dioxide concentration and d13C values in the atmosphere of two Australian coal seam gas fields *Water, Air and Soil Pollution* 225(2216): 1-9.
- Mazurek M, Alt-Epping P, Bath A, Gimmi T, Waber HN, Buschaert S, De Canniere P, De Craen M, Gautschi, A, Savoye S, Vinsot A, Wemere I, Wouters L (2011). Natural tracer profiles across argillaceous formations. *Applied Geochemistry* 173: 219-240.
- Parsons Brinckerhoff (2012). Phase 2 Groundwater Investigations- Stage 1 Gas field Development Area Gloucester Gas Project. January 2012 Rep., AGL Upstream Investments Pty Ltd.
- Parsons Brinckerhoff (2013). Hydrogeological Investigation of a Strike-slip Fault in the Northern Gloucester Basin. 9 August 2013 Rep., AGL Upstream Investments Pty Ltd.
- Parsons Brinckerhoff (2015). Updated Conceptual Hydrogeological Model of the Gloucester Basin Rep. Rep. 2200556A-WAT-REP-001 RevE, Parsons Brinckerhoff, Sydney, Australia.
- Pennsylvania State University (2012). Methane Gas and Its Removal from Wells in Pennsylvania. *Water Facts #24*. Penn State Extension.
- Plummer LN and Glynn PD (2013). Radiocarbon dating in groundwater systems: Chapter 4. *Isotope methods for dating old groundwater*. IAEA, Vienna, Austria.
- Pollock DW (1994). User's guide for MODPATH/MODPATH-PLOT, Version 3: A particle post-processing package for MODFLOW, the U. S. Geological Survey finite-difference ground-water flow model. U. S. Geological Survey.
- Poole JC, McNeill GW, Langman SR and Dennis F (1997). Analysis of noble gases in water using a quadrupole mass spectrometer in static mode. *Applied Geochemistry* 12(6): 707-714, doi:10.1016/S0883-2927(97)00043-7.
- Ransley T, Somerville P, Piang Tan K, Feitz A, Cook S, Yates G, Schoning G, Bell J, Caruana L, Sundaram B and Wallace L (2015). Groundwater Hydrochemical Characterisation of the Surat Region and Laura Basin – Queensland. Final technical report for the National Collaboration Framework Hydrochemical Characterisation Project: 218.
- Roberts J, Engel B and Chapman J (1991). *Geology of the Camberwell, Dungog and Bulahdelah 1:100,000 Geological Sheets 9133, 9233, 9333*, New South Wales Geological Survey, Sydney.
- Rowe D and Muehlenbachs A (1999). Low-temperature thermal generation of hydrocarbon gases in shallow shales. *Nature* 398(6722): 61-63.
- Smith SD, Mathouchanh E and Mallants D (2018). Characterisation of fluid flow in aquitards using helium concentrations in quartz, Gunnedah Basin, NSW. CSIRO, Australia.

- Stolper DA, Sessions AL, Ferreira AA, Santos Neto EV, Schimmelmann A, Shusta SS, Valentine DL and Eiler JM (2014a). Combined ^{13}C -D and D-D clumping in methane: Methods and preliminary results. *Geochimica et Cosmochimica Acta* 126: 169-191, doi:10.1016/j.gca.2013.10.045.
- Stolper DA et al. (2014b). Formation temperatures of thermogenic and biogenic methane. *Science* 344(6191): 1500-1503, doi: 10.1126/science.1254509.
- Stolper DA, Martini AM, Clog M, Douglas PM, Shusta SS, Valentine DL, Sessions AL and Eiler JM (2015). Distinguishing and understanding thermogenic and biogenic sources of methane using multiply substituted isotopologues. *Geochimica et Cosmochimica Acta* 161: 219-247, doi: 10.1016/j.gca.2015.04.015.
- Stuiver M and Polach HA (1977). Discussion: Reporting of ^{14}C data. *Radiocarbon* 19(3): 355-363.
- Suckow A (2014). The age of groundwater – Definitions, models and why we do not need this term. *Applied Geochemistry* 50: 222-230.
- Suckow A, Taylor A, Davies P, and Leaney F (2015). Geochemical baseline monitoring. Final Report. CSIRO, Australia.
- Van Voast WA (2003). Geochemical signature of formation waters associated with coalbed methane. *AAPG Bulletin* 87(4): 667-676.
- Vengosh A, Jackson RB, Warner N, Darrah TH and Kondash A (2014). A Critical Review of the Risks to Water Resources from Unconventional Shale Gas Development and Hydraulic Fracturing in the United States. *Environmental Science & Technology* 48(15): 8334-8348, doi: 10.1021/es405118y.
- Vogel JC (1967). Investigation of groundwater flow with radiocarbon. In 'Isotopes in Hydrology. Vienna'. pp. 255-368. Vienna.
- Walter KM, Chanton JP, Chapin FS, Schuur EA and Zimov SA (2008). Methane production and bubble emissions from arctic lakes: Isotopic implications for source pathways and ages, *Journal of Geophysical Research: Biogeosciences* 113(G3), n/a-n/a, doi: 10.1029/2007JG000569.
- Wang DT, Gruen DS, Lollar BS, Hinrichs KU, Stewart LC, Holden JF, Hristov AN, Pohlman JW, Morrill PL, Könneke M, Delwiche KB, Reeves EP, Sutcliffe CN, Ritter DJ, Seewald JS, McIntosh JC, Hemond HF, Kubo MD, Cardace D, Hoehler TM, Ono S (2015). Nonequilibrium clumped isotope signals in microbial methane. *Science* 348(6233): 428-431, doi: 10.1126/science.aaa4326.
- Weiss RF (1970). Helium Isotope Effect in Solution in Water and Seawater. *Science* 168(3928): 247-248, doi: 10.1126/science.168.3928.247.
- Whiticar MJ (1999). Carbon and hydrogen isotope systematics of bacterial formation and oxidation of methane. *Chemical Geology* 161(1-3): 291-314, doi:10.1016/S0009-2541(99)00092-3.

Whiticar MJ, Faber E and Schoell M (1986). Biogenic methane formation in marine and freshwater environments: CO₂ reduction vs. acetate fermentation—Isotope evidence. *Geochimica et Cosmochimica Acta*, 50(5), 693-709, doi:10.1016/0016-7037(86)90346-7

Woessner WW (2000). Stream and fluvial plain ground water interactions: rescaling hydrogeological thought. *Ground Water* 38: 423-429.

6 Structural geology analysis¹¹

6.1 Introduction

The Gloucester Basin is a highly deformed small Permian basin located within the Southern New England Fold Belt, containing coal and coal seam gas (CSG) prospects (Ward et al., 2001; Hodgkinson et al., 2014). The basin probably formed in response to the transtensional regime causing extension to the Sydney-Bowen-Gunnedah Basin systems. The Gloucester Basin currently interpreted geological architecture suggests that the basin experienced a complex structural history and shear movement which is more evident from the available 3D seismic data (to be discussed in Section 6.2.2).

The Gloucester Basin (Figure 6-1) is broadly an east-west synclinal feature (Figure 6-2), heavily faulted, particularly in the southeast part of the basin, by a complex series of normal and reverse faults (Ward et al., 2001). Due to the structural complexity, the sedimentary sequences are mostly steeply dipping causing difficulty in horizon correlation across the basin. Grieves and Saunders (2003) and SRK Consulting (2005, 2010) proposed two major tectonic episodes for the development of Permian sequence within the Gloucester Basin:

- Early to Late Permian extension resulted in normal and strike-slip reactivation of older pre-Permian faults (for an overview of fault types, see Section 9.2.4, particularly around the margins of the basin and the development of syn-depositional faults (northern and eastern edge of the basin). This coincides with the phase of extension and sedimentation defined by Cawood et al. (2011) in the Sydney-Gunnedah-Bowen Basin and coeval (having the same age or date of origin) with roll back of the Pacific Plate. Fault activity has been interpreted during the deposition of the Early Permian Alum Mountain Volcanics (Roberts et al., 1991, p. 167). Faulting also controlled (to varying degrees) the deposition of most Permian coal-bearing strata in the basin (Roberts et al., 1991, p. 284; Harrington et al., 1989, p. 64); and
- Late Permian compression (north-east shortening) and tilting of the basin during the early stages of the Hunter-Bowen Orogeny, resulted in reactivation and inversion of many faults, and new thrust faulting and erosion.

¹¹ Contributing authors: S Mukherjee, J Copley

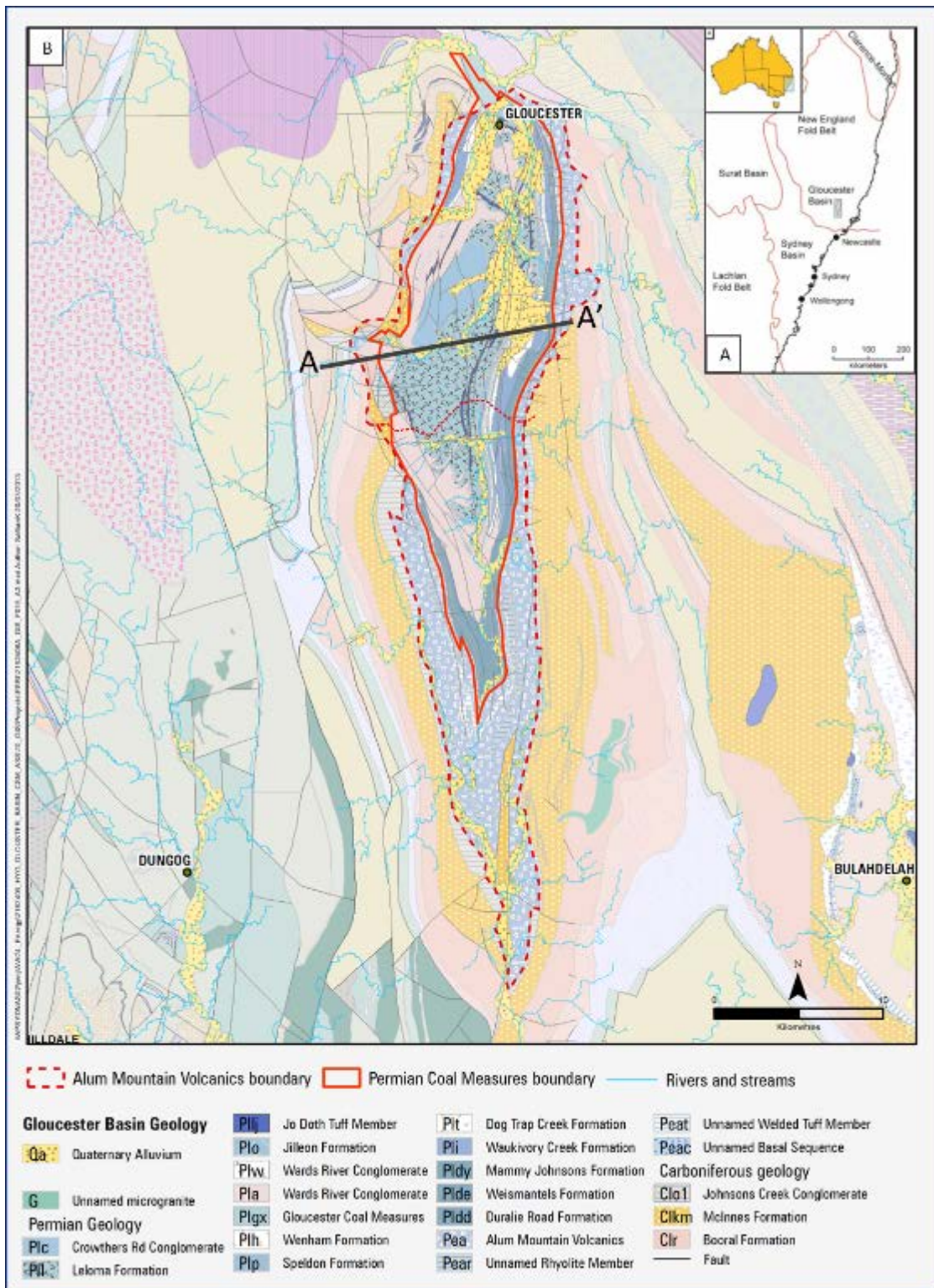


Figure 6-1 (A) Location map of Gloucester Basin (Source: McVicar et al., 2014) (B) Regional geological map of the Gloucester Basin (Source: Parsons Brinckerhoff, 2013).

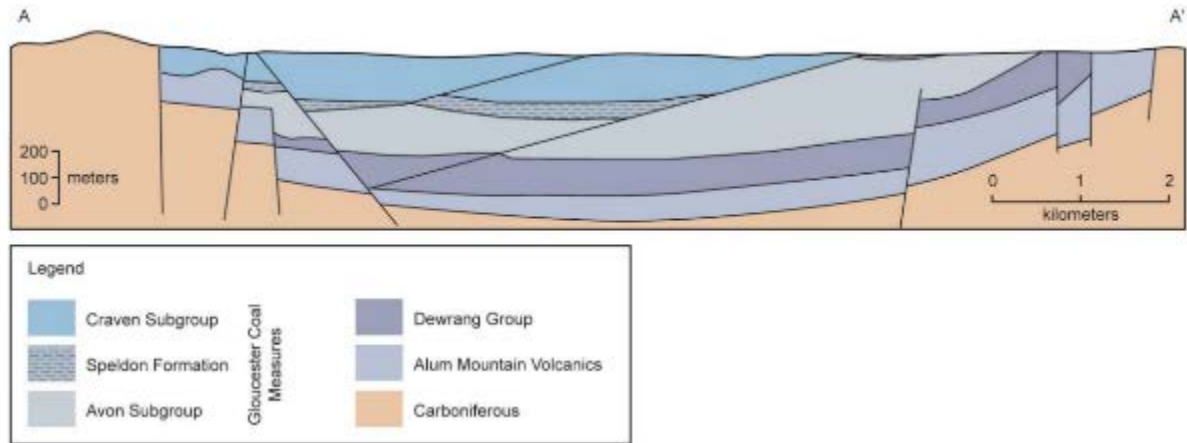


Figure 6-2 Simplified regional cross-section for the Gloucester Basin (Source: Roberts et al., 1991). This figure is not covered by a Creative Commons Attribution licence. It has been reproduced with the permission of NSW Trade & Investment.

The current project had access to a number of different fault interpretations for the basin as a starting point. These were mainly shapefiles and maps with surface trace locations rather than fault planes in three dimension. The available fault interpretations included that from the CSIRO as part of the Bioregional Assessments Programme (McVicar et al., 2014), various reports commissioned by AGL culminating in the Hydrogeological Investigation of a strike slip fault in the northern Gloucester Basin by Parsons Brinckerhoff (2013) and other faults locations provided by AGL directly. To augment this pre-existing data, the project embarked first on an evaluation of the available image logs to assess the in-situ stress and the characteristics of fractures. We then used this and the previously described hydrogeological characterisation to zoom into specific areas with evidence of potentially enhanced vertical hydraulic communication to examine the detailed fault zone architecture from the 3D seismic volume supplied by AGL. Note that it was outside the scope of the project to re-interpret the entire 3D seismic volume.

6.2 Methods

6.2.1 Borehole image log analysis

A total of 11 wells with image log data and interpretations were available for the study (Figure 6-3). Data density is relatively higher near the Waukivory pilot area but sparse outside this area. AGL provided image log data files (*.DLIS and *.WCL format) for 7 wells and interpretation data for all 11 wells. These data were re-examined with the objective to assess the contribution of faults, fractures and present-day maximum horizontal principal stress

orientations (S_{Hmax})¹² to fluid movement from the CSG reservoirs that might impact adjacent aquifers. Further interpretation of the data relates to the distortion of regional stress orientation by local structural deformation, and stratigraphic variability in present-day in-situ stress, utilizing the lithologic correlations developed by AGL.

Resistivity and acoustic borehole image logs are the main well log data used for this study. Most of the borehole image data was of good quality but there were also a few poor-quality image log data present, which were used with caution.

6.2.1.1 Methodology and Classification

Borehole image logs were used to interpret the stress orientations (through borehole breakout) relative to faults and fractures within the Gloucester Basin. The interpreted *in-situ* stress and fracture orientations were overlain on the seismic sections to determine any spatial variation with depth and/or kinematic style of the larger structural features. The *in-situ* horizontal stress (S_{Hmax}) and fracture orientations were also cross-plotted with measured permeability data to observe any causal relationships that assist in predicting potential permeability pathways for fluid movement.

The image log data were loaded into the Geolog (v.7.4) software¹³. The workflow presented in Figure 6-4 for quality assessment and interpretation was followed. Examples of observed features include breakouts, drilling induced fractures, micro-faults and conductive (open to flow) and resistive (closed to flow) fractures (Figure 6-5). Resistivity contrast (dark and light coloured bands) shows the bed boundary and / or lithological variation in the resistivity image log (Figure 6-6). Due to limitation of image logs' depth of investigation, the interpretation of conductive, resistive and mixed fractures is limited within the borehole. Outside the borehole, S_{Hmax} orientation normally controls the opening and closing of fractures.

The identification of faults and fractures follows the classification rules presented in Figure 6-5. This includes the symbols to be employed on maps and images. Fracture in general refers to rock discontinuities of all types: joints, faults, veins, shear zones and foliation planes can be classified as fracture.

¹² This is equivalent to the notation σ_{Hmax} used in Section 9

¹³ <http://www.pdgm.com/promotional-sites/geolog-7/>

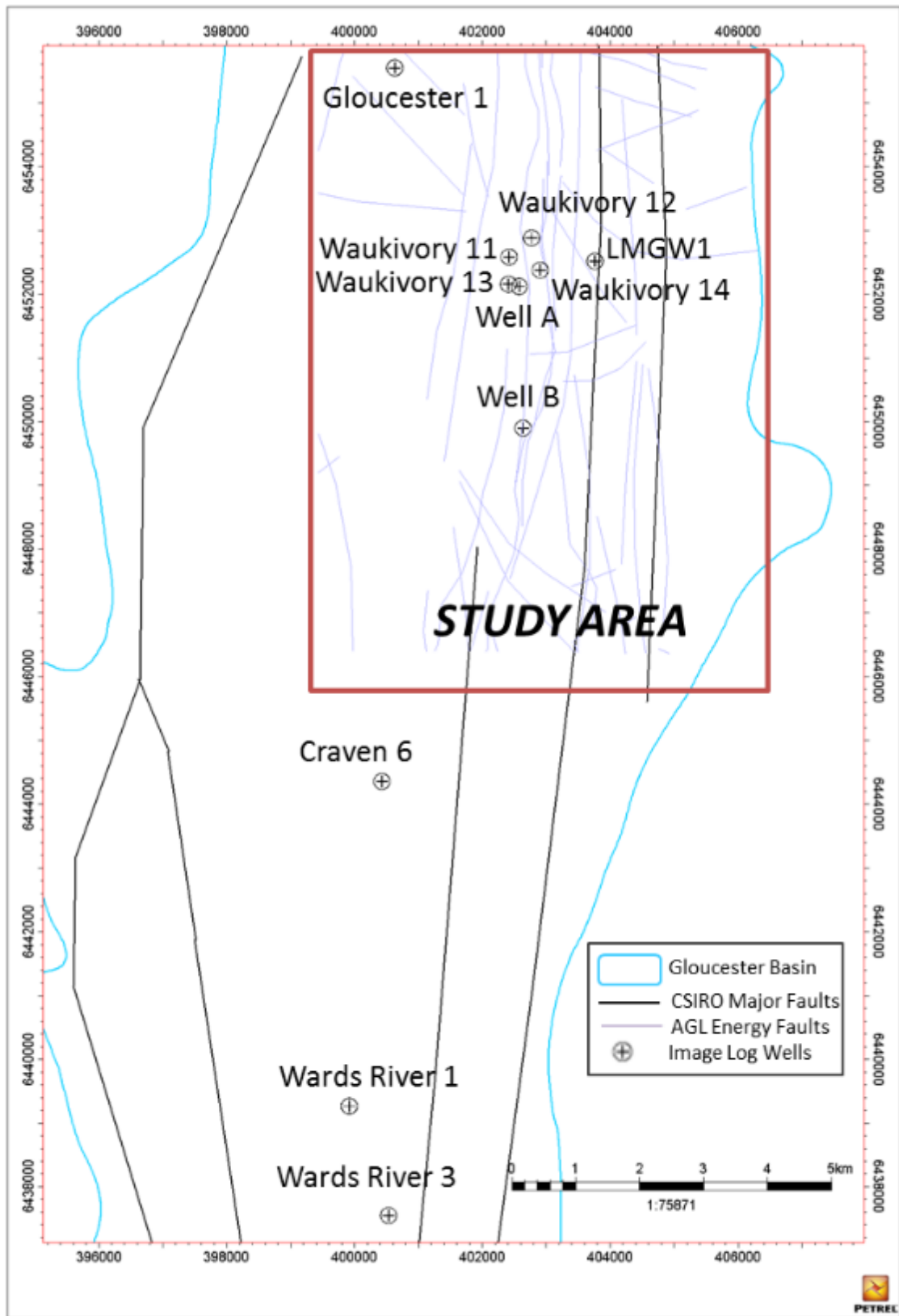


Figure 6-3 Map showing location of wells with image log data.

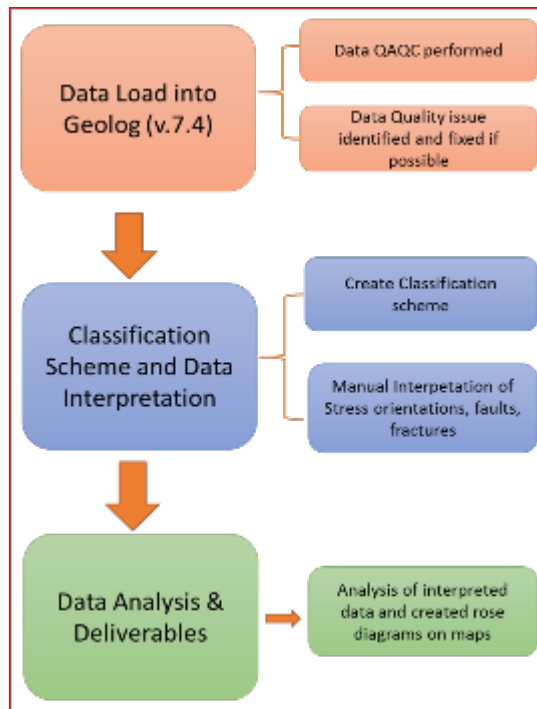


Figure 6-4 Image log analysis methodology flow chart adopted in this study.

Feature Classification	Observation	Interpretation	Symbols	Sketch
Conductive Fracture	Lower resistivity fracture that cut strata covering entire / partial borehole circumference	Fracture		
Resistive Fracture	Higher resistivity fracture that cut strata covering entire / partial borehole circumference	Fracture		
Mixed Fracture	Fracture that cut strata covering entire / partial borehole circumference showing lower resistivity in some part of the fracture length	Fracture		
Fault	Fracture that cut strata with obvious displacement covering entire / partial borehole circumference	Fault		
Breakout	Wide blobby zones of low resistivity, low acoustic amplitude and long travel time that occur on opposite sides of the borehole wall	Borehole Breakout		
DITF	Steeply dipping, planar, conductive fracture that is borehole parallel, perpendicular to borehole breakout orientation	Drilling Induced Tensile Fracture		

Figure 6-5 Image log interpretation classification scheme.

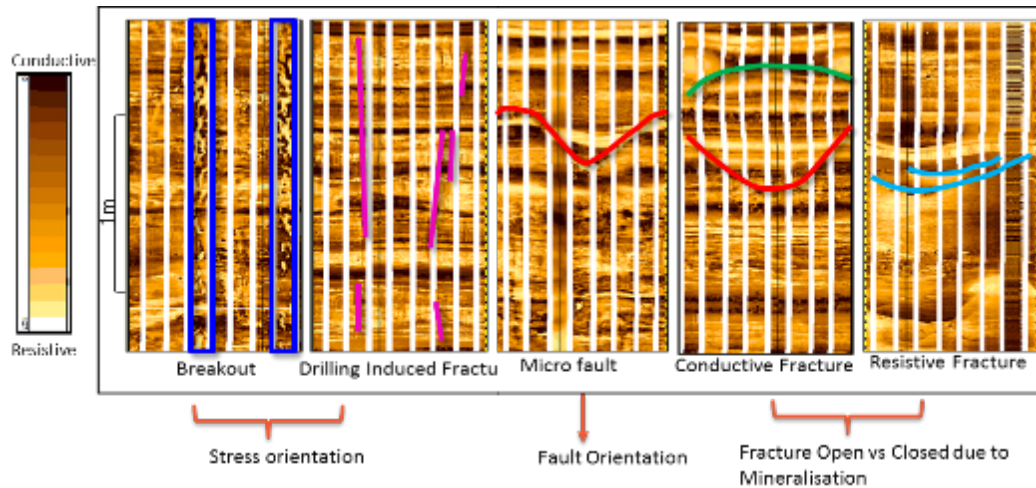


Figure 6-6 Example of structural features observed in borehole image and how they were used in the interpretation.

Fracture density is a measure of the fracture abundance and can be determined by three methods (Figure 6-7):

1. **P₁₀** – Number of fractures per unit length of scanline (L-1). The borehole axis can be the scanline for the P10 measurement in the borehole. The fracture density measurement is direction dependent;
2. **P₂₀** – Number of fracture per area of exposure (L-2). The fracture density measurement is direction dependent; and
3. **P₃₀** – Number of fractures per unit volume of rock mass (L-3).

Fracture intensity is another fracture abundance measure. Volumetric intensity (P32) is a scale independent fracture abundant measure defined as area of fracture per volume of rock mass (L⁻¹). This parameter is calculated to identify high fracture zones in each well used for the Gloucester Basin image log study.

6.2.1.2 In-situ stress analysis

AGL provided present-day *in-situ* stress interpretation data from a total of 11 wells for this study. Out of these 11 wells, 7 well image log files were available for the interpreted data quality assessment and checking. All the available data was put through the image log analysis methodology (Figure 6-4) and any data quality issues were tracked and fixed. The *in-situ* stress data were manually reinterpreted for these 7 wells and an interpretation confidence assigned for each interpretation. Any interpreted data below the 50% confidence level was excluded from the final maps and interpretations. Interpreted data received for the other 4 wells was incorporated in the final maps “as received”.

The *in-situ* stress map based on the available data shows variation of stress spatially (Figure 6-8) as well as vertically within individual wells (Figure 6-14). The large variations in *in-situ* stress orientation indicates a strong influence of local structures. Rajabi et al. (2016) also

observed similar *in-situ* stress variation within the Gloucester Basin and an overall higher standard deviation than the regional average S_{Hmax} for New South Wales (as did Enever and Lee, 2000).

The *in-situ* stress distributions within the Waukivory pilot area are variable over short distances (Figure 6-8). Waukivory 12 and 14 are located on a different fault block with respect to the other Waukivory wells. The S_{Hmax} orientations in Waukivory 12 and 14 is NNW - SSE to WNW-ESE, whereas in the other Waukivory wells it is ENE-WSW. This change in the *in-situ* stress orientation is attributed to the presence of faults or fault zones.

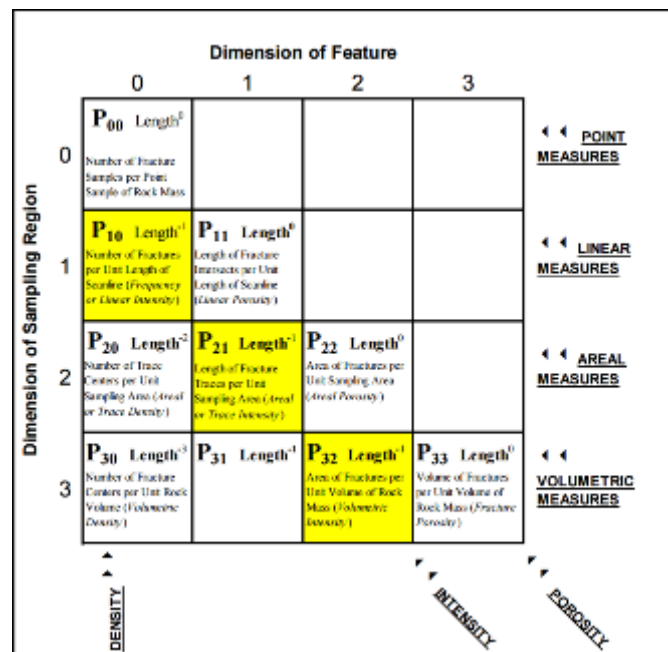


Figure 6-7 Fracture abundance measures (source: Dershowitz and Herda, 1992; Mauldon and Dershowitz, 2000).

6.2.1.3 Borehole fracture characterisation

Manual fracture interpretation was based on the classification scheme mentioned in Figure 6-5. A total of 7 well image log data were interpreted and any interpreted data below 50% confidence level was excluded from the final maps and interpretations. AGL provided interpreted data for one well (Craven 6), which is also included in the final maps and interpretation.

The wells in the Waukivory pilot area show higher fracture density and multiple fracture orientations proximal to the fault whereas further south in Craven 6, strong unimodal and in Wards River 1 bimodal fracture orientations were observed (Figure 6-9). However, the data in the central part of the study area is sparse and additional well data is required to further investigate fracture characteristics over that part of the Gloucester Basin. The dominant fracture orientation in the Southern wells is mostly orthogonal to the present-day S_{Hmax} orientation whereas fracture orientation in most of the wells within the Waukivory pilot area

are parallel or sub-parallel to S_{Hmax} (Figure 6-10). The higher fracture density and multiple fracture orientations within wells Waukivory 12 and 14 develops a dilatant tendency creating pathways for fluid movement in the shallower aquifers.

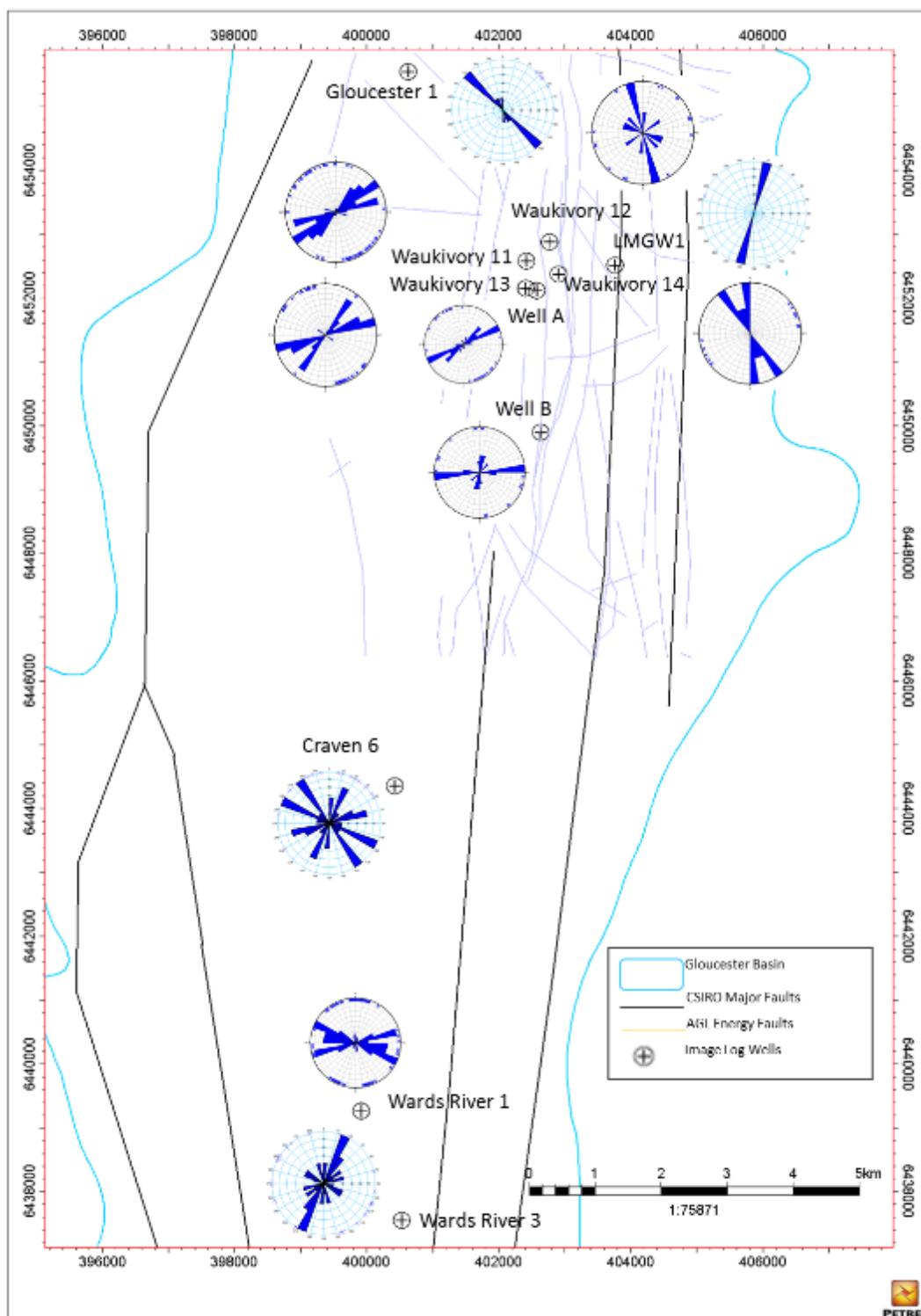


Figure 6-8 Map showing in-situ horizontal stress (S_{Hmax}) distribution within the Gloucester Basin.

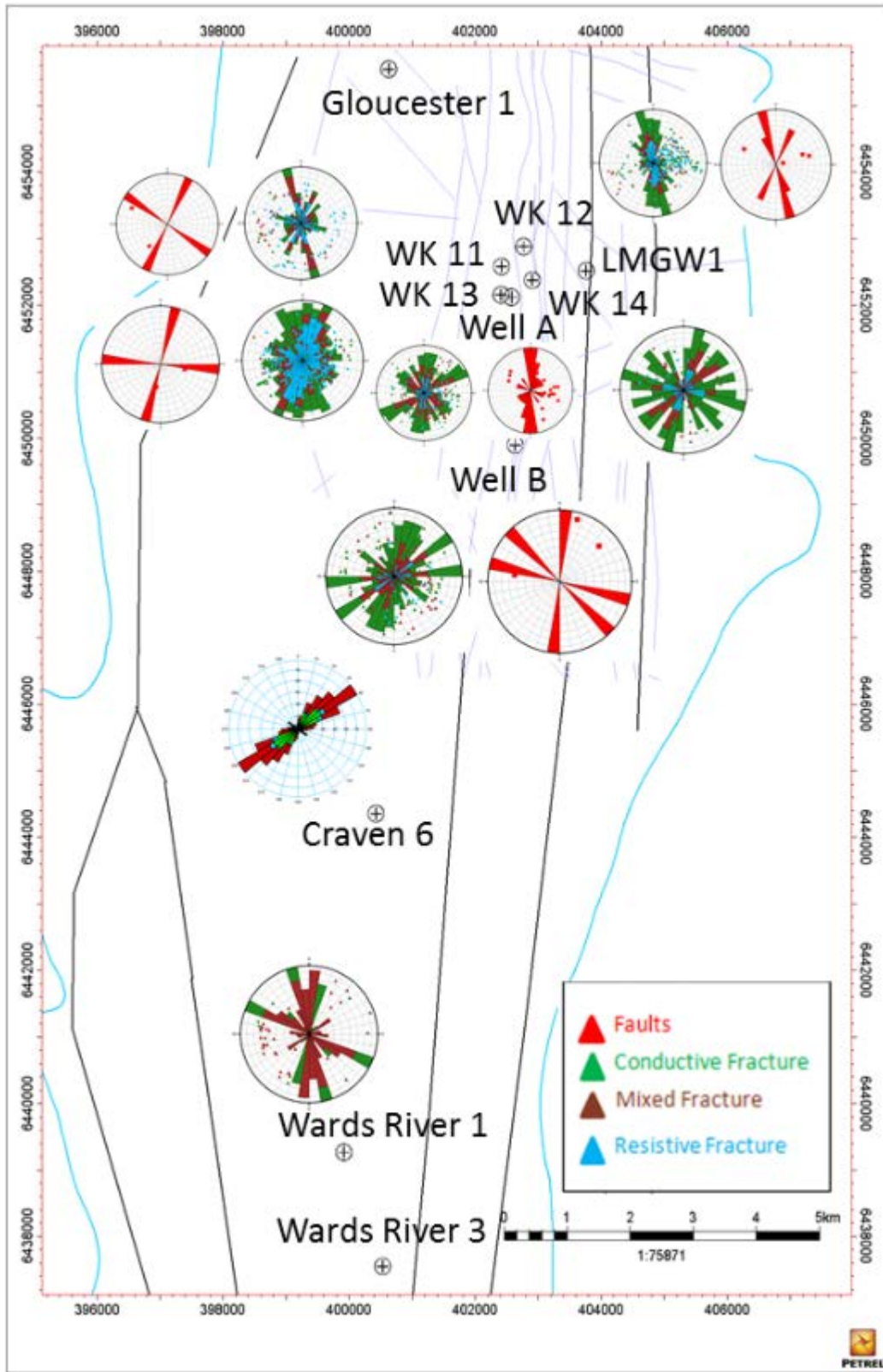


Figure 6-9 Summary map showing faults and fracture distribution within Gloucester Basin.

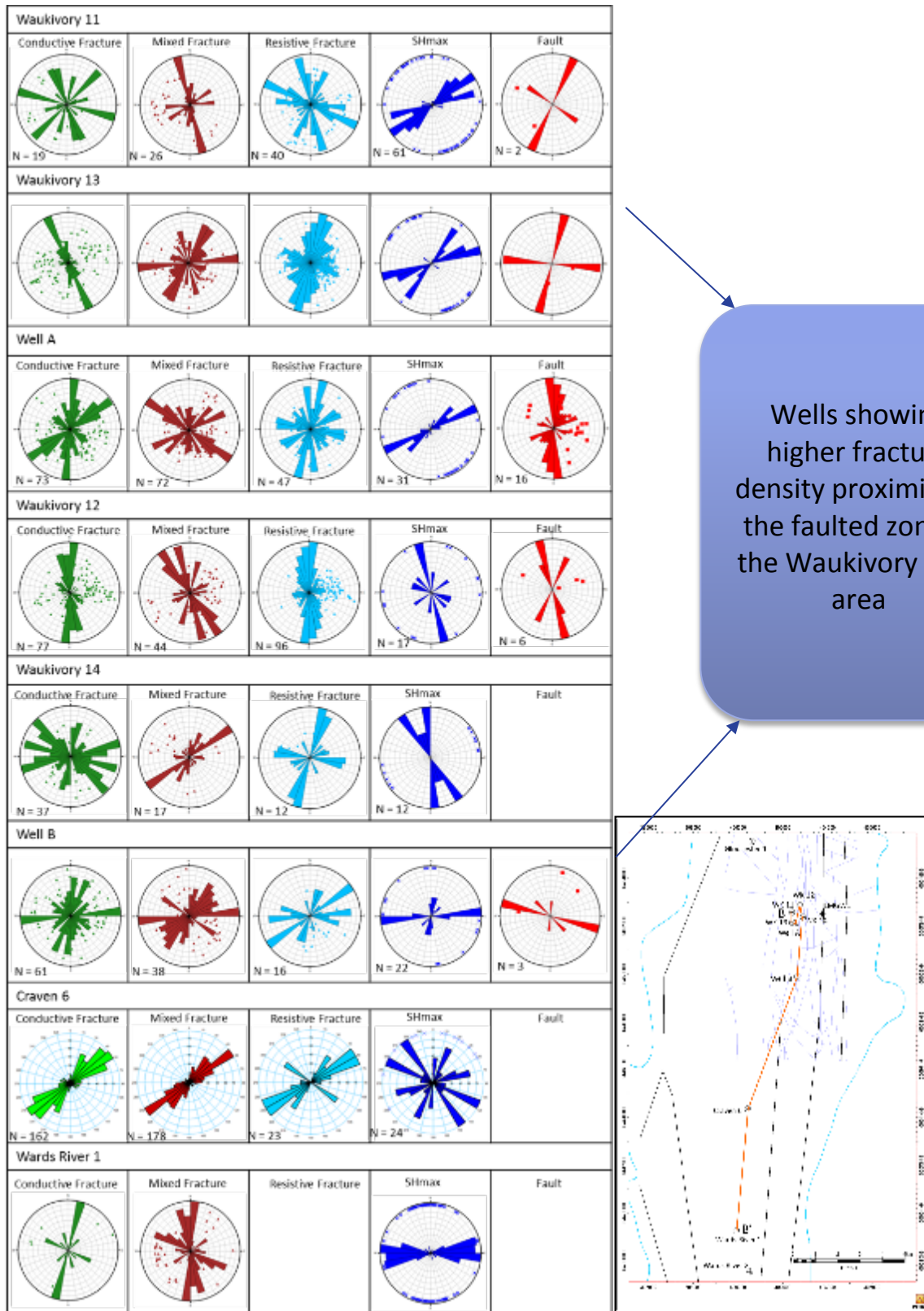


Figure 6-10 Individual well details on in-situ stress, faults and fracture distribution along B – B’ cross section.

In the Waukivory pilot area, significant variation of *in-situ* stress and fracture characteristics is observed over a short distance. Waukivory 11 and Waukivory 12 are located on two different fault blocks each with a distinctive S_{Hmax} orientation. Also, Waukivory 12 is geographically closer to an assumed fault zone from various previous reports than Waukivory 11. Proximity to the structure may be related to higher fracture density (P32) along with multiple fracture orientations and rotation of S_{Hmax} in Waukivory 12. The fracture orientations are parallel or subparallel to the S_{Hmax} orientation which may contribute to the high dilatation tendency of fractures within Waukivory 12. In comparison, Waukivory 11 shows significantly lower fracture density (Figure 6-11 and Figure 6-12). The average fracture dip in Waukivory 12 is also relatively low angle ($20^{\circ} - 50^{\circ}$) in comparison to Waukivory 11 ($40^{\circ} - 70^{\circ}$).

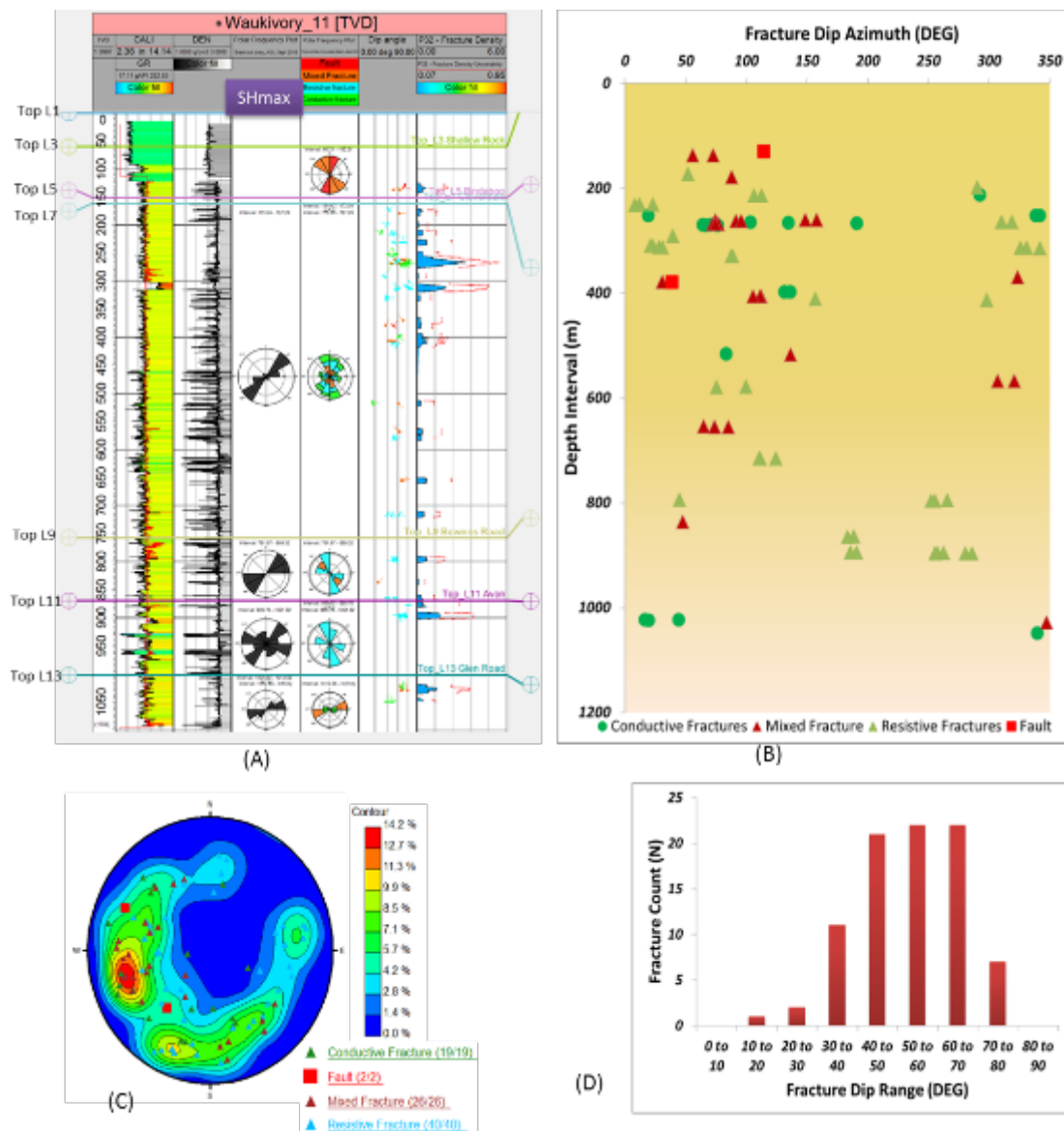
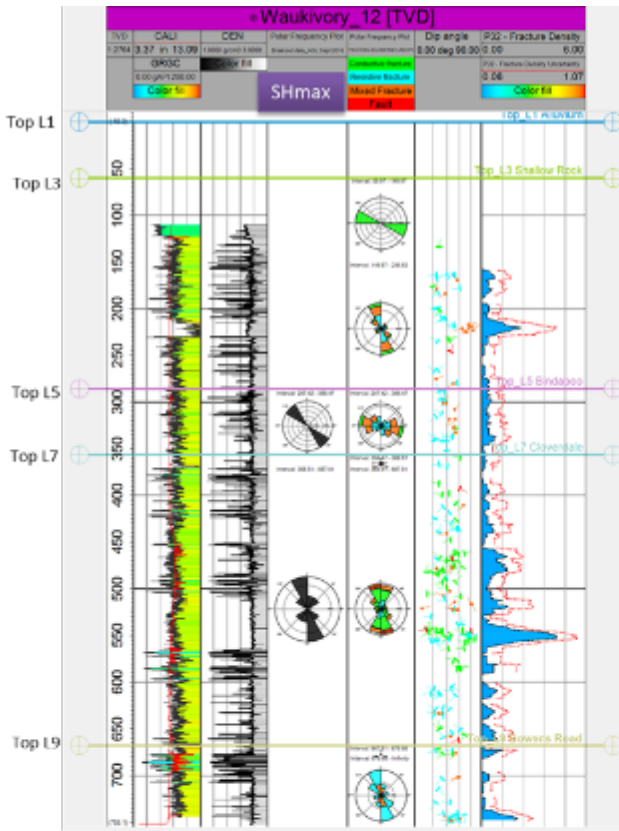
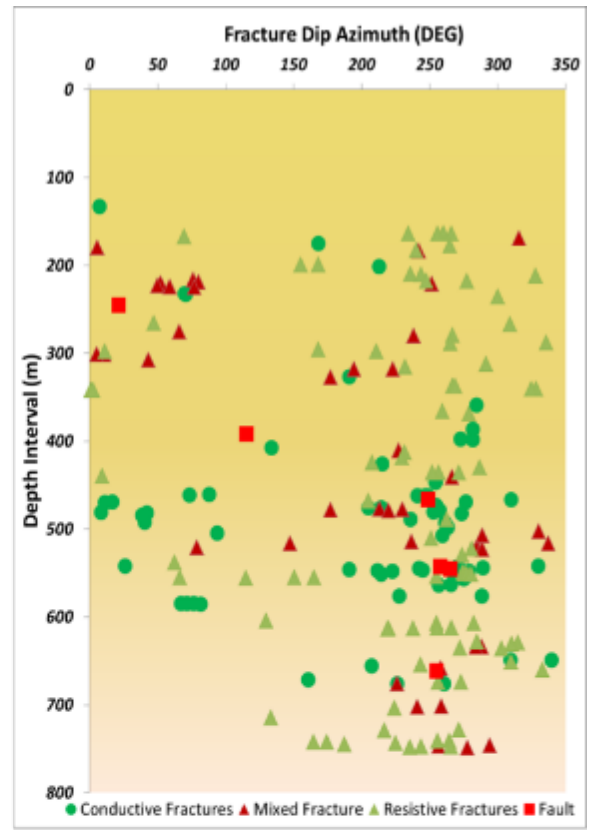


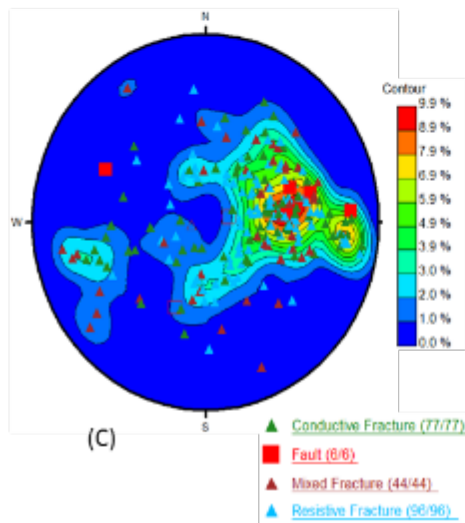
Figure 6-11 (A) Waukivory 11 S_{Hmax} and fracture distribution along depth; (B) Waukivory 11 fracture dip azimuth distribution along depth; (C) Stereonet contour of faults and fractures dip azimuth in Waukivory 11 well; (D) Waukivory 11 fracture dip range histogram.



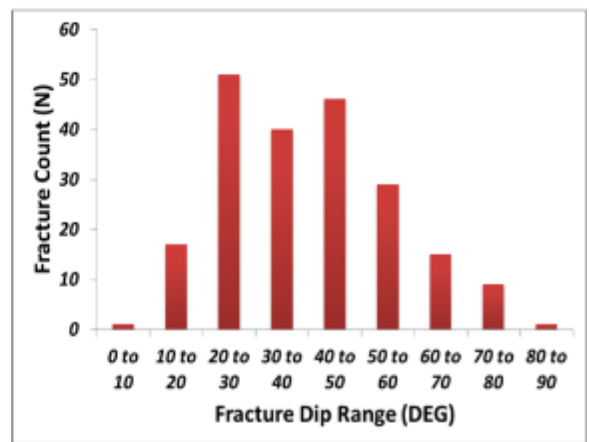
(A)



(B)



(C)



(D)

Figure 6-12 (A) Waukivory 12 S_{Hmax} and fracture distribution along depth; (B) Waukivory 12 fracture dip azimuth distribution along depth; (C) Stereonet contour of faults and fractures dip azimuth in Waukivory 12 well; (D) Waukivory 12 fracture dip range histogram.

The seismic section through Waukivory 12 (Figure 6-13) shows a complicated fault zone architecture and the presence of fault segments along the well path or proximity to the well at the same location that the image log shows a high fracture density.

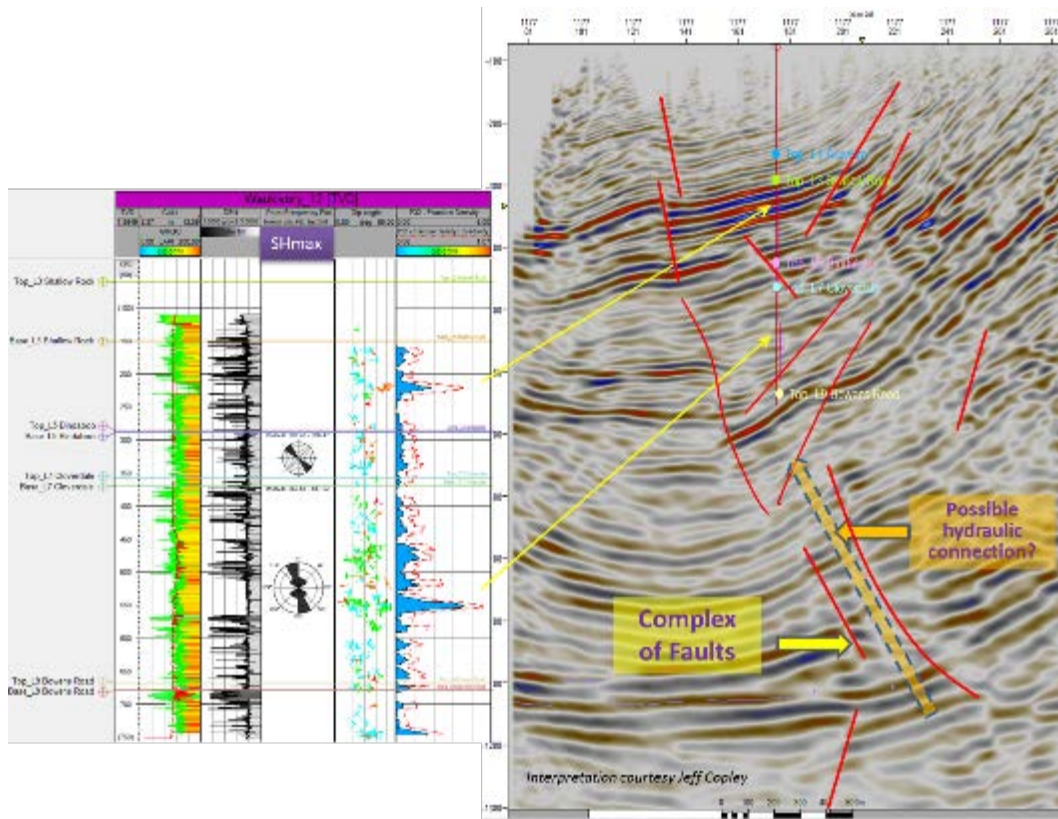


Figure 6-13 Seismic and well section showing structural complexity, in-situ stress and fracture character variation along depth within Waukivory 12.

6.2.1.4 In-situ stress and fracture relationship with permeability

The Gloucester Basin CSG reservoirs mostly have low permeability ($\sim 1\text{mD}$) (see Figure 2.16 in Section 2.3 and Parsons Brinckerhoff, 2015). Therefore, fault seal mechanisms are less relevant to influencing fluid flow from the deeper reservoirs (i.e. the matrix permeability is already low). However, fault damage zones, relay structures and fractures that are permeability enhancement mechanisms are more likely to have an observable influence on fluid flow. Therefore, characterising *in-situ* stress along with small scale fractures associated with seismically observable faults or areas of distributed strain in relays may be important. A cross-section in the Waukivory pilot area and further South up to Well B was made to understand the variation of *in-situ* stress and fracture orientations within well and its relationship to the interpreted permeability data from well test (Figure 6-14). Further, the relative angle between *in-situ* stress and fractures are plotted against the depth and interpreted permeability from the well test data (Figure 6-15). Albeit based on limited data points, the Waukivory pilot area displays slightly increased permeability with depth when fracture orientations are sub-parallel to the *in-situ* stress orientations. At a similar depth, interpreted permeability is an order of magnitude greater when fracture orientation is parallel or sub-parallel to $S_{H\text{max}}$ orientation.

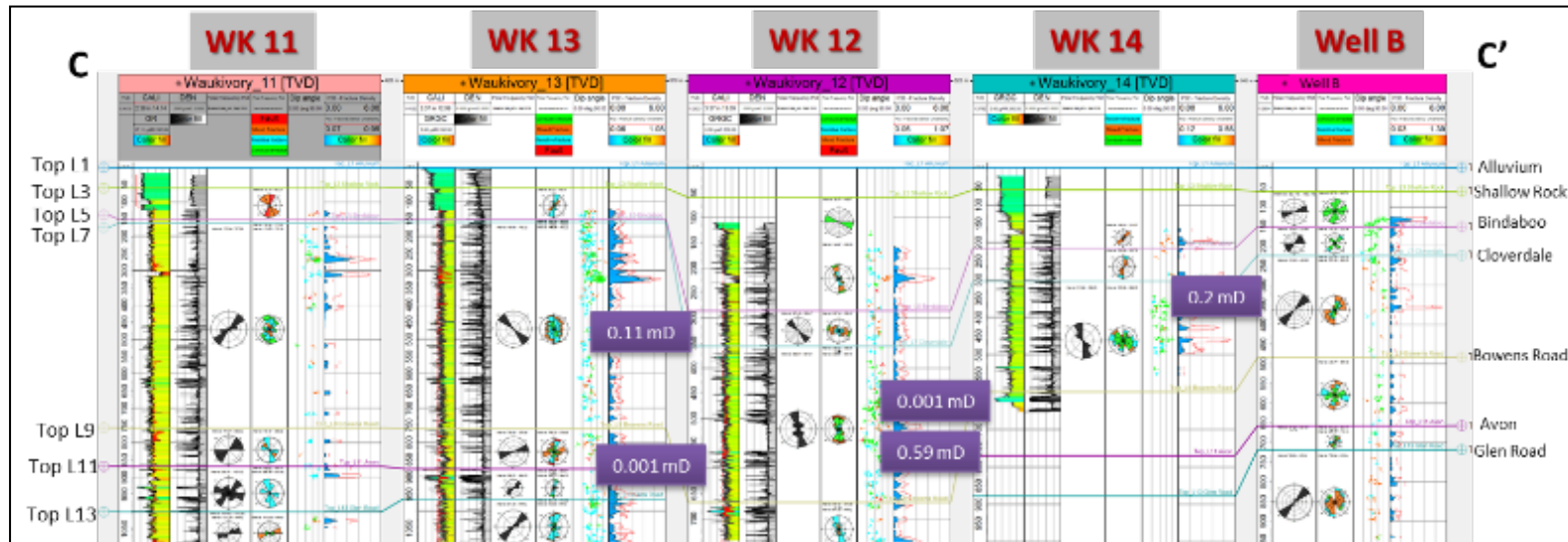


Figure 6-14 Cross-section along Waukivory pilot area and further south showing in-situ stress and fracture character variation spatially and along depth with the measured permeability data using well tests.

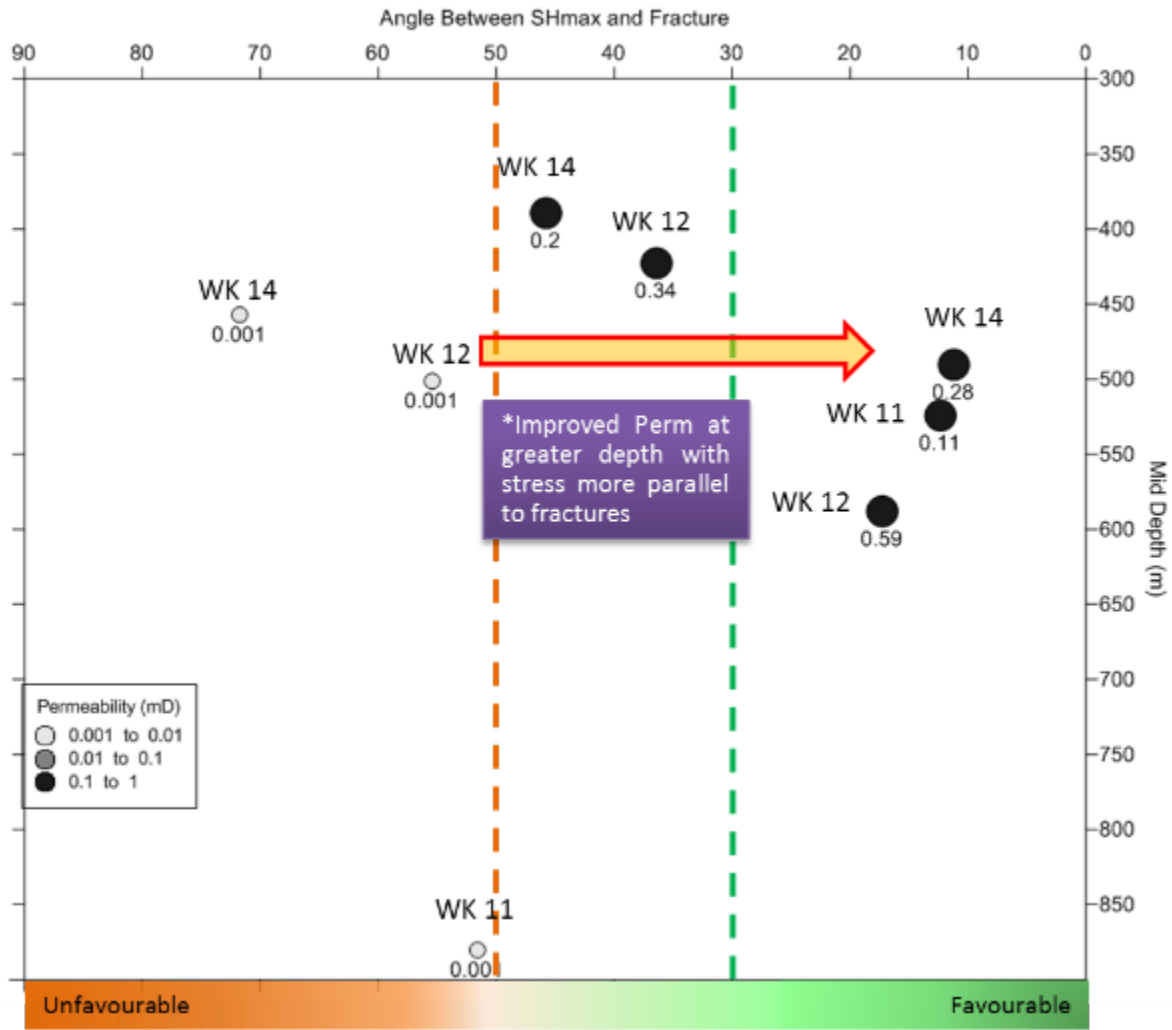


Figure 6-15 Interpreted permeability relationship with angle between S_{Hmax} and fracture orientation.

From the 3D seismic data, it is observed that Waukivory 14 measured permeability interval falls in a fault damage zone. Also, two sets of fracture orientation (NE-SW and NNE-SSW) are observed for this interval. The NNE-SSW fracture set is dominant across this interval and its relationship with the S_{Hmax} results in relatively higher permeability within this interval.

6.2.2 Three-dimensional deep seismic analysis

While the scope of the project was not to re-interpret the entire available 3D seismic volume, this data was used to examine in more detail areas of specific interest highlighted by the previous hydrodynamic and hydrochemistry analysis. The aim was to understand the structural architecture in areas that showed indications of vertical fluid movement. In the public domain, older 2D seismic data was available for the Gloucester Basin. As part of the CSG appraisal, AGL acquired modern processed 3D seismic data and this still confidential data was made available to the project. The 3D volume (Morgani 3D) was loaded into the

Petrel E&P Software Platform¹⁴ (mig_ps_filt_ST). The 3D survey covers a small portion of the northern part of the Gloucester Basin (Figure 6-16). The data is of good quality, however the complex faulting and lateral variability of the formations make mapping in some cases uncertain. A full interpretation of the entire seismic volume was beyond the scope of this project, however, key locations identified by the “Hydrochemical Analysis” field program (Section 4) and subsurface “Hydraulic Analysis” (Section 5) indicated that certain areas had the potential for enhanced vertical hydraulic communication. These key locations were examined in detail. For this purpose the 3D seismic data are very good within the specific areas of interest regarding the delineation of key fault morphologies relevant to the hydrologic properties.

A coherency volume (“Variance”) was created with a 15 sample smoothing filter. This provided a reasonably high fidelity image of faulting. The few wells with sonic logs were used to create well ties and approximate formation correlations.

6.2.2.1 Coherency attribute discussion

The Morgani 3D volume was used to create “coherency” attributes (“Variance” in Petrel) which is a process by which the seismic response for each trace is compared to the adjacent traces in terms of its similarity. This comparison is made across a time window which is then moved sample by sample, from top to bottom. The mathematical operation of cross-correlation between traces produces a value between -1 and +1. The resulting volume can be displayed along constant time surfaces or interpreted horizons, these are termed “slices”. A colour bar is adjusted to best capture the dynamic range of interest, from a visual standpoint. In this case the darker (red is maximum) colour represents a discontinuity or offset of some type between traces. This is generally representative of a fault. The advantage of the 3D volume is that with appropriate adjustment of the “slices” one can observe complexity that is not possible with closely spaced 2D profiles. These concepts will be expanded on within the interpretation discussion.

¹⁴ <https://www.software.slb.com/products/petrel>

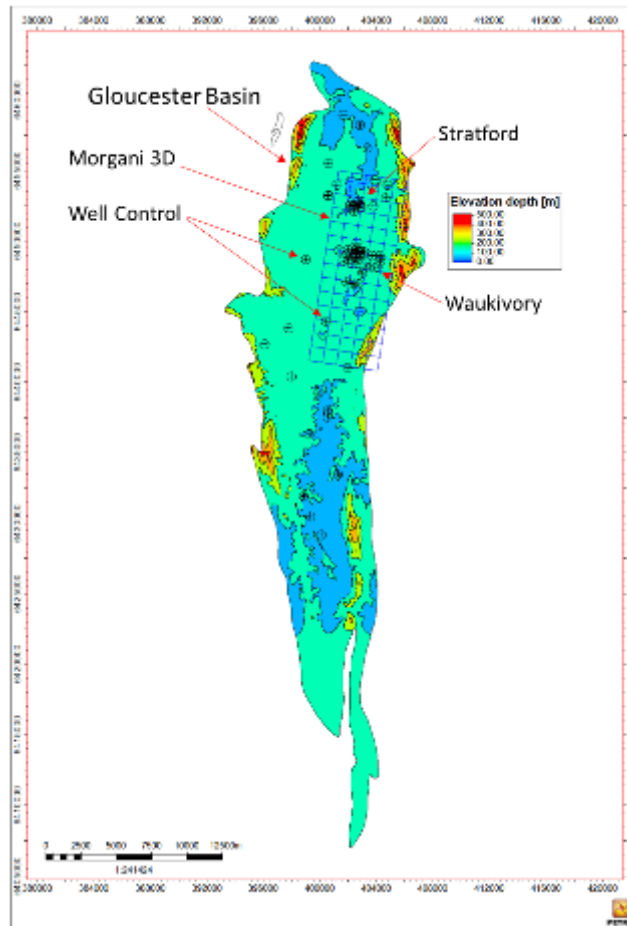


Figure 6-16 Gloucester Basin – Morgani 3D location and basin outline.

A representative time slice from the coherency attribute volume is shown in Figure 6-17. On the left is the coherency attribute in map view with black-red colour indicating sharp discontinuity and the lighter grey-white indicating relatively coherent response trace to trace. On the right hand side of the image is a vertical profile (indicated by the yellow line on the map) with the level of the slice shown as the horizontal yellow line. An example point of discontinuity in the reflection data is highlighted in both displays. A similar display style will be used in the discussion section of the report.

Wells with sonic logs were used to create “well ties”, where the travel time data measured in the log is integrated to create a time-depth relationship by which logs and formation tops can be displayed on the seismic data. The limited number of wells with this information precluded any attempt to create a larger scale velocity model by which the 3D data could be transformed into depth. The use of time-depth relations and well ties is a common interpretive practice.

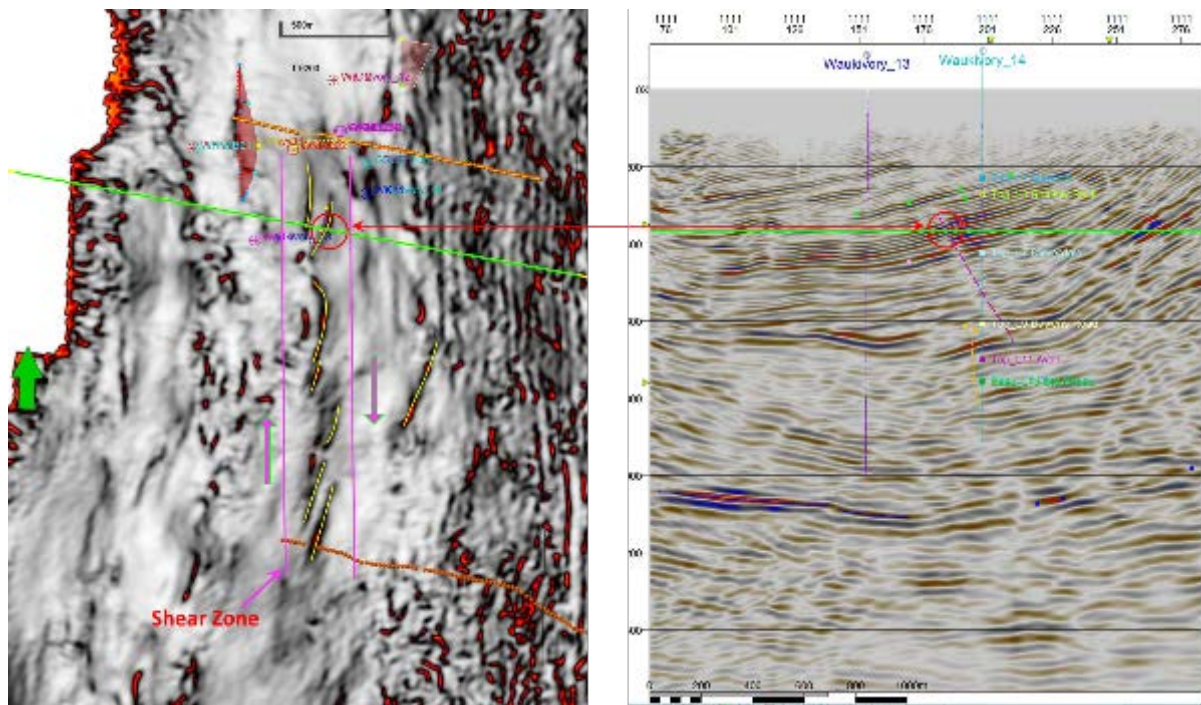


Figure 6-17 Morgani 3D Coherency Attribute volume, example time slice (left) and profile (right). The magenta lines represent the bounds of the shear zone with right lateral displacement (magenta arrows). Yellow lines represent interpreted fault segments. Red polygon is an interpreted fault plane. The orange transects mark the NanoTEM lines.

Faults were mapped on a local basis to provide support for the hydrologic interpretation. There were three primary areas of interest from the hydrodynamic and hydrochemical analysis: 1) the Stratford area near Stratford-4; 2) the Waukivory area near Waukivory 12; and the Waukivory area along the Waukivory River. The central areas (Pontilands and Craven) did not have the well control for mapping from the hydrodynamic and hydrochemistry point of view, but inferences can be made based on seismic observations from the other areas applied here.

6.2.2.2 Characterization of structure

The entire 3D area is characterized by complex fault patterns as is expected for the compressive/strike-slip environment. On the eastern side of the seismic volume the shallow section is rotated sharply and dips west at a high angle. Seismic imaging in this area is much poorer than on the western side of the survey due to steeply dipping bedding. The western side generally coincides with the areas of better well control.

The Stratford and Waukivory areas are distinguished from one another by the difference in spatial fault morphology observed from the 3D data. In the Stratford area, faulting within the shallower section is characterized by a series of en-echelon displacements. These had been mapped previously as continuous faults. However upon closer examination with the coherency attribute many of these faults are seen to be discontinuous along strike with “en echelon” patterns consistent with shear deformation (right lateral). The Waukivory area is a

good example of this as shown in the previous figure. The series of en echelon faults trend south to north, just east of the Waukivory 13 well, with each individual fault having a lateral extent of less than 500 meters (Figure 6-18).

Figure 6-18 shows the generally north-south structural fabric is offset just north of the Stratford area giving the impression of a bend. This change in strike is accompanied by WNW-ESE cross faults which are not observed to the north or further to the south.

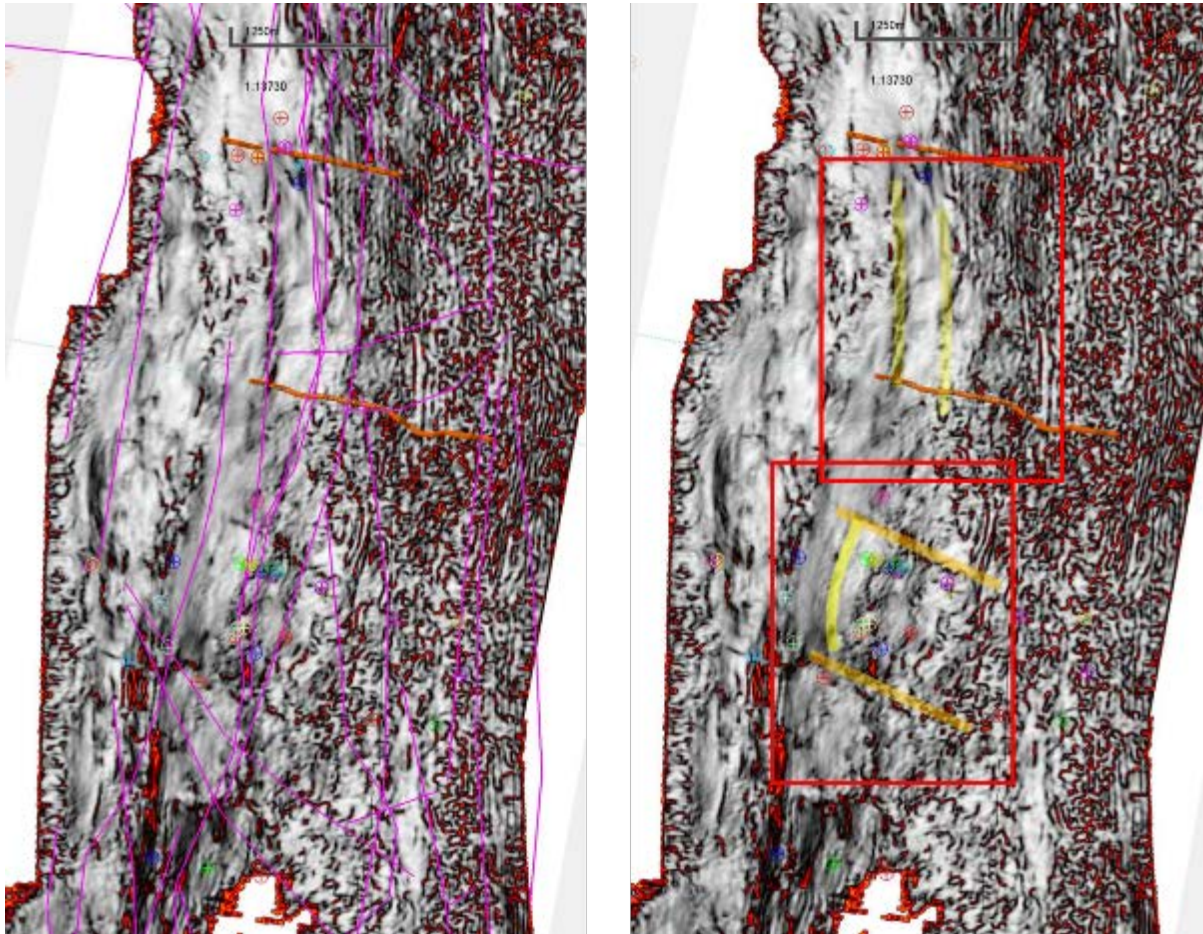


Figure 6-18 Fault pattern change from Stratford to Waukivory. Left panel: Magenta lines are previous AGL fault interpretations and orange transects mark the NanoTEM lines. Right Panel: Top red box highlights the area of Figure 6-17 and the bottom red box highlights the area of Figure 6-19. The orange transects mark the NanoTEM lines and the yellow lines represent interpreted fault zones.

The Waukivory and Stratford areas are presented in more detail below. In the left figure (Figure 6-17) a N-S trend of discontinuous, en-echelon faults are shown by the time slice from the coherency volume. The faults are highlighted in yellow. An example of the fault is shown in the profile (Figure 6-17, right) where the fault break is highlighted (red circle) along the slice level (green). These faults have an individual lateral extent of ~500m or less. The en-echelon morphology can be interpreted as resulting from right-lateral shear. One might expect this geometry to result in an increased tendency for the faults to be dilatant and possible enhanced permeability.

Figure 6-19 is from the Stratford area where the overall N-S structural trend is observed to be slightly offset. This “bend” also conforms to an area where a series of W-E faults occur. These “cross-faults” are not observed in other areas. These appear to conform to the observed boundaries of a salinity anomaly as observed in monitoring bores.

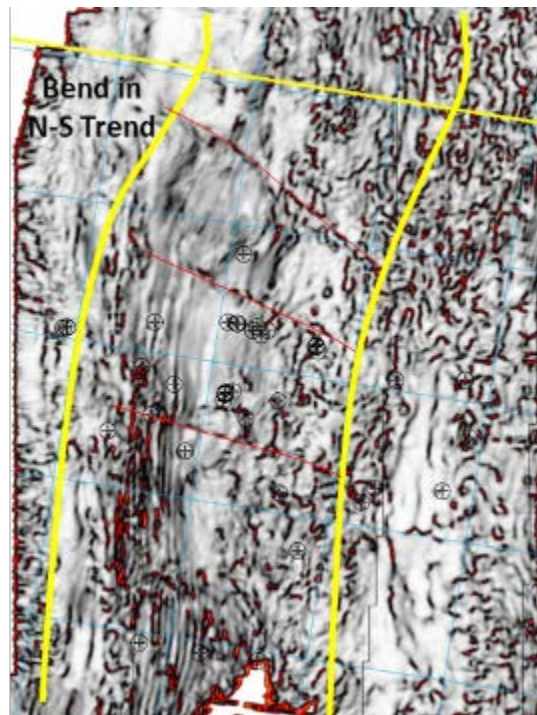


Figure 6-19 Detailed coherency slice from Stratford area. Key features are ~W-E faulting which occur at “bend” in structural trend. This deformation may form flow boundary to compartmentalize the observed salinity anomaly.

6.3 References

- Cawood PA, Leitch EC, Merle RE and Nemchin AA (2011). Orogenesis without collision: stabilizing the Terra Australis accretionary orogen, eastern Australia. *GSA Bulletin* 123(11–12): 2240– 2255, doi: 10.1130/B30415.1.
- Dershowitz WS, Herda H (1992). Interpretation of Fracture Spacing and Intensity, Proc. 33rd. U.S. Symp. on Rock Mechanics, Balkema.
- Enever JR and Lee MF (2000). On the prediction of rock stress, in Proceedings of GEOENG, Melbourne
- Grieves K and Saunders J (2003). Seismic reprocessing, interpretation and mapping for the Stratford Coal Seam methane prospect, PEL 285. AJ Lucas Coal Technologies Pty Ltd and Molopo Australia, Australia.

- Harrington HJ, Brakel AT, Hunt JW, Wells AT, Middleton MF, O'Brien PE, Hamilton DS, Beckett J, Weber CR, Radke SJ, Totterdell M, Swaine DJ and Schmidt PW (1989). Permian coals of eastern Australia. Bulletin 231. Bureau of Mineral Resources, Canberra.
- Mauldon M and Dershowitz W (2000). A Multi-dimensional system of fracture abundance measures, Summit 2000, Geological Society of America Annual Meeting, Nevada.
- McVicar TR, Langhi L, Barron OV, Rachakonda PK, Zhang YQ, Dawes WR, Macfarlane C, Holland KL, Wilkes PG, Raisbeck-Brown N, Marvanek SP, Li LT and Van Niel TG (2014). Context statement for the Gloucester subregion. Product 1.1 from the Northern Sydney Basin Bioregional Assessment. Department of the Environment, Bureau of Meteorology, CSIRO and Geoscience Australia, Australia.
- Parsons Brinckerhoff (2013). Hydrogeological conceptual model of the Gloucester Basin. AGL Upstream Investments Pty Ltd, St Leonards, New South Wales.
- Rajabi M, Tingay M and Heidbach O (2016). The present-day stress field of New South Wales, Australia. *Australian Journal of Earth Sciences*, 63(1): 1-21, doi: 10.1080/08120099.2016.1135821.
- Roberts J, Engel B and Chapman J (1991). Geology of the Camberwell, Dungog, and Bulahdelah. 1:100,000 geological series – sheets 9133, 9233, 9333. Geological Survey of New South Wales, Sydney.
- SRK Consulting (2005). Gloucester Basin geological review. A J Lucas Coal Technologies Pty Ltd and Molopo Australia Ltd, Australia.
- SRK Consulting (2010). Gloucester Basin stage 1 gas field development project preliminary groundwater assessment and initial conceptual hydrogeological model. AGL Energy Limited, Australia.
- Ward CR, Bocking M and Ruan CD (2001). Mineralogical analysis of coals as an aid to seam correlation in the Gloucester Basin, New South Wales, Australia. *International Journal of Coal Geology* 47: 31–49.

7 Data integration, fault seal analysis and hydrogeological conceptualisation¹⁵

7.1 Introduction

The investigation of the Gloucester Basin case study area included field work and desktop subsurface studies that all occurred in parallel. The field sampling was designed to both take advantage of existing bores, roads and water courses for ease of access, and focus on transects running perpendicular to the main north-south structural trend in order to increase the chance of seeing hydrodynamic signatures of upwards migration along structures. The field campaign included sampling well bores for water chemistry and dissolved gases, collection of atmospheric samples for methane, acquisition of shallow geophysics along certain transects, and a run of river surface water sampling campaign of Waukivory River and the Avon River for water chemistry and dissolved gases (see Section 4 for details). The desktop subsurface study “mined” CSG exploration well and water bore records for data to constrain the formation water hydrochemistry and hydrogeology (see Section 5 for details), examined well bore image logs to determine *in situ* stress and small scale strain (fracture orientation, dip, dilatancy and fracture density) (Section 6), and the available seismic data was examined to interpret the fault zone architecture (Section 6). Each of these investigations proceeded in parallel and independently. In terms of the hydraulic nature of faults and their influence on the flow systems of the Gloucester Basin, the following key salient observations were made from across all these individual investigations:

- The run of river sampling shows a methane and helium anomaly at ~11,200 m position along the Waukivory River (see Figure 4-6);
- The run of river sampling shows a further methane anomaly at ~7000m, which is approximately the confluence of Waukivory River with the Avon River (see Figure 4-6);
- The shallow geophysics transects (particularly the NanoTEM) indicated changes in resistivity that might relate to fault locations in the shallow subsurface;
- The image log analysis showed highly variable S_{Hmax} orientation and highly variable fracture orientations, dip and fracture density. Where the angle between S_{Hmax} and fracture orientation is minimised, the fractures tend to be in dilatancy and the bulk

¹⁵ Contributing authors: J Underschultz, S Mukherjee, H Xu, A Wolhuter, J Copley

permeability is enhanced. The Waukivory 12 and 14 wells are examples of this (see Figure 6-15);

- The desktop subsurface hydrochemistry study revealed two high salinity TDS anomalies (>4,000 mg/L) in the shallow aquifer system in the Stratford area and a less prominent high salinity TDS anomaly (>2,000 mg/L) in the shallow aquifer system in the Waukivory area (See Figure 4-19);
- The hydrodynamic assessment identified the Waukivory 12 and 14 wells to define consistent vertical hydraulic gradients across multiple horizons (Section 4.2.1). The lowest value of hydraulic head (near the surface) is equivalent to the elevation of the creek near the well. While having less data control a similar vertical gradient was also identified at the wells Stratford 7 and 8;
- Analysis of the 3D seismic volume identified some regions to contain clearly traceable and relatively continuous reflectors (coals) interrupted by significant fault offsets. Other parts of the seismic volume show more “disturbed” seismic reflectors indicating a network of small en-echelon structures at various orientations. These appear to coincide with regions where strain is being transferred between one major structure and the next en-echelon one; and
- Analysis of the 3D seismic volume shows a dominant north-south structural fabric with a bend in the Stratford area. Within the bend region there are high angle faults trended roughly east-west that take up some of the strain.

7.2 Methods for integration

In this integration section we take the various lines of evidence described in section 7.1, to build a single interpretive conceptual model that honours the entire data set. On the basis of this unifying conceptual model we then proceed with numerical modelling to confirm or refute that the numerical model is robust (i.e. the numerical model broadly confirms the conceptual model features with a plausible parameter set) and consistent with the data control (Section 8). For example, can the salinity anomalies be reproduced with a steady-state flow model given the constraints of hydraulic head boundary conditions and permeabilities estimated and measured in the strata and fault zones? If the numerical model proves to be robust then it can be used to predict flow conditions with more confidence in areas devoid of hydrodynamic data.

7.3 Integrated analysis supporting a hydrogeologic conceptualisation

Three regions of the total area examined have some combination of data suggesting preferential upwards vertical fluid migration pathways. These include:

1. The Stratford area: Here the Stratford 7 and 8 wells indicate an upwards hydraulic gradient and the TDS map for the shallow aquifer indicate two salinity plumes of

greater than 4,000 mg/L. Unfortunately, no image logs were available in this area and the field sampling program did not cover this area;

2. The Waukivory River at ~11,200m: The field program measured a surface water methane and helium anomaly and the NanoTEM indicate that this is a region of resistivity change in the shallow subsurface that could be related to a fault. Unfortunately this is not a location that is constrained by deeper well data; and
3. The Waukivory area: Here the Waukivoury 12 and 14 wells indicate an upwards hydraulic gradient and the TDS map for the shallow aquifer indicates a salinity plumes of greater than 2,000 mg/L. The image log data show a high fracture density and fracture orientation relative to S_{Hmax} favourable to dilatancy and enhanced permeability. The field program measured a surface water methane and helium anomaly and the NanoTEM indicated a local resistivity change in the shallow subsurface that could be related to a fault.

With these and other observations in mind we develop with factual information a conceptual model of the Gloucester Basin flow system that can subsequently be tested with further analysis (e.g., the 3D seismic volume). The conceptual flow system is depicted in the schematic diagram of Figure 7-1. The model shows a series of Permian bedrock coal zones and interburden with a bulk permeability of 1 mD or less. The bedrock strata is cut by faults that exhibit transpression with east-west shortening but north-south strike-slip displacement as evidenced by en-echelon faulting and the overall bend in the structural grain. Some of these faults reach the base of the alluvium and in fact exert an influence on the location of the surface drainage. The upper part of the bedrock immediately beneath the alluvium is weathered and has an enhanced permeability in the 10's of mD (see Figure 2.6). The water table in the alluvium fluctuates with season and climate and may or may not be connected to the surface drainage at different times. The alluvium has a permeability in the 100's of mD (see Figure 2.6). The overall flow system is controlled by recharge at the high topography eastern and western edges of the basin with discharge generally into the basin's central drainage. Given the overall permeability distribution the bulk of the flux is within the alluvium and shallow weathered bedrock. The flux through the deeper part of the basin is focused where the fault zone architecture provides slightly enhanced permeability (e.g. from 0.1 mD matrix permeability to 1 mD enhanced permeability) at particular locations. Some examples of inferred enhanced permeability are co-located where surface anomalies of methane were detected in the field sampling program.

In the Permian bedrock strata there are fault segments that form barriers to flow with hydraulic head discontinuities across them. Other locations however where certain fault segments and their associated damage zones provide slightly enhanced permeability relative to the host rock and thus focus flux upwards to shallower aquifers. At these locations upwelling groundwater may result in a plume of high salinity water emanating from a fault into a fresher water shallow aquifer (a salinity anomaly, such as observed in Figure 4-19). These same migration pathways may be locations of methane and helium migration that can be detected in the shallow aquifer or surface water. Candidate locations

for vertically connected structurally enhanced permeability are areas where strain is transferred from one major fault segment to another across a zone of distributed small scale strain with multiple orientations. These same areas may demonstrate high fracture density on image logs and have more opportunity for some fractures to be in dilatant conditions.

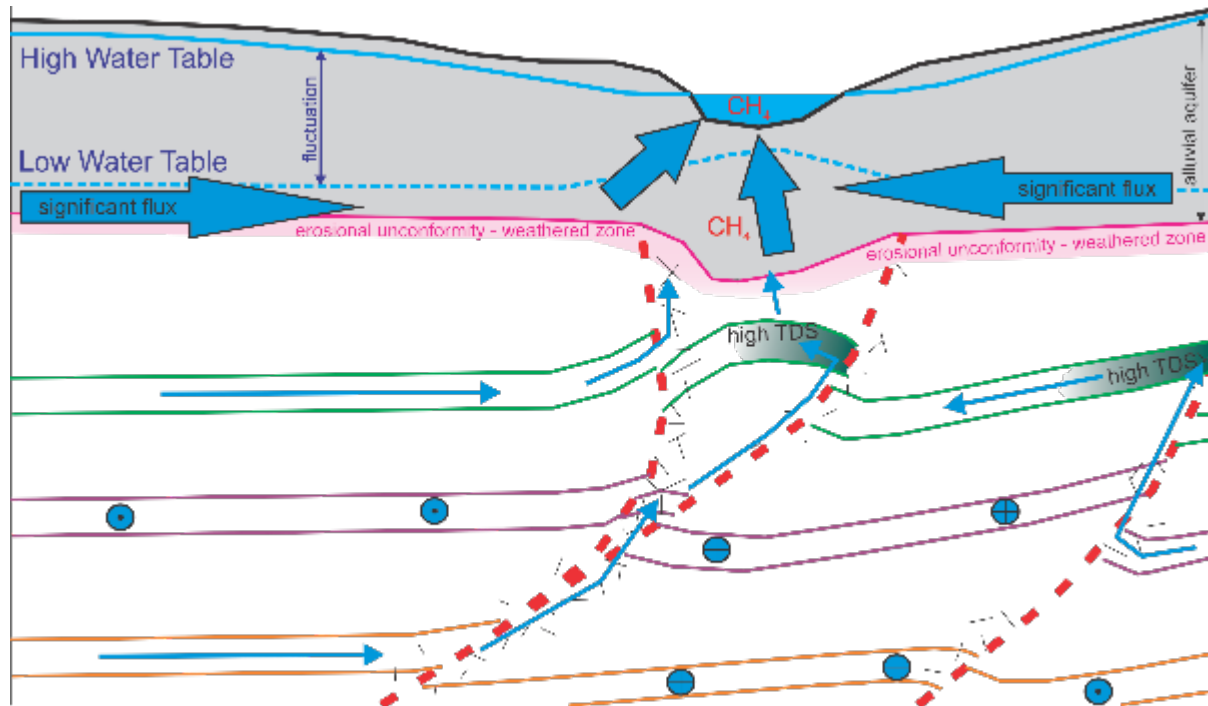


Figure 7-1 Conceptual model of the hydrodynamic system of the Gloucester Basin. Dimensions are not to scale. Circles with plus signs indicate flow into the page; circles with dots indicate flow out of the page.

7.3.1 Seismic Interpretation with NanoTEM

The two NanoTEM profiles (NT3 & NT5) were acquired within the area covered by the Morgani 3D survey. Though the 3D seismic data has limited resolution at the very shallow depths where resistivity is measured by the NanoTEM, the interpretation compared the results and found useful observations that are mutually supportive of the interpretation.

Profile NT3 is shown located in the north part of the 3D survey through the Waukivory area. Shown in Figure 7-2 below, the location of NT3 crosses a series of en-echelon faults as interpreted on the seismic data.

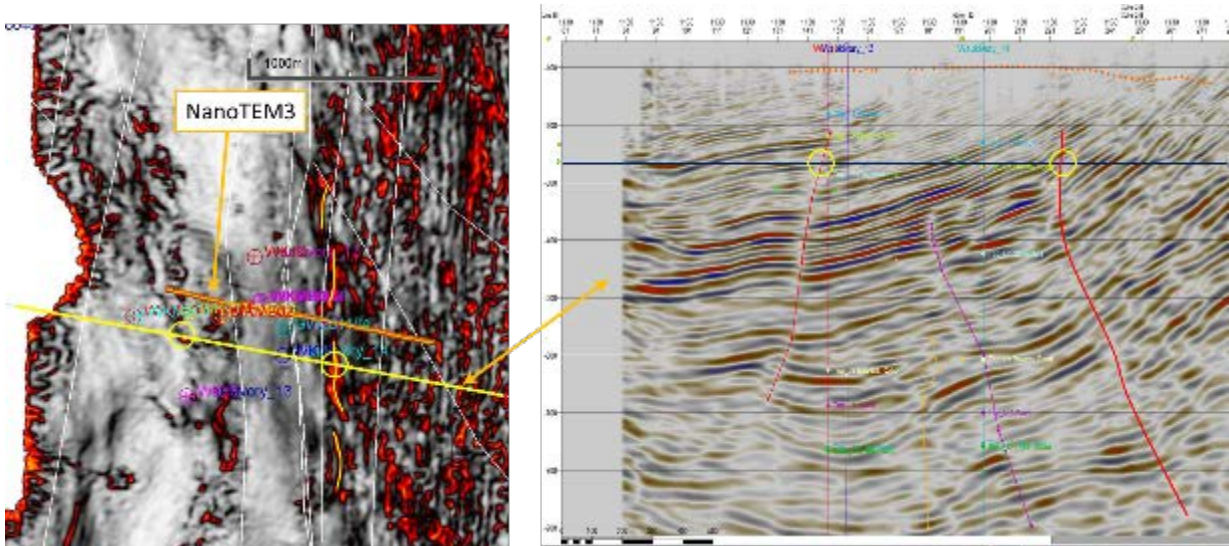


Figure 7-2 Coherency example from Waukivory area integrated with NanoTEM Profile 3 (orange). Profile shows the shallow extent of discontinuous, en-echelon faulting, also shown in Figure 6-17).

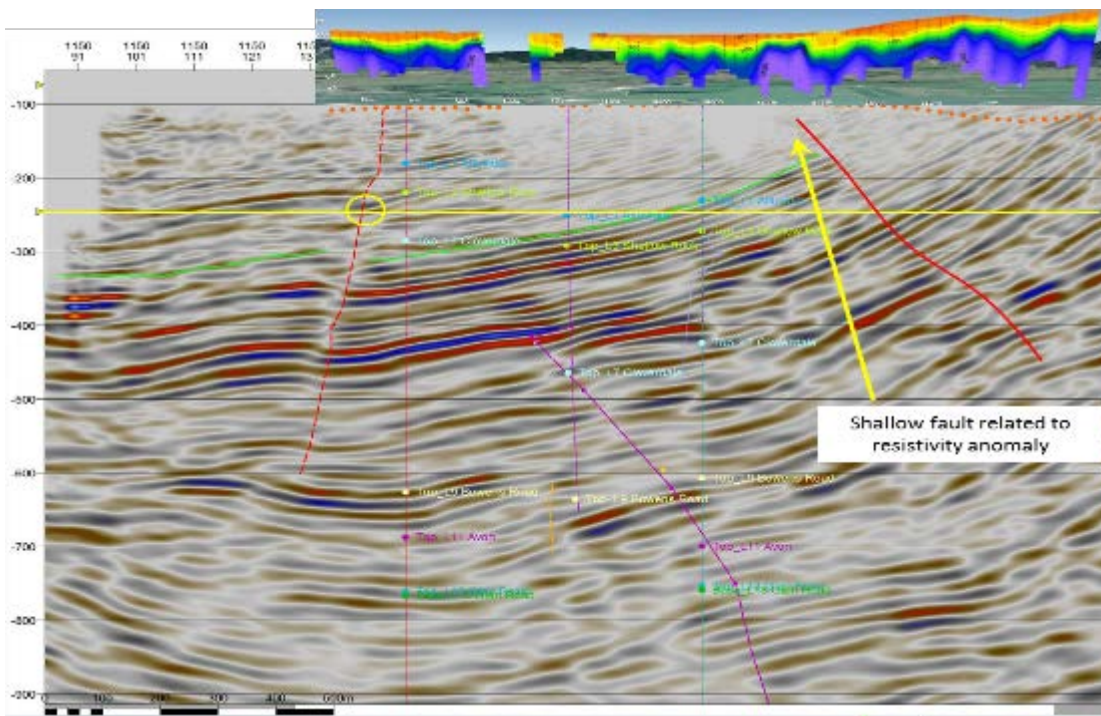


Figure 7-3 Profile along NanoTEM3 (orange in previous figure), shallow resistivity anomalies are observed to coincide with seismic faulting.

Figure 7-2 and Figure 7-3 summarize findings from NanoTEM profile 3. The inset in Figure 7-3, shows the profile along NanoTEM3 (orange line in previous figure), shallow resistivity anomalies are observed to often coincide with seismic faulting. It should be noted that resistivity anomalies may be related to other geological features such as steeply dipping strata at subcrop.

In Figure 7-4 the location of NT5 is shown on the coherency display (left) and the seismic profile is shown with an inset of the NanoTEM resistivity data. As with NT3 the seismic data

poorly resolves the shallow section, but some faulting is observed and interpreted to extend to near surface. At the east (right) side of the profile the geologic section is found to have increasingly steep dip. Some of the faults interpreted on NT5 seem to correspond to the seismic and resistivity changes on the east side could also be related to changes in subcropping units of differing resistivity.

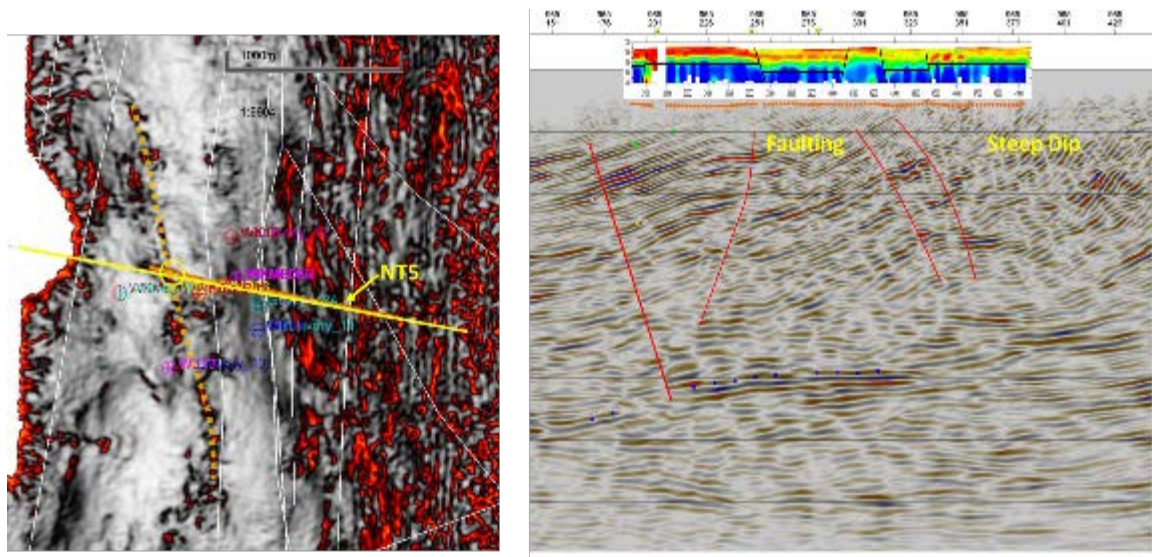


Figure 7-4 NanoTEM 5 and corresponding seismic profile.

7.3.2 Revised hydraulic Head Maps and Cross Sections

With the advantage of all the supporting information described in the previous part of the report, the hydraulic head maps first constructed and reported on in Section 4.2.1 are now reinterpreted here, while still honouring the control data and also being now constrained by all the other available constraining datasets and information. Because a significant part of the hydrodynamic system includes vertical components of fluid migration, we also present cross sections with hydraulic head distributions in order to depict these aspects not always evident from aquifer maps.

The most recent set of regional fault interpretations from AGL were used as a base for the hydraulic head maps. These consist of a different set of traces at different stratigraphic levels (Figure 7-5). We used the Bindaboo Fault interpretation for control of L1-L6 hydraulic head contours, Fairbairns Fault interpretation for control of L8, Bowens Fault interpretation for control of L10 and the Avon Fault interpretation for control of L11-L14. A boundary condition control on the hydrodynamic system is the water table elevation. This can mimic the ground surface elevation and we can gain insight into controls on fluid flow by examining of the Digital Elevation Model (DEM) for the study area (Figure 7-6). Here we see that the north-south trending central drainage coincides with a topographic low down to about 100 masl. Other surface elevation measurements such as well survey data would suggest that the actual creek bed is as low as 90 masl near the confluence of the Waukivory River with the Avon River. In contrast, the hills on the eastern margin of the basin are in

excess of 250 masl. Similarly, there are topographic highs occur on the western edge of the basin (Figure 7-6). The change in water table elevation across the basin and the bulk of the flux within the alluvium and shallow weathered bedrock aquifer, creates a horizontal potential gradient within the shallow aquifer system that tends to drown out the subtle features imposed by upwelling or recharging formation water along faults.

7.3.2.1 Hydraulic Head Distribution for Layers 11-14

The deepest part of the basin with sufficient data to construct a hydraulic head distribution is from the Avon Coal Member and deeper (layers 11-14). Despite the sparse data set and information only being available on the eastern part of the study area, we interpret a pattern consistent with the deep flow system being gravity driven (Figure 7-7). The highest heads (up to ~180 masl) occur on the eastern edge of the basin (Stratford 7 and Waukivory 4 wells) beneath the highest topography. A generally westward gradient to the central parts of the basin is defined by hydraulic head values in the 130-140 range at Stratford 5D, LMG 3. West of Waukivory 4 there is no data control in the Layers 11-14 but we can use data shallower in the section to help constrain the contours in this region. One could assume that there is an equivalent flow system on the western half of the study area, however there are no data to constrain it.

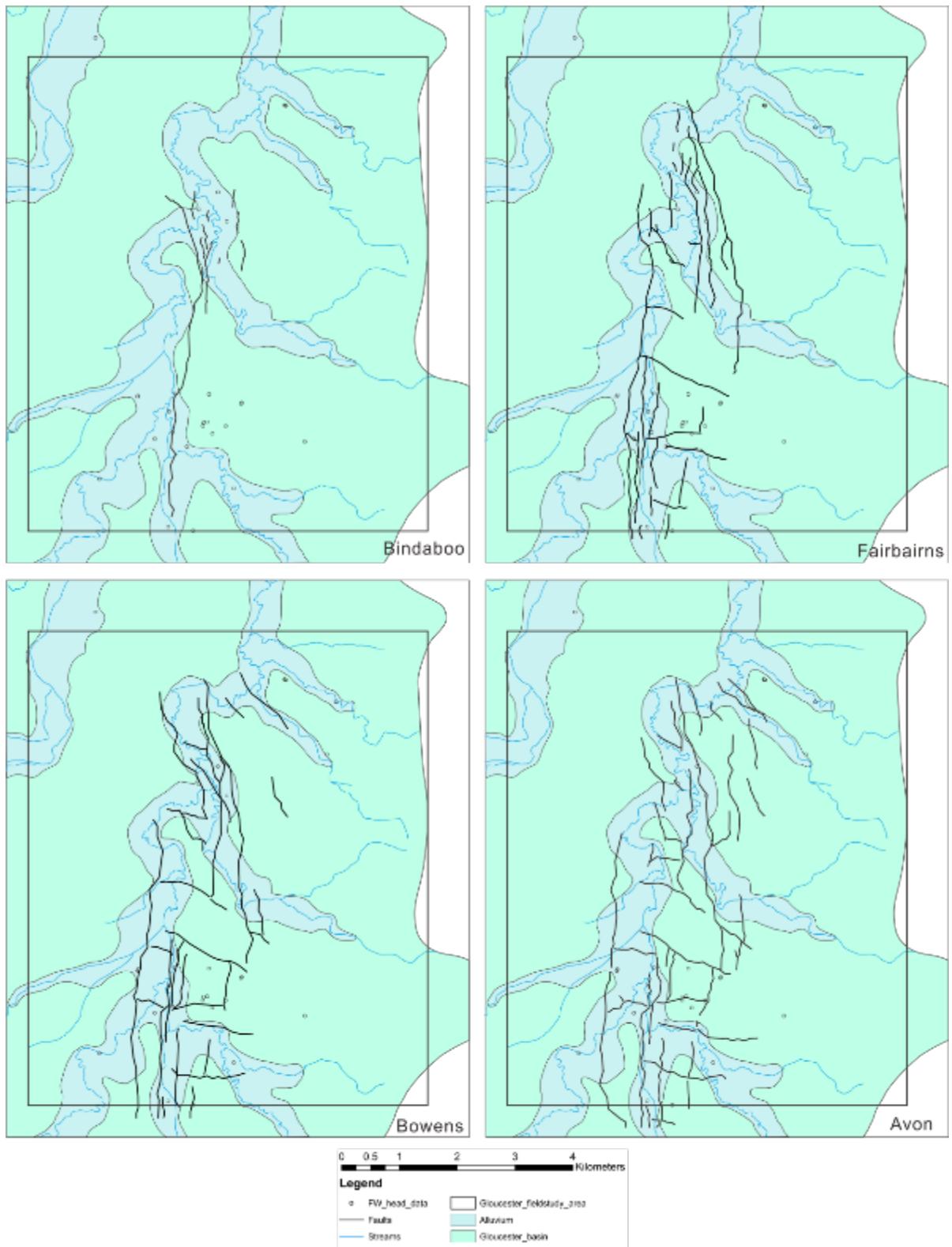


Figure 7-4 Updated faults (black lines) for the Gloucester Basin from AGL with different fault trace locations per stratigraphic interval. Stratigraphic levels are as follows: L1-L6 (Bindaboo), L8 (Fairbairns), L10 (Bowens), and L11-L14 (Avon).

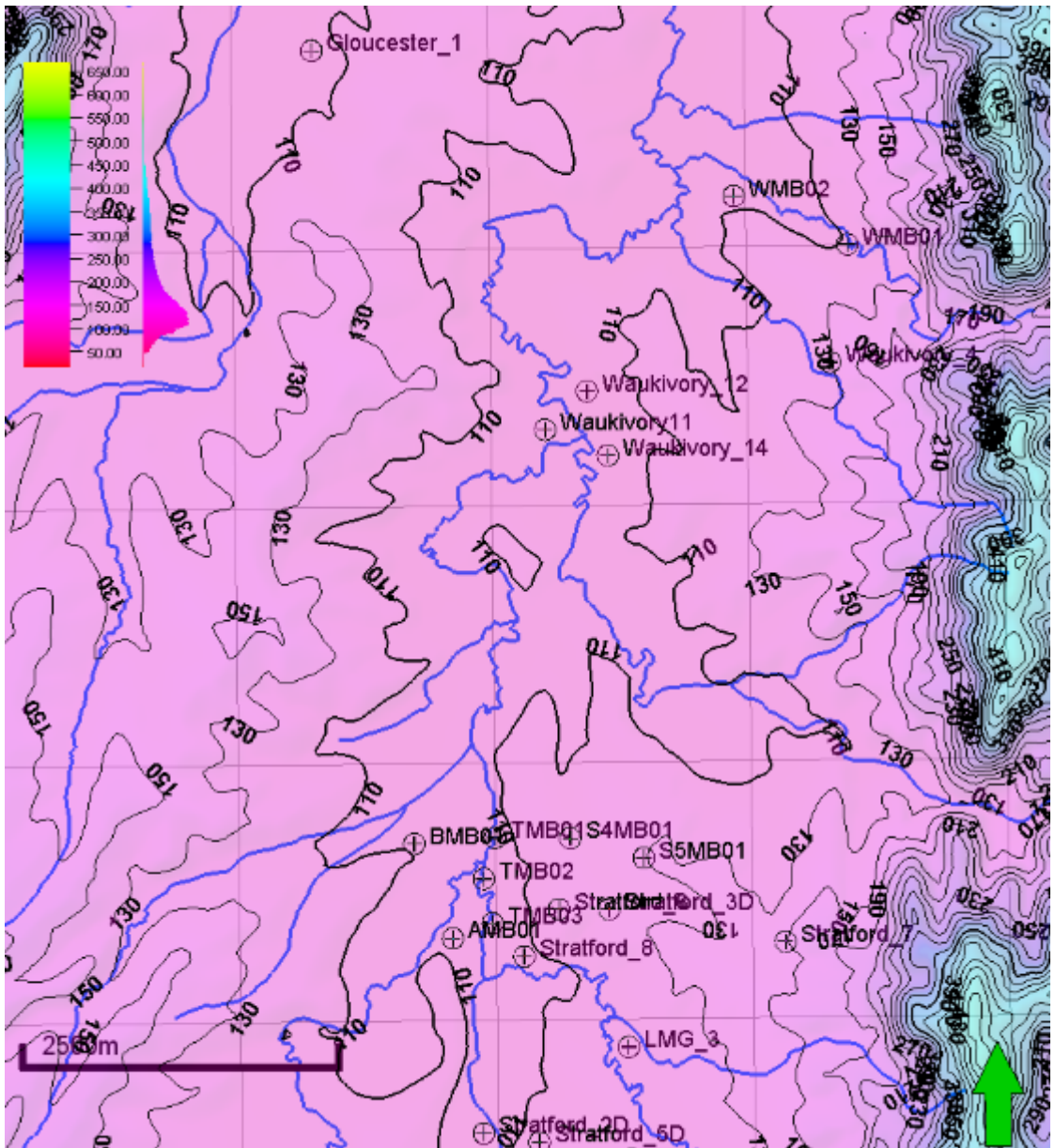


Figure 7-5 The Digital Elevation Model (masl) for the study area with key wells/bores marked. The surface drainage is posted in blue.

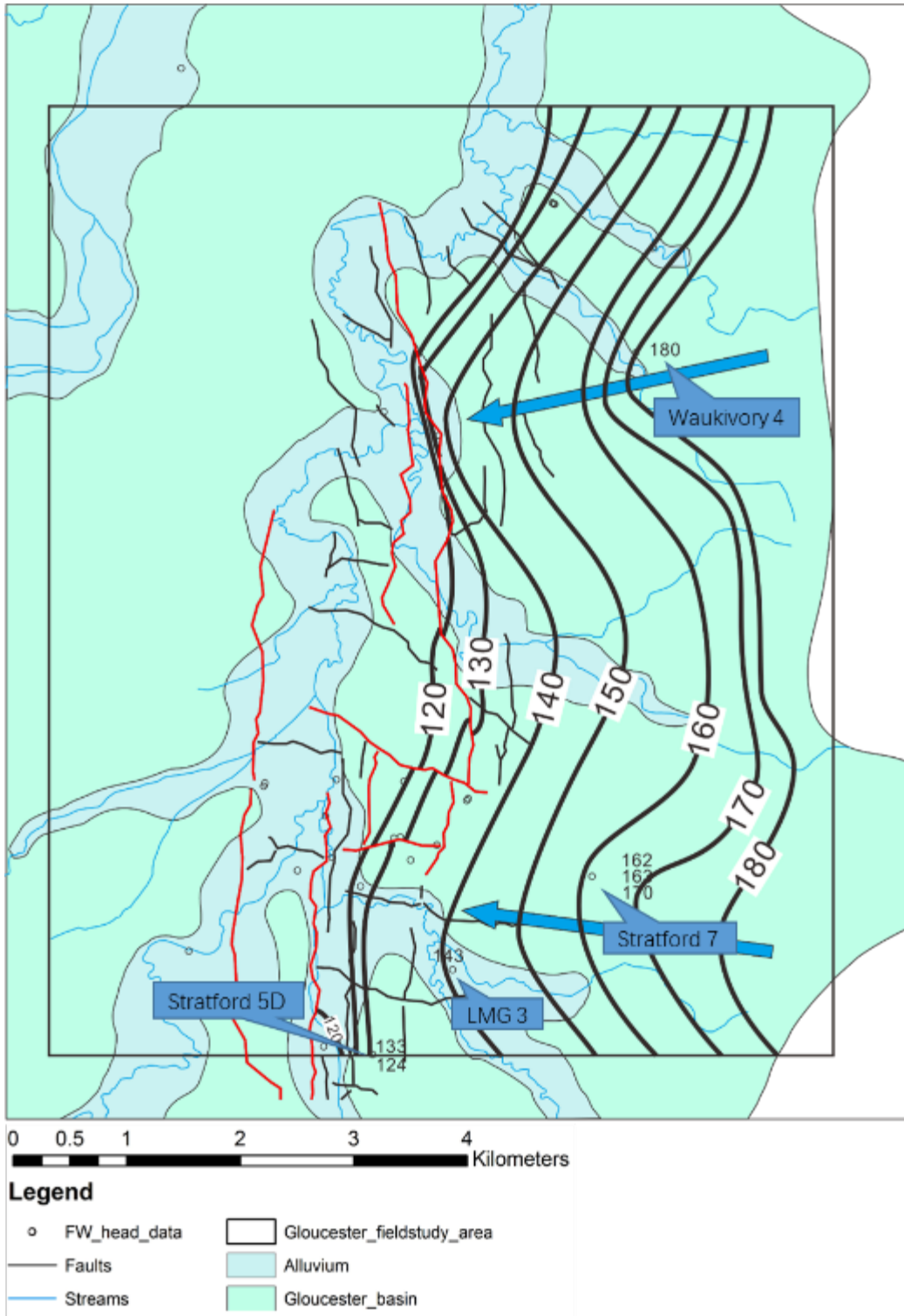


Figure 7-6 Fresh water hydraulic head distribution (bold black contours) for L11-L14 (Avon).

7.3.2.2 Hydraulic Head Distribution for Layer 10

The Dog Trap Creek Formation roughly correlates to the AGL Layer 10. This layer had sufficient hydraulic head data to be mapped separately and is the next mappable system above Layer 11-14 (Figure 7-8). There are only a few data control points located in the Stratford area but these define a low hydraulic head region in the central part of the basin with slightly higher values to the east. This remains consistent with a gravity driven flow system from the east. Note that the values of hydraulic head in the central part of the basin are slightly lower than the values in Layer 11-14 below. This suggests that in the central part of the basin there is an upward gradient potentially driving a general upward discharge.

7.3.2.3 Hydraulic Head Distribution for Layer 8

The Wards River Conglomerate is equivalent to Layer 8 and it separates the Bowens Road Coal Member below from the Cloverdale to Fairbairns Lane Coal measures above. This zone not only has a number of data control geographically but there are a number of wireline tests that provide a vertical pressure (hydraulic head) profile within Layer 8 (Figure 7-9). A central trough of low hydraulic head of less than 110 masl roughly coincident with the Avon River drainage dominates the hydraulic head map. Note that in the Stratford area these values are slightly lower than those previously described for L10. In the Waukivory area the Waukivory 12 and 14 wells demonstrate a decreasing hydraulic head profile upwards. Interestingly Waukivory 11 shows the opposite although the data from Waukivory 11 have a higher degree of uncertainty since a Horner extrapolation was not possible from the raw data.

7.3.2.4 Hydraulic Head Distribution for Layer 1-6

The data between the alluvial unconfined aquifer and the top of the Cloverdale Coal Member shows a consistent pattern and thus these data were grouped into a single hydraulic head map. This map is, however, mainly constrained by CSG well data and thus more representative of the deeper part of the system rather than the unconfined alluvial aquifer. Parsons and Brinckerhoff (2013) map the alluvial aquifer and this is shown in Figure 2.3 of this report. The Layer 1-6 hydraulic head map (Figure 7-10) is constrained firstly by the data control but also by the surface aquifer map (Figure 2.3) and the hydraulic head map for Layer 8 below (Figure 7-9). The result is a central north south trending trough of low hydraulic head with higher values to the east and west influenced by high topography gravity driven flow.

Unfortunately, examination of the hydraulic head maps for each stratigraphic layer does not easily inform the vertical component of flow since the lateral gradient dominated the pattern. To examine vertical hydraulic gradients more easily we next review the hydraulic head distributions along a number of selected cross sections that focus on areas previously identified as areas of interest for vertical hydraulic communications (methane and helium anomalies, salinity anomalies, image log data and vertical hydraulic head gradients).

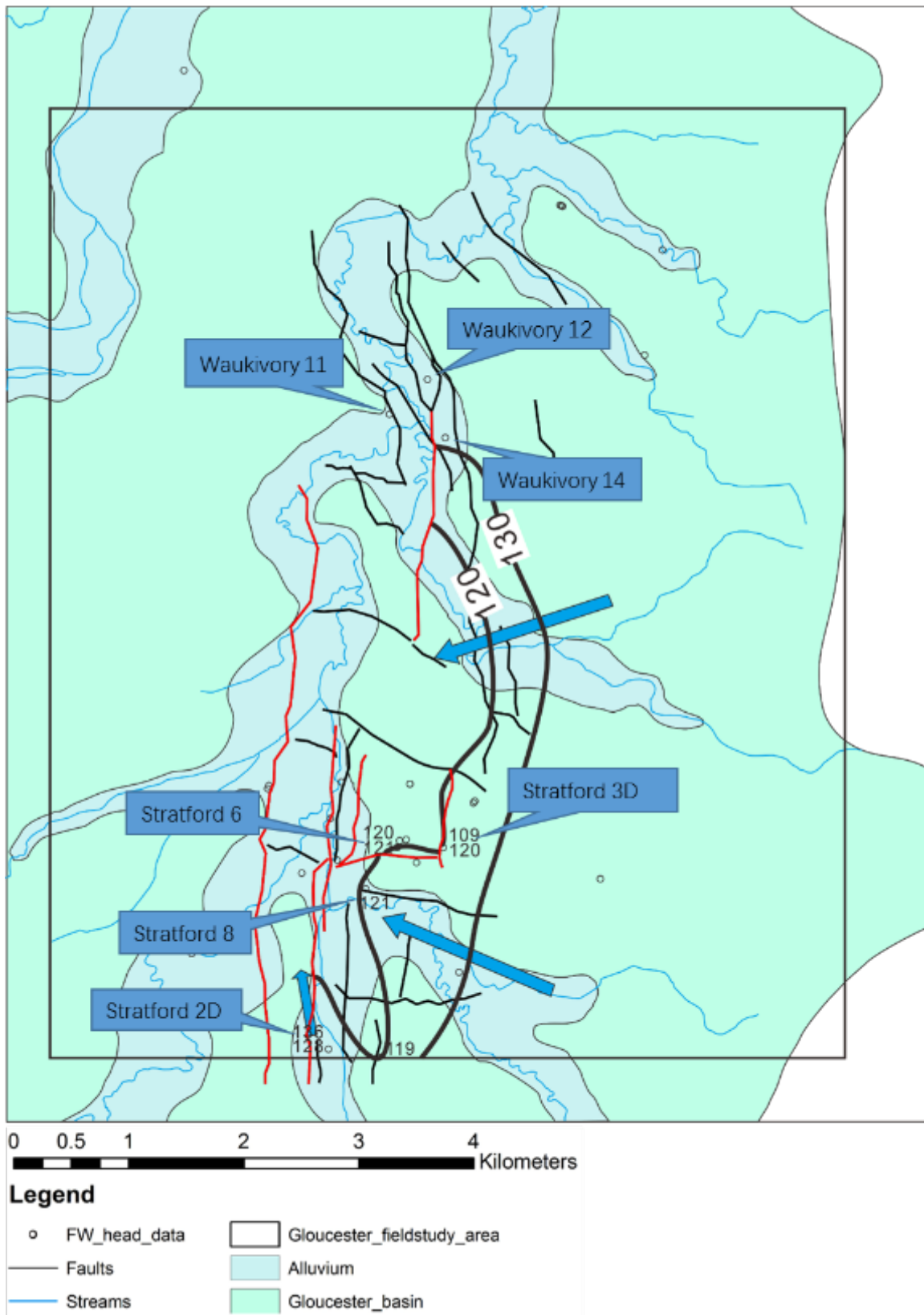


Figure 7-7 Fresh water hydraulic head distribution (bold black contours) for L10 (Bowens Road).

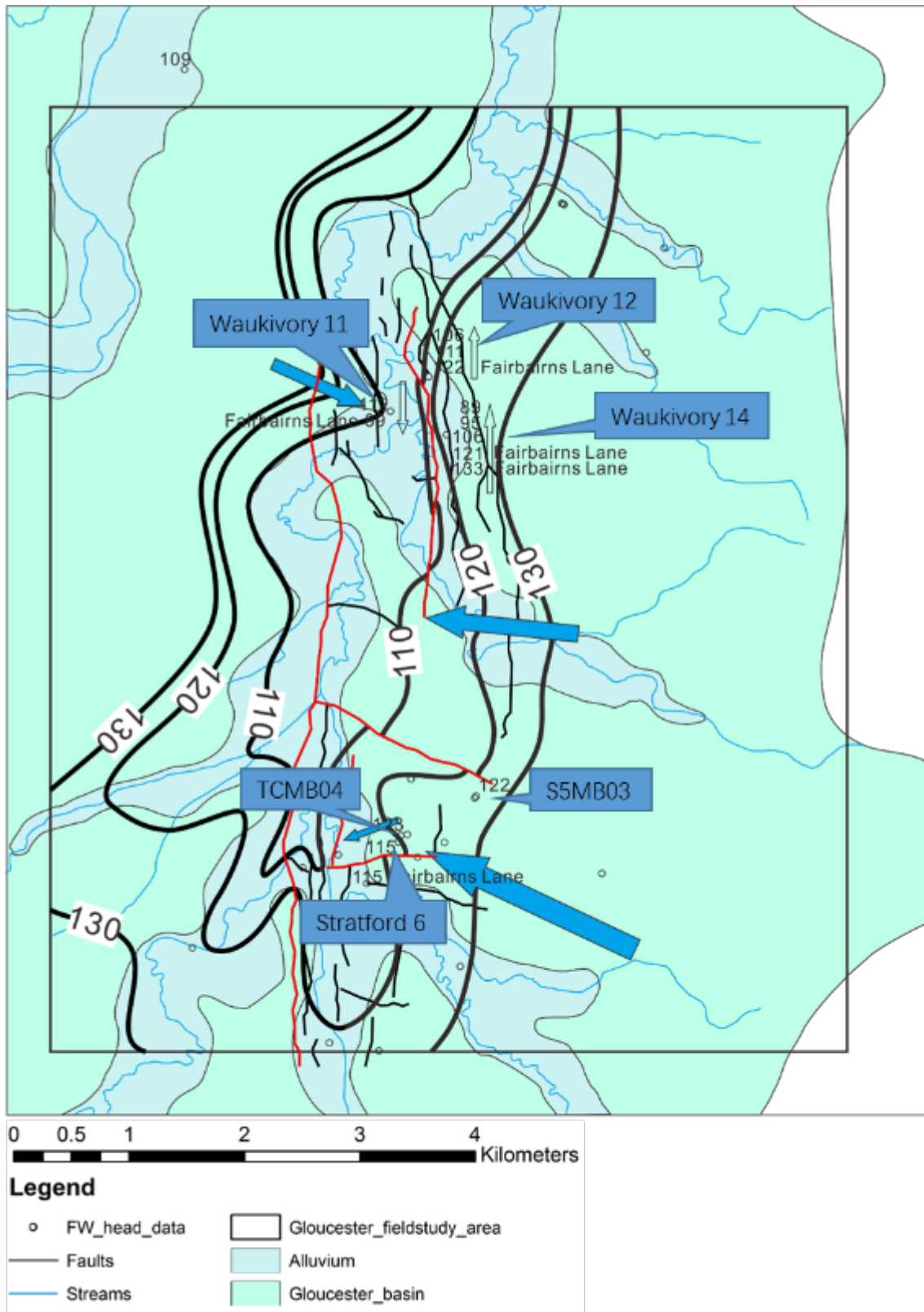


Figure 7-8 Fresh water hydraulic head distribution (bold black contours) for L8 (Fairbairns).

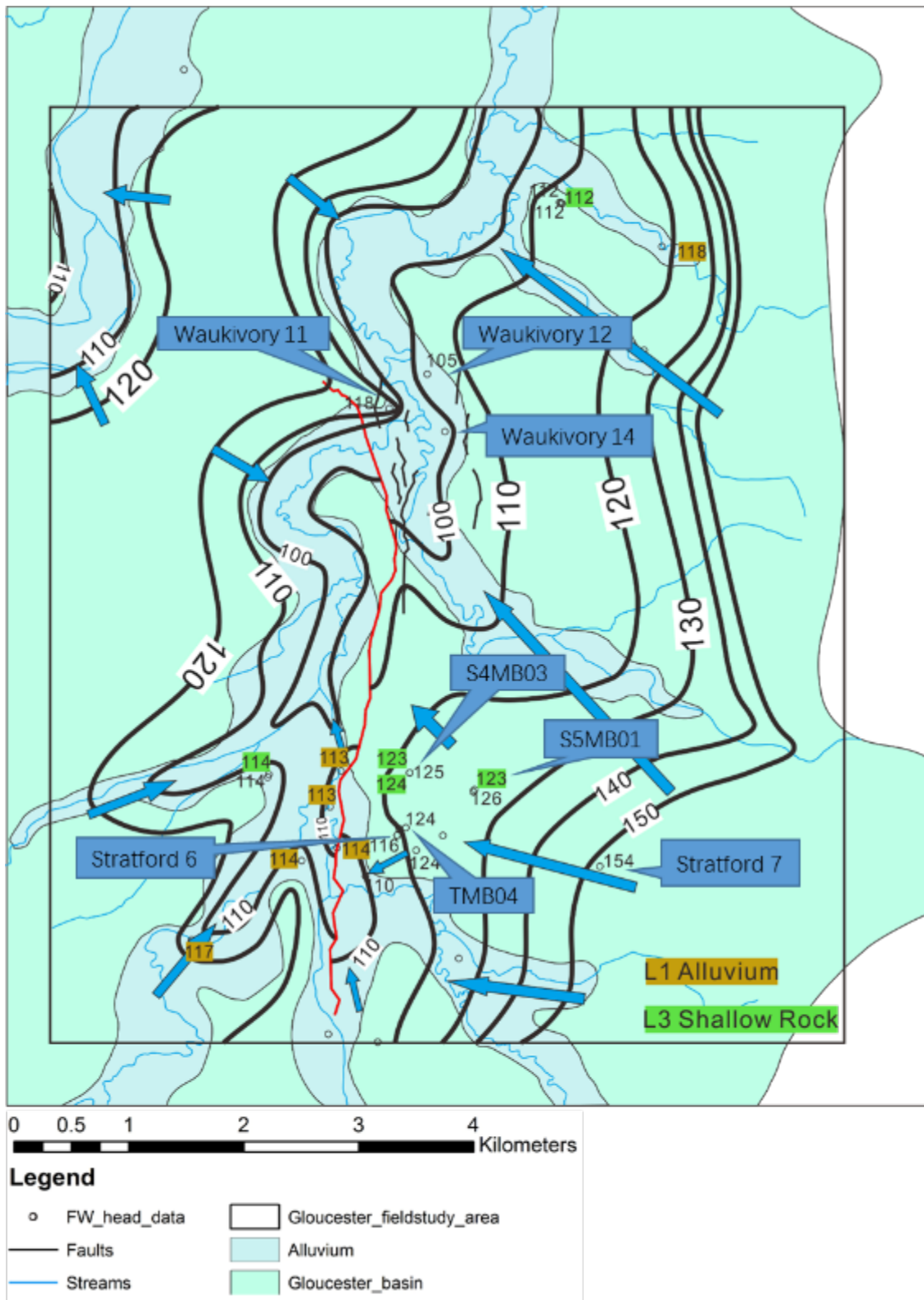


Figure 7-9 Fresh water hydraulic head distribution (bold black contours) for L1-L6 (Bindaboo) with well/bore data control (hydraulic head value posted next to each well/bore with data from the alluvium flagged khaki green and shallow fractured bedrock flagged bright green.

7.3.2.5 Vertical flow analysis (cross sections)

In order to illuminate the vertical hydraulic gradients we constructed West-East and South-North cross sections in each region of interest and used pressure (hydraulic head) data control in the wells, the hydraulic head maps previously described and the DEM to constrain the hydraulic head distributions mapped on each cross section. In these cross sections, yellow labels with numbers are hydraulic heads calculated by test or monitoring well data. The green data control are obtained from the aforementioned contour maps. The blue squares indicate conditions of a downward flow component and red ones indicate an upward flow component. The AGL static geological model layers are marked and fault locations area estimated from the AGL maps and from the 3D seismic volume analysis conducted in this study as specific locations. The cross sections show vertical exaggeration in order to distinguish the vertical detail.

Section W-E in the Waukivory area

There is generally a high hydraulic head at Waukivory 4, particularly in deeper layers, that drives a trend towards the west with an upward flow (leakage) component. This would suggest that the more significant recharge is occurring further to the east past the edge of the cross section. At the WKMB02 and Waukivory 12 wells there is nearly a vertical gradient towards lower values and eventual discharge at surface. The two upward flow areas coincide with a high salinity (TDS 2,000 mg/L contour in Waukivory area, Figure 4-19) in the L1-6 shallow aquifer. We can see that both these locations of upward flow and shallow salinity anomalies are located near interpreted fault zones. It is also at the location between WKMB02 and Waukivory 12, where the surface water sampling revealed a helium and methane anomaly.

In contrast, at Waukivory 11, there is a localized downwards gradient also located very close to a fault. The downward gradient only penetrates a short distance before the flow path is captured by the low hydraulic head discharge to WKMB02. This local flow cell might be driven by a combination of higher topography adjacent to the creek and a fault facilitating local recharge to a couple hundred meters before it circulates back to surface. It should also be cautioned that Waukivory 11 was also subject to a higher degree of data uncertainty.

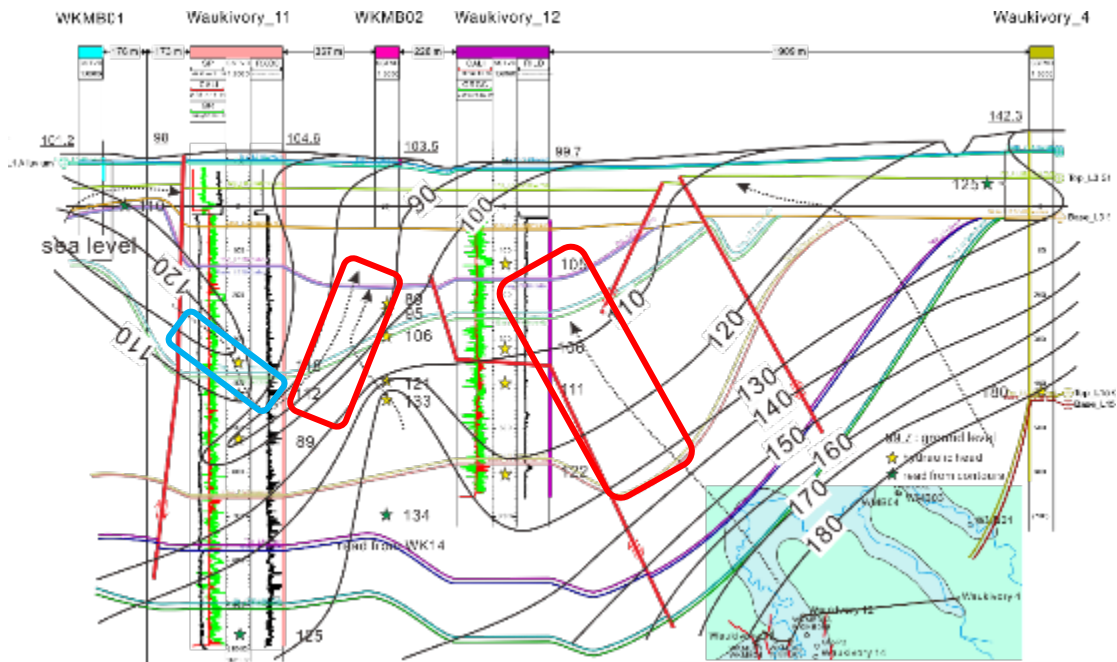


Figure 7-10 Fresh water hydraulic head distribution (black contours) along a W-E cross-section through the Waukivory area with well/bore data control (yellow stars are test data/monitoring bore data and green stars are controls from previously described hydraulic head maps). The location of cross-section is the black line shown in base map on the bottom right of the diagram. Black arrows show the interpreted flow direction, upward in the red squares and downward in the blue square. Interpreted faults are shown by red lines.

Section S-N in the Waukivory area

The cross section shown in Figure 7-12 is also through the Waukivory area but oriented generally north south. This line of section tracks sub-parallel to the surface water drainage and the hydraulic head pattern is generally one of upwards hydraulic gradient with discharge towards the surface drainage. Slight variations of this are explained by the line of section running slightly in and out of the river valley with this slight topography of the water table resulting in a slight lateral gradient from east to west in the shallow aquifer.

Section W-E in the Stratford area

Generally high hydraulic heads are shown at Stratford 7 which drives a flow trend towards the west with discharge to the Avon River near TMB01 (Figure 7-13). This pattern is consistent with a gravity driven flow system from high topography to the east. Discharge towards the western side of the cross section coincides with a salinity plume in the shallow aquifer system. There is a second plume however in the shallow aquifer system between TMB05 and somewhere to the west of Stratford 7. An upward flow component is indicated (but not strong) at Stratford 7. A closer look at the 3D seismic volume and the coherency map (Figure 7-14) reveals that to the west of Stratford 7 there is an interpretable fault segment that could be the location of upwelling groundwater. Once in the shallow aquifer the flow is towards the west.

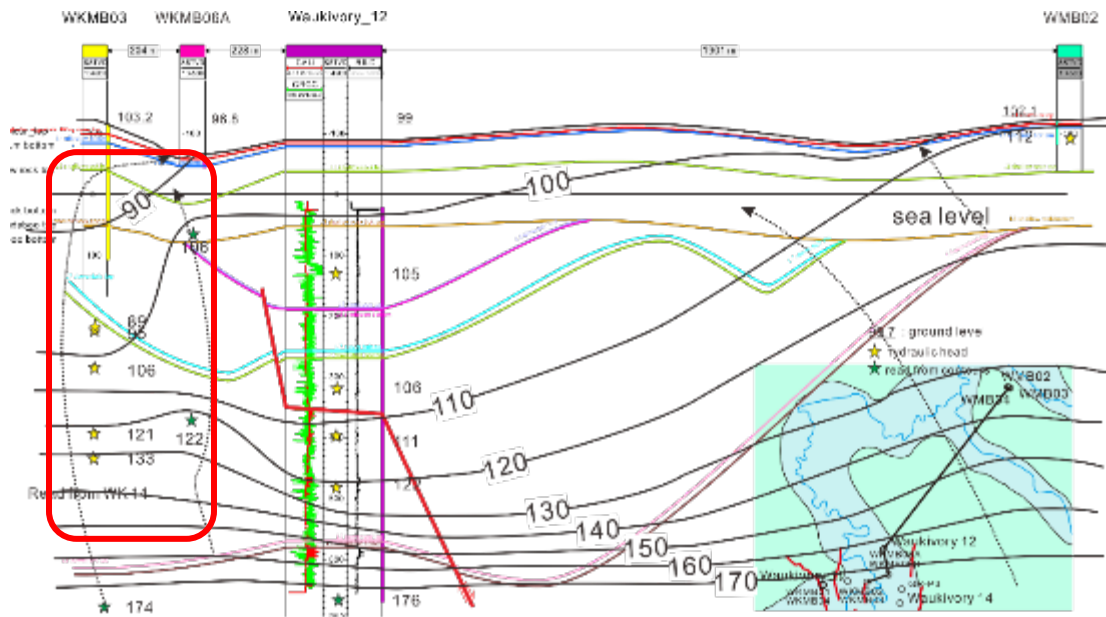


Figure 7-11 Fresh water hydraulic head distribution (black contours) along a S-N cross-section through the Waukivory area with well/bore data control (yellow stars are test data/monitoring bore data and green stars are controls from previously described hydraulic head maps). The location of cross-section is the black line shown in base map on the bottom right of the diagram. Black arrows show the interpreted flow direction, upward in the red square. Interpreted faults are shown by red lines.

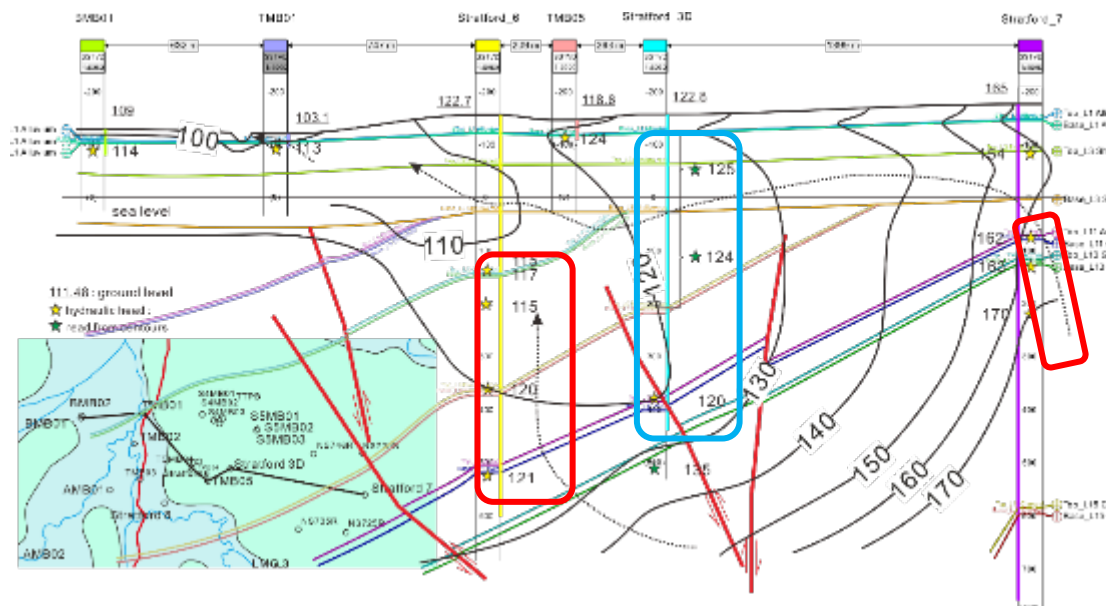


Figure 7-12 fresh water hydraulic head distribution (black contours) along a W-E cross-section through the Stratford area with well/bore data control (yellow stars are test data/monitoring bore data and green stars are controls from previously described hydraulic head maps). The location of cross-section is the black line shown in base map on the bottom right of the diagram. Black arrows show the interpreted flow direction, upward in the red squares. Interpreted faults are shown by red lines.

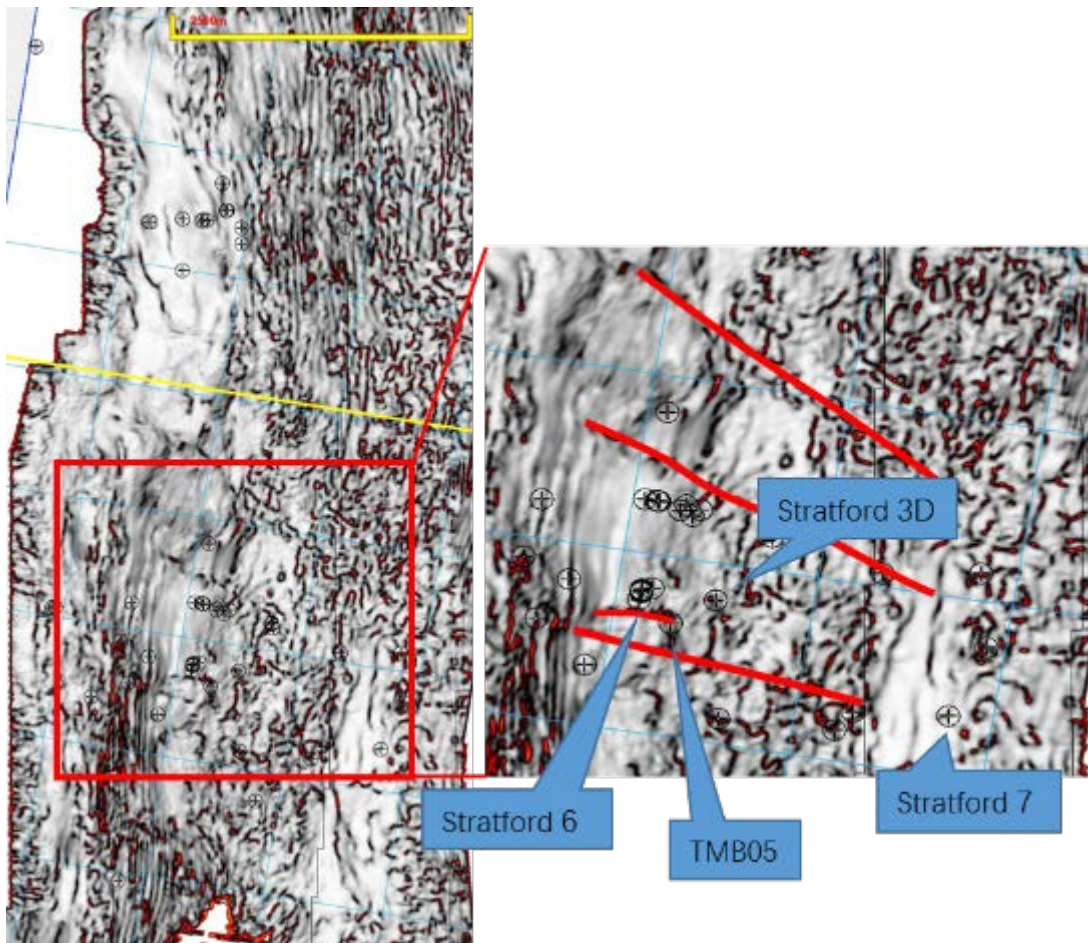


Figure 7-13 3D seismic cube with a horizontal map of coherency that indicates small fault segments in the Stratford area. Map on the left is a regional view while the red square is highlighted in more detail on the right.

7.3.3 Salinity distribution in shallow aquifers

In light of the new structural data and the reinterpretation of the hydraulic head data that includes all the hard data point controls as well as other softer constraints, we now re-examine the salinity distribution previously presented in Figure 4-19. Given the data control on TDS, the fault interpretation described in Figure 7-14 and the hydraulic head constraints captured by the cross section in Figure 7-13, the TDS plume east of Stratford 6 cannot be sourced from the west side of the plume as the hydraulic gradient at that location is locally downwards (see cross section in Figure 7-13). As there is no hard data control on the eastern edge of the TDS plume, one can interpret that the $> 4,000$ mg/L extends east to a lination in the coherency map (Figure 7-14) west of Stratford 7. Stratford 7 itself shows a general upward hydraulic head gradient in this region. The updated salinity map takes into account all the available supporting data (Figure 7-14).

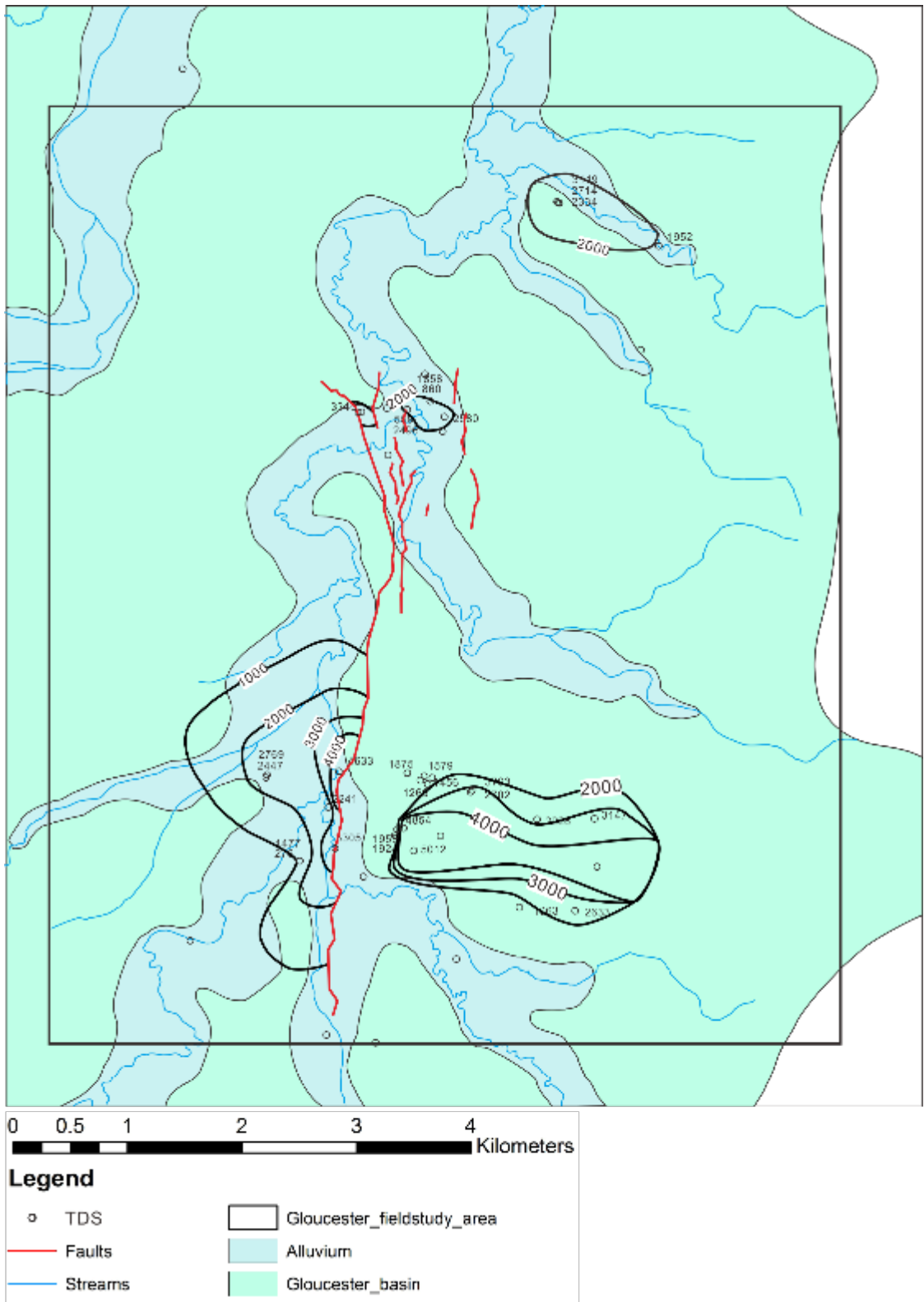


Figure 7-14 Salinity map (mg/L) for L1-L6 with added control of the hydraulic head cross-sections and detailed coherency map interpretation to help constrain the TDS plume geometry.

7.4 References

Parsons Brinckerhoff (2013). Hydrogeological conceptual model of the Gloucester Basin.
AGL Upstream Investments Pty Ltd, St Leonards, New South Wales.

8 Regional scale groundwater flow modelling of fault conceptualisations¹⁶

8.1 Introduction

Coal seam gas development applications are now required to predict how the proposed development will change the quantity (de-pressurisation) of groundwater and surface water near the development site and how dependent processes and systems will be affected. The accepted way to predict future impacts of groundwater extraction from coal seam gas production is to simulate the natural system using numerical modelling techniques. Reliable predictions require numerical models with suitable data as input, while models must further have the appropriate design (from conceptual models) and capability (e.g. model code) to represent the natural system being investigated for the intended purpose of the model. Numerical models can also be used to explore the validity of, and sensitivity of predictions to, different conceptual models and parameters, and demonstrate the improvements to predictions that can be achieved by improving model design and parameters. Numerical groundwater modelling will provide a means for integrating flow processes associated with aquitards and faults across a range of scales, ultimately leading to a scientifically robust understanding of potential impacts on groundwater from extractive industries.

Complementary to existing modelling efforts being undertaken by the industry and the Bioregional Assessments Programme in the Gloucester Basin (Parsons Brinckerhoff, 2013; AGL Energy Limited, 2014; Peeters et al., In Prep), the modelling activities within this project focus on an analysis that explores the role of fault features (3D architecture and hydrodynamic properties) on a regional groundwater resource using improved flow system conceptualisations. New concepts introduced in this project are based on in-depth analyses of hydraulic data (Sections 4), hydrochemical and tracer data (Sections 5), and structural geology data (Sections 6). The analysis will include potential effects of faults with and without coal seam depressurisation boundary conditions. Seismic and sub-seismic faults may play an important role in the movement of groundwater as they can act as either conduits or barriers to flow. It is important to understand the location and architecture of faults and their impact on groundwater flow and groundwater quality, as they could potentially compartmentalise or propagate pressure changes in aquifers. The ability of faults to restrict or extend pressure changes is therefore important to consider when assessing the possible impacts of CSG extraction. Despite this, the inclusion of faults in groundwater models (and their parameterisation) are generally neglected in assessments of CSG in Australia (Turnadge et al., 2018a).

¹⁶ Contributing authors: S Noorduijn, J McCallum, C Simmons, D Mallants, O Batelaan

To be of relevance to the IESC, regulators and practitioners, assessment results from this project should not be constrained to a single basin; i.e. results need to be transferrable to other basins, as far as is practically feasible. This may include a sensitivity analysis where such fault properties are varied within physically realistic ranges to explore how and when a groundwater system becomes affected by faults. In this project, best available data will be used to advance understanding of the role of faults; however, the purpose is not to develop a calibrated model for predictive purposes.

8.2 Approach to incorporate geological information in regional-scale groundwater modelling

A novel and efficient numerical approach has been developed to include geological information (i.e., fault zone architecture and Drill Stem Test information) in regional groundwater flow models by accurately representing the connections and disconnection of key hydrogeological units as they are affected by faults. This will address the issue regarding the need to improve aquifer characterisation for inclusion in numerical modelling. The approach present here involved the development of a 3D regional groundwater numerical model using MODFLOW-USG¹⁷ and the inclusion of a structural geological base model (McCallum et al., 2018).

McCallum et al. (2018) investigated the implementation of faults within a numerical groundwater flow model where it was found that the MODFLOW Unstructured-grid (MODFLOW-USG) offers the flexibility to represent grid geometries that arise from faulting. This work highlighted the necessity to understand the role of fault systems with regard to groundwater flow, more specifically the importance of determining whether faults act as barriers or conduits to flow. A particular limitation of the initial and highly simplified Gloucester model as represented in McCallum et al. (2018) is that the hydraulic properties are based on a sedimentary facies model which overestimates permeability within the model. Because the sedimentary facies model did not consider secondary processes like cementation, the permeability based on the sedimentary facies of the Stratford model (Frery et al., In Prep) is larger than what has been observed from core permeability estimates at the site (Parsons Brinckerhoff, 2015). As a result, the model is liable to overestimate the system response to any perturbations, e.g. a CSG development. We have developed a methodology which explicitly represents fault zones in MODFLOW-USG and combines the use of Drill Stem Test data, well log information, and geostatistical methods to improve understanding of the groundwater flow system.

The method will allow for complex and spatially variable fault geometries, permeabilities and thicknesses to be incorporated into regional flow models. It offers a numerically viable

¹⁷ UnStructured Grid

option for including faults in models. It will also allow the incorporation of complex geology models in regional groundwater flow models.

In this section the design of the numerical model is described (section 8.2.1) which covers the basin conceptualisation, model design, and boundary conditions. The fault implementation is described in section 8.2.2, followed by the CSG production scenario used in the model (section 8.2.3), and model parameterisation (section 8.2.4). In addition to the CSG production, the fault features described in section 8.2.5 are also included in the numerical model (section 8.2.6). The numerical model is used in a number of scenarios which are outlined in section 8.2.7.

8.2.1 Model design

8.2.1.1 Model Conceptualisation

The model structure of the Gloucester Basin developed in this project, hereafter referred to as the Gloucester model, was based on previously identified faults within the basin (Roberts et al., 1991; Frery et al., In Prep). The Gloucester Basin is a geologically closed basin consisting of three (water bearing) hydrogeological units: surface alluvium, shallow weathered and fractured rock, and bedrock (interbedded interburden and coal seams). Table 2-1 and Figure 2-4 in section 2.2 provide an additional outline of the basin structure. Figure 8-1 shows the location of the faults included in the Gloucester model. Roberts et al. (1991) identified numerous additional faults within the basin in addition to those in the model, however only the larger, more extensive faults with normal displacement which varies between 200 and 500 m were included in this model structure. Future work may involve inclusion of other smaller faults into the model structure. The shallow alluvial deposits, associated with the Avon and Gloucester rivers (and connected small tributaries) are incised into the surficial geology (Figure 8-2).

In the Gloucester subregion there are two existing coal mines with expansion plans (Duralie Coal Mine and Stratford Mining Complex) and one proposed coal mine (Rocky Hill, currently on hold as of 15 June 2015). A major difference with the groundwater model developed by Peeters et al. (In Prep) is the absence of any coal mining in the current project.

8.2.1.2 Model Design

The Gloucester model consists of 42 numerical layers (upscaled from the a local facies model of Stratford area (Frery et al., In Prep), with a horizontal grid size of 200 m by 200 m and a thickness of 50 m (Figure 8-3). Only those grid cells present at the surface of the model have a variable thickness based on the topographic features (such as the alluvium) in the Gloucester basin.

The alluvial groundwater system is included in the model as the initial layer to investigate how the shallow groundwater system, when connected to the deeper groundwater system,

responds to the presence of faults under natural flow conditions and conditions of increased stress (e.g. due to depressurisation). Grid cell refinement was required to simulate the alluvial aquifer; this was implemented using a quad-tree refinement. The horizontal dimensions of the alluvial cells were 66.6 m by 66.6 m, while the thickness was 15 m in the north and 8 m in the south (based on McVicar et al, 2014).

Subsequent model layers represent the interburden units and coal seams to a depth of 2,500 m (Frery et al., In Prep). The weathered/fractured zone is included in this sequence and its enhanced hydraulic conductivity is accounted for in the model parameterisation (see section 8.2.4). The impermeable basement volcanic sequence is excluded due to its low water bearing capacity and is considered as a no flow boundary.

Figure 8-3b highlights those streams/rivers which were included in the model. Observational evidence suggests that all streams within the Gloucester basin are gaining i.e., receive groundwater. As such, all streams were implemented in the model using the drain package. The appropriateness of using drain rather than river cells for the Gloucester streams was discussed by Peeters et al. (In Prep), who concluded that the use of drain cells is a reasonable simplification and avoids many potential problems associated with the use of river cells.

Groundwater discharge into the drains is determined using the length of stream, a nominal width of stream (assumed to be approximately 2 m based on average observations in the region), head gradient (groundwater level and base of the stream determined from the 90 m land surface DEM and an assumed stream depth of 0.5 m) and a conductance term (alluvial hydraulic conductivity). When the groundwater level drops below the base of the drain, no discharge occurs, therefore drain flow only occurs when the groundwater level is above the base of the drain. In addition, the drain package assumes that any water which enters a drain is removed from the model, while it does not have the capacity to simulate flow between adjacent drain segments and therefore to simulate drain flow or losing stream conditions (i.e., groundwater recharge from a losing stream reach).

Constant head boundary conditions are imposed in the north and south of the Gloucester model are based on land surface elevation (no groundwater data available). The basin is bounded on the east and west by faults (Figure 6-2) therefore no flow boundaries are specified to the east and west of the model. Recharge is included in this model, where the alluvial aquifer receives 80 mm/year and the fractured rock aquifer receives 2.5 mm/year (Peeters et al., In Prep). Evaporation and transpiration were not explicitly considered in this investigation, it is assumed that recharge inherently accounts for these losses. In total the model contains 159,003 model cells, and takes 90 minutes to simulate a transient 120 year time period.

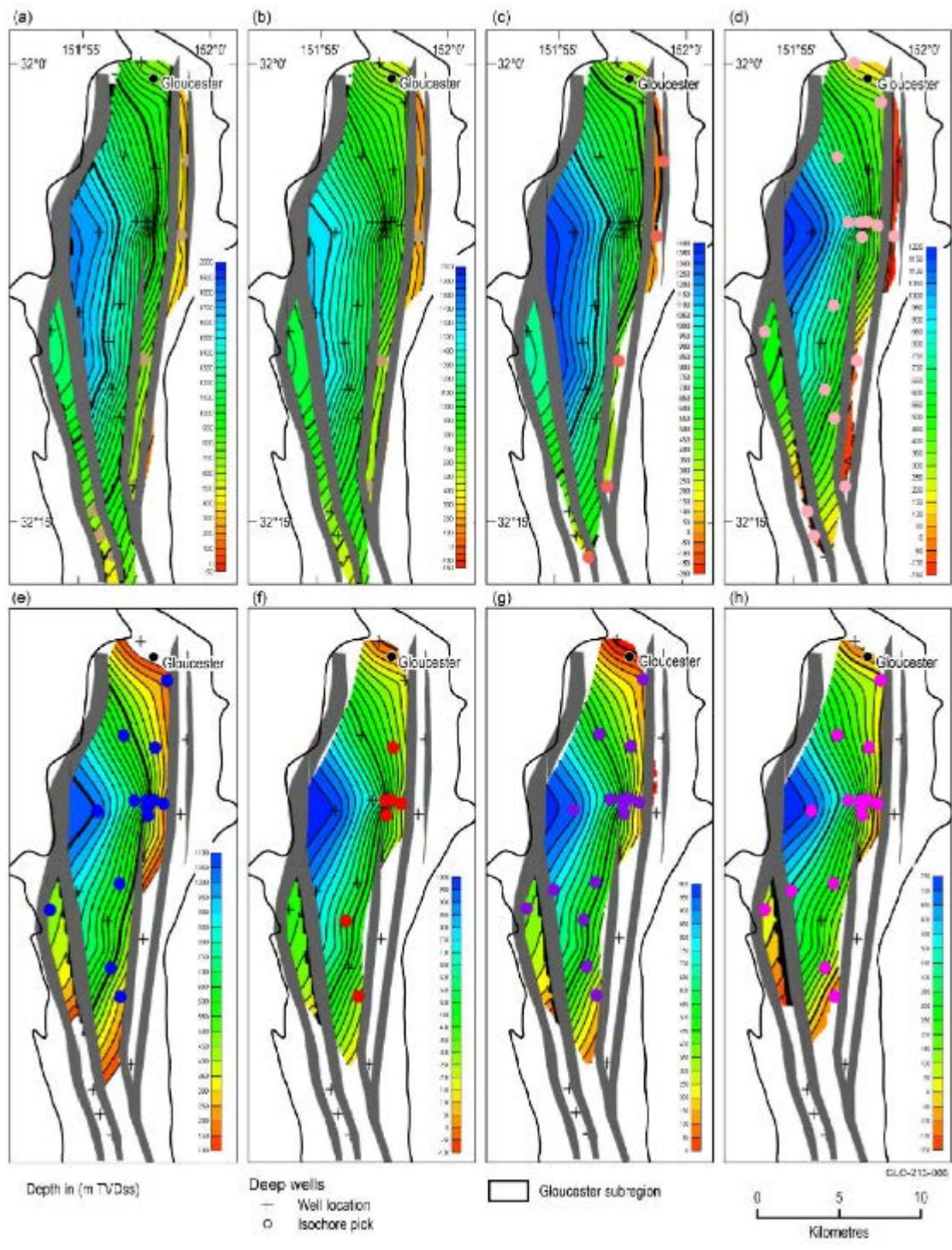


Figure 8-1 Gloucester Basin major fault traces (grey lines) and depth structure maps extracted from the eroded and faulted geological model for the coal-bearing geological Gloucester Basin area modelled in three dimensions. (a) Alum Mountain Volcanics, (b) Durallie Road Formation, (c) Mammy Johnsons Formation, (d) Waukivory River Formation, (e) Dog Trap Creek Formation, (f) Speldon Formation, (g) Wenham Formation Wards River Conglomerate and (h) Jilleon Formation TVDss = total vertical depth subsea reported to the Australian Height Datum; negative values represent elevation above sea level – grey lines represent the main fault trends (Source: Frey et al., In Prep).

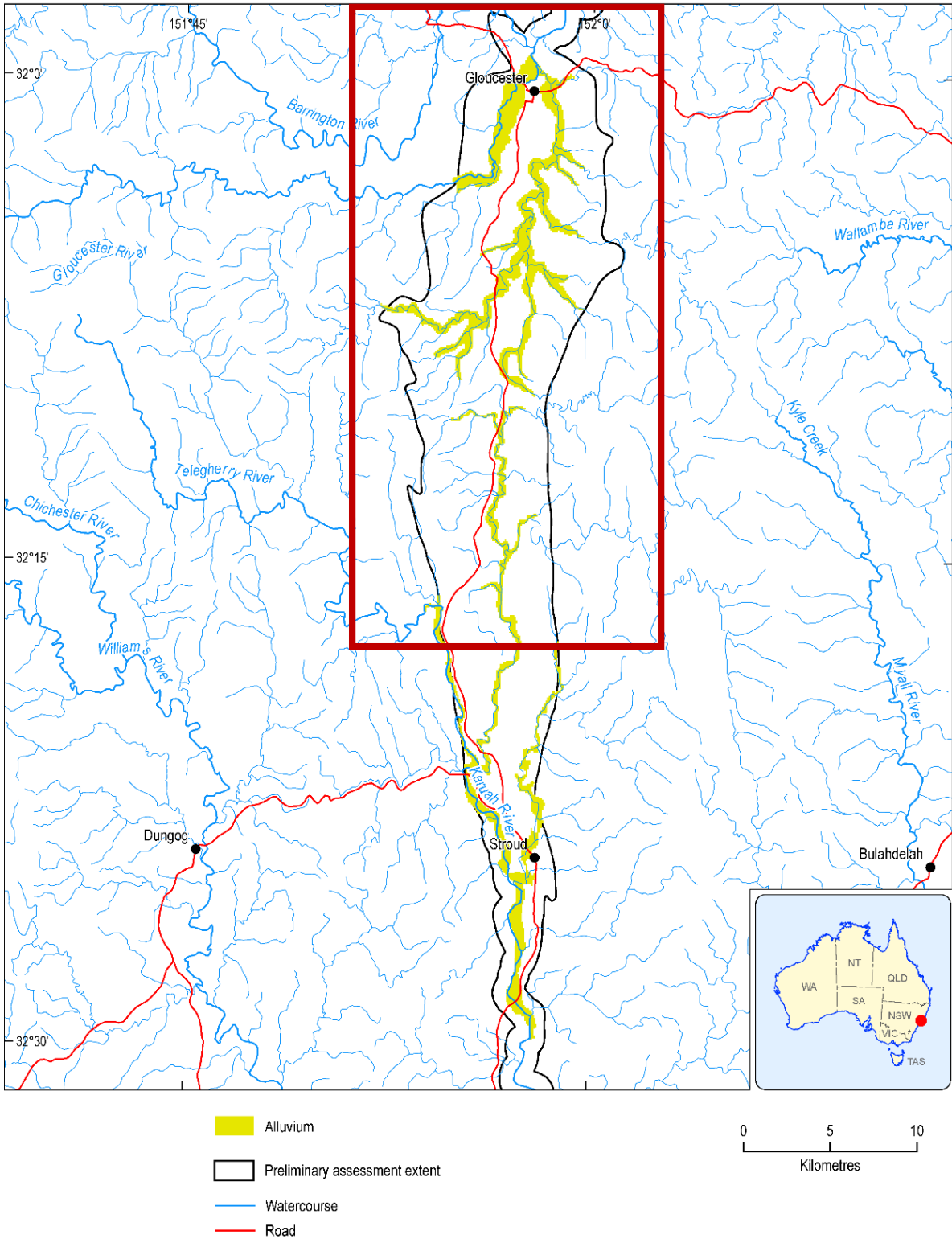


Figure 8-2 Alluvial model of the Gloucester Basin. Extent of the Gloucester basin model is indicated by the red box.

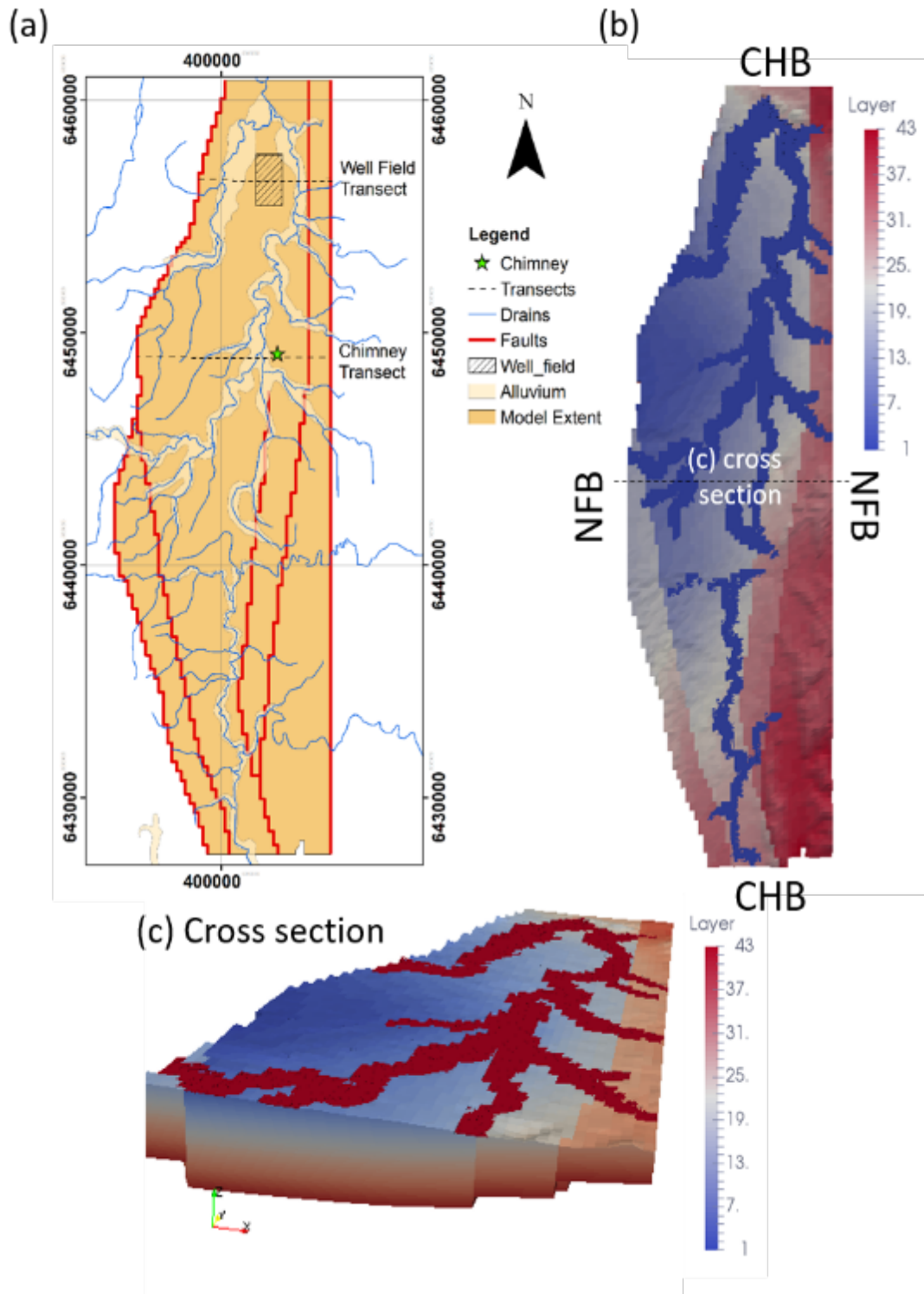


Figure 8-3 (a) Extent of the Gloucester numerical model showing the major faults (red lines), well field location (hashed box), and chimney location (green star). The alluvial aquifer (beige) and drains (blue lines) are also indicated. (b) Plan view with numerical layer numbers (variability in layer numbers at the surface is due to fault juxtaposition), with model boundary conditions also indicates (NFB: no flow boundary, and CHB: constant head boundary). (c) Cross-sectional view of the model (cross-section identified in (b)). Figure based on Fig 17 from McCallum et al. (2018).

8.2.1.3 Model Boundary Conditions

Constant head boundary conditions are imposed in the north and south of the Gloucester model and are based on land surface elevation (no groundwater data are available). The basin is bounded on the east and west by faults (Figure 6-2 and Figure 8-3a), therefore no flow boundaries are specified to the east and west of the model.

Recharge is included in this model, where the alluvial aquifer receives 80 mm/year and the fractured rock aquifer receives 2.5 mm/year (Parsons Brinckerhoff, 2012). Evaporation and transpiration were not explicitly considered in this investigation; it is assumed that recharge inherently accounts for these losses.

The model was run to steady-state, where the initial groundwater level was set to the surface elevation. A total of 58 stress periods was used in the transient simulation, capturing the production and post production period. In total the model contains 159,003 model cells, and takes 90 min to simulate a transient 127 year time period. The simulation period starts in 2018, ends in 2145 and is initialised with a steady-state stress period and followed by 126 transient stress periods; 42 annual stress, five 2-year stress periods, five 5-year stress periods and five 10-year stress periods. All stress periods have ten time steps.

8.2.2 Fault Implementation

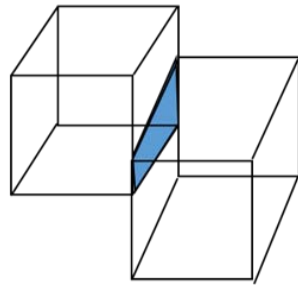
Faults are implemented in the model using a modified continuum approach for simplicity (based on McCallum et al., 2018

), whereby non-neighbour connections are identified for each of the faults (Figure 8-4(a)) to calculate the permeability of the opposite cell (Figure 8-4(b)) (see Figure 8-5). A ghost node is used to connect the adjacent cells. With the continuum approach both across-fault flow and up-fault flow can be simulated. The permeability of the fault is proportional to the fault throw (vertical offset), which is implemented in the model as a fault permeability multiplier which is used to modify the permeability of ghost connections within a fault:

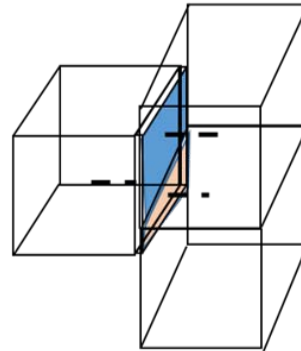
$$F_m = e^{\left(\frac{t_f}{t_{max}} \times \log(f)\right)} \quad (8-1)$$

where F_m is the fault permeability multiplier, t_f is the throw of a fault (vertical offset) at a given location (m), t_{max} is the maximum throw (vertical offset) within the model, and f is a factor chosen to represent a fault in dilation ($f = 1.0$) or compression ($f = 10^{-5}$). The storage coefficients are unaffected by the faulting, and remain constant (see section). This approach assumes that the fault permeability multiplier and throw vary exponentially to ensure proper representation of the full range in fault permeabilities (also see Manzocchi et al. 1999). Further work is required to investigate the relationship between fault throw and permeability.

(a) Connected cell areas



(b) Connect adjacent cells via ghost node



(c) continuum approach with up-fault flow through a series of connected thin 'fault cells'

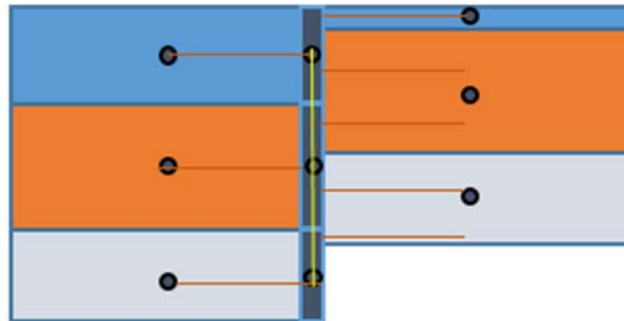


Figure 8-4 Implementation of the modified continuum method in MODFLOW-Unstructured Grid, based on McCallum et al. (2018).

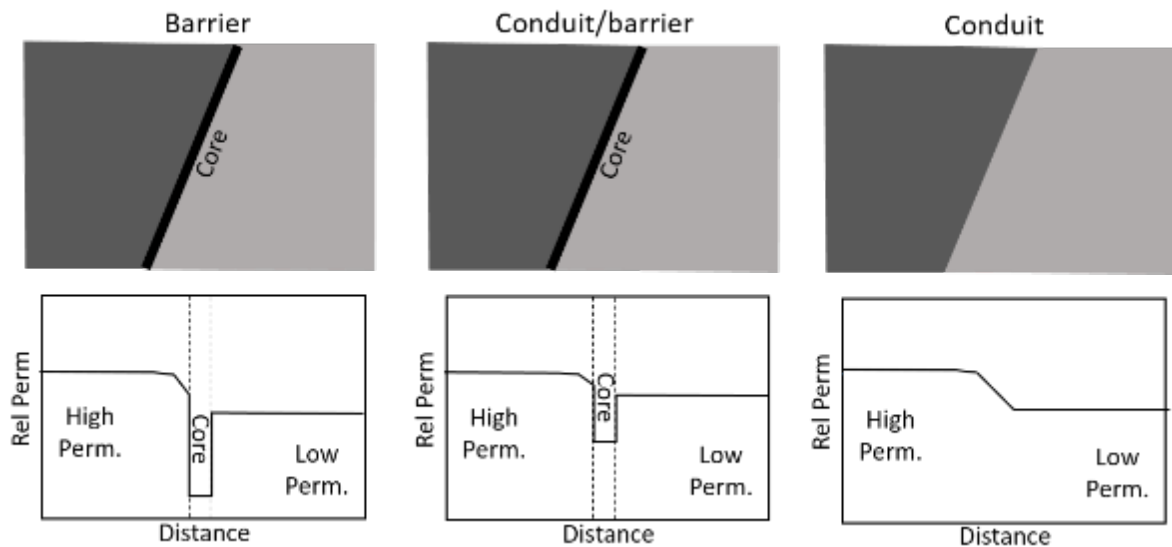


Figure 8-5 Conceptual model of fault relative permeability (Rel Perm) for different fault types. Based on Figure 4 McCallum et al. (2018).

Figure 8-6 shows how the throw of the fault affects the fault permeability multiplier F_m , where for $f = 1.0$ the properties of the fault do not influence across-fault flow such that the flow is only impacted by the properties of adjacent layers (Figure 8-5). Under these conditions, the fault can be assumed to be in dilation, i.e. it does not restrict groundwater flow. For $f = 10^{-3}$ and 10^{-5} , the impact of the fault throw is clearly visible: the greater the offset caused by faulting (t_f), the smaller the fault permeability multiplier F_m . For these scenarios, the reduction in F_m represents a reduction in the across-fault flow caused by the compaction of fine grains formed by movement during faulting. For example, assume the fault throw is 200 m, F_m is 0.1 (for $f = 10^{-5}$) or 0.3 (for $f = 10^{-3}$), and the model layers either side of the fault have a K of 10 m/d and 0.1 m/d, respectively. The fault conductance was calculated as the harmonic mean of the K values at either side of the fault multiplied by F_m . Based on a 200-m cell size, the harmonic mean is 0.2 m/d. Therefore, for $f = 10^{-3}$ the multiplier $F_m = 0.3$ and the fault conductance equals 0.2 m/d x 0.3 = 0.06 m/d. For $f = 10^{-5}$ the multiplier $F_m = 0.1$ and the fault conductance equals 0.2 m/d x 0.1 = 0.02 m/d.

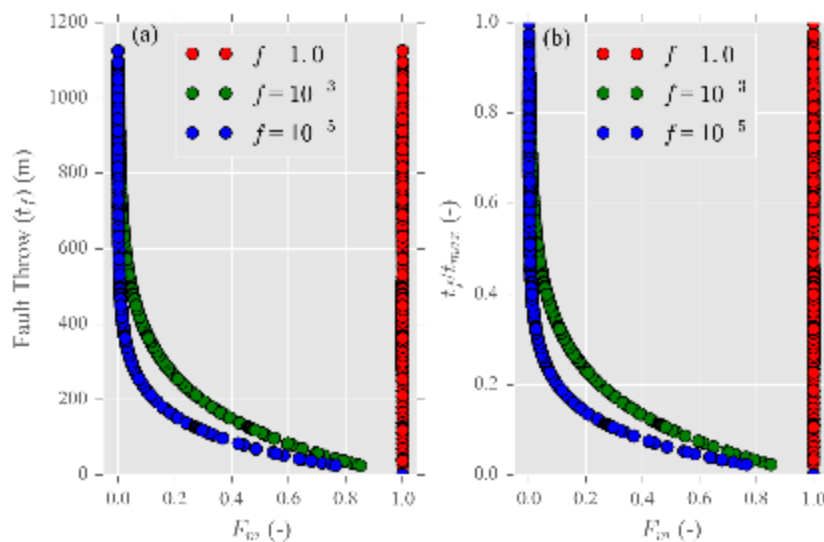


Figure 8-6 Relationship between the fault permeability multiplier and (a) fault throw (m) and (b) the throw ratio (throw/maximum throw).

8.2.3 CSG water production curves

The hypothetical scenarios investigated here first assume a natural system with faults which serves as a yardstick against which potential effects from stresses on the groundwater system associated with future CSG extraction in the Gloucester Basin (second set of scenarios) can be compared. The second set of scenarios investigated consider the drilling of 50 CSG wells (Figure 8-3 (a)), across a 1 km by 2 km area, in layer 21 (approx. 1,050 m below the model surface). The proposed production period and associated water extraction is shown in Figure 8-7. This scenario (P50) represents the median proposed pumping scenario for the coal seam gas extraction from Parsons Brinckerhoff (2013). The pumping scenario was implemented as a flux boundary condition.

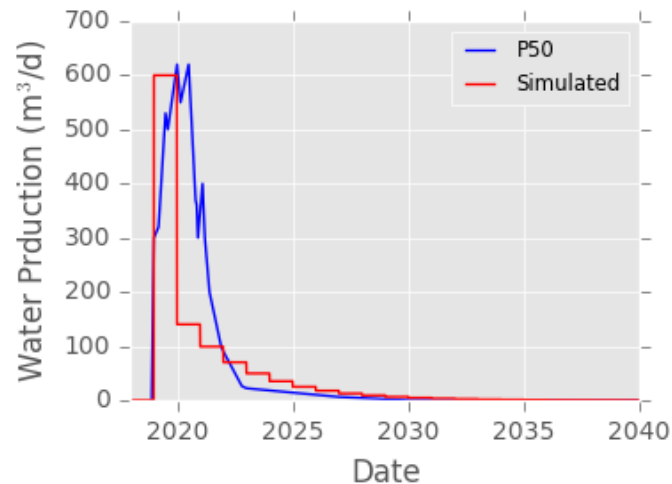


Figure 8-7 Total water production rate used for the P50 scenario (blue; Peeters et al. (In Prep)) and the MODFLOW-simulated water production rates (red).

8.2.4 Model Parameterisation

8.2.4.1 Workflow

As previously observed in McCallum et al. (2018), the facies model developed by Frery et al. (In Prep) overestimates the hydraulic properties of the Gloucester basin. Therefore, Drill Stem Tests (DST) permeability data obtained for isolated sections of wells, are combined with geostatistical techniques to better inform the modelled bulk (interburden and coal seam) permeability values. Figure 8-8 shows an outline of the workflow which leads to the generation of a 3D bulk permeability field which incorporates all 42 layers in the Gloucester model. The methods discussed in this section apply to the pre deformation 3D fields, for example see Figure 8-9 (a). Estimation of the bulk permeability involves the following steps:

- The **Permeability estimation** involves the DST data to determine the permeability-depth relationship for the coal seams, and re-introducing the observed variability in the coal seam permeability using geostatistical methods;
- The **Coal Seam Connectivity** used the geostatistical techniques presented in Zinn and Harvey (2003) to generate 3D fields of different coal seam connectivity; and
- The connectivity fields are then combined with the Coal fraction CDF data to generate 3D coal fraction domains as part of the **Bulk Permeability Estimation**. The 3D bulk permeability domain is generated by combining the 3D coal fraction domain and the depth-permeability relationships. The resultant 3D bulk permeability domains are then applied to the undeformed model (Figure 8-9 (a)), to which the major fault geometry are applied, deforming the model structure (e.g., Figure 8-9 (b)).

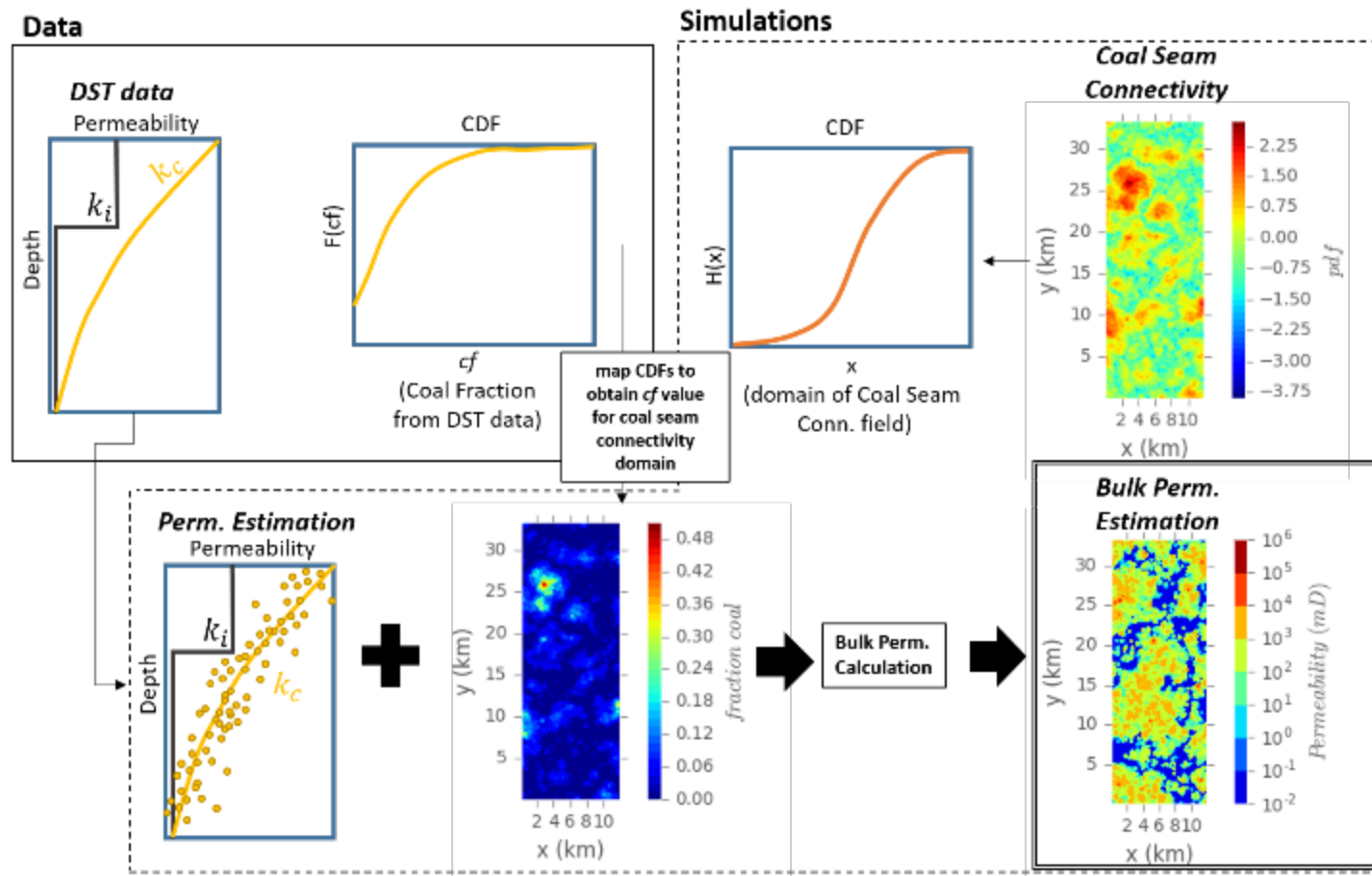


Figure 8-8 Workflow to generate a 3D bulk permeability field to inform model parameterisation. The data block shows the available drill stem test (DST) data used to determine the depth-permeability relationship for coal k_c and interburden k_i , and the cumulative distribution function (CDF) of the coal fraction data. The simulations block includes Gaussian simulations to generate variability in the coal seam permeability (Permeability Estimation) and spatial connectivity of the coal seams (Coal Seam Connectivity). The DST CDF and coal seam connectivity and fraction were used to estimate the bulk permeability (Bulk Permeability Estimation).

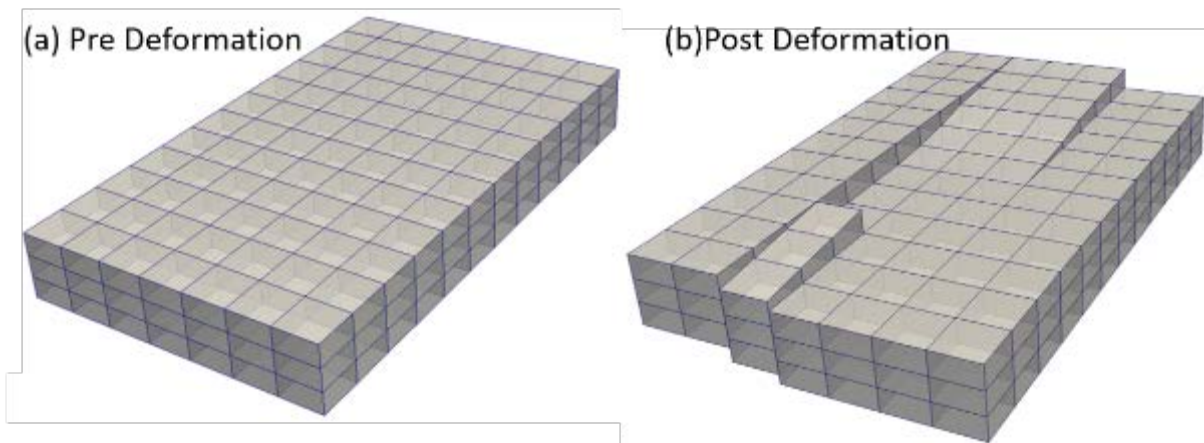


Figure 8-9 Schematic diagram showing a layered model structure (a) pre deformation and the faulted model structure post deformation (b). Figure based on Figure 13(b) in McCallum et al. (2018).

8.2.4.2 Permeability Estimation

The permeability of the Gloucester model was initially based on the sedimentary facies model of the Stratford area (Frery et al., In Prep). However, a major limitation of this data is that it does not account for secondary processes, including cementation of pore spaces, which would considerably affect the subsurface permeability. Secondary cementation within a formation would reduce its permeability, therefore introducing a significantly lower permeability compared to the facies model. Low permeabilities have been observed in core permeability estimates from the area (Parsons Brinckerhoff, 2015), confirming that the facies model would overestimate permeability.

The large-scale bulk permeability (k), required for the groundwater flow model, is comprised of the combined coal (k_c) and interburden (k_i) permeability. The porous and fractured nature of the coal seams results in preferential flow pathways that strongly influence the bulk permeability. To represent the bulk permeability with an acceptable level of accuracy, it is necessary to determine the permeability of the coal and interburden independently.

Drill Stem Test (DST) data provides an estimation of bulk permeability, pressure and productive capacity of an isolated section of the uncased bore. This data is available for a number of CSG exploration wells in the Waukivory area of the Gloucester basin (Figure 8-10).

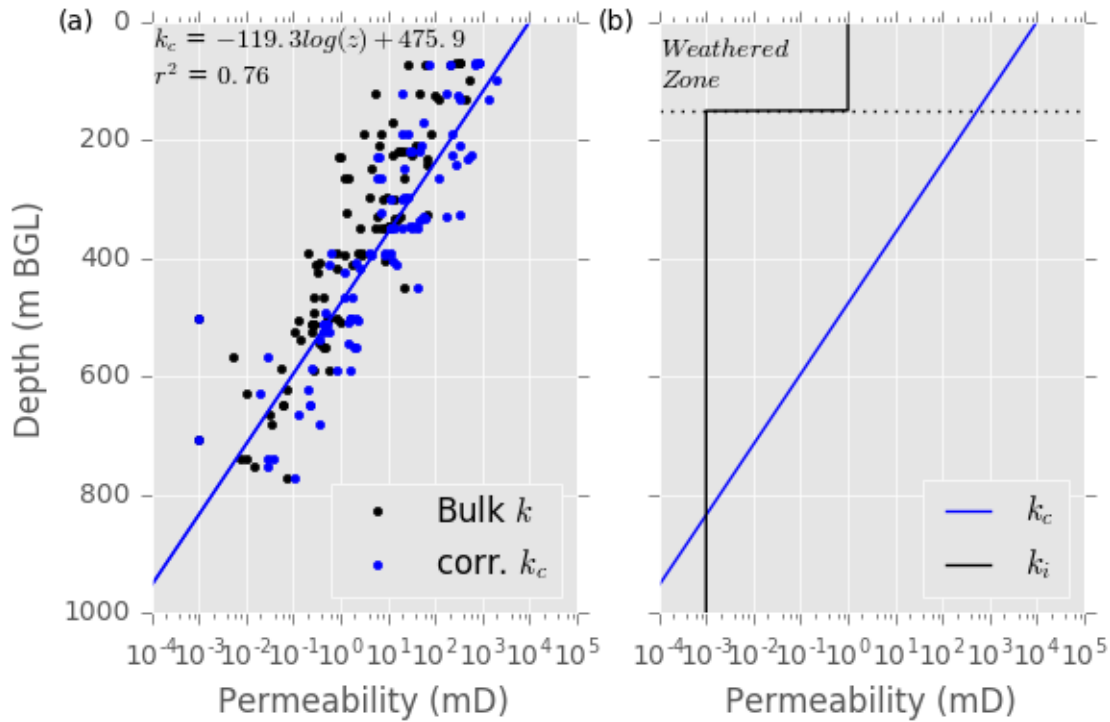


Figure 8-10 (a) Bulk permeability (k) data from Drill Stem Tests in the Waukivory area in the Gloucester Basin at various depths (black dots) and corrected coal seam DST permeability estimates (corr. k_c) based on the DST data for bulk permeability and coal seam fraction present for each data point. Blue line represents a log-linear regression of the corrected coal seam permeability estimates (equation and r^2 stated in the figure). (b) Simple model of permeability for the coal fraction (k_c : blue) and assumed interburden model (k_i : black). The dotted line indicates the base of the weathered zone.

As discussed above, the bulk permeability will be impacted by the presence of high permeability coal seams in the isolated section being tested. Where the isolated section contains a high proportion of coal, the permeability will be high by comparison to a section with a lower proportion of coal. Therefore, knowledge of the amount of coal present in the isolated section will allow the permeability of the coal seam to be estimated using the following equation:

$$k = f_c k_c + (1 - f_c) k_i \quad (8-2)$$

where k , k_c and k_i are the bulk, coal and interburden permeability respectively (mD), f_c and f_i (m/m) represent the fraction of coal and interburden length present in the isolated section, respectively. This equation assumes that the relationship between the bulk permeability k is the weighted arithmetic mean of the coal k_c and interburden permeability k_i . This provides an estimate of the horizontal permeability, while anisotropy is applied in the vertical direction to account for reduced vertical permeability at a ratio of 100:1 horizontal to vertical permeability. It should be noted that this data is mainly from CSG wells in high coal bearing areas. Therefore, the high permeability layers (coal) are likely overestimated compared to the low permeability layers (interburden), resulting in bulk permeability values that are biased towards the high end.

Figure 8-10 (a) shows the bulk permeability and coal seam permeability data based on a bimodal distribution of interburden permeability (Figure 8-10 (b)). No data are available regarding the hydraulic properties of the interburden material, therefore values of permeability were based on the rock composition and weathering (depth dependent). Parsons Brinckerhoff (2013) reported that the interburden is composed of indurated and cemented sandstone/siltstone and claystone. Its low permeability is associated with sparse fractures and which decrease with depth.

A weathered zone (labelled on Figure 8-10 (b)) is located from the surface to 150 m BGL. This high permeability layer is due to a high density of fracturing (irregular weathering and fault expressions near the surface). The hydraulic conductivity of the rock within the weathered zone (< 150 m BGL) ranges from 10 m/d – 10⁻⁶ m/d (~20 mD – 4x10⁻⁶ mD), the typical range in hydraulic conductivity is 10⁻³ – 10⁻⁴ m/d (~3x10⁻⁴ mD - 9x10⁻⁵ mD) (Parsons Brinckerhoff, 2013). For this investigation, the weathered zone only affects the interburden permeability because the estimated coal permeability is enhanced in this zone.

Figure 8-10 (b) shows the depth-dependent permeability relationships used to develop the groundwater flow model. However, the single log-linear relationship between depth and coal seam permeability produces only a single conductivity value at any given depth. In other words, the natural variability in the permeability is not reproduced. However, to produce a realistic groundwater flow field, it is necessary to account for the variability in coal permeability. To this end, the average of the depth de-trended coal permeability estimates was used to obtain an overall estimate of the variance ($\sigma^2 \ln K$) of the coal permeability. This approach assumes that the variance is uniform with depth. A Gaussian random field was then generated with the mean ($\ln K$) = 0.0 and the variance of the coal permeability ($\sigma^2 \ln K = 2.87$) using GSLIB software (Deutsch and Journel, 1992). The minimum possible correlation length of $\ln K$ was used to generate a random Gaussian field (Figure 8-11), i.e. 3 cells or nodes in all three directions x, y, and z. Given the horizontal cell size of 200x200 m, and a vertical cell size of 50 m, this was achieved by imposing a horizontal correlation length of 600 m and vertical correlation length of 150 m. This Gaussian field is then used to generate spatially heterogeneous coal permeability estimates using:

$$\ln(k_c) = (z - 492.76) / 57.51 + \sqrt{\sigma^2} \epsilon \quad (8-3)$$

where k_c is the coal permeability, z is the vertical depth (m), σ^2 is the variance of the log-permeability data (2.87), and ϵ is the value of a spatially correlated random variable with zero mean and unit variance. This presents an improvement over the simplified model obtained from Frery et al. (In Prep). Figure 8-12 shows the resulting 3D $\ln(k_c)$ domain which will then be used in the bulk permeability estimation.

Note that when a single stochastic heterogeneous domain is used for modelling, inference of statistical moments of the distribution of relevant variables requires a flow domain that is sufficiently large compared with the correlation scales of the pertinent formation properties. In addition, in order to preserve details of the spatial structure of the formation properties, the size of the numerical cells must be small compared with the characteristic

length scale of the heterogeneity of the relevant formation properties. Ababou (1988) and Ababou et al. (1989) suggested the following two criteria: i) the domain size should be at least 10 to 50 times the correlation length, and ii) at least four nodes or grid cells per correlation length. Based on these criteria, the current single Gaussian variance field was generated with parameters that are close to the recommended values from Ababou et al. (1989).

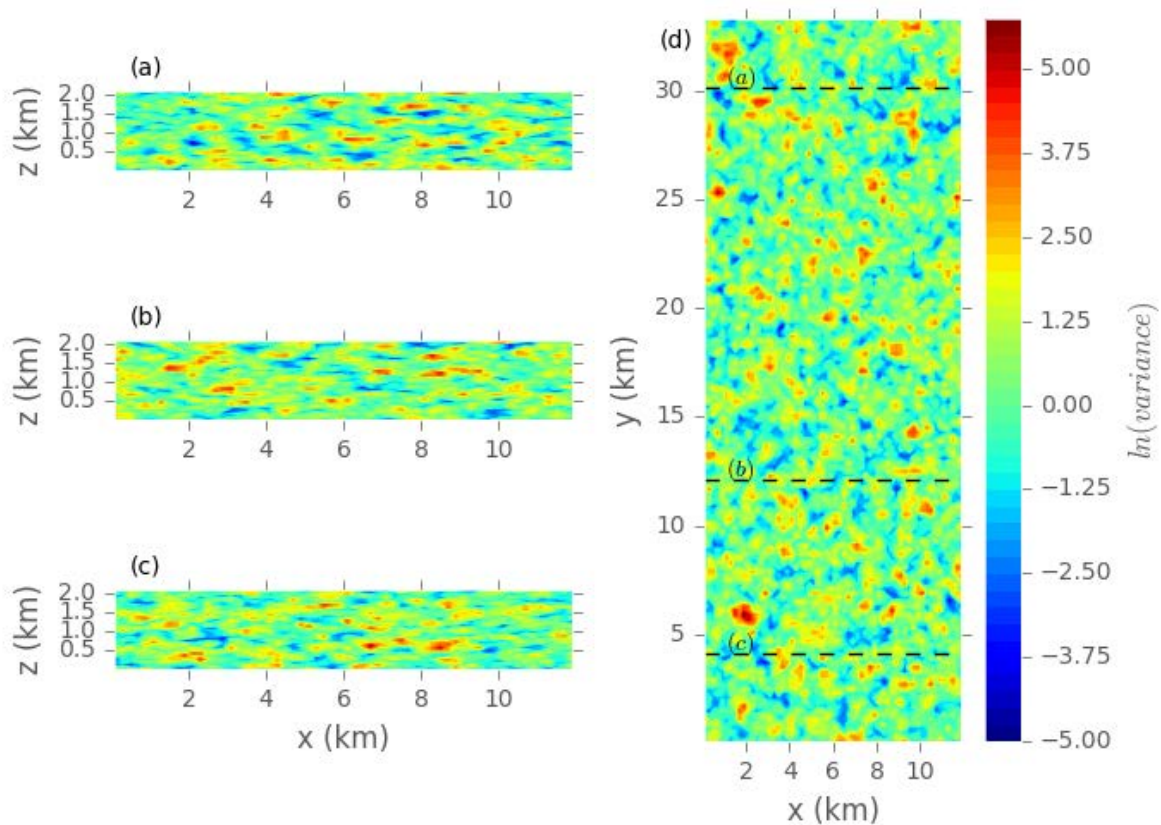


Figure 8-11 Images of the 3D Gaussian domain of spatially correlated values with a mean of zero and a variance of $\ln(\text{permeability})$ of 2.85 ($\sqrt{\sigma^2 \varepsilon}$ in Equation 8-3) determined from the Drill Stem data (where permeability is depth-detrended). Subplots (a) – (c) show vertical slices through the 3D domain at different locations (labelled on (d)). (d) shows a plan view of the 21st layer in the field.

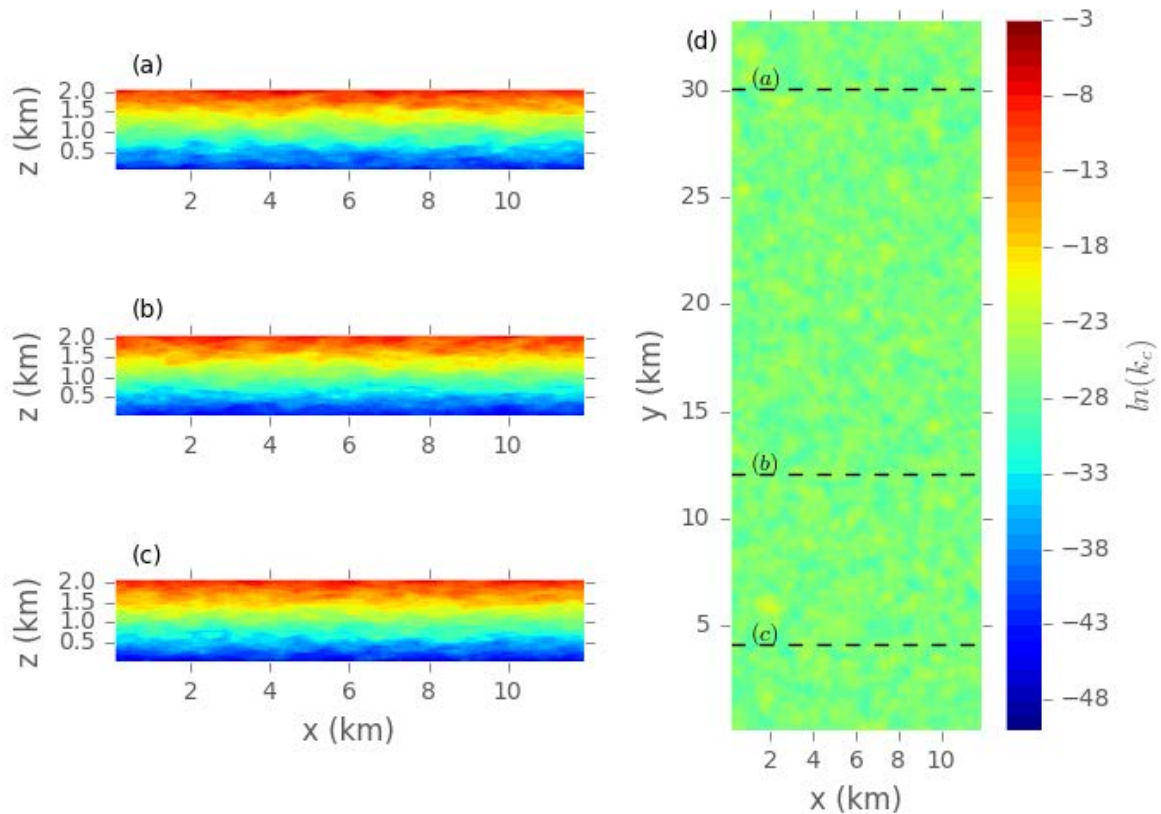


Figure 8-12 Image of the 3D natural log of the coal permeability ($\ln(k_c)$) based on the depth relationship (Equation 8-3) and the spatial variability depicted in Figure 8-11. Subplots (a) – (c) show vertical slices through the 3D domain at different locations (labelled on (d)). (d) shows a plan view of the 21st layer in the domain.

8.2.4.3 Coal seam connectivity

Figure 8-13 provides an example of the coal seams present in four CSG wells, located approximately 200 m apart. This figure clearly shows that interpolation of individual coal seams between adjacent wells is extremely challenging. It would appear from the logs of these wells that coal seams form spatially discrete bodies, however very little can be inferred with regard to their connectivity. In the absence of additional spatial information, generating synthetic domains of the different type of connectivity may provide insight into the effect of coal seams connectivity on the groundwater system.

Zinn and Harvey (2003) developed a method to generate domains where either high-conductivity structures could be connected or low-conductivity structure could be connected or disconnected, whilst maintaining the variogram of the original Gaussian field (see Figures 3 and 13 in Renard and Allard (2011) for discussion on connectivity structures):

$$Y' = \sqrt{2} \operatorname{erf}^{-1} \left(2 \operatorname{erf} \left(\frac{Y}{\sqrt{2}} \right) - 1 \right) \quad (8-4)$$

where Y' is the transformed value of the Gaussian simulated ($\ln(K)$) and Y are the original values ($Y = \ln(K)$). Equation 8-4 generates a domain where the low values are connected and

the high values form isolated patches (Zinn and Harvey, 2003). To generate the inverse of this domain, multiply Equation 8-4 by -1.

Based on the size of the model, grid cell size and to ensure that some level of connection/disconnection occurred, a correlation length of 10 km was used (no field data was available to inform this selection). One 3D domain of random values was generated using the following statistics: mean value of 0.0 (-), standard deviation of 1.0 (-), and a 10 km correlation length. The correlation length would ensure that the values within a range of 10 km would be more related to each other (similar) than values beyond a range of 10 km. The Zinn and Harvey (2003) method was then applied to the Gaussian field to create two end-member scenarios: connected coal seams and disconnected coal seams using Equation 8-4. The large correlation length applied in these Gaussian field ensured the generation of large channel structures in the modified fields. A disconnected domain is shown in Figure 8-14 and a connected domain is shown in Figure 8-15. The impact of coal seam connectivity on bulk permeability will be significant, and in the case of disconnected and isolated coal seams the permeability at a regional scale will be low. The impact of groundwater extraction in such a hydrogeological environment will be localised to the coal seam. Alternatively, the bulk permeability in a connected field will be high, leading to a greater regional impact of groundwater extraction.

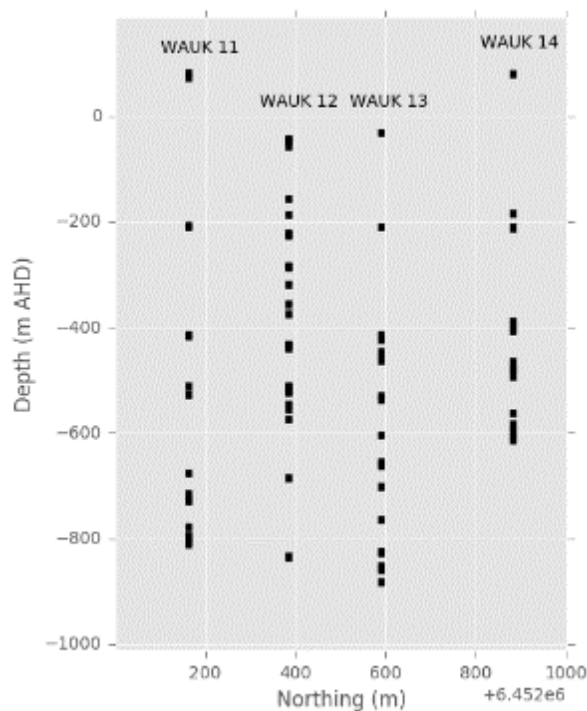


Figure 8-13 Location of coal seams in four CSG wells in the Waukivory (WAUK) area, Gloucester Basin. Black lines represent the location and depth of the coal seam.

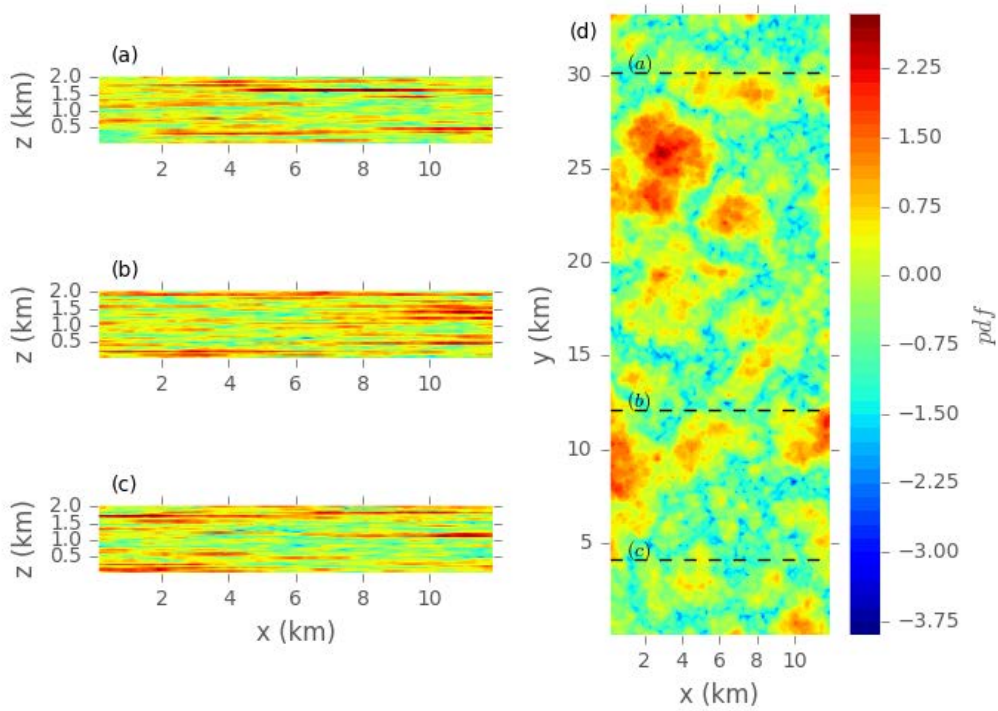


Figure 8-14 Images of the disconnected multi-Gaussian domain of spatially correlated random values with a mean of zero and a unit variance. Subplots (a) – (c) show vertical slices through the 3D domain at different locations (labelled on (d)). (d) shows a plan view of the 21st layer in the domain.

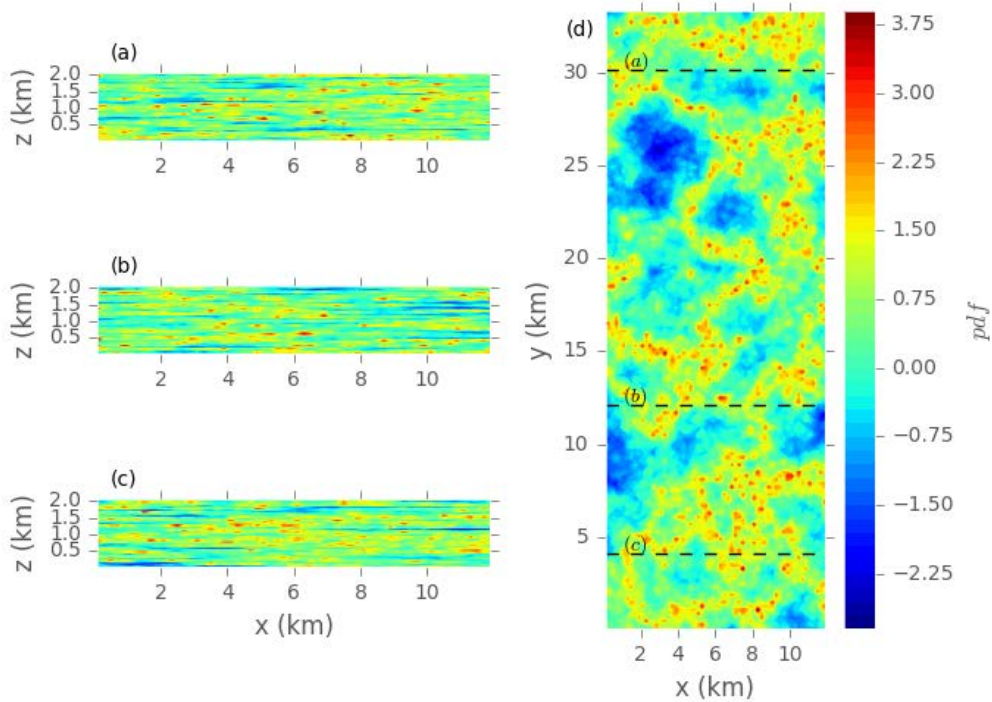


Figure 8-15 Images of the connected multi-Gaussian domain of spatially correlated random values with a mean of zero and a unit variance. Subplots (a) – (c) show vertical slices through the 3D domain at different locations (labelled on (d)). (d) Plan view of the 21st layer in the domain.

8.2.4.4 Bulk Permeability Estimation

The disconnected and connected Gaussian domains currently only provide information regarding connectivity, as such it is necessary to convert the domain from its current values to a more informative fraction of coal estimate. Well log data from 21 CSG exploration bores were used to quantify the fraction of coal present in 50-m sections (thickness of the model cells). The 50-m spacing enables DST data to be scaled from variable interval length to values appropriate for implementation in the model; these data are a subset of the raw DST data. Figure 8-16 shows the cumulative distribution function (CDF) of the coal fraction. Figure 8-16 clearly indicates that approximately 32% of all the 50-m sections did not contain any coal, and that about 90% contained less than 10% coal. The bias in the DST data is also noted: the average coal fraction from the DST data is 31.5% and therefore the likelihood of encountering this fraction of coal in the environment is about 1% (99th percentile).

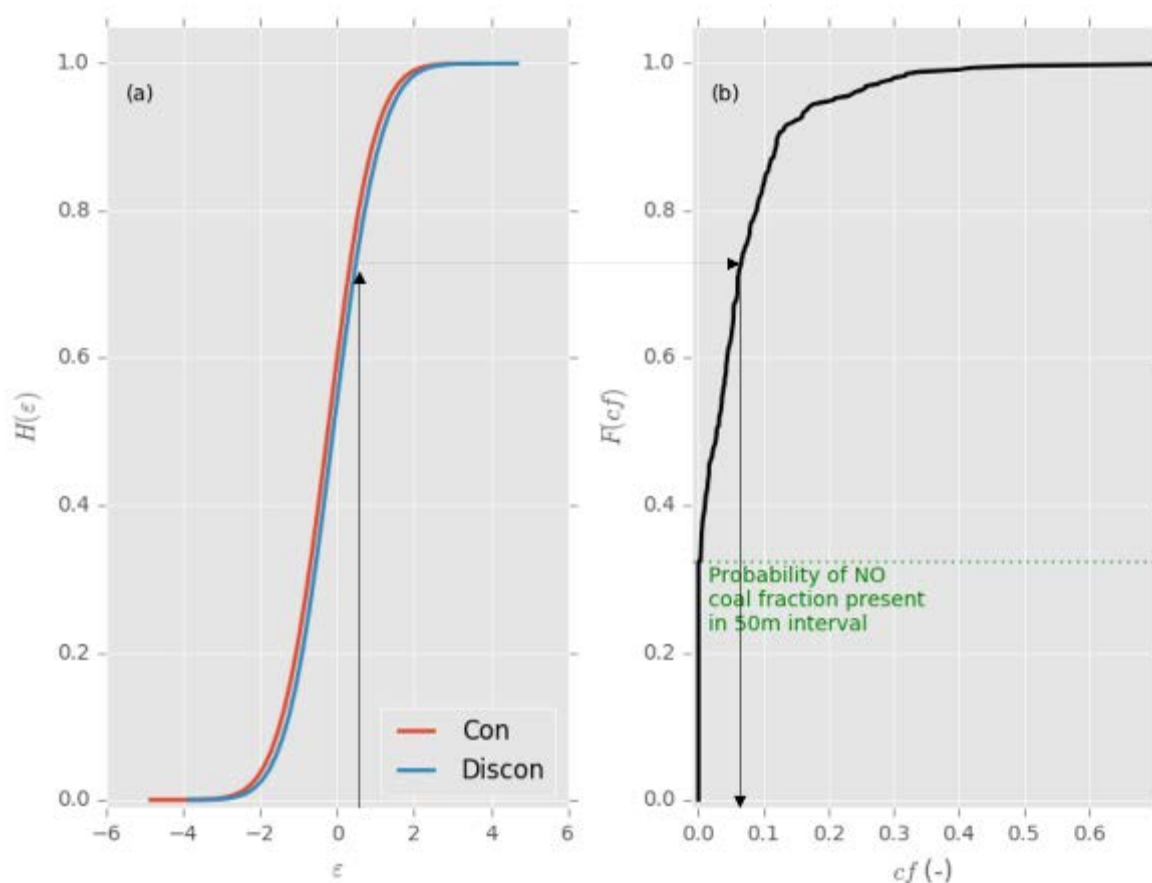


Figure 8-16 Cumulative Distribution function (CDF) of the (a) connected (Con) and disconnected (Discon) domain ($H(\epsilon)$) and (b) the coal fraction in the each of the Drill Stem Test data ($F(cf)$)(black line). The arrows indicate how a value of ϵ is mapped to a coal fraction.

To generate a field of the coal fraction, a normal score transform approach is used to map the connected and disconnected domains (Figure 8-14 and Figure 8-15) to the CDF of the coal fraction (Figure 8-16b). This means that each value (ϵ) in the connected and disconnected domain is a spatially correlated random variable, which relates to the CDF of the variable i.e., $H(\epsilon)$, see Figure 8-16(a). $H(\epsilon)$ can then be mapped to the CDF of the coal

fraction data ($F(cf)$, Figure 8-16(b)), and an estimate of the coal fraction is obtained for each value (ϵ) in the connected and disconnected domain. Figure 8-17 and Figure 8-18 show the results of the normal score transform i.e., fraction of coal present in the 3D domains.

The coal permeability (k_c) values in the 3D $\ln(k_c)$ domain (Figure 8-12) developed in the Permeability Estimation section are used in Equation 8-2 in combination with interburden permeability estimates in Figure 8-10 (b) to estimate the bulk permeability of the connected and disconnected domains .

The resulting bulk permeability (k) domain is implemented in the MODFLOW-USG model, which faults, erodes and deforms the layers in accordance with the geological structures in the Gloucester basin (see Figure 8-9 as an example). All bulk permeability values (k) were isotropic for the x and y direction ($k_x = k_y$), and anisotropic in the z direction $k_z = k_x/100$, the storativity (10^{-5}) of the model was constant across all layers. Peeters et al. (In Prep) discussed the importance of storage properties on drawdown prediction, however due to the lack of additional data and the primary focus of this study (i.e. impact of connectivity structures) storativity was kept constant. Future work is needed to obtain additional field data and investigate the impacts of both permeability and storativity upon drawdown predictions.

Figure 8-19 provides an example of the final model structure for connected and disconnected fields; the structural deformation has a clear impact on the continuity of high K zones laterally where the faults have introduced an offset between layers. Likewise, the reduction in K with depth is very apparent, only those layers within approximately 500 m of the surface have a higher K value. The range in hydraulic conductivities is 10 to 1×10^{-6} m/d.

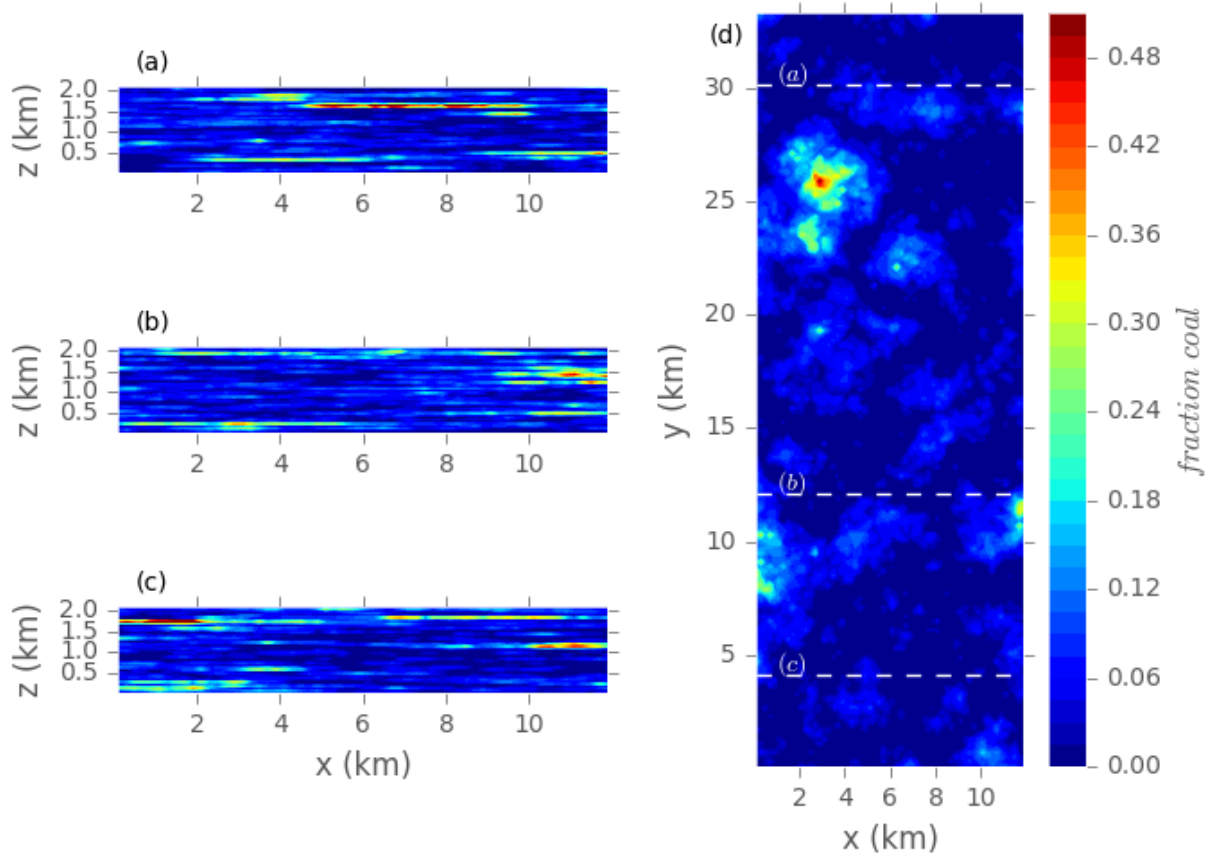


Figure 8-17 Images of the 3D coal fraction field, obtained by a normal-score transform of the potential coal connectivity (disconnected: Figure 8-14) and the likely coal fraction present (Figure 8-16). Subplots (a) – (c) show vertical slices through the 3D field at different locations (labelled on (d)). (d) shows a plan view of the 21st layer in the field.

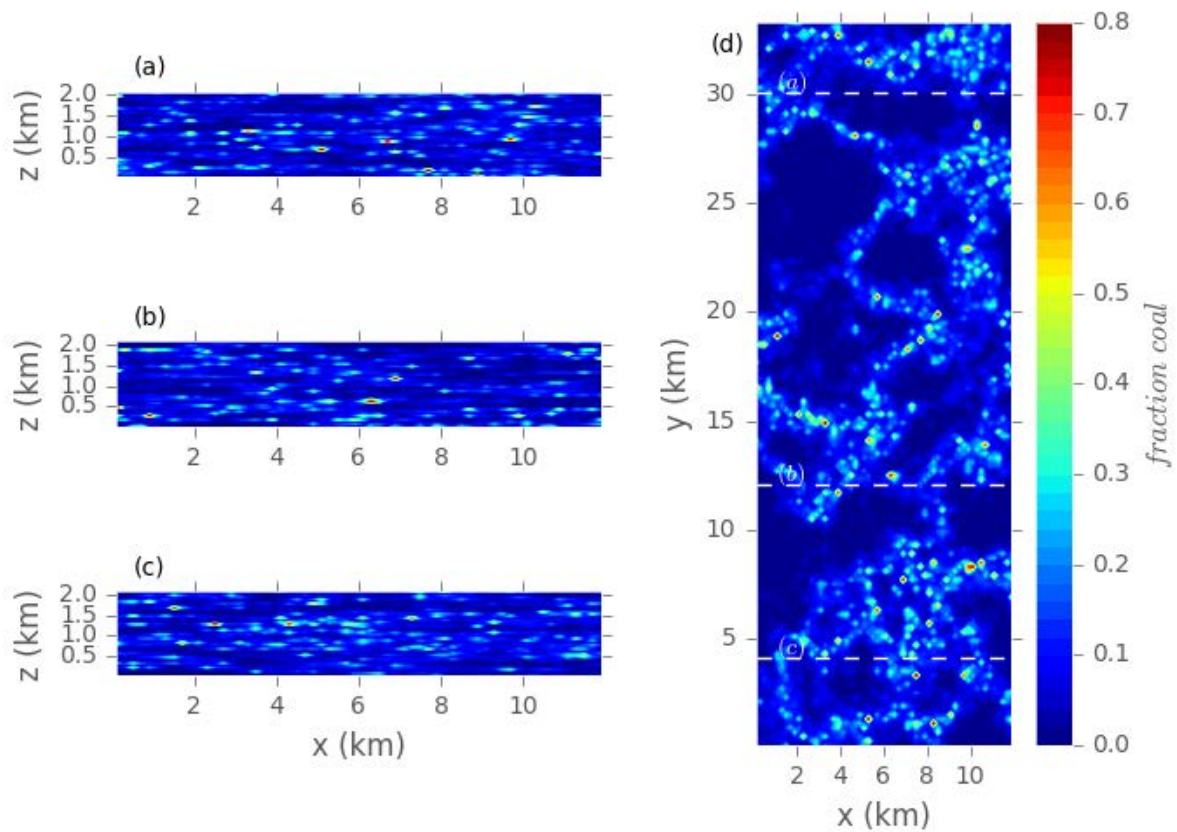


Figure 8-18 Images of the 3D coal fraction field, obtained by a normal-score transform of the potential coal connectivity (connected: Figure 8-15) and the likely coal fraction present (Figure 8-16). Subplots (a) – (c) show vertical slices through the 3D field at different locations (labelled on (d)). (d) shows a plan view of the 21st layer in the field.

The geostatistical approach presented here is provided as an example of how additional geological information can be incorporated into a numerical groundwater model. This is by no means an exhaustive investigation into this methodology. For future implementation we would make the following recommendations:

- Well log data: additional conditioning/training data will help generate a more realistic distribution of the coal seams (i.e., condition the Gaussian simulations); and
- Multiple realisations: multiple structures and realisations are necessary to sample a wider range of plausible outputs. Relying on a limited number of realisations can introduce bias in the simulated output. As such, it is recommended that at least 30 output permeability fields would be used.

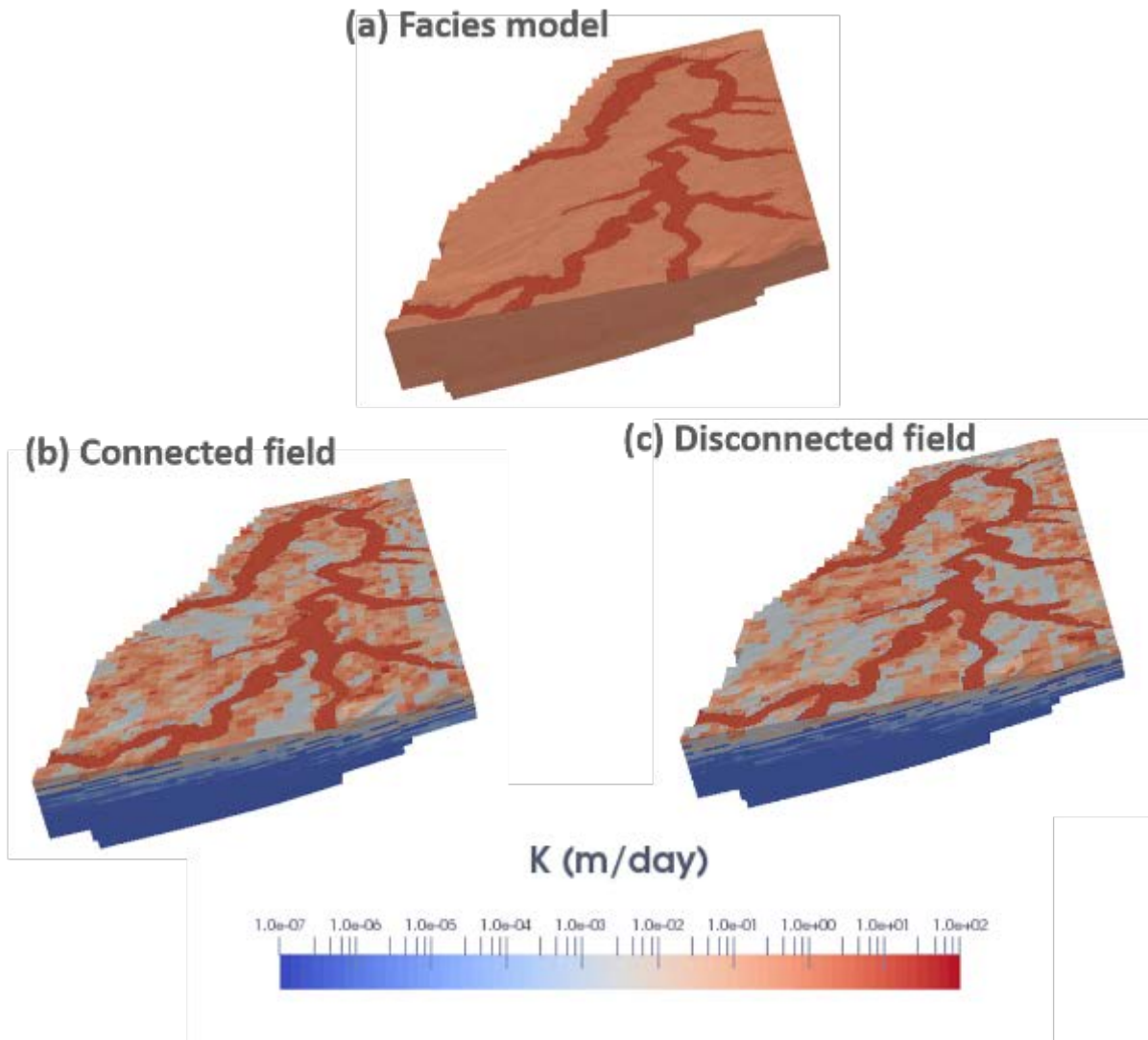


Figure 8-19 Comparison of the bulk hydraulic conductivity domains in the north of the Gloucester model for the (a) facies model, (b) connected K domain, and (c) disconnected K (m/day) domain. The red area (high K zone) is associated with the alluvial aquifer.

8.2.5 Additional fault features: Chimneys

TDS anomalies linked to fault structures have been discussed in Section 7. Such features have been related to the presence of multiple faults forming areas of fractured rock (i.e. the damaged zones associated with fault segments). These zones are slightly more permeable than the host rock and form conduits allowing water to migrate vertically between layers. Examples of such a TDS anomaly are present in the Gloucester Basin and are associated with a complex fault system. In other areas the Permian bedrock strata are fault segments that form barriers to flow with hydraulic head discontinuities across them. Both the flow enhancing and flow reducing features may be present at other locations within the basin; however, it is reasonable to assume that their impact on the groundwater flow system will strongly depend on how continuous they are. Ideally these features could be used to constrain fault properties.

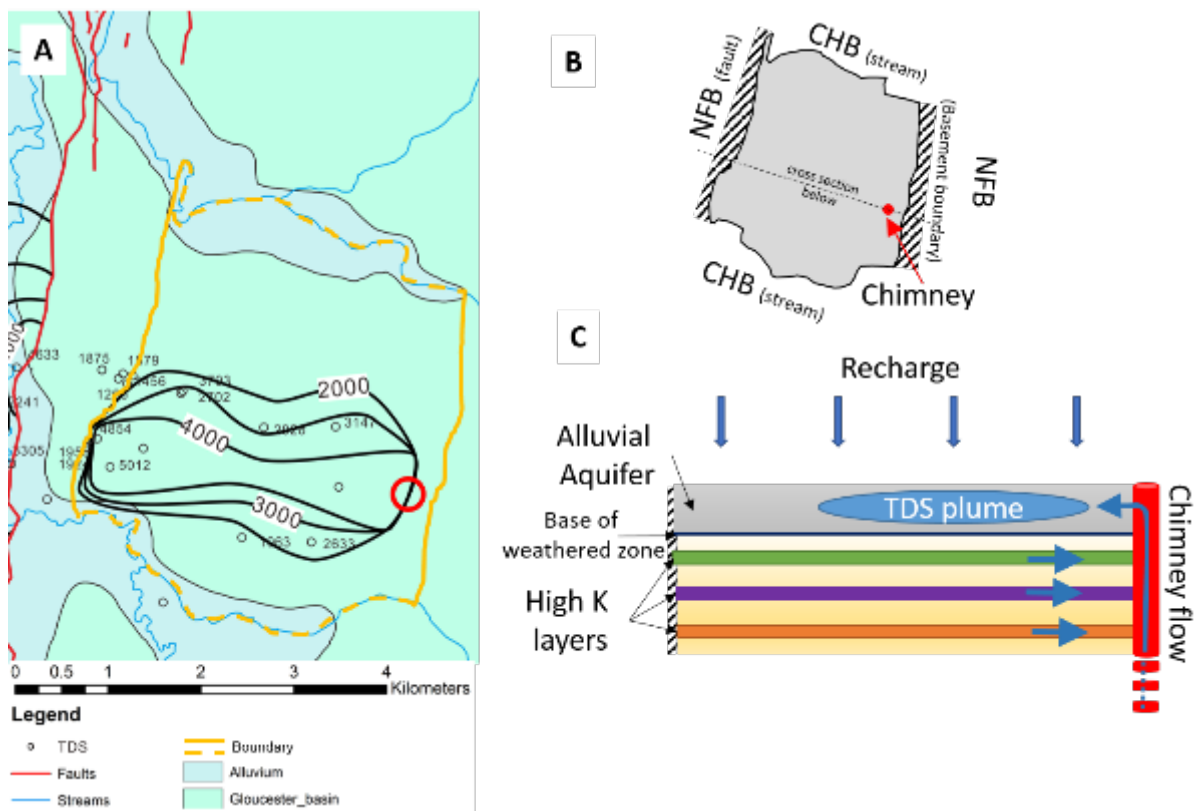


Figure 8-20 (A) TDS anomaly and the head boundaries used for the plume analysis, chimney location indicated by the red circle (based on Figure 7-14). Solid yellow lines represent the no-flow boundaries, and the dashed lines represent the constant head boundaries, and open black circles represent well locations. (B) Schematic diagram of the aquifer area used in the mass balance analysis showing the boundary conditions (NFB: no flow boundary and CHB: constant head boundary) and chimney location (red circle). (C) Schematic cross-section through (B) showing the chimney connectivity between high hydraulic conductivity layers at depth and the overlying alluvial aquifer/weathered zone.

A simple steady-state analytical mass balance approach was used to estimate the flux through the TDS anomaly in Figure 8-20 to better constrain fault hydraulic properties (for details see Appendix D). The TDS contours were used to determine the plume concentration through space, and provide additional information which will help constrain discharge through this fault feature. The TDS plume is located within the surficial alluvial aquifer, which sits within a high conductivity weathered system (weathered zone). Streams to the north and south of the plume provided constant head boundary conditions, and the fault to the west and catchment boundary to the east provided no-flow boundaries (Figure 8-20).

8.2.6 Implementing chimneys in MODFLOW

The chimney features can be conceptualised using the Connected Linear Network (CLN) package from MODFLOW-USG (Panday et al., 2015). The advantage of the CLN package is that it simulates flow through conduits without requiring grid refinement. They were used

previously to represent extraction wells by Doble et al. (2018) and Noorduijn et al. (2018). In this investigation, they are used to simulate the flow through conduits/chimneys associated with faulting. This is achieved by connecting a string of CLN nodes between adjacent layers/model cells, which allow passive flow between the CLN nodes. The flow rate through the string of CLN nodes is controlled by their effective hydraulic conductivity (K_{eff}) and head gradient along the conduit, and the resistance to flow between the conduit-aquifer matrix interface, and through the aquifer matrix (Panday et al., 2015). Figure 8-21 shows the geologic conceptual model of a chimney conduit and how it is conceptualised in the numerical model. The initial numerical model only included the large basin forming faults, while the small faults, fault zones and chimney type structures are not included. As a result, no offset in model layers is simulated at the chimney locations.

Table 8-1 Chimney CLN parameters.

PARAMETER	CHIMNEY
Length of chimney (m)	1262.5
Chimney radius (m)	10.0
Effective conductivity (m/d)	0.01
Skin factor (-)	-

Implementation of the chimney into MODFLOW-USG is constrained to the cylindrical form shown in Figure 8-21(b). The numerical model requires an estimate of the effective hydraulic conductivity of the CLN, which can be estimated by rearranging the equation for flow through a cylinder (assuming steady-state flow and a vertical gradient $i = 1$ within the chimney):

$$K_{eff}i = \frac{Q_{ch}}{\pi r^2} \quad (8-5)$$

where K_{eff} is the effective hydraulic conductivity of the cylinder (m/year), Q_{ch} is the flux through the chimney ($m^3/year$), and r is the radius of the cylinder (m). Estimates of Q_{ch} obtained in Appendix D were substituted in Equation 8-5, together with a radius r of 10 m, to arrive at an estimated K_{eff} of 10 m/year (approximately 0.01 m/day). The selection of the chimney radius to derive K_{eff} is rather arbitrary, while the estimation of Q_{ch} is based on previously an a estimated recharge of 5 mm/year (Parsons Brinckerhoff, 2012; 2013)

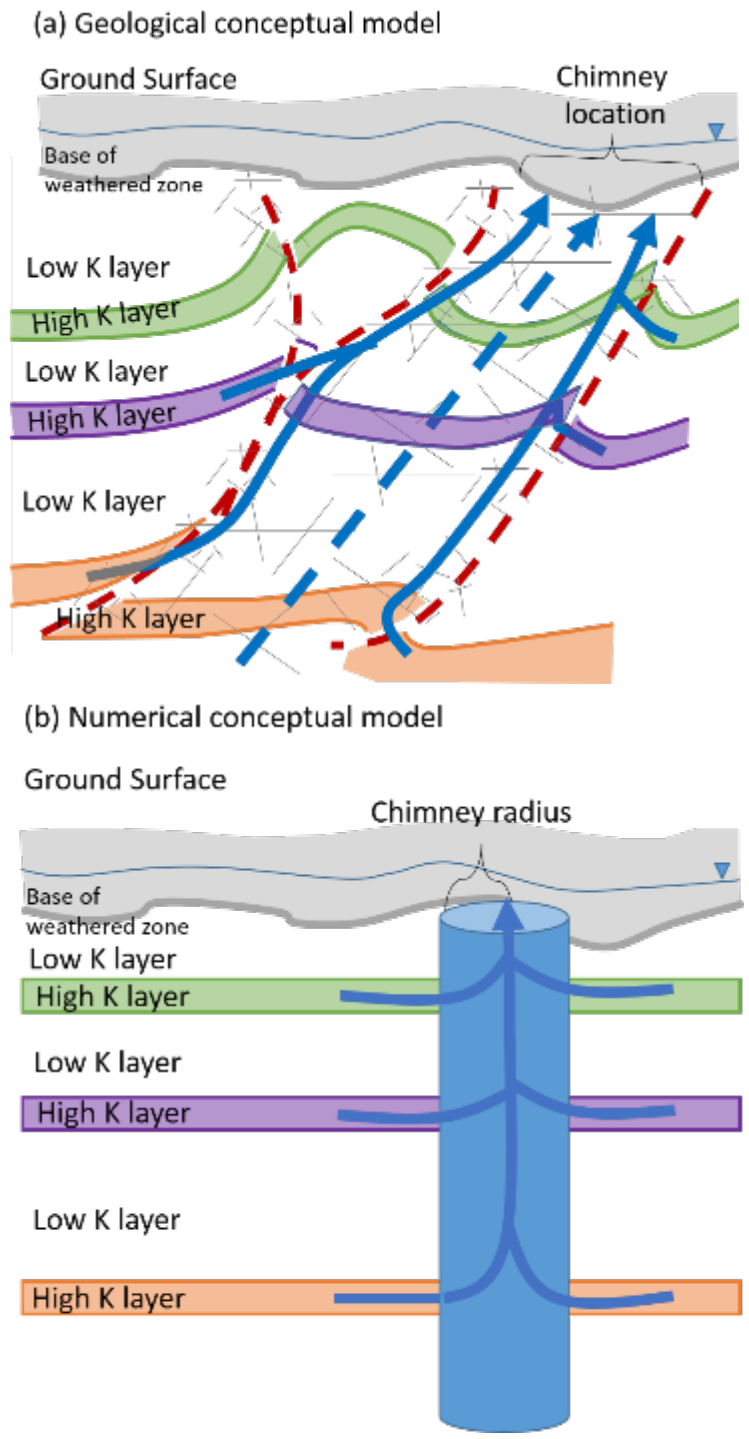


Figure 8-21 (a) Schematic geological cross-section through a chimney conduit showing the faults (red dashed line) and layer deformation and offset. The grey lines indicate areas of enhanced flow due to brecciation process during faulting. The grey area represents the alluvial aquifer and weathered zone, the groundwater table is shown (thin blue line and triangle). The approximate location of the chimney is indicated. (b) Conceptual representation of the chimney as implemented in the numerical model. The blue cylinder represents the chimney conduit, which receives groundwater from the high hydraulic conductivity aquifers (labelled). The radius of the conduit and its hydraulic conductivity are required as inputs.

The impacts of chimneys on the groundwater system is likely to be reasonably localised, as indicated by the spatial extent of the TDS plume in Figure 8-20. Based on the mass balance outlined above, a reasonable assessment of the chimney geometry has been obtained. The structural geology associated with the formation of chimney type features may be more extensive than is represented by a single chimney. We address this by simulating a cluster of 5 chimneys within a 600 m by 600 m area (1 CLN per grid cell), as shown in Figure 8-22 (b). The location of the chimneys is shown in Figure 8-20(a).

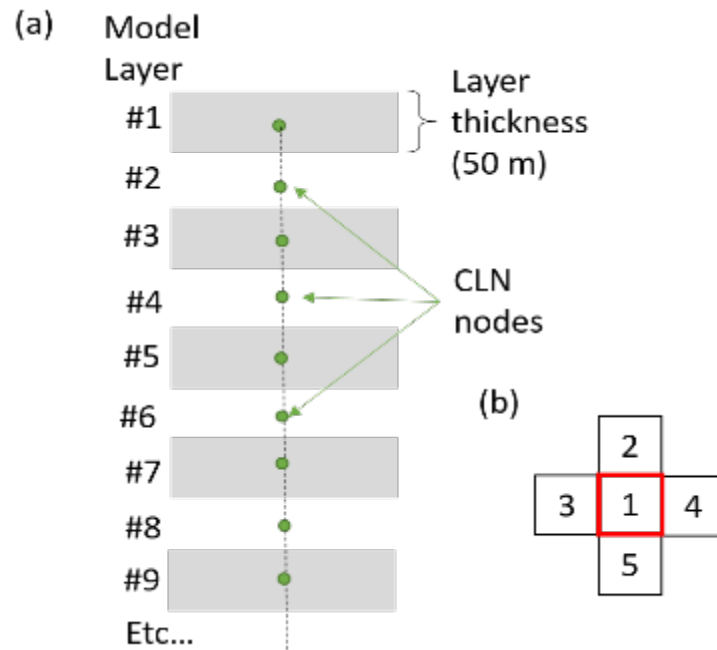


Figure 8-22 Connected Linear Network configuration for the single CLN chimney simulation showing the CLN nodes (green) and the connection between layers, (b) plan view of the CLN for a single chimney (CLN # 1: red square) and the cluster of five chimneys (5 CLN: red and black squares) simulations.

Figure 8-23 shows the variability in bulk hydraulic conductivities (K) intercepted by the CLN string. As mentioned previously, the impact of a chimney will depend on the permeability of the underlying geology (background rock permeability). Figure 8-23 shows that for both the connected and disconnected simulations, the CLN is located in a highly variable K field, but that this variability decreases with depth. At depths greater than -800 m AHD, there is minimal variability in bulk K (see Figure 8-24). Figure 8-24 also highlights this depth relationship, and clearly shows the difference in connectivity between the high and low K zones between the two simulations.

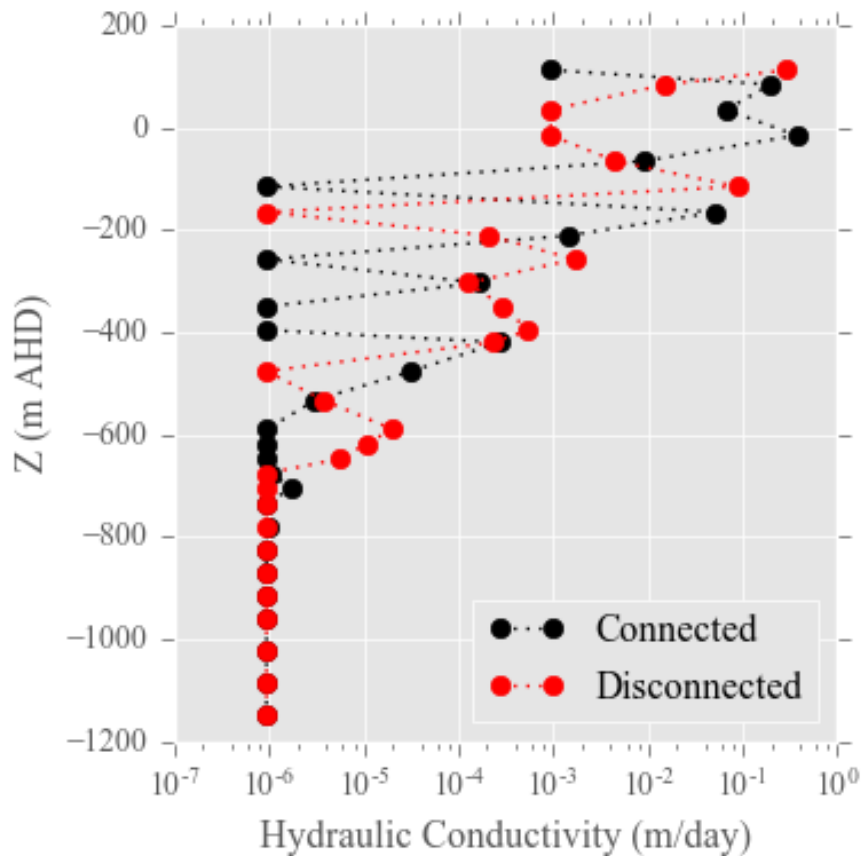


Figure 8-23 Hydraulic conductivity of the groundwater nodes connected to the CLN chimney (single CLN) for the connected (black) and disconnected (red) simulations.

8.2.7 Modelling scenarios

The impact of both the faults and the chimney structures on the groundwater and surface water flow system will be examined for the following scenarios:

- 1) Influence of the fault characteristic (i.e. low, medium, and high permeability) upon groundwater head; and
- 2) Influence of coal seam connectivity on the groundwater flow and quality.

The impact of faults upon the groundwater flow system has already been investigated by McCallum et al. (2018) for some hypothetical fault types and characteristics. The current modelling investigation will examine the impact of aquifer and fault properties specific for the Gloucester Basin on the groundwater system. Therefore, multiple scenarios will be run in which the fault type is varied between a barrier fault (i.e., a fault in compression) and a conduit fault (i.e., a fault in dilation). Three levels of fault permeability were derived to allow for various (low, medium and high) across-fault flow scenarios. The following values for the factor f (see Equation 8-1) were used for the different scenarios (see section 8.2.1 and Equation 8-1 for further details): $f = 1$ (fault in dilation; maximum across-fault flow), $f = 0.01$

(medium across-fault flow) and $f = 0.00001$ (fault in compression; low across-fault flow). In addition to fault type we also vary the degree of coal seam connectivity, i.e. connected or disconnected (see section 8.2.4.3 for details). The hydraulic head and drawdown are shown as an indication of the impacts of production for the different K fields (connected and disconnected) and fault properties on the groundwater flow.

The influence of chimney flow on the groundwater system is likely to be reasonably localised, as indicated by the spatial extent of the TDS plume in Figure 8-20. However, the impact of CSG production may extend to influence chimney flow. As such, chimney features are incorporated into the numerical groundwater flow model. Furthermore, the structural geology associated with the formation of chimney type features may be more extensive than is represented by a single chimney. We address this by simulating a cluster of 5 chimneys within a 600 m by 600 m area (1 CLN per grid cell), as shown in Figure 8-22 in addition to a single chimney feature. The location of the chimneys is shown in Figure 8-20(a).

Table 8-2 Outline of the simulations using the different fault configurations, geostatistical permeability fields and the number of Connected Linear Networks (chimneys) in the model.

Effect of fault permeability	Effect of connectivity within coal formations	
	Connected coal seam	Disconnected coal seam
Fault: low across-fault permeability	Scenario 1: 1 CLN	Scenario 2: 1 CLN
Fault: medium across-fault permeability	Scenario 3a: 1 CLN	Scenario 4a: 1 CLN
	Scenario 3b: 5 CLN	Scenario 4b: 5 CLN
Fault: high across-fault permeability	Scenario 5: 1 CLN	Scenario 6: 1 CLN

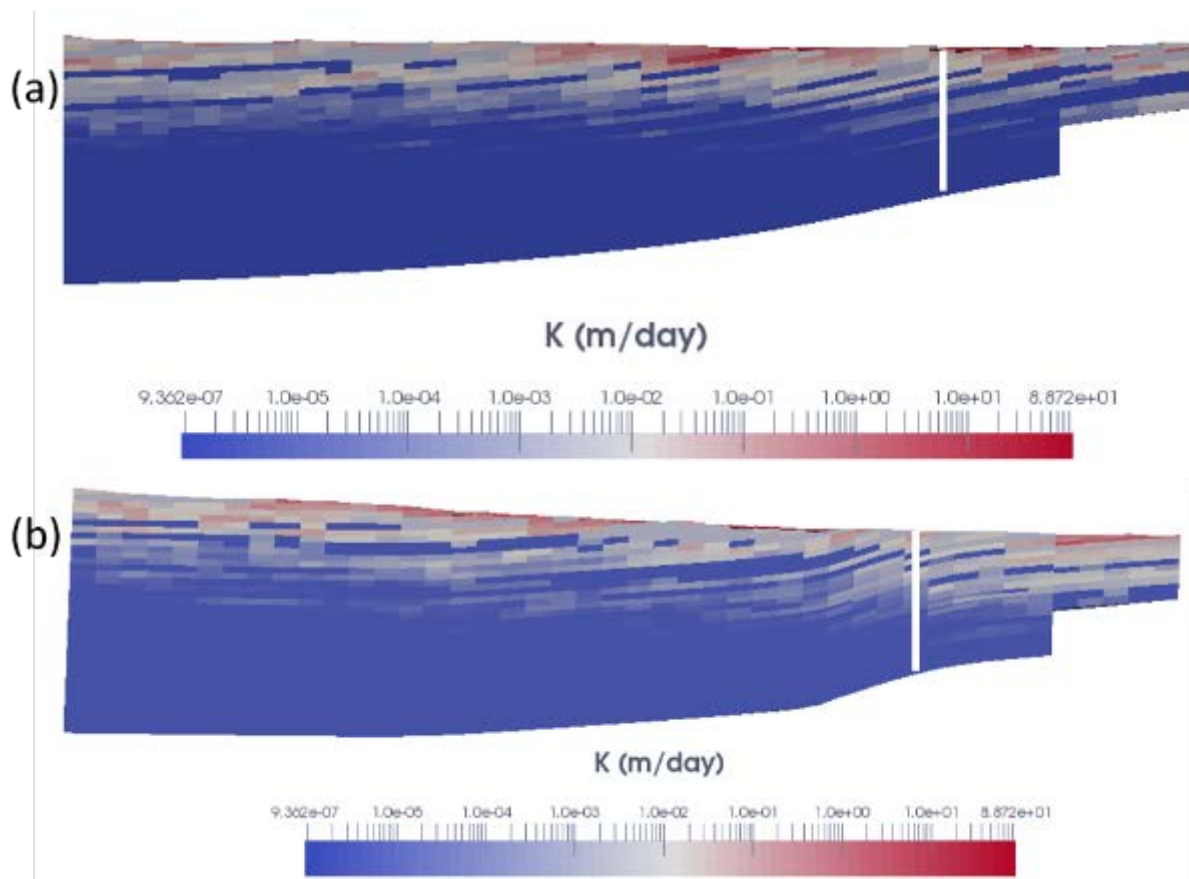


Figure 8-24 Cross-sections for the connected (a) and disconnected (b) models, and the location of the chimney (white line).

The simulation was run to steady-state prior to the commencement of pumping. Figure 8-25 shows the steady-state hydraulic heads for the connected conduit/barrier simulation (for details about the conduit/barrier conceptual model, see McCallum et al., 2018). The geological features rather than the hydrology define the basin. Hence, the presence of a flow divide along the centre of the basin. Groundwater and surface water flow to the north and south depending on the location relative to the divide. The hypothesized CSG production and TDS anomalies are located in the north of the basin; therefore, the focus of this work will be in this area (see Figure 8-20).

8.3 Simulated groundwater response

Simulated groundwater model responses are reported in the following order. First, the natural unperturbed system will be discussed which serves as a reference case against which to compare the effects of depressurisation in the presence of faults. Then groundwater system will be put under a stress by imposing the CSG water production curves shown in Figure 8-7.

Both the natural (steady-state) and stressed system will compare the following simulation cases, for both connected and disconnected coal seams:

- an aquifer where faults have a minimal impact on the flow system (i.e. the high across-fault flow where the fault has a high permeability);
- an aquifer with faults that exhibit medium (fault has a medium permeability) and low (fault has a low permeability) across-fault flow;
- an aquifer with faults that exhibit high across-flow in presence of a chimney; and
- an aquifer with faults that exhibit medium and low across-fault flow in presence of a chimney.

8.3.1 Groundwater flow for a natural system

The sensitivity of a natural groundwater system is discussed for both a connected and disconnected system. The steady-state solution of the high across-fault flow model is taken as the reference, as this is the condition where the fault has the least effect on the groundwater flow. Subsequent results are then shown for the medium and low across-fault flow models.

8.3.1.1 Connected model simulations

Simulated steady-state groundwater heads are shown for a high, medium, and low permeability fault in Figure 8-25. The high permeability fault has a permeability nearly identical to that of the host rock at both sides of the fault, therefore the impact on the groundwater flow and head distribution is negligible. This case is the reference for comparison with subsequent model runs. As the fault permeability decreases, the effect on heads becomes evident with a sharp head contrast developing across the fault (Figure 8-25 (b) and (c)). Under the conditions of connected K fields, this head build-up will relatively quickly dissipate in the directions along the fault. The effect of such faults on groundwater flow is further shown in Figure 8-26. The hydraulic head contours for the high permeability fault (Figure 8-26(a)) show that the fault has a negligible impact on flow field. The influence of the fault on the head contours becomes more apparent in the medium (Figure 8-26(b)) and low (Figure 8-26(c)) scenarios, with a sharp contrast in head levels either side of the fault.

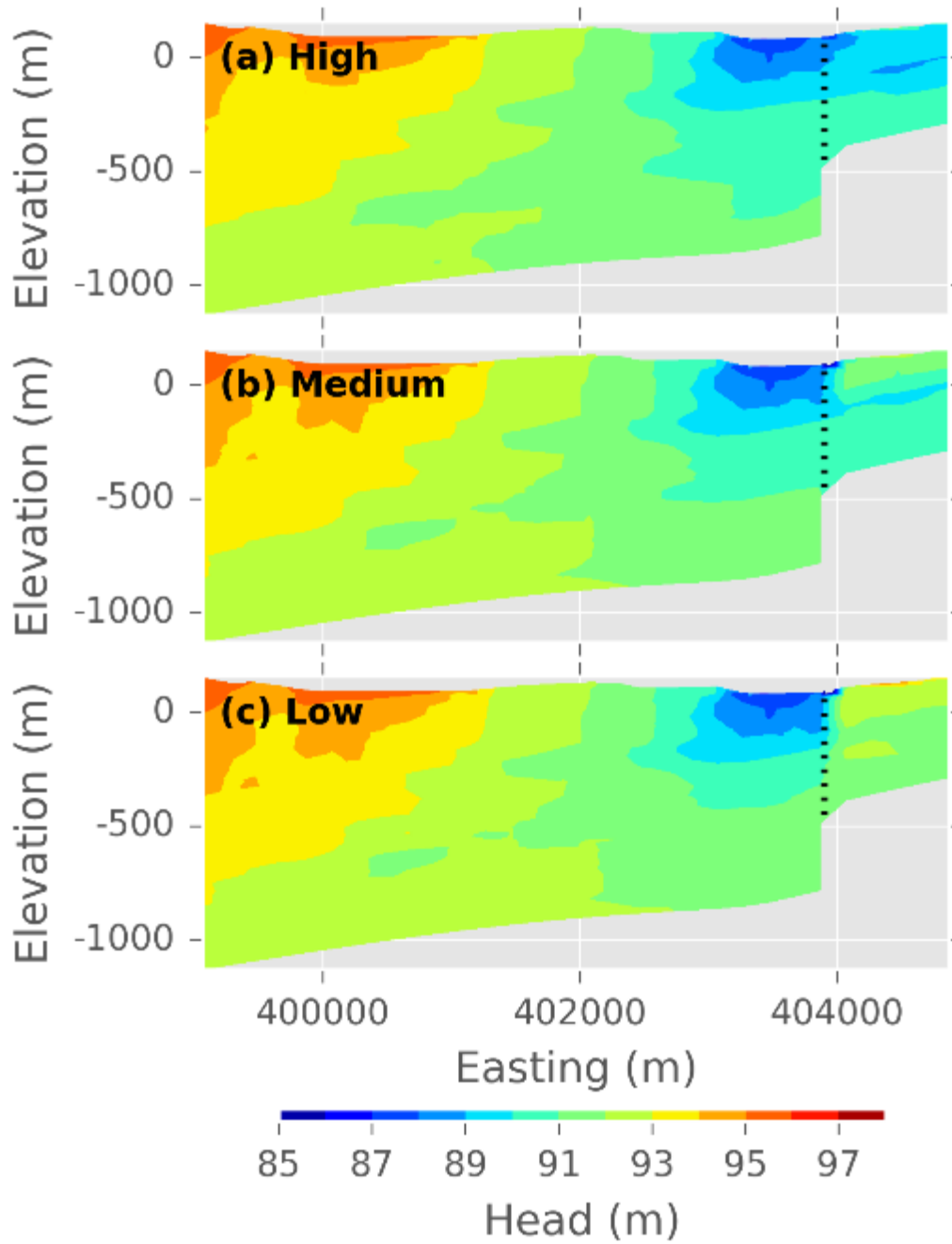


Figure 8-25 Cross-sectional view of steady-state head distribution for a connected model for (a) high permeability fault, (b) medium permeability fault, and (c) low permeability fault. Dotted line indicates the main fault location. See Figure 8-3 for cross-section location.

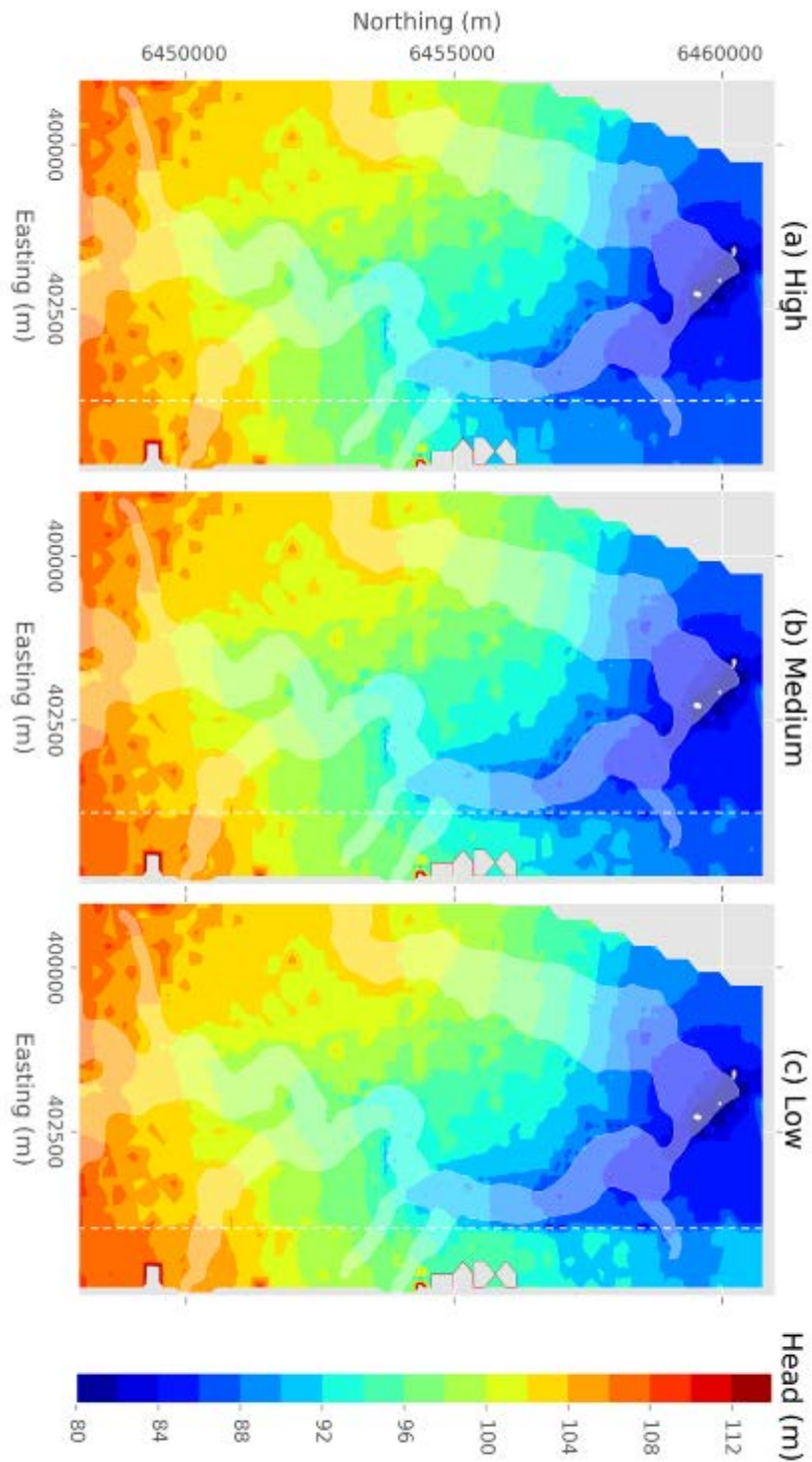


Figure 8-26 Plan view of the surficial hydraulic head contours in the north of the Gloucester model for the connected model and (a) high permeability fault, (b) medium permeability fault, and (c) low permeability fault. The alluvial aquifer is identified by the transparent white area. Grey areas within the model area indicate model cells whose hydraulic head are outside of the range depicted here.

8.3.1.2 Disconnected model simulations

Simulated steady-state groundwater heads for the disconnected models are shown for a high, medium, and low permeability fault in Figure 8-27. The head behaviour is broadly similar to that of the connected model, with an increasing disruption of the flow paths – leading to an increased head build-up across the fault - as the fault permeability decreases. There is a noticeable difference though with the connected model: the dissipation of the head build-up for the disconnected model will occur over a greater distance than with the connected model, therefore there is a larger head build-up across the fault for the former model (Figure 8-27).

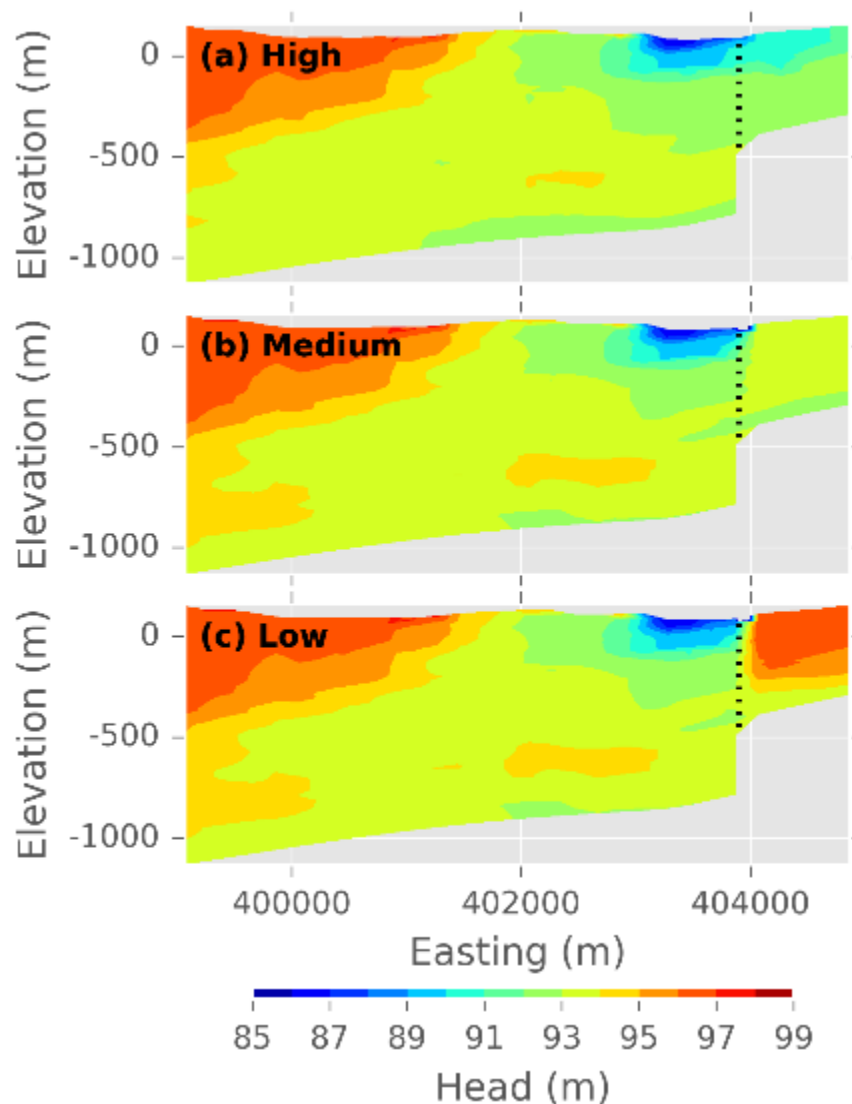


Figure 8-27 Cross-sectional view of steady-state head distribution for a disconnected model across the well field for (a) high permeability fault, (b) medium permeability fault, and (c) low permeability fault. Dotted line indicates the main fault location. See Figure 8-3 for cross-section location.

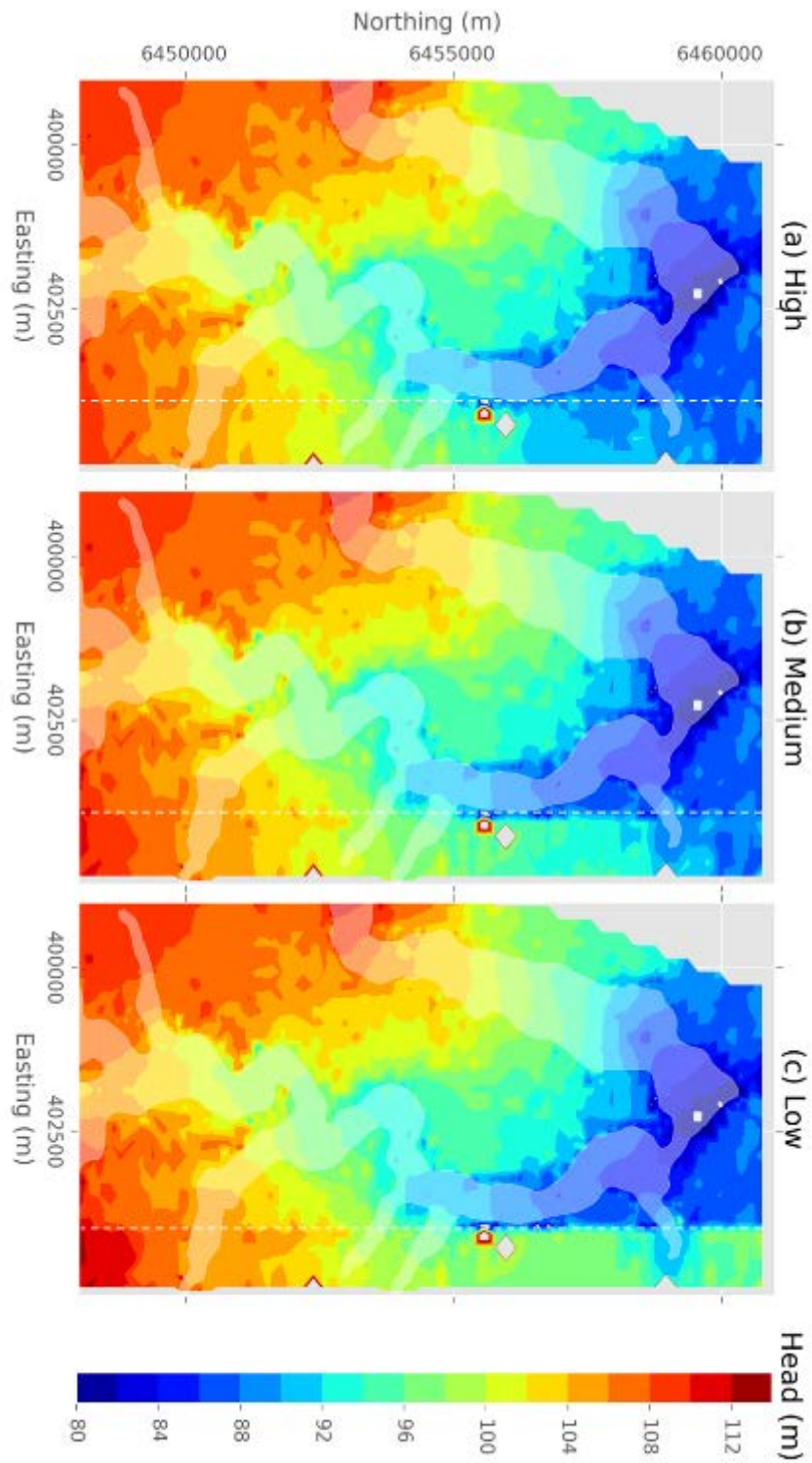


Figure 8-28 Plan view of the surficial hydraulic head distribution in the north of the Gloucester model for the disconnected model for (a) high permeability fault, (b) medium permeability fault, and (c) low permeability fault. The alluvial aquifer is identified by the transparent white area. Grey areas within the model area indicate model cells whose hydraulic head are outside of the range depicted here.

8.3.2 Groundwater flow for a stressed system

The sensitivity of a groundwater system under hydraulic stress from depressurisation due to CSG extraction is discussed for both a connected and disconnected system. Results are shown for a high, medium and low permeability fault model. The steady-state solution still reflects a natural groundwater systems and therefore is taken as the reference against which the other results will be compared.

8.3.2.1 Connected model simulations

The results of the connected simulations in terms of the heads and drawdowns are shown first for the high permeability fault (Figure 8-29). Most noticeable result is the similarity in heads for the steady-state and stressed systems (1 and 10 years) in the vicinity of the fault.

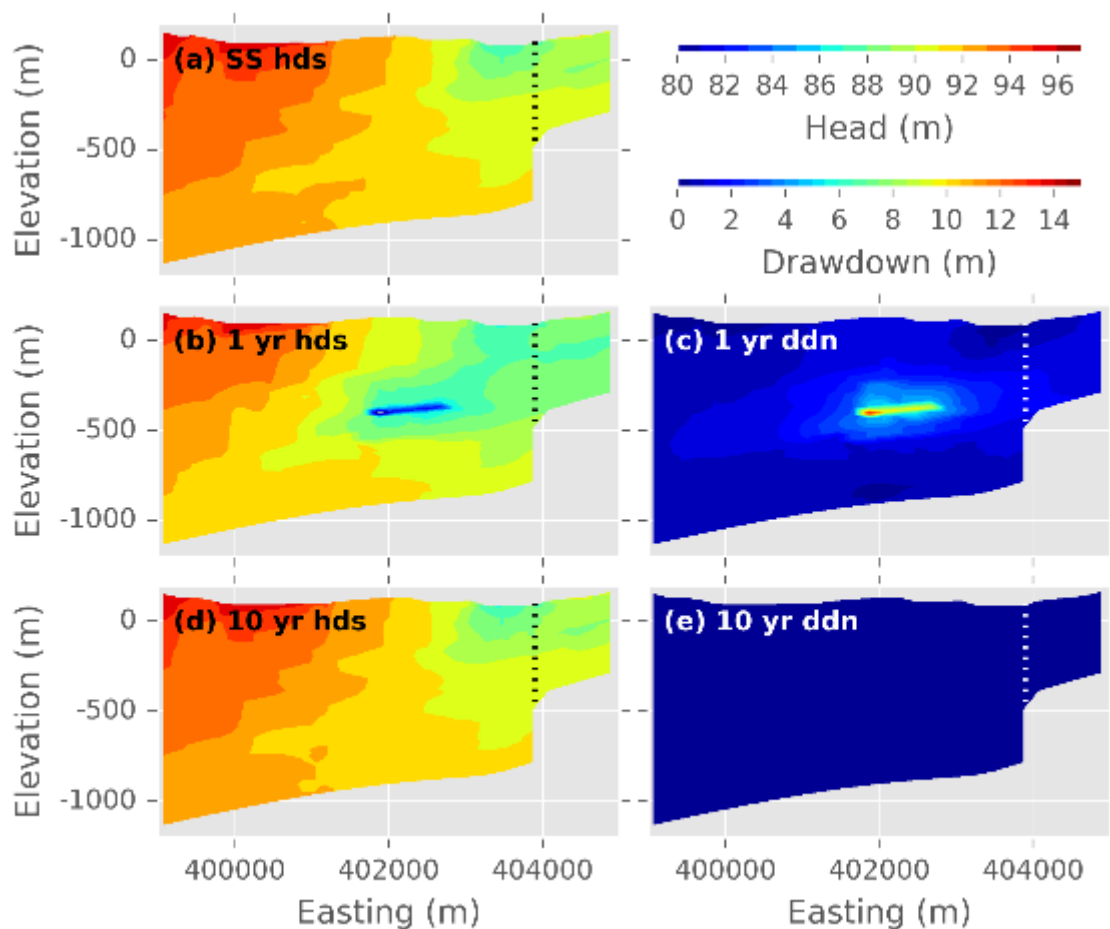


Figure 8-29 Cross-section through the well field of the hydraulic heads (a,b, and d) and drawdown (c and e) for the connected simulation using a high flow across fault conceptualisation at different time (steady state, 1 year of pumping, and 10 years of pumping). The location of the fault is indicated in (a), (b) and (d) (dashed line) and the location of the stream is identified. See Figure 8-3 for cross-section location.

Indeed, the drawdown induced by pumping extends across the fault, which confirms that the high permeability fault is not a barrier to the propagation of the drawdown. The

pressure propagation is further enabled by the connected K field, which provides for a continuous high permeability zone that extends across the fault. When a high fault permeability is combined with a connected K model, effects of depressurisation are little or not affected by the fault. Under those conditions, the drawdown is expected to expand more or less equally in all directions.

Propagation of depressurisation for a medium and low permeable fault are shown in Figure 8-30 and Figure 8-31. As the fault becomes less permeable, the cone of depression will be less noticeable across the fault; the pre-existing head drop across the fault at steady-state does only minimally change when pumping occurs. The presence of such faults causes the cone of depression to compartmentalise in the direction orthogonal to the fault; in the direction parallel to the fault, it would stretch further compared to the more permeable fault simulation.

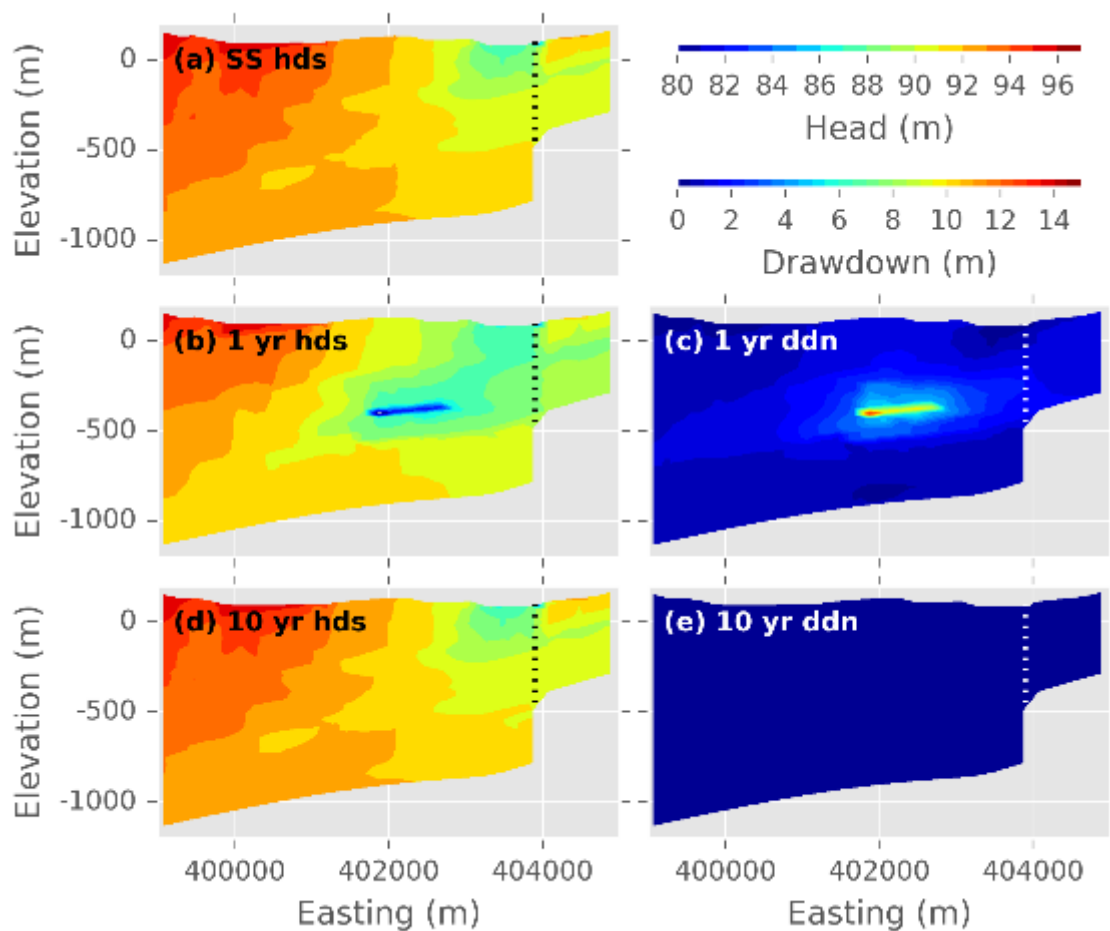


Figure 8-30 Cross-section through the well field of the hydraulic heads (a,b, and d) and drawdown (c and e) for the connected simulation using a medium flow across fault conceptualisation for different times (steady state, 1 year of pumping, 10 years of pumping). See Figure 8-3 for cross-section location.

The zone of maximum drawdown (subplot c in Figure 8-27, Figure 8-31, and Figure 8-30) remains more and more localised as the permeability of the fault decreases. Note that these cross-sections are only a 2D representation of a 3D process; because of the three-dimensional connection between high K zones, the drawdown is laterally very extensive. The maximum drawdown in all connected models occurs at the well field (1,050 m BGL) and is approximately 14.5 m. The inclusion of the location of the coal seams into the geostatistical simulation would ensure the presence of a high coal fraction at the proposed CSG site. Due to a lack of available spatial data, these geostatistical simulations may result in a lower coal fractions (high interburden fraction) which will alter the drawdown response.

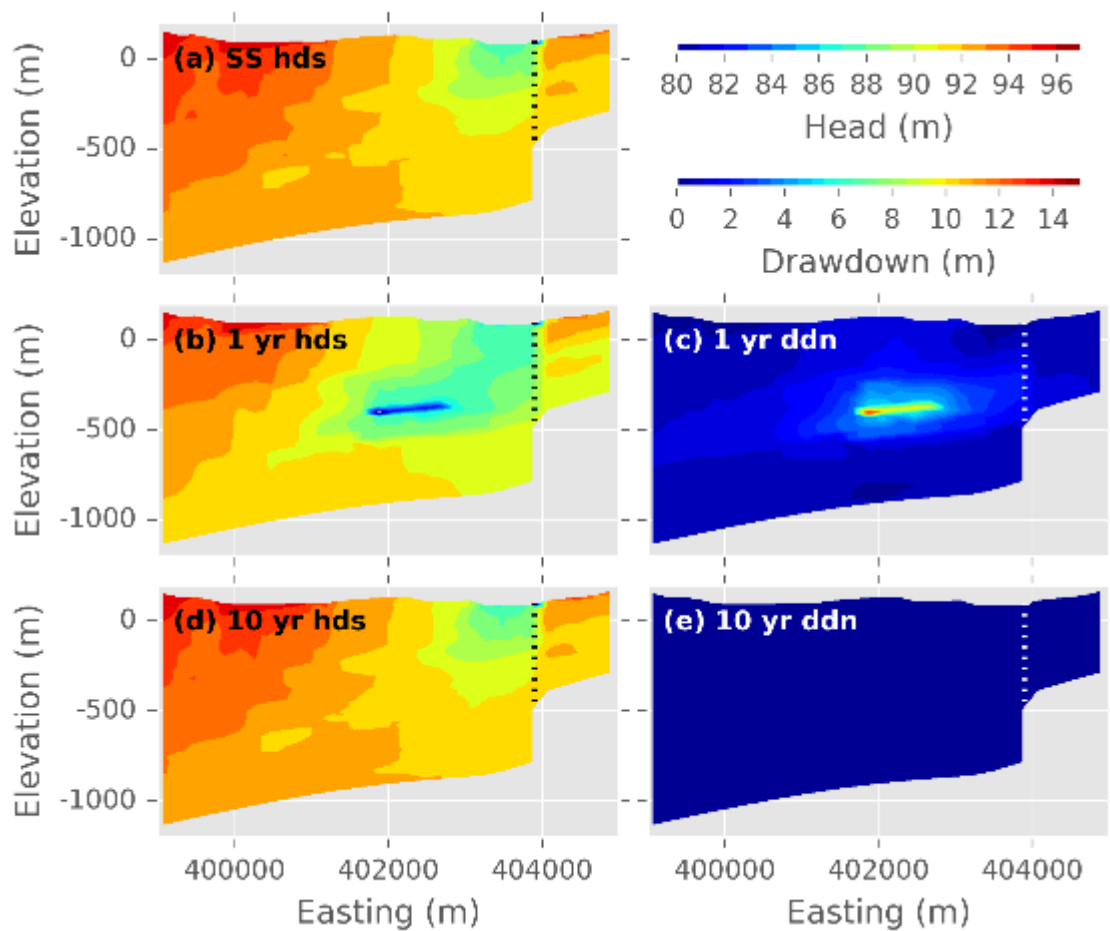


Figure 8-31 Cross-section through the well field of the hydraulic heads (a, b, and d) and drawdown (c and e) for the connected simulation using a low flow across fault conceptualisation for different time (steady state, 1 year of pumping, 10 years of pumping). See Figure 8-3 for cross-section location.

Of further interest is the relatively rapid recovery of the groundwater levels, even after 10 years since the start of the pumping, at which time the heads have essentially recovered to pre-production levels for all simulations (see cross sections (d) and (e) in Figure 8-27, Figure 8-25, and Figure 8-30). Although the groundwater extraction scenario extends over 12 years, groundwater extraction becomes very small towards the end of the production period (about 2 m³/day, Figure 8-7). This rapid recovery is the result of the low pumping

rates, low storage capacity and the highly connected K field enabling rapid replenishment; however the effect of replenishment becomes more and more obstructed as the fault permeability decreases.

Groundwater levels directly to the west of the fault are primarily controlled by the presence of a stream, which forms a discharge point in the model. Figure 8-29 (b) and (c) show that there is only a minor change in the groundwater head and drawdown close to the stream, indicating that groundwater extraction has minimal impact on this area, suggesting that stream discharge will not be impacted (see section 8.2.1 for drain implementation). Surface water – groundwater fluxes are unaffected by the groundwater extraction, verifying the minimal impact of the groundwater extraction. Future work may include the use of particle tracking to investigate the surface water- groundwater interactions.

A summary of simulated heads for the three fault permeabilities at three different times (steady-state, after 1 year pumping, and after 10 year pumping) is shown in Figure 8-32. As the fault permeability decreases, the effect on head discontinuity across the fault becomes more pronounced. Also, the head discontinuity increases as the stress on the system increases. Figure 8-33 shows the drawdown in the surficial groundwater level 1 year after pumping commences. High recharge and high K in the alluvial aquifer results in minimal drawdown at and close to the alluvial deposits, with a maximum surficial drawdown of approximately 1.75 m. The impacts of pumping propagate across the fault for all three fault conditions but with differing magnitudes. The magnitude of the drawdown to the east of the fault for the high and medium simulations is approximately 1.25 m, the low fault permeability has a lower drawdown east of the fault (0.7 m). The impact of the fault on the drawdown becomes clear in the medium and low simulations.

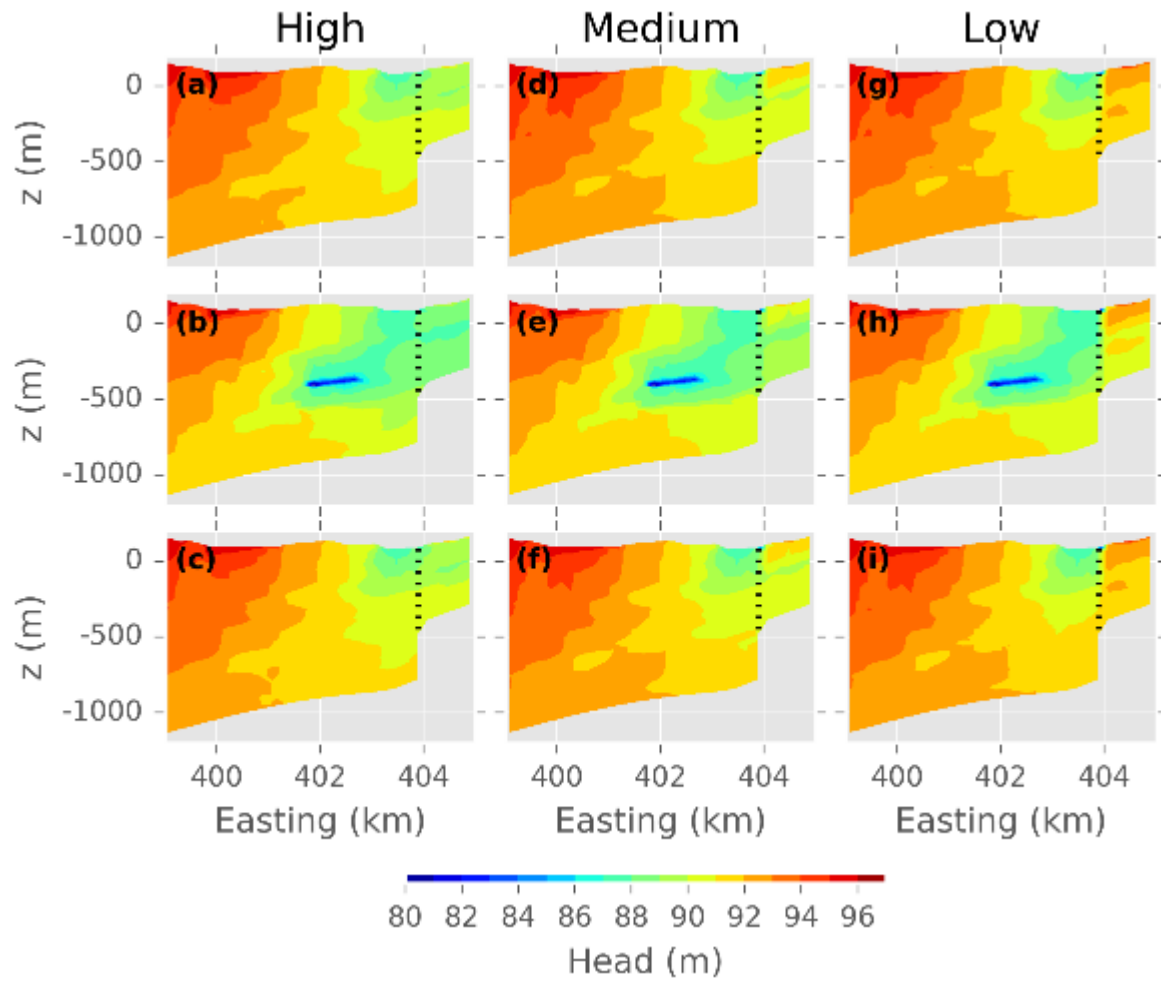


Figure 8-32 Comparison of the cross-section through the well field of the hydraulic heads for the connected simulation using a high (a, b, and c), medium (d, e, and f) and low (g, h, and i) flow across fault conceptualisation at different times. Steady-state heads are shown in (a), (b), and (c); heads after 1 year of pumping are shown in (d), (e), and (f); and heads 10 years into the production period (pumping has almost ceased at this point) (g), (h), and (i). See Figure 8-3 for cross-section location.

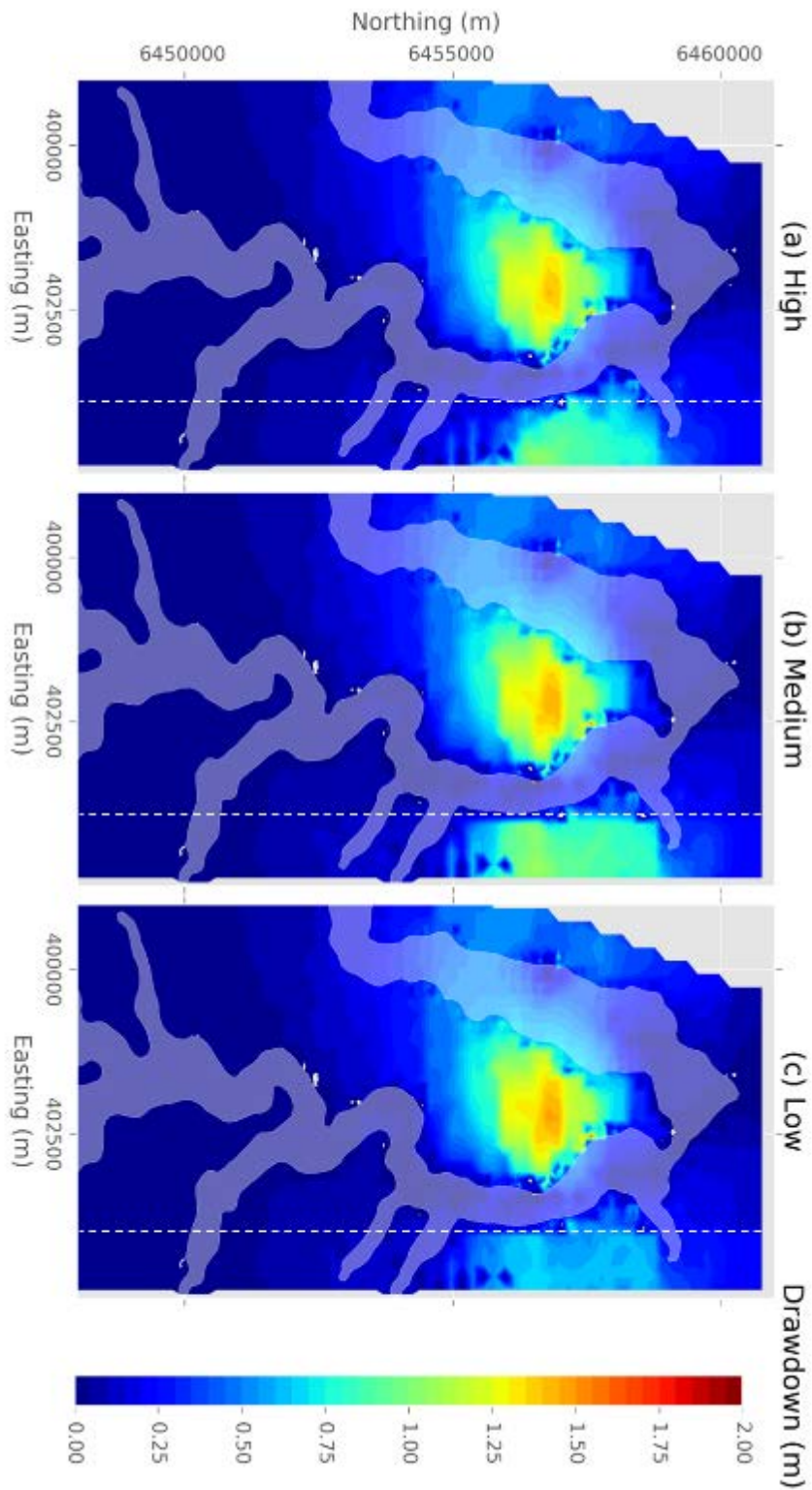


Figure 8-33 Plan view of the surficial drawdown in the north of the Gloucester model for the connected model after 1 year of pumping. The alluvial aquifer is identified by the transparent white area. Grey areas within the model area indicate model cells whose hydraulic head are outside of the range depicted here.

8.3.2.2 Disconnected model simulations

The results of the disconnected simulations are shown in Figure 8-35, Figure 8-36, Figure 8-37, and in the summary of Figure 8-38. In comparison to the connected K field simulations, the groundwater response is very different. For all simulations, the steady-state heads in the disconnected field are on average 4-5 m higher than those in the connected field because the bulk permeability of the field is lower for the disconnected field (i.e., the disconnected field arithmetic mean of $\ln(K) = -6.18$ while the connected field arithmetic mean of $\ln(K) = -5.22$). In addition, the disconnected K field clearly preserves the hydraulic layering either side of the fault. A typical feature of the disconnected model is seen in Figure 8-35c, which shows the drawdown after 1 year of pumping together with several layers below the pumping zone with minimal drawdown. In addition to the fault, there are now other features (i.e. extended low permeability zones) that constrain the propagation of the depressurisation.

The maximum drawdown is 4.2 m, which is approximately 0.5 m smaller than that observed in the connected K field. On the other hand, the drawdown for the disconnected model is propagated over a larger area due to the morphology of the high K zones; however the lateral spread is likely limited due to the discontinuous nature of the high K zones. How the impact of pumping on the groundwater heads in the disconnected K field is impacted by the K field is shown in Figure 8-34. The disconnected field shown in Figure 8-34 has a number of discontinuous layers, with the highest permeability at shallow depths, bounded by low permeability cells. This results in the patchy response observed in all simulations for both hydraulic head and drawdown.

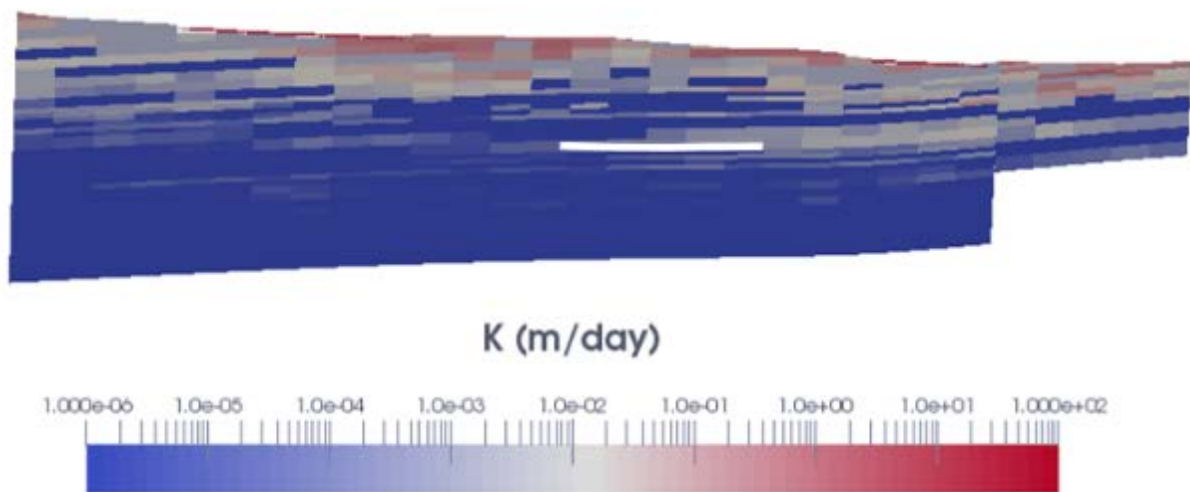


Figure 8-34 Cross-section of hydraulic conductivity through the well field for the disconnected K model. Location of the fault indicated by a white rectangle, white box identifies the well locations.

The summary of simulated heads for three fault permeabilities at three different times (i.e. steady-state, 1 year pumping, 10 year pumping) illustrates again that also in the case of a

disconnected K model faults have an important effect on groundwater flow. As the faults become less permeable, the head discontinuity across the fault increases. However, the head distribution at either side of the fault is now also constrained by low-permeable layers that can further compartmentalise groundwater heads.

The impacts of the pumping on the surficial aquifer are shown in Figure 8-39. The alluvial aquifer shows a similar response to the connected model drawdown, where the high recharge and high K model runs are relatively unaffected by the pumping. The magnitude of the drawdown is higher in the disconnected simulation (> 2.0 m) than the connected simulation. This shows that the drawdown within the disconnected field, at the surface, is high relative to the well field, whereas the connected field has a large drawdown at the well field and a low surficial drawdown. The disconnected K field is diffusing the drawdown over the large high K zones (with a low effective hydraulic conductivity due to the isolated K zones), whereas the connected K field has an extensive response in that the drawdown, in a 2D plot, appears to be distributed by the connected high K channels. The surficial drawdown appears to represent the bulk effective permeability properties of the underlying K field structure, where the surface drawdown is higher in the disconnected field due to the lower effective hydraulic conductivity and the lower in the connected field, which has a higher effective conductivity.

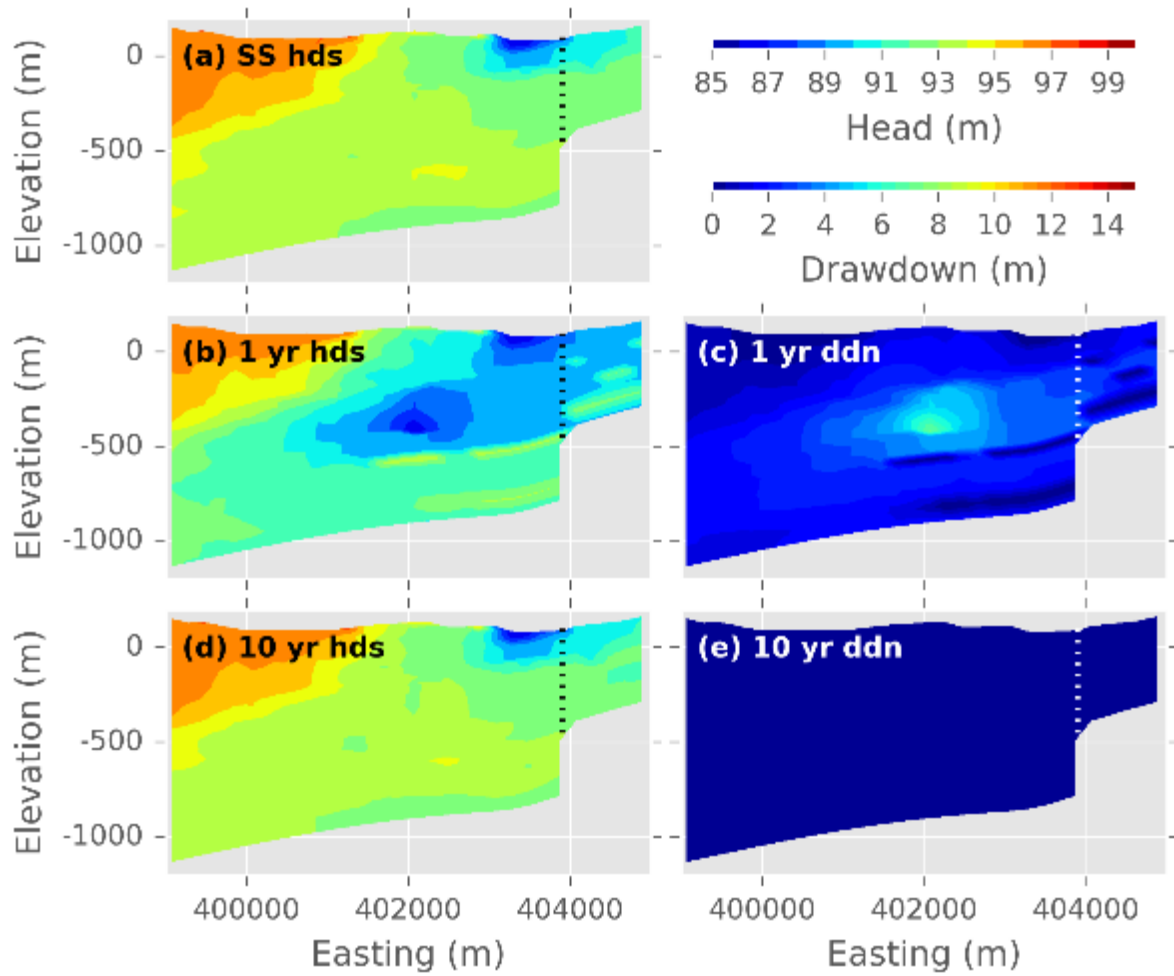


Figure 8-35 Cross-section through the well field of the hydraulic heads (a, b, and d) and drawdown (c and e) for the disconnected simulation using a high flow across fault conceptualisation for different times (steady-state, 1 year of pumping, and 10 years of pumping). See Figure 8-3 for cross section location.

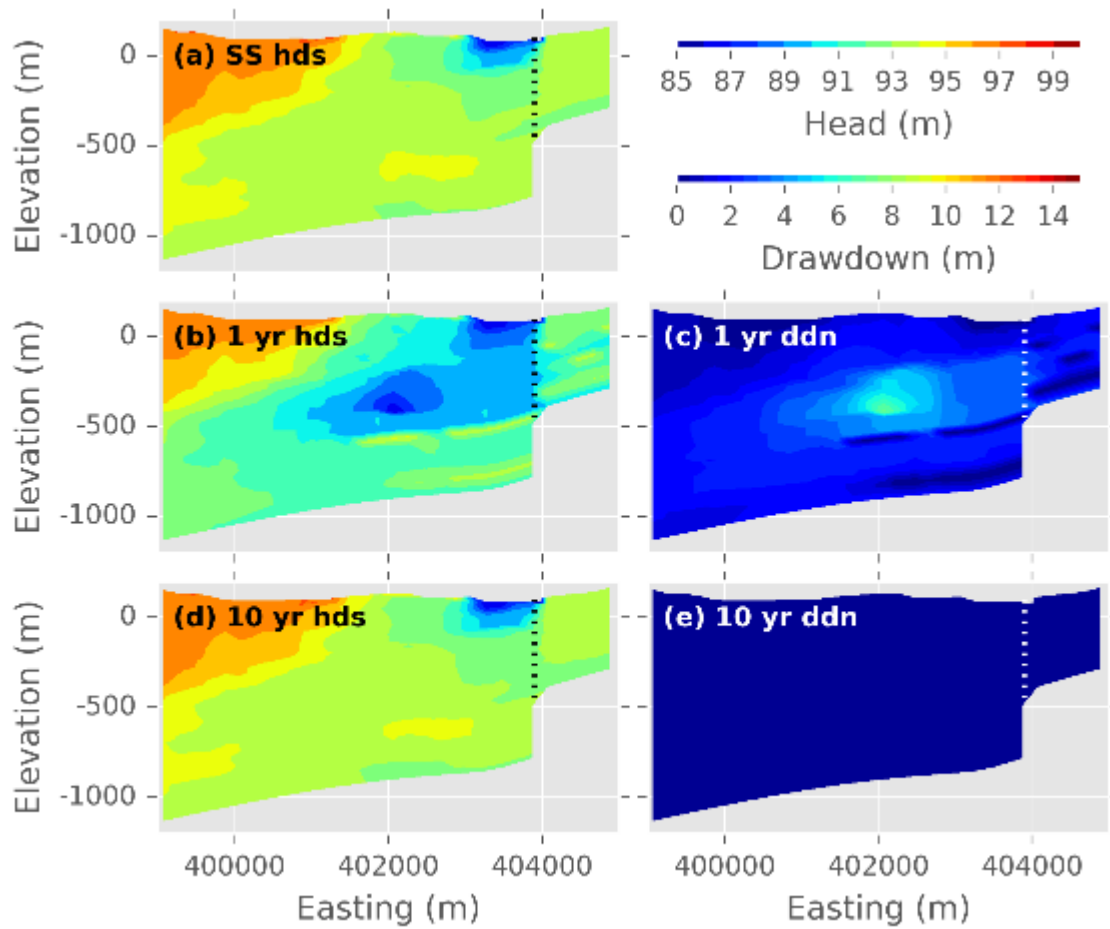


Figure 8-36 Cross-section through the well field of the hydraulic heads (a, b, and d) and drawdown (c and e) for the disconnected simulation using a medium flow across fault conceptualisation for different times (steady-state, 1 year of pumping, and 10 years of pumping). See Figure 8-3 for cross-section location.

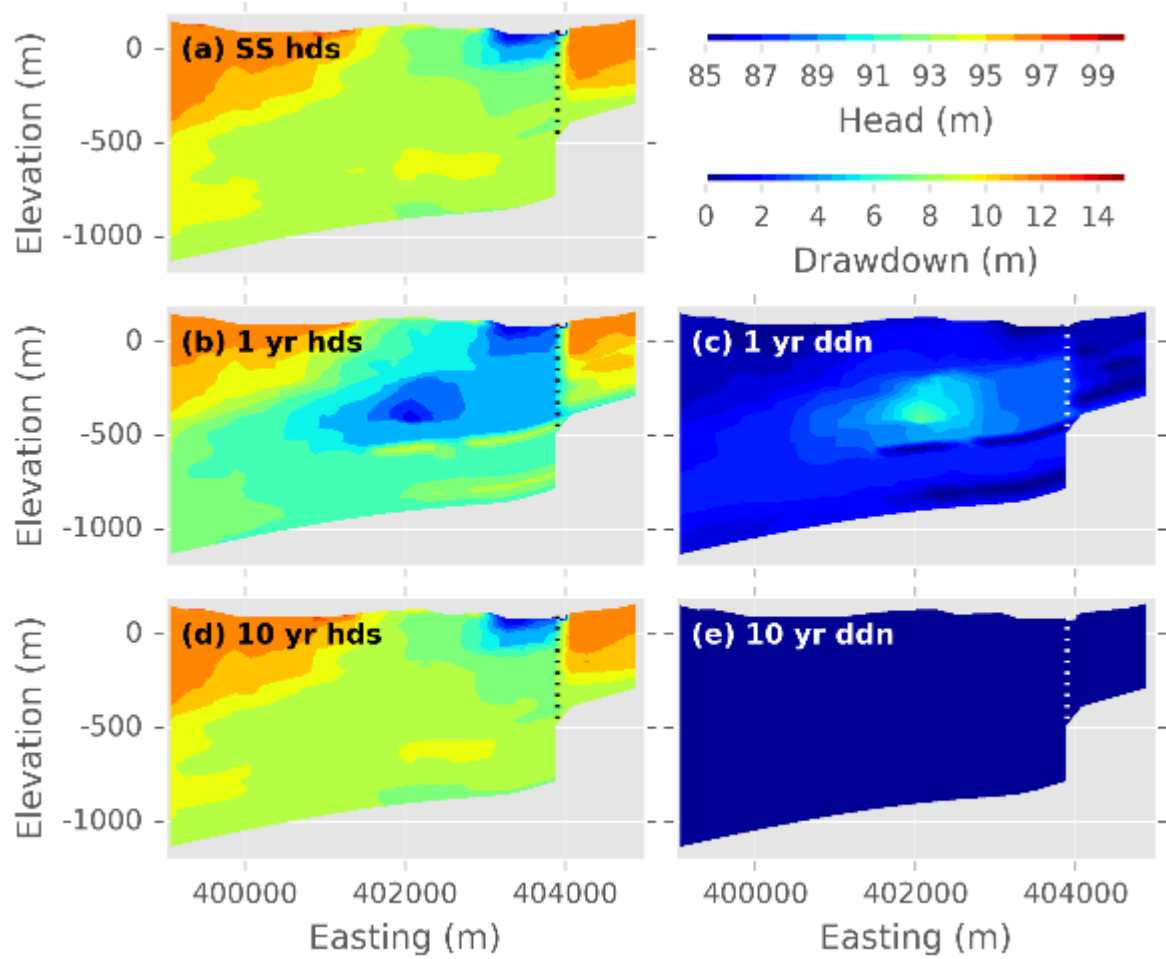


Figure 8-37 Cross-section through the well field of the hydraulic heads (a, b, and d) and drawdown (c and e) for the disconnected simulation using a low flow across fault conceptualisation for different times (steady-state, 1 year of pumping, and 10 years of pumping). See Figure 8-3 for cross-section location.

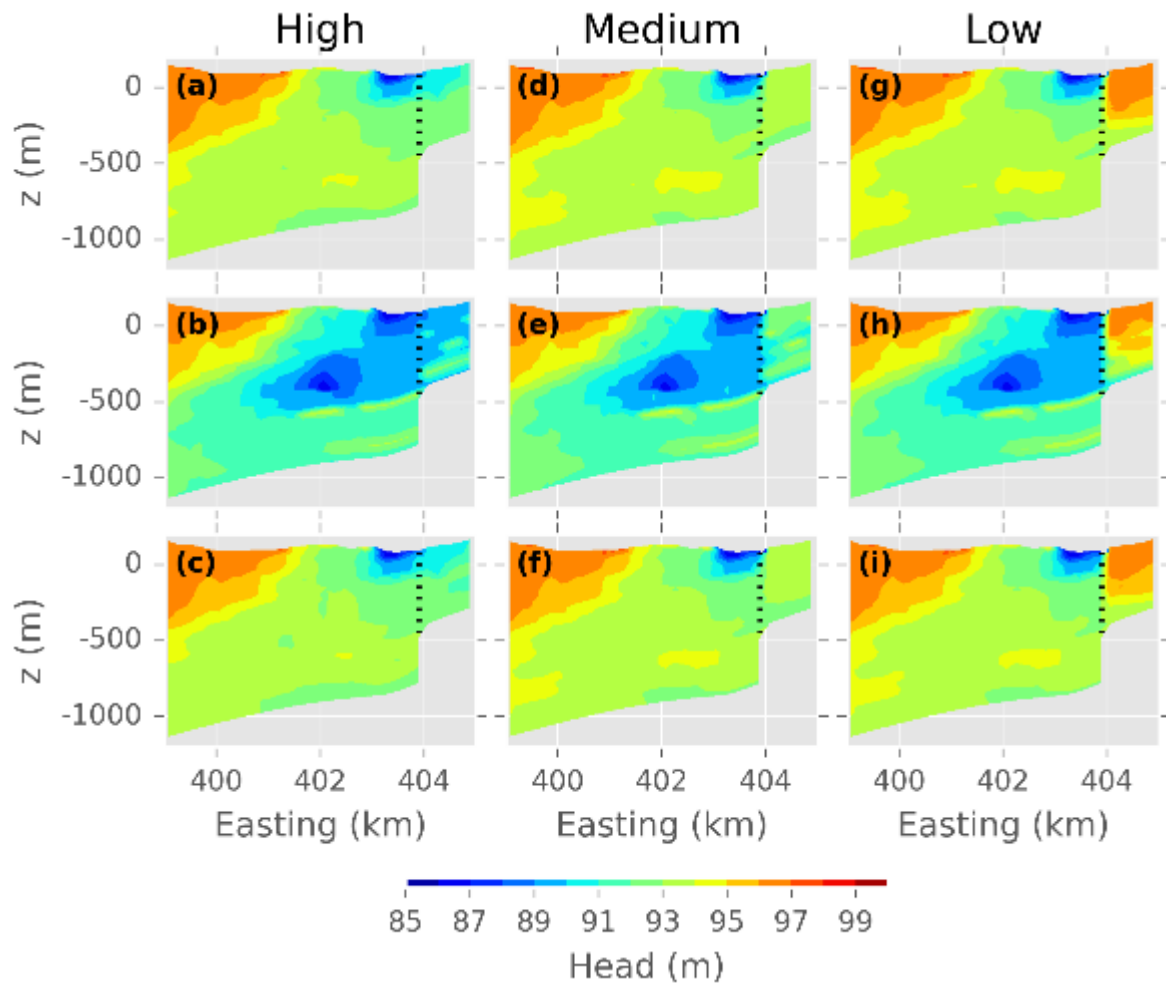


Figure 8-38 Comparison of the cross-section through the well field of the hydraulic heads for the disconnected simulation using a high (a, b, and c), medium (d, e, and f) and low (g, h, and i) flow across fault conceptualisation at different times. Steady-state heads are shown in (a), (b), and (c); heads after 1 year of pumping are shown in (d), (e), and (f); and heads 10 years into the production period (pumping has almost ceased at this point) (g), (h), and (i). See Figure 8-3 for cross-section location.

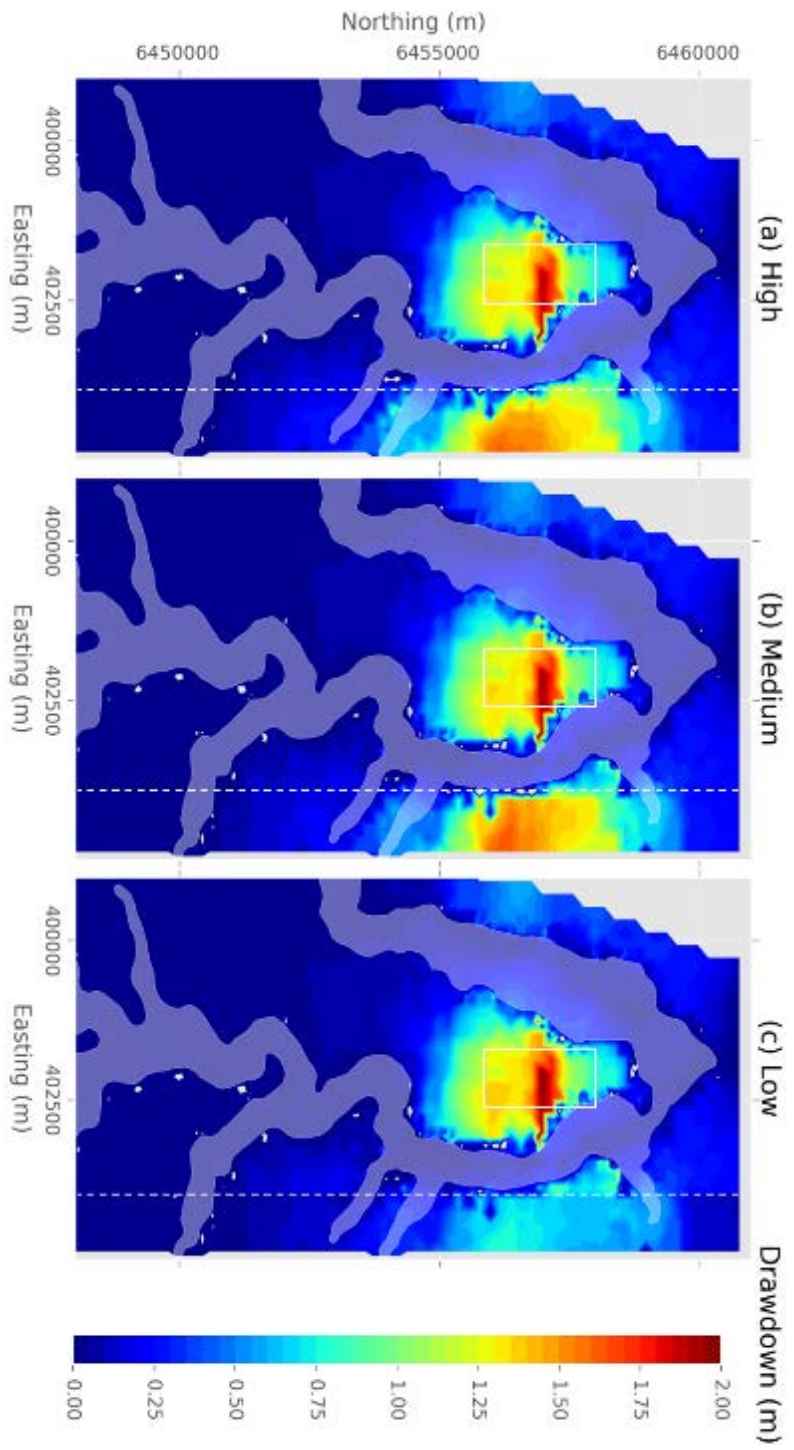


Figure 8-39 Plan view of the surficial drawdown in the north of the Gloucester model for the disconnected model after 1 year of pumping. Well field location indicated by white box. The alluvial aquifer is identified by the transparent white area. Grey areas within the model area indicate model cells whose hydraulic head are outside of the range depicted here. Dashed white line is a fault.

8.3.3 Impact of chimney flow on groundwater heads

Several structural features were identified in Section 7 that could be linked to fault zones with more permeable rock masses that provided preferential pathways for water, dissolved solutes and gases. The most noticeable feature was the presence of several anomalies in TDS across several geological layers, right up until the surface layers. These features were named chimneys and are the subject of numerical simulations in the subsequent sections. The aim of the simulations is not to exactly reproduce these features, but to explore what conceptual model and flow parameters would yield similar behaviour, and then to test if such parameters are physically plausible values, and in line with observations. The first set of simulations involves a single chimney (Section 8.3.3.1); the second set of simulations is based on a cluster of chimneys (Section 8.3.1.2).

8.3.3.1 Single chimney simulations

As discussed in Section 8.2.6, a chimney is represented in the model as a vertical Connected Linear Network: this is basically a 10-m-radius tube with permeabilities defined as 0.01 m/d, or up to four orders of magnitude larger than the surrounding rock permeability between -1,200 and -600 m depth, see section 8.2.6. The chimney is located at significant distance from the CSG well field (about 5 km), while the nearest fault is at a distance of approximately 1 km. The extraction is therefore expected not to be impacted significantly by the chimney. The changes in flow behaviour of the chimney in the presence of different fault types is also expected to be minimal, given the distance between chimney and fault. The calculations with a single chimney are undertaken again for three fault permeabilities (high, medium, low) and for connected and disconnected K fields.

Table 8-3 shows that only 4 of the 6 scenarios tested resulted in any substantial flow through the single chimney under steady-state flow conditions (i.e. without additional stress from extraction). Regardless of the underlying K field, the maximum flux through the chimney is approximately 0.19 m³/day (or 69.4 m³/yr), which is substantially lower than the value estimated using the mass balance approach (see Appendix D). Both approaches have their limitation: the mass balance approach makes assumptions about the geometry of the chimney, while the numerical modelling approach further makes assumptions of the chimney permeability. Unless data are available which help to characterise the location, geometry and hydraulic properties of the chimney, reproducing the observed anomalies will be difficult. Additional information regarding the morphology and properties of the chimney, coupled with well logs can be included in this approach as “training” data to inform modelling (e.g., Mariethoz et al., 2010).

Table 8-3 Simulated steady-state flux (m³/day) through the single chimney for the different scenarios. (positive fluxes are upward).

K-MODEL	FAULT PERMEABILITY		
	High	Medium	Low
Connected	0.19	0.018	0.016
Disconnected	0.016	-1.01 x10 ⁻⁶	-1.13x10 ⁻⁶

The presence of a single chimney within the model has little impact on the groundwater head and flow, as shown in Figure 8-40 and Figure 8-41. The chimney flow does not influence the hydraulic heads and induces little to no additional drawdown in the simulations.

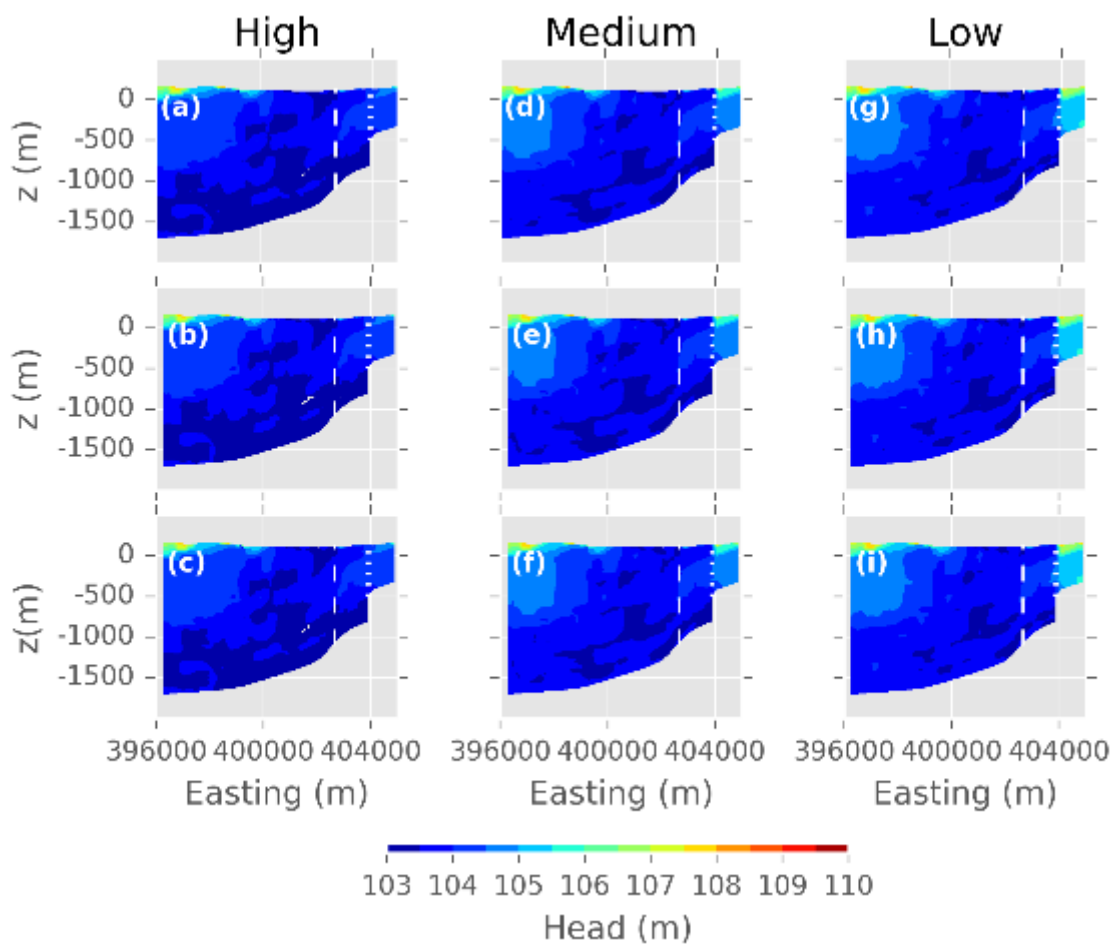


Figure 8-40 Cross-sectional views of the hydraulic heads for the connected simulation using a high (a, b, and c), medium (d, e, and f) and low (g, h, and i) flow across-fault conceptualisation at different times. Steady-state heads are shown in (a), (b), and (c); heads after 1 year of pumping are shown in (d), (e), and (f); and heads 10 years into the production period (pumping has almost ceased at this point) (g), (h), and (i). See Figure 8-3 for cross-section location. The chimney (CLN) location is marked with a white dashed line.

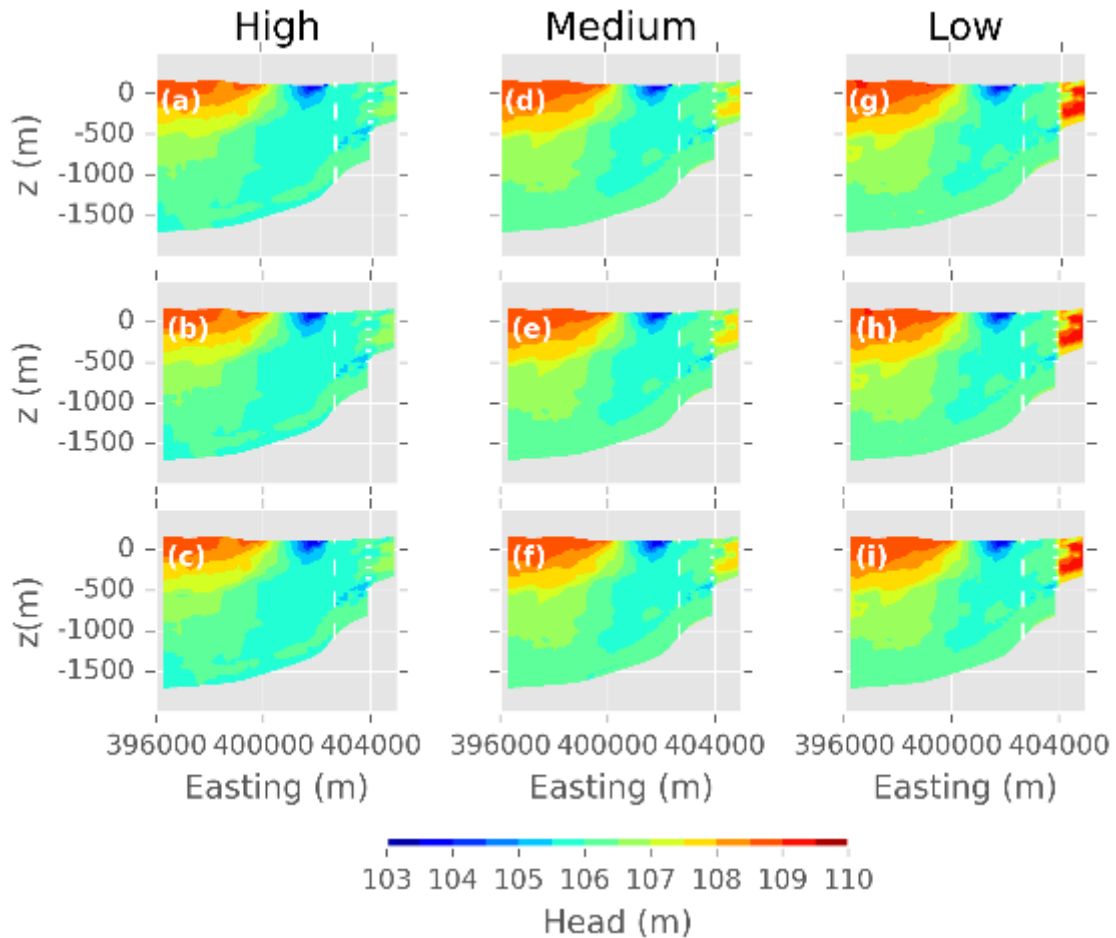


Figure 8-41 Cross-sectional view of the hydraulic heads for the disconnected simulation using a high (a, b, and c), medium (d, e, and f) and low (g, h, and i) flow across fault conceptualisation at different times. Steady-state heads are shown in (a), (b), and (c); heads after 1 year of pumping are shown in (d), (e), and (f); and heads 10 years into the production period (pumping has almost ceased at this point) (g), (h), and (i). See Figure 8-3 for cross-section location. The chimney (CLN) location marked with a white dashed line.

Calculated heads within the single CLN and flow through the CLN are displayed in Figure 8-42 for connected and disconnected K fields and for three fault permeabilities (low, medium, and high); the simulated response of the top CLN node is shown in Figure 8-42. The initial upward direction of flow is not impacted by the pumping; also head variations within the CLN are very small such that the pumping does not influence the head distribution within the CLN. Both observations indicate that the CLN remained disconnected from the main drawdown zone linked to the gas production area. Or in other words, a single preferential pathway does not seem to affect the depressurisation in the upper aquifers; note the distance of 5 km between the chimney and the gas production area.

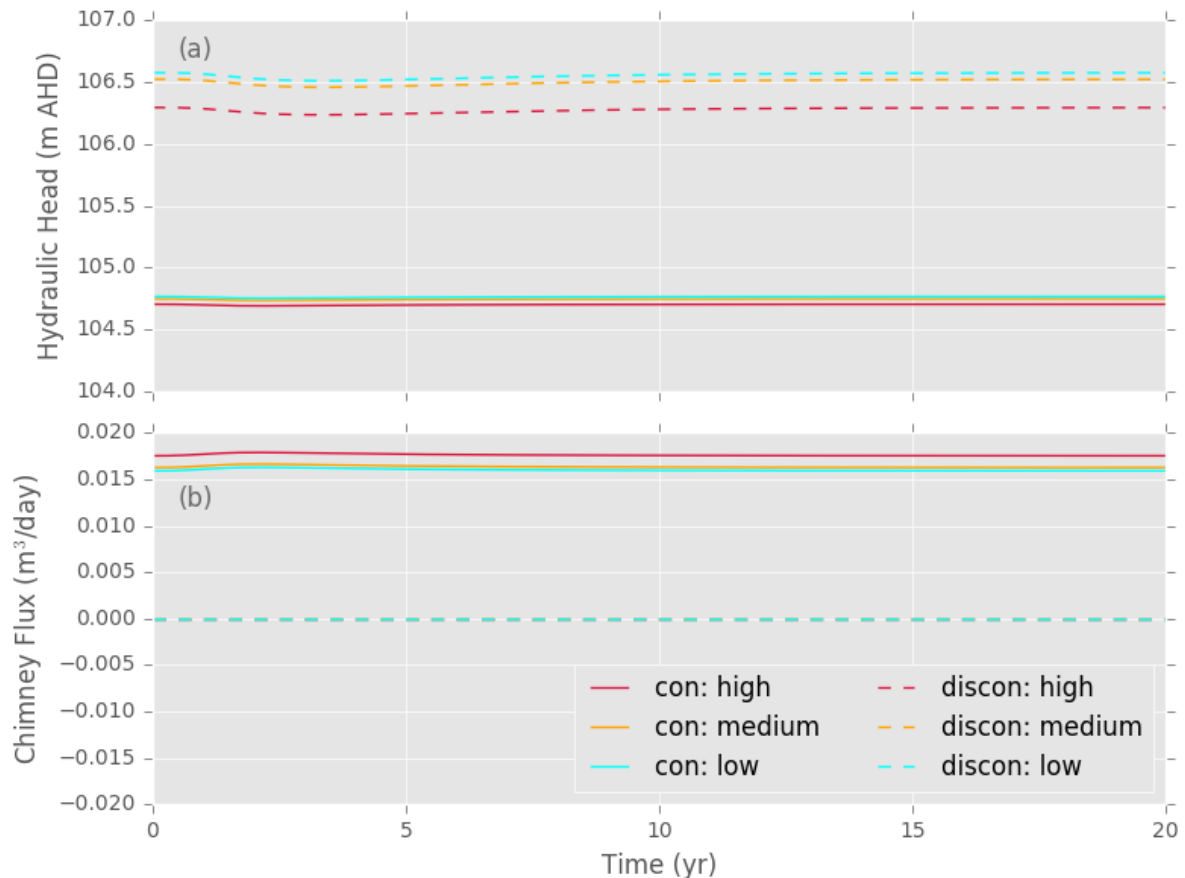


Figure 8-42 Single chimney (CLN) hydraulic head (a) and groundwater flux (b) a for the different K fields (connected: con, and disconnected: discon) and fault scenarios (low, medium, and high flow across the fault) for a period of 20 years (pre-pumping (0 years) to post pumping (> 10 years)). The head values are taken from the top CLN node.

8.3.3.2 Cluster of chimneys

The potential impact of a cluster of chimneys was evaluated for a medium permeable fault (Figure 8-43). The impact of multiple chimney features (5 chimneys within a 600 m by 600 m area) on the simulated groundwater level remains minimal, the impact of alternate fault permeabilities upon the chimney flow will be negligible. As previously mentioned, these features are a high localised phenomena and would therefore have a very localised impact. As expected, the groundwater level in the chimneys does appear to be only minimally affected by the pumping, i.e. the magnitude of the response is on the order of 5 cm (Figure 8-44a). A corresponding increase in groundwater flux through some of the chimneys is also discernible in Figure 8-44b, however this would have a minimal impact on groundwater flow. The difference in reaction across the five chimneys is governed by the location of the CLNs and whether or not they intersect higher K zones that are connected to the main zone of depressurisation.

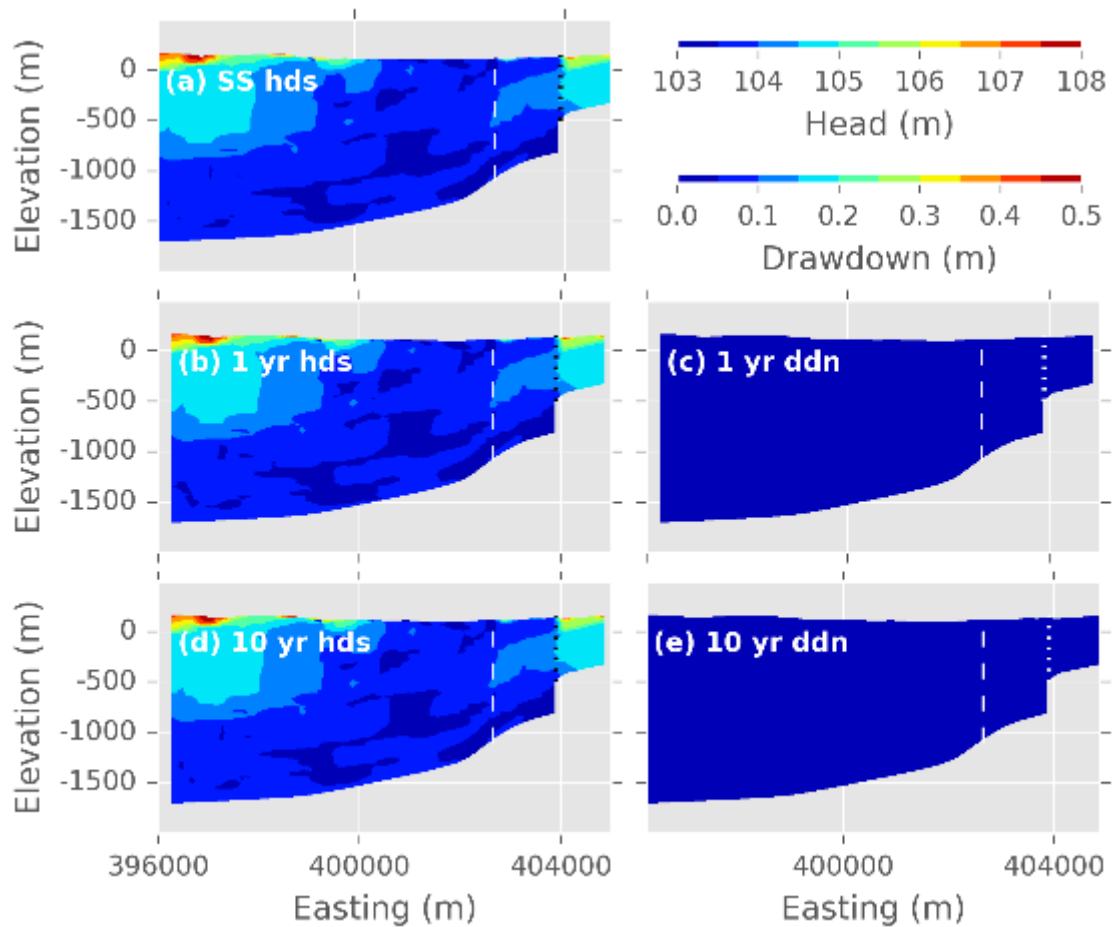


Figure 8-43 Cross-sectional view of the hydraulic heads (a, b, and d) and drawdown (c and e) for the connected simulation using a medium across-fault flow conceptualisation for different times (steady-state, 1 year of pumping, 10 years of pumping). See Figure 8-3 for cross-section location. The centre of the chimney cluster is indicated by the dashed white line.

The steady-state flux through all 5 chimneys for the connected and disconnected K fields was 0.832 and 0.079 m^3/day , respectively. This equates to a total annual flux of 303.7 m^3/year for the connected field and 28.8 m^3/year for the disconnected field (or 96 mm/years and 9 mm/year respectively, based on the known cross sectional area of each chimney (Annex D)). This is a marked increase in flow compared to the simulation using a single chimney. Interestingly, there are now several chimneys with a negative flux, i.e. downward flow. This shows that the hydraulic conductivity field is highly heterogeneous and that some of the chimneys intercept higher K zones connected to the main zone of depressurisation. Regardless of the change in flux, the impacts of the chimneys on the groundwater flow are minimal as shown by the hydraulic head in all the chimneys (Figure 8-44a).

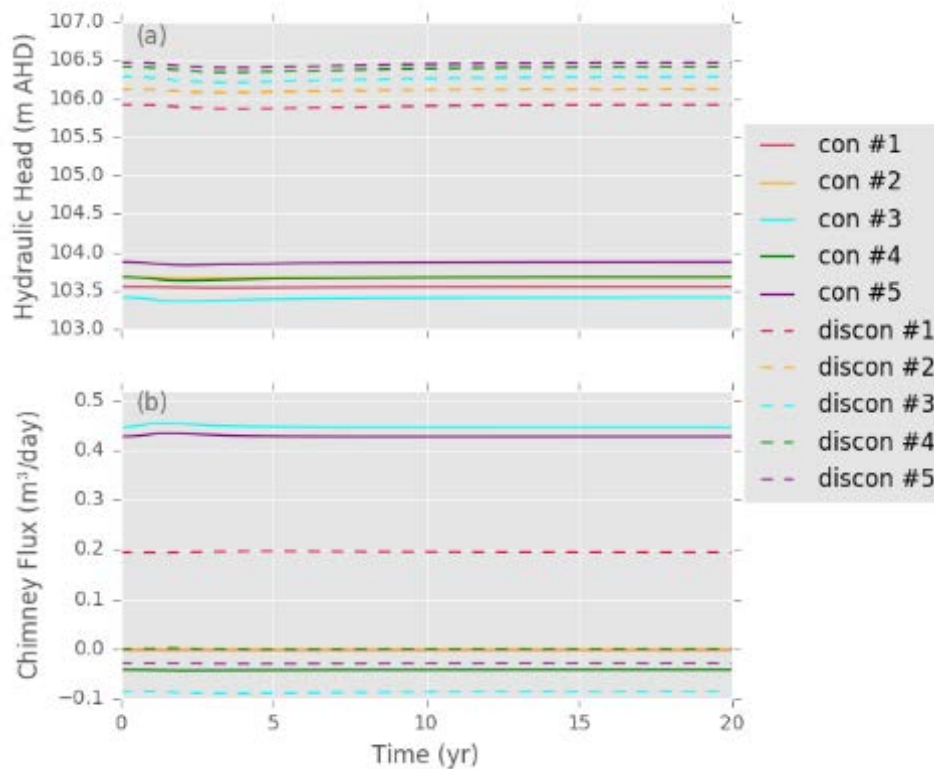


Figure 8-44 Hydraulic head (a) and groundwater flux (b) through each chimney (CLN) for the clustered simulations (5 CLNs numbered 1-5; see Figure 8-22), for the different K fields (connected: con, and disconnected: discon) and fault scenarios for a period of 20 years (pre-pumping to post pumping).

8.4 Key findings of groundwater flow modelling

The primary aim of this work was to present an approach to include geological information (i.e., fault zone architecture and Drill Stem Test information) in regional groundwater flow models. The approach has been successful at improving and enhancing existing geological conceptualisations. We have shown that the inclusion of additional hydrogeological information, in the form of Drill Stem Test data, is a suitable means to better represent more complex basins such as the Gloucester Basin. The statistical approach takes into account some key features that will influence basin permeability. However, in an unconditioned scenario (i.e. not constrained by point data), this statistical approach has limited capacity to predict actual behaviour which may be observed in the field.

Within the context of the presented methodology, a number of conclusions regarding the groundwater response to CSG development can be drawn:

1. Impact of faults without water production for CSG extraction

One of the first fault-related outputs from McCallum et al. (2018) demonstrated how geological faults and their hydraulic properties can be represented in regional-scale groundwater flow models. They also showed how different fault properties resulted in different aquifer responses based on a simplified regional groundwater flow

model. Faults represent a continuum from conduits to groundwater flow through to barriers to groundwater flow. The vast majority of groundwater flow models have assumed that faults act as barriers to flow, however recent work has indicated that this assumption is based on limited data and it does not explain observed anomalies in groundwater heads or salinity. This work has provided further illustrations of the nature and degree of impacts caused by faults, this time based on a regional groundwater flow model that was built using a relatively large data set, typical of what is used by industry for simulating impacts from hydrocarbon developments. Impacts of faults on groundwater flow were tested by modifying fault properties to represent high, medium, and low across fault flow. As the fault permeability decreases, the effect on heads becomes more evident with a sharp head contrast developing across the fault. Under the conditions of connected K fields, this head build-up will relatively quickly dissipate in the directions along the fault. Simulated anomalous head distributions were similar in nature to those measured in the field.

2. Impact of faults with additional stress due to water production for CSG extraction

The previously discussed impacts were demonstrated for a groundwater flow model that did not experience any stresses from CSG extraction. If stresses due to water production are imposed, a maximum drawdown of approximately 1.75 m is observed at and close to the alluvial deposits. High recharge and high K in the alluvial aquifer results in minimal drawdown. The presence of one fault within approximately 1 km from the well field did not affect the maximum drawdown in the alluvial deposits. The only material impact of the fault was on how strong the impacts of pumping would propagate across the fault. The magnitude of the drawdown across the fault for the high and medium fault permeability simulations is approximately 1.25 m, the low fault permeability has a lower drawdown across the fault of 0.7 m.

The faults included in the groundwater flow simulations have no material impact on the maximum drawdown in the fractured rock or alluvial aquifer, in part because of their distance from the depressurisation zone (about 1 km), and in part because only a few large faults were included (all at a considerable distance from the well field). Several smaller faults and disturbed zones exist in the area, and were shown to be likely responsible for head and salinity anomalies. These features were not included in the model although an attempt was made to represent them by the so-called chimney structures. The latter had no effect on propagating or affecting the depressurisation, mainly because of their relatively large distance from the well field (about 5 km).

Calculated maximum head drawdown in the weathered and fractured rock aquifer is of similar magnitude as the results obtained by Peeters et al. (In Prep) using a different modelling approach, i.e. up to 1.75 m for the former versus less than 1 m for the latter. As far as the impact of faults as conduits to propagate depressurisation is concerned, results obtained here are also consistent with those reported by Peeters et al. (In Prep). Although only the effects from CSG extraction are considered

here, the effects of faults on maximum drawdown are indistinguishable between a model with or without faults.

3. Aquifer properties

The permeability structure has a significant influence on the extent of drawdown. Where the high permeability zone forms connected pathways, drawdown is focussed and extends laterally within the connected pathways. Alternatively, the drawdown in a low connectivity field is more diffuse. The bulk hydraulic properties within a discontinuous permeability field are lower, resulting in higher heads relative to a connected permeability field. This underscores the need to properly characterise the hydraulic conductivity all hydrogeological formations, not just the coal seams. This should also include the establishment of the spatial correlation structure as a basis for realistic groundwater flow simulations in which such spatial correlations are implemented.

4. Coal seam properties

The geostatistical approach presented here generated spatial fields with two levels of coal seam connectivity (i.e., connected and disconnected). The effect of coal seams being either connected or disconnected on groundwater flow in the presence of faults was clearly demonstrated. However, the difference in maximum head drawdown in the fractured rock and alluvial aquifers between connected and disconnected models were small. Given the importance of proper characterisation of the degree of connectivity, sufficient geological information should be incorporated into numerical groundwater flow models. For example, use of well log data would allow proper conditioning/training data to generate a more realistic distribution of the coal seams. Furthermore, multiple realisations are necessary to sample more plausible outputs. Relying on a single realisation can introduce bias in the simulated output.

5. Role of preferential flow paths (“chimney-like” structures)

Field observations of salinity anomalies across the basin were interpreted as “chimney-like” structures, i.e. highly localised preferential flow features associated with fault damage zones enhancing connectivity between deeper and shallower groundwater. Based on a simple mass balance approach under natural flow conditions (i.e. no pumping), the flow through the chimneys required to explain the salinity anomalous observations was estimated to be very small (10% of recharge for the area evaluated). The impact on regional groundwater flow from the presence of chimneys under conditions of water extraction was tested. By implementing such chimney features in the groundwater model, the magnitude of the flow through the chimneys for the connected K field was shown to be similar in magnitude to the mass balance estimates.

The chimney structures had no demonstrable impact on head drawdown; this was mainly because they were located at relatively large distance from the depressurisation zone.

8.5 References

- Ababou R (1988). Three-Dimensional Flow in Random Porous Media. PhD Thesis. Department of Civil Engineering, Massachusetts Institute of Technology. Cambridge, Massachusetts. 2 volumes, 833pp.
- Ababou R, McLaughlin D, Gelhar LW, and Tompson AF (1989). Numerical simulation of three dimensional saturated flow in randomly heterogeneous porous media. *Transport in Porous Media*. 4: 549-565.
- AGL Energy Limited (2014) Surface Water and Groundwater Management Plan for the Waukivory 331 Pilot Program - Gloucester Gas Project. Sydney. Viewed 16 June 2015, http://www.agl.com.au/~media/AGL/About%20AGL/Documents/How%20We%20Source%20Energy/Gloucester%20Document%20Repository/Water%20Plans/20141022_Surface%20Water%20and%20Groundwater%20Management%20Plan%20for%20the%20Waukivory%20Pilot%20Program.pdf.
- Deutsch, C and Journel, A. (1992) GSLIB: Geostatistical Software Library, Oxford Univ. Press, New York.
- Doble R, McCallum J, Turnadge C, Peeters L, Wu B and Mallants D (2018). Modelling inter-aquifer leakage associated with well integrity failure, prepared by the Commonwealth Scientific and Industrial Research Organisation (CSIRO). Canberra.
- Frery E, Rohead-O'Brien H, Wilkes PG, McVicar TR, Van Niel TG, Li LT, Barron OV, Rachakonda PK, Zhang YQ, Dawes WR, Marvanek SP, Buettikofer H and Gresham MP (In Prep). Observations analysis and statistical analysis and interpolation for the Gloucester subregion. Product 2.1-2.2 for the Gloucester subregion from the Northern Sydney Basin Bioregional Assessment. Australia.
- Manzocchi T, Walsh JJ, Nell PAR and Yielding G (1999). Fault transmissibility multipliers for flow simulation models. *Petroleum Geoscience* 5: 53–63.
- Mariethoz G, Renard P and Straubhaar J (2010). The Direct Sampling method to perform multiple-point geostatistical simulations, *Water Resources Research*, 46(11), doi: 10.1029/2008WR007621.
- McCallum JL, Simmons CT, Mallants D and Batelaan O (2018). Simulating the groundwater flow dynamics of fault zones. Flinders University of South Australia and CSIRO, Report to OWS, Canberra, ACT.
- McVicar TR, Langhi L, Barron OV, Rachakonda PK, Zhang YQ, Dawes WR, Macfarlane C, Holland KL, Wilkes PG, Raisbeck-Brown N, Marvanek SP, Li LT and Van Niel TG (2014) Context statement for the Gloucester subregion. Product 1.1 from the Northern

- Sydney Basin Bioregional Assessment. Department of the Environment, Bureau of Meteorology, CSIRO and Geoscience Australia, Australia.
- Noorduijn S, McCallum J, Doble R, Wu B, Mallants D (2018). Assessment of regional-scale effects on groundwater balance linked to increased inter-aquifer leakage, prepared by the Commonwealth Scientific and Industrial Research Organisation (CSIRO), Canberra, in collaboration with Flinders University of South Australia.
- Panday S, Langevin CD, Niswonger RG, Ibaraki M and Hughes JD (2015). MODFLOW-USG Version 1: An unstructured grid version of MODFLOW for simulating groundwater flow and tightly coupled processes using a control volume finite-difference formulation: U.S. Geological Survey Techniques and Methods. book 6. U.S. Geological Survey Techniques and Methods. Available at: <http://pubs.usgs.gov/tm/06/a45>.
- Parsons Brinckerhoff (2012). Water Balance of the Gloucester Stage 1 GFDA, Report PR_1099, Sydney, Australia.
- Parsons Brinckerhoff (2013). Hydrogeological Conceptual model of the Gloucester Basin. Sydney, Australia.
- Parsons Brinckerhoff (2015). Updated conceptual hydrogeological model of the Gloucester Basin. Sydney, Australia.
- Peeters L, Dawes WR, Rachakonda PR, Pagendam DE, Singh RM, Pickett TW, Frery E, Marvanek SP and McVicar TR (In Prep). Groundwater numerical modelling for the Gloucester subregion: Product 2.6.2 for the Gloucester subregion from the Northern Sydney Basin Bioregional Assessment.
- Renard P and Allard D (2011). Connectivity metrics for subsurface flow and transport. *Advances in Water Resources* 51: 168-196.
- Roberts G and Stewart I (1991) NoGeology of the Camberwell, Dungog and ulahdelah 1:100,000 Sheets 9133, 9233, 9333, in Energy NSWDoMa (ed). Sydney, Australia.
- Roberts J, Engel B and Chapman J (1991). NoGeology of the Camberwell, Dungog and ulahdelah 1:100,000 Sheets 9133, 9233, 9333. In: Energy NSWDoMa (ed). Sydney, Australia.
- Turnadge C, Mallants D and Peeters L (2018a). Overview of aquitard and geological fault simulation approaches in regional scale assessments of coal seam gas extraction impacts, prepared by the Commonwealth Scientific and Industrial Research Organisation (CSIRO). Canberra.
- Zinn B and Harvey CF (2003) When good statistical models of aquifer heterogeneity go bad: A comparison of flow, dispersion, and mass transfer in connected and multivariate Gaussian hydraulic conductivity fields, *Water Resources Research*, 39(3) doi: 10.1029/2001WR001146.

9 3D geomechanical deformation modelling¹⁸

9.1 Introduction

3D numerical geomechanical modelling of sedimentary coal basins subject to depressurisation from CSG extraction enables the simulation of the 3D distribution and partitioning of strains and stresses that can impact on intraformational flow and hydraulic properties of faults and fractures (see, e.g. Zhang et al., 2009). In the study area, 3D geomechanical simulations with the stratigraphy and a generic fault thematically based on data from the Gloucester Basin have been performed to investigate the geomechanical effects of depressurisation in coal seams on the stability of a pre-existing fault (referred-to as fault reactivation potential). Effects of modifications to strains and stresses on the connectivity and flow pathways between the fault, aquifers and aquitards are further analysed. When coupled to flow modelling, the geomechanical deformation simulations can be used to assess the dynamic behaviour of faults and the impact of pressure variation on flow pathways (see, e.g. Khan and Teufel, 2000; Zoback and Zinke, 2002; Zhang et al., 2009; Zhang et al., 2011). Our attention here is on the effects of pore pressure variations associated with depressurisation in a simplified reservoir rock system with coal seam units.

9.2 Geo-model setup

9.2.1 Geomechanical simulator FLAC3D

Geomechanical deformation and fluid flow modelling has been performed using FLAC3D (Itasca, 2006). FLAC3D is a very well tested mechanical modelling code from the Itasca Corporation in the USA. It is widely used in civil and mining engineering applications. Its application to geological systems across a range of scales can be found in the literature (e.g. Sorjonen-Ward et al., 2002; Zhang et al., 2009, 2011).

The code is capable of simulating the interactions between deformation and fluid flow in porous media. Modelled materials are represented by a 3D mesh representing the geometries of the observed geological structures. Each element in the mesh behaves according to prescribed mechanical and hydraulic laws and in response to the applied boundary conditions. For this study, rocks are simulated as isotropic elastic-plastic materials that require the specification of several geomechanical parameters, including Young's modulus, Poisson's ratio, cohesion, tensile strength, friction angle and dilation angle. Under deformation loading conditions, such materials deform initially in an elastic manner up to a

¹⁸ Contributing authors: Y Zhang, J Strand, L Langhi, J Underschultz

yield point (i.e. the maximum shear stress in the materials reaches a yield stress), and then after yield, it deforms plastically resulting in irreversible plastic strain (e.g. Ord 1991) (Figure 9-1). The yield stress for the materials is governed by the Mohr-Coulomb failure criteria as described by the equation below:

$$\tau_m = C + |\sigma_n \tan(\phi)| \quad (9-1)$$

where τ_m is the maximum shear stress and σ_n is the normal stress on a plane of the materials, C is cohesion, and ϕ is friction angle. The criterion required for plastic yield to occur is defined by the maximum shear stress becoming equal to the value defined by Equation (9-1). In addition, tensile failure occurs when the effective minimum principal stress (total stress minus pore fluid pressure) is tensile and overcomes the rock tensile strength. Figure 9-1 illustrates the stress-strain relationship for the Mohr-Coulomb elastic-plastic material modelled here.

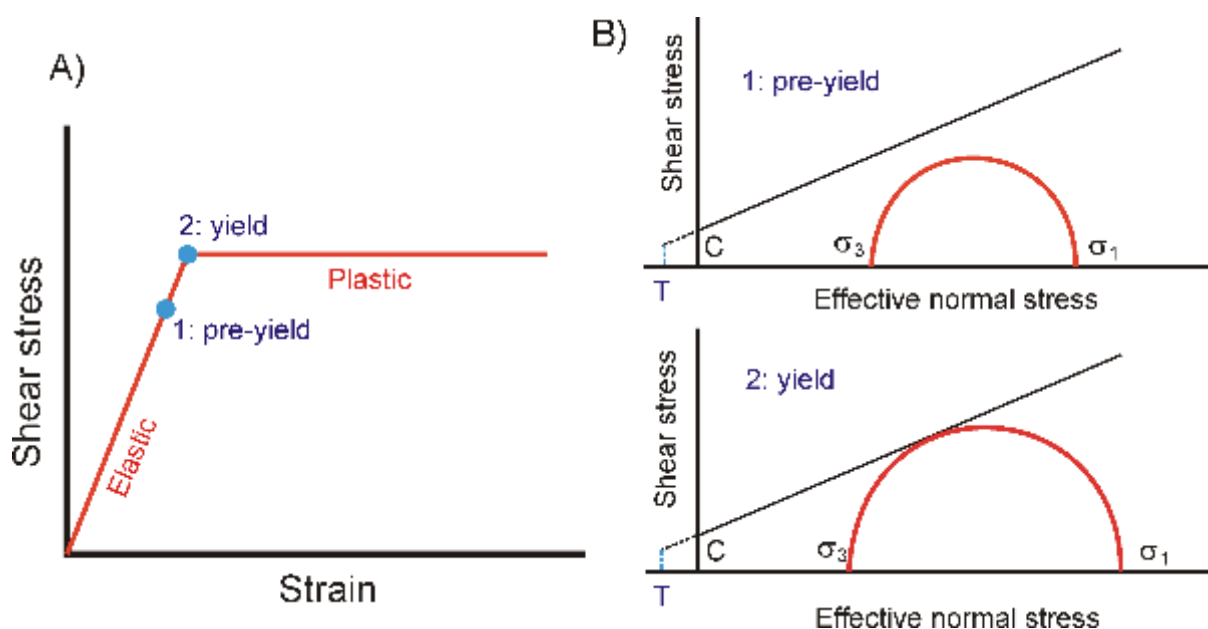


Figure 9-1 (A) Schematic illustration of stress-strain relationship for the Mohr-Coulomb elastic-plastic material. (B) Mohr's circle diagrams for point-1 (pre-yield) and point-2 (yield) in A. Mohr's circle is a two-dimensional graphical presentation of principal stresses (σ_1 and σ_3 are the maximum and minimum principal stresses). Mohr's circle will touch the failure envelope (straight line) when mechanical yield or failure occurs. The vertical dash line and T define the tension cut off (tensile failure) point, where the effective minimum principal stress is tensile and equal to tensile strength.

Fluid flow in the model is governed by Darcy's law for an isotropic porous medium. Fluid flow velocities are primarily a function of gradients in pore fluid pressure and variations in permeability. Fluid flow is coupled with mechanical deformation during a simulation in the following ways.

Interactions between deformation and fluid flow are reflected through a number of coupled processes during simulation:

- (1) shear strain (deformation) causes volumetric strain;
- (2) volumetric strain results in pore pressure changes (e.g. positive volumetric strain/volume increase or “dilation” leads to a local pore pressure decrease);
- (3) changes in pore pressure result in changes in effective stress, which in turn affects rock deformation;
- (4) changes in pore pressure result in changes in fluid flow direction and magnitude; and
- (5) the development of any topographic elevation or depression in the top surface of the model due to deformation results in topographically driven fluid flow assuming that the water table is coincident with the land surface.

9.2.2 Model stratigraphy and structure

The model simulates a simplified stratigraphic sequence thematically representative of the study area (Figure 9-2). It contains an alluvium layer (dominated by unconsolidated sediments of silts-sands-gravels) at the top, eleven thin coal beds, each of which represent a combined unit of multiple thin coal seams and shale inter-beds, eleven interburden beds (strong and well cemented silty sandstone layers) sandwiched between coal layers, and a basal “basement” unit at the base (carboniferous strata of conglomerate, sandstone and siltstone). A generic fault of 60 degree dip is included in the model. The model stratigraphy and fault structure are loosely based on existing hydrogeologic data and conceptualisations for the Gloucester Basin (Frery et al., 2014); the resulting model is therefore not purely hypothetical but uses a simplified hydrostratigraphic conceptualisation. Such simplification facilitates a straightforward analysis of the complex interactions between mechanical and hydraulic processes.

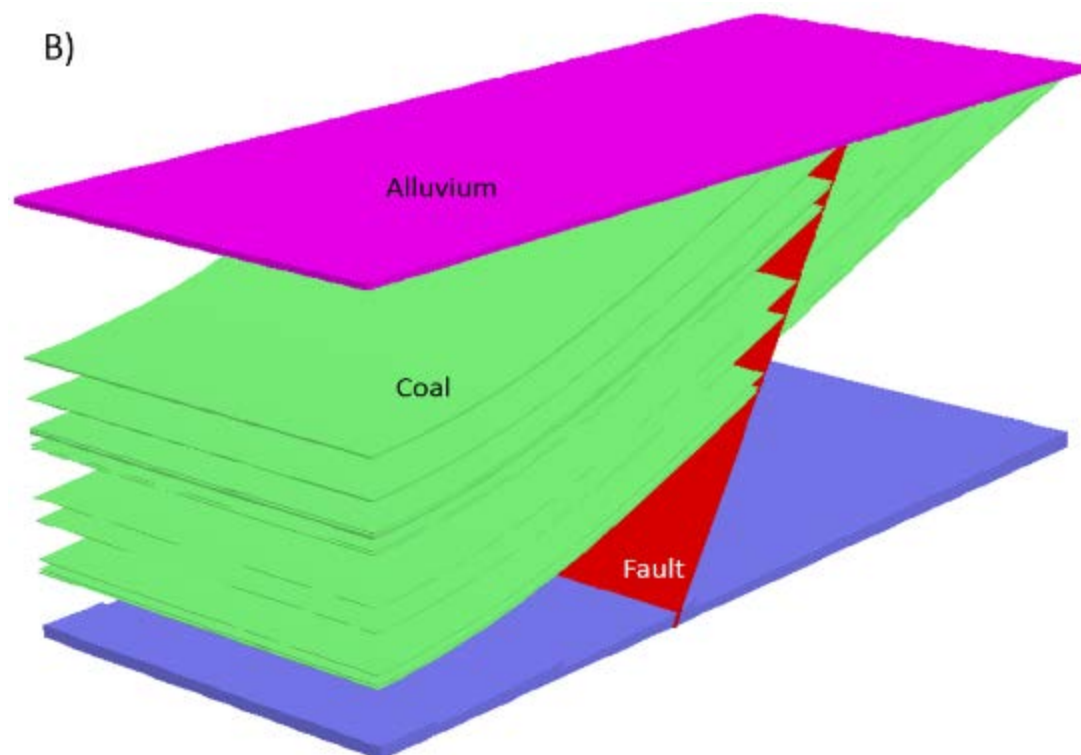
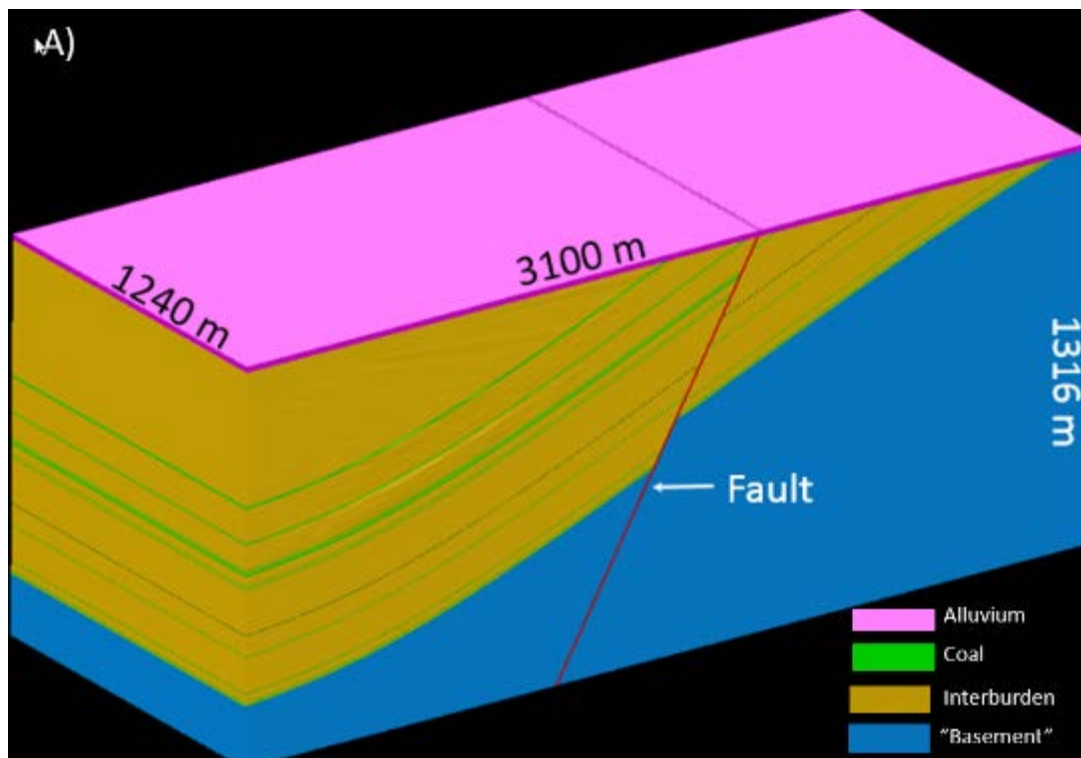


Figure 9-2 Model geometry. (A) Full model. (B) Model internal structure with 11 coal layers and a single generic fault.

9.2.3 Mechanical and hydraulic properties

A complete set of geomechanical and hydrological properties are given in Table 9-1. The specification of these parameters are based on available data for the study area and also data in literature (Lama and Vutukuri, 1978; Turcotte and Schuberts, 1982; Gentzis et al., 2007; Connell, 2009; Langhi et al., 2010; Parsons Brinckerhoff, 2012). Of note is the lack of laboratory test data on rocks from the area. The fault permeability was chosen such that it would be lower than coal but higher than other rock units in the base models.

Table 9-1 Summary of model properties. (1 mD corresponds to 7.5×10^{-4} m/d or 8.62×10^{-9} m/sec). IB = interburden; BU = Basal “basement unit.

Unit	Density (kg/m ³)	Young’s modulus (Pa)	Poisson’s ratio	Cohesion (Pa)	Tensile strength (Pa)	Friction angle (degree)	Dilation angle (degree)	Permeability	Porosity
Alluvium	2082	2.5E+7	0.35	2.0E+4	1.0E+4	35	2	1 D	0.15
IB	2450	3.5E+10	0.25	1.5E+7	7.5E+6	30	2	1 mD	0.03
Coal	1500	1.9E+9	0.39	5.7E+6	2.8E+6	35	2	20 mD	0.1
BU	2487	3.6E+10	0.25	1.8E+7	9.0E+6	30	2	0.1 mD	0.015
Fault	2398	2.0E+9	0.15	5.0E+6	2.5E+6	20	2	10 mD	0.05

9.2.4 Initial model conditions

The regional stress patterns for the Sydney Basin (Hillis et al., 1999) are used as a reference for the specification of initial stresses in the models due to lack of measured stress data or analytical data based on realistic vertical stresses (i.e. realistic density variations with depth) for the study area at the time of modelling. Previous studies indicate that eastern Australia is dominated by reverse-faulting stresses with local areas of strike-slip faulting and normal faulting stresses (e.g. Hillis et al., 1999; Brooke-Barnett et al., 2015) (Figure 9-3). There are also large variations in stress magnitudes and gradients throughout the region both geographically and in depth. Our approach here is generic, that is, defining an initial stress field that does not lead to fault failure before depressurisation and then exploring how depressurisation potentially alters stress or generates perturbations. Specific initial stress conditions will be described in the next section for modelling scenarios.

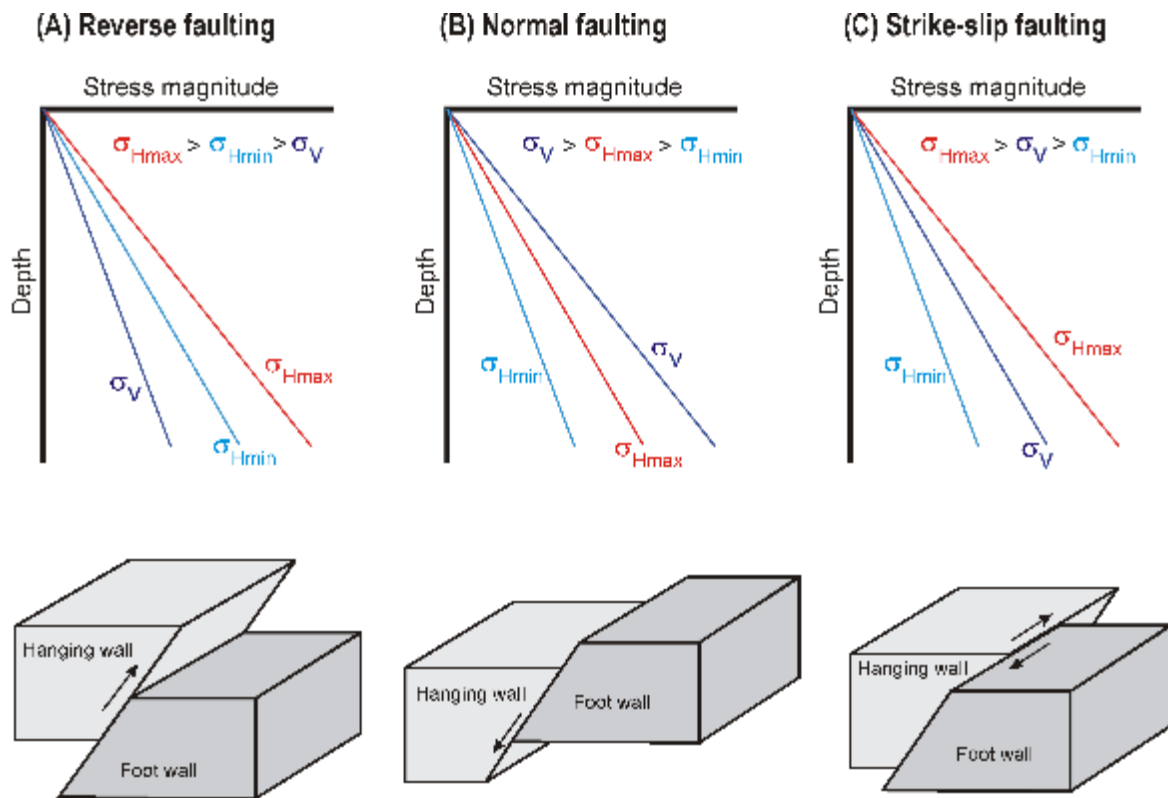


Figure 9-3 Schematic illustration of stress gradients and fault movement for (A) reverse-faulting stress, (B) normal-faulting stress, and (C) strike slip-faulting stress cases. σ_V is the vertical stress, σ_{Hmax} is the maximum horizontal stress and σ_{Hmin} is the minimum horizontal stress.

Initial hydrostatic pore pressures (Figure 9-4) are defined in the models with the entire domain assumed fully water-saturated. Permeable fluid flow boundary conditions are used for all of the model boundaries which are kept constant throughout a simulation.

“Container”-like static geomechanical boundary conditions are adopted in the model. The top of the model is simulated as a free surface. The base is not allowed to move in the vertical direction but is free to move in other directions. Vertical edges of the models are not allowed to move in the direction perpendicular to the edge but are free to move in the on-plane directions.

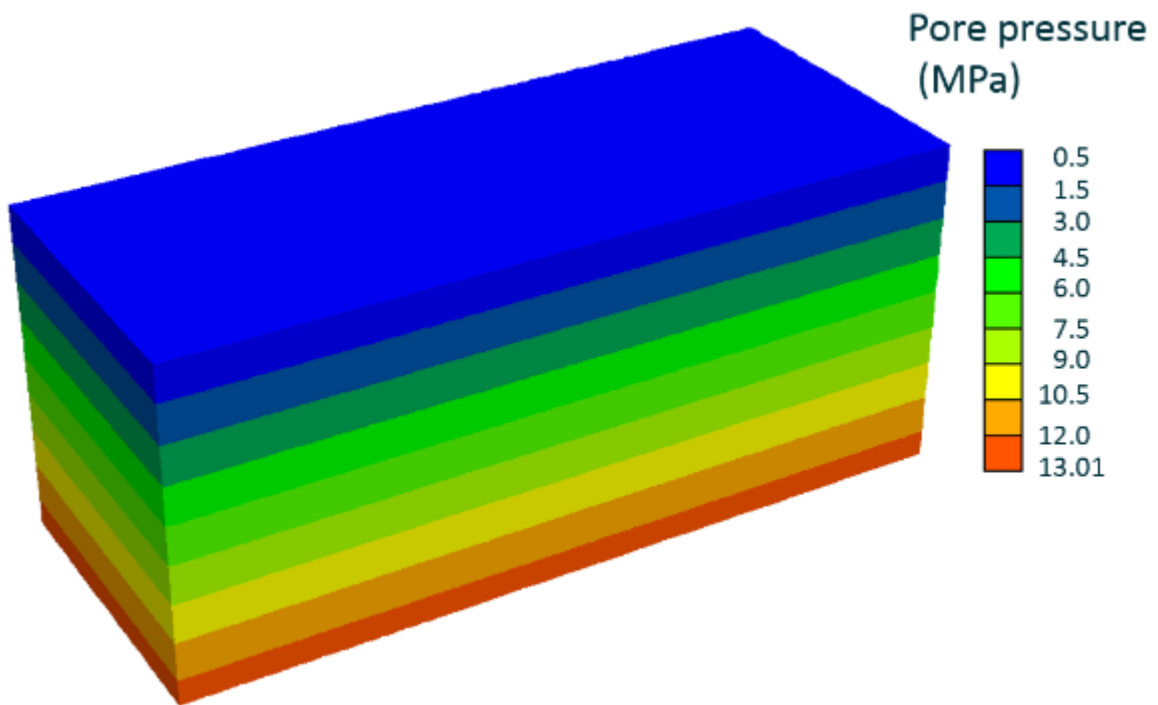


Figure 9-4 Initial pore pressure of the model.

9.2.5 Scenarios for modelling

Scenarios for depressurisation

Depressurisation at an intersection site between a well and coal seam unit is simulated by incorporating a pore pressure drawdown from the initial pore pressure values at the depressurisation site to 1 MPa (i.e. final pore pressure), the critical desorption pore pressure for coal seam gas (Morad et al., 2008). This involves pore pressure drawdowns of >80% from initial pressure values, and hence probably represents a worst-case scenario. In the simulation, the pore pressure drawdowns are linearly implemented as a series of small increments over a period of 40 days, which is followed by 30 days of equilibrium.

To understand the behaviour of the current depressurisation simulations, a series of depressurisation scenarios have been tested, including the cases of: 1) one well depressurising one single shallow or deeper coal seam unit; 2) four wells depressurising one single shallow or deeper coal seam unit; 3) four wells depressurising all the coal seam units in the models below an approximate depth level of -300 m.

The model results for depressurisation scenario (3) (Figure 9-5) are only presented here, because this scenario is the most realistic one of the tested scenarios to represent depressurisation for coal seam gas extraction in real gas fields.

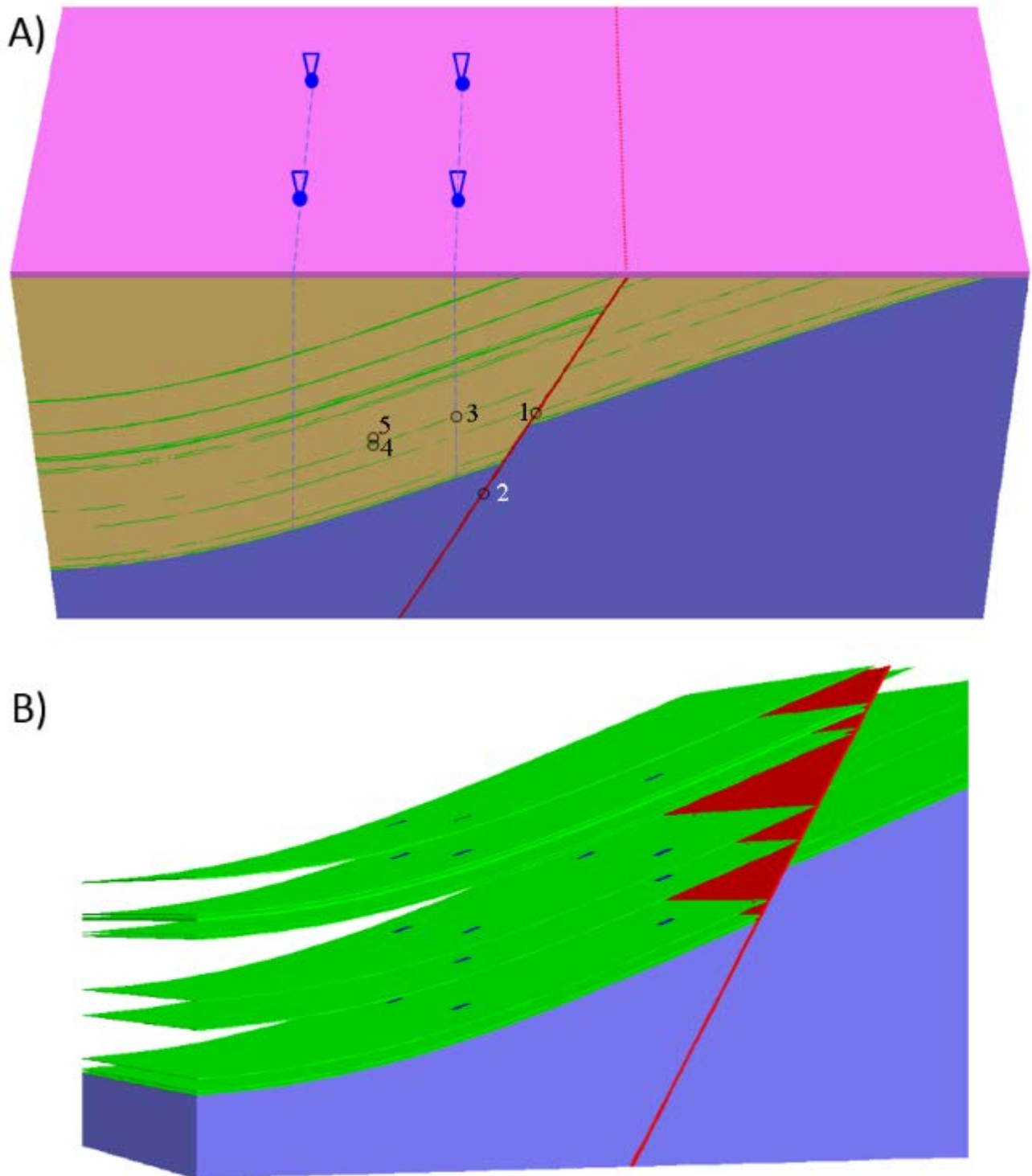


Figure 9-5 Illustration of four well locations for depressurisation simulations (A) and depressurisation locations on coal seam units (B). Numbered open circles in (A) show approximate depth levels of pore pressure and shear stress tracking locations in the model. Also note that interburden units are not plotted in (B) and red triangles are fault segments exposed between coal units.

Scenarios for initial model stress regimes

Three initial stress regimes are investigated in the models (See Figure 9-3 for the concept of faulting stress regimes). These are generic approaches to investigate the impact of depressurisation. We are interested in the effect of depressurisation on these stress regimes, where the initial stresses do not lead to fault failure but the fault (or part of it) is critically stressed (i.e. close to failure) prior to depressurisation.

1. Reverse faulting stress regime ($\sigma_{Hmax} > \sigma_{Hmin} > \sigma_v$)

This is the dominant stress regime for eastern Australia (Hillis et al., 1999). Because there were no measured stress data for the Gloucester Basin at the time of modelling, the following stress gradients are used in the model, based on the average stress patterns for the Sydney Basin (Hillis et al., 1999): lithostatic stress (or overburden pressure due to the weight of overlying material) for σ_v or σ_3 (vertical stress); 50 MPa/km for σ_{Hmax} or σ_1 (the maximum horizontal stress, in the E-W direction); and (3) 35 MPa/km for σ_{Hmin} or σ_2 (the maximum horizontal stress, in the N-S direction). Note that the vertical stress gradient varies throughout the model due to dipping stratigraphic beds and horizontally-inhomogenous density distribution.

2. Normal faulting stress regime ($\sigma_v > \sigma_{Hmax} > \sigma_{Hmin}$)

This stress regime could be locally present in sedimentary basins in eastern Australia. The data for the Sydney basin (Hillis et al., 1999) suggest that the lowest stress ratio ($R =$ Ratio of minimum stress to maximum stress in one cycle of loading) between σ_{Hmin} (σ_3 , in the E-W direction) and σ_v (σ_1) is approximately 0.48, which was adopted as the stress condition for the base model (σ_{Hmax} or σ_2 is intermediate between σ_v and σ_{Hmin}), as a worst case scenario for investigating fault failure/reactivation. Another stress ratio assuming a weaker fault scenario is also investigated, which will be described in the results section for the convenience of description.

3. Strike-slip faulting stress regime ($\sigma_{Hmax} > \sigma_v > \sigma_{Hmin}$)

This stress regime could also be present in eastern Australia. A stress ratio of $R = 0.5$ between σ_{Hmin} (σ_3) and σ_{Hmax} (σ_1) is adopted as a generic approach, with σ_v being intermediate.

9.3 Simulation results

9.3.1 Results of the models with a reverse faulting stress regime

Pore pressure variations due to depressurisation

Along with pore pressure drawdown at depressurisation locations (red line in Figure 9-6), all the surrounding areas in the model experience pore pressure decrease. The magnitude of pore pressure decreases is dependent on the distance of a location from depressurisation locations.

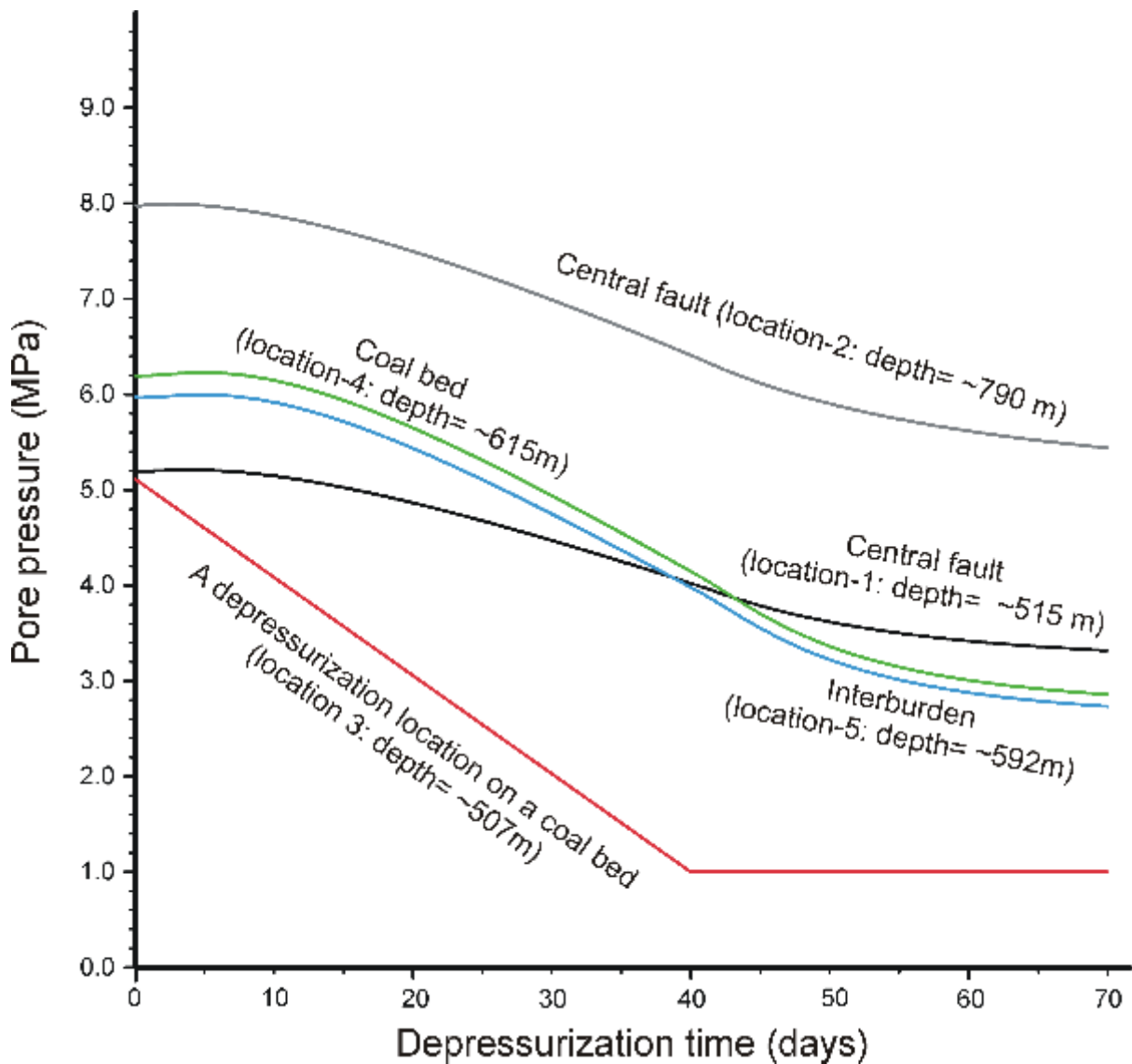


Figure 9-6 Pore pressure variations with depressurisation at locations for the four-well scenario in the model (reverse faulting stress regime). Note that all pore pressure curves start from hydrostatic conditions. See Figure 9-5 for the locations and depth levels of datum-tracking points in the model.

To investigate the effect of the rate of pore pressure drawdown, a second model run with fast depressurisation is performed (i.e. pore pressure drawdown over two days against 40 days in the base model). It is noted that final pressure after approximately 60 days for these monitored locations are consistent with the base model (Figure 9-7). However, some initial pore pressure increases are observed immediately after the start of depressurisation, before overall pore pressure start to a decrease. This feature is believed to reflect the effects of early perturbations from the flow fields corresponding to fast pore pressure drawdown.

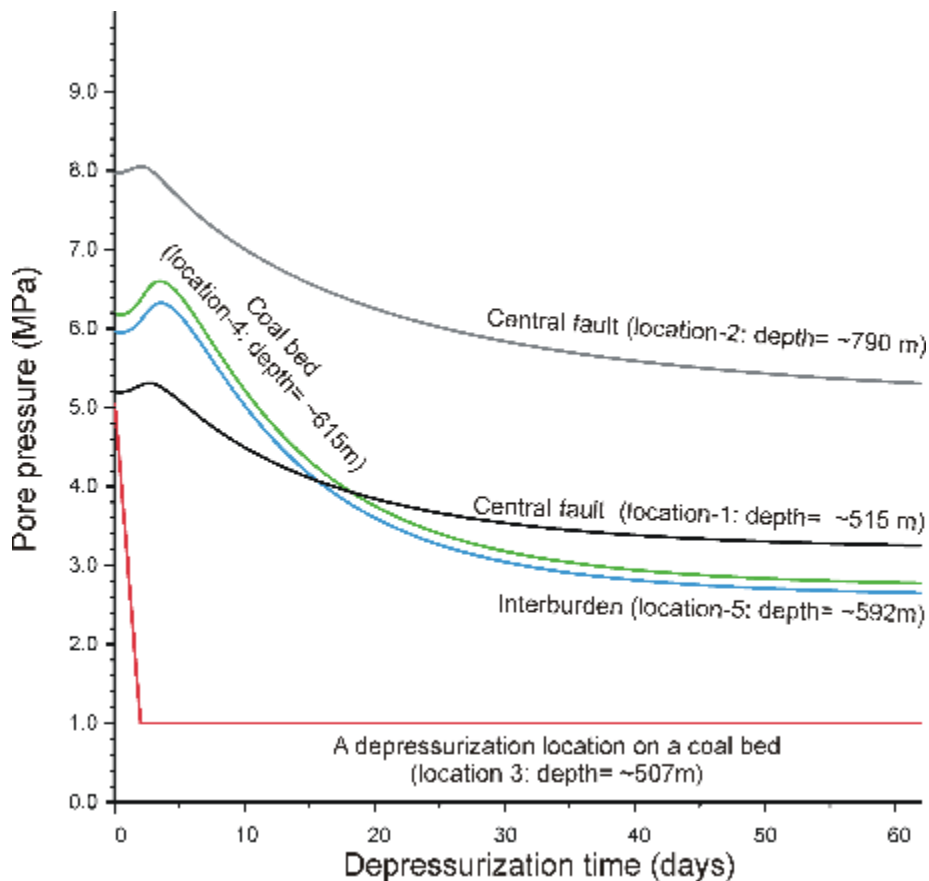


Figure 9-7 Pore pressure variations with fast depressurisation at a number of locations in the model (reverse faulting stress regime). See Figure 9-5 for the locations and depth levels of datum-tracking points in the model.

The final pore pressure distribution for the base model is shown in Figure 9-8 (top image). It is noted that extensive and large pore pressure decreases occurred in the hanging wall area of the fault surrounding depressurisation locations. Pore pressure changes appear to be greater in the vertical direction than the horizontal direction. In addition, the impacts of depressurisation appear to be greater in shallower levels above a depressurisation point than in deeper horizons below a depressurisation point. This likely reflects the effect of the low permeability of the "basement", due to which the pressure perturbation cannot diffuse into the basement.

To investigate the effects of fault permeability on pore pressure variations, two additional models with lower (0.1 mD) and higher (50 mD) fault permeability than in the base model (10 mD), have been performed. The results (Figure 9-8, middle image) show that when a much lower fault permeability is involved, a pattern of pore pressure compartmentalisation becomes clear. Pore pressure decreases are almost entirely confined to the hanging-wall area, with little pore pressure perturbation occurring in the footwall area across the fault (also see Figure 9-3). This illustrates the role of a sealing fault in a reservoir. For the model with a higher fault permeability of 50 mD (Figure 9-8, bottom image), pore pressure perturbation from depressurisation into the footwall area is greater than in the base model

(Figure 9-8, top image), showing the behaviour of a more permeable fault (providing better connectivity across a fault).

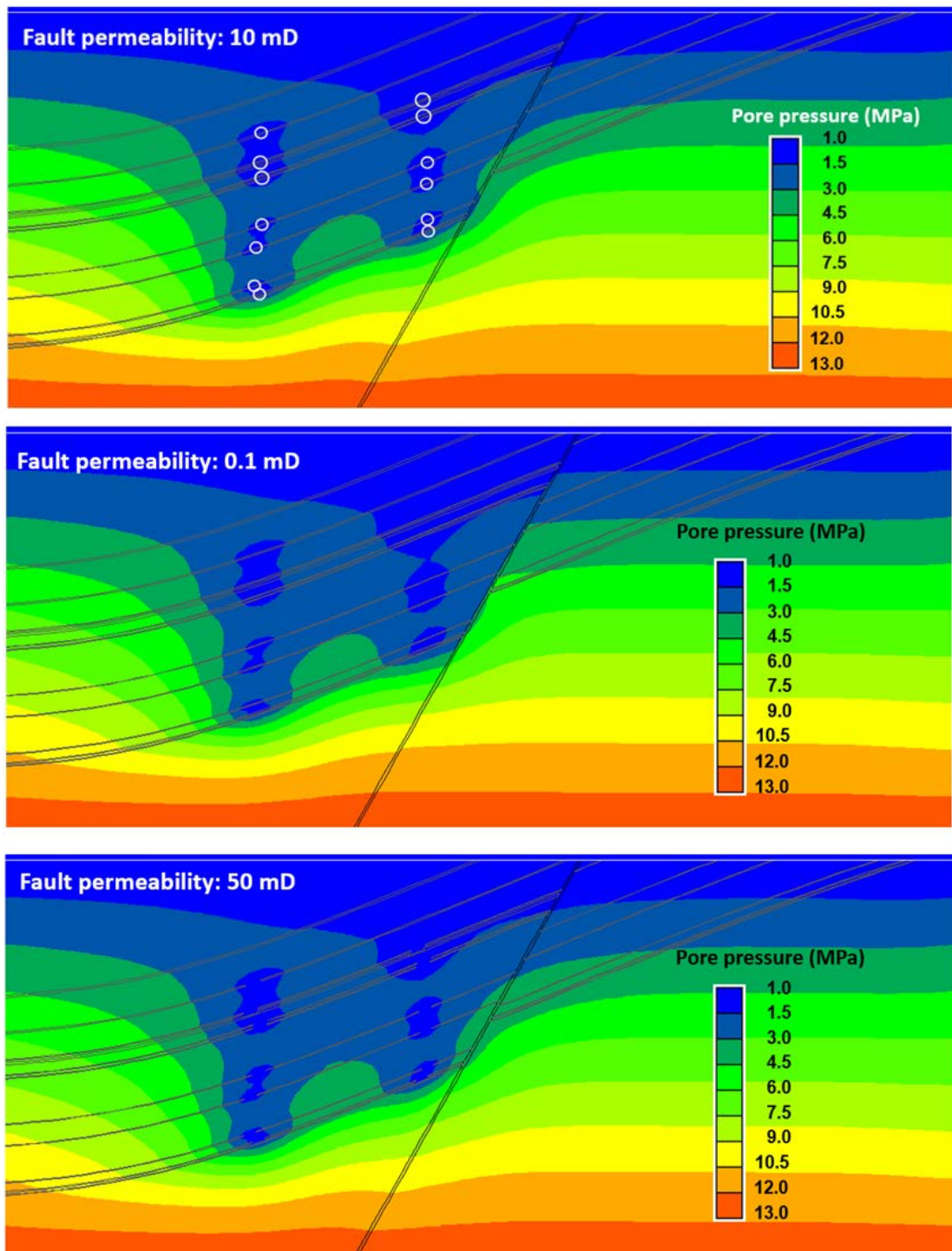


Figure 9-8 Final pore pressure distribution on an E-W vertical cross section truncating depressurisation locations through the model (reverse faulting stress regime). Three images are for the models with fault permeability of 10 mD (top), 0.1 mD (middle) and 50 mD (bottom). Coal permeability is 20 mD in all models. Circles on top image show approximate depressurisation locations (i.e. CSG wells intersection coal layers).

Simulation tests also show that the permeability of coal beds influences the final pore pressure patterns in the models with identical depressurisation conditions. As seen in Figure 9-9, pore pressure perturbations and reductions derived from the depressurisation conditions are more extensive in the model with a higher coal permeability than in the model with a lower coal permeability.

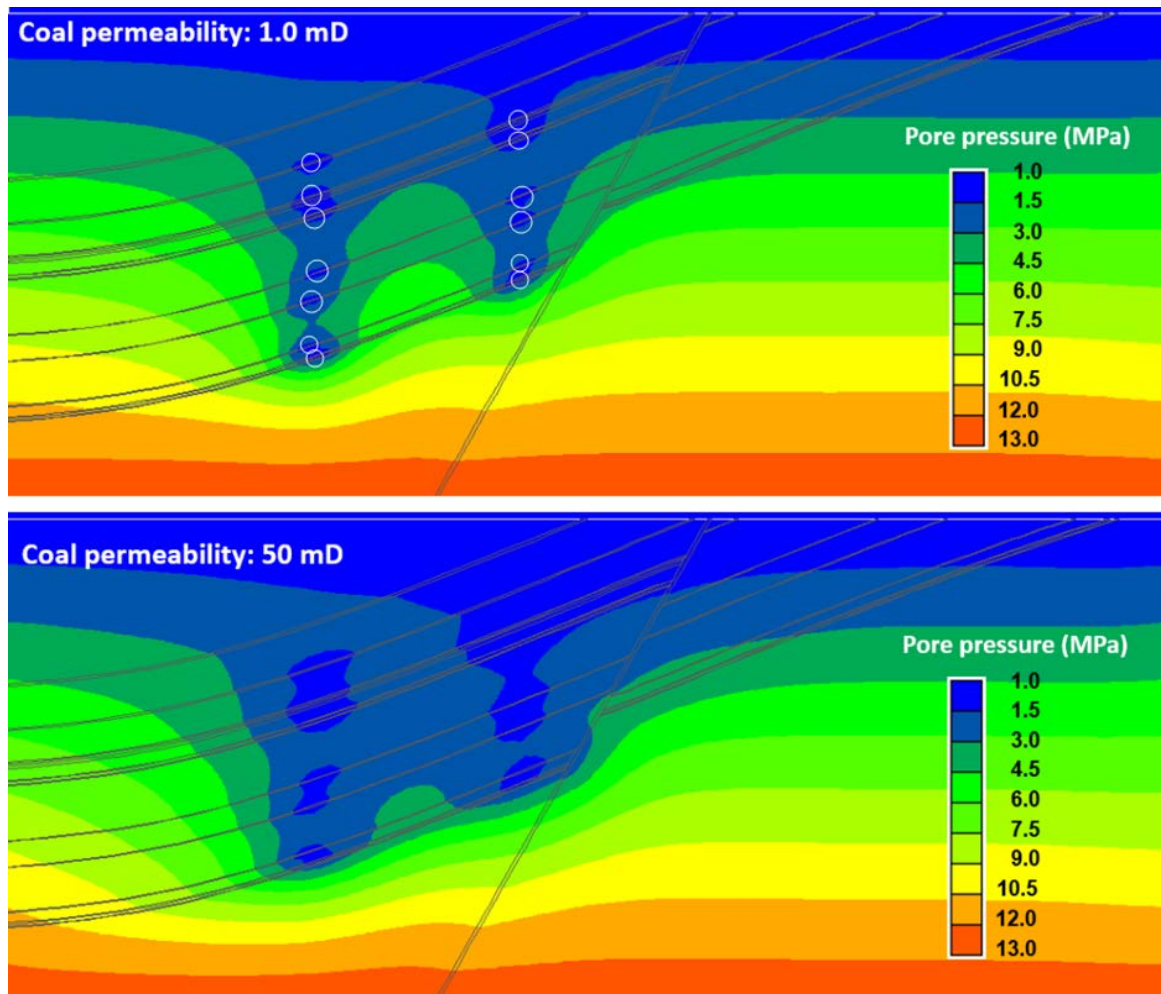


Figure 9-9 Final pore pressure patterns on an E-W vertical cross section for the models with coal permeability = 1.0 and 50 mD, respectively. Fault permeability is kept at 10 mD in both models. Circles on top image show approximate depressurisation locations.

Stress alteration

Analyses of stress variations show that shear stresses in the model with a reverse stress regime all decrease in response to depressurisation, for example in the fault and coal beds (Figure 9-10). Plots of the stresses on Mohr's circle diagrams (Figure 9-11, fault locations are in the centre of the fault at the indicated depths; also see Figure 9-1 for information about Mohr's circle diagrams) clearly illustrate two features:

- 1) decrease of shear stresses; and

2) increase of the effective stresses and hence the Mohr's circles shift further away from failure envelopes. These features determine that there will be no mechanical failure in fault (reactivation) or coal as the result of depressurisation as confirmed in the present models. We note again that the reverse stress regime is the dominant one for eastern Australia.

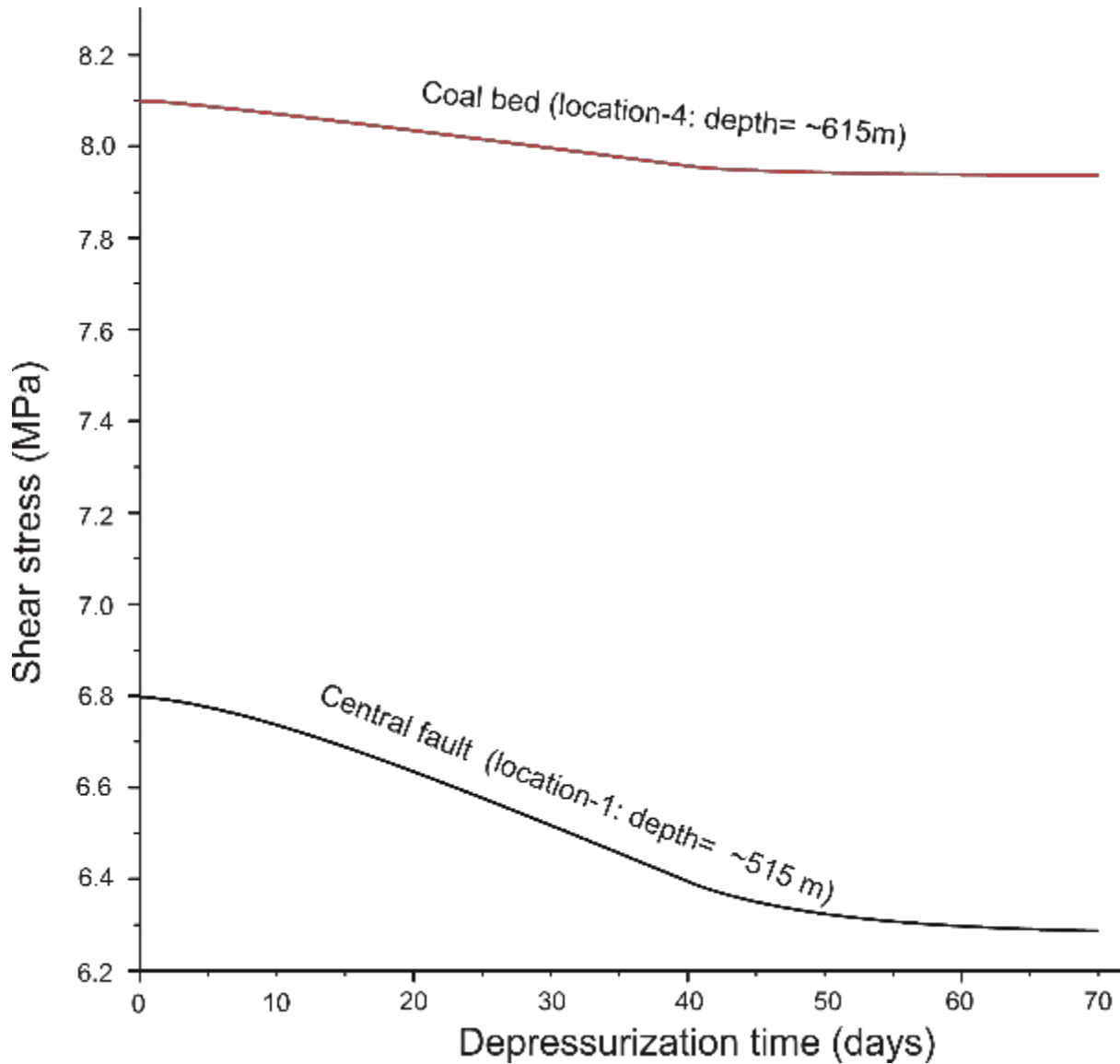


Figure 9-10 Plots of shear stresses in the fault and coal beds in the model with a reverse faulting stress regime. See Figure 9-5 for the locations and depth levels of datum-tracking points in the model.

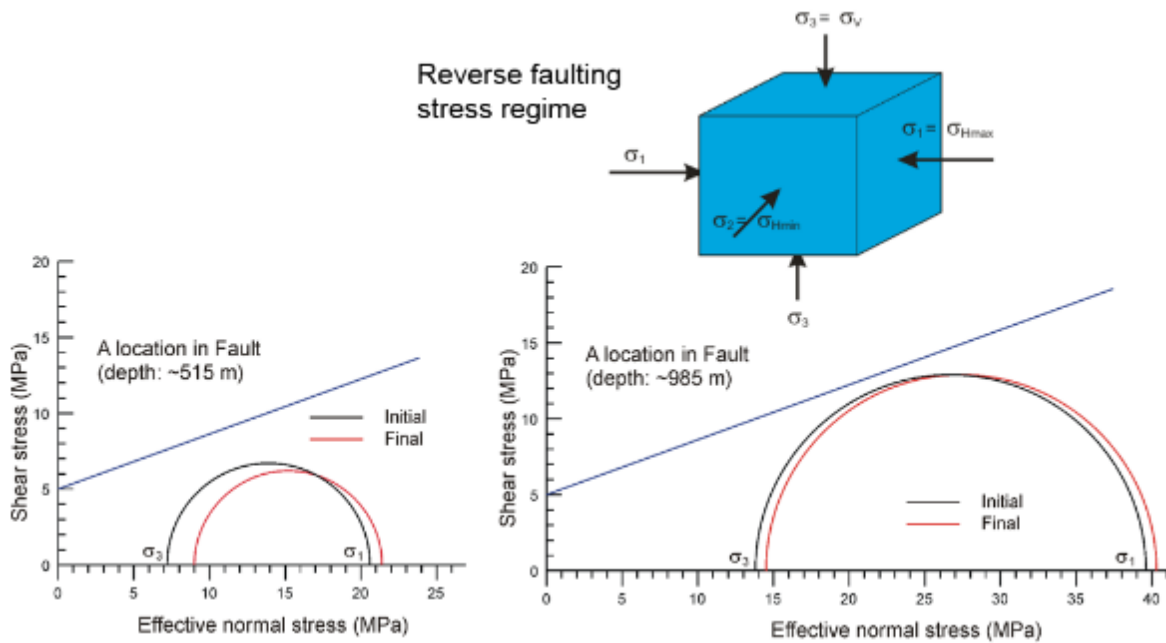


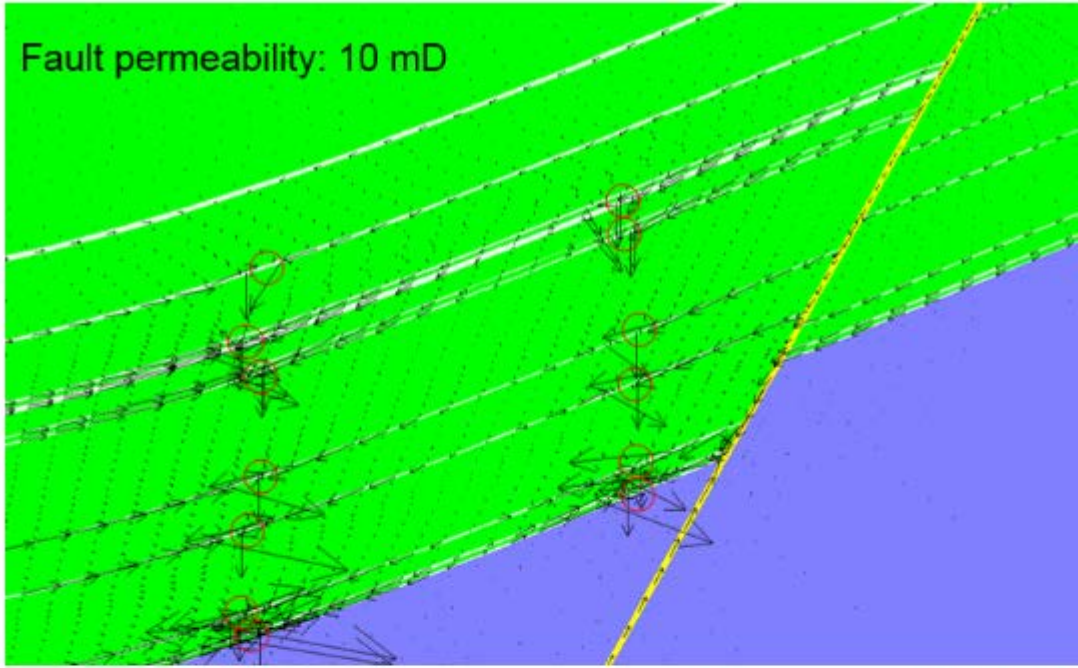
Figure 9-11 Mohr's circle diagrams showing stress variation with respect to failure envelopes under a reverse faulting stress regime. σ_1 , σ_2 and σ_3 are the maximum, intermedium and minimum principal stresses, respectively. σ_v is the vertical stress, and σ_{Hmax} and σ_{Hmin} are the maximum and minimum horizontal stress, respectively.

Fluid flow patterns

Fluid flow is dominated by lateral flow along coal beds, converging towards depressurisation locations on coal beds (i.e. production wells) (Figure 9-12). For the base model with fault permeability = 10 mD, there is flow both across and along the fault, suggesting movement of fluids from the footwall side towards the hanging-wall side. For the model with a 100 times lower fault permeability of 0.1 mD (Figure 9-12), there is little flow in the fault or movement of fluids from the footwall to the hanging-wall side. The maximum flow velocities occur around depressurisation sites (production wells) on coal beds in both models, as is determined by depressurisation-resultant pore pressure decreases in these points.

As is indicated by model tests, changing coal bed permeability does not change flow patterns, that is, fluid flow still converges towards production wells and there is still strong flow across/along the fault (across-fault flow is mainly exhibited at intersecting locations between the fault and coal beds). However, changes in coal permeability strongly change fluid flow velocities along de-pressured coal beds. Figure 9-13 compares flow patterns between two models with the coal permeability of 50 mD and 1.0 mD, respectively (fault permeability is kept at the base model value of 10 mD). In the model with higher coal permeability (Figure 9-13A), flow velocities along the de-pressured coal beds are much greater than in the model with a lower permeability (Figure 9-13B); note that flow velocity in the fault is different in both models (flow velocity in the fault for the high-permeability model is invisible due to scaling effect).

A) Fault permeability: 10 mD



B) Fault perm: 0.01 mD

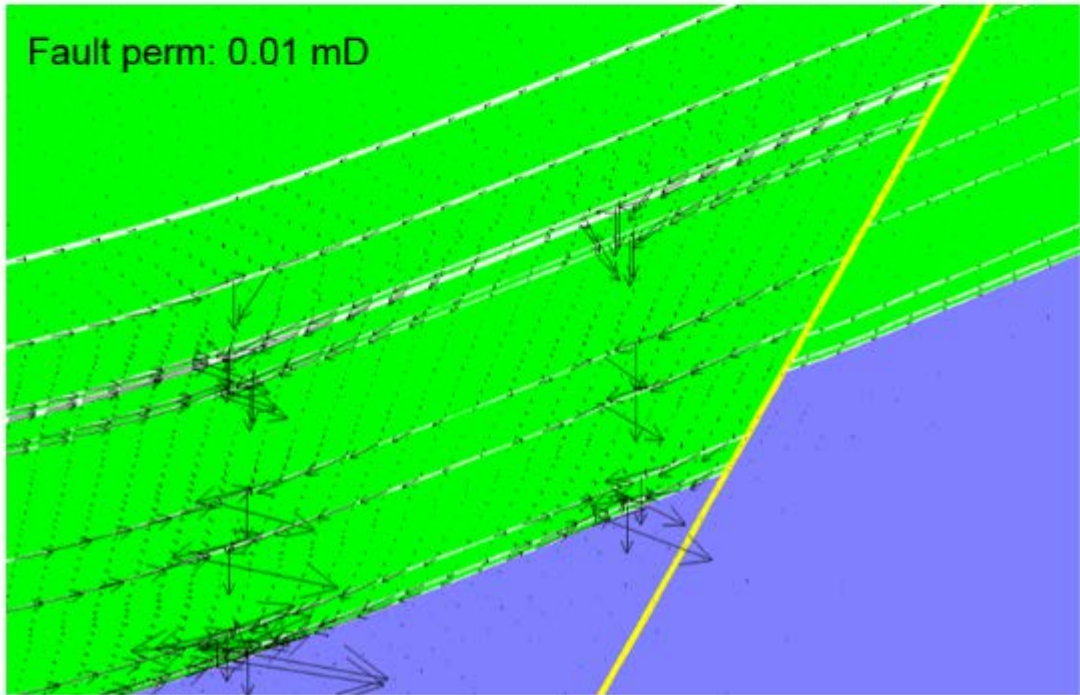


Figure 9-12 Plots of fluid flow velocity vectors on a vertical cross section for models with fault permeability of (A) 10 mD (the base model) and (B) 0.1 mD. Maximum flow velocity is $\sim 7.9 \times 10^{-7}$ m/s in both models. Circles on (A) show approximate depressurisation locations.

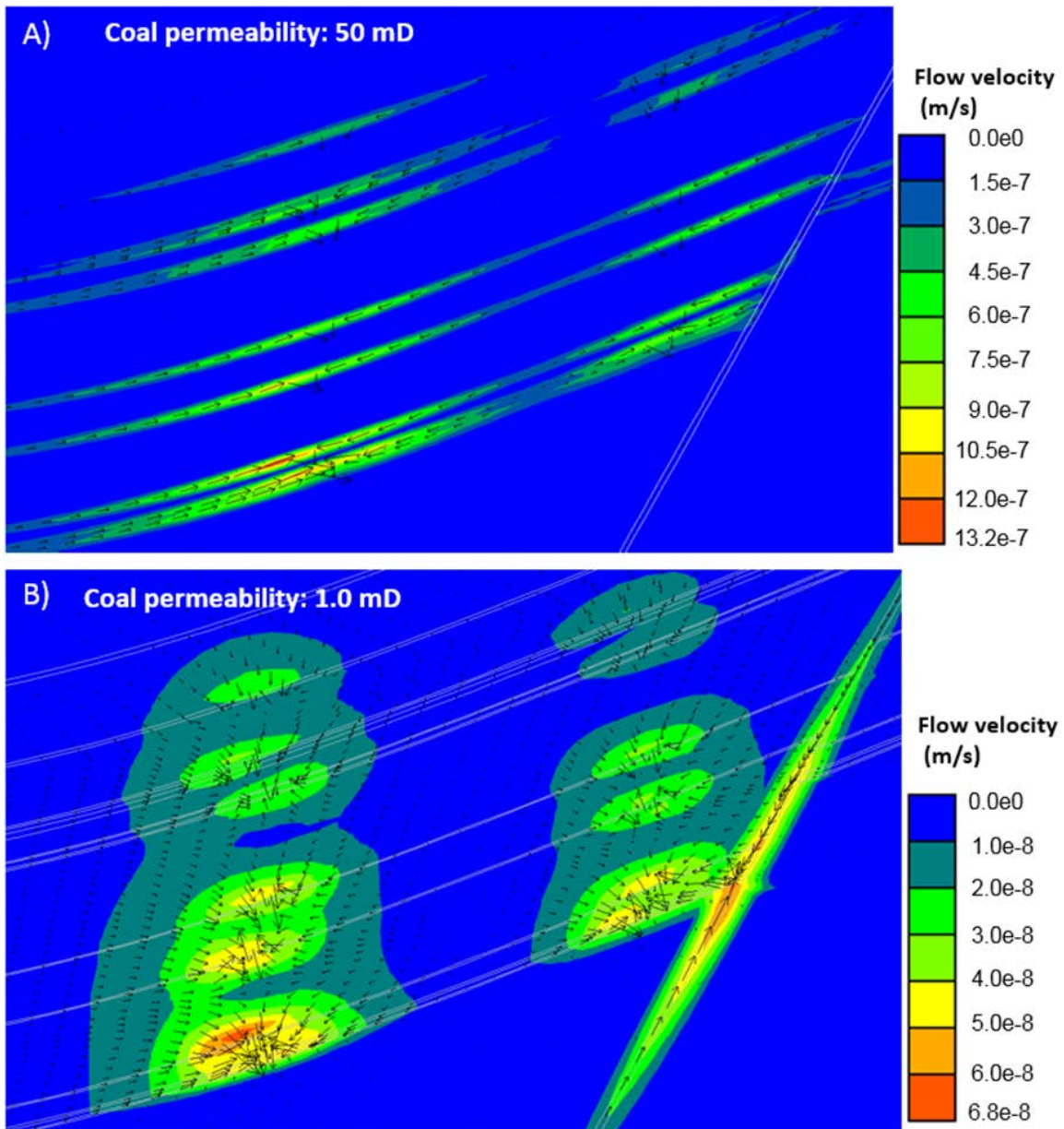


Figure 9-13 Fluid flow velocity contours and vectors on a vertical cross section. (A) Model with coal permeability = 1 mD. (B) Model with coal permeability = 50 mD. Fault permeability is kept at 10 mD in both models. Note different flow velocity scales in the images for best visualization of fluid flow velocity contours and vectors. High flow velocity locations on coal beds are depressurisation locations (also see Figure 9-12A for these locations).

9.3.2 Model results for normal faulting stress regime

Pore pressure changes and fluid flow patterns are consistent with those from the models with a reverse faulting stress regime described above, as these are predominantly governed by depressurisation-resultant pore pressure changes and flow properties (these remain consistent in the models for both regimes). In this section, we therefore focus on stress alteration in response to depressurisation under a normal faulting regime.

In contrast to the models with reverse-faulting stress regimes, stress alteration under the normal faulting stress regime as the result of depressurisation is characterized by shear stress increase (Figure 9-14). It is noted that upon the onset of depressurisation or fluid depletion, shear stresses in fault and coal beds both start to increase until the end of the depressurisation phase and then flatten out by the end of the post-depressurisation equilibrium phase. Shear stress increases within the fault (at ~515m depth level) are greater than 0.5 MPa.

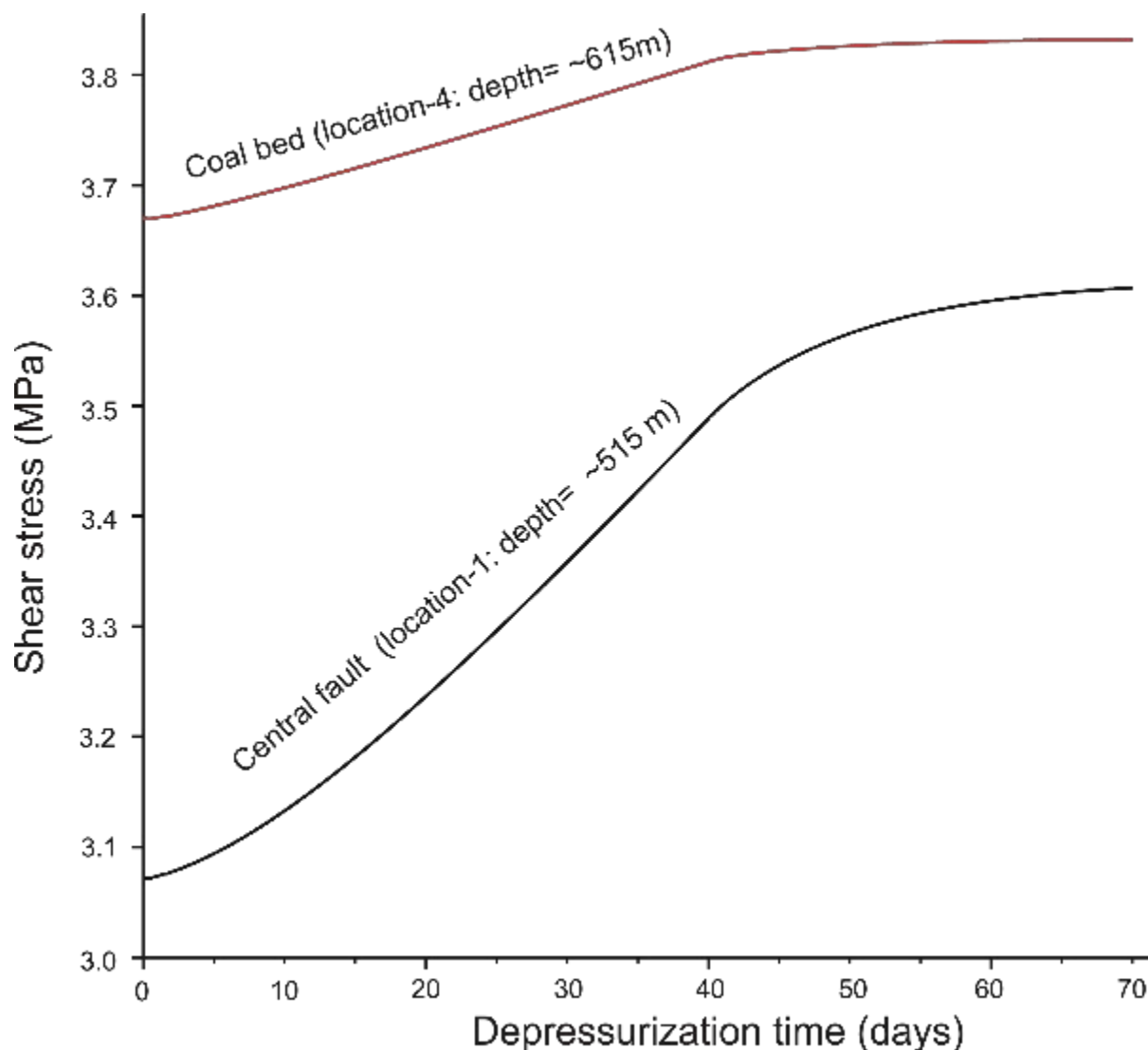


Figure 9-14 Plots of shear stresses in fault and coal in the model with a normal faulting stress regime. See Figure 12-5 for the locations and depth levels of datum-tracking points in the model.

However, the examination of geomechanical failure status in the model indicates that there is no failure in the fault and coal beds under the present set of model mechanical properties. Plots of model stresses on the Mohr-circle diagrams (Figure 9-15) provide an insight, showing that shear stress increases are insufficient to generate failure in the model. More specifically, shear stress increases lead to some expansion of the stress Mohr's circles

but not sufficient for contact with the failure envelopes, rather, the increases of effective stresses due to pore pressure decrease actually shifts the stress Mohr's circles further away from the failure envelopes (Figure 9-15). For failure to happen, the following conditions are required: 1) shear stress increase is sufficiently large; 2) fault and rock strength parameters (cohesion and friction angle) are sufficiently low; 3) pore pressure increase is sufficiently large.

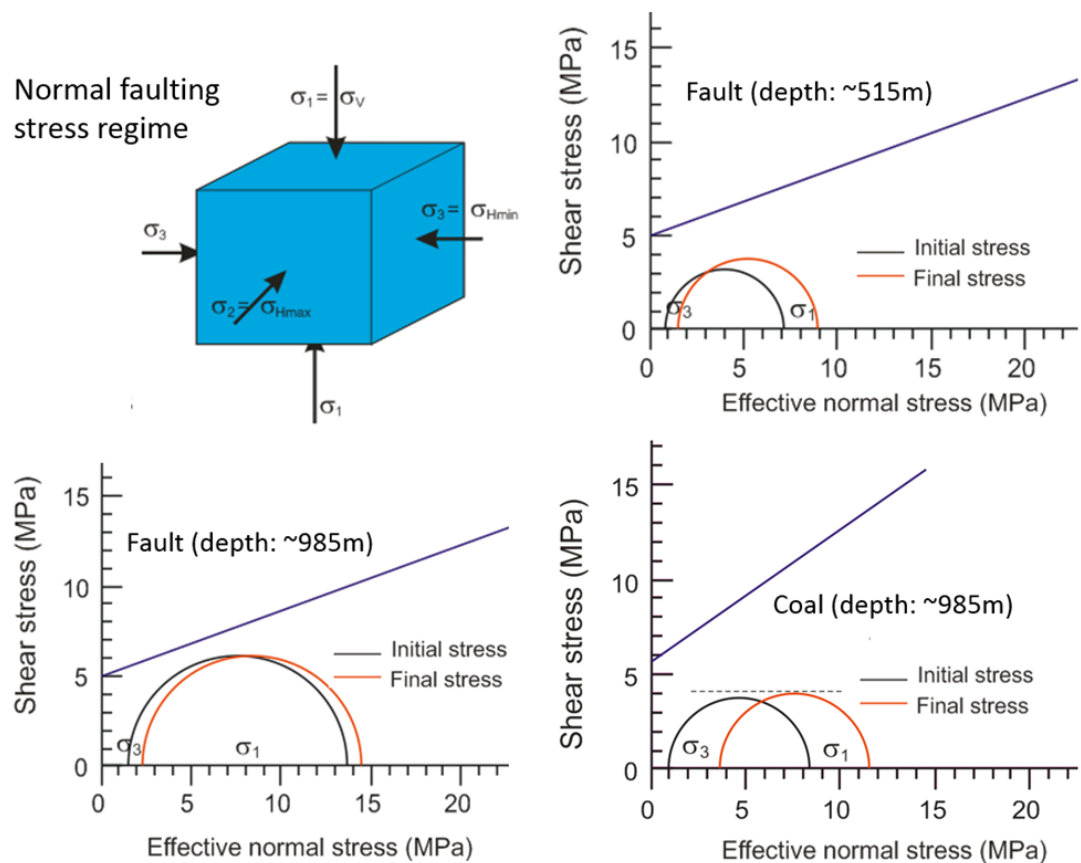


Figure 9-15 Mohr's circle diagrams showing stress variation with respect to failure envelopes under a normal faulting stress regime.

It is helpful to investigate and understand, as a generic case, what conditions might lead to the failure or reactivation of a fault as the result of depressurisation in a normal stress regime. A model has therefore been constructed with a reduced fault cohesion of 2 MPa (we used 5 MPa in the base model), which was used by Zhang et al. (2015) as a weak fault scenario for a CO₂ case study in the Southwest CO₂ geosequestration Hub, Western Australia. A variable stress ratio (R) from 0.5 to 0.65 from shallow depth (500 m) to greater depth (1000 m) is used in this model to impose conditions typical of a critically-stressed fault (fault stresses are such that the fault is close to failure - its Mohr's circle is close to the failure envelope) in a normal stress regime (Figure 9-16). In this way we can investigate the impact of depressurisation effects on stress alteration and fault failure under the worst-case

scenario. The results show that under the model property and initial stress condition, shear stress increases associated with depressurisation is large enough to generate a partial failure or reactivation of the fault (Figure 9-17).

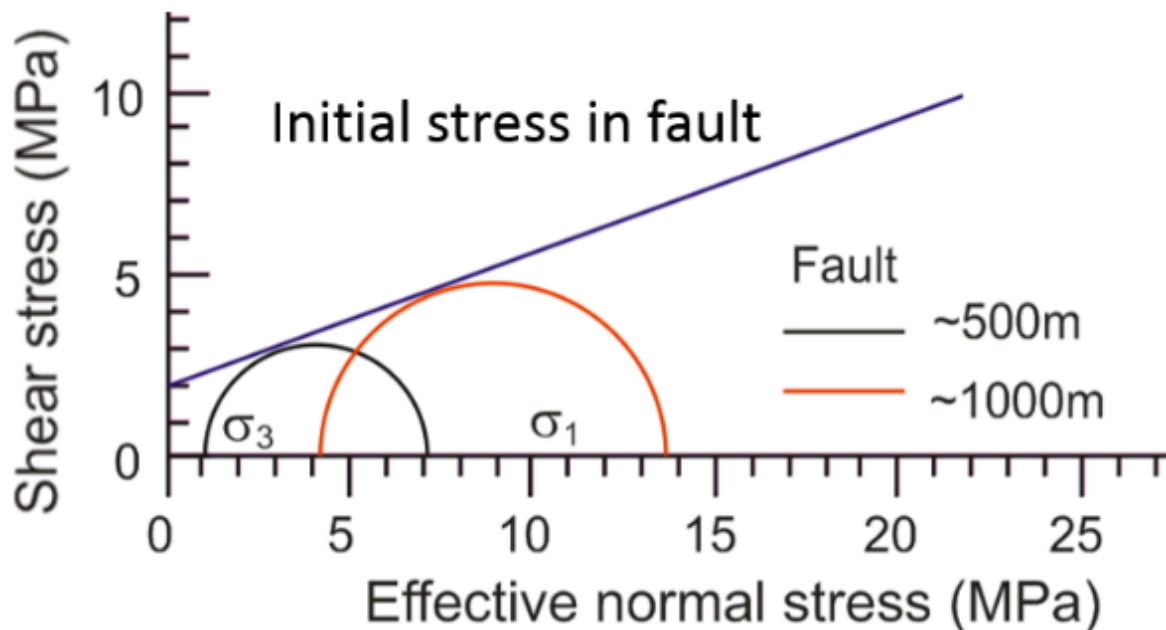


Figure 9-16 Mohr's circle diagrams showing initial stresses in a fault in a model with low fault cohesion of 2 MPa and a variable stress ratio from 0.5 to 0.65 from shallow depth (500 m) to greater depth (1000 m). Note that the fault is critically-stressed from shallow to greater depth.

Under the above stress conditions, there is still no mechanical failure in the coal beds (Figure 9-18). It appears coal beds are unlikely to fail when using the present coal properties and conventional Mohr-Coulomb elastic-plastic constitutive theory. This is demonstrated by a model with a lower coal cohesion (1 MPa) compared to that (5.7 MPa) in the base model (Figure 9-18). This is because coal beds have a large friction angle (35°), and as such, the effect of effective mean stress increase (Mohr circle moves horizontally and in the positive x-direction) due to pore pressure reduction is far greater than the effect of shear stress increase (Mohr circle moves vertically) as illustrated by the Mohr's circle diagram.

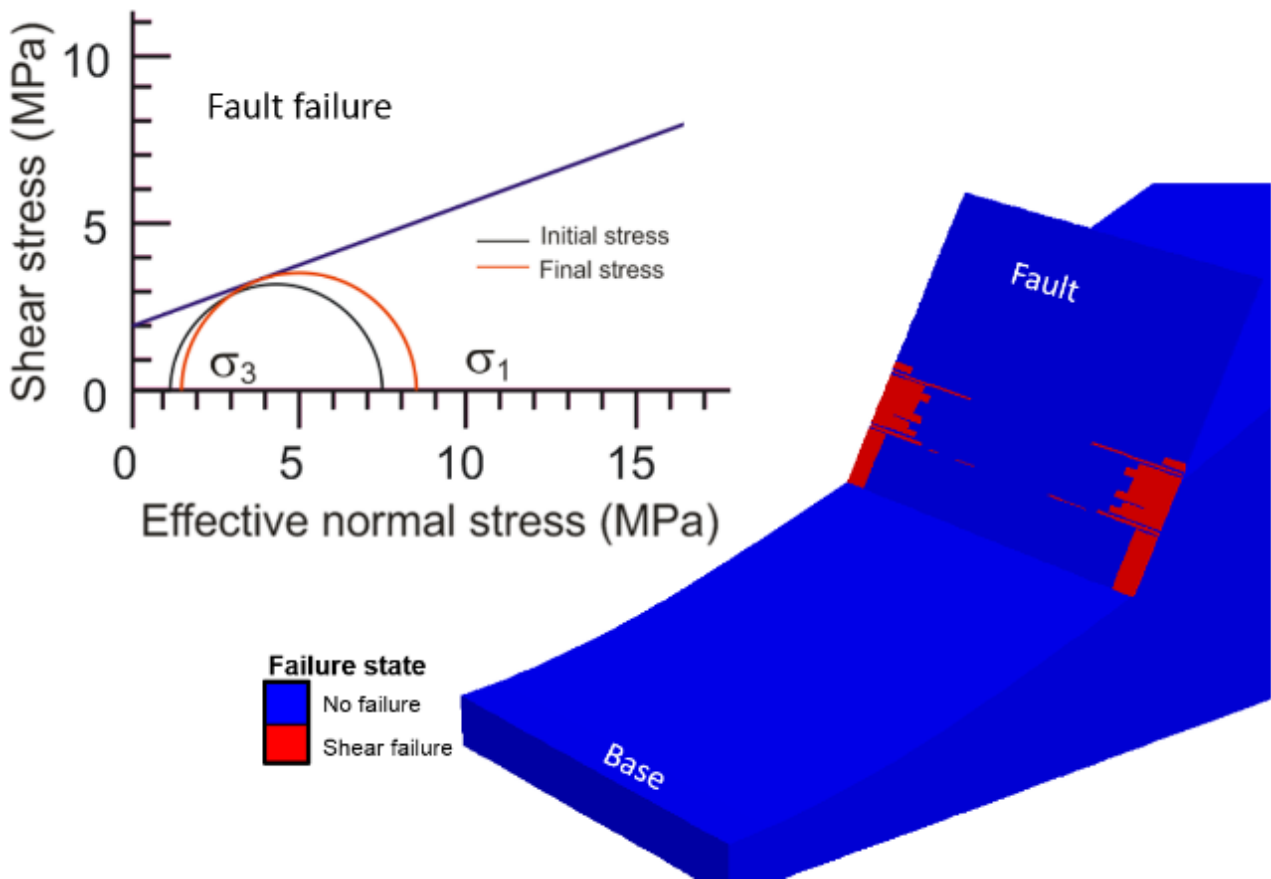


Figure 9-17 Illustration of failure status in fault and Mohr-circle stress plot for a fault experiencing failure in one or several locations.

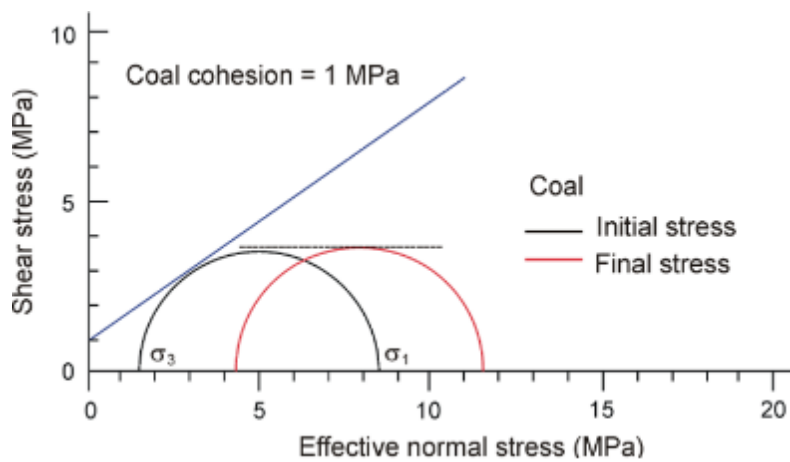


Figure 9-18 Mohr-circle stress plot for a location in coal beds in a model with a very low coal cohesion of 1 MPa.

9.3.3 Model results for strike-slip faulting stress regime

Similar to the models with normal-faulting stress conditions, the models with strike-slip stress conditions also show consistent pore pressure changes and fluid flow patterns with those from the models with a reverse faulting stress conditions. We therefore again focus on stress alteration in response to depressurisation in a strike-slip faulting regime in this section.

Importantly, the model results show that shear stresses in the fault and coal beds also decrease in response to depressurisation under a strike-slip regime (Figure 9-19). The combination of shear-stress decrease and effective-stress increase determines that the corresponding Mohr's circle for stresses in the fault (and also coal) will shift away from the failure envelop as the result of depressurisation under a strike-slip regime (Figure 9-20), and hence there is no mechanical failure in the model.

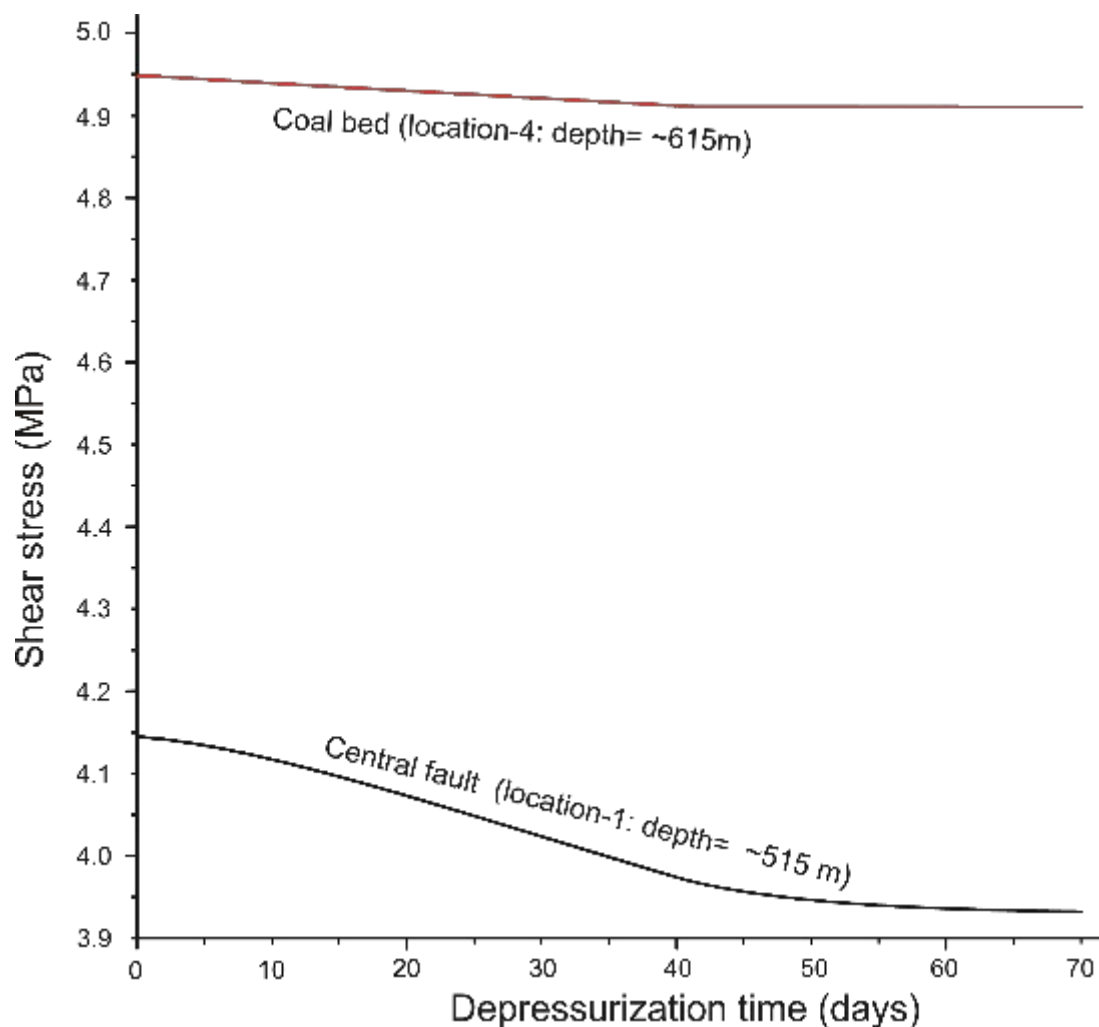


Figure 9-19 Plots of shear stresses in the fault and coal in the model with a strike-slip faulting stress regime. See Figure 9-5 for the locations and depth levels of datum-tracking points in the model.

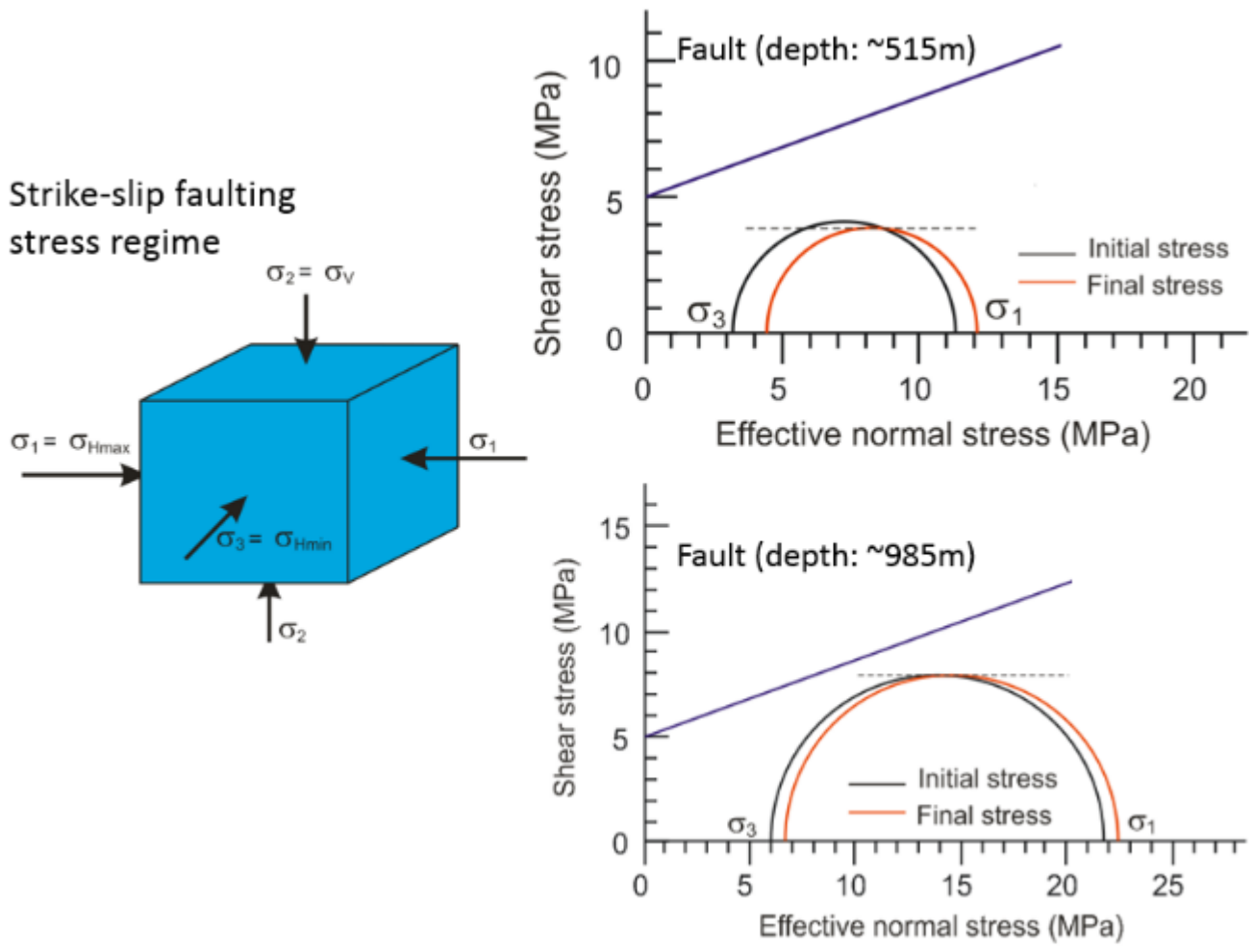


Figure 9-20 Mohr's circle diagrams showing stress variation with respect to the failure envelope for the fault under a strike-slip faulting stress regime.

9.4 Conclusions

Key conclusions from the present geomechanical modelling are:

- Under static tectonic conditions (i.e. no active tectonic deformation is involved or considered), depressurisation in coal seams leads to alterations of the stress state. Shear stress only increases in the models with normal-faulting stress regimes. In contrast, in models with reverse-faulting (dominant stress regime in eastern Australia) or strike-slip faulting stress regimes, shear stresses decrease as the result of depressurisation. All these shear stress alterations take place together with overall effective stress increases associated with pore pressure reduction.
- The patterns of stress alterations above suggest that there is a chance for failure in the coal and fault (reactivation) only under normal-faulting stresses. Failure in the coal and fault is less likely under reverse-faulting or strike-slip faulting stresses due to the combined effects of shear stress decrease and effective stress increase, as

also suggested by Zhang et al. (2016). It needs to be noted that this conclusion is based on the theory of conventional Mohr-Coulomb elastic-plastic theory which is adopted here. The Mohr-Coulomb elastic-plastic model is commonly adopted to simulate the geomechanical behaviours of rocks in upper crustal levels. It has limitations such as not capturing discrete faulting behaviours (i.e. sliding on discrete fault surfaces) and likely underestimating stress alterations associated with material loss (i.e. shrinkage or mass loss due to chemical or fluid processes, numerical modelling of which requires the development of new geomechanical constitutive models in numerical modelling codes).

- In the present base geomechanical models (the model properties are assembled based the data from the study region or literature) with reverse-faulting, normal-faulting or strike-slip stress conditions, no geomechanical failure in coal strata or fault reactivation is observed. A partial failure/reactivation in the fault is observed in the model with a normal-faulting stress regime and a low fault cohesion (i.e. weak fault scenario).
- Fluid flow is dominated by lateral flow along coal beds, converging towards depressurisation locations (production wells) on coal beds. Fault permeability governs fluid transport through or along the fault. In relatively higher fault permeability cases (e.g. base model), there is more significant flow both across and along the fault from the footwall side towards the hanging-wall side. In a lower fault permeability of 0.1 mD, there is little flow in the fault or movement of fluids from the footwall across the faults to the hanging-wall side. Coal permeability strongly affects flow velocities within coal beds during depressurisation.
- Depressurisation generates fluid pore pressure reduction in all the models. Fault permeability and coal permeability both affect final pore pressure patterns. For example, a low fault permeability of 0.1 mD leads to the development of pore pressure compartmentalisation across the fault.

9.5 References

- Brooke-Barnett S, Flottmann T, Paul PK, Buseti S, Hennings P, Reid R & Rosenbaum G (2015). Influence of basement structures on in situ stresses over the Surat Basin, southeast Queensland. *J. Geophys. Res. Solid Earth* 120, doi:10.1002/2015JB011964.
- Connell LD (2009). Coupled flow and geomechanical process during gas production from coal seams. *Int. J. Coal Geol.* 79 (1-2): 18-28.
- Frery E, Langhi L, Strand J, Rohead-O'brien H, Wilkes P (2014). Multiscale geomodelling in the coal-bearing Gloucester Basin, NSW. Australian Earth Sciences Convention 2014 (Newcastle, NSW, Australia, 7-10 July 2014). Geological Society of Australia, 310-311.

- Gentzis T, Deisman N & Chalaturnyk RJ (2007). Geomechanical properties and permeability of coals from the foothills and mountain regions of western Canada. *Int. J. Coal Geol.* 69: 153–164.
- Khan M and Teufel LW (2000). The effect of geological and geomechanical parameters on reservoir stress path and its importance in studying permeability anisotropy. *SPE Reservoir Eval Eng* 3(5): 394–400.
- Itasca (2006). *FLAC3D: Fast Lagrangian Analysis of Continua in 3 dimensions, user manual, version 3.1.* Itasca Consulting Group, Inc., Minneapolis.
- Hillis RR, Enever JR & Reynolds SD (1999). In situ stress field of eastern Australia. *Australian J. Earth Sciences* 46: 813-825.
- Lama RD & Vutukuri VS (1978). *Handbook on mechanical properties of Rocks (Testing Techniques and Results – Volume II).* Trans Tech Publications, Clausthal, Germany.
- Langhi L, Zhang Y, Gartrell A, Underschultz JR, Dewhurst D (2010). Evaluating hydrocarbon trap integrity during fault reactivation using geomechanical 3D modelling: An example from the Timor Sea, Australia. *AAPG Bulletin* 94: 567-591.
- Morad K, Mireault R, Deen L (2008). Reservoir engineering for geologists: coalbed methane fundamentals. *Reservoir Issue* 9: 23-26.
- Parsons Brinckerhoff (2012). Phase 2 Groundwater investigations - Stage 1 Gas Field Development Area Gloucester Gas Project. Report for AGL Upstream Investments Pty Ltd.
- Sorjonen-Ward, P, Zhang Y & Zhao C (2002). Numerical modeling of orogenic processes and gold mineralization in the southeastern part of the Yilgarn craton, Western Australia. *Australian J. Earth Sciences* 49: 935-964.
- Turcotte D L, Schubert G (1982). *Geodynamics: Applications of Continuum Physics to Geological Problems.* Wiley, New York.
- Zhang Y, Gartrell A, Underschultz JR and Dewhurst DN (2009). Numerical modelling of strain localisation and fluid flow during extensional fault reactivation: implications for hydrocarbon preservation. *Journal of Structural Geology* 31: 315-327.
- Zhang Y, Underschultz JR, Gartrell A, Dewhurst DN and Langhi L (2011). Effects of regional fluid pressure gradients on strain localisation and fluid flow during extensional fault reactivation. *Marine and Petroleum Geology* 28: 1703-1713.
- Zhang Y, Clennell MB, Delle Piane C, Ahmed S, Sarout J (2016). Numerical modelling of fault reactivation in carbonate rocks under fluid depletion conditions - 2D generic models with a small isolated fault. *Journal of Structural Geology* 93:17-28.
- Zoback M and Zinke JC (2002). Production-induced Normal Faulting in the Valhall and Ekofisk oil fields. *J. Pure appl. Geophys* 159: 403-420.

10 Summary and conclusions¹⁹

10.1 Fault investigations: a multiple lines of evidence approach

This project developed methods and workflows that may help to improve the characterisation of subsurface rock properties, in particular faults, and then meaningfully incorporates them into regional groundwater flow models. The Gloucester Basin, NSW, was selected as a case study area for one example of how generic workflows can be applied for the fault investigations. The Gloucester Basin is broadly an east-west synclinal feature, heavily faulted by a complex series of normal and reverse faults. Due to the structural complexity, the sedimentary sequences are mostly steeply dipping on the edges and fairly flat lying in the centre, causing difficulty in horizon correlation across the basin.

The investigations in the Gloucester Basin case study area included both field work and desktop subsurface studies occurring in parallel. The field sampling was designed to both take advantage of existing bores and water courses, and focus on transects running perpendicular to the main north-south structural grain such that there was an increased chance of identifying hydrodynamic signatures of upwards fluid migration along structures. The field campaign included sampling well bores for water chemistry and dissolved gases, collection of atmospheric samples for methane, acquisition of shallow geophysics along certain transects, and a run of river surface water sampling campaign of Waukivory River and the Avon River for water chemistry and dissolved gases. The desktop subsurface study utilized coal seam gas exploration well and water bore records for data to constrain the formation water hydrochemistry and hydrogeology, examined well bore image logs to determine *in situ* stress and small scale strain, and the available seismic data was examined to interpret the fault zone architecture in specific areas of interest. From those investigations multiple lines of evidence were obtained as the basis of a conceptual hydrogeological model that included fault zone architecture and its hydrodynamic properties.

In conclusion, through the case study a new methodology of integrating different existing techniques was developed (i) that was successful in deriving multiple lines of evidence about hydraulic-chemical expressions of faults, (ii) which was used for fault conceptualisation, and (iii) that is verifiable through numerical groundwater flow modelling.

¹⁹ Contributing authors: D Mallants, J Underschultz, C Simmons

10.2 Shallow geophysical survey

Evidence for near-surface expressions of geological faults (i.e. in the top 50 to 100 m) was derived from shallow surface-based geophysical investigations. Processing of data was undertaken for two lines of shallow Time domain Electromagnetics (TEM) collected during this project and one additional line of similar data collected for AGL in 2011. Where near-surface expressions of faults were identified in the higher resolution TEM data, there were corresponding deeper fault traces evident from analysis of seismic survey data. Furthermore, some surface features (e.g. river location) appear to be influenced by geological structures and faulting. Analysis of environmental tracers (e.g. helium - ^4He) in the Avon and Waukivory Rivers and groundwater near inferred fault traces were indicative of a source of groundwater coming from greater depth with a much longer residence time and mixing with the shallow groundwater. This is consistent with international studies that found that helium is more concentrated in groundwater in the close vicinity of lineament features as a result of a higher fracture density and an existing inter-connection with flow pathways of increased residence time.

Based on a conjunctive analysis of high-resolution Time domain Electromagnetic data and deep seismic survey data, it was concluded that the near-surface expressions of faults and deeper fault traces are likely connected.

10.3 Hydrochemistry and environmental tracer data

A cluster analysis of the hydrochemistry of surface water and groundwater was undertaken to identify possible types and sources of water (deep groundwater or shallow alluvial groundwater). By using a Piper diagram the surface water samples were characterised as a Na- HCO_3 -Cl water type with some of the shallow alluvial aquifer samples having a very similar composition while other samples were of the Na-Cl water type. Potential mechanisms explaining the high concentration Na-Cl water type of the alluvial samples include evapo-concentration or mixing with more saline water from the underlying interburden formations. The groundwater samples from the interburden and coal seams have Na- HCO_3 , Na- HCO_3 -Cl and Na-Cl water types, which is similar to other coal seam gas studies globally. Indeed, international studies show that coal seam water predominantly consists of sodium and bicarbonate and is essentially devoid of sulphate, calcium and magnesium, but has high concentrations of Na.

Stable isotopes of water ($\delta^{18}\text{O}$ and $\delta^2\text{H}$) provided further insights into the various mixing processes between deeper and shallow groundwater and surface water. The groundwater samples from the major aquifer units showed some overlap and are isotopically lighter than the surface water samples and less enriched than the average weighted rainfall. The coal seam samples are far more depleted in stable isotopes than the alluvial samples indicating groundwater recharge under different climatic conditions to present day. Comparing $\delta^2\text{H}$ versus chloride showed that the bulk of the groundwater samples from the major aquifer units have higher chloride concentrations than the surface water and therefore can only provide a relatively small component of discharge to the surface water system. There are a few groundwater samples that have low chloride concentrations in the alluvial and interburden aquifers which indicates end members with a larger contribution to the surface water system.

Overall, the patterns in chloride and stable isotopes of water are consistent with a binary mixing system between a surface water end-member and a groundwater end-member at the scale of the alluvial aquifer and adjoining interburden. Two hypotheses are put forward that could explain the observed isotope line. The first hypothesis assumes a process with overall low vertical groundwater advection velocity or spatially constrained flows, possibly linked to permeable fault zones. Under such conditions of low flow, a sufficiently large solute concentration gradient could favour diffusion in the opposite (i.e. downward) direction. The second hypothesis, however, considers a dynamic alluvial aquifer setting, where solutes such as stable isotopes are continuously exchanged between surface water and groundwater by flood cycles and hyporheic processes. Over time, this could also generate a mixing profile across the river to the interburden continuum.

The ^{222}Rn concentrations were highest in the shallow alluvial aquifer (37-65 Bq L^{-1}), medium in other deeper aquifer units and coal seams (less than 13 Bq L^{-1}), and lowest in the surface water (generally less than 1 Bq L^{-1}). Hotspots in the river that were above the general trend are likely an indicator of subsurface inflow into the river. Groundwater from the alluvial aquifer adjacent to the Waukivory River and Avon River is the most likely source or groundwater “mixing bucket” prior to discharge into the river.

Tritium results show that most of the groundwater samples within the study area are more than 50 years old. Analysis of other environmental tracers (^{14}C and ^4He) suggest that the deeper groundwater (interburden and coal seams) has an apparent groundwater age that is greater than approximately 30,000 years.

When helium and methane depth profiles were analysed with a one-dimensional advection-dispersion transport model, two models (one with upward velocity and one with downward velocity) fitted the data equally well. Estimated pore-water velocities ranged from 4×10^{-5} to 8×10^{-5} m year^{-1} for the methane data and about one order of magnitude lower velocities were derived based on the helium data. The modelling suggested that the exchange process is more likely to be driven by diffusion rather than advection. Regardless of the uncertainty about the groundwater velocity, the upward flux based on the helium and methane data set indicated there is little exchange between the deeper groundwater and the shallower aquifer. This does not exclude the existence of other pathways possibly with higher groundwater velocities; however, those pathways were apparently not sampled with the existing groundwater well network.

Inference of fault locations from the combination of near-surface geophysics and deeper seismic analysis, together with evidence from tracer analysis indicated the presence of both slow moving groundwater (i.e. diffusion-driven mass transport) and faster moving groundwater (i.e. advection-driven mass transport). The former was inferred from one-dimensional modelling of methane and helium profiles, while evidence of the latter was found in tracer hotspots along the Avon and Waukivory Rivers. Such a combined low and high flow system was conceptualised at the local scale as a dual-permeability type rock. The majority of the interburden acts as a relatively low permeability rock where mass transport is governed by molecular diffusion. Certain fault zone architecture acts effectively as the more permeable rock with mass transport likely governed by advection (i.e. flowing water). The conceptual model of a dual permeability rock represents the fractures and matrix domain as separate continua. Each continuum has its own representative permeability, which is very small for the matrix rock (about 0.1 mD) and higher for the fault zone

(about 1 mD). If a pressure and/or concentration gradient exists between fracture and matrix zone, mass transport occurs between the two continua. This conceptual model was confirmed at the regional scale based on analysis of hydraulic data, salinity data and structural geology data.

10.4 Hydraulic analysis

The presence of zones characterised by upward water movement near fault traces was further confirmed on the basis of regional scale well head and salinity data. At several locations in the Stratford area, fault locations are indicative of a source of formation water emanating from beneath the fault. At other locations fault locations are coincident with downward groundwater flow. Also, based on the head observations certain fault locations seemed to behave hydraulically as a barrier to east-west flow across the fault. The strongest expression of such features was observed in the shallow layers including the alluvium and the shallow fractured bedrock.

In the Stratford area, there are also two high TDS areas separated by faults, one at 4,633 mg/L and the other at 5,012 mg/L. The fault separating the two high TDS zones may play a significant role in providing for groundwater discontinuity laterally but may also be a source of upwelling higher salinity formation water. A possible conclusion is that certain fault segments and their associated damage zones provide a slightly enhanced permeability relative to the host rock and focus fluxes upwards to shallower aquifers.

10.5 Structural geology analysis

Further evidence of enhanced vertical hydraulic communication due to faults was obtained from an evaluation of image logs to assess the *in-situ* stress and the characteristics of fractures. In particular resistivity and acoustic borehole image logs were examined with the objective to assess the contribution of faults, fractures and present-day maximum horizontal principal stress orientations (S_{Hmax}) to fluid movement from the coal seam gas reservoirs to adjacent aquifers. The interpreted *in-situ* stress and fracture orientations were overlain on seismic sections to determine any variation with depth and/or kinematic style of the larger structural features. The *in-situ* horizontal stress (S_{Hmax}) and fracture orientations were also cross-plotted with measured permeability data to observe any causal relationships that assist in predicting potential permeability pathways for fluid movement.

The *in-situ* stress map and well sections showed variation of stress spatially as well as vertically within individual wells. The large variations in *in-situ* stress orientation indicates a strong influence of local structures, i.e. faults or fault zones.

The dominant fracture orientation in most of the wells within the Waukivory area are parallel or sub-parallel to S_{Hmax} . The higher fracture density and multiple fracture orientations within some of the Waukivory wells develops a dilatant tendency creating pathways for fluid movement in the shallower aquifers.

The Gloucester Basin coal seam gas reservoirs mostly have a low permeability (~1mD). Therefore, fault seal mechanisms are less relevant to influencing fluid flow from the deeper reservoirs (i.e. the matrix permeability is already low). However, fault damage zones, relay structures and fractures that are permeability enhancement mechanisms are more likely to have an observable

influence on fluid flow. Therefore, characterising *in-situ* stress along with small scale fractures associated with seismically observable faults or areas of distributed strain in relays was shown to be a powerful method to demonstrate that the Waukivory area displayed slightly increased permeability with depth when fracture orientations are sub-parallel to the *in-situ* stress orientations. At a similar depth, interpreted permeability was an order of magnitude greater when fracture orientation is parallel or sub-parallel to S_{Hmax} orientation.

A final analysis re-interpreted the original fault traces by using three-dimensional (3D) seismic data. Analysis of the 3D seismic volume shows a dominant north-south structural fabric with a bend in the Stratford area. Within the bend region there are high angle faults trending roughly east-west that take up some of the strain. The Stratford and Waukivory areas are distinguished from one another by the difference in spatial fault morphology. In the Stratford area, faulting within the shallower section is characterized by a series of en-echelon fault segments. These had been mapped previously as continuous faults.

10.6 Data integration and proposed regional scale conceptual model

The combined desktop investigations and analysis of field data resulted in multiple lines of evidence regarding expressions of the impacts of faults on local and regional groundwater flow. The evidence was combined to develop a regional scale conceptual model of the Gloucester Basin subsurface, consistent with the local-scale dual-permeability conceptual model. In at least three regions within the test case area there are some combinations of data that suggest there is preferential upwards vertical fluid migration. These areas include:

1. The Stratford area with at least two wells indicating an upward hydraulic gradient and the TDS map for the shallow aquifer indicating two salinity plumes exceeding 4,000 mg/L.
2. The Waukivory River at approximately 12,200 m upstream of the confluence with the Avon River, where the field investigations measured a surface water methane and helium concentration anomaly and where the TEM indicated that this was a region of resistivity change in the shallow subsurface that could be related to a fault.
3. The Waukivory area, where at least two wells indicated an upward hydraulic gradient and the TDS map for the shallow aquifer indicates a salinity plume exceeding 2,000 mg/L. The image log data showed a high fracture density and fracture orientation relative to S_{Hmax} favourable to dilatency and enhanced permeability. The field investigations found in this same location a methane and helium concentration anomaly in surface water samples at the confluence of the Waukivory River with the Avon River.

The proposed conceptual model for the Gloucester Basin includes a series of Permian bedrock coal zones and interburden with a bulk permeability of 1 mD or less (Figure 10-1). The bedrock strata is cut by faults that exhibit transgression with east-west shortening but north-south strike-slip displacement. Some of these faults reach the base of the alluvium and exert an influence on the location of the surface drainage. The upper part of the bedrock immediately beneath the alluvium is weathered and has an enhanced permeability in the 10's of mD. The alluvium has a permeability in the 100's of mD. The overall flow system is controlled by recharge at the high topography eastern and western edges of the basin with discharge generally into the basin's central drainage.

Given the overall permeability distribution the bulk of the flux is within the alluvium and fractured bedrock. The flux through the deeper part of the basin has its flux focused in a few locations where the fault zone architecture provides slightly enhanced permeability (e.g. from 0.1 mD matrix permeability to 1 mD enhanced permeability).

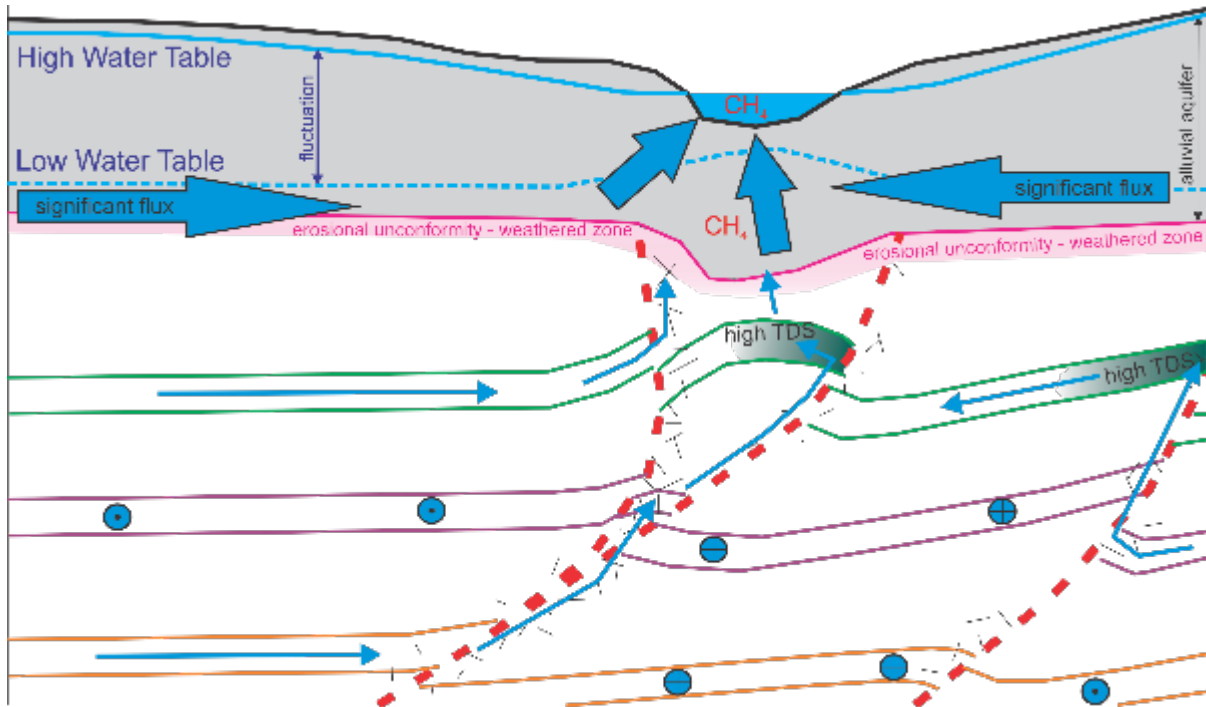


Figure 10-1 Conceptual model of the hydrodynamic system of the Gloucester Basin. Dimensions are not to scale. Circles with plus signs indicate flow into the page; circles with dots indicate flow out of the page.

In the Permian bedrock strata there are fault segments that form barriers to flow with hydraulic head discontinuities across them. There are other locations however where certain fault segments and their associated damage zones provide slightly enhanced permeability relative to the host rock and thus focus flux upwards to shallower aquifers. At these locations upwelling groundwater may result in a plume of high salinity water emanating from a fault into a fresher water shallow aquifer. These same migration pathways may be locations of methane and helium migration that can be detected in the shallow aquifer or surface water. Candidate locations for vertically connected structurally enhanced permeability are areas where strain is transferred from one major fault segment to another across a zone of distributed small scale strain oriented at multiple orientations. These same areas may demonstrate high fracture density on image logs and have more opportunity for some fractures to be in dilatant conditions.

10.7 Regional scale groundwater flow modelling

To complement the field investigations and the desktop analysis that had demonstrated the impacts of faults on regional groundwater flow and solute migration (salinity and tracers), numerical simulations were undertaken to demonstrate the relationship between different fault properties and aquifer responses. The simulations were based on a regional groundwater flow

model for the Gloucester Basin that was built using a relatively large data set, typical of what is used by industry for simulating impacts from hydrocarbon developments. Impacts of faults on groundwater flow were tested by modifying fault properties to represent high, medium, and low permeability across fault flow.

Results showed that as the fault permeability decreased, the effect on heads became more evident with a sharp head contrast developing across the fault. Under the conditions of well-connected K fields for the coal seam layers, this head build-up quickly dissipated in the directions along the fault. Simulated anomalous head distributions were similar in nature to those measured in the field. This leads to the conclusions that the degree to which coal seam layers are connected in space has a direct and profound impact on the head build-up across faults and on the distance over which this head build-up dissipates in the directions along the fault.

The geostatistical approach presented here generated spatial fields with two levels of coal seam connectivity (i.e., connected and disconnected). The effect of coal seams being either connected or disconnected on groundwater flow in the presence of faults was clearly demonstrated. Where the high permeability zone forms connected pathways, drawdown was focussed and extends laterally within the connected pathways. Alternatively, the drawdown in a low connectivity field is more diffuse. The bulk hydraulic properties within a discontinuous permeability field were lower, resulting in higher heads relative to a connected permeability field. This underscores the need that the characterisation of the hydraulic conductivity of hydrogeological formations should include establishment of the spatial correlation structure as a basis for realistic groundwater flow simulations in which such spatial correlations are implemented.

Field observations of salinity anomalies across the basin had been interpreted as “chimney-like” structures, i.e. highly localised preferential flow features associated with fault damage zones enhancing connectivity between deeper and shallower groundwater. Based on a simple mass balance approach under natural flow conditions (i.e. no pumping), the flow through the chimneys required to explain the salinity anomalous observations was estimated to be very small (10% of recharge). By implementing such chimney features in the groundwater model, the magnitude of the flow through the chimney for the connected K field was shown to be similar in magnitude to the mass balance estimates.

The faults included in the groundwater flow simulations had no material impact on the maximum drawdown in the fractured rock or alluvial aquifer, in part because of they were sufficiently far from the depressurisation zone (about 1 km), and in part because only a few large faults were included (all at a considerable distance from the well field). Several smaller faults and disturbed zones were shown to be present in the area, and were shown to be likely responsible for head and salinity anomalies. These features, however, were not included in the model although an attempt was made to represent them by the so-called chimney structures. The implementation of chimney structures had no effect on propagating or affecting the depressurisation, mainly because of their relatively large distance from the well field (about 5 km).

Calculated maximum head drawdown in the weathered and fractured rock aquifer is of similar magnitude as the results obtained by Peeters et al. (In Prep)²⁰ using a different modelling approach, i.e. up to 1.75 m for the former versus less than 1 m for the latter. As far as the impact of faults as conduits to propagate depressurisation is concerned, results obtained here are also consistent with those reported by Peeters et al. (In Prep). Although only the effect from CSG extraction is considered here, the effects of faults on maximum drawdown were shown to be indistinguishable between a model with or without faults.

10.8 Geomechanical deformation modelling

Three-dimensional (3D) numerical geomechanical deformation modelling of sedimentary coal basins subject to depressurisation from coal seam gas extraction was undertaken to simulate the 3D distribution and partitioning of strains and stresses that can impact on intraformational flow and hydraulic properties of faults and fractures. 3D geomechanical simulations with a simplified stratigraphy and a generic fault thematically based on data from the Gloucester Basin have been performed to investigate the geomechanical effects of depressurisation in coal seams on the stability of a pre-existing fault (referred-to as fault reactivation potential). Effects of modifications to strains and stresses on the connectivity and flow pathways between the fault and aquifers were analysed. When coupled to flow modelling, the geomechanical deformation simulations can be used to assess the dynamic behaviour of faults and the impact of pressure variation on flow pathways.

Key conclusions from the present geomechanical modelling are:

1. Under static tectonic conditions (i.e. no active tectonic deformation is involved or considered), depressurisation in coal seams leads to important stress alterations. Shear stress only increases in the models with normal-faulting stress regimes. In contrast, in models with reverse-faulting (dominant stress regime in eastern Australia) or strike-slip faulting stress regimes, shear stresses decrease as the result of depressurisation. All these shear stress alterations take place together with overall effective stress increases with associated pore pressure reduction.
2. Based on the conventional Mohr-Coulomb elastic-plastic theory, the patterns of stress alterations suggest that there is a chance for failure in the coal and fault (reactivation) only under normal-faulting stresses. Failure in the coal and fault is less likely under reverse-faulting or strike-slip faulting stresses due to the combined effects of shear stress decrease and effective stress increase.
3. In the present base geomechanical models with reverse-faulting, normal-faulting or strike-slip stress conditions, no geomechanical failure in coal strata or fault reactivation was

²⁰ Peeters L, Dawes WR, Rachakonda PR, Pagendam DE, Singh RM, Pickett TW, Frery E, Marvanek SP and McVicar TR (In Prep). Groundwater numerical modelling for the Gloucester subregion: Product 2.6.2 for the Gloucester subregion from the Northern Sydney Basin Bioregional Assessment.

observed. A partial failure/reactivation in the fault is observed in the model with a normal-faulting stress regime and a low fault cohesion (i.e. weak fault scenario).

4. Fluid flow is dominated by lateral flow along coal beds, converging towards depressurisation locations (production wells) on coal beds. Fault permeability governs fluid transport through or along the fault. In relatively higher fault permeability cases (e.g. base model), there is more significant flow both across and along the fault from the footwall side towards the hanging-wall side. In a lower fault permeability of 0.1 mD, there is little flow in the fault or movement of fluids from the footwall across the faults to the hanging-wall side. Coal permeability strongly affects flow velocities within coal beds during depressurisation.
5. Depressurisation generates fluid pore pressure reduction in all the models. Fault permeability and coal permeability both affect final pore pressure patterns. For example, a low fault permeability of 0.1 mD leads to the development of pore pressure compartmentalisation across the fault.

11 Benefits of research findings²¹

This project contributes to knowledge generation in hydrogeology, groundwater management and sustainable resource extraction, and thereby addresses some of the IESC research gaps,

‘To increase the scientific evidence that underpins decisions about coal seam gas and large coal mining development, enabling decisions to be based on the most rigorous science available’

in the following way:

- Specifically in regards to aquitards, this project has improved understanding of vertical hydraulic conductivity variability in aquitards and how such variability translates into uncertainty about groundwater depressurisation at regional scale (Smith et al., 2018; Turnadge et al., 2018a, 2018b);
- Specifically in regards to faults, this project has improved understanding of the influence of faults on groundwater flow in the Gloucester Basin, and what suite of tools is best suited to characterise fault architecture and its hydraulic properties for the modelling of propagation of depressurisation from hydrocarbon reservoirs to linked aquifers and surface environments (this report and McCallum et al., 2018); and
- Specifically in regards to modelling, this project has improved conceptualisation, representation and parameterisation of aquitards and faults in regional groundwater flow models to allow robust quantification of uncertainty about regional groundwater flow and pressure distribution (this report and McCallum et al., 2018).

Note that the Gloucester case study is one example of how the methodology and workflows might be applied. Indeed, this process is highly geology and basin specific. In particular, the bulk permeability of the strata below the weathered bedrock is very low (generally less than 1 mD). This means that the impact of fault sealing processes (i.e. permeability reducing mechanisms in faults such as shale gouge, clay smear, and cataclasis) is less important since the bulk permeability of the matrix is so low already. In the case of the Gloucester Basin, it are the fault processes that locally enhance permeability (e.g., in-situ stress, damage zones, relays and rheology), which become important for regional groundwater flow characterisation. In other basins the reverse may be true. It is therefore important to look at this report (and its supporting reports) as identifying a wide range of possible fault processes that influence permeability and a wide range of methodologies for characterizing faults. These methods are transferable to many other basins. The Gloucester case study represents an example of how the workflows can be applied, however a meaningful application of workflows needs to be tailored to the particular characteristic of the rocks in each case. This includes a determination of which aspects of the generic workflows are

²¹ Contributing authors: D Mallants, J Underschultz, C Simmons

most important in a particular geological setting, the availability of data and the maturity of the coal seam gas development.

The research findings will also:

- Assist better decision-making, regulation, natural resource management and industry practice;
- Build knowledge about the highest risks to freshwater resources, land and ecosystems; and
- Help provide data and knowledge that can support future assessments in priority areas.

This project will further strengthen:

- IESC advice on project proposals with regard to the adequacy of methods of assessment and representation of groundwater flow across low permeability formations (aquitards);
- Regulator and industry understanding of the feasibility of methods of assessment and representation of groundwater flow across low permeability formations (aquitards), providing improved representation of vertical hydraulic conductivity in numerical groundwater flow models; and
- Regulator and industry understanding of coal reservoir behaviour as it relates to depressurisation and water production, and how perturbations within the reservoir are propagated across aquitards into overlying and underlying water resources.

11.1 Benefits to the coal seam gas industry

The coupling and integration between geology, geophysics, geomechanics and hydrogeology/groundwater (flow modelling etc.) is rarely done for regional groundwater flow models and therefore this approach is innovative in general. The application to faults/aquitards science is further innovative in the specific terms studied in this project.

It is anticipated that the new insights gained regarding the estimation of fault architecture and hydraulic characteristics of faults and fault damage zones will be transferable back to CSG operations. In particular the findings will improve the predictive capacity and understanding of:

- The fault zone architecture;
- The distribution of strain between larger faults and fractures of the fault damage zone;
- The in-situ stress distribution;
- The rock mechanical nature of the different stratigraphic units and how this relates to the points above;
- The rock properties and hydraulic parameters of fault segments and associated damage zones; and
- The nature of how the above characterisation may impact the movement of fluids in the subsurface.

The insights gained through this work could have important implications to CSG industry in forecasting reservoir performance and the distribution of pressure decline between production wells and between production wells and fault lineaments. Finally it may improve the forecasting of impacts (or lack of impacts) on adjacent aquifer systems.

11.2 Remaining knowledge gaps and recommendations

- The characterisation, conceptualisation and modelling of groundwater flow with presence of faults was undertaken in a single test case area, the Gloucester Basin. The transferability of the current results to other areas has not been explicitly tested, although some recommendations can be made. First of all, the novel numerical modelling tool for incorporation of faults in groundwater flow models is applicable to any basin. However, the larger the size of the basin and the more faults need to be incorporated, the more computer intensive the simulations become. This may possibly limit the number of faults that can be effectively incorporated; further testing is required to get better understanding of the computational limits of such models. Under certain conditions, faults can also be approached as equivalent porous media which renders the simulations more cost-effective; this project has demonstrated several ways to compare and contrast explicit representations of faults versus an effective media approach. Secondly, the field investigations have demonstrated how the combination of different environmental tracers (including methane) can be used to derive conceptual models that include the effects of faults on groundwater flow, which are tested through numerical modelling. Thirdly, the integrated analysis of formation water hydrochemistry, hydrogeology, well bore image logs proved successful to derive a consistent conceptual model of fault behaviour with articulation of location of flow-facilitating zones and their hydraulic properties. This integrated approach is considered generally applicable and can be applied to other basins, provided it is customised to fit the key elements case specific to the geology of the basin.
- Interpretation of the surface-based geophysical datasets collected here (TEM surveys) are based on the three lines of data collected to this time. Interpretation quality could possibly be improved if more geophysical data were collected, especially closer to logged bores, allowing relationships between geophysical response and true ground conditions to be tightened. However, a value of information exercise is recommended to determine how useful this would be.
- The spatial coverage of geophysical investigations could be improved by using one of the helicopter-based airborne EM systems that “specialise” in collecting very shallow data (see, e.g. the SkyTEM 301 system <http://skytem.com/tem-systems/>). These systems can collect data over large areas economically, and provide high resolution of the near surface. Again, a value of information exercise is recommended first to determine how useful this would be.
- The three-dimensional groundwater flow model used the Connected Linear Network approach to simulate preferential flow caused by faults; these fault features were interpreted as “chimney-like” structures. While this approach provided a first assessment to constrain the fault characteristics thought to be responsible for the observed salinity

anomalies, future work should attempt to use the fault module capability and explore under what conditions (fault architecture and hydraulic properties) groundwater flow simulations including faults would reproduce the observations. This would inform when and where faults are important and need to be treated explicitly in modelling or whether an equivalent porous medium approach is sufficient, or whether faults can be just excluded all together. Developing that understanding remains key.

- Further testing of the modelling approach with fault features is warranted. This would first involve seeking datasets with evidence of fault-mediated effects of large-scale depressurisation and test if predicted impacts meet observations.

11.3 Outcomes and impacts

Key outcomes and impacts from the faults component of the project “Research to improve treatment of faults and aquitards in Australian regional groundwater models to improve assessment of impacts of coal seam gas (CSG) extraction” are as follows:

- **Based on McCallum et al. (2018):** A novel simulation tool to represent faults in groundwater models. This allows improved simulation of the influence of faults on groundwater flow where explicit representation of faults is required. The modelling of propagation of depressurisation from hydrocarbon reservoirs to linked aquifers and surface environments can now be undertaken with tools that allow a greater accuracy in the spatial representation of fault zones and their hydraulic properties.
- **This report:** A novel tool was developed to sample groundwater for gas analysis. The sampling methodology allows collecting dissolved gases from a representative groundwater sample, preventing sample gas loss (effervescence) by maintaining sample pressurisation. The design of the sample device is such that it can be deployed easily in the field and that the collected sample could be transferred to a suitable sample container, appropriate for analysis by a portable gas analyser to determine the dissolved methane concentration in water.
- **This project:** While the principles and workflow develop here are tested on one case study area, they are made sufficiently generic such that they can be more widely applicable. The broader scale implications, such as transferability of results, and optimal combinations of techniques (and their limitations) for different hydrogeological conditions and intended scale of modelling, is discussed. To successfully apply these workflows to any particular case study one needs to consider the geology and available data and the problem trying to be addressed and then select the most fit for purpose combination of tools and methods that has the best chance of success.

11.4 References

- McCallum J, Simmons C, Mallants D and Batelaan O (2018). Simulating the groundwater flow dynamics of fault zones. MODFLOW Un-Structured Grid: A comparison of methods for representing fault properties and a regional implementation. School of the Environment, Flinders University, South Australia.
- Underschultz J, Esterle J, Strand J and Hayes S (2018). Conceptual representation of fluid flow conditions associated with faults in sedimentary basins. Prepared for the Department of the Environment by The University of Queensland Centre for Coal Seam Gas, Queensland.
- Appelo, CAJ, Postma, D (2007) 'Geochemistry, Groundwater and Pollution.' (A.A.Balkema Publishers: Amsterdam, The Netherlands)
- Atkins, ML, Santos, IR, Maher, DT (2015) Groundwater methane in a potential coal seam gas extraction region. *Journal of Hydrology: Regional Studies* **4, Part B**, 452-471.
- Banwell, G, Parizek, R (1988) Helium 4 and Radon 222 Concentrations in Groundwater and Soil Gas as Indicators of Zones of Fracture Concentration in Unexposed Rock. *Journal of Geophysical Research* **93**, 355-366.
- Bigeleisen, J, Wolfsberg, M (1958) Theoretical and experimental aspects of isotope effects in chemical kinetics. *Advances in Chemical Physics* **1**, 15-76.
- Burnett, WC, Kim, G, Lane-Smith, D (2001) A continuous monitor for assessment of ²²²Rn in the coastal ocean. *Journal of Radioanalytical and Nuclear Chemistry* **249**, 167-172.
- Chanton, J, Chaser, L, Glasser, P, Siegel, D (2005) Carbon and Hydrogen Isotopic Effects in Microbial, Methane from Terrestrial Environments. In 'Stable Isotopes and Biosphere Atmosphere Interactions.' pp. 85-105.
- Cheung, K, Klassen, P, Mayer, B, Goodarzi, F, Aravena, R (2010) Major ion and isotope geochemistry of fluids and gases from coalbed methane and shallow groundwater wells in Alberta, Canada. *Applied Geochemistry* **25**, 1307-1329.
- Cicerone, RJ, Oremland, RS (1988) Biogeochemical aspects of atmospheric methane. *Global Biogeochemical Cycles* **2**, 299-327.
- Coleman, DD, Risatti, JB, Schoell, M (1981) Fractionation of carbon and hydrogen isotopes by methane-oxidizing bacteria. *Geochimica et Cosmochimica Acta* **45**, 1033-1037.
- Commonwealth of Australia (2014) Aquifer connectivity within the Great Artesian Basin, and the Surat, Bowen and Galilee Basins, Background review. Department of the Environment, Canberra.
- Crosson, ER (2008) A cavity ring-down analyzer for measuring atmospheric levels of methane, carbon dioxide and water vapor. *Applied Physics B: Lasers and Optics* **92**, 403-408.
- Drever, JI (1988) 'The geochemistry of natural waters.' (Prentice-Hall: Englewood Cliffs, NJ)
- Durridge Company Inc, 2015. Rad7 Radon detector.
- Duvert, C, Raiber, M, Owen, DDR, Cendón, DI, Batiot-Guilhe, C, Cox, ME (2015) Hydrochemical processes in a shallow coal seam gas aquifer and its overlying stream-alluvial system: implications for recharge and inter-aquifer connectivity. *Applied Geochemistry* **61**, 146-159.
- Eyer, S, Tuzson, B, Popa, ME, van der Veen, C, Röckmann, T, Rothe, M, Brand, WA, Fisher, R, Lowry, D, Nisbet, EG, Brennwald, MS, Harris, E, Zellweger, C, Emmenegger, L, Fischer, H, Mohn, J (2015) Real-time analysis of $\delta^{13}\text{C}$ - and δD -CH₄ in ambient air with laser spectroscopy: method development and first intercomparison results. *Atmos. Meas. Tech. Discuss.* **8**, 8925-8970.

- Faiz, M, Hendry, P (2006) Significance of microbial activity in Australian coal bed methane reservoirs — a review. *Bulletin of Canadian Petroleum Geology* **54**, 261-272.
- Faiz, M, Hendry, P (2009) Microbial Activity in Australian CBM Reservoirs. CSIRO Petroleum, North Ryde, NSW, Australia.
- Ferretti, DF, Miller, JB, White, JWC, Etheridge, DM, Lassey, KR, Lowe, DC, MacFarling Meure, CM, Dreier, MF, Trudinger, CM, van Ommen, TD, Langenfelds, RL (2005) Unexpected changes to the global methane budget over the past 2000 years. *Science* **309**, 1714-1717.
- Ferretti, DF, Miller, JB, White, JWC, Lassey, KR, Lowe, DC, Etheridge, DM (2007) Stable isotopes provide revised global limits of aerobic methane emissions from plants. *Atmospheric Chemistry and Physics* **7**, 237-241.
- Flis, MF, Newman, GA, Hohmann, GW (1989) Induced-polarization effects in time-domain electromagnetic measurements. *Geophysics* **54**, 514-523.
- Gibbs, R (1970) Mechanisms controlling world water chemistry. *Science* **170**, 1088-1090.
- Golding, SD, Boreham, CJ, Esterle, JS (2013) Stable isotope geochemistry of coal bed and shale gas and related production waters: A review. *International Journal of Coal Geology* **120**, 24-40.
- Hamawand, I, Yusaf, T, Hamawand, SG (2013) Coal seam gas and associated water: A review paper. *Renewable and Sustainable Energy Reviews* **22**, 550-560.
- Hamilton, SK, Golding, SD, Baublys, KA, Esterle, JS (2014) Stable isotopic and molecular composition of desorbed coal seam gases from the Walloon Subgroup, eastern Surat Basin, Australia. *International Journal of Coal Geology* **122**, 21-36.
- Heaton, THE, Vogel, JC (1981) "Excess air" in groundwater. *Journal of Hydrology* **50**, 201-216.
- Heilweil, VM, Solomon, DK, Darrah, TH, Gilmore, TE, Genereux, DP (2016) Gas-Tracer Experiment for Evaluating the Fate of Methane in a Coastal Plain Stream: Degassing versus in-Stream Oxidation. *Environmental Science & Technology* **50**, 10504-10511.
- Heilweil, VM, Stolp, BJ, Kimball, BA, Susong, DD, Marston, TM, Gardner, PM (2013) A Stream-Based Methane Monitoring Approach for Evaluating Groundwater Impacts Associated with Unconventional Gas Development. *Groundwater* **51**, 511-524.
- Herczeg, AL, Dighton, JC, Easterbrook, ML, Salomons, E RA Akber, F Harris (Eds) (1994) 'Radon-222 and Ra-226 measurements in Australian groundwaters using liquid scintillation counting, Proceeding of Workshop on Radon and Radon Progeny Measurements in Environmental Samples.' Canberra. (Office of the Supervising Scientist:
- Iverach, CP, Cendón, DI, Hankin, SI, Lowry, D, Fisher, RE, France, JL, Nisbet, EG, Baker, A, Kelly, BFJ (2015) Assessing Connectivity Between an Overlying Aquifer and a Coal Seam Gas Resource Using Methane Isotopes, Dissolved Organic Carbon and Tritium. *Scientific Reports* **5**, 15996.
- Jackson, RE, Gorody, AW, Mayer, B, Roy, JW, Ryan, MC, Van Stempvoort, DR (2013) Groundwater Protection and Unconventional Gas Extraction: The Critical Need for Field-Based Hydrogeological Research. *Groundwater* **51**, 488-510.
- Jähne, B, Heinz, G, Dietrich, W (1987) Measurement of the diffusion coefficients of sparingly soluble gases in water. *Journal of Geophysical Research* **92**, 10767-10776.
- Kirk, MF, Wilson, BH, Marquart, KA, Zeglin, LH, Vinson, DS, Flynn, TM (2015) Solute Concentrations Influence Microbial Methanogenesis in Coal-bearing Strata of the Cherokee Basin, USA. *Frontiers in Microbiology* **6**, 1287.
- MacInnes, S (2005) 'STEMINV: Smooth model TEM Inversion.' (Zonge Engineering: Tucson, AZ)
- Mazurek, M, Alt-Epping, P, Bath, A, Gimmi, T, Waber, HN, Buschaert, S, De Canniere, P, De Craen, M, Gautschi, A, Savoye, S, Vinsot, A, Wemeare, I, Wouters, L (2011) Natural tracer profiles across argillaceous formations. *Applied Geochemistry* **173**, 219-240.
- Parsons Brinckerhoff (2012) Phase 2 Groundwater Investigations- Stage 1 Gas field Development Area Gloucester Gas Project. January 2012. AGL Upstream Investments Pty Ltd.

- Parsons Brinckerhoff (2013) Hydrogeological Investigation of a Strike-slip Fault in the Northern Gloucester Basin. 9 August 2013. AGL Upstream Investments Pty Ltd.
- Parsons Brinckerhoff (2015) Updated Conceptual Hydrogeological Model of the Gloucester Basin. Parsons Brinckerhoff No. Rep. 2200556A-WAT-REP-001 RevE, Sydney, Australia.
- Poole, JC, McNeill, GW, Langman, SR, Dennis, F (1997) Analysis of noble gases in water using a quadrupole mass spectrometer in static mode. *Applied Geochemistry* **12**, 707-714.
- Rice, CA, Flores, RM, Stricker, GD, Ellis, MS (2008) Chemical and stable isotopic evidence for water/rock interaction and biogenic origin of coalbed methane, Fort Union Formation, Powder River Basin, Wyoming and Montana USA. *International Journal of Coal Geology* **76**, 76-85.
- Rowe, D, Muehlenbachs, A (1999) Low-temperature thermal generation of hydrocarbon gases in shallow shales. *Nature* **398**, 61-63.
- Stolper, DA, Lawson, M, Davis, CL, Ferreira, AA, Neto, EVS, Ellis, GS, Lewan, MD, Martini, AM, Tang, Y, Schoell, M, Sessions, AL, Eiler, JM (2014a) Formation temperatures of thermogenic and biogenic methane. *Science* **344**, 1500-1503.
- Stolper, DA, Martini, AM, Clog, M, Douglas, PM, Shusta, SS, Valentine, DL, Sessions, AL, Eiler, JM (2015) Distinguishing and understanding thermogenic and biogenic sources of methane using multiply substituted isotopologues. *Geochimica et Cosmochimica Acta* **161**, 219-247.
- Stolper, DA, Sessions, AL, Ferreira, AA, Santos Neto, EV, Schimmelmann, A, Shusta, SS, Valentine, DL, Eiler, JM (2014b) Combined ^{13}C -D and D-D clumping in methane: Methods and preliminary results. *Geochimica et Cosmochimica Acta* **126**, 169-191.
- Stuiver, M, Polach, HA (1977) Discussion: Reporting of ^{14}C data. *Radiocarbon* **19**, 355-363.
- Stumm, W, Morgan, JJ (1996) 'Aquatic Chemistry: Chemical Equilibria and Rates in Natural Waters.' (John Wiley & Sons, Inc.: New York)
- Telford, WM, Geldart, LP, Sheriff, RE, Keys, DA (1976) 'Applied Geophysics.' (Cambridge, England: Cambridge University Press)
- Van Voast, WA (2003a) Geochemical signature of formation waters associated with coalbed methane. *AAPG Bulletin* **87**, 667-676.
- Van Voast, WA (2003b) Geochemical signature of formation waters associated with coalbed methane. *AAPG Bulletin-American Association of Petroleum Geologists* **87**, 667-676.
- Vengosh, A, Jackson, RB, Warner, N, Darrah, TH, Kondash, A (2014) A Critical Review of the Risks to Water Resources from Unconventional Shale Gas Development and Hydraulic Fracturing in the United States. *Environmental Science & Technology* **48**, 8334-8348.
- Wang, DT, Gruen, DS, Lollar, BS, Hinrichs, K-U, Stewart, LC, Holden, JF, Hristov, AN, Pohlman, JW, Morrill, PL, Könneke, M, Delwiche, KB, Reeves, EP, Sutcliffe, CN, Ritter, DJ, Seewald, JS, McIntosh, JC, Hemond, HF, Kubo, MD, Cardace, D, Hoehler, TM, Ono, S (2015) Nonequilibrium clumped isotope signals in microbial methane. *Science* **348**, 428-431.
- Weiss, RF (1970) Helium Isotope Effect in Solution in Water and Seawater. *Science* **168**, 247-248.
- Whiticar, MJ (1999) Carbon and hydrogen isotope systematics of bacterial formation and oxidation of methane. *Chemical Geology* **161**, 291-314.
- Whiticar, MJ, Faber, E, Schoell, M (1986) Biogenic methane formation in marine and freshwater environments: CO_2 reduction vs. acetate fermentation—Isotope evidence. *Geochimica et Cosmochimica Acta* **50**, 693-709.